RESEARCH

2007-43

Investigation of Low Temperature Cracking in Asphalt Pavements

National Pooled Fund Study 776

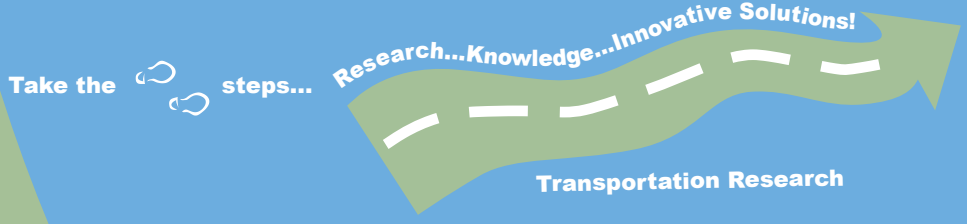

Technical Report Documentation Page

1. Report No.	2.	3. Recipients Accession No.
MN/RC 2007-43		

4. Title and Subtitle	5. Report Date
Investigation of Low Temperature Cracking in Asphalt Pavements National pooled Fund Study 776	October 2007
	6.

7. Author(s)	8. Performing Organization Report No.
Mihai Marasteanu, Adam Zofka, Mugur Turos, Xinjun Li, Raul Velasquez, Xue Li, William Buttlar, Glaucio Paulino, Andrew Braham, Eshan Dave, Joshua Ojo, Hussain Bahia, Christopher Williams, Jason Bausano, Allen Gallistel, Jim McGraw	

9. Performing Organization Name and Address	10. Project/Task/Work Unit No.
Department of Civil Engineering Office of Materials University of Minnesota Mn/DOT 500 Pillsbury Drive S.E. 1400 Gervais Avenue Minneapolis, Minnesota 55455 Maplewood, Minnesota 55109	11. Contract (C) or Grant (G) No. (c) 81655 (wo) 128

12. Sponsoring Organization Name and Address	13. Type of Report and Period Covered
Minnesota Department of Transportation 395 John Ireland Boulevard St. Paul, Minnesota 55155	Final Report 14. Sponsoring Agency Code

15. Supplementary Notes
http://www.lrrb.org/PDF/200743.pdf

16. Abstract (Limit: 200 words)

Good fracture properties are an essential requirement for asphalt pavements built in the northern part of the US and in Canada for which the predominant failure mode is cracking due to high thermal stresses that develop at low temperatures. Currently, there is no agreement with respect to what experimental methods and analyses approaches to use to investigate the fracture resistance of asphalt materials and the fracture performance of asphalt pavements. This report presents a comprehensive research effort in which both traditional and new experimental protocols and analyses were applied to a statistically designed set of laboratory prepared specimens and to field samples from pavements with well documented performance to determine the best combination of experimental work and analyses to improve the low temperature fracture resistance of asphalt pavements.

The two sets of materials were evaluated using current testing protocols, such as creep and strength for asphalt binders and mixtures as well as newly developed testing protocols, such as the disk compact tension test, single edge notched beam test, and semi circular bend test. Dilatometric measurements were performed on both asphalt binders and mixtures to determine the coefficient of thermal contraction.

Discrete fracture and damage tools were utilized to model crack initiation and propagation in pavement systems using the finite element method and TCMODEL was used with the experimental data from the field samples to predict performance and compare it to the field performance data.

17. Document Analysis/Descriptors	18. Availability Statement
asphalt binder, asphalt mixture, low temperature cracking, strength, fracture toughness, fracture energy, creep compliance, cohesive zone model, coefficient of thermal contraction	No restrictions. Document available from: National Technical Information Services, Springfield, Virginia 22161

19. Security Class (this report)	20. Security Class (this page)	21. No. of Pages	22. Price
Unclassified	Unclassified	338	

Investigation of Low Temperature Cracking in Asphalt Pavements

National Pooled Fund Study 776

Final Report

Prepared by:

Mihai Marasteanu
Adam Zofka
Mugur Turos
Xinjun Li
Raul Velasquez
Xue Li
University of Minnesota

William Buttlar
Glaucio Paulino
Andrew Braham
Eshan Dave
University of Illinois

Joshua Ojo
Hussain Bahia
University of Wisconsin, Madison

Christopher Williams
Jason Bausano
Iowa State University

Allen Gallistel
Jim McGraw
Mn/DOT Office of Materials

October 2007

Prepared for:

Minnesota Department of Transportation
Research Services Section
395 John Ireland Boulevard
St. Paul, MN 55155

ACKNOWLEDGEMENTS

This research study would not have been possible without the contribution of a number of organizations and individuals.

The research teams would first like to acknowledge MN/DOT (Office of Materials) as the lead state in this pooled fund study. The significant efforts of Ben Worel, Tim Clyne, Jim McGraw, Maureen Jensen, and Glenn Engstrom are very much appreciated.

The support, guidance and assistance with identifying and collecting field samples provided by the participant states are also recognized. The support and insightful discussions during the TAP meetings provided by Mike Heitzman (Iowa DOT), Leonard Makowski (Wisconsin DOT), Chris Euler (New York State DOT), David Kilpatrick (Connecticut DOT), Ron Horner (North Dakota DOT), Jim Weston (Washington State DOT), and Gerald Reinke (Mathy Construction) deserve particular recognition.

The research team would like to thank the members of the Technical Advisory Panel for their suggestions that helped improve the quality of this research effort. In particular, the suggestions offered by Professors Carl Monismith and David Anderson, and Dr. Kai Tam are much appreciated.

The research team would also like to thank Keith Herbold, John D'Angelo and Jack Youtcheff from the Federal Highway Administration for the opportunity given to the four universities to work together along with the participant states on this challenging research topic.

Special recognition is given to Jim Klessig from MN/DOT, who sadly passed away last month. His relentless efforts were instrumental in getting this pooled fund study started.

TABLE OF CONTENTS

LIST OF TABLES

LIST OF FIGURES

EXECUTIVE SUMMARY

Good fracture properties are an essential requirement for asphalt pavements built in the northern part of the US and in Canada for which the predominant failure mode is cracking due to high thermal stresses that develop at low temperatures. Currently, there is no agreement with respect to what experimental methods and analyses approaches to use to investigate the fracture resistance of asphalt materials and the fracture performance of asphalt pavements. This report presents a comprehensive research effort in which both traditional and new experimental protocols and analyses were applied to a statistically designed set of laboratory prepared specimens and to field samples from pavements with well documented performance to determine the best combination of experimental work and analyses to improve the low temperature fracture resistance of asphalt pavements

First, a comprehensive literature review was performed, as detailed in chapter two of the report, which included research in asphalt materials characterization, experimental results analysis and modeling, pavement system analysis and modeling and pavement performance related to low temperature behavior of asphalt pavements.

Next, two sets of materials were selected to be investigated in this study. The first set consisted of field samples that were cored or sawed from pavements for which performance information was readily available, as described in chapter three of the report and Appendices A through D. The second set consisted of laboratory prepared specimens that followed a statistically designed test matrix incorporating 10 different asphalt binders, two types of aggregates, two air void levels and two asphalt contents. The preparation procedure is described in detail in chapter four of the report.

The two sets of materials were evaluated using current testing protocols, such as creep and strength for asphalt binders and mixtures as well as newly developed testing protocols, such as the disk compact tension test, single edge notched beam test, and semi circular bend test. Also, dilatometric measurements were performed on both asphalt binders and mixtures to determine the coefficient of thermal contraction. The test procedures and the experimental results are presented in chapters five and six of the report

The analysis of the test results is contained in chapter seven of the report. The analysis focus on comparisons between the parameters calculated based on the experimental data obtained using the different test procedures as well as identifying correlations between the binder and the mixture parameters and between the binder properties and field performance and mixture properties and field performance.

A key component of this study involved the reexamination of the mechanisms of thermal cracking by applying modern computational fracture mechanics models. In chapter eight, discrete fracture and damage tools were utilized to model crack initiation and propagation in pavement systems using the finite element method. In chapter nine, TCMODEL was used with the experimental data from the field samples to predict performance and compare it to the field

performance data. Also included in this chapter were a few examples on using cohesive fracture models and damage models in specially designed subroutines developed for the commercially available finite element code ABAQUS to obtain similar predictions.

Chapter ten contains the conclusions and recommendations from the research performed in this study.

CHAPTER 1

INTRODUCTION

Background

Good fracture properties are an essential requirement for asphalt pavements built in the northern part of the US and in Canada for which the predominant failure mode is cracking due to high thermal stresses that develop at low temperatures. Currently, many agencies are struggling to maintain their pavement networks at acceptable conditions. Minnesota alone spent $355 million dollars on pavement structures last year and nationally the expenditures reached $45 billion. This amount is not enough to satisfactorily maintain the roadways at their current service levels and new methods must be developed to increase pavement service life with the existing resources. Improving the fracture resistance of the asphalt materials used in pavements and understanding the role played by the individual components of the pavement system in the fracture mechanism become a very important priority in the effort to reduce and eventually eliminate the occurrence of thermal cracks in asphalt pavements. This will maximize the service life of both new and rehabilitated pavements and significantly reduce the high costs of repairing low temperature cracks.

Problem Statement

The current Superpave specifications, based on the linear viscoelastic analysis of creep and strength data at low temperatures on both asphalt binders and mixtures represented a major step forward in the selection of asphalt materials with improved low temperature performance. However, this approach is limited to one single event and cannot provide the tools to predict the evolution of cracks in time and does not allow taking into consideration the effects of traffic loading, of the variable aging through the asphalt layer and of the pavement system on the thermal behavior of the pavement.

This type of analysis can be performed only based on fracture mechanics concepts, which have been successfully used to predict the fracture behavior of metal structures, rocks and concrete. Presently, there is no agreement with respect to what experimental methods and analysis approaches to use to investigate the fracture resistance of asphalt materials and the fracture performance of asphalt pavements.

It becomes therefore a top priority to conduct a comprehensive research effort that brings under the same umbrella the different experimental protocols and analyses and compares them based on a common set of asphalt materials and on well documented field performance data to determine the best combination of experimental work and analyses to improve the low temperature fracture resistance of asphalt pavements

Objectives

This research effort has the following objectives:

- Develop fracture tests appropriate for thermal cracking evaluation (low temperature)
- Conduct traditional and new tests on a broad range of mixtures, particularly those containing modified PG grades, considering lab versus field specimens and aging effects.

The current PG system was developed based on experimental data and field performance of unmodified asphalt materials.

- Evaluate new and existing lab test results and models, especially in the context of field observations of good and poor performing pavements from participating states
- Develop constitutive material models and appropriate pavement models to predict thermal fracture behavior of asphalt materials and pavements
- Develop a final report, detailing conclusion of hypotheses and recommendations for state DOT's.

Scope

The proposed research considers two major hypotheses:

1. Experimental protocols to determine asphalt materials low temperature fracture properties can be developed, which will lead to an improved prediction of the occurrence and severity of thermal cracking in asphalt pavements. The approach would include binder and mixture fracture tests coupled with analyses capable of predicting the initiation and propagation of thermal cracks.
2. The results from the experimental work and analyses incorporated into a realistic pavement model that takes into account the entire pavement system would have superior predictive capabilities as compared to the existing NCHRP 1-37A approach.

If the first hypothesis is true, then the relative importance of creep properties, fracture properties, aging effects, pavement layer thicknesses and layer types, and traffic effects can be properly evaluated. This can benefit state DOT's in evaluating the inherent range of factor of safety against thermal cracking in existing design methods, and give insight towards the most economical means for achieving a higher and more consistent factor of safety against thermal cracking. The approach would provide a comprehensive method for evaluating the cost/benefit of polymer modified binders and mixtures as a deterrent to thermal cracking and would identify other significant factors contributing to thermal cracking occurrence.

If both hypotheses are determined to be true, then the new tools can be used to refine the existing thermal cracking performance prediction model recommended in NCHRP 1-37A. This would benefit state DOT's, as they would then have a more accurate and reliable means for designing asphalt pavements that resist thermal cracking.

Research Approach

In order to fulfill the objectives of this research the following approach will be followed:

- A comprehensive literature review of previous and current research efforts in the area of low temperature performance of asphalt pavements will be conducted at the beginning of the project. The review will include research performed in asphalt materials characterization, experimental results analysis and modeling, pavement system analysis and modeling and pavement performance related to low temperature behavior of asphalt pavements.
- Two sets of materials will be selected for investigated in this study. The first set consists of materials that have been used in already built pavements for which performance information is well documented and readily available. The second set consists of laboratory prepared specimens following a statistically designed test matrix.

- The materials selected will be evaluated using current testing protocols, such as creep and strength for asphalt binders and mixtures as well as newly developed testing protocols, such as the disk compact tension test, single edge notched beam test, and semi circular bend test. This approach will allow determining the best testing protocol and data analysis for selecting the most fracture resistant asphalt materials. It also allows bringing together the asphalt binder and asphalt mixture specifications.
- The analysis of the test results will focus on finding the most promising experimental parameters for selecting the most crack resistant materials and for correctly analyzing the crack propagation mechanism in the pavement system and predicting performance. It will also allow developing useful correlations between the different material parameters obtained from the different test methods. Priority will be given to investigating the contribution of each of the asphalt mixture components and their interactions to the fracture resistance of the mixture, with emphasis on the role played by the asphalt binder and the binder-aggregate interaction.
- A key component of this study will involve the reexamination of the mechanisms of thermal cracking by applying modern computational fracture mechanics models. Discrete fracture and damage tools will be utilized to model crack initiation and propagation in pavement systems using the finite element method. The research team will utilize cohesive fracture models and damage models in specially designed subroutines developed for the commercially available finite element code ABAQUS. Once the mechanisms of thermal cracking are better understood, the researchers will determine the best approach for recalibration and/or modifying the existing TCMODEL program in the 2002 Design Guide and to recommend appropriate testing protocols to support this approach.

CHAPTER 2

LITERATURE REVIEW

Introduction

The main distress in asphalt pavements built in northern U.S. and Canada is the low temperature cracking resulting from the contraction of the asphalt mixture under extreme temperature changes. Low temperature cracking is manifested as a set of parallel surface-initiated transverse cracks of various lengths and widths. The cracks are predominantly perpendicular to the center line of the roadway.

The existence of transverse cracks leads to other types of degradation of the pavement structure. Water enters the pavement through the cracks and weakens the pavement base and subbase. Under moving loads water and fine materials are pumped out and result in progressive deterioration of the asphalt layer. In winter the presence of water leads to differential frost heave of the pavement.

This paper presents a review of the research efforts that address this problem. In the first part, the experimental methods used to determine the low temperature cracking resistance of asphalt mixtures are discussed. In the second part, the modeling efforts of the pavement response under low temperature loading are presented.

Experimental Methods

The experimental methods for both asphalt binders and asphalt mixtures are reviewed. The review includes the current specification methods as well as new methods developed to characterize the low temperature cracking properties of asphalt pavement materials.

Current Specification Methods

The current Superpave specifications address this distress based on strength and creep tests performed on asphalt binders and asphalt mixtures. For asphalt binders two laboratory instruments were developed during the Strategic Highway Research Program (SHRP) to investigate the low temperature behavior of asphalt binders (1): the Bending Beam Rheometer (2) and the Direct Tension Tester (3), which make the object of two AASHTO specifications (3) and (4) and are used to obtain the performance grade (PG) of asphalt binders in the US.

The BBR is used to perform low-temperature creep tests on beams of asphalt binders conditioned at the desired temperature for one hour. Based on the elastic solution for a simply supported beam and the correspondence principle the creep compliance is obtained. The final results are reported in the form of a plot of the inverse of the creep compliance, called creep stiffness (S), versus time. The stiffness and the m-value, which represents the slope of stiffness vs. time curve in a double logarithm plot, are used to determine the critical temperature.

The DTT is used to perform uniaxial tension tests at a constant strain rate of 3% per minute on dog-bone shaped specimens of asphalt binders. The average stress and strain at failure are obtained from six replicates. The temperature at which the failure strain is 1% represents an optional limiting temperature.

A new AASHTO standard (5) eliminates the 10°C shift used in the previous two methods to determine the PG low temperature limit. The critical temperature is simply calculated at the intersection of the thermal stress curve obtained from the BBR creep compliance data with the strength master curve obtained from the DTT data.

For asphalt mixtures one laboratory testing device was developed during the SHRP effort: the Indirect Tension Tester (IDT) (6). In this test, a cylindrical specimen is loaded in compression along the diameter. This is similar to the Brazilian test and the splitting tension test used to determine the tensile strength of rocks (7) and concrete (8). A critical temperature can be determined at the intersection between the tensile strength-temperature curve and the thermal stress-temperature curve. This approach is used in the TC model subroutine part of the new mechanistic empirical pavement design guide (9).

Thermal Stress Restrained Specimen Test (TSRST)

TSRST method has been used to study the low temperature cracking in asphalt pavement by many researchers. A seminal paper presented at AAPT in 1965 (10) established the frame work for using viscoelastic concepts to study the low temperature cracking behavior of asphalt mixtures and presented the idea of the TSRST. This work was continued by other researchers such as Carpenter (11), Janoo (12), Stock and Arand (13), Jung and Vinson (14).

Currently, the TSRST procedure is not part of the AASHTO specifications. A review of the TSRST system developed as part of SHRP Project A-003A "Performance-Related Testing and Measuring of Asphalt-Aggregate Interactions and Mixtures" and described in detail in (14) as well as efforts based on TSRST are presented below.

The TSRST system consists of a load frame, a data acquisition system, an environmental chamber with a temperature controller, and a specimen alignment stand. Either a beam or cylindrical specimen can be used in this test. The test specimen is aligned with an alignment stand and glued to two end platens with an epoxy compound. The glued specimen is cooled to a temperature of 5°C for one hour to establish thermal equilibrium prior to testing, and then placed in the environmental chamber. LVDT's are placed at the top and bottom clamps to measure the deformation of specimen. As the temperature reduces the thermal contraction measured by the LVDTs is used by the closed-loop load frame to load the specimen back to its original length. During the test, the temperature and the tensile load are recorded and the thermal stress-temperature curve is plotted. Three or four thermistors are attached to the surface of the specimen to measure the specimen temperature and a resistance temperature detector is used to monitor the temperature of the chamber and to control the cooling at a specific rate.

Jung and Vinson (14) tested four asphalt binders and two aggregates at two levels of air voids (4% and 8%) and four cooling rates (1, 2, 5, and 10 °C/hr). They ranked the low temperature cracking resistance of asphalt mixtures based on the fracture temperature and found good agreement with the ranking of the asphalt binders used. The softer asphalt binders and the aggregates with a rough surface texture and angular shape resulted in higher fracture strength values and colder fracture temperatures of the asphalt mixtures. The long term aged specimens had warmer fracture temperatures and the specimens with high air voids content (8%) had lower fracture strength than those with low air voids content (4%). Furthermore, the cooling rate significantly affected the experimental measurements of TSRST, although it did not change the ranking of asphalt mixtures. They recommended that the fracture temperature should be used to rank the low temperature cracking resistance of asphalt mixtures. Since the penetration of asphalt

cement at 15°C correlated well with the fracture temperature of asphalt mixtures, they also suggested using the penetration of binders as a reasonable indicator of low temperature resistance.

Recently, Pucci et al. (15) studied the correlation between asphalt mixture TSRST results and asphalt mixture Direct Tension Test (DTT) results. Using a cooling rate of 10°C/h, they observed that the slope of the thermal stress-temperature curve started to drop at a temperature (T_{ini}) higher than the fracture temperature (T_{frac}); a similar observation was also mentioned by Fortier and Vinson (16) in their research of asphalt mixtures prepared with modified asphalt binders. The authors compared the thermal stress σ_{ini} at T_{ini} and σ_{frac} at T_{frac} with the ultimate stress σ_{crack} in a DTT with a strain rate of $\alpha \cdot (dT/dt)$, where α is the coefficient of the thermal contraction. They found a good correlation between the σ_{ini} and σ_{crack} and recommended the asphalt mixture DTT as a viable test to characterize the low temperature fracture properties of asphalt mixtures. Note that this test method is different than the IDT method currently used in AASHTO specifications.

Fracture Mechanics-Based Test Methods

Various pavement distresses are related to the fracture properties of the asphalt layer, including longitudinal cracking, thermal (transverse) cracking, and reflective cracking. The fracture resistance of asphalt materials significantly influences the service life of asphalt pavements and consequently the maintenance and management of the pavement network.

One of the most powerful tools to study the fracture properties of engineering materials is fracture mechanics. One of the earliest attempts to investigate the mechanism of fracture in asphalt mixtures was performed by Moavenzadeh (17). However, it took more than two decades to incorporate fracture mechanics tools in asphalt materials characterization.

Fracture Mechanics-Based Tests on Asphalt Binders

The specimen geometry used in fracture test on asphalt binders was heavily influenced by two factors: (1) convenient specimen preparation; (2) compatibility with the current equipment used in the Superpave specifications. Asphalt binder specimens are usually cast in molds and require little preparation prior to testing, which provides some flexibility in choosing the geometry of the fracture test specimen. Two methods are discussed next.

Single Edge Notched Beam SE(B) Test

This method follows closely ASTM E399 procedure (18) and assumes that linear elastic fracture mechanics (LEFM) conditions are present. The geometry of the SE(B) specimen is shown in Figure 2.1. A crack starter notch is machined at the middle point of the span from the bottom side of the beam. The beam is symmetrically supported by two rollers and a line load is applied at the top side of the beam.

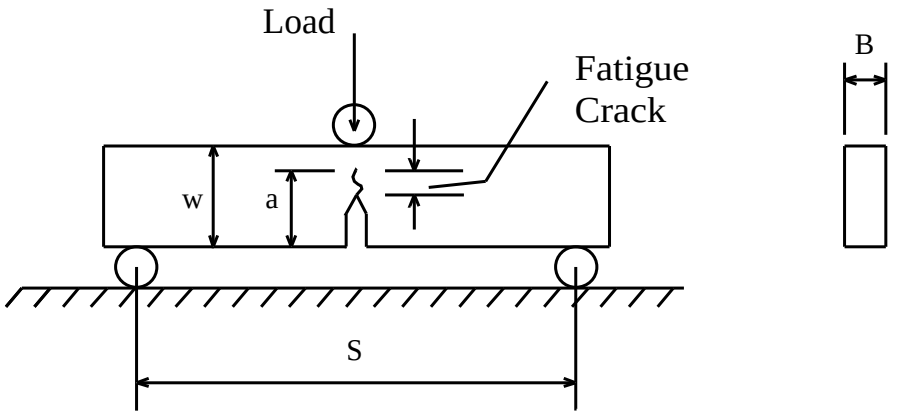

Figure 2.1. Single edge notched beam test

where B = 0.5w

s = 4w

a = 0.45 to 0.55w

The stress intensity factor (K), is used to characterize the stress field in the vicinity of the crack tip. A subscript is used to denote the mode of fracture under which K is derived. For example, K_I means the stress intensity factor of mode I fracture. The critical stress intensity factor (K_c) corresponding to the initiation of a crack is defined as the measure of fracture toughness. Following the notation of the stress intensity factor, the mode I fracture toughness is denoted as K_{IC}.

Due to the fact that plane strain, transitional plane strain to plane stress, and full plane stress exist in service simultaneously, there are strict requirements for the specimen geometry. The K_I for the SE(B) specimen shown in Figure 2.1 can be determined as follows:

$$K_I = \frac{P \cdot S}{BW^{\frac{3}{2}}} f(\frac{a}{W}) \qquad [1]$$

where

$$f(\frac{a}{W}) = \frac{3(\frac{a}{W})^{\frac{1}{2}}[1.99 - \frac{a}{W}(1-\frac{a}{W})(2.15 - 3.93(\frac{a}{W}) + 2.7(\frac{a}{W})^2)]}{2(1+2\frac{a}{W})(1-\frac{a}{W})^{\frac{3}{2}}} \qquad [2]$$

P = load

B = thickness of specimen;

W = width of specimen;

S = span of specimen;

a = crack length.

The K_{Ic} is obtained if the critical load is used in equation [1]. The accuracy with which K_{Ic} describes the fracture behavior depends on how well it characterizes the stress and strain field around the crack tip assuming LEFM conditions. However, in many materials, a plastic zone forms ahead of the crack tip. When the size of the process zone is significantly large relative to

the specimen size then LEFM assumptions are violated. In order to measure a stable toughness value and assure the validity of LEFM, three geometric requirements have to be met:

$$a \geq 2.5(\frac{K_{Ic}}{\sigma_{ys}})^2$$

$$B \geq 2.5(\frac{K_{Ic}}{\sigma_{ys}})^2 \qquad [3]$$

$$0.45 \leq a/W \leq 0.55$$

where

σ_{ys} = the yield strength

and the other parameters are the same as previously described.

Lee and Hesp (19) and Lee et al. (20) were among the first to use the SE(B) geometry to measure the fracture properties of asphalt binders. A notched asphalt binder beam was cast in a silicone mold and conditioned at -20°C for at least 12 hours before tested with an MTS test frame. The specimen was 25 mm wide (w) by 12.5 mm thick (B) by 175 mm long (L) and the span of the beam was 100 mm (s). The experiment was controlled by the displacement of the crosshead at a speed of 0.01 mm/s. Based on test results from both plain and modified asphalt binder, they observed that the addition of modifier increased the fracture toughness of asphalt binder. To estimate fracture energy, beam specimens with different initial notch lengths (a = 12.5 mm, 15.5 mm, and 18.2 mm) were tested and the graphical method used in Dongre's work (21) was used to calculate the fracture energy. The total strain energy, U_T, was calculated as the area under the load-displacement curve and the total energy per thickness, U_T /a, was plotted against the initial notch length. The slope, dU_T/da, was determined from the regression analysis and was used to compute the fracture energy as follows:

$$J = -\frac{1}{B}\frac{dU_T}{da} \qquad [4]$$

where B is the thickness of the beam and a is the initial notch length. The results showed that the addition of modifiers significantly increased the fracture energy of asphalt binders.

Hoare and Hesp (22) also tested SE(B) asphalt binder specimens of different sizes. They kept the a/w ratio at 0.2 and varied the size of specimen. Three sets of dimensions were tested and the analysis of experimental results showed that no significant differences in the fracture toughness values were found between specimens with different sizes.

Anderson et al. (23) used the SE(B) test to measure the fracture toughness of fourteen types of asphalt binders, one plain binder as the base and its thirteen modified ones, and checked the effectiveness of characterization of low-temperature cracking resistance with different grading methods. The specimen was prepared following the protocol developed by Lee and Hesp (19). The test was performed at the same crosshead speed of 0.01 mm/s and the K_{Ic} was determined using the failure load. The authors also found that fracture toughness discriminated much better the fourteen asphalt binders with compared to the PG criteria.

Olard and Di Benedetto (24) studied the temperature and loading rate effects on the asphalt binder fracture toughness and fracture energy measured on SE(B) specimens. They tested five types of binders plain and modified binders at four crosshead speeds of 0.01 mm/s, 0.05mm/s, 0.25 mm/s and 1 mm/s at temperatures ranging from -23°C to -4°C. They used a beam with the same dimensions as in the previous studies (25×12.5×175 mm) and an initial notch 5 mm long.

They followed closely the ASTM standard to check the nonlinearity of the load-displacement curve before using equation [1] to determine the fracture toughness and showed that only few specimens had nonlinear behavior in the temperature range used. They developed the equation below to compute fracture energy:

$$G_{Ic} = \frac{U}{BW\Phi} \quad [5]$$

where Φ is the energy calibrator defined as

$$\Phi = \frac{C}{\frac{dC}{d(\frac{a}{w})}} \quad [6]$$

where C is the compliance of the specimen. The results indicated that the fracture toughness was less dependent on temperature and loading rate than the fracture energy. The data showed the probable existence of a lower bound for the fracture energy of asphalt binders, which was reached in the glassy and brittle state of asphalt binders. The existence of an asymptotic value for the fracture energy of asphalt mixtures was also reported by Li and Marasteanu (25).

DENT Test

One of the first attempts to use the DENT test for asphalt binders is described in (26). The specimen dimensions are provided in Figure 2.2. A 45º notch angle was used to facilitate making initial notches at both sides of the beam and five different notch lengths were tested. The sample was tested at 20°C and the fracture energy of asphalt binders was measured to predict the fatigue cracking in asphalt mixtures. The essential work of fracture (EWF) method (27) was used to estimate the fracture resistance of asphalt binders by dividing the strain energy into the essential work of fracture (w_e) and the plastic work of fracture (w_p). The EWF method is described in detail in (27). Both w_e and w_p were compared to the loss modulus of asphalt binder $|G^*|\cdot\sin\delta$ at 25°C, the PG parameter used to predict the fatigue cracking behavior of asphalt binder, and no significant correlations were found.

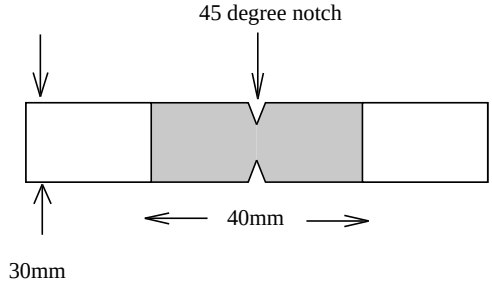

Figure 2.2. Geometry of the double edge notched tension specimen

Roy and Hesp (28) used the DENT and the DTT geometries to perform thermal stress restrained specimen tests on asphalt binders. The specimens were mounted in a MTS test frame in an environmental chamber and the temperature was reduced at a rate of 10°C per hour until the specimens failed. The test frame was programmed to hold the specimen at 0.1 percent strain until failure occurred and the temperature at failure was recorded as the indicator for the low-temperature performance of the binders. Large differences were found between the failure temperatures of the notched and the unnotched specimen for the same type of asphalt binder.

Other work done on DENT by Zofka and Marasteanu (29) compared DENT and DT for nine different asphalt binders. They improved methodology originally proposed by (29). The results showed that DENT produces better repeatability than DT and it can be used to estimate critical cracking temperatures of asphalt binders.

Fracture Mechanics-Based Tests on Asphalt Mixtures

Beam Geometry

The first research on the application of fracture mechanics concepts to asphalt mixtures (17) was performed on SE(B) even before the adoption of ASTM E399 in 1970. Majidzadeh et al. (31) predicted fatigue life of paving mixtures in terms of material constants, geometry, boundary conditions, and the state of stress. They described fatigue failure by three processes: damage initiation, crack growth, and final failure. Two mixtures, an Ottawa sand and limestone with 60-70 pen asphalt cement, at three temperatures (23, 41, 78.5°F) were tested.

One of the first post SHRP studies on the application of fracture mechanics concepts to asphalt mixture characterization was published by Labuz and Dai (32). Closed-loop, computer-controlled fracture tests were conducted using an unload-reload procedure so that multiple measurements of fracture toughness K_{Ic} could be obtained from a single specimen in three-point bending. Accurate measurement of the load-point displacement was complicated by nonlinear deformation and crushing at the roller to specimen contacts. These factors were eliminated by measuring a differential displacement: the deflection of the notch relative to points directly above the supports provided a displacement that avoided the contact problem. This method also provided an estimate of Young's modulus, E, through a compliance calibration. The behavior (E and K_{Ic}) of the asphalt concrete tested at an air voids content of about 10% was dependent upon temperature. Assuming linear fracture mechanics is valid, the fracture toughness was found to be 0.25 MPa.$m^{0.5}$ at 0°C, 0.53 MPa.$m^{0.5}$ at -18°C, and 0.50 MPa.$m^{0.5}$ at -34°C. The loading records indicated that nonlinear behavior was more pronounced at -18°C than at -34°C, which means that more energy would be needed to initiate fracture. In terms of pavement performance, this asphalt mixture would be more resistant to fracture at -18°C than at -34°C. The air void content influenced the asphalt's fracture toughness. As the air voids increased, the fracture toughness decreased. Using the compliance method, they obtained the fracture resistance curve, called the R-curve, of the asphalt mixture.

Many studies over the following years investigated the fracture toughness of asphalt concrete using Linear Elastic Fracture Mechanics (LEFM). Ramsamooj et al. (33) tested 46 different mixtures at temperatures ranging from 16-35°C. One of their major conclusions was the fatigue life of many types of asphalt concrete mixtures can be predicted from simple fracture tests. Kim et al. (34) investigated the fracture toughness of asphalt concrete from -5 to -30°C in 5°C steps. They used 85-100 asphalt cement with granite and limestone aggregate. They found that toughness increased from -5 to -15°C and then decreased down to -30°C. They also indicated that granite showed a slightly better resistance to fracture than limestone using the effective crack model (35). Mobasher et al. (36) compared low temperature fracture parameters of conventional asphalt cement to asphalt cement with rubber (asphalt rubber). They found that asphalt rubber mix has a lower modulus but a higher toughness than conventional asphalt cement. Hossain et al. (37) also investigated the effect of rubber content on fracture energy. Using three rubber contents (19, 22, 24%), three asphalt cement contents (6, 7.5, 9%), and two temperatures (5, 25°C), they found higher values of fracture energy from higher binder contents, irrespective of rubber content.

Roy and Hesp (28) used the crack mouth opening displacement (CMOD) and the crack tip opening displacement (CTOD) to account for inelastic deformation. A few studies characterized fracture using the strain energy release rate based on Elastic-Plastic Fracture Mechanics (EPFM). Dongre et al. (21) compared 12 asphalt cements with the same aggregate at four temperatures (-21 to 16°C). At low temperatures, J_{Ic}, the critical J integral, was sensitive to mixture properties while K_{Ic} was not.

More recently, Wagoner et al. (38) (39), through two papers, determined that the Single Edge Notched Beam, SE(B), was the most promising fracture test based on test control method, crack front development, test repeatability, test temperature, and mixed mode fracture, but there was no standard test method or analysis available. They compared three different nominal maximum aggregate sizes with three binders and found that the polymer modified mixture with the smallest aggregate size gave the highest fracture energy values. They also attempted to measure mixed-mode fracture by offsetting the notch on the bottom of the specimen.

Cylindrical Geometry

Although the SE(B) geometry has been extensively used in metals and rocks, its application to asphalt mixtures is restricted due to the asphalt mixture preparation methods. The compaction method of choice for asphalt mixtures in the US is the Superpave gyratory compactor (40). Most of the experimental work on asphalt mixtures was performed on cylindrical specimens. The cores extracted from pavements are also cylindrical. Therefore, preparing rectangular beams of asphalt mixtures requires additional equipment, such as a slab compactor, and makes further comparison of material properties obtained from different testing configurations very difficult. It is no surprise that most of the asphalt mixtures fracture investigations use cylindrical specimens.

Modified Superpave Indirect Tension Test (IDT)

Roque et al. (41) investigated the use of the IDT to determine the fracture properties of asphalt mixtures. They modified the IDT specimens by drilling an 8-mm diameter hole in the center of the specimen, as shown in Figure 2.3. Their research focused on obtaining suitable crack growth rate parameters to describe the fatigue cracking of asphalt mixtures under traffic loading at intermediate temperatures. Tests were performed at a single temperature of 10°C. The stress intensity factor (K_I) measured at different loading cycles was used to predict the crack growth with Paris' law (42). Zhang et al. (43) showed that permanent deformation at the crack tip is significant at 10ºC for this geometry and the application of Paris' law to describe crack propagation using linear elastic fracture mechanics (LEFM) was not reasonable. In the same year, Roque et al. (44) introduced the concept of dissipated creep strain energy (DCSE) limit and fracture energy (FE) limit to account for the inelastic deformation and healing of asphalt mixtures at this temperature.

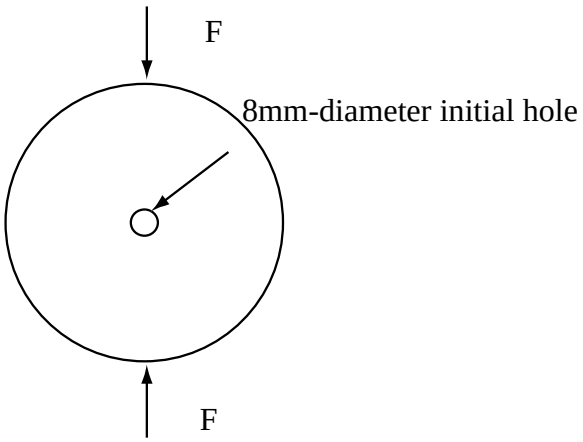

Figure 2.3. Modified IDT specimen

Semi Circular Bend (SCB) Test

The semi circular bend (SCB) test was first proposed by Chong and Kurrupu (45). The SCB specimen is a half disc with a notch that is a-mm long and makes an angle α with the center axle of the disc. The test setup is schematically shown in Figure 2.4.

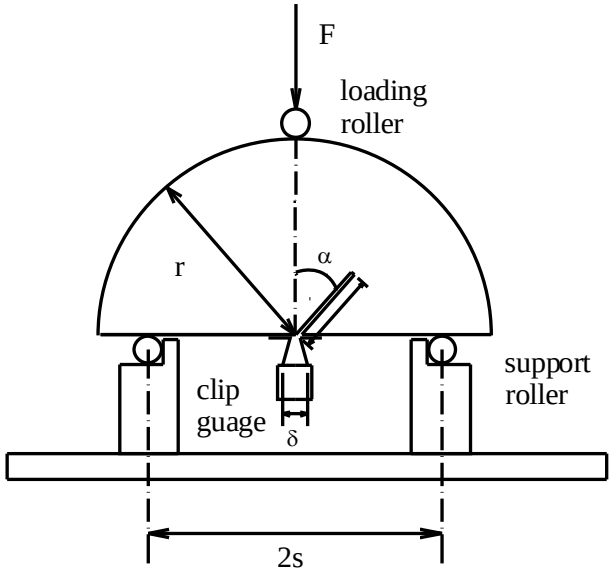

Figure 2.4. Semi-circular bend (SCB) test

The fracture toughness values obtained by Chong and Kurrupu (46) were in agreement with the values determined by other researchers for the same material. They noticed that the fracture toughness measured with the SCB test does not depend on the crack length and the thickness of specimen. This observation was confirmed later on by other researchers (47). The K_I of the SCB specimen can be computed as follows

$$K_I = \sigma_0 \sqrt{\pi a}(Y_I + C) \qquad [7]$$

where

D = the specimen diameter

B =the specimen thickness

P_0 = the pertinent force

Y_I = the normalized stress intensity factor depending on and

C = the correction factor depending on a/r.

Lim et al. (47) investigation on the influence of specimen size showed that:

- The fracture toughness is independent of specimen thickness over the range of conditions tested in his study.
- Neither specimen size (in terms of the diameter of the specimen) nor notch length appears to have an appreciable effect on the apparent fracture toughness.
- Notch lengths between 3 mm and 80% the SCB specimen radius seem to provide valid K_{Ic} values.

Chong and Kurrupu (46) used the fatigue precracking in the SCB test to introduce sharp crack tips in rock specimens. However, Lim et al. (47) did not use fatigue precracking. They argued that, unlike metals, the high porosity of the rock they tested provided naturally sharp cracks and made fatigue precracking unnecessary. They mentioned similar observations made by other researchers (48).

The SCB test can be used to determine not only the mode I stress intensity factor, but also the mixed mode I and II stress intensity factors, depending on the angle of the notch α (49). If the angle is equal to zero, pure mode I stress intensity factor can be measured.

Molenaar et al. (50) used the SCB test to determine the fracture properties of asphalt mixtures. They tested seven standard types of asphalt mixtures using three different specimen sizes, four test temperatures (25°C, 15°C, 0°C, and –10°C) and three loading rates (0.005mm/s, 0.05mm/s, and 0.5mm/s). They followed the secant method described in (18) and determined the fracture toughness of asphalt mixtures. They pointed out that possible excessive plastic deformation at higher temperature may violate the assumptions used in computing the fracture toughness. The data showed that for a deformation rate of 0.05mm/s, most specimens did not show significant non-linear deformation before peak load. They concluded that:

- K_I is almost independent of the specimen diameter for a deformation rate of 0.05 mm/s if the diameter is greater than 220 mm; for a deformation rate of 0.005 mm/s the diameter must be greater than 150 mm.
- The dependence of the apparent fracture toughness on the specimen thickness is weaker than its dependence on the specimen diameter.
- The apparent fracture toughness and indirect tensile strength are positive related, and apparent fracture toughness can be interpreted as tensile strength for a notched specimen. For temperatures below 15°C, the variation coefficient of the fracture toughness is about half that of the indirect tensile strength.
- The discriminative ability of the SCB test as a fracture toughness test is fair, whereas the discriminative ability of the indirect tensile test to determine the indirect tensile strength is poor.

Li et al (51) and Li (52) performed SCB tests on three asphalt mixtures used at MnROAD facility. The mixtures were prepared using the same aggregates but three different grades of asphalt binders (PG 58-28, PG 58-34, and PG 58-40). The tests were performed at three temperatures, -20°C, -30°C, and -40°C, using an experimental protocol in which the loading rate was controlled by the CMOD signal set at a constant rate of 0.0005 mm/s. Both the fracture

toughness and fracture energy of asphalt mixtures were determined from the experimentally determined load vs. load line displacement (LLD) curve. The authors concluded that:

- The fracture toughness and fracture energy can be used to differentiate asphalt mixtures with respect to their low-temperature performance. The fracture energy is a better parameter than the fracture toughness due to less dependence on the conditions of linear elasticity and homogeneity of the tested materials.
- Both fracture parameters are temperature dependent.
- The lower the temperature, the lower the fracture energy. Nevertheless, a plateau value of fracture energy appeared to be reached when the temperature dropped below the PG critical temperature.
- The fracture toughness evolution with temperature decrease was not as simple and appeared to be related to binder PG critical temperature at which a peak is observed in the fracture toughness of the asphalt mixtures.

Disc-Shaped Compact Tension DC(T) Test

The compact tension test is a part of ASTM E399 (18) and recommended as an alternative to the SE(B) test. The compact tension test can be performed with both rectangular and disc-shaped compact specimen. In this section only the disc-shaped compact tension was reviewed.

The standard DC(T) specimen is a single edge notched and fatigue crack disc segment loaded in tension (53). The geometry of a disc-shaped compact specimen is shown in Figure 2.5.

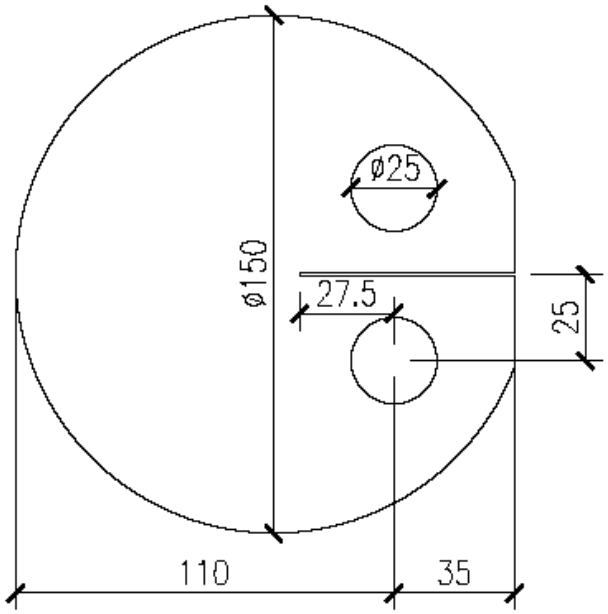

Figure 2.5. Geometry of DC(T) Specimen, mm (54)

DC(T) testing was performed on RAP asphalt concrete by Lee et al. (55). Two binders, an AC-10 and an AC-20, were used, along with two sources of RAP added in amounts of 0, 10, 20, 30, 40, 50, 75, and 100 percent based on total weight of blended asphalt binder. Fracture toughness, defined by LEFM, was evaluated at different loading rates and at two temperatures, 0 and 22°C. At 0°C, brittle fracture occurred and the different levels of RAP had no significant effect. At 22°C, fracture toughness increased with the increase of RAP.

Wagoner et al. (54), (56), (57) modified the ASTM DC(T) geometry by moving the location of the loading holes to reduce failure at the loading holes. They also set the thickness of the specimens to 50mm and the notch length to 19mm in order to maximize the ligament area. Three temperatures (-20, -10, 0°C) and four loading rates (10, 5, 1, 0.1 mm/min) were investigated. Fracture energy was computed by the area under the load-CMOD curve normalized by the area of facture surface. They found that as temperature increased, fracture energy increased, and as loading rate increased, fracture energy decreased. The coefficient of variation (4-25%) was comparable to SE(B) (3-28%) and SCB (15-34%).

Wagoner et al. also compared four mixtures: a 19mm with a PG64-22, a 9.5mm with a PG64-22, a 9.5mm with a PG58-22, and a 4.75mm with a polymer modified asphalt binder. They found that softer binders had higher fracture energy, with the polymer modified asphalt binder producing the highest. They also determined that at higher temperatures, cracks tend to go around aggregate; while at lower temperatures, the crack goes through the aggregate. In addition, they tested three specimen thicknesses (25, 50, 75mm) and found fracture energy increased as thickness increased. The DC(T) test was incorporated into a testing suite developed for obtaining both continuum and material separation properties from field cores.

Coefficient of Thermal Expansion and Contraction for Asphalt Mixtures

A very important parameter required to calculate the thermal stresses that develop in asphalt pavements exposed to severe low temperatures is the coefficient of thermal expansion (CTE) and contraction (CTC) or alpha (α, used for both CTE and CTC) of the asphalt mixtures. Alpha was first investigated by Littlefied (58). He concluded that different asphalt cements produced different amounts of expansion and contraction of mixtures when samples were heated or cooled between 0°F and 130°F. He also stated that the magnitudes of the expansion and contraction could cause cracking. Jones et al. (59) found a transition temperature between 70-86°F where alpha changed and that there were different thermal coefficients in expansion versus contraction. Jones also built a volumetric equation to predict theoretical coefficients of expansion and contraction:

$$B_{mix} = \frac{VMA \times B_{ac} + V_{agg} \times B_{agg}}{3 \times V_{total}} \quad [8]$$

where:

B_{mix} = linear coefficient of thermal contraction of mixture

B_{ac} = CTE of binder

B_{agg} = CTE of aggregate

V_{agg} = % volume of aggregate in mix

V_{total} = total volume

Stoffels et al. (60) investigated the suitability of using a resistance strain gage technique from 0°C to -25°C with samples from 22 pavement sections. Alpha values ranged from 1.33 to 2.97x10-5/°C. They found that alpha values were not affected by the thermal schedule method, by either a series of constant temperature changes or a cooling rate of 0.1°C/min. They could not find a relationship between alpha of the mixture and the alpha of aggregates, the air voids, or the VMA. Mehta et al. (61) conducted a similar study using Linear Variable Differential Transducers (LVDTs) from the Indirect Tension Test (IDT) setup.

Zeng et al. (62) investigated the thermal nonlinearity of asphalt concrete from -40°C to +40°C and found that alpha was a continuous nonlinear function of temperature that turns at the glass transition temperature. They also stated that assuming thermal linearity can result in moderate errors in stress prediction in asphalt pavements. Finally, they found the same deformation curve for both cooling (CTC) and heating (CTE).

Bahia et al. (63) developed predictions of asphalt concrete mixture alpha from asphalt cement and IDT data. Nam et al. (64)**Error! Reference source not found.** further investigated these points and found that thermal coefficients above T_g, α_l, are higher than coefficients below T_g, α_g. They found that for α_g of the mix the following factors were significant: aggregate type, binder α_g, binder α_l. For α_l of the mix these were: aggregate type, binder α_l, gradation, VFA, and effect AC.

Mamlouk et al (65) studied nine asphalt mixtures including mixtures with crumb rubber. They found that alpha was dependent on material type and method of compaction, that CTE was slightly larger than the CTC, and that conventional HMA showed lower thermal coefficients than asphalt rubber mix. Using a heat flow computer program, they determined that it takes anywhere from 4.6 to 8.0 hours for a sample to change from room temperature to 0°C.

Low Temperature Cracking Models

The thermal cracking models can be categorized as empirical and mechanistic models. Empirical models, developed through regression analyses of field data, are useful in identifying parameters that affect thermal cracking. However, they are limited to the data set on which they were based, and they do not fully explain the cracking phenomenon at a fundamental level. Conversely, mechanistic-based or mechanistic-empirical models rely on principles of mechanics of materials in describing the cracking process. Most existing mechanistic-based cracking models focus on the asphalt mixture layer rather than considering the entire pavement structure as an integrated system.

Empirically-Based Thermal Cracking Models

In general, empirical models are relatively easy to use once they have been developed and the necessary inputs to the model have been determined. Some model inputs are easily obtained (e.g. pavement thickness), while others require more complicated testing (e.g. fracture toughness). Therefore, the ease of use of a model depends primarily upon the ability to determine the model inputs. The predictive capability of empirical models, as reported by the R^2 value, is strictly limited to the data set on which the model was developed. Any extrapolation outside this data set may result in unreasonable predictions.

Fromm and Phang's Models

Fromm and Phang (66) developed a number of regression equations to predict the cracking index based upon a testing program carried out on 33 pavement sections in Ontario. The cracking index, used by the Ontario Department of Transportation, measures the cracking severity on a project wide basis expressed as the amount of transverse cracking per 150 m of two-lane pavement:

$$I = N_m + N_f + 0.5*N_h \quad [10]$$

where:

I = cracking index

N_m = number of multiple cracking occurrences in 150 m of pavement

N_f = number of full cracking occurrences in 150 m of pavement

N_h = number of half cracking occurrences in 150 m of pavement

Figure 2.6 illustrates multiple, full, and half cracking, respectively.

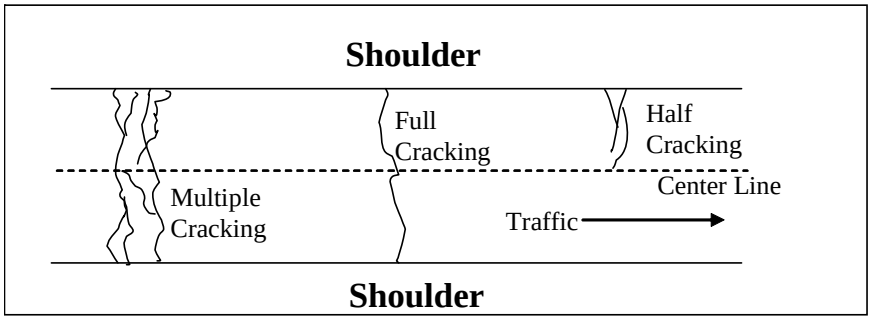

Figure 2.6. Cracking index definitions (66)

Initially, approximately 40 variables were considered in the statistical analysis but through step-wise linear regression, they reduced the parameters to the eleven listed in Table 2.1. Three equations were developed, using the parameters in Table 2.1, to better characterize the northern and southern regions of Ontario in addition to a general model describing all of the data. The cracking index predictive capability (R^2) ranged from 0.6 to 0.7 among the three models developed.

Table 2.1. Linear regression parameters (66)

Variable – Description
X_1 - Viscosity Ratio = $\frac{Visc@15.6^oC(megapoise)}{Visc@135^oC(centistokes)}$
X_2 - freezing index (degree days)
X_3 - critical temperature, ^oF
X_4 - air voids, % by volume
X_5 - stripping rating
X_6 - recovered asphalt penetration at 25^{o}C, dmm
X_7 - asphaltenes, % by weight
X_8 - granular base, % Passing 0.075mm sieve
X_9 - asphalt aggregate, % Passing 0.075 mm sieve
X_{10} - granular base, clay content
X_{11} - subbase, % Passing 4.75 mm sieve

Many of the parameters listed in Table 2.1 are commonly used in pavement engineering (e.g. air voids, % passing 0.075mm sieve). However, the critical temperature parameter (X_3) deserves further explanation. Fromm and Phang devised the critical temperature to account for the flow properties of the asphalt concrete. The critical temperature is the temperature at which the viscous flow under creep loading in one hour equals the temperature shrinkage in one hour. At temperatures higher than the critical temperature, it is believed that the viscous flow of the material is sufficient to relieve the stresses developed due to shrinkage. Conversely, at temperatures below the critical temperature, the thermal stresses develop faster than the relaxation and cracks are more likely to develop. This observation suggests that below the critical temperature the elastic nature of asphalt concrete becomes more prominent than the viscous behavior.

To determine the critical temperature, Fromm and Phang used two test methods. First, the thermal coefficient of contraction (α) was determined. Next, one-hour creep tests were performed to measure the viscous flow properties at different temperatures. The results of the creep tests were then plotted as shown in Figure 2.7 to determine the viscous flow versus temperature relationship. The critical temperature was determined by assuming a temperature decrease in one hour (ΔT), multiplying it by α and determining the corresponding temperature on the creep curve. Assuming that ΔT = -12°C, based on climatological data in Ontario, they found the critical temperature ranging between -15ºC and 0ºC.

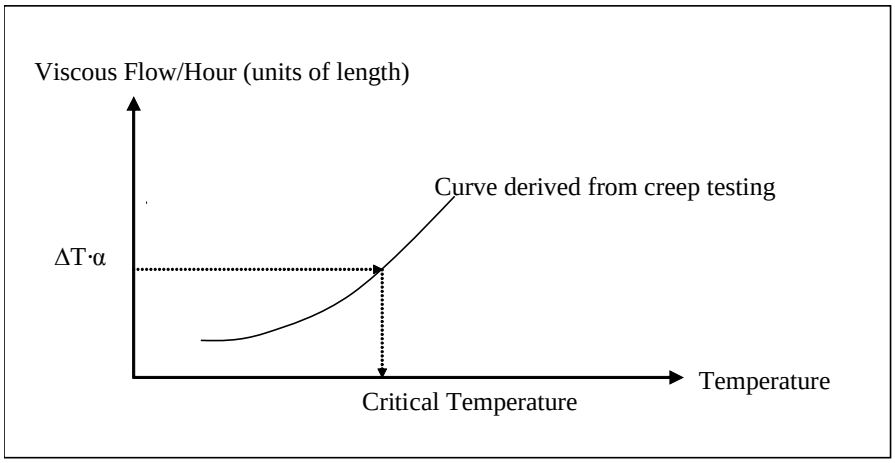

Figure 2.7. Schematic of critical temperature determination (66)

The general model predicts the cracking index (I) for all the pavement sections as follows:

$$I = 52.22x_1 + 0.0007093x_2 + 0.4529x_3 - 1.348x_4 + \quad [11]$$
$$+ 0.4687x_5 - 0.07903x_6 - 0.4887x_7 - 0.1258x_8 - 0.1961x_9$$

The R^2 was found to be 0.6357.

The northern model represents test sections where penetration graded asphalts of equal to or greater than 110 were used:

$$I = 30.30x_1 + 0.00602x_2 + 0.5253x_3 - 1.280x_4 + \quad [12]$$
$$+ 0.5190x_5 - 0.02563x_6 - 0.0844x_7 - 1.496x_8 + 0.225x_9 + 3.1043x_{10} + 0.097x_{11}$$

The R^2 was 0.6222.

The southern model represents test sections where penetration-graded asphalts of less than 110 were used:

$$I = 64.74x_1 + 0.008279x_2 + 0.3935x_3 - 1.491x_4 + \quad [13]$$
$$+ 0.3246x_5 - 0.0001481x_6 - 0.6069x_7 - 0.8071x_8 - 0.6567x_9$$

In this case the R^2 was equal to 0.7038.

As shown above, most of the coefficients associated with each independent variable were consistent with the expectations. A notable exception, however, is represented by the air voids in the asphalt concrete. The coefficient determined by the authors was less than zero. In other words, more air voids corresponded to less pavement cracking, when the reverse was expected. Fromm and Phang explained that Ontario pavements were typically constructed with lower air voids than recommended by the Asphalt Institute. Several investigations were cited showing that within certain void limits, the stiffness of a mix may decrease with an increase in voids (Van Draat and Sommer (67); Bazin and Saunier (68)) and therefore result in lower thermal stresses.

It is important to note that in all three models a decrease in the amount of cracking with an increase in the amount of fines (X_8) in the base material was predicted. While there was no direct link made between the amount of fines and the frictional properties of the base, it is possible that as the fines increased, the angle of internal friction of the material decreased resulting in less frictional constraint on the surface layer and fewer cracks. Conceptually, the fines can act as miniature ball bearings that decrease the angle of internal friction within the material.

Airport Pavement Model

Haas et al. (69) conducted an empirical study similar to that of Fromm and Phang (66). In the study, data were gathered from 26 airport pavements throughout Canada. After performing a series of laboratory tests on asphalt concrete cores, evaluating the condition of the existing pavement and conducting a series of statistical analyses, the following empirical model was proposed:

$$TRANCRAK = 218 + 1.28 \cdot ACTHICK + 2.52 \cdot MINTEMP + 30 \cdot PVN - 60 \cdot COEFFX \quad [14]$$

$R^2 = 0.70$

where: TRANCRAK = transverse crack spacing (m)

ACTHICK = thickness of asphalt concrete (cm)

MINTEMP = minimum temperature recorded on site

PVN = Pen-Vis Number

COEFFX = coefficient of thermal contraction (mm/1000mm/°C)

The viscosity of the binder was not taken into account in equation [14]. It was stated that the original binder viscosity data were not obtainable and therefore were not incorporated in the regression analyses. The authors' assumption was that the "correct" initial penetration grade was selected for each site and that any thermal effects that were observed resulted strictly from the variables in equation [14].

It is interesting to note that this equation predicts less cracking with an increase in surface thickness, similar to the observations made at Ste. Anne test road. It is unknown whether this

was due to the confounding effects of constructing thicker surfaces on lower quality materials as documented at Ste. Anne test road.

Mechanistic-Based Thermal Cracking Models

In contrast to the empirically based models, the mechanistic cracking models are computationally more complex. Based upon principles of mechanics, these models usually require the solution of a system of linear or non-linear equations.

Most mechanistic thermal cracking models focus exclusively on the asphalt concrete surface. Among the few exceptions is the fictitious crack model, also called the cohesive zone model that includes the interface friction between the supporting layer and asphalt concrete surface layer through a prescribed boundary condition imposed on the asphalt concrete. The frictional constraint model also takes into account the constraint from the aggregate base and predicts the crack spacing based on the balance between the accumulated thermal stress and the friction on the top of the aggregate base.

Hills and Brien - Fracture Temperature Prediction

Hills and Brien (70) developed a means of predicting the temperature at which asphalt concrete will fracture. Their method was later extended for use as a mix evaluation tool (71). It is important to realize that this method does not predict amount or frequency of cracking, only the temperature at which cracks may form.

The governing principle of the approach is illustrated in Figure 2.8. As temperature decreases, thermal stresses develop when the material is fully restrained. When the tensile strength mastercurve, representative of laboratory test results, intersects the stress curve a thermal crack develops.

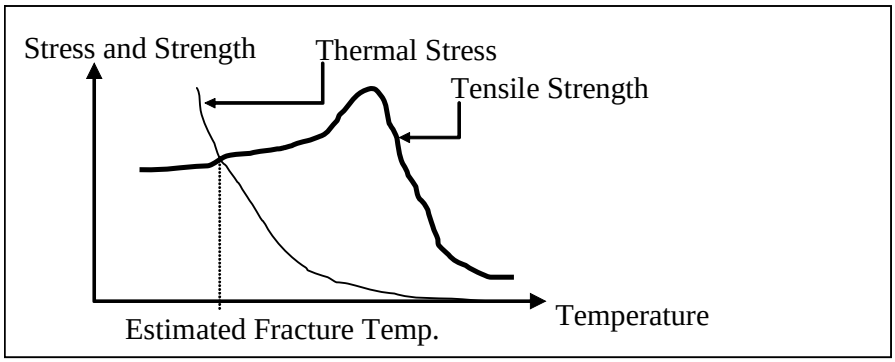

Figure 2.8. Method of estimating fracture temperature (70)

A key component of the model is the determination of the thermally induced stress. Hills and Brien considered asphalt mixtures as an elastic isotropic material The state of stress in any one of the principal directions is expressed by the inverse of Hooke's Law:

$$\sigma_i = \frac{1}{1+\upsilon} \cdot E \cdot \varepsilon_i + \frac{\upsilon}{1+\upsilon} \cdot 3 \cdot p \qquad [15]$$

where:

$$p = \frac{\sigma_x + \sigma_y + \sigma_z}{3}$$

E = stiffness

ε_i = strain (i=x,y,z)

ν = Poisson's ratio

σ_i = stress

They imposed certain stress and strain conditions to approximate the behavior of asphalt concrete as either an infinite beam or an infinite slab as shown in Figure 2.9.

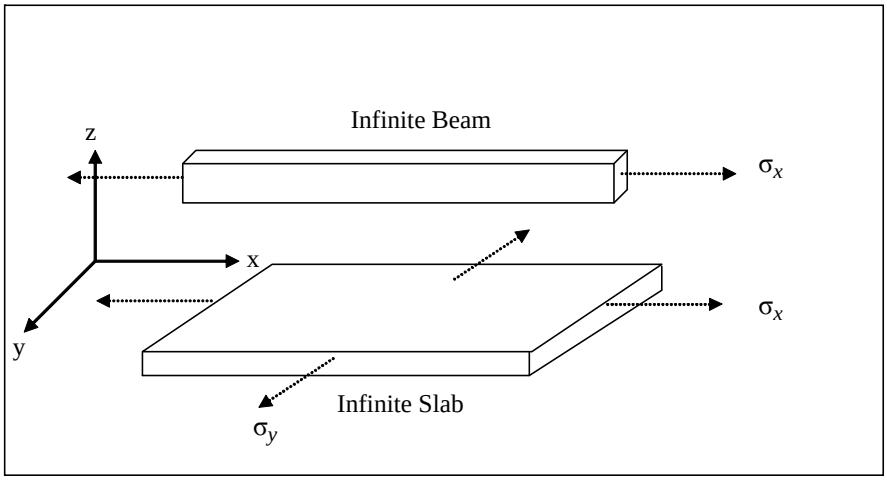

Figure 2.9. Infinite beam and infinite slab conditions

Table 2.2 summarizes these conditions and the resulting expressions for stress.

Table 2.2. Two stress formulations (70)

Case	Stress and Strain Conditions	p	σ_x
Infinite Beam	$\sigma_y = \sigma_z = 0$	$\frac{\sigma_x}{3}$	$E\varepsilon_x$
Infinite Slab	$\sigma_z = 0$ $\varepsilon_x = \varepsilon_y$	$\frac{2 \cdot \sigma_x}{3}$	$\frac{1}{1-\nu} \cdot E\varepsilon_x$ $(\sigma_x = \sigma_y)$

The total strain (ε_t) in an elastic material can be expressed as the summation of the mechanical (ε_m) and thermal strains (ε_{th}) or:

$$\varepsilon_t = \varepsilon_m + \varepsilon_{th} \qquad [16]$$

where:

$\varepsilon_m = \varepsilon_x$ as in Table 2.2

ε_{th} = thermally induced strain = $\alpha\Delta T$

α = linear coefficient of thermal contraction/expansion

ΔT = change in temperature

Due to the assumed infinite nature of the problem, the total strain at any point in the material must equal zero, and equation [16] becomes:

$$0 = \varepsilon_m + \varepsilon_{th} \quad [17]$$

Substituting the appropriate terms into equation [17] and solving for σ_x in either the infinite slab or beam case yields:

$$\sigma_x = -E\alpha\Delta T \quad \text{Infinite Beam} \quad [18]$$

$$\sigma_x = -\frac{E}{1-\nu}\alpha\Delta T \quad \text{Infinite Slab} \quad [19]$$

Finally, Hills and Brien assumed that the stiffness (S) of asphalt concrete is a function of both temperature (T) and time of loading (t). They therefore substituted stiffness (S(T,t)) for elastic modulus (E) in equations [18] and [19]:

$$\text{Infinite Beam: } \sigma_x = \int_{T_i}^{T_f} S(T,t)\alpha dT \quad [20]$$

$$\text{Infinite Slab: } \sigma_x = \int_{T_i}^{T_f} \frac{S(T,t)}{1-\nu}\alpha dT \quad [21]$$

In order to validate the prediction model, Hills and Brien conducted a number of laboratory experiments on asphalt concrete beams to compare predicted and measured fracture temperatures. The specimens were fully restrained beams of asphalt concrete cooled at a rate of approximately 10°C/hour. Though their predictions were not exact, they did obtain reasonable fracture temperature approximations. Their model predicted the benefit of using a soft binder to prevent thermal cracking.

The Hills and Brien approach is fundamentally sound, assuming that a pseudo-elastic representation of asphalt concrete is valid. Also, the method is relatively simple and the inputs to the model may be obtained by well-established laboratory testing methods. However, it is limited to predicting fracture temperature and not the amount or spacing of cracking and thus has limited applicability as a performance model.

Christison, Murray and Anderson - Thermal Stress Prediction

Christison et al (72) performed different stress analyses and compared the fracture temperature predictions to those measured in two test roads in Canada. The first pavement was constructed in central Alberta in 1966 (73). The second pavement was the St. Anne Test Road (74). The comparison showed that the pseudo-elastic beam (equation [20]) analysis yielded reasonable results without the added complexities of modeling the asphalt concrete as a viscoelastic material.

COLD Computer Program

Finn et al. (75) implemented the Hills and Brien approach in the computer program COLD. The three main uses of the program, as viewed by Finn et al., were to aid in the binder selection

process, to identify the potential for low temperature cracking of particular mixes in particular locations, and to help develop pre-paving specifications (76).

COLD Framework

The framework of the COLD program is shown in Figure 2.10. In the program Fourier's second law of heat transfer, with special surface boundary conditions, is solved by finite differences to determine the thermal gradient within the pavement. The thermal gradient is then used to calculate the thermal stresses, assuming either a pseudo-elastic slab or beam and solving equations [20] or [21] numerically.

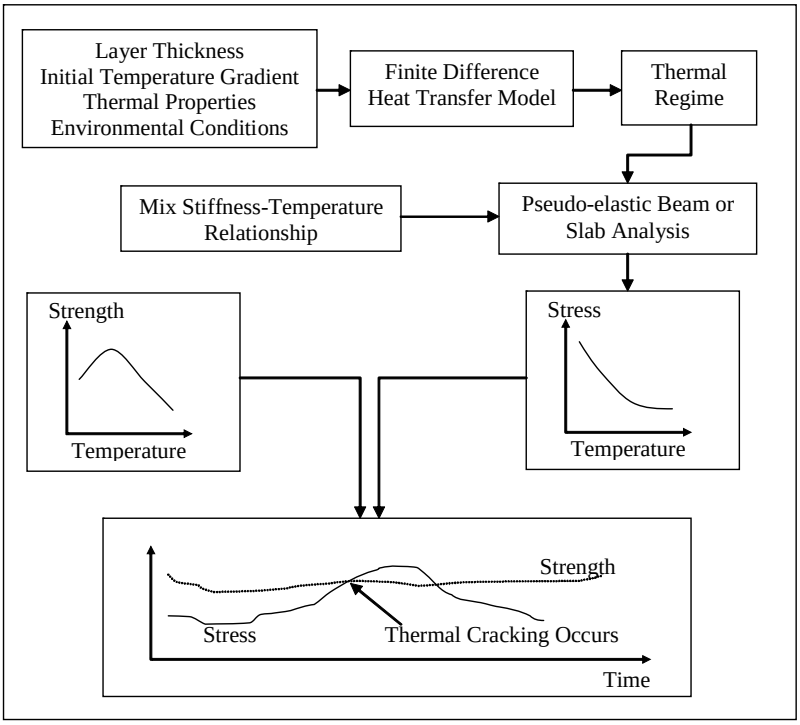

Figure 2.10. COLD framework (76)

A primary component of COLD is the development of a tensile strength versus temperature relationship, as illustrated in Figure 2.10. This was derived, as done by Hills and Brien (1966), through laboratory testing (e.g. indirect tension testing at cold temperatures). COLD has the added ability to account for the variability of strength with temperature. Therefore, it is possible to incorporate reliability into the analysis by using different percentile strength values as shown in Figure 2.11.

The last component of COLD superimposes strength and stress versus time, as shown at the bottom of Figure 2.10. Cracks are assumed to form instantaneously when the strength is exceeded.

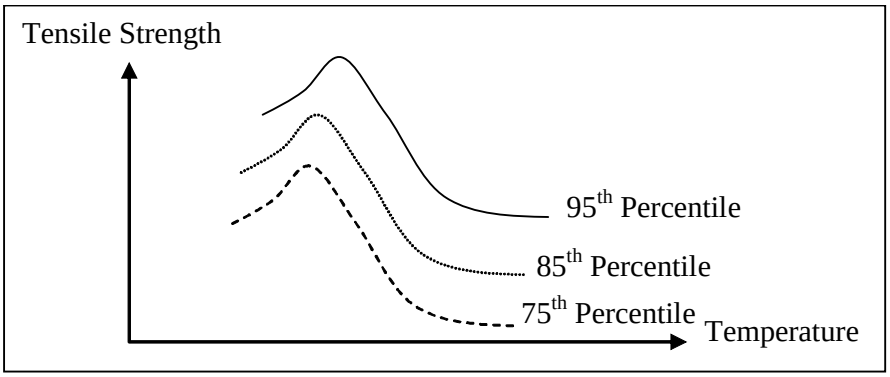

Figure 2.11. Tensile strength variability with temperature

Similar to the previously discussed models, COLD does not predict the amount of cracking expected in a pavement. However, a field validation study conducted in Utah established an empirical link between the probability of cracking and the expected amount of cracking (76).

Thermal Cracking (TC) Model

The Thermal Cracking (TC) model, incorporated in the new AASHTO Design Guide (9) was originally developed as part of the SHRP A-005 contract by Hiltunen and Roque (77). It was later modified and refined in the National Cooperative Highway Research Program (NCHRP) project 9-19 as part of the development of the Design Guide research effort. The TC model is composed of three parts:

- Calculation of thermal stress
- Calculation of crack propagation
- Calculation of crack amount

Calculation of Thermal Stress

In the calculation of thermal stresses in the asphalt layer the temperature profile of the pavement and two material properties, asphalt mixture coefficient of thermal contraction and relaxation modulus, are required.

The temperatures at different depths in the asphalt pavement are predicted using the climatic model subroutine.

The linear coefficient of thermal contraction of asphalt mixtures is obtained based on previous work performed by Jones et al. (59) who showed that

$$\alpha_{mix} = \frac{VMA \cdot \alpha_{AC} + V_{agg} \cdot \alpha_{agg}}{3V_{total}} \quad [22]$$

where

α_{mix} : linear coefficient of thermal contraction of the asphalt mixture (m/m/ºC)

α_{AC} : volumetric coefficient of thermal contraction of the asphalt cement in the solid state (m/m/ºC)

α_{agg} : volumetric coefficient of thermal contraction of the aggregate (m/m/ºC)

VMA : percent volume of voids in the mineral aggregate

V_{agg} : percent volume of aggregate in the mixture

V_{total}: 100 percent

The measurement of the coefficient of thermal contraction of asphalt cement and aggregates is not part of routine mixture design. Therefore, a constant value of 3.45 10-4 m/m/ºC is assumed for all asphalt cement types. For the coefficient of thermal contraction of the aggregates, the values published elsewhere are used and α_{mix} can be determined knowing the VMA and V_{agg} obtained as part of the routine asphalt mixture design. The thermal strain is simply calculated as

$$\varepsilon = \alpha_{mix} \cdot \Delta T \quad [23]$$

where

ε - thermal strain

ΔT - temperature change

Relaxation modulus tests are typically not performed on asphalt mixtures. Instead, the creep compliance is experimentally determined and numerically converted to the relaxation modulus. The 1000-second creep test is performed according to AASHTO TP9-96 procedure (78) at three different temperatures of -20°C, -10°C, and 0°C and master curves of the creep compliance are obtained assuming that the time-temperature superposition principle is valid.

The reduced time is calculated as:

$$\xi = \frac{t}{a_T} \quad [24]$$

where

ξ: reduced time

t: real time

a_T: temperature shift factor

Two functions are fitted from the master curve. The first one is a 4-parameter Prony series described by the following expression:

$$D(\xi) = D(\infty) - \sum_{i=1}^{N} D_i e^{-\xi/\tau_i} + \frac{\xi}{\eta_\upsilon} \quad [25]$$

or

$$D(\xi) = D(0) - \sum_{i=1}^{N} D_i (1 - e^{-\xi/\tau_i}) + \frac{\xi}{\eta_\upsilon} \quad [26]$$

where

$D(\infty) = D(0) + \sum_{i=1}^{N} D_i$

$D(\xi)$: creep compliance at reduced time ξ

ξ : reduced time

$D(\infty), D(0), D_i, \tau_i, \eta_\upsilon$: Prony series parameters

The Prony series can be incorporated into the convolution integral that relates the creep compliance to the relaxation modulus to determine the relaxation modulus.

The second fitted function is a power function in the form

$$D(\xi) = D_0 + D_1 \xi^m \quad [27]$$

where D_0, D_1, and m are coefficients for this power model, which are not related to the coefficients in the Prony series. The purpose of this step is to obtain the parameter m, which is used later in estimating the crack propagation.

For a viscoelastic material, the creep compliance and the relaxation modulus are related by the convolution integral:

$$\int_0^{\infty} D(t-\tau)\frac{dE(\tau)}{d\tau}d\tau = 1 \quad [28]$$

A computer program calculates the relaxation modulus using the Laplace transformation of the creep compliance expressed in the form of Prony series. The resulting relaxation modulus is obtained as

$$E(\xi) = \sum_{i=1}^{N+1} E_i e^{-\xi/\lambda_i} \quad [29]$$

where

$E(\xi)$: relaxation modulus at reduced time ξ

E_i, λ_i : parameters for the master curve of relaxation modulus

The thermal stress is computed with the one-dimensional hereditary integral that calculates the stress given a known strain history:

$$\sigma(\xi) = \int_0^{\xi} E(\xi - \xi')\frac{d\varepsilon}{d\xi'}d\xi' \quad [30]$$

where

$\sigma(\xi)$: stress at reduced time

$E(\xi - \xi')$: relaxation modulus at reduced time

ε : strain at reduced time

By changing the variables, this equation can be written in terms of real time, t, as

$$\sigma(t) = \int_0^{t} E(\xi(t) - \xi'(t))\frac{d\varepsilon}{dt'}dt' \quad [31]$$

A finite difference solution of equation [31] was developed by Soules et al. (79) with $E(\xi)$ represented by a Prony series

$$\sigma(t) = \sum_{i=1}^{N+1} \sigma_i(t) \quad [32]$$

where

$$\sigma_i(t) = e^{-\Delta\xi/\lambda_i}\sigma_i(t-\Delta t) + \Delta\varepsilon \cdot E_i \frac{\lambda_i}{\Delta\xi}(1 - e^{-\Delta\xi/\lambda_i})$$

$\Delta\varepsilon$ and $\Delta\xi$ are the changes in strain and reduced time over the time interval Δt.

Calculation of Crack Propagation

The stress intensity factor is calculated with a two-dimensional finite element program, CRACKTIP, developed by Chang et al. (80) at the Texas Transportation Institute. The thermal crack was modeled as a single vertical crack in the asphalt mixture layer. The finite element computation is time-consuming and is not practical for the purpose of pavement design. For convenience CRACKTIP was run for a broad range of conditions and the results were used to develop a simple regression equation that can be easily incorporated in the design calculations:

$$K_I = \sigma(0.45 + 1.99C_0^{0.56}) \quad [33]$$

where

K_I : stress intensity factor

σ : far-field stress

C_0 : current crack length

The crack length under thermal loading cycles is calculated using Paris' law (42):

$$\frac{da}{dN} = A(\Delta K)^n \quad [34]$$

where

a: the crack length

N: the number of cycles

ΔK: the change of the stress intensity factor

A, *n*: regression parameters

In this expression the rate of crack propagation is determined from the amplitude of stress intensity factor at each cycle. In the TC model the change in temperature during one day is taken as one loading cycle, and the change of the crack length is computed and accumulated on a daily basis. Thus, the dN in equation [34] turns out to always be 1 and equation [35] can be rewritten as

$$\Delta a = A(\Delta K)^n \quad [35]$$

The TC model introduces an extra constraint to the crack propagation in one loading cycle. The asphalt layer is divided into four sub-layers. The model allows the crack to grow only within one sub-layer in one thermal cycle, regardless of stress magnitude. Therefore, four extreme cold days are needed to crack the asphalt layer from top to bottom.

In equation [34], parameters *A* and *n* are determined from fatigue tests that are costly and time-consuming. Schapery (81) extended his theory to describe the fracture in nonlinear viscoelastic materials and indicated that the fracture parameters *A* and *n* can be related to other material properties such as:

- The slope (*m*) of the linear portion of the log compliance-log time master curve determined from a creep test
- The undamaged strength of the material
- The fracture energy of the material determined experimentally by monitoring the released energy through crack propagation

The m-value was obtained from the creep compliance. The average tensile strength at -10°C was selected to represent the undamaged tensile strength of the asphalt mixture at all temperatures.

Previous experiments showed that the peak strength always occurred at temperatures lower than -10°C. Thus, the strength at -10°C was selected as a conservative estimate of the undamaged tensile strength of the mixture. The fracture energy density is, however, difficult to measure.

Work by Molenaar (82) showed that *A* can be empirically calculated as

$$\log A = 4.389 - 2.52 \cdot \log(E \cdot \sigma_m \cdot n) \quad [36]$$

where

E : mixture stiffness

σ_m : tensile strength

The experiments conducted by Lytton et al. (83) led to other relationships:

$$\log A = -\frac{n + 0.69}{0.511} \quad [37]$$

and

$$n = 0.8 \cdot (1 + \frac{1}{m}) \quad [38]$$

where m is determined in equation [27].

In the TC model, *n* is calculated using equation [38]; *A* is calculated with equation [39] in which the material modulus *E* is replaced by a calibration coefficient *k*:

$$\log A = 4.389 - 2.52 \cdot \log(k \cdot \sigma_m \cdot n) \quad [39]$$

where

k : coefficient from field calibration (10,000)

n : calculated with equation [38]

Thus, the two coefficients in the crack propagation model, *A* and *n*, can be computed from the creep compliance and tensile strength data obtained at -10°C.

Calculation of Crack Amount

An empirical equation based on field observations was developed to predict the amount of thermal cracking amount as follows

$$AC = \beta \cdot P(\log C > \log D) \quad [40]$$

where

AC : observed amount of thermal cracking

β : regression coefficient determined through field calibration

P( ) : probability function

D : thickness of surface layer

C : crack length

The field calibration resulted in β =353.5.

The authors of the TC model pointed out that this model does not predict more than 50% of the total possible amount of cracking that can develop in the pavement, and the minimum crack spacing predicted by this model is 15 feet. The model assumes that a crack is counted only when it reaches the bottom of the asphalt layer.

Fictitious Crack Model

The fictitious crack model (FCM) proposed by Hillerborg et al. (84) is one of the major crack models used in the study of fracture in Portland cement concrete. The FCM assumes that a process zone exists ahead of the physical crack tip and that all damage, i.e. micro-cracking, is localized in this zone. The material in this zone is not physically completely open in the macroscopic sense, but the ability of the material to transfer stresses between the two sides of the zone is reduced. The stress within this process zone depends on the distance from the crack tip: the further from the crack tip, the larger the stress is, with the maximum stress up to the tensile strength of the material at the end of this process zone. This is schematically shown for a three-point bending beam configuration in Figure 2.12.

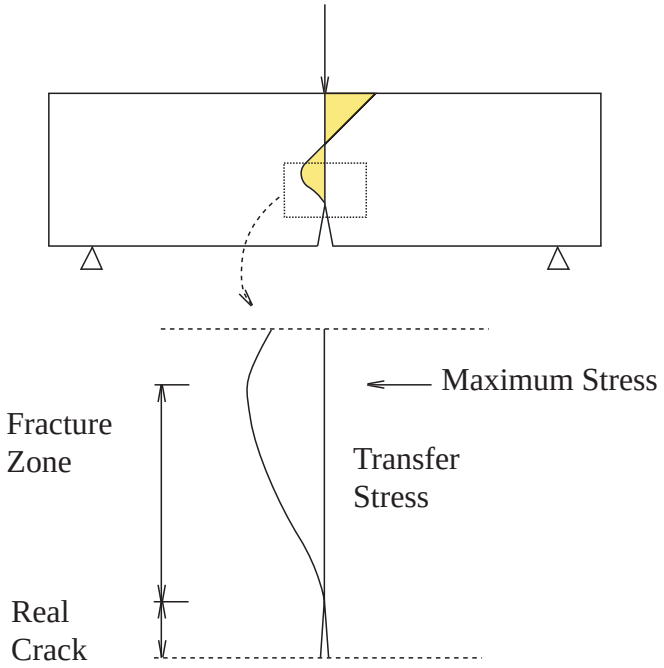

Figure 2.12. A loaded concrete beam with a crack and process zone (85)

Hillerborg et al. (84) stated that microcracking is the dominant state in the process zone in concrete, and that fracture in concrete is the process in which microcracks emerge into several visible major cracks. The area near the physical crack tip contains more microcracks than the area further away, which therefore is less capable of transferring stresses between the two parts separated by the crack.

Unlike the infinite stress at the crack tip in the theory of LEFM, the largest stress in the FCM is the tensile strength of materials. By this means, the FCM avoids the singularity in the numerical computation and can be conveniently implemented into the finite element analysis.

The FCM has been widely applied to the study the fracture of rock and Portland cement concrete. Only two of the earlier references about the numerical application of the FCM to concrete are mentioned here: Hillerborg et al. (84) and Petersson (86). To facilitate the simulation, usually an assumption is made for the constitutive equation in the process zone. When the simulation is finished, the numerically computed load-displacement curve and the parameters assumed in the constitutive equation can be calibrated with the experimental data. A finite element computer program is usually needed to accomplish the numerical computation.

For asphalt materials Jenq and Perng (87) applied the FCM to simulate the crack growth in single edge notched beam specimens tested at 23.9°C (75°F). They simulated the load-load line displacement curve by assuming a bilinear constitutive behavior for the fictitious crack. Then, the load-load line displacement curve from the numerical simulation was compared with their experimental data and the parameters in the bilinear constitutive equation were calibrated. They concluded that the FCM could be used to simulate the fracture behavior in asphalt mixtures and indicated that the FCM was a promising tool in the study of crack growth in asphalt materials.

Shen and Kirkner (88) used the FCM to study the interaction between multiple cracks and predicted the crack spacing of transverse cracks. They assumed an initial set of fictitious cracks on the pavement; when the temperature drops, some fictitious cracks become predominant and become major cracks. A system of non-linear algebraic equations was obtained based on the equilibrium between the friction at the bottom of asphalt pavement layer and the thermal stresses accumulated in the asphalt layer. The solutions to these equations provided the crack spacing in an asphalt pavement. The authors extended their research (89) to address the viscoelastic deformation of the asphalt mixtures at low temperature.

The FCM is an application of the more general cohesive zone model (CZM) (90), (91) to concrete research. Soares et al. (92), Paulino et al. (93), and Li (52) have applied the CZM to model the fracture behavior in asphalt mixtures. This type of model has the potential to address the coupling of thermal loading and traffic loading.

Frictional Constraint Model

The frictional constrain model considers the friction on the interface between the asphalt layer and the aggregate base layer and estimates its effect on the crack spacing. Hannele et al. (94) and Timm and Voller (95) proposed, separately, similar frictional constraint models to predict the crack spacing. Hannele et al. included the variation of material properties in the estimation of the crack spacing, while Timm et al. predicted the crack spacing based on both 1D and 2D modeling of the asphalt layer. In this section, the second model is reviewed in detail.

Because of the construction joint and/or the flaw of materials, a “free end” is assumed. The friction at the interface between the asphalt layer and the aggregate base is balanced by the thermal stress in the asphalt layer that increases with distance from the “free end” until it reaches the tensile strength of the asphalt mixture, as shown in Figure 2.13.

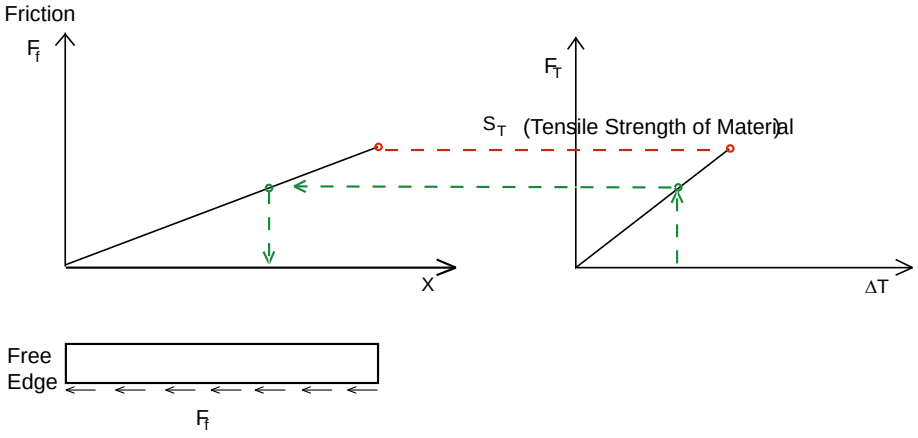

Figure 2.13. Friction constraint model

The model is based on the Mohr-Coulomb equation and the crack spacing, equal to $1.5X_c$, is computed using the following equation

$$X_c = \frac{E\alpha\Delta T}{\frac{C}{h} + \rho g \tan\phi} \quad [41]$$

where

X_c = longitudinal distance from free edge to the point of maximum tensile stress,

E = asphalt mixture Young's modulus,

α = asphalt mixture linear coefficient of thermal contraction,

ΔT = temperature change,

C = cohesion,

ϕ = friction angle,

h = thickness of pavement,

ρ = density of asphalt mixture,

g = gravity.

The asphalt layer was modeled as both a 1D bar and a 2D layer, however, the comparison showed that the simpler model predicts crack spacing as well as the 2D model.

Li et al. (51) compared the crack spacing predicted in three cells at MnRoad facility using both the frictional constraint model and the TC model. The frictional constraint model predicted values closer to the crack spacing measured in the field compared to the TC model. The authors also indicated that reasonable estimation of the cohesion and the friction angle of the interface, which were not directly available in their study, were critical in estimating crack spacing.

Conclusions

A variety of experimental methods and analyses has been used or is currently used to evaluate the fracture resistance of asphalt materials and to predict the low temperature cracking performance of asphalt pavements. However, a number of important conclusions can be drawn from the literature review of these methods and analyses:

- The experimental measurement of fracture mechanics based properties of both asphalt binders and asphalt mixtures is a critical requirement for both the material selection process and the stress analyses of the pavement.
- No study was performed so far that compares different experimental fracture methods
- There is little understanding of the relations between the conventional material properties and the fracture mechanics properties.
- The stress analyses methods available at this time to investigate asphalt pavements exposed to severe low temperatures and low temperature cycles have important limitations that make their applicability questionable. It appears that an analysis based on the cohesive zone model may offer a more realistic approach to modeling the crack propagation in asphalt pavements.

These important issues will be addressed in the next chapters of this report.

CHAPTER 3

FIELD SITES AND MATERIAL IDENTIFICATION

Introduction

Two sets of materials were investigated in this study. The first set consists of materials obtained from already built pavements for which performance information is documented and readily available. The second set consists of laboratory prepared specimens following a statistically designed test matrix and using typical materials and mix designs for the northern Midwest states.

Field Samples

The research team initial idea was to collect field samples from both good and poor performing pavements. Ideally, samples from both newly constructed (less than 3 years old) and older pavements (more than 7 years old) would be obtained. Asphalt overlays were not considered in this study to eliminate the effect of reflective cracking. Pavements containing significant amount of RAP in the asphalt layers were not considered either to keep the level of significant factors to a minimum.

The field samples would consist of both cores and beams sampled between the wheel paths to accommodate the different test geometries required as part of the experimental characterization of the asphalt mixtures. At the beginning of the project the research team and members of the TAP put together a document that contained detailed guidelines for the participant states to select and perform the necessary activities to obtain the field samples. The document also contained a project nomination form that the participant states will use to nominate their field sections. The document is presented in Appendix A.

At the beginning of October 2004 this document was emailed to all participant states with the request to get back the nominated sites by the end of 2004. By the end of the year four states submitted their nominations for pavement sites that reasonably fit the project requirements: Illinois (4 sites), Minnesota (7 sites), Wisconsin (3 sites), and North Dakota (3 sites). Detailed information about the nominated sites is presented in Appendix B.

The research team and members of the TAP made recommendations to the states with respect to the selected sites and by the end of spring 2005, as shown at the end of Appendix B. The recommendations included all Minnesota sites, two of the Illinois sites two of the Wisconsin sites and one of the North Dakota sites.

As of February 2006, all Minnesota and Wisconsin field samples and one of the Illinois samples have been collected and distributed to the universities part of the research team. Illinois I-74 samples were received in summer of 2006. In addition, cores were received from North Dakota from one of the sites that was not recommended. Details of the coring experience at the MnROAD test cells and from Illinois US Highway 20 are given in Appendices C, D, and E.

Laboratory Specimens

The second set of materials consisted of laboratory prepared specimens that follow a statistically designed matrix. Field samples provide the critical link between laboratory experiments and field performance; however, the number of factors that can be evaluated is often limited, unless

the field sites were built according to a statistical design. Laboratory conditions provide a better control of the factors that affect material properties and offer the advantage of a statistical design that can identify the significant factors of interest.

Table 3.1 summarizes the test matrix for the laboratory prepared specimens. The matrix contains a combination of binder and mixture factors. The main focus of this matrix is to quantify the effects of the factors considered to be the most significant based on empirical evidence accumulated over the years: binder type, film thickness, air voids, and differential contraction between the aggregate particles and the binder.

Table 3.1. Laboratory experimental layout

Air Voids →		**Design (4%)**				**As constructed (7%)**			
Aggregate Type →		**Aggregate 1 Granite**		**Aggregate 2 Limestone**		**Aggregate 1 Granite**		**Aggregate 2 Limestone**	
Binder Content →		Design	Film thick.	Design	Film thick.	Design	Film thick.	Design	Film thick.
Binder Type (modification)	PG58-40, modifier 1 SBS (Flint Hills)	**X**	**X**	**X**					
	PG58-40, modifier 2	Not available, replaced with 64-22							
	PG58-34, modifier 1 Elvaloy (Murphy Oil)	**X**	**X**	**X**					
	PG58-34, modifier 2 SBS (Flint Hills)	**X**		**X**					
	PG58-28, plain 1 (Seneca Petroleum)	**X**	**X**	**X**	**X**	**X**	**X**	**X**	**X**
	PG58-28, plain 2 (Payne and Dolan)	**X**		**X**					
	PG64-34, modifier 1 Elvaloy (Murphy Oil)	**X**		**X**					
	PG64-34, modifier 2 Black Max™ (Husky)	**X**		**X**					
	PG64-28, plain 1 (Seneca)	**X**		**X**					
	PG64-28, modifier 1 SBS (Seneca Petroleum)	**X**		**X**					
	PG64-22, plain (Seneca Petroleum)	**X**		**X**					
	PG70-22, modified SBS (Seneca Petroleum)	Received but not part of the approved work plan							

In recognizing the significant effect of the asphalt binder properties on the low temperature performance of asphalt pavements ten different asphalt binders, both plain and modified, that cover five different performance grades were selected for this study. Note that the main idea in selecting the binders was to get materials representative of the asphalt market in the area rather than keeping the base asphalt binder limited to one or two sources. The search for these binder grades from the asphalt producers in the northern Midwest states found 9 of the 10 asphalt binders selected in the work plan; only one type of PG58-40 was found and the research team and the TAP agreed to replace the second PG58-40 with the PG64-22 binder. Table 3.1 shows the final experimental layout; apart from the type of binder, the type of aggregate represents another significant factor followed by the film thickness and by air void content.

To reduce the effect of mix design all mixtures were designed according to the guidelines for a 12.5-mm Superpave asphalt mixture.

Two different types of aggregates, limestone and granite were used to prepare the mixtures to investigate the effect of the differential contraction between the asphalt binder and the aggregate. Additional details about these aggregates are provided in Chapter 4.

Two levels of air voids were used: the design value of 4% and 7% representing typical as-constructed values. Although previous work indicated that higher air voids translates into lower fracture resistance, it is important to quantify this difference for further improvements in construction practice and performance prediction modeling.

Two levels of asphalt content were used, the design value and the value resulting from a recently proposed film thickness approach (Iowa DOT and Minnesota DOT). Although it is expected that a richer mixture will most likely be more crack resistant, no well-documented data to support this statement is currently available.

In order to minimize the effect of specimen preparation on the test results, all gyratory compacted and beam specimens were prepared at the MTU facility. The beams were prepared at Iowa State from the materials batched at Michigan Tech. The experimental investigation of the laboratory prepared specimens and of the field samples was performed by the four research universities as indicated in Table 3.2.

Table 3.2. Experimental Work by Research Teams

		ISU	UIUC	UMN	WISC
Mixture	Indirect Tensile Test (IDT) (creep and strength)			**X**	
	Single-Edge Notched Beam, SE(B)		**X**		
	Semi Circular Bending (SCB)			**X**	
	Disc-Shaped Compact Tension, DC(T)		**X**		
	Thermal Stress Test TSRST			**X***	
	Dilatometric Measurements				**X**
Binder	DSR, BBR and DTT			**X**	
	Double Edge Notch Tension (DENT)			**X**	
	Dilatometric Measurements				**X**

* instrumented with acoustic emission

CHAPTER 4

LABORATORY SPECIMEN PREPARATION

Preparation of Gyratory Specimens

Sampling of Material

Two aggregate sources and ten binders were sampled according to the experimental plan (Table 3.1). It was determined by the research team that the aggregate sources should have different coefficients of thermal expansion, thus a granite and limestone aggregate sources were selected. Granite and limestone aggregates are commonly used materials in the design and construction of hot mix asphalt pavements. The location of the aggregate sources was selected for ease of sampling since Wisconsin is centrally located to the states where the research is being conducted. Ten different binders, both plain and modified, that cover five performance grades were selected for this study.

Both aggregates were sampled from Mathy Construction Company aggregate quarry in the summer and fall of 2005 in Wisconsin. Table 4.1 below shows the location, source, and approximate weights for the material sampled for the granite and limestone aggregates. Approximately 20 tons of material was sampled, dried, sieved, sands were blended, and the coarse aggregate was separated by sieve size fraction. The gradations and specific gravities of the individual materials were compared to the job mix formula supplied by Mathy Construction.

Table 4.1. Aggregate sources and approximate weights of material sampled

Aggregate Type	Material	Location	Source	# of 30 gallon barrels	Approximate Weight (lbs)
Granite	1/2" Crushed Rock	Cisler	Marathon	12	5400
	3/8" Crushed Rock	Cisler	Marathon	5	2250
	3/16" Crushed Rock	Cisler	Marathon	5	2250
	Man. Sand	Cisler	Marathon	10	4500
	Blend Sand	Cisler	Marathon	8	3600
Limestone	3/4" x 3/8" Bit. Rock	Gates	Dunn	12	5400
	1/2" x 1/4" Bit. Rock	Gates	Dunn	12	5400
	3/8" Bit. Agg.	Gates	Dunn	5	2250
	Man. Sand	Tammec	St. Croix	12	5400
	Blend Sand	Mimbach	St. Croix	10	4500
				TOTAL WEIGHT (LBS)	40950
				TOTAL WEIGHT (TONS)	20

Verification of Aggregate Properties

The verification of aggregate properties was done in accordance with the American Society of Testing and Materials (ASTM) and the American Association of State Highway and Testing Officials (AASHTO) testing criteria. The specific aggregate properties were:

- Coarse aggregate specific gravity,
- Fine aggregate specific gravity
- Gradation, and

- Fine aggregate angularity.

Table 4.2 and Table 4.3 contain the specific gravities of each aggregate source along with the gradation of each aggregate source. AASHTO T 304 "Uncompacted Void Content of Fine Aggregate." Results are shown in Table 4.4. The data shows that differences exist between uncompacted void contents when you use method A or method C. The results show that the manufactured sands have higher uncomapcted void contents than the blend sands which is expected because the manufactured sands are crushed whereas the blend sands are more rounded to subrounded. The Superpave specification for uncompacted void contents for a traffic level of 3 to 30 million ESAL's is 45 (≤100 mm) and 40 (>100 mm).

Table 4.2. Granite gradations for individual aggregate source

	Sieve Size (mm)	Cisler 1/2" Crushed Rock	Cisler 3/8" Crushed Rock	Cisler 3/16" Crushed Rock	Cisler Man Sand	Cisler Blend Sand	Mineral Filler	Trial Blend
Percent Passing	19	100	100	100	100	100	100	100
	12.5	82.9	100	100	100	99.2	100	95.2
	9.5	42.5	97.9	100	100	97.5	100	83.5
	4.75	10.9	14.5	98.2	95.9	87.3	100	65.2
	2.36	6	2	67.2	62.3	76.6	100	47.1
	1.18	4	1.3	43.4	33.5	64	100	33.4
	0.6	3.4	1.2	29	17.5	44.2	100	23.8
	0.3	3	1.1	19.8	8.2	15.2	100	12.5
	0.15	2.6	1	13.1	2.7	1.2	100	7
	0.075	2.1	0.9	9.2	1.1	0.2	100	5.1
	Gsb	2.691	2.681	2.596	2.659	2.623		2.648
	Percent	23%	10%	25%	30%	12%	1.5%	

Table 4.3. Limestone gradations for individual aggregate source

	Sieve Size (mm)	Gates 3/4" x 3/8"	Gates 1/2" x 1/4"	Tammec 3/8" Washed Chip	3/8" Minus R#4	3/8" Minus R#8	3/8" Minus R#3/8	Mimbach Washed Man. Sand	Tammec Blended Sand	Trial Blend
Percent Passing	19	100.0	100.0	100.0	100.0	100.0	100.0	100.0	100.0	100.0
	12.5	69.0	100.0	100.0	100.0	100.0	100.0	100.0	98.9	97.2
	9.5	29.0	53.0	100.0	99.0	100.0	0.0	100.0	94.9	79.1
	4.75	7.0	5.0	37.0	5.9	100.0	0.0	86.5	87.2	59.6
	2.36	6.0	3.0	6.0	1.4	67.9	0.0	64.8	79.0	48.6
	1.18	6.0	2.0	3.6	1.2	54.0	0.0	46.6	68.7	38.6
	0.6	5.0	2.0	3.1	1.1	48.7	0.0	35.1	50.2	28.8
	0.3	5.0	1.0	2.6	1.2	43.6	0.0	27.0	21.0	16.9
	0.15	4.0	1.0	1.9	1.2	34.1	0.0	18.9	5.6	9.2
	0.075	2.9	0.5	1.5	1.0	22.6	0.0	11.6	2.6	5.4
	Gsb	2.567	2.592	2.638	2.659	2.659	2.659	2.587	2.665	2.618
	Percent	8.0%	12.0%	0.0%	5%	0.0%	8.0%	37.0%	30.0%	100.0%

Table 4.4. Fine Aggregate Angularity test results

Aggregate	Uncompcated Voids (AASHTO T 304 Method C)	Uncompcated Voids (AASHTO T 304 Method A)
Cisler Manufactured Sand	41.9	48.9
Cisler Blend Sand	37.5	39.4
Mimback Manufactured Sand	40.2	46.7
Tammec Blend Sand	33.8	40.4

Verification of Mixture Designs and Volumetric Properties

The next step is to compact specimen in order to determine the volumetric properties of the trial blend. The trial blends for the two aggregate sources are shown in Figure 4.1. A minimum of two 4,500g samples are to be compacted using the Superpave gyratory compactor and one 2,000g sample was prepared to determine the maximum theoretical specific gravity for each asphalt content selected. Typically, a range of asphalt contents are chosen with increments of 0.5% in order to determine the air voids at 4%.

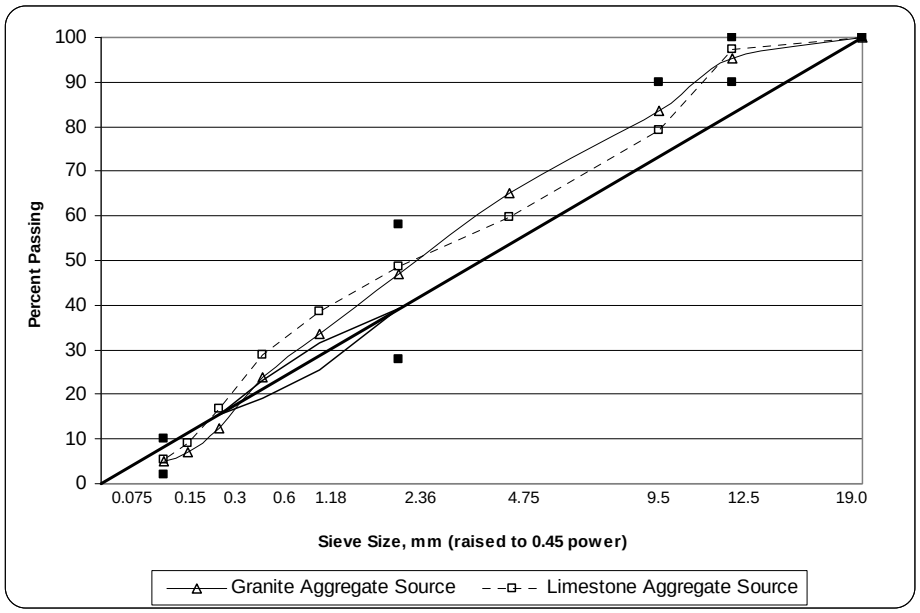

Figure 4.1. 12.5mm gradation for HMA mix designs

The mixing and compaction temperatures were selected to be 155°C and 135°C, respectively. N_{ini} is 8, N_{des} is 100 and N_{max} is 160. These compaction parameters represent a traffic level of 3,000,000 to less than 30,000,000 equivalent single axle loads (ESAL's) which is medium to high traffic. The Superpave mix design procedure (SP-2) was used to mix and compact the HMA specimens and Rice samples.

Determinations of the optimum asphalt content were determined using the following procedure:

1. Batch out two 4,500g samples and one 2,000g sample for each trial asphalt content.
2. Place the batched out aggregate into separate bread pans and store in an oven at 155°C over night. Also, heat up mixing tools
3. Heat up the binder at 155°C for a few hours to make it fluid. Heat the gyratory mold, top and bottom plates and tools at 135°C.
4. Combine the aggregate and the appropriate weight of binder in the bucket mixer and mix until the aggregate looks thoroughly coated.
5. Dump the mixed material back into the bread pan and scrap the bucket until the tarred weight is within plus or minus 10g.
6. Return mixture to ovens at short term aging for 2 hours at 135°C.
7. Compact two specimens to N_{max} for volumetric analysis. The compactor software automatically records specimen height.
8. Obtain trial mixture volumetric properties using theoretical maximum specific gravity (ASTM D2041 and bulk specific gravity of compacted specimens (ASTM D2726).

9. The calculations are as follows:

Where $G_{mm} = \dfrac{A}{A+B-C}$

A = Oven dry mass of loose asphalt sample,
B = Buoyant mass of pycnometer filled with water, and
C = Buoyant mass of pycnometer, mixture, and water.

Where $G_{mb} = \dfrac{A}{B-C}$

A = Oven dry mass of compacted specimen,
B = Saturated surface dry mass of compacted specimen, and
C = Buoyant mass of compacted specimen.

$$G_{mb}(\text{estimated}) = \frac{\frac{W_M}{V_{MX}}}{\gamma_W}$$

W_M = Mass of specimen,
V_{MX} = Volume of compaction mold, and
γ_W = Density of water

$$C = \frac{G_{mb}(\text{measured})}{G_{mb}(\text{estimated})}$$

C = Correction factor,
G_{mb}(measured) = measured bulk specific gravity after N_{des}
G_{mb}(estimated) = estimated bulk specific gravity at N_{des}
$G_{mb}(corrected) = C \times G_{mb}(estimated)$

- Input volumetrics and obtain a corrected bulk specific gravity.
- Evaluate the trial mixture with air voids (AV), voids in the mineral aggregate (VMA), and voids filled with asphalt (VFA) for each asphalt content.

$$AV = \frac{G_{mm} - G_{mb}}{G_{mm}}$$

$$VMA = 100 - \frac{G_{mb} \times P_s}{G_{sb}}$$

P_s = Aggregate content

G_{sb} = Bulk specific gravity of total aggregate

$$VFA = 100 \times \frac{VMA - AV}{VMA}$$

Figures 4.2 and 4.3 show the verification plots for the mix design for the granite and limestone aggregate sources, respectively. The optimum asphalt content is determined at 4.0% air voids. In addition, the VMA and VFA must meet the Superpave mix design requirements for a 12.5 nominal maximum aggregate size (NMAS) with a design traffic level of three to thirty millions ESAL's. The optimum asphalt content, VMA, and VFA for the granite aggregate source are 6.0%, 16.3%, and 75.9%; respectively. The optimum asphalt content is slightly higher than one would think, and this is due the fact that there is quite a bit of manufactured sand in the mixture which creates a lot more surface area than coarse aggregate thus increasing the binder content. The optimum asphalt content, VMA, and VFA for the limestone aggregate source are 6.9%, 16.2%, and 75.0%; respectively. This binder content is rather high due to the absorptiveness of the aggregate and the amount of manufactured sand used to create this mix design. Figures 4.2

and 4.3 also show that the VMA and VFA are within the allowable limits of the Superpave method.

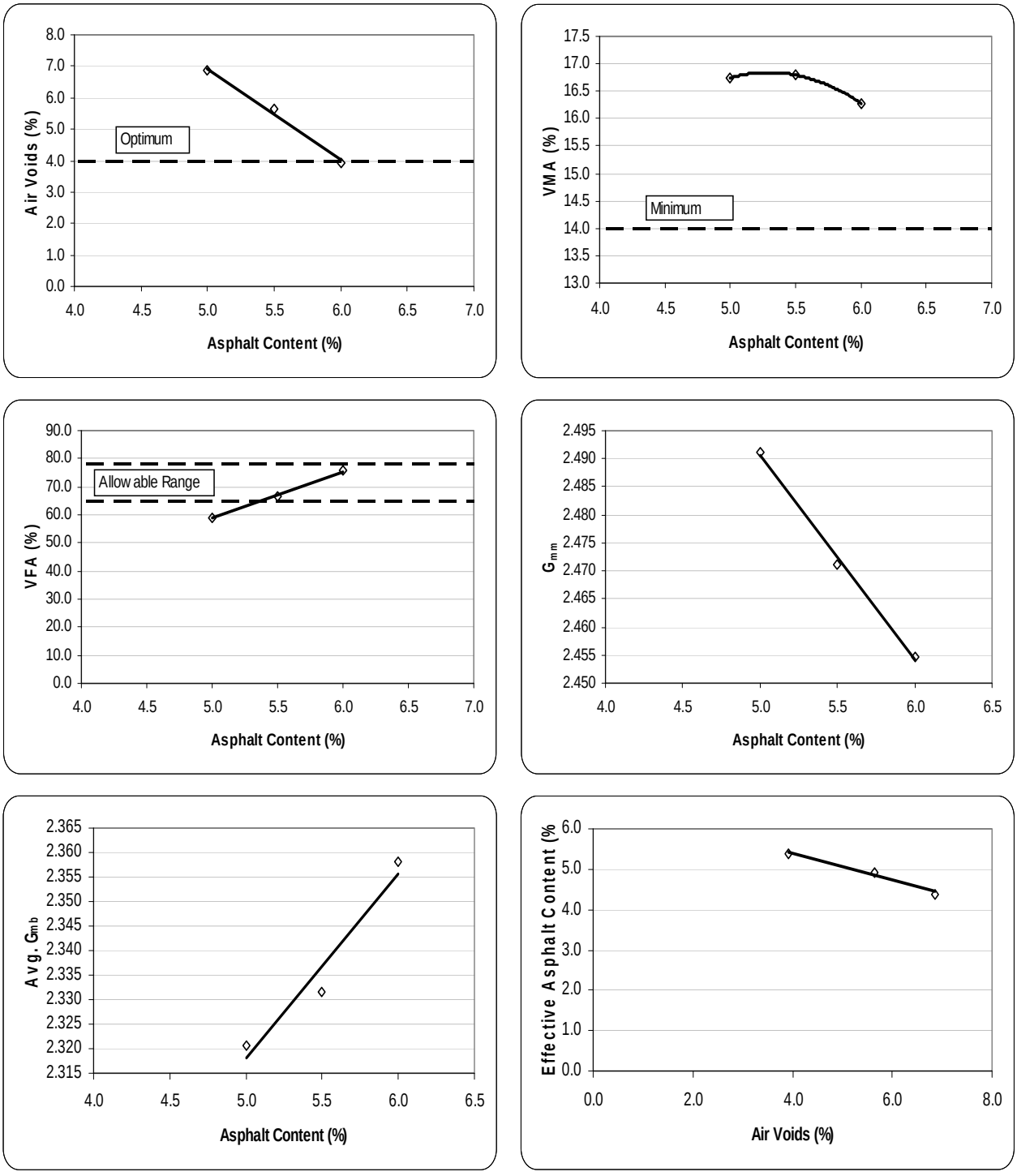

Figure 4.2. Granite aggregate mix design volumetric properties

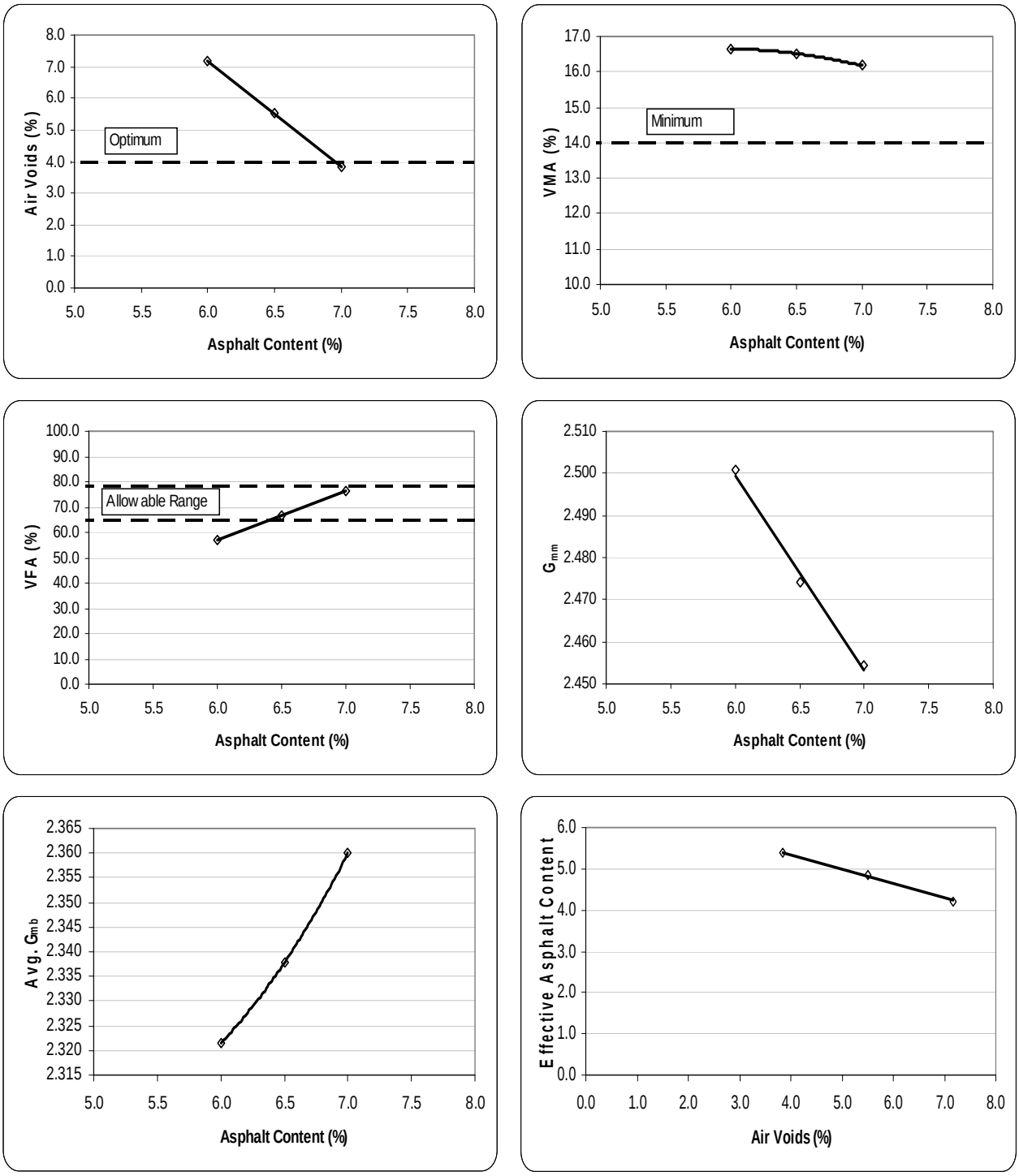

Figure 4.3. Limestone aggregate mix design volumetric properties

Batching of Materials

The first step in the sample preparation was to batch out the required amount of aggregate materials for each Superpave gyratory specimen and each slab. The batch samples for each gyratory sample were 6852 g (granite and limestone aggregate source). The slab specimen

sample size for the granite source were 17,286g at 4% air voids, 16,737g for 7% air voids for a 380mm x 100mm x 75mm slab; 10,795g at 4% air voids and 10,477g at 7% air voids for a 380mm x 63.5mm x 63.5mm slab. The slab specimens for the limestone source 18,325g at 4% air voids, 17,780g for 7% air voids for a 380mm x 100mm x 75mm slab, 11,475g at 4% air voids and 11,113g at 7% air voids for a 380mm x 63.5mm x 63.5mm slab. A total of 377 Superpave gyratory and 224 slab samples were batched for the 28 different mix designs.

The batching process started with the measurements of the Superpave gyratory compactor and the linear kneading compactor taking into consideration the final compaction heights of 170mm for the gyratory samples and 100mm and 63.5mm for the two different slab samples. The maximum theoretical specific gravity was used to calculate the bulk specific gravity at a specified air void level. The calculated bulk specific gravity is then multiplied by the volume of the mold and then divided by a correction factor (1.022 for the granite source and 1.013 for the limestone source) to estimate the target mix weight for a particular air void level.

Mixing and Compaction of Hot Mix Asphalt Specimens

First the aggregate and asphalt were brought up to the appropriate mixing temperature. The mixing and compaction temperatures were selected to be 155 and 135°C, respectively. Typically, a viscosity and temperature relationship is developed by testing the asphalt binder in a rotational viscometer. According to SP-2 manual, the mixing temperature should not exceed 165°C and the compaction temperature should not be lower than 115°C. In this research project there was an enormous undertaking with the amount of material being compacted and the broad range of binders, therefore common mixing and compaction temperatures were used for all mixtures instead of using different mixing and compaction temperatures for each of the 11 binders. The temperatures selected of 155 and 135°C were well within the range of the temperature-viscosity relationship developed by Superpave. Then liquid asphalt was added to the aggregate and the sample was thoroughly mixed to ensure uniform coating of the aggregate with the binder. The mixture was then placed back in the oven at the compaction temperature to short-term age for 2 hours. While the samples were aging the molds and appropriate tools needed for compaction were heated and brought to compaction temperature as well. The samples were then compacted and allowed to cool down to room temperature before further testing. The samples' bulk specific gravities were then measured according to ASTM D 2726 (Standard Test Method for Bulk Specific Gravity and Density of Non-Absorptive Compacted Bituminous Mixtures). Finally, each samples' air voids were calculated using the maximum theoretical and bulk specific gravities.

Delivery of Specimens

Eighty-four Superpave gyratory compacted specimens were delivered to the University of Minnesota for indirect tensile creep and strength testing. One hundred and twelve Superpave gyratory compacted specimens were delivered to the University of Minnesota for mixture fracture testing using the semi-circular bend test. Eight-four Superpave gyratory compacted specimens were delivered to the University of Illinois for the disc compact tension test

Extra Material

Due the extent of laboratory testing for this research project, extra material remained for the granite and limestone aggregate sources. The material has been sieved and stored in a fifty-five

gallon plastic container for future use. The asphalt binder is also stored in metal five gallon containers. The material was transported to MnRoads in Monticello, Minnesota where it will be stored until additional experimental cells in the experimental plan become available.

Preparation of Slab Compacted Specimens

Batching of Materials for Slabs

The first step in the sample preparation was to batch out the required amount of aggregate materials for each slab. The slab specimen sample size for the granite source were 17,286g at 4% air voids, 16,737g for 7% air voids for a 380mm x 100mm x 75mm slab; 10,795g at 4% air voids and 10,477g at 7% air voids for a 380mm x 63.5mm x 63.5mm slab. The slab specimens for the limestone source 18,325g at 4% air voids, 17,780g for 7% air voids for a 380mm x 100mm x 75mm slab, 11,475g at 4% air voids and 11,113g at 7% air voids for a 380mm x 63.5mm x 63.5mm slab. A total of 224 slab samples were batched for the 28 different mix designs.

The batching process started with the measurements of the linear kneading compactor taking into consideration the final compaction heights of 100mm and 63.5mm for the two different slab samples. The maximum theoretical specific gravity was used to calculate the bulk specific gravity at a specified air void level. The calculated bulk specific gravity is then multiplied by the volume of the mold and then divided by a correction factor (1.022 for the granite source and 1.013 for the limestone source) to estimate the target mix weight for a particular air void level.

Mixing and Compacting of Hot Mix Asphalt Slab Specimens

First the aggregate and asphalt were brought up to the appropriate mixing temperature. The mixing and compaction temperatures were selected to be 155 and 135°C, respectively. Typically, a viscosity and temperature relationship is developed by testing the asphalt binder in a rotational viscometer. According to SP-2 manual, the mixing temperature should not exceed 165°C and the compaction temperature should not be lower than 115°C. In this research project there was an enormous undertaking with the amount of material being compacted and the broad range of binders, therefore common mixing and compaction temperatures were used for all mixtures instead of using different mixing and compaction temperatures for each of the 11 binders. The temperatures selected of 155 and 135°C were well within the range of the temperature-viscosity relationship developed by Superpave. Then liquid asphalt was added to the aggregate and the sample was thoroughly mixed to ensure uniform coating of the aggregate with the binder. The mixture was then placed back in the oven at the compaction temperature to short-term age for 2 hours. While the samples were aging the appropriate aluminum gauge plates (1" aluminum plate and ½"aluminum plate to achieve 2½" thick slab), 1/8" steel plate, kneading keys and appropriate tools needed for compaction were heated and brought to compaction temperature as well. First, the aluminum plate was placed in the mold box, then the steel plate was placed on top of the aluminum plate as to not damage the aluminum plate. HMA was placed in the mold and spread out with a spatula with extra HMA placed in the corners. The keys were then placed on top of the HMA to knead/compact the slab. The roller was lowered and the pressure initialized. The HMA was compacted until the keys were flush with the mold surface in order to achieve the height of interest. Two slabs were able to be compacted simultaneously. The slabs were then compacted and allowed to cool down to room temperature before further testing. The samples' bulk specific gravities were then measured according to

ASTM D 2726 (Standard Test Method for Bulk Specific Gravity and Density of Non-Absorptive Compacted Bituminous Mixtures). Finally, each samples' air voids were calculated using the maximum theoretical and bulk specific gravities.

Delivery of Slab Specimens

Eighty-four slab compacted specimens were delivered to the University of Minnesota for Thermal Stress Restrained Specimen Tensile Strength Testing (TSRST). Fifty slab compacted specimens were delivered to the University of Wisconsin for dilatometric measurements. This represents a total of one hundred thirty-four slab compacted specimens.

Extraction and Recovery of Asphalt Binders

Extraction and Recovery for Rheological Testing

A limited number of cores and beams were obtained for the field sites selected in this study. To obtain enough recovered binder, previously tested IDT and SCB specimens were broken down and delivered in plastic labeled bags to MnDOT chemical Laboratory by the UMN team. All IDT and SCB specimens were obtained from the upper layer of each core. Table 4.5 below details the number of specimens used and the amount of binder recovered.

Table 4.5. Specimens used for extraction and recovery

Site:	Type of binder	Equivalence	No of SCB* specimens delivered	No of IDT** specimens delivered	Quantity of recovered AC (g)
MN Road 03	120/150	PG 58-28	6	2	220
MN Road 19	AC 20	PG 64-22	6	2	220
MN Road 33	PG 58-28	PG 58-28	6	2	184
MN Road 34	PG 58-34	PG 58-34	6	2	180
MN Road 35	PG 58-40	PG 58-40	6	2	148
MN CSAH 75 section 4WB	PG 58-28	PG 58-28	6	2	160
MN CSAH 75 section 2EB	PG 58-34	PG 58-34	6	2	183
WI US 45	PG 58-34	PG 58-34	6	2	229
WI STH 73	PG 58-28	PG 58-28	6	2	232
IL US 20 sect 6	AC 10	PG 58-28	6	0***	135
IL US 20 sect 7	AC 20	PG 64-34	6	0***	120
IL I 74	AC 20	PG 64-34	6	0***	127
ND SH 18	120/150	PG 58-28	6	2	204

*- semicircular specimen: diameter = 150 mm, thickness = 25 mm, weight = 500 g
**-circular specimen: diameter = 150 mm, thickness = 40 mm, weight = 1600 g
***- thickness of the core's upper layer was 37mm; no IDT was performed.

All specimens were extracted using according to MN/DOT Modified AASHTO T164 method. This method uses toluene as extraction solvent to prevent any interaction with the polymer present in the modified binders, as suggested in SHRP A-370.

Extraction and Recovery for "Aging" Testing

Although not included in the work plan the following experiment was performed to look at the variation of aging level with location within the pavement layers. Cores taken from the five MnRoad cells part of this study were cut in thin slices, with a thickness of approximately 5 mm. The slices were cut using a saw made by Sawing Systems, model 541OB with a 600 mm blade. According to the thickness of each core the following number of slices was obtained:

Table 4.6. AC slices from MnROAD cores

Site	Core thickness (mm)	No of thin slices
MnRoad cell 03	165	16
MnRoad cell 19	210	23
MnRoad cell 33	105	12
MnRoad cell 34	128	14
MnRoad cell 35	105	11

Each slice was put in a labeled bag, and delivered to Mn/DOT chemical laboratory where the following steps were performed:

1. The 1/8 inch slices were first crumbled by hand, approximately 25 grams of each thin section and placed into 50ml Nalgene centrifuge tubes. Then 25 ml of THF were added to the crumbled samples and the centrifuge tubes were capped.
2. The centrifuge tubes were shaken for 10 minutes on a laboratory shaker.
3. The samples were then centrifuged at 2400 rpm for 10 minutes.
4. The solvent /binder solution was decanted off into 1oz metal tins and evaporated to dryness (no presence of THF). THF is present when strong peaks at 910 and 1075 show up on the collected spectra.
5. Using a Thermo Nicolet Nexus 470 FT-IR with Omnic control software a spectrum of each sample was collected and saved it in the original condition with no spectral processing. Experiment conditions were as follows:
    a. Single bounce ATR with ZnSe crystal
    b. Automatic water vapor and CO_2 suppression
    c. Background collected before each sample

    Some of the binder was scraped off the inside of the tin and smeared onto the ZnSe crystal. The crystal was cleaned with toluene and then acetone. A couple of minutes were allowed for the solvent to evaporate before collecting the next background and sample spectra.

6. Using TQAnalyist spectral analysis software the area of the carbonyl peak at 1700 (analysis peak) was calculated by rationing against the peak at 1377 (path length peak) to account for sample preparation and path length differences. The following parameters were used in the calculation method:

    a. Path length peak

        i. Baseline points: 1325 to 1400

        ii. Measured area: 1325 to 1400

        iii. Approx. peak location: 1377

    b. Analysis Peak

        i. Baseline points: 1640 to 1800

        ii. Measure area: 1640 to 1750

        iii. Approx. peak location: 1700

7. The calculated areas were recorded. If the areas are negative there is little or no peak present and as a result baseline noise causes the spectra to pass both above and below the baseline used in step 6b. To help in evaluating and graphing the data, the lowest negative number present was set to zero and that amount was added to the rest of the calculated areas.

The results of the analysis are presented in the following figures.

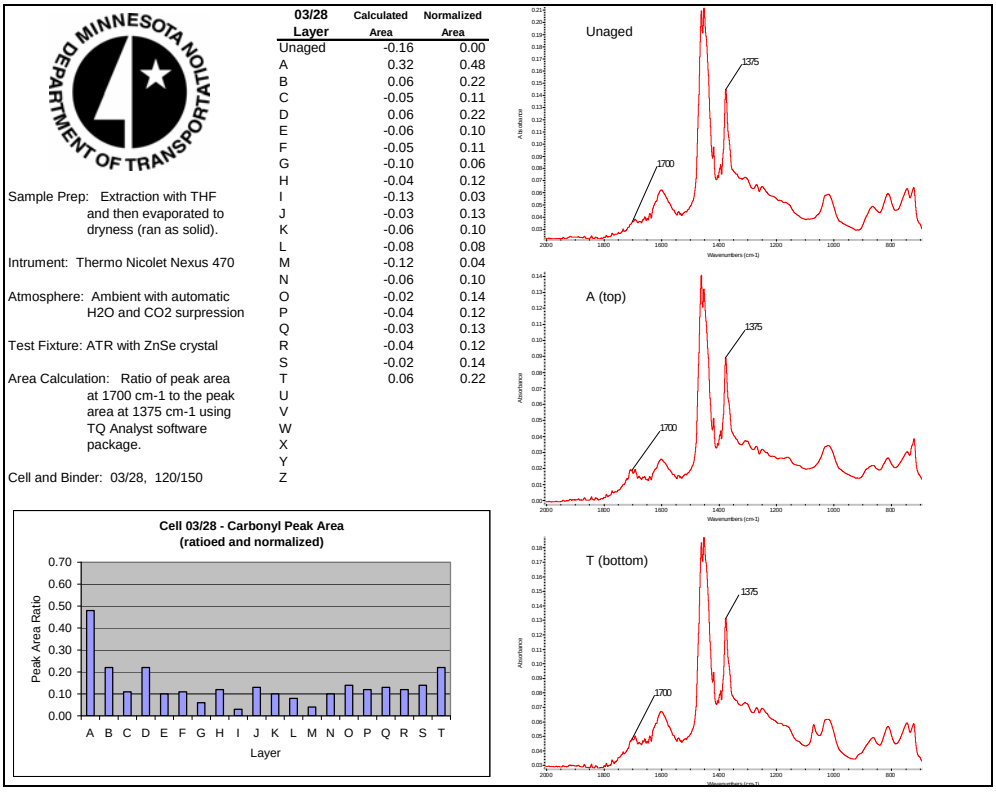

03/28 Layer	Calculated Area	Normalized Area
Unaged	-0.16	0.00
A	0.32	0.48
B	0.06	0.22
C	-0.05	0.11
D	0.06	0.22
E	-0.06	0.10
F	-0.05	0.11
G	-0.10	0.06
H	-0.04	0.12
I	-0.13	0.03
J	-0.03	0.13
K	-0.06	0.10
L	-0.08	0.08
M	-0.12	0.04
N	-0.06	0.10
O	-0.02	0.14
P	-0.04	0.12
Q	-0.03	0.13
R	-0.04	0.12
S	-0.02	0.14
T	0.06	0.22
U		
V		
W		
X		
Y		
Z		

Figure 4.4. Slice aging results for Cell 03

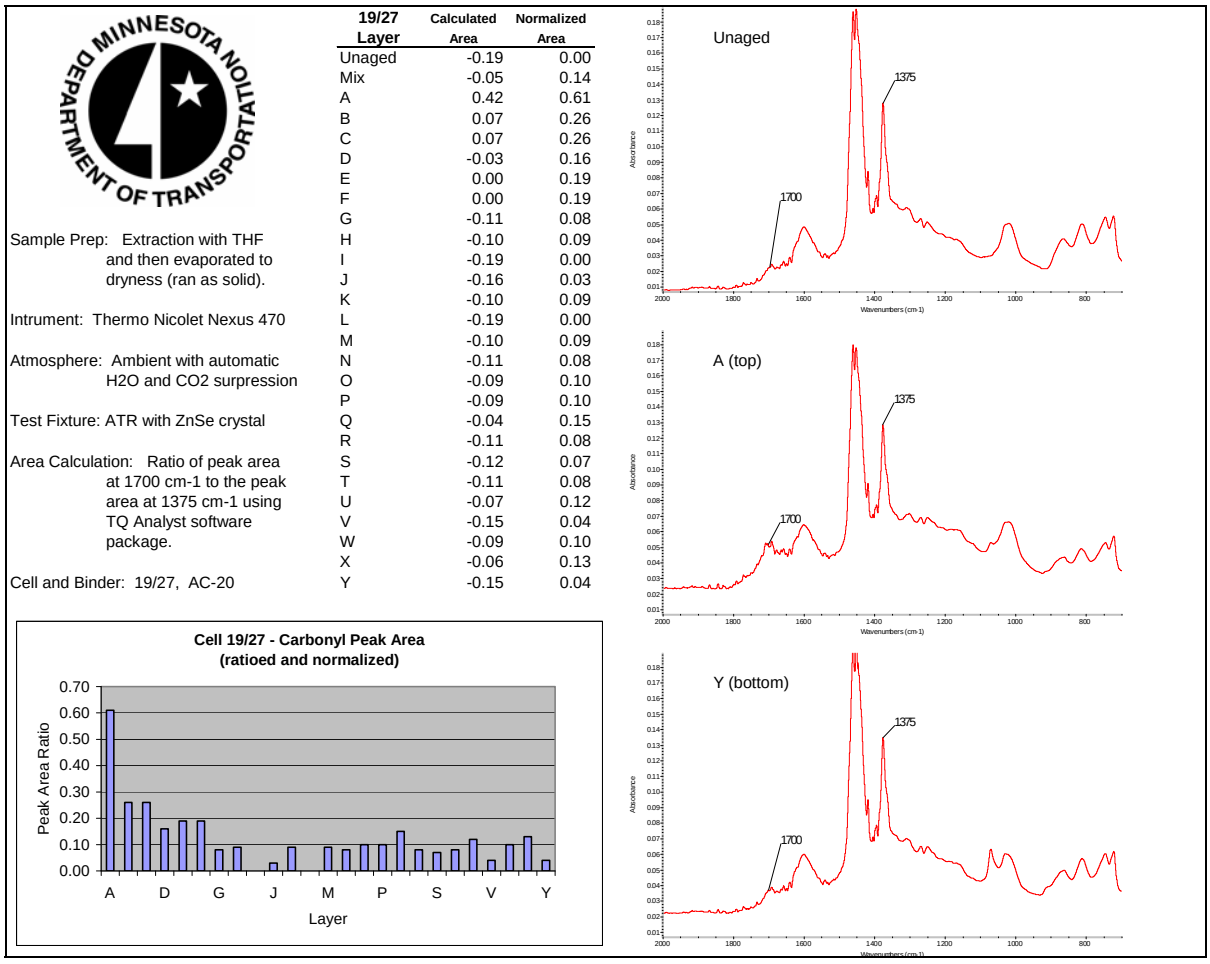

Figure 4.5. Slice aging results for Cell 19

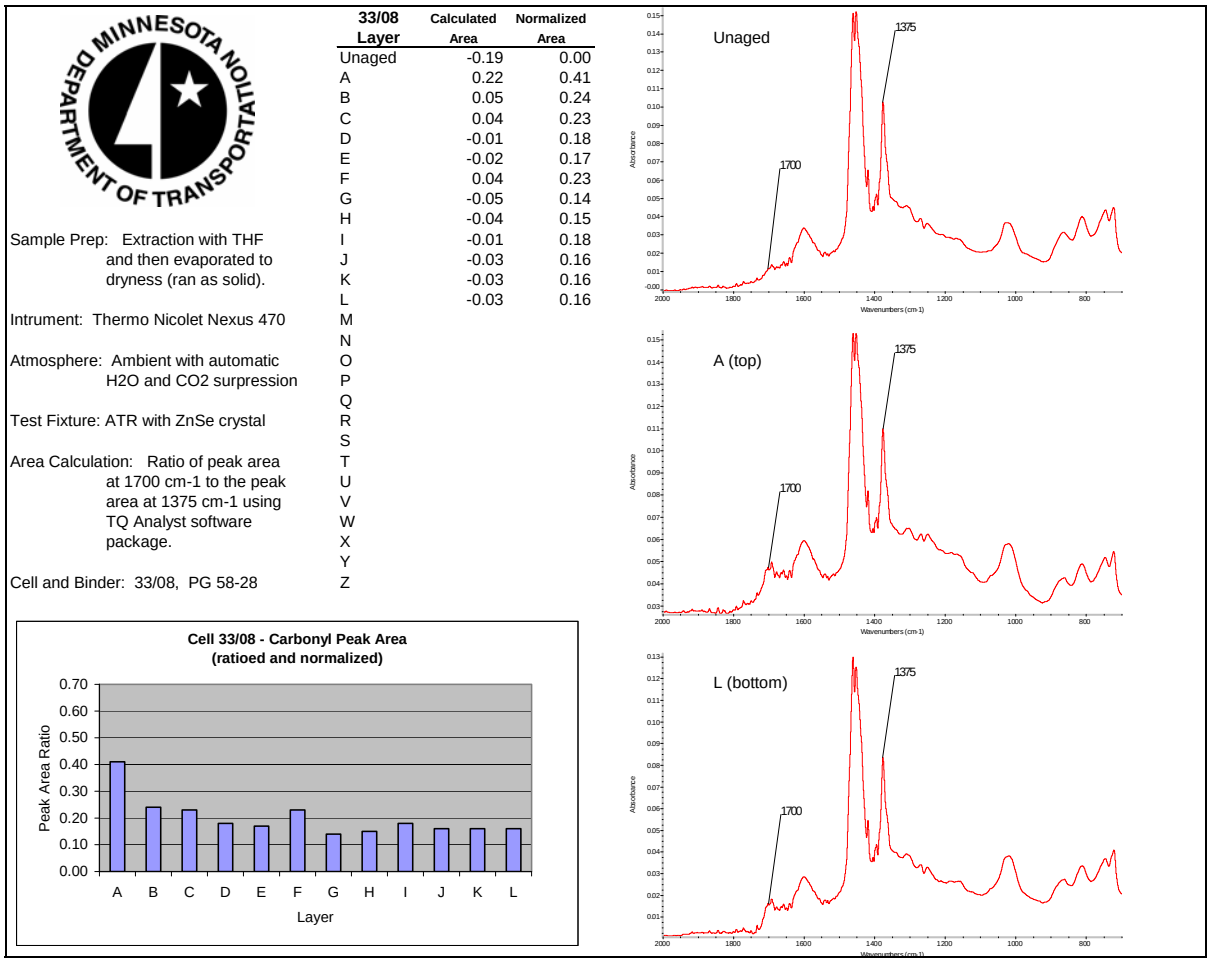

Figure 4.6. Slice aging results for Cell 33

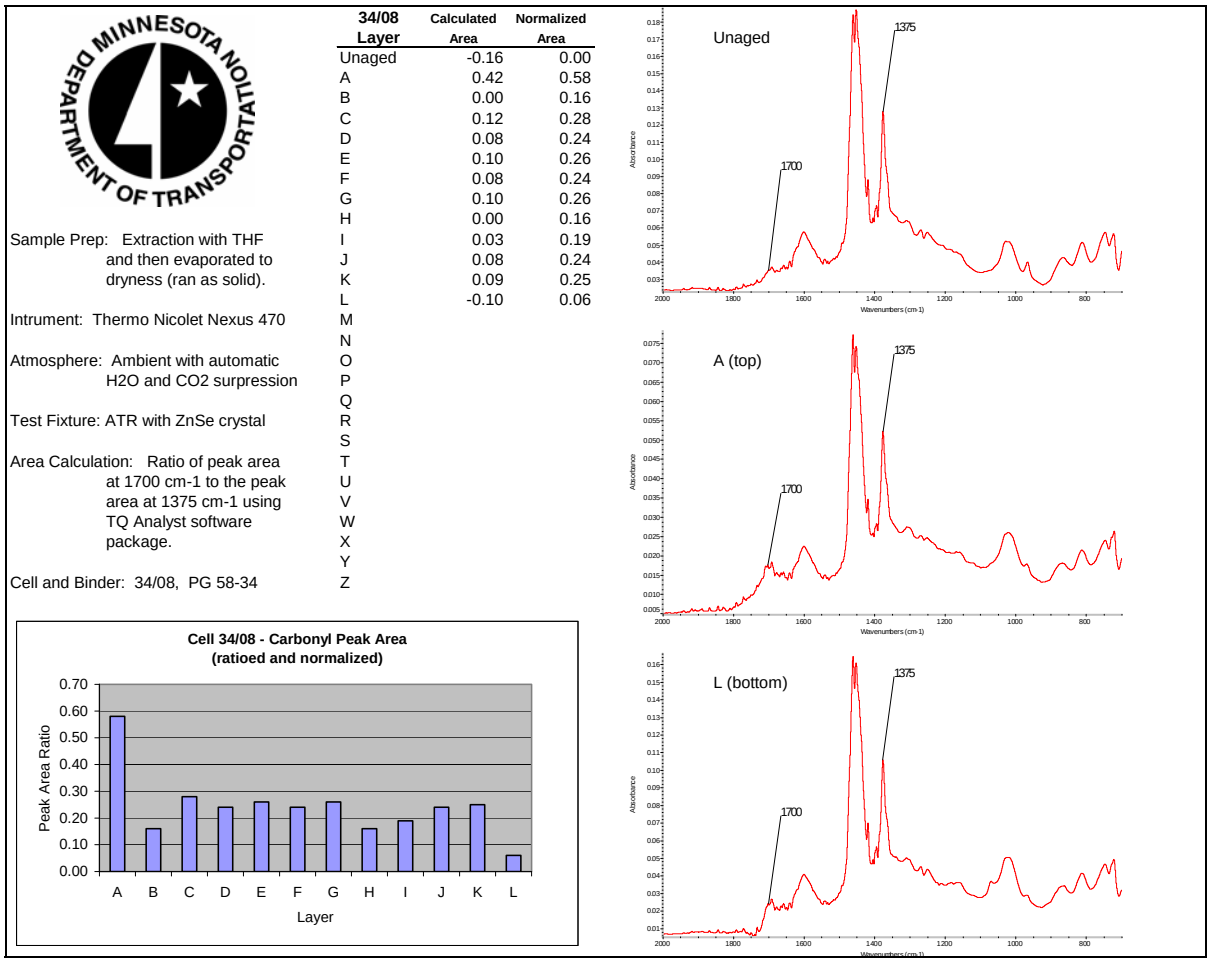

Figure 4.7. Slice aging results for Cell 34

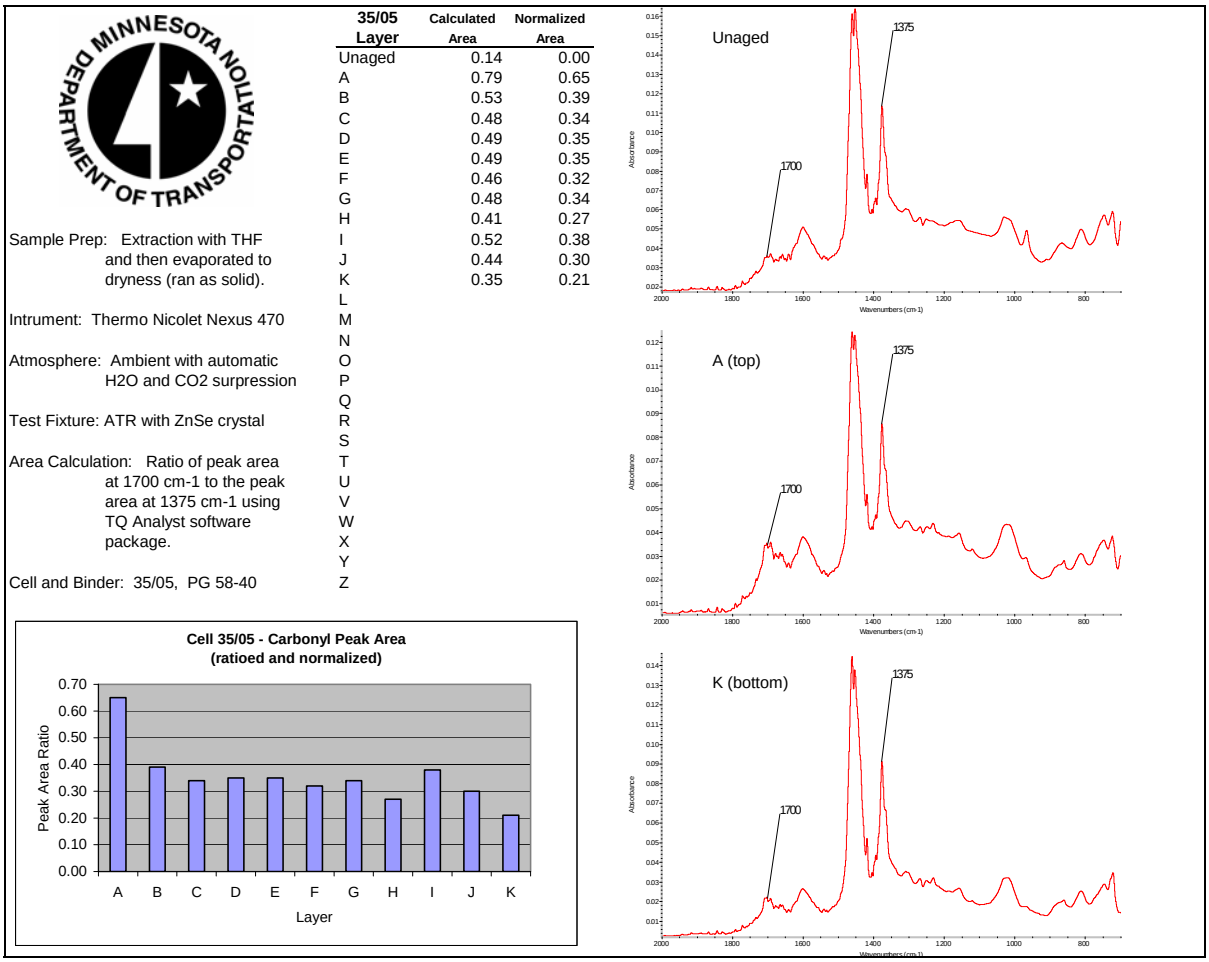

Figure 4.8. Slice aging results for Cell 35

Laboratory Aging of Asphalt Binders

The binders selected were aged to simulate two stages of the pavement field conditions:

1. Short term aging that occurs during production and construction. This was achieved using the Rolling Thin Film Oven Test (RTFOT) following the AASHTO T240 procedure.
2. Long term aging that occurs during pavement service life. This was achieved using the Pressure Aging Vessel (PAV) procedure following the AASHTO PP1 Procedure at 100 C.

Aging was performed according to the methods above by the University of Wisconsin (UW) research team. The samples were then distributed between UW and UMN to conduct the required testing according to the experimental plan. Table 4.7 lists the binders aged, the grade, the amount kept for rheological or glass transition temperature (T_g) measurements and the type of binder, whether modified or not. An additional binder, PG70-22, was also aged, as shown in Table 4.7.

Table 4.7. List of binder aged and their distribution in the order they were received

	Binder name	PG grade	AGED				
			RTFO (UW)	PAV (UW)	T_g (UW)	RTFO (UMN)	PAV (UMN)
1	SBS, Flint Hills	PG 58 -40	70g	37g	20g	450-500g	160g
2	Elvaloy, Murphy	PG 58 -34	70g	44g	20g	450-500g	154g
3	SBS, Flint Hills	PG 58 -34	70g	35g	20g	450-500g	180g
4	Neat, Seneca	PG 58 -28	70g	41g	20g	450-500g	168g
5	Neat, Payne & Dolan	PG 58 -28	70g	43g	20g	450-500g	166g
6	Elvaloy, Murphy	PG 64 -34	70g	37g	20g	450-500g	149g
7	Black Max, Husky	PG 64 -34	70g	38g	20g	450-500g	145g
8	Neat, Seneca	PG 64 -28	70g	40g	20g	450-500g	160g
9	SBS, Seneca	PG 64 -28	70g	35g	20g	450-500g	151g
10	Neat, Seneca	PG 64 -22	70g	38g	20g	450-500g	173g
6	*SBS, Seneca*	*PG 70 -22*	*70g*	*34g*	*20g*	*450-500g*	*168g*

CHAPTER 5

BINDER TESTING

Dilatometric Testing

The test procedure and results of dilatometric testing to measure glass transition (Tg) performance for laboratory-aged asphalt binders, and field extracted asphalt binders, are presented in the first part of this chapter. The part is divided in three sections: PAV-aged binders, RTFOT-aged binders and field-aged extracted binders.

PAV Aged Asphalt Binders

The procedure for this test includes the sample preparation, calibration of measuring instrument and measurements of thermo-volumetric response parameters.

PAV Aged Sample Preparation

Binders used for this part of the testing were PAV aged according to procedure outlined in the AASHTO PP1 procedure. The steps taken in the preparation of samples include annealing the PAV aged binder by heating it until it was sufficiently fluid to pour into two clean silicon rubber molds. The entire assembly was allowed to cool on the bench top at ambient temperature (21-23°C) for 60 minutes after which the samples were trimmed and dressed with hot knife until a shinning surface was achieved. After dressing, the specimens were allowed to cool on the bench top at ambient temperature for another 15 minutes before demoded and inspected. At this stage if there is any suspicion of air bubble inclusion in the prepared sample it was discarded, otherwise the samples weight were determined and sample made ready for Tg test.

It's worth noting that sample preparation was the major challenge in this test procedure due to the need to remove all air bubbles entrapped in the sample after PAV aging. It was clearly observed that minor variability in de-airing of the sample after PAV can result in important changes of the Tg values. Also, timing of the testing after pouring sample could have an effect due to physical hardening. Several samples were discarded whenever it was suspected that it might contain air bubbles especially for the polymer-modified binders.

Assembly of the Dilatometric Apparatus

As shown in Figure 5.1, The Tg Test System consists of:

1. Two dilatometers cells each containing a binder specimen submerged in ethyl-alcohol,
2. An insulated chamber for temperature control during testing and conditioning of specimen.
3. Real-time temperature measuring and recording devices.
4. A volume change measuring system.
5. A cooling unit consisting liquid nitrogen, and
6. A heating unit installed in the environmental chamber.

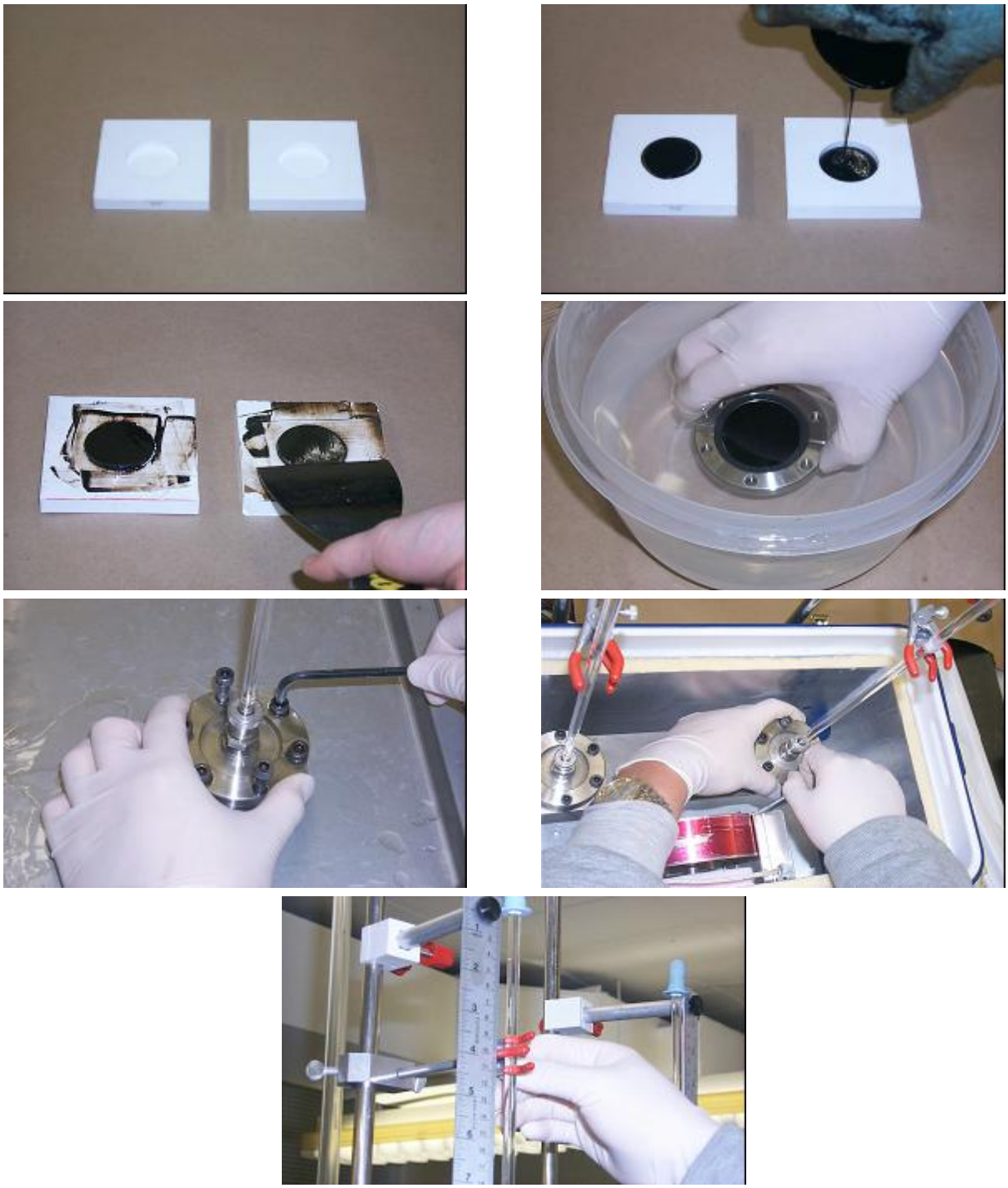

Figure 5.1. Assembly of the dilatometric apparatus

Dilatometer: – A dilatometer consists of the aluminum cell connected to a precision-bore capillary tube, which opens to the atmosphere at its top end. Asphalt specimens approximately 10 ml were placed inside the cell.

Insulated Chamber: - This chamber is designed and insulated for the placement of the dilatometric cells and for heating and cooling of the air from 40°C to -76°C. Heater is installed inside of the chamber to control temperature and the cooled air is provided from the liquid

nitrogen tank that is directly connected to the temperature chamber through a controlled valve. The chamber also houses the temperature sensors and fan.

Temperature Measuring and Recording Device: – Temperature was measured with temperature devices with sensitivity of 0.001°C placed in the chamber and connected to data acquisition system.

Volume Change Measuring System: – The volume change of asphalt binder specimen was measured on a level-measuring frame. The frame supports two capillary glass tubes holding ethyl alcohol as an indicator of volume change of asphalt binder specimen.

Cooling Unit and Medium: –Liquid nitrogen was selected as cooling medium due to its economical procurement. Liquid nitrogen is capable of cooling the air down to the desired low temperature, -76°C.

Heating Unit: – A heating fan was installed in the insulated chamber.

Test Procedure

Testing procedure involves assembling of dilatometer cell, filling the capillary tube with ethyl alcohol (to a medium height for reading volume change) with the aid of suction rubber and tightening all connecting bolts to seal the cell. These steps were performed in ethyl alcohol bath so as to prevent the inclusion of air bubbles in the system (Figure 5.1). The assembling of the dilatometer was then mounted into the environmental chamber and all supporting equipment such as circulating fan, heating motor, computer and temperature control sensor were plugged in and initiated. The main valve for the inflow of liquid nitrogen was opened and the software loaded.

The test conditions was set up with temperature change rate fixed for all tests at 1°C/min, which was chosen for practical reasons and represented what had been used in previous studies (96).

Testing starts at + 40°C and remains for 10 minutes for specimens to achieve temperature equilibrium. After this duration of stable temperature, it is cooled at the rate of 1°C/min. to -76°C. The total required testing time is 126 minutes (2 hours and 6 minutes). The reading of capillary height and temperature was recorded every 2 minutes in a prepared sheet. To estimate the experimental error, measurements were made in two independent replicates. Independent replication means that a different specimen is used in a different dilatometric cell.

Calibrations were performed to account for the change in the capillary height due to changes in the volume of alcohol and the inside volume of the dilatometeric cell. Each cell was calibrated using an aluminum specimen identical in volume to the asphalt specimen (Figure 5.2). The exact testing procedure used for asphalt samples was followed for the aluminum samples.

In addition, in order to account for the difference between the interior temperature of the cell and cooling chamber temperature, dilatometeric cell temperature calibration was carried out in relation with cooling chamber and the correlation derived was used for Tg calculation (Figure 5.3).

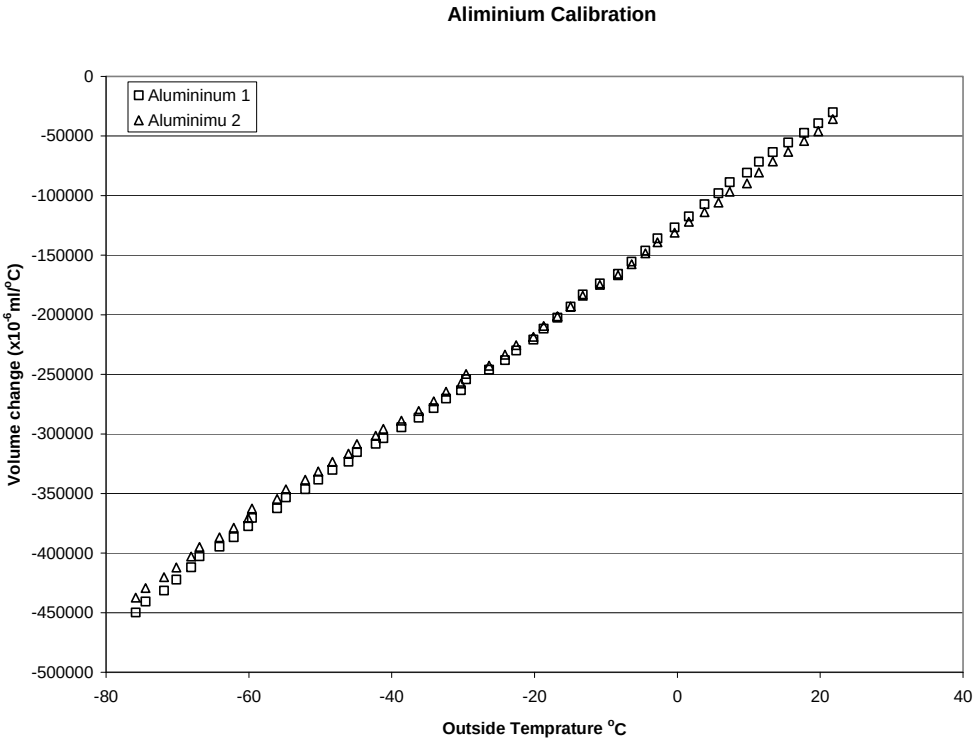

Figure 5.2. Calibration for measuring volume change of alcohol medium and cells using an Aluminum specimen

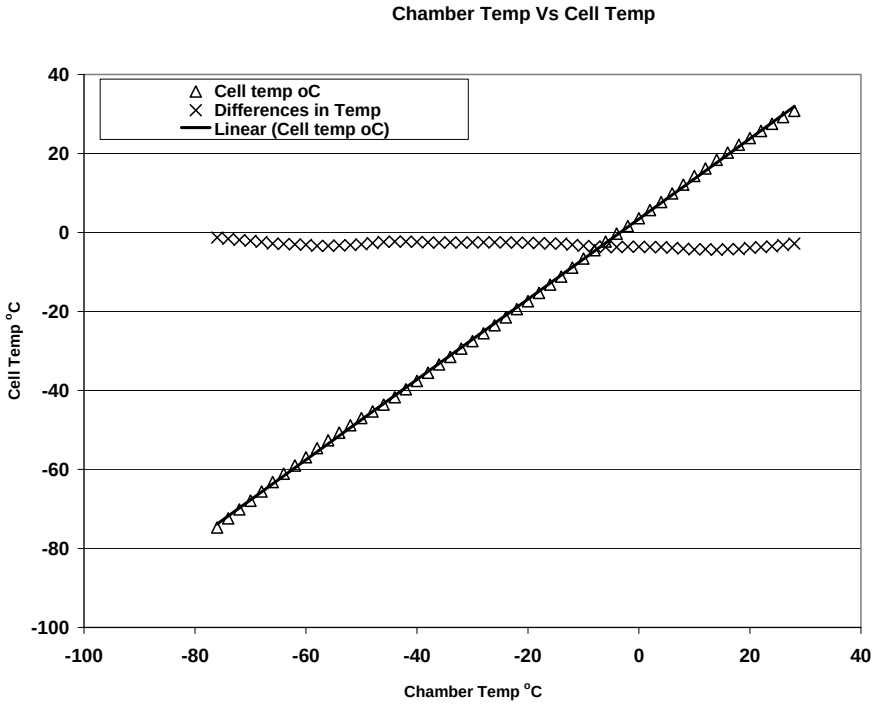

Figure 5.3 Temperature correction chart used to correct the outside chamber temperature to reflect the inside cell temperature

Computation

Data collected were analyzed using regression analysis method in Excel spreadsheet and curve fitting for each sample was drawn. The following hyperbolic equation, which has been used to fit binder thermo-volumetric properties (97), was applied to the data, and found to be effective to fit the nearly dual-linear curve. Figure 5.4 shows sample of the result and the fitted curve.

$$v = c_v + \alpha_g(T - T_g) + R(\alpha_l - \alpha_g)\ln\{1 + \exp[(T - T_g)/R]\}$$

where:

v = specific volume change in ml/g,

c_v = constant,

R = regression constant related to the rate of the volume change at and near the glass transition temperature,

T = test temperature in °C,

T_g = glass transition temperature in °C,

α_g = coefficients of contraction above the glass transition temperature in 10^{-6}/C, and

α_l = coefficients of contraction below the glass transition temperature in 10^{-6}/C.

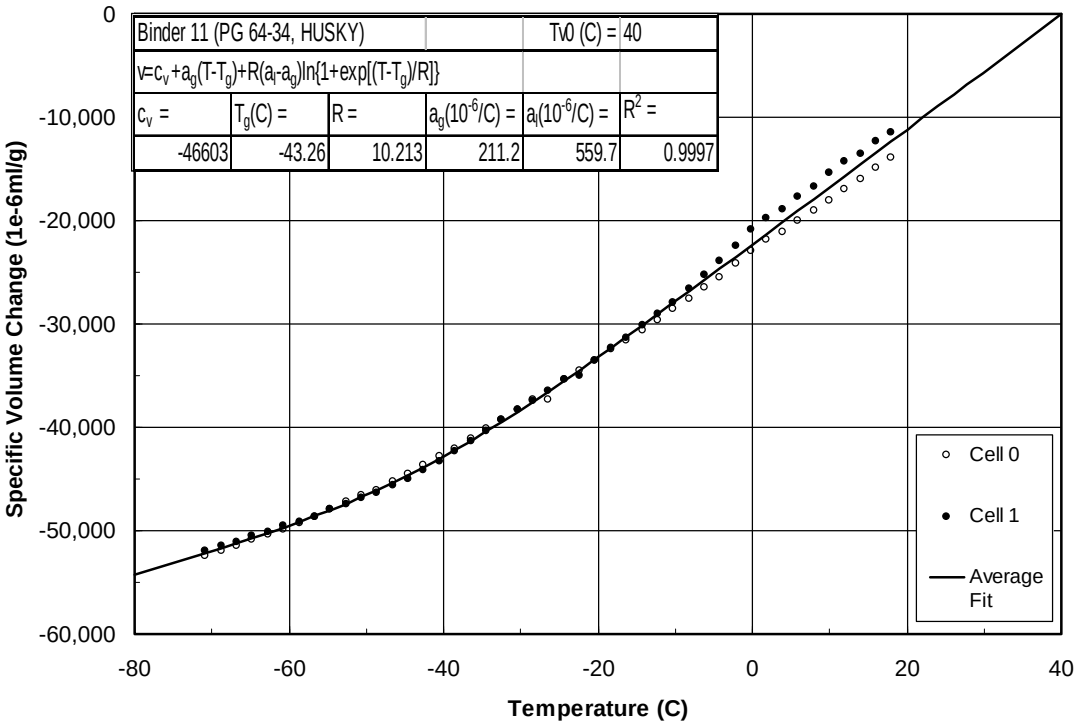

Figure 5.4. Typical Tg output

PAV-Aged Asphalt Binders Testing Results

Summary of the results for the PAV aged binders measured is shown in Table 5.1. As described earlier, each binder was tested in two replicates. However, to measure the reproducibility of the measurements as determined using independent samples, three of the binders were tested at

different times, using different samples. Table 5.1 includes the repeatability of the results measured for two random samples (LTCPB08 and LTCPB11). There is a relatively good agreement for the coefficients of thermal contractions above and below Tg for both binders. However, the values of the Tg show a relatively high range, particularly for the PG 64-34.

Table 5.1. PAV aged asphalt binders test results

Sample No.	PG	NAME	Tg(^{o}C)	α_g(10-6/^{o}C)	α_l(10-6/^{o}C)	R^2
LTCPB10	PG 58-40	58-40 SBS Flint Hills	-24.98	333.39	538.29	.09989
LTCPB08 Repeat 1	PG 58-34	58-34 Elvaloy Murphy	-35.74	160.8	474.3	0.9998
LTCPB08 Repeat 2	PG 58-34	58-34 Elvaloy Murphy	-38.56	125.4	452.5	0.9998
LTCPB09	PG 58-34	58-34 SBS Flint Hills	-29.64	195.9	583.26	0.9997
LTCPB01	PG 58-28	58-28 Plain Seneca	-20.14	202.74	477.28	0.9994
LTCPB02	PG 58-28	58-28 Plain P+D	-26.42	350.6	578.4	0.9998
LTCPB06	PG 64-34	64-34 Elvaloy Murphy	-34.41	214.58	458.88	0.9998
LTCPB11 Repeat 1	PG 64-34	64-34 Black Max Husky	-43.26	211.25	559.73	0.9997
LTCPB03	PG 64-28	64-28 Plain Seneca	-31.03	224.5	545.4	0.9997
LTCPB04 Repeat 1	PG 64-28	64-28 SBS Seneca	-26.55	272.77	444.77	0.9995
LTCPB04 Repeat 2	PG 64-28	64-28 SBS Seneca	-21.97	252.8	467.7	0.9998
LTCPB05	PG 64-22	64-22 Plain Seneca	-31.87	308.86	513.69	0.9995

Figure 5.5 and Figure 5.6 show the replicate measurements for these binders. It can be seen that a rather good repeatability is observed for the Binder #8 (PG 58-34) but a poor repeatability is seen for the other binder (PG 64-34). It is hypothesized that the lack of good repeatability is due to air entrapment during sample preparation. The PG 64-34 is a very unique binder that is extremely sticky and difficult to handle. It is recommended that testing of the RTFO aged material be used because there is less possibility of air entrapment in the samples. Also for modeling of thermal cracking in the field the less aged condition could be more relevant.

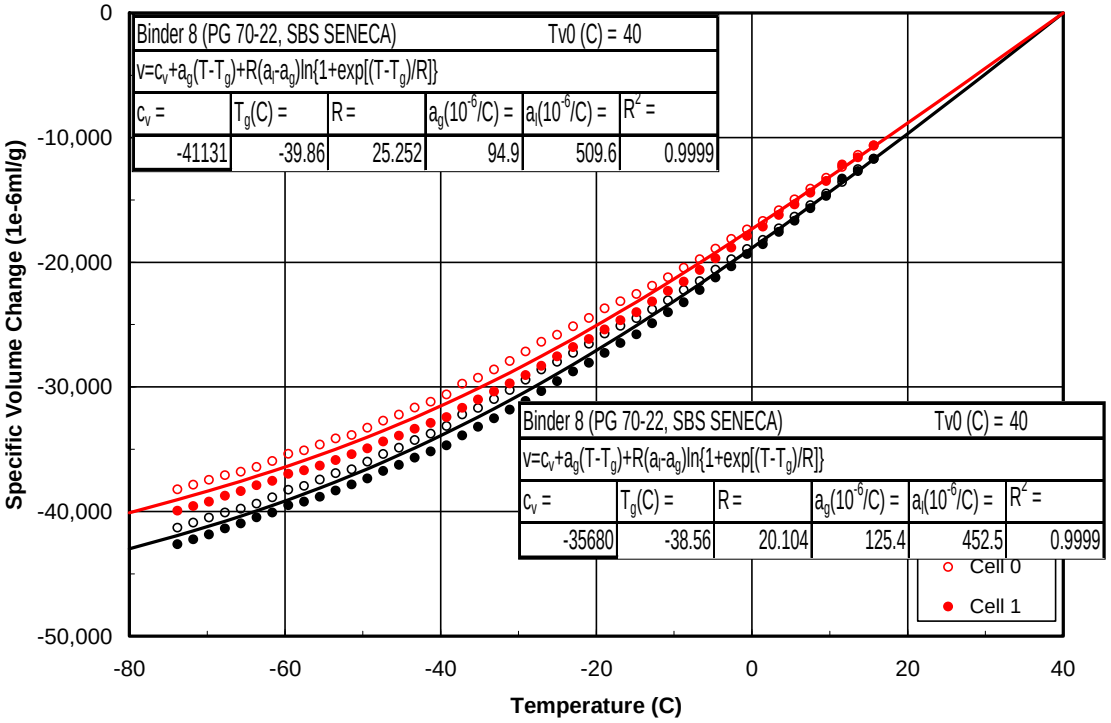

Figure 5.5. Typical Tg output with replicate

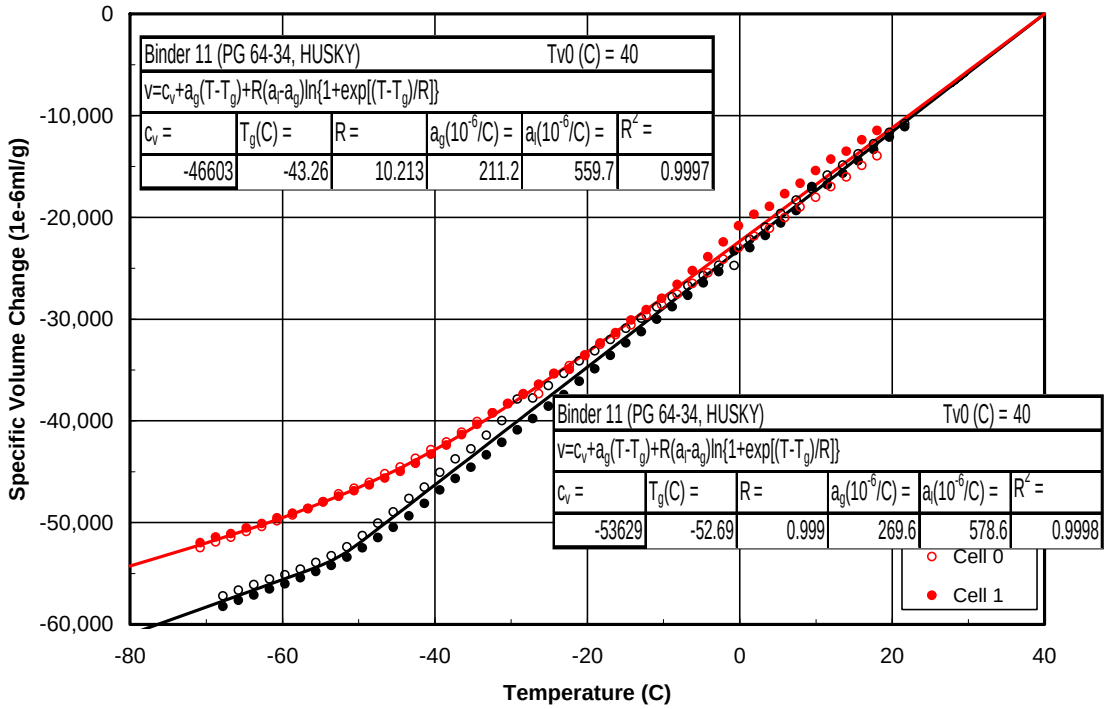

Figure 5.6. Output with replicate for the PG 64-34 sample

RTFOT Aged Binders

Using the same protocol the RTFO-Aged binders were tested for the Tg properties. The calibration was repeated to ensure accurate results and a new calibration data set was used. The new data set was very similar to the set measured before the PAV aged samples were tested, which indicates the stability of the testing device.

Summary of the results for the RTFO aged binders results are shown in the Table 5.2. It is noted that the samples 58-40:M1 and sample 58-34:M2 were not included due to lack of sufficient material for conducting the RTFO aging. Similar to the PAV-aged samples, the testing was done in duplicate samples and the results for the two dilatometric cells were averaged.

Table 5.2. Dilatometric results for RTFO aged laboratory binders

Binders			Thermal Properties			
ID	**PG**	**NAME**	**T_g(°C)**	**$\alpha_g(10^{-6}/C)$**	**$\alpha_l(10^{-6}/C)$**	**R^2**
58-40:M1	**PG 58-40**	**Modifier 1, SBS (Flint Hills Res.)**		Short of Material		
58-34:M1	**PG 58-34**	**Modifier 1, Elvaloy (Murphy)**	-30.95	216.99	454.20	0.9998
58-34:M2	**PG 58-34**	**Modifier 2, SBS (Flint Hills Res.)**		Short of Material		
58-28:U1	**PG 58-28**	**Plain 1, (Seneca)**	-31.26	250.02	526.00	0.9999
58-28:U2	**PG 58-28**	**Plain 2, (Payne and Dolan)**	-29.33	257.60	524.44	0.9999
64-34:M1	**PG 64-34**	**Modifier 1, Elvaloy (Murphy)**	-34.06	173.90	465.31	0.9999
64-34:M2	**PG 64-34**	**Modifier 2, Black Max (Husky)**	-30.54	241.08	495.64	0.9998
64-28:U1	**PG 64-28**	**Plain 1, (Seneca)**	-29.65	247.69	523.01	0.9999
64-28:M1	**PG 64-28**	**Modifier 1, SBS (Seneca)**	-29.08	260.11	529.53	0.9998
64-22:U1	**PG 64-22**	**Plain 1, (Seneca)**	-27.21	282.94	555.61	0.9999

Field Extracted Asphalt Binders

The testing method used for the field extracted binders is similar to the method used for the laboratory-aged binders except that the extracted binders were not aged. The dilatometeric testing for extracted binders test were also carried out in duplicates. Table 5.3 gives summaries of the dilatometeric properties of the extracted binders based on averaging the measurements of the duplicate samples.

Table 5.3. Summary of the dilatometeric properties of field extracted binders

Binders				Thermal Properties			
Site	**Code name**	**Original binder grade**	**Equivalent binder grade**	**T_g(°C)**	**$\alpha_g(10^{-6}/C)$**	**$\alpha_l(10^{-6}/C)$**	**R^2**
MnROAD Cell 03	**MnROAD 03**	120/150	PG 58-28	-27.40	296.69	548.16	0.9995
MnROAD Cell 19	**MnROAD 19**	AC-20	PG 64-22	-21.01	335.16	556.31	0.9996
MnROAD Cell 33	**MnROAD 33**	PG 58-28	PG 58-28	-21.00	335.05	556.47	0.9992
MnROAD Cell 34	**MnROAD 34**	PG 58-34	PG 58-34	-20.11	220.76	660.64	0.9993
MnROAD Cell 35	**MnROAD 35**	PG 58-40	PG 58-40	-40.69	285.75	569.02	0.9999
MN CSAH-75, section 2 EB	**MN75 2**	PG 58-28	PG 58-28	-23.61	294.60	523.29	0.9999
MN CSAH-75, section 4 WB	**MN75 4**	PG 58-34	PG 58-34	-24.37	331.08	586.20	0.9999
WI US-45	**WI US 45**	PG 58-34	PG 58-34	-24.54	269.82	566.13	0.9998
WI STH-73	**WI STH 73**	PG 58-28	PG 58-28	-30.36	286.59	560.24	0.9998
IL US-20, section 6	**IL US20 6**	AC-10	PG 58-28	-28.78	311.20	550.80	0.9999
IL US-20, section 7	**IL US20 7**	AC-20	PG 64-22	-29.05	255.27	481.54	0.9999
IL I-74	**IL I74**	AC-20	PG 64-22	-28.13	292.80	498.94	0.9999
ND SH-18	**ND 18**	120/150	PG 58-28	-27.50	287.01	539.73	0.9999

Rheological Testing

This section presents the results of the rheological testing of binders aged in the laboratory and binders extracted from the cores. Original binders that were used in gyratory specimens' preparation were aged using two procedures: Rolling Thin Film Oven Test (RTFOT) - AASHTO T240 and Pressure Aging Vessel (PAV) - AASHTO PP1. The details of these procedures are given in Chapter 4 that also outlines the methodology of the binder extraction from the field cores.

Table 5.4 presents the details on the laboratory binders testing - manufacturer and type of modification, if any, as well as the test temperatures based on the PG grade of the original binder. Table 5.5 presents the extracted binders, their source site, and test temperatures.

Table 5.4. Test temperatures for laboratory binders

Binder details	Code name	Test temperatures (DT, DENT, BBR)		
	Temperature* ->	H	I	L
PG58-40, modifier 1 SBS (Flint Hills Res.)	58-40 M1	-30	-36	-42
PG58-34, modifier 1 Elvaloy (Murphy)	58-34 M1	-24	-30	-36
PG58-34, modifier 2 SBS (Flint Hills Res.)	58-34 M2	-24	-30	-36
PG58-28, plain 1 (Seneca Petroleum)	58-28 U1	-18	-24	-30
PG58-28, plain 2 (Payne and Dolan)	58-28U2	-18	-24	-30
PG64-34, modifier 1 Elvaloy (Murphy)	64-34 M1	-24	-30	-36
PG64-34, modifier 2 Black Max (Husky)	64-34 M2	-24	-30	-36
PG64-28, plain 1 (Seneca)	64-28 U1	-18	-24	-30
PG64-28, modifier 1 SBS (Seneca)	64-28 M1	-18	-24	-30
PG64-22, plain (Seneca)	64-22 U1	-12	-18	-24

***** H – high, I – intermediate, L – low

Table 5.5. Equivalent PG grade and test temperatures for extracted binders

Site	Code name	Original binder grade	Equivalent binder grade	Test temperatures (DT, DENT, BBR)		
			Temperature[1] ->	H	I	L
MnROAD Cell 03	MnROAD 03	120/150	PG 58-28	-18	-24	-30
MnROAD Cell 19	MnROAD 19	AC-20	PG 64-22[2]	-18	-24	-30
MnROAD Cell 33	MnROAD 33	PG 58-28	PG 58-28	-18	-24	-30
MnROAD Cell 34	MnROAD 34	PG 58-34	PG 58-34	-24	-30	-36
MnROAD Cell 35	MnROAD 35	PG 58-40	PG 58-40	-30	-36	-42
MN CSAH-75, section 2 EB	MN75 2	PG 58-28	PG 58-28	-18	-24	-30
MN CSAH-75, section 4 WB	MN75 4	PG 58-34	PG 58-34	-24	-30	-36
WI US-45	WI US 45	PG 58-34	PG 58-34	-24	-30	-36
WI STH-73	WI STH 73	PG 58-28	PG 58-28	-18	-24	-30
IL US-20, section 6	IL US20 6	AC-10	PG 58-28	-18	-24	-30
IL US-20, section 7	IL US20 7	AC-20	PG 64-22[2]	-18	-24	-30
IL I-74	IL I74	AC-20	PG 64-22[2]	-18	-24	-30
ND SH-18	ND 18	120/150	PG 58-28	-18	-24	-30

[1] H – high, I – intermediate, L – low

[2] test temperatures based on PG 64-28

Table 5.6 presents the number of replicates used in each test. That number depended on the test, binder type, and the loading rate. Note that in some cases, even though the tests were performed, they did not produce acceptable results (e.g. specimen did not break at all or 3% strain was reached, in DT or DENT). Thus, these results were removed from the analysis. Also, due to DT equipment malfunction, DT and DENT were not conducted below -30°C.

Table 5.6. Number of replicates in binder testing

Binder	DT		DENT	BBR
	1%/min	3%/min	1%/min	
RTFOT	3	6	6	2
PAV	n/a*	3	2	1
Extracted	n/a*	3	3	2

* not tested

Bending Beam Rheometer (BRR)

The bending beam rheometer (BBR) testing was performed on a Cannon thermoelectric rheometer, according to AASHTO T 313-05 standard (2). Tests were conducted at three temperatures as presented in Table 5.4 and Table 5.5 with two replicates for RTFOT and extracted binders, and one replicate for PAV (see Table 5.6). In addition to the standard procedure (1 hour conditioning at test temperature), each beam was kept in the bath for additional 19 hours and re-tested in order to investigate physical hardening effect. The results are given in Tables 5.7-5.9.

Table 5.7. BBR creep stiffness @ 60sec, RTFOT binders

Conditioning ->		1 hour				20 hours			
Binder	Temp.	S [MPa]	CV S [%]	m-value	CV m-value [%]	S [MPa]	CV S [%]	m-value	CV m-value [%]
58-40M1	-30	75	5.2	0.461	6.8	88	9.3	0.391	0.3
	-36	197	2.2	0.345	2.9	258	4.1	0.320	0.4
	-42	462	2.3	0.286	1.4	614	2.8	0.242	1.1
58-34 M1	-24	200	4.6	0.409	2.2	246	1.3	0.365	0.2
	-30	468	1.3	0.304	3.3	607	2.9	0.262	0.8
	-36	989	7.8	0.216	1.9	1149	7.8	0.171	0.1
58-34 M2	-24	179	0.4	0.377	0.6	227	4.2	0.342	0.6
	-30	433	2.4	0.294	1.8	575	1.5	0.248	0.3
	-36	858	0.3	0.211	2.0	1094	0.9	0.172	2.6
58-28 U1	-18	115	0.2	0.387	1.1	149	3.9	0.334	1.2
	-24	231	4.4	0.323	2.5	327	1.9	0.273	2.6
	-30	556	1.1	0.248	4.1	722	5.7	0.199	1.8
58-28 U2	-18	142	7.5	0.414	0.8	179	5.3	0.370	1.0
	-24	317	n/a*	0.327	n/a	391	3.2	0.287	2.0
	-30	n/a**	n/a**	n/a**	n/a**	n/a**	n/a**	n/a**	n/a**
64-34 M1	-24	173	2.0	0.411	0.6	216	1.3	0.374	0.2
	-30	474	3.1	0.311	1.0	596	5.7	0.266	2.1
	-36	923	2.9	0.217	2.1	1108	0.1	0.176	1.1
64-34 M2	-24	150	1.5	0.404	1.1	177	2.5	0.370	0.0
	-30	393	3.2	0.313	0.6	479	2.8	0.273	1.5
	-36	792	5.3	0.229	0.1	954	10.1	0.197	0.2
64-28 U1	-18	213	1.4	0.337	0.3	280	3.7	0.282	3.0
	-24	381	4.8	0.272	1.3	548	2.5	0.216	0.6
	-30	n/a**	n/a**	n/a**	n/a**	n/a**	n/a**	n/a**	n/a**
64-28 M1	-18	120	0.6	0.377	0.7	173	0.8	0.337	0.3
	-24	274	0.3	0.309	1.2	360	3.8	0.270	3.5
	-30	599	0.5	0.237	0.4	804	0.8	0.193	2.6
64-22 U1	-12	n/a**	n/a**	n/a**	n/a**	n/a**	n/a**	n/a**	n/a**
	-18	118	4.8	0.365	0.5	148	0.8	0.323	0.9
	-24	274	7.0	0.309	3.3	364	3.6	0.271	0.4

* only one replicate

** specimen either cracked during testing or deflections were too large

Table 5.8. BBR creep stiffness @ 60sec, PAV binders

Conditioning ->		1h		20h	
Binder	Temp.	S [MPa]	m-value	S [MPa]	m-value
58-40 M1	-30	111	0.320	136	0.290
	-36	236	0.285	293	0.261
	-42	484	0.252	602	0.223
58-34 M1	-24	274	0.320	363	0.284
	-30	619	0.255	746	0.226
	-36	1035	0.203	1234	0.174
58-34 M2	-24	219	0.332	282	0.294
	-30	479	0.269	595	0.238
	-36	854	0.207	1105	0.164
58-28 U1	-18	176	0.322	230	0.278
	-24	316	0.268	417	0.227
	-30	n/a*	n/a*	n/a*	n/a*
58-28 U2	-18	224	0.344	271	0.302
	-24	444	0.281	528	0.238
	-30	847	0.219	1026	0.177
64-34 M1	-24	248	0.341	296	0.302
	-30	515	0.269	665	0.231
	-36	1032	0.202	1199	0.158
64-34 M2	-24	201	0.330	245	0.304
	-30	469	0.275	573	0.237
	-36	814	0.210	907	0.165
64-28 U1	-18	245	0.314	326	0.270
	-24	450	0.268	591	0.218
	-30	798	0.215	1027	0.156
64-28 M1	-18	176	0.296	209	0.266
	-24	306	0.262	387	0.220
	-30	539	0.233	685	0.186
64-22 U1	-12	129	0.341	172	0.279
	-18	286	0.278	370	0.237
	-24	n/a**	n/a**	n/a**	n/a**

** specimen either cracked during testing or deflections were too large

Table 5.9. BBR creep stiffness @ 60sec, extracted binders

Conditioning ->		1 hour				20 hours			
Binder	Temp	S [MPa]	CV S [%]	m-value	CV m-value [%]	S [MPa]	CV S [%]	m-value	CV m-value [%]
MnROAD 03	-18	228	0.7	0.329	0.0	298	2.2	0.282	1.9
	-24	335	3.4	0.294	0.2				
	-30	638	4.9	0.167	12.4				
MnROAD 19	-18	359	1.4	0.281	1.6	489	3.0	0.236	0.1
	-24	485	1.9	0.249	1.1				
	-30	702	4.5	0.122	8.0	721	3.6	0.076	8.3
MnROAD 33	-18	276	9.1	0.289	0.9	320	8.9	0.247	2.3
	-24	388	1.5	0.260	0.5				
	-30	557	4.1	0.138	0.7	635		0.097	
MnROAD 34	-24	227	7.3	0.308	0.1				
	-30	464	3.0	0.195	1.2	555	5.9	0.142	5.3
	-36	624		0.124		681		0.084	
MnROAD 35	-30	231	3.6	0.210	1.3	297	1.6	0.172	0.3
	-36	391	9.2	0.184	6.7	485	0.8	0.151	1.8
	-42	506		0.131		712		0.111	
MN75 2	-18	479		0.286		526		0.248	
	-24	685		0.240					
	-30	800		0.100		891		0.058	
MN75 4	-24	286	0.4	0.258	5.7	348		0.215	
	-30	482		0.166					
	-36	872	5.1	0.120	8.3	904		0.081	
WI US 45	-24	283	2.9	0.234	1.9	369	0.4	0.198	5.3
	-30	502	4.8	0.166	6.8	616	2.6	0.124	0.3
	-36	765	5.0	0.124	4.9	859		0.084	
WI STH 73	-18	198	1.3	0.343	2.7	286	0.1	0.283	1.0
	-24	357	9.6	0.218	3.5	483	1.7	0.169	6.1
	-30	599	0.1	0.160	1.0	662	11.7	0.109	2.4
IL US20 6	-18	169		0.335		244		0.279	
	-24	305		0.221		425		0.186	
	-30	555		0.171		698		0.117	
IL US20 7	-24	480		0.159					
	-30	706		0.110		825		0.074	
	-36	1027		0.074		1035		0.049	
IL I74	-24	521		0.148					
	-30	656		0.096		816		0.067	
	-36								
ND 18	-18	248	4.2	0.312	0.5	373	0.2	0.261	1.2
	-24	371	1.0	0.197	0.2	463	3.6	0.142	1.7
	-30	627	1.4	0.142	1.8	778		0.104	

* empty cells indicate equipment malfunction or specimen break due to temperature/conditioning effects

** for some materials only one replicate was tested

Direct Tension (DT)

Direct Tension (DT) testing was carried out on a Bohlin Direct Tension with Neslab chilling system, according to AASHTO T 314-02 (3). The binders were tested at the same test temperatures as the BBR tests (Table 5.4 and Table 5.5). Two different loading rates were used: 1%/min, to match DENT loading rate, and standard 3%/min. The number of replicates varied depending upon the aging condition of the binder and the loading rate. Representative values for stress and strain at failure, in DT and DENT tests, were calculated as simple averages or as trimmed averages if 5 or more replicates produced meaningful results for a given binder/temperature combination. Tables 5.10-5.13 present DT results for RTFOT (1%/min), RTFOT (3%min), PAV, and extracted binders, respectively.

Table 5.10. DT, 1%/min, RTFOT binders

Binder	Temp. [C]	Stress @ failure		Strain @ failure	
		Average [MPa]	CV [%]	Average [-]	CV [%]
58-40 M1	-30	n/a*	n/a*	n/a*	n/a*
58-34 M1	-24	3.76	3.6	6.32	8.0
	-30	5.21	18.9	1.55	28.3
58-34 M2	-24	n/a*	n/a*	n/a*	n/a*
	-30	4.26	29.1	1.37	34.5
58-28 U1	-18	2.45	8.7	6.25	17.9
	-24	3.58	n/a	1.88	n/a
	-30	4.29	13.8	1.11	15.2
58-28 U2	-18	3.46	n/a	4.60	n/a
	-24	4.35	15.1	1.92	22.5
	-30	5.41	11.4	1.17	9.4
64-34 M1	-24	n/a*	n/a*	n/a*	n/a*
	-30	6.07	28.1	2.25	43.3
64-34 M2	-24	n/a*	n/a*	n/a*	n/a*
	-30	5.77	16.3	3.41	49.0
64-28 U1	-18	4.06	8.1	3.33	17.1
	-24	3.90	18.9	1.24	20.6
	-30	4.70	17.4	0.96	15.7
64-28 M1	-18	2.80	n/a	6.08	n/a
	-24	5.14	2.7	3.52	12.7
	-30	5.41	1.9	1.38	1.4
64-22 U1**	-12	n/a*	n/a*	n/a*	n/a*
	-18	n/a*	n/a*	n/a*	n/a*
	-24	4.64	6.1	3.18	10.9
	-30	4.82	6.9	1.41	6.2

* strain at failure larger than 3%

** additional tests at -30°C

Table 5.11. DT, 3%/min, RTFOT binders

Binder	Temp. [C]	Stress @ failure		Strain @ failure	
		Average [MPa]	CV [%]	Average [-]	CV [%]
58-40 M1	-30	n/a*	n/a*	n/a*	n/a*
58-34 M1	-24	4.92	5.6	3.97	3.5
	-30	5.97	7.0	1.38	7.6
58-34 M2	-24	4.81	6.2	5.57	30.1
	-30	6.63	13.8	1.84	22.0
58-28 U1	-18	3.21	7.8	3.32	13.2
	-24	4.57	12.8	1.52	14.6
	-30	4.64	18.6	1.02	10.4
58-28 U2	-18	4.24	10.9	3.40	34.6
	-24	4.81	12.6	1.44	14.4
	-30	5.27	6.1	0.93	9.1
64-34 M1	-24	n/a*	n/a*	n/a*	n/a*
	-30	6.97	5.2	1.80	9.0
64-34 M2	-24	n/a*	n/a*	n/a*	n/a*
	-30	7.02	3.3	2.29	5.5
64-28 U1	-18	4.52	2.4	1.99	4.4
	-24	4.36	20.8	1.14	19.8
	-30	4.44	12.8	0.83	4.5
64-28 M1	-18	4.31	4.7	7.02	0.9
	-24	5.98	9.1	2.27	8.9
	-30	5.78	11.2	1.19	7.4
64-22 U1	-12	n/a*	n/a*	n/a*	n/a*
	-18	n/a*	n/a*	n/a*	n/a*
	-24	5.39	5.8	2.42	7.9
	-30	4.59	19.7	1.19	15.4

* strain at failure larger than 3%

Table 5.12. DT, 3%/min, PAV binders

Binder	Temp. [C]	Stress @ failure		Strain @ failure	
		Average [MPa]	CV [%]	Average [-]	CV [%]
58-40 M1	-30	n/a*	n/a*	n/a*	n/a*
58-34 M1	-24	4.56	8.5	1.65	12.9
	-30	6.32	6.0	1.28	5.5
58-34 M2	-24	5.22	19.1	3.10	42.9
	-30	6.13	13.2	1.57	18.8
58-28 U1	-18	3.74	4.2	2.62	1.4
	-24	4.20	29.0	1.25	40.0
	-30	5.58	13.9	1.06	14.7
58-28 U2	-18	4.48	8.1	4.23	29.4
	-24	4.22	30.8	1.03	32.7
	-30	5.28	13.5	0.88	13.9
64-34 M1	-24	5.27	28.7	2.40	51.7
	-30	5.95	13.7	1.42	18.4
64-34 M2	-24	3.27	54.7	1.64	65.4
	-30	5.65	8.0	1.50	6.8
64-28 U1	-18	2.13	7.0	0.80	6.3
	-24	2.88	11.1	0.67	12.1
	-30	2.11	47.2	0.35	38.9
64-28 M1	-18	4.30	6.7	4.14	5.5
	-24	4.65	2.4	1.62	2.6
	-30	4.35	10.6	0.92	10.1
64-22 U1	-12	3.37	9.1	3.44	23.6
	-18	3.04	19.5	1.12	24.2
	-24	3.23	2.5	0.69	5.6

* strain at failure larger than 3%

Table 5.13. DT, 3%/min, extracted binders

Binder	Temp. [C]	Stress @ failure		Strain @ failure	
		Average [MPa]	CV [%]	[-]	CV [%]
MnROAD 03	-18	3.722	17.7	1.499	22.4
MnROAD 03	-24	5.060	16.4	1.179	14.2
MnROAD 03	-30	5.066	22.0	0.849	16.6
MnROAD 19	-18	3.165	9.2	0.953	10.5
MnROAD 19	-24	4.018	29.8	0.776	29.6
MnROAD 19	-30	2.517	3.1	0.397	1.2
MnROAD 33	-18	3.075	36.5	1.255	44.7
MnROAD 33	-24	5.447	9.3	1.318	8.9
MnROAD 33	-30	3.177	28.5	0.558	29.8
MnROAD 34	-24	4.895	4.9	2.201	12.0
MnROAD 34	-30	6.434	13.7	1.628	19.0
MnROAD 35	-30	3.972	12.7	1.906	20.2
MN75 2	-18	3.481	49.8	1.019	47.9
MN75 2	-24	3.865	20.8	0.615	17.1
MN75 2	-30	1.473	18.0	0.244	13.8
MN75 4	-24	6.068	7.7	1.700	15.5
MN75 4	-30	5.387	16.0	0.980	11.4
WI US 45	-24	6.049	16.8	2.311	24.6
WI US 45	-30	9.004	n/a	2.043	n/a
WI STH 73	-18	4.672	18.0	2.350	35.6
WI STH 73	-24	5.837	6.3	1.467	4.6
WI STH 73	-30	6.491	15.2	1.087	12.6
IL US20 6	-18	4.619	10.2	2.787	18.0
IL US20 6	-24	4.855	33.0	1.292	30.6
IL US20 6	-30	5.734	26.9	1.045	25.8
IL US20 7	-18	2.006	0.8	0.499	0.1
IL US20 7	-24	2.791	25.1	0.583	18.9
IL US20 7	-30	1.465	24.4	0.252	24.0
IL I74	-18	4.061	n/a	1.122	n/a
IL I74	-24	1.122	33.2	0.210	28.2
IL I74	-30	0.973	42.5	0.220	57.7
ND 18	-18	4.347	28.7	1.775	41.1
ND 18	-24	5.969	4.9	1.352	3.3
ND 18	-30	5.327	0.2	0.853	0.8

Double Edge Notch Tension (DENT)

To further investigate low-temperature fracture behavior of the asphalt binders, DT procedure was modified to perform Double Edge Notch Tension (DENT) tests (29). The DT molds are modified to prepare DENT specimens according to the geometry shown in Figure 5.7. The modified molds also allow the use of a razor blade to generate 1.5mm pre-cracks on both sides of the test specimens (Figure 5.8). The strain rate during testing is lowered to 1%/min due to the rapid failure occurring at the low temperatures. The testing protocol is similar to DT (AASHTO T 314-02) with the specimen pre-cracking prior to conditioning in the cooling bath.

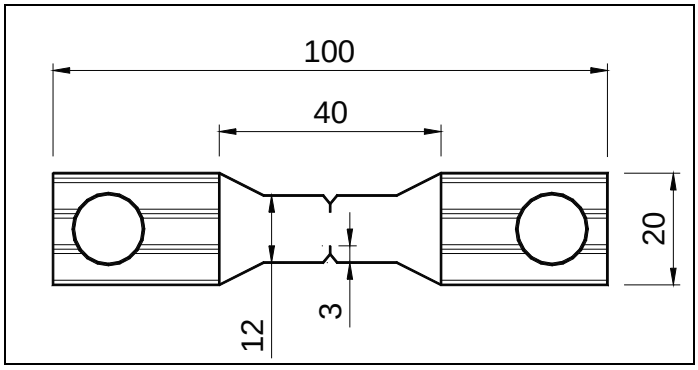

Figure 5.7. Double Edge Notched Tension (DENT) specimen dimensions (mm)

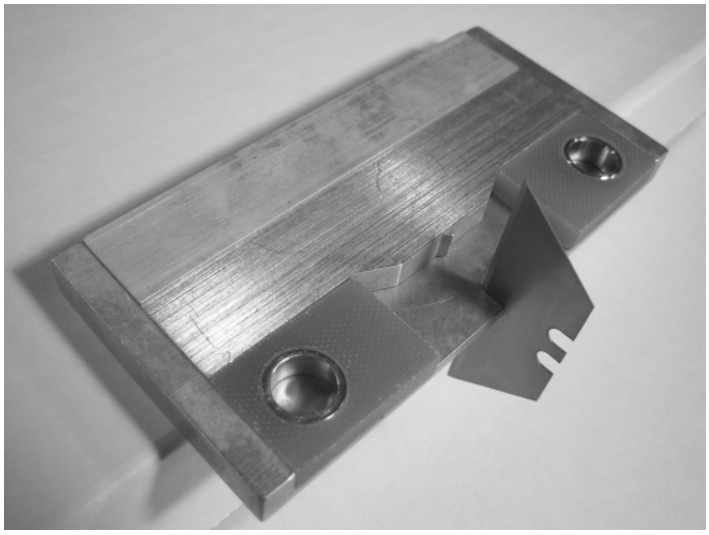

Figure 5.8. DENT specimen pre-cracking.

DENT test configuration allows for calculating binder critical stress intensity factor in mode I (fracture toughness) K_{IC} using the following equation (98):

$$K_{IC} = \frac{P}{B\sqrt{W}} \frac{\sqrt{\frac{\pi a}{2W}}}{\sqrt{1-\frac{a}{W}}} \left[1.122 - 0.561\left(\frac{a}{W}\right) - 0.205\left(\frac{a}{W}\right)^2 + 0.471\left(\frac{a}{W}\right)^3 + 0.190\left(\frac{a}{W}\right)^4 \right] \quad [1]$$

where:

P – peak load [kN],

B – specimen thickness [mm]

W – half width of the specimen [mm],

a – length of the notch and pre-crack [mm].

Tables 5.14-5.16 present DENT stress and strain values at failure for all three types of binders, i.e. RTFOT, PAV, and extracted. Additionally, fracture toughness, K_{IC}, is also calculated for each binders using equation 1.

Table 5.14. DENT, 1%/min, RTFOT binders

Binder	**Temp. [C]**	**Stress @ failure**		**Strain @ failure**		Fracture Toughness kPa*m^0.5
		Average [MPa]	CV [%]	Average [-]	CV [%]	
58-40 M1	-30	n/a*	n/a*	n/a*	n/a*	n/a*
58-34 M1	-24	0.706	44.4	0.266	26.1	59.0
58-34 M2	-24	1.023	16.0	0.337	22.6	85.5
	-30	0.942	22.2	0.226	8.7	78.8
58-28 U1	-18	1.231	n/a	1.845	n/a	102.9
	-24	1.165	8.0	0.349	23.1	97.4
	-30	0.447	15.3	0.102	8.2	37.4
58-28 U2	-18	1.111	19.5	0.394	25.2	92.9
	-24	1.392	16.1	0.359	27.5	116.3
	-30	0.466	19.7	0.109	10.4	38.9
64-34 M1	-24	1.166	29.1	0.346	24.3	97.5
	-30	0.877	6.2	0.178	6.6	73.3
64-34 M2	-24	1.276	5.1	0.535	8.2	106.6
	-30	0.925	22.9	0.245	4.7	77.3
64-28 U1	-18	0.699	34.3	0.210	30.9	58.4
	-24	0.625	47.5	0.142	30.6	52.3
	-30	0.540	20.3	0.103	9.9	45.1
64-28 M1	-18	1.135	36.1	0.548	40.1	94.9
	-24	0.806	13.4	0.229	8.0	67.4
	-30	0.768	20.7	0.151	23.5	64.2
64-22 U1	-12	n/a*	n/a*	n/a*	n/a*	n/a*
	-18	1.133	7.9	0.566	8.5	94.7
	-24	0.834	13.6	0.264	8.2	69.7

* strain at failure larger than 3%

Table 5.15. DENT, 1%/min, PAV binders

Binder	Temp. [C]	Stress @ failure		Strain @ failure		Fracture Toughness kPa*m^0.5
		Average [MPa]	CV [%]	Average [-]	CV [%]	
58-40 M1	-30	0.915	10.8	0.550	2.3	76.5
58-34 M1	-24	0.962	20.3	0.239	28.6	80.5
	-30	0.753	34.2	0.140	28.8	62.9
58-34 M2	-24	1.069	33.3	0.280	22.5	89.3
	-30	0.880	14.6	0.180	11.3	73.5
58-28 U1	-18	0.613	n/a	0.243	n/a	51.3
	-30	0.561	9.6	0.100	7.7	46.9
58-28 U2	-18	0.813	n/a	0.239	n/a	68.0
	-24	0.552	45.7	0.127	44.5	46.2
	-30	0.559	22.8	0.136	25.0	46.7
64-34 M1	-24	0.904	15.5	0.245	2.7	75.6
	-30	0.759	26.0	0.182	11.0	63.5
64-34 M2	-24	1.077	29.0	0.312	24.3	90.0
	-30	0.806	21.4	0.191	5.2	67.4
64-28 U1	-18	0.420	55.8	0.173	1.3	35.1
	-24	0.603	10.6	0.173	11.7	50.4
	-30	0.569	14.3	0.097	3.3	47.6
64-28 M1	-18	0.995	3.5	0.490	34.4	83.1
	-24	1.080	10.0	0.303	12.5	90.3
	-30	1.279	5.5	0.239	11.0	106.9
64-22 U1	-12	0.598	35.1	0.262	33.9	50.0
	-18	1.037	n/a	0.279	n/a	86.7
	-24	0.605	26.2	0.144	15.6	50.6

* strain at failure larger than 3%

Table 5.16. DENT, 1%/min, extracted binders

Binder	Temp. [C]	Stress @ failure		Strain @ failure		Fracture Toughness kPa*m^0.5
		Average [MPa]	CV [%]	[-]	CV [%]	
MnROAD 03	-18	0.521	22.7	0.131	22.0	43.6
MnROAD 03	-24	0.568	29.9	0.128	24.2	47.5
MnROAD 03	-30	0.547	6.6	0.091	9.8	45.7
MnROAD 19	-18	0.527	16.5	0.121	15.3	44.1
MnROAD 19	-24	0.547	37.7	0.118	12.6	45.7
MnROAD 19	-30	0.837	11.4	0.120	13.5	70.0
MnROAD 33	-18	0.552	3.6	0.146	10.0	46.2
MnROAD 33	-24	0.538	7.8	0.105	13.5	45.0
MnROAD 33	-30	0.742	15.4	0.099	19.4	62.0
MnROAD 34	-24	0.464	3.3	0.159	5.1	38.8
MnROAD 34	-30	0.544	19.4	0.104	20.7	45.4
MnROAD 35	-30	0.531	42.4	0.177	18.4	44.4
MN75 2	-18	0.517	14.6	0.106	5.7	43.2
MN75 2	-24	0.586	20.2	0.136	14.9	49.0
MN75 2	-30	0.762	26.8	0.160	24.5	63.7
MN75 4	-24	0.598	20.9	0.135	29.8	50.0
MN75 4	-30	0.808	25.6	0.167	30.4	67.6
WI US 45	-24	0.317	63.0	0.151	7.0	26.5
WI US 45	-30	0.536	9.7	0.099	15.6	44.8
WI STH 73	-18	0.477	19.3	0.120	26.8	39.9
WI STH 73	-24	0.505	16.9	0.118	35.0	42.2
WI STH 73	-30	0.459	13.8	0.088	22.5	38.4
IL US20 6	-18	0.660	8.0	0.187	6.5	55.1
IL US20 6	-24	0.518	21.7	0.100	19.4	43.3
IL US20 6	-30	0.517	n/a	0.085	n/a	43.2
IL US20 7	-18	0.659	5.5	0.131	7.7	55.1
IL US20 7	-24	0.727	8.9	0.115	14.7	60.7
IL US20 7	-30	0.742	30.1	0.113	29.1	62.0
IL I74	-18	0.616	n/a	0.117	n/a	51.5
IL I74	-24	0.694	21.2	0.110	26.2	58.1
ND 18	-18	0.606	15.3	0.157	21.9	50.7
ND 18	-24	0.510	14.4	0.093	12.2	42.6
ND 18	-30	0.612	19.2	0.092	14.4	51.1

CHAPTER 6

MIXTURE TESTING

Fracture and IDT Testing of the Laboratory Prepared Asphalt Mixture Gyratory Specimens

This task describes the test methods used to determine the low temperature rheological and fracture properties of the 28 mixtures prepared in the laboratory using the Superpave gyratory compactor and to present the test results. Each mixture was tested at three temperatures and three replicates were tested at each temperature. To accommodate the fact that mixture properties are less depended on temperature change than the binder properties and to allow at the same time a direct comparison of binder and mixture properties the following formula was used to determine the three test temperatures:

- For asphalt binders
    - PG +10°C (for a PG -28 it will be -18°C)
    - 6°C below (PG +10°C)
    - 12°C below (PG +10°C)
- For asphalt mixtures:
    - PG +10°C
    - 12°C below (PG +10°C)
    - 12°C above (PG +10°C).

In this fashion two of the test temperatures are common for the binder and mixture testing.

Identification System

With the large matrix of samples, a labeling system was developed for laboratory produced samples. Table 6.1 shows the mixture properties with the corresponding label. Note that:

- The first column of each label is simply the binder grade of the asphalt cement.
- The second column indicates whether the asphalt cement is modified (M) or unmodified (U). If there are multiple modified or unmodified asphalt cements, with the same binder grade, they are differentiated by a one or a two.
- The third column is the air void content. The majority of mixtures were compacted to 4 percent air voids (4) but four mixtures were compacted to 7 percent air voids (7).
- The fourth column is the type of aggregate, either granite (GR) or limestone (LM).
- Finally, the fifth column only appears on mixtures that did not use Superpave design asphalt cement content. If there is no fifth column, the asphalt content is 6.0% for granite mixtures, and 6.9% for limestone mixtures. In order to evaluate the effect of film thickness, several mixtures included an extra 0.5% asphalt cement (+0.5AC). These mixtures had an asphalt content of 6.5% for the granite and 7.4% for the limestone.

Table 6.1. Labeling system

Label	PG Binder Grade	Modifier	Air Voids	Aggregate	Asphalt Content (%)
58-40:M1:4:GR	58-40	SBS	4.0	Granite	6.0
58-40:M1:4:GR:+0.5AC	58-40	SBS	4.0	Granite	6.5
58-40:M1:4:LM	58-40	SBS	4.0	Limestone	6.9
58-34:M1:4:GR	58-34	Elvaloy	4.0	Granite	6.0
58-34:M1:4:GR:+0.5AC	58-34	Elvaloy	4.0	Granite	6.5
58-34:M1:4:LM	58-34	Elvaloy	4.0	Limestone	6.9
58-34:M2:4:GR	58-34	SBS	4.0	Granite	6.0
58-34:M2:4:LM	58-34	SBS	4.0	Limestone	6.9
58-28:U1:4:GR	58-28	Unmodified 1	4.0	Granite	6.0
58-28:U1:4:GR:+0.5AC	58-28	Unmodified 1	4.0	Granite	6.5
58-28:U1:4:LM	58-28	Unmodified 1	4.0	Limestone	6.9
58-28:U1:4:LM:+0.5AC	58-28	Unmodified 1	4.0	Limestone	7.4
58-28:U1:7:GR	58-28	Unmodified 1	7.0	Granite	6.0
58-28:U1:7:GR:+0.5AC	58-28	Unmodified 1	7.0	Granite	6.5
58-28:U1:7:LM	58-28	Unmodified 1	7.0	Limestone	6.9
58-28:U1:7:LM:+0.5AC	58-28	Unmodified 1	7.0	Limestone	7.4
58-28:U2:4:GR	58-28	Unmodified 2	4.0	Granite	6.0
58-28:U2:4:LM	58-28	Unmodified 2	4.0	Limestone	6.9
64-34:M1:4:GR	64-34	Elvaloy	4.0	Granite	6.0
64-34:M1:4:LM	64-34	Elvaloy	4.0	Limestone	6.9
64-34:M2:4:GR	64-34	Black Max™	4.0	Granite	6.0
64-34:M2:4:LM	64-34	Black Max™	4.0	Limestone	6.9
64-28:U1:4:GR	64-28	Unmodified 1	4.0	Granite	6.0
64-28:U1:4:LM	64-28	Unmodified 1	4.0	Limestone	6.9
64-28:M1:4:GR	64-28	SBS	4.0	Granite	6.0
64-28:M1:4:LM	64-28	SBS	4.0	Limestone	6.9
64-22:U1:4:GR	64-22	Unmodified 1	4.0	Granite	6.0
64-22:U1:4:LM	64-22	Unmodified 1	4.0	Limestone	6.9

Disc-Shaped Compact Tension [DC(T)]

The Disc-Shaped Compact Tension test, or DC(T), was developed as a practical method for the determination of low-temperature fracture properties of cylindrically-shaped asphalt concrete test specimens. The DC(T)'s advantages include easy specimen fabrication, from both field and gyratory samples, and it is a standard fracture test configuration (ASTM E399 Standard Test Method for Plane-Strain Fracture Toughness of Metallic Materials). The specimen dimensions are shown in Figure 6.1.

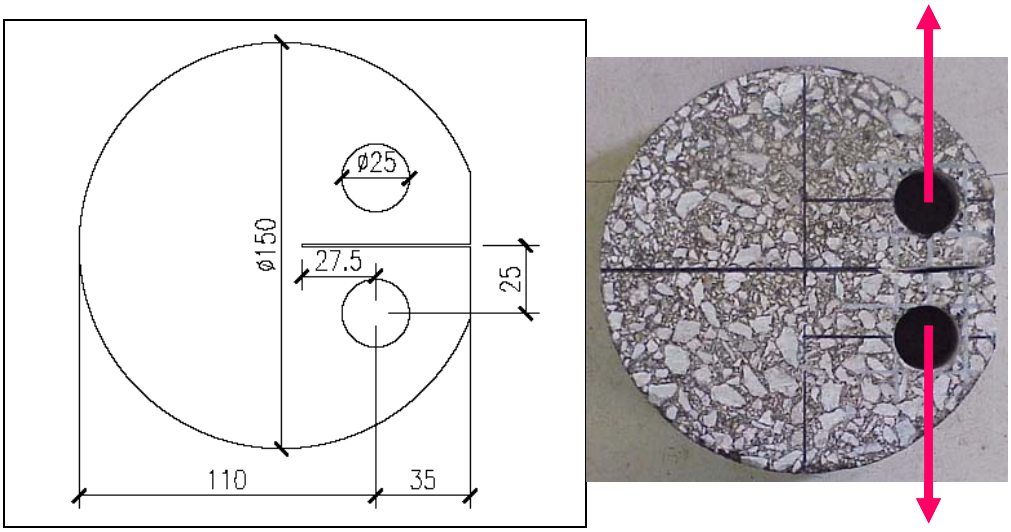

Figure 6.1. Specimen dimensions of the DC(T) sample (mm) and DC(T) loading setup

The DC(T) test is performed under tensile loading at the loading holes and the crack mouth opening displacement (CMOD) is measured with a clip-on gage at the face of the crack mouth. The test is controlled through a constant CMOD rate to provide a stable post-peak fracture. The fracture energy is calculated by determining the area under the load-CMOD curve normalized by initial ligament length and thickness.

Three Superpave gyratory samples were obtained from Iowa State University for each mixture in the testing matrix as shown in Table 6.1. Each gyratory sample was approximately 175mm in height. The first step in DC(T) specimen preparation is slicing 50mm thick samples, as shown in Figure 6.2, with a masonry saw.

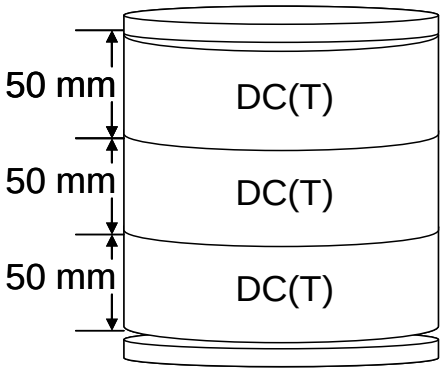

Figure 6.2. Gyratory sample cutting configuration

After slicing the samples, two holes were drilled into the face of each DC(T) sample for the loading pins. The holes were drilled on a stationary drilling rig with a 1-inch outside diameter core bit. Next, a flat face was cut on the notch side for the CMOD clip gage with a tile saw. The final step of specimen preparation is cutting the notch with a tile saw. The notch is designed for 82.5mm of ligament length in order to provide a large fractured face area. Figure 6.3 shows a typical DC(T) specimen after testing.

Figure 6.3. DC(T) specimen after testing

Table 6.2 shows DC(T) data for all of the laboratory produced mixtures with modified asphalt binders and Table 6.3 for the mixtures prepared with unmodified binders . The fracture energy was found from taking the average of three test replicates. In some cases, due to fabrication or testing errors, only two samples were tested.

Table 6.2. DC(T) test results for mixtures with modified asphalt binders

	Temp (°C)	Fracture Energy (avg, J/m^2)	COV (%)
64-34:M2:4:LM	-36	393.7	9.2
	-24	579.7	14.3
	-12	3374.9*	6.2
64-34:M2:4:GR	-36	663.8	18.7
	-24	913.9	17.9
	-12	3505.7*	12.2
64-34:M1:4:LM	-36	310.7	4.2
	-24	493.6	7.6
	-12	2601.3*	24.7
64-34:M1:4:GR	-36	477.9	15.4
	-24	740.4	14.9
	-12	2032.8*	38.8
64-28:M1:4:LM	-30	323.3	10.1
	-18	429.7	5.2
	-6	1389.6*	9.6
64-28:M1:4:GR	-30	456.5	7.7
	-18	759.8	13.3
	-6	1361.3	5.8
58-40:M1:4:LM	-42	440.9	8.1
	-30	623.1	11.7
	-18	2705.8*	15.2
58-40:M1:4:GR:+0.5AC	-42	790.2	7.0
	-30	1377.1	11.4
	-18	2844.9*	3.2
58-40:M1:4:GR	-42	655.4	13.8
	-30	1099.6	13.1
	-18	2032.7*	4.4
58-34:M2:4:LM	-36	324.9	9.0
	-24	567.7	9.0
	-12	2717.7*	1.4
58-34:M2:4:GR	-36	459.0	15.9
	-24	796.0	17.7
	-12	2640.7*	21.8
58-34:M1:4:LM	-36	311.5	24.1
	-24	525.5	12.5
	-12		
58-34:M1:4:GR:+0.5AC	-36	456.2	27.3
	-24	632.4	1.8
	-12	2132.5*	27.2
58-34:M1:4:GR	-36	455.3	10.6
	-24	646.9	7.7
	-12	1746.3*	12.1

*extrapolation needed for data analysis

Table 6.3. DC(T) test results for mixtures with unmodified asphalt binders

	Temp (°C)	Fracture Energy (avg, J/m^2)	COV (%)
64-28:U1:4:LM	-30	237.0	9.7
	-18	425.5	7.0
	-6	488.6	17.8
64-28:U1:4:GR	-30	442.7	21.1
	-18	583.0	7.8
	-6	1093.8*	16.7
64-22:U1:4:LM	-24	332.7	7.2
	-12	417.1	8.6
	0	1242.0*	37.6
64-22:U1:4:GR	-24	489.2	6.5
	-12	738.3	14.1
	0	1418.8*	11.8
58-28:U2:4:LM	-30	265.3	20.1
	-18	521.0	7.7
	-6	861.1	22.3
58-28:U2:4:GR	-30	584.9	12.9
	-18	822.8	16.2
	-6	1853.0*	33.5
58-28:U1:7:LM:+0.5AC	-30	229.6	24.2
	-18	499.6	8.7
	-6	1837.6*	19.5
58-28:U1:7:LM	-30	314.7	11.7
	-18	440.4	13.2
	-6	935.2	19.4
58-28:U1:7:GR:+0.5AC	-30	445.3	24.8
	-18	653.9	6.7
	-6	1382.1	40.5
58-28:U1:7:GR	-30	417.4	24.5
	-18	578.0	8.4
	-6		
58-28:U1:4:LM:+0.5AC	-30	316.9	7.4
	-18	447.3	18.6
	-6	1396.3*	32.9
58-28:U1:4:LM	-30	316.1	4.5
	-18	422.2	14.5
	-6	1210.8*	29.1
58-28:U1:4:GR:+0.5AC	-30	369.6	44.8
	-18	792.4	9.4
	-6	1289.7*	3.2
58-28:U1:4:GR	-30	497.1	20.6
	-18	652.8	4.1
	-6		

*extrapolation needed for data analysis

Semi-Circular Bending (SCB)

Similar to DC(T) the semi circular bending (SCB) test method takes advantage of the simple specimen preparation from Superpave Gyratory compacted cylinders and the simple loading setup. A schematic of the test set-up is shown in Figure 6.4.

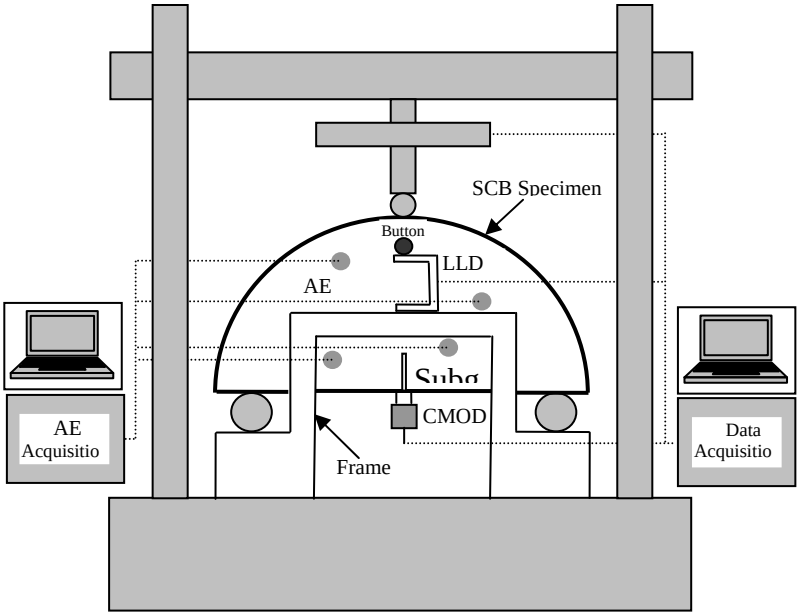

Figure 6.4. SCB experimental setup

In this study a MTS servo-hydraulic testing system equipped with an environmental chamber was used to perform the SCB test. The SCB samples were symmetrically supported by two fixed rollers and had a span of 120mm. Teflon tapes were used to reduce the friction from the two rollers. The Indirect Tension test (IDT) loading plate was used to load the SCB specimens. The load line displacement (LLD) was measured using a vertically mounted Epsilon extensometer with 38 mm gage length and ±1 mm range; one end was mounted on a button that was permanently fixed on a specially made frame, and the other end was attached to a metal button glued to the sample. The crack mouth opening displacement (CMOD) was recorded by an Epsilon clip gage with 10 mm gage length and a +2.5 and -1 mm range. The clip gage was attached at the bottom of the specimen. Considering the brittle behavior of asphalt mixtures at low temperatures, the CMOD signal was used as the control signal to maintain the test stability in the post-peak region of the test. A constant CMOD rate of 0.0005mm/s was used and the load and load line displacement (P-u) curve was plotted. A contact load with maximum load of 0.3 kN was applied before the actual loading to ensure uniform contact between the loading plate and the specimen. The testing was stopped when the load dropped to 0.5 kN in the post peak region. All tests were performed inside an environmental chamber. Liquid nitrogen was used to obtain the required low temperature. The temperature was controlled by the environmental chamber temperature controller and verified using an independent platinum RTD thermometer.

Acoustic Emission (AE) Instrumentation

During the SCB fracture testing, the AE event signals were recorded using four DAQ cards (Model PCI-5112, National Instruments). Each card had two independent channels which acquired AE signals detected by eight piezoelectric sensors (Model S9225, Physical Acoustics

Corporation). Four sensors were mounted on each side of the specimen using M-Bond 200, a modified alkyl cyanoacrylate. The preamplification of the AE signals was provided by eight preamplifiers (Model 1220C, PAC) with a gain set to 40 dB. One of the sensors was used as a trigger, which was often the one closest to the tip of the initial notch. Trigger level was set at 10 mV in this research. Once the recording was triggered, signals were band-pass filtered (0.1-1.2 MHz) and sampled at 20 MHz over 200 microseconds. Considering the ringing of the resonant sensor, a sleep time of 9 milliseconds between two consecutive events was prescribed during which the system could not be triggered. The velocity of propagation of the longitudinal waves was determined by generating an elastic wave by pencil lead (0.5 mm diameter) breakages on the opposite side of the samples.

Sample Preparation

Out of five cylindrical specimens, 150mm in diameter by 177mm height, delivered by Michigan Technological University four were used to cut SCB and IDT samples according to the schematic shown in Figure 6.5. Cylinder 1, 2 and 3 were cut off top and bottom to a final height of around 155mm. With this final height, specimen was then cut into 2 IDT specimens with 40mm each in height and 2 SCB slices with 25 mm each in height. Cylinder 4 was cut into 3 IDT specimens with 40 mm each in height. The plates for each layer were then cut into semicircular bend samples with an original notch length of 15 mm. The SCB slice cut from cylinder 1, 2 and 3 was symmetrically cut into two semicircular bend samples with an original notch with 15mm in length and 2 mm in width.

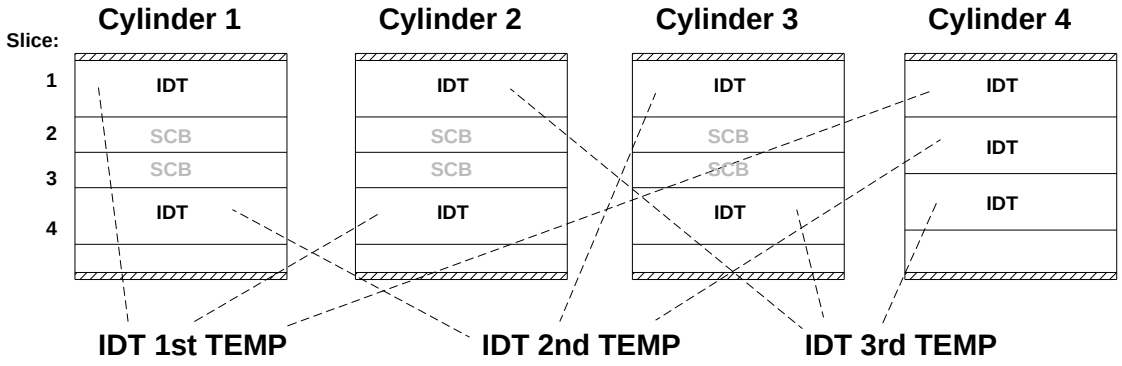

Figure 6.5. SCB and IDT sample preparation

SCB Fracture Test Results

A total of 252 SCB samples were tested using the SCB geometry. Out of these specimens, 84 were instrumented with AE sensors. A typical plot of the loading as a function of the load line displacement (LLD) for each testing temperature is shown in Figure 6.6. Note that TH, TM, and TL indicate the three test temperatures: high, middle, and low.

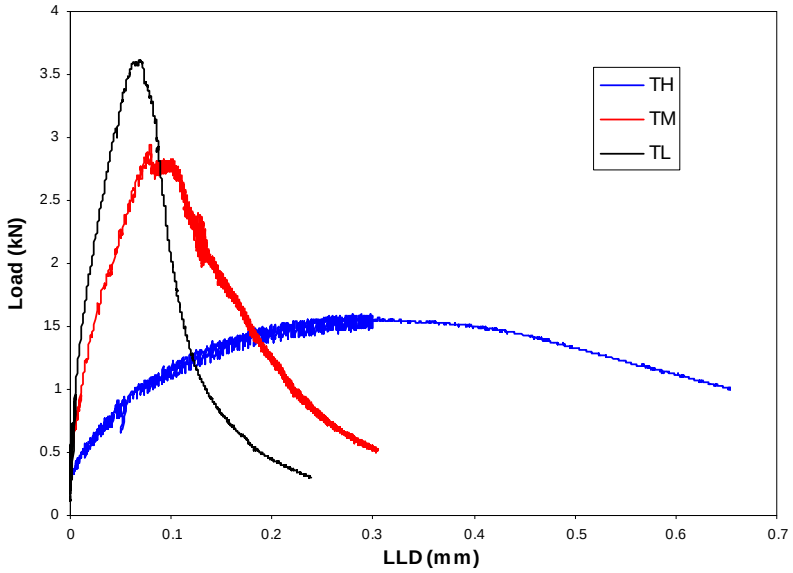

Figure 6.6. Typical plot of load vs. load line displacement

Figure 6.6 clearly shows that the asphalt mixtures behavior is significantly affected by the test temperature. At the higher test temperature the mixture has a more ductile behavior characterized by lower peak loads and larger displacements. At the lowest test temperature, the mixture has brittle behavior characterized by high peak loads and small deformations. At the middle test temperature, the mixture behavior represents a transition between the high and the low temperatures.

Figure 6.7 plots the test results for the three replicates of the same mixture at one test temperature. It can be observed that the repeatability of the test is reasonable.

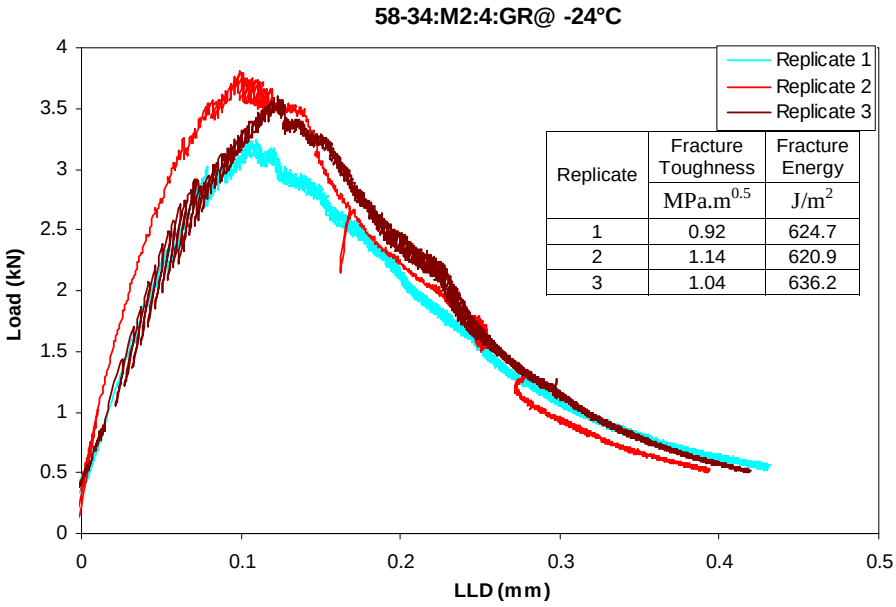

Replicate	Fracture Toughness	Fracture Energy
	$MPa.m^{0.5}$	J/m^2
1	0.92	624.7
2	1.14	620.9
3	1.04	636.2

Figure 6.7. Typical plot of loading with load line displacement for 3 replicates

The load and load line displacement data were used to calculate the fracture toughness and fracture energy. It was shown that the stress intensity factor K can be reasonably calculated using the following equation:

$$\frac{K_I}{\sigma_0\sqrt{\pi a}} = Y_I(s_0/r) + \frac{\Delta s_0}{r}B \qquad [1]$$

where

K_I = Mode I stress intensity factor;

σ_0 = $P/2rt$

P = applied load;

r = specimen radius;

t = specimen thickness.

Y_I = the normalized stress intensity factor

$$Y_{I(s_0/r)} = C_1 + C_2(a/r) + C_3\exp(C_4(a/r)) \qquad [2]$$

C_i = constants;

a = notch length;

$\Delta s_0/r = s_a/r - s_0/r$

s_a/r = actual span ratio;

s_0/r = nearest span ratio analyzed in the derivation of this equation (0.80, 0.67, 0.61, 0.50)

$$B = 6.55676 + 16.64035(\frac{a}{r})^{2.5} + 27.97042(\frac{a}{r})^{6.5} + 215.0839(\frac{a}{r})^{16}$$

The fracture energy G_f was calculated according to RILEM TC 50-FMC specification that has been extensively used in the study of concrete. The work of fracture is the area under the loading-deflection (P-u) curve and the fracture energy (G_f) can then be obtained by dividing the work of fracture with the ligament area, which is the product of the ligament length and the thickness of the specimen. This is shown in equation 3.

$$G_f = \frac{W_f}{A_{lig}} \qquad [3]$$

where W_f is the work of fracture and

$$W_f = \int P du$$

A_{lig} is the area of the ligament.

The tail part of the P-u curve can be reasonably obtained by fitting the data curve in the post peak region following a method described elsewhere (25). However, for the mixtures prepared with the PG 58-40 the fracture energy couldn't be obtained at the highest test temperature due to excessive plastic deformation.

Table 6.4 contains the average values for the fracture toughness and fracture energy for all 28 mixtures.

Table 6.4. SCB fracture parameters for all mixtures

Mixture	Temp(°C)	Fracture Toughness		Fracture Energy	
		Mean ($MPa.m^{0.5}$)	CoV (%)	Mean (J/m^2)	CoV (%)
58-40:M1:4:GR	-18	0.4	26.2		
	-30	0.9	16.1	1210.1	5.2
	-42	1.2	8.1	590.0	8.5
58-40:M1:4:GR:+0.5AC	-18	0.4	7.1		
	-30	0.8	1.2	1358.8	8.5
	-42	1.1	13.7	622.3	15.5
58-40:M1:4:LM	-18	0.4	20.1	778.6	20.0
	-30	0.8	5.3	928.8	6.5
	-42	0.9	6.6	355.6	10.6
58-34:M1:4:GR	-12	0.6	11.4	1150.3	16.7
	-24	1.0	4.0	549.0	11.0
	-36	1.1	4.5	351.8	10.6
58-34:M1:4:GR:+0.5AC	-12	0.6	6.8	1055.4	7.8
	-24	0.9	3.3	567.8	5.0
	-36	1.1	1.5	433.1	16.0
58-34:M1:4:LM	-12	0.5	13.7	926.7	17.7
	-24	0.7	5.8	327.8	9.4
	-36	0.8	5.8	236.9	12.0
58-34:M2:4:GR	-12	0.5	1.7	1208.2	11.9
	-24	1.0	10.5	627.2	1.3
	-36	1.2	8.4	382.0	9.0
58-34:M2:4:LM	-12	0.6	1.4	1052.3	4.3
	-24	0.9	3.5	373.2	5.6
	-36	0.9	4.2	295.6	23.8
58-28:U1:4:GR	-6	0.4	7.2	900.9	7.3
	-18	0.8	7.3	549.0	4.7
	-30	1.0	9.3	379.5	10.2
58-28:U1:4:GR:+0.5AC	-6	0.4	10.4	797.1	27.4
	-18	0.8	6.3	555.1	16.2
	-30	1.0	3.8	360.7	6.3
58-28:U1:4:LM	-6	0.3	8.1	699.5	9.5
	-18	0.7	7.0	380.6	15.0
	-30	0.8	5.2	240.4	17.1
58-28:U1:4:LM:+0.5AC	-6	0.4	3.3	726.1	11.0
	-18	0.6	5.4	377.6	2.0
	-30	0.8	6.8	259.3	11.5
58-28:U1:7:GR	-6	0.3	8.7	685.3	22.2
	-18	0.7	7.6	428.2	4.3
	-30	0.9	3.0	270.0	4.2
58-28:U1:7:GR:+0.5AC	-6	0.3	11.3	733.9	12.3
	-18	0.7	6.4	500.9	19.3
	-30	0.8	18.2	331.3	17.4
58-28:U1:7:LM	-6	0.3	3.6	671.5	7.8

	-18	0.6	6.4	348.4	18.2
	-30	0.6	5.8	195.4	4.2
58-28:U1:7:LM:+0.5AC	-6	0.3	2.1	634.7	10.0
	-18	0.6	9.3	272.0	16.4
	-30	0.6	9.8	209.9	10.4
58-28:U2:4:GR	-6	0.4	8.6	1052.7	11.9
	-18	0.9	3.5	516.2	13.0
	-30	1.0	5.2	328.5	18.4
58-28:U2:4:LM	-6	0.3	7.6	812.3	9.2
	-18	0.8	8.7	330.7	13.5
	-30	0.8	7.1	290.5	20.2
64-34:M1:4:GR	-12	0.6	0.7	1259.7	15.8
	-24	1.1	3.5	626.6	16.9
	-36	1.1	5.3	374.9	5.0
64-34:M1:4:LM	-12	0.5	9.8	1122.2	3.9
	-24	0.9	3.0	381.9	14.6
	-36	0.9	4.2	252.7	9.6
64-34:M2:4:GR	-12	0.5	2.3	1478.7	8.1
	-24	1.1	1.7	962.3	12.8
	-36	1.2	7.8	519.5	7.7
64-34:M2:4:LM	-12	0.4	8.8	1280.0	3.8
	-24	1.0	6.9	738.4	5.1
	-36	1.0	5.8	279.5	8.9
64-28:U1:4:GR	-6	0.5	11.3	879.1	8.9
	-18	0.9	3.5	413.1	10.9
	-30	1.0	3.4	274.0	5.8
64-28:U1:4:LM	-6	0.5	1.7	712.4	3.1
	-18	0.7	7.3	279.5	21.8
	-30	0.8	7.5	205.4	17.0
64-28:M1:4:GR	-6	0.4	11.7	907.4	6.7
	-18	1.0	4.7	586.5	5.2
	-30	1.1	1.8	504.1	7.7
64-28:M1:4:LM	-6	0.4	13.9	812.7	10.4
	-18	0.9	3.6	421.1	13.6
	-30	0.8	6.8	300.1	10.4
64-22:U1:4:GR	0	0.4	13.0	796.2	13.9
	-12	0.9	5.7	671.8	9.3
	-24	0.9	6.4	308.9	11.3
64-22:U1:4:LM	0	0.3	1.2	626.9	8.9
	-12	0.7	8.7	459.0	16.3
	-24	0.8	7.6	256.0	11.9

Indirect Tensile Test (IDT) Creep Stiffness and Strength

All 28 mixtures were evaluated using the Indirect Tensile Test Device. Two parameters, creep compliance and strength were determined using the current AASHTO specification T 322-03, “Standard Method of Test for Determining the Creep Compliance and Strength of Hot-Mix

Asphalt (HMA) Using the Indirect Tensile Test Device" (6). Each mixture was tested at three different temperatures determined based on the PG grade of the binder. At each temperature, three replicates coming from different gyratory specimens were tested to minimize the bias due to the gyratory compaction. The details of the IDT specimen preparation are presented in Figure 6.5.

First, 9 IDT specimens cut from 4 different gyratory cylinders were tested for the creep stiffness and later for the strength. Both procedures are specified in AASHTO T 322-03 and the resultant parameters are calculated as follows:

- Creep stiffness:

$$D(t) = \frac{\Delta X \cdot D_{avg} \cdot b_{avg}}{P_{avg} \cdot GL} \cdot C_{cmpl}$$, where

$D(t)$ – creep compliance,

ΔX – trimmed mean of the horizontal deformations,

D_{avg} – average specimen diameter,

b_{avg} - average specimen thickness,

P_{avg} – average force during the test,

GL – gage length (38mm)

C_{cmpl} – creep compliance parameter at any given time, computed as

$$C_{cmpl} = 0.6354 \cdot \left(\frac{X}{Y} \right)^{-1} - 0.332$$, where

X – horizontal deformation,

Y – vertical deformation.

Creep stiffness $S(t)$ at the time t was calculated as the inverse of the creep compliance $D(t)$, i.e. $S(t)=1/D(t)$.

- Tensile strength:

$$S = \frac{2 \cdot P_{fail}}{\pi \cdot b \cdot D}$$, where

P_{fail} – failure (peak) load,

b, D – specimen thickness and diameter, respectively.

The AASHTO procedure leads to one value of the creep stiffness $S(t)$ for a given mixture at each temperature. An alternative method was also introduced that determines the creep stiffness values separately for each replicate. The trimmed mean from the AASHTO procedure is replaced by the average deformation value from both faces of the given replicate. The simple average over three replicates gives the creep stiffness $S(t)$ at each temperature. Both methods yield similar results as presented in Figure 6.8 and 6.9.

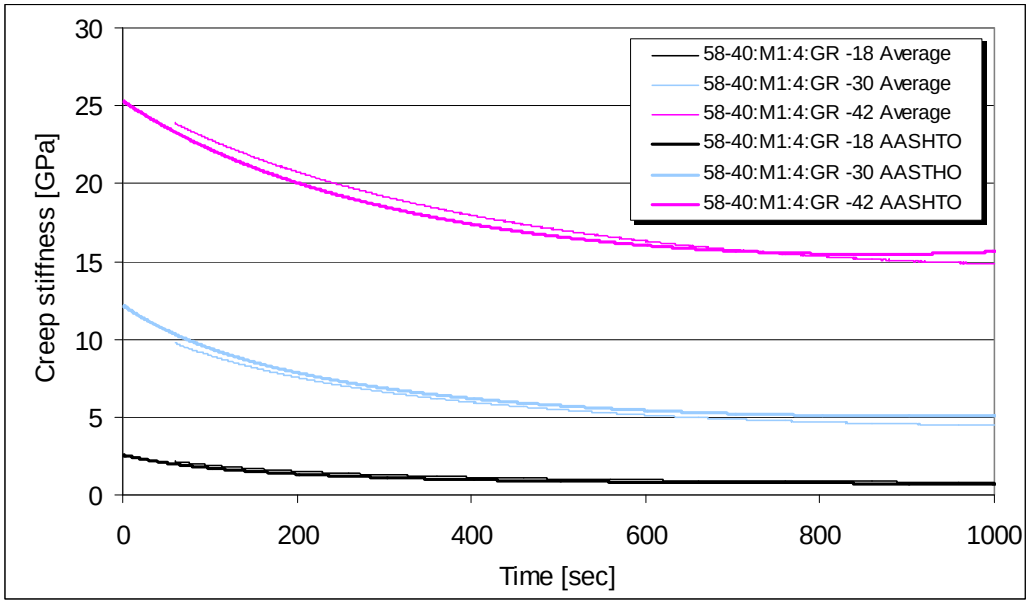

Figure 6.8. Comparison between simple average and AASHTO method for 58:40:M1:4:GR at all three temperatures (normal scale)

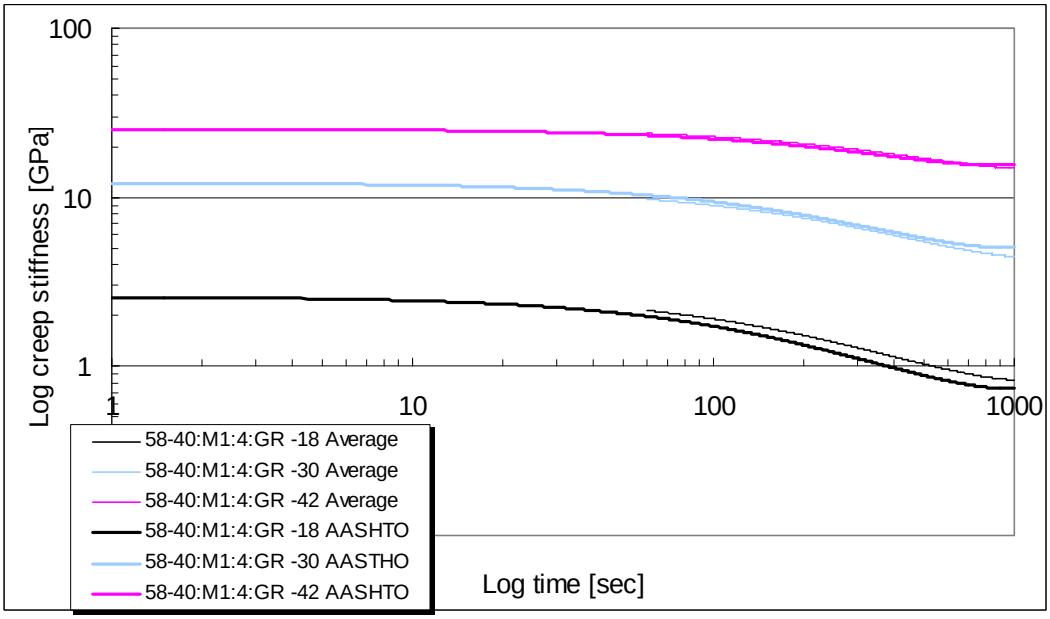

Figure 6.9. Comparison between simple average and AASHTO method for 58:40:M1:4:GR at all three temperatures (log scale)

Figures 6.10 and 6.11show two examples of the creep stiffness curves derived separately for each replicate. It can be seen that the curves might differ significantly and, in some cases, they intersect (Figure 6.11).

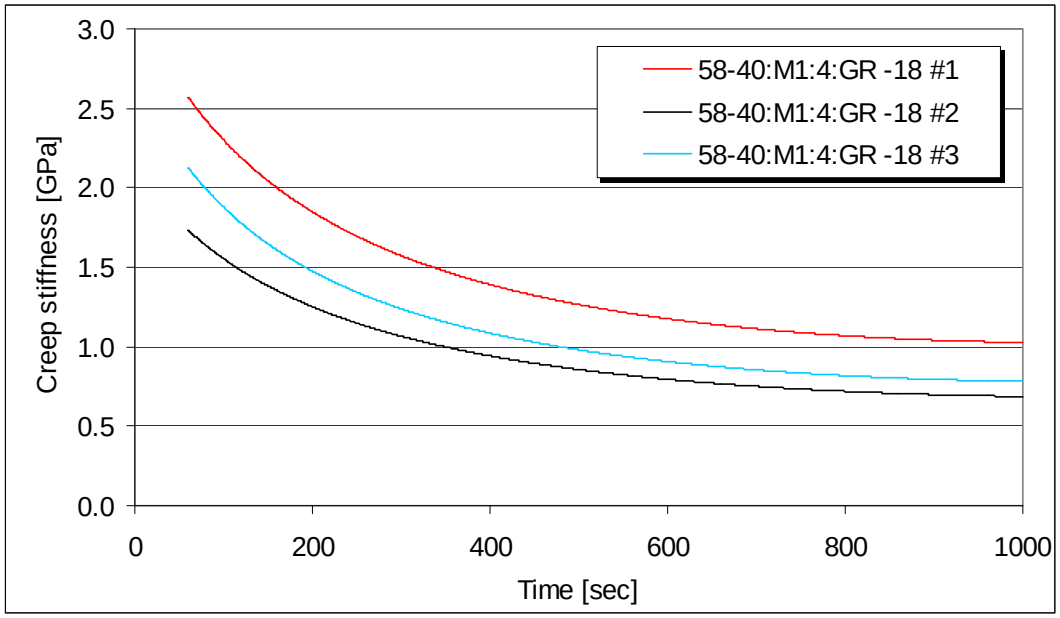

Figure 6.10. Creep stiffness for 58:40:M1:4:GR at -18°C

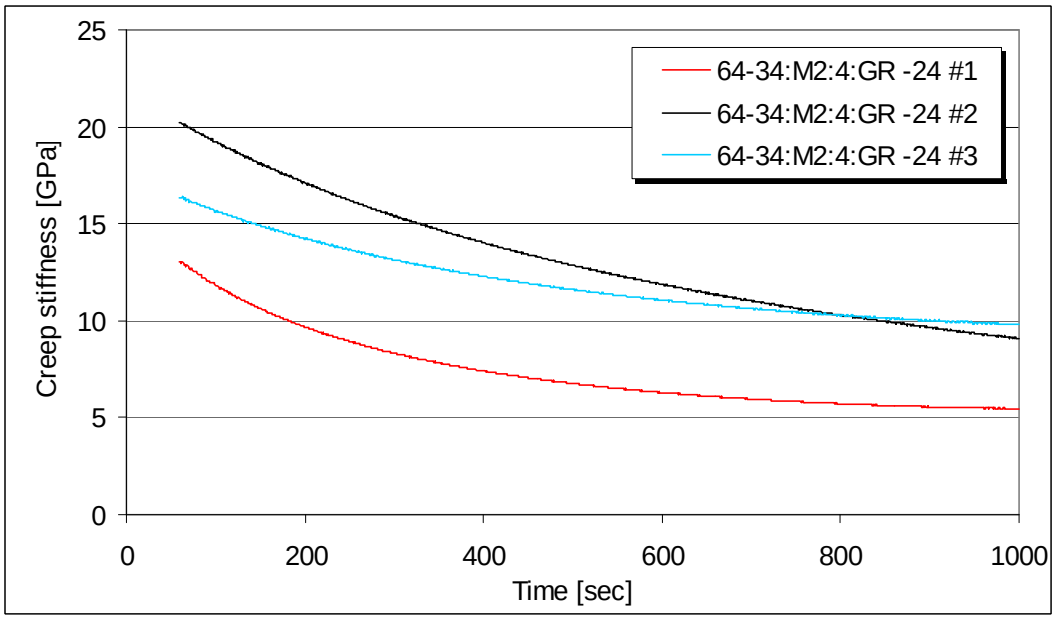

Figure 6.11. Creep stiffness for 64:34:M2:4:GR at -24°C

The summary of all creep stiffness results is presented in Table 6.5. The data was also used to generate plots which rank the mixtures according to the creep stiffness values at 60sec and 500sec derived using simple average method and the AASHTO method, respectively. The ranking was done separately for the lowest, intermediate, and the highest test temperatures.

Table 6.5. Creep stiffness values for all the mixtures at 60 and 500 seconds

Mixture	Temp (°C)	Creep stiffness @ 60sec [GPa]			Creep stiffness @ 500sec [GPa]		
		Simple average		AASHTO T 322-03	Simple average		AASHTO T 322-03
		Average	CV [%]		Average	CV [%]	
58-40:M1:4:GR	-18	1.90	28.9	2.09	0.86	26.8	0.90
	-30	9.84	12.6	10.76	5.43	14.3	5.81
	-42	22.47	19.2	23.52	16.31	21.9	16.83
58-40:M1:4:GR:+0.5AC	-18	1.70	6.1	1.81	0.72	3.3	0.74
	-30	11.46	24.5	12.26	6.32	34.4	6.16
	-42	17.10	15.3	17.69	11.66	17.4	12.19
58-40:M1:4:LM	-18	2.32	39.9	2.13	1.08	44.2	1.02
	-30	10.30	4.6	10.76	5.83	4.5	6.22
	-42	21.51	9.7	23.35	14.87	10.9	15.91
58-34:M1:4:GR	-12	2.65	46.3	2.34	0.92	38.7	0.86
	-24	16.73	6.2	17.00	10.06	9.5	10.14
	-36	21.52	4.0	19.80	18.65	15.6	16.83
58-34:M1:4:GR:+0.5AC	-12	3.90	18.5	3.73	1.58	20.0	1.49
	-24	17.19	22.9	17.06	10.88	30.1	10.61
	-36	31.33	20.8	29.83	25.95	16.2	24.28
58-34:M1:4:LM	-12	2.85	15.7	3.23	1.11	12.4	1.24
	-24	14.98	31.5	15.15	8.91	30.7	9.26
	-36	28.38	12.7	30.88	23.01	11.2	24.14
58-34:M2:4:GR	-12	2.72	8.8	2.99	0.96	20.9	1.03
	-24	16.60	11.8	19.79	9.34	22.3	10.91
	-36	29.76	9.0	29.37	23.38	13.9	23.24
58-34:M2:4:LM	-12	2.75	16.4	3.14	1.09	14.7	1.29
	-24	14.59	2.2	15.58	8.81	3.7	9.69
	-36	26.36	18.6	26.63	20.62	15.5	21.20
58-28:U1:4:GR	-6	2.51	23.8	2.53	0.83	40.6	0.77
	-18	7.07	30.7	7.39	3.59	46.7	3.43
	-30	15.31	4.4	11.60	12.88	8.4	9.58
58-28:U1:4:GR:+0.5AC	-6	2.01	13.8	1.90	0.69	19.0	0.69
	-18	11.86	15.4	13.37	6.76	14.1	7.24
	-30	27.27	7.4	27.44	20.44	3.9	20.59
58-28:U1:4:LM	-6	2.48	26.0	2.59	0.91	24.7	0.96
	-18	8.29	23.0	8.93	4.80	27.0	4.88
	-30	26.81	13.3	28.25	19.43	12.2	20.62
58-28:U1:4:LM:+0.5AC	-6	2.39	12.8	2.40	0.88	11.8	0.91
	-18	9.98	8.2	9.89	5.38	10.9	5.48
	-30	24.49	10.3	26.77	18.22	9.8	20.05
58-28:U1:7:GR	-6	1.28	40.2	1.78	0.38	56.1	0.44
	-18	5.60	29.7	5.56	2.30	38.2	2.30
	-30	16.94	14.3	16.44	12.54	6.3	11.73
58-28:U1:7:GR:+0.5AC	-6	1.62	8.3	1.94	0.49	6.1	0.59
	-18	8.92	8.9	8.56	5.50	12.6	5.27
	-30	19.89	6.2	21.21	14.68	4.3	15.65
58-28:U1:7:LM	-6	1.56	17.7	1.52	0.56	27.0	0.53

	-18	6.34	12.3	6.36	3.58	7.6	3.55
	-30	19.91	11.2	21.85	14.52	10.9	16.23
58-28:U1:7:LM:+0.5AC	-6	1.07	16.4	1.17	0.39	31.5	0.41
	-18	6.25	27.7	7.15	3.61	32.4	3.95
	-30	14.59	1.3	16.14	9.67	8.6	11.02
58-28:U2:4:GR	-6	2.05	37.2	1.92	0.60	54.9	0.47
	-18	10.26	9.0	11.04	5.23	8.3	5.75
	-30	17.93	21.4	16.07	14.93	26.1	13.19
58-28:U2:4:LM	-6	2.38	19.4	2.29	0.89	22.4	0.83
	-18	11.08	10.1	10.57	6.09	14.8	6.02
	-30	21.69	5.8	22.50	16.56	9.4	17.17
64-34:M1:4:GR	-6	2.31	31.1	2.55	0.80	34.5	0.87
	-18	9.82	10.6	9.86	5.71	13.0	5.68
	-30	20.55	25.9	17.50	17.92	23.0	15.74
64-34:M1:4:LM	-12	3.29	41.9	3.23	1.38	41.5	1.38
	-24	13.34	21.1	14.88	7.66	18.3	8.42
	-36	28.53	6.7	26.92	22.77	4.8	21.53
64-34:M2:4:GR	-12	3.00	17.5	3.11	1.19	16.0	1.22
	-24	15.32	29.5	16.38	8.95	31.4	9.45
	-36	32.73	15.1	33.49	24.88	9.2	26.15
64-34:M2:4:LM	-12	2.63	37.2	2.61	0.98	28.3	0.93
	-24	11.83	8.3	13.12	6.77	7.3	7.50
	-36	26.27	6.9	27.09	19.86	7.7	20.53
64-28:U1:4:GR	-6	2.69	23.6	2.68	0.85	28.7	0.85
	-18	10.05	17.9	11.09	5.91	24.5	6.08
	-30	19.78	4.9	18.10	17.31	3.0	16.32
64-28:U1:4:LM	-6	3.03	6.4	3.59	1.25	12.4	1.45
	-18	17.14	16.9	17.72	11.20	23.2	11.19
	-30	26.72	9.4	27.33	21.15	9.1	21.44
64-28:M1:4:GR	-6	3.62	3.8	3.74	1.22	11.5	1.27
	-18	11.12	5.1	11.94	7.06	4.4	7.72
	-30	17.55	21.5	13.26	16.03	30.0	12.63
64-28:M1:4:LM	-6	2.44	36.8	2.37	1.05	42.0	0.99
	-18	12.04	18.1	11.65	8.24	25.4	8.02
	-30	18.99	14.1	19.08	14.65	14.6	15.11
64-22:U1:4:GR	0	3.17	13.3	3.62	1.18	19.4	1.21
	-12	10.24	22.1	11.72	5.55	21.0	6.12
	-24	23.87	11.3	24.09	18.32	14.2	18.19
64-22:U1:4:LM	0	2.20	5.4	2.25	0.84	12.1	0.85
	-12	7.87	8.8	6.81	4.50	8.7	4.05
	-24	21.64	9.4	23.41	16.17	12.4	17.73

A typical force-displacement curve obtained during the strength test is presented in Figure 6.12. The displacements represent the loading head displacements; this was done to avoid damaging the strain gages when testing at low temperatures at which the failure was catastrophic. The measured peak load was used to calculate the tensile strength.

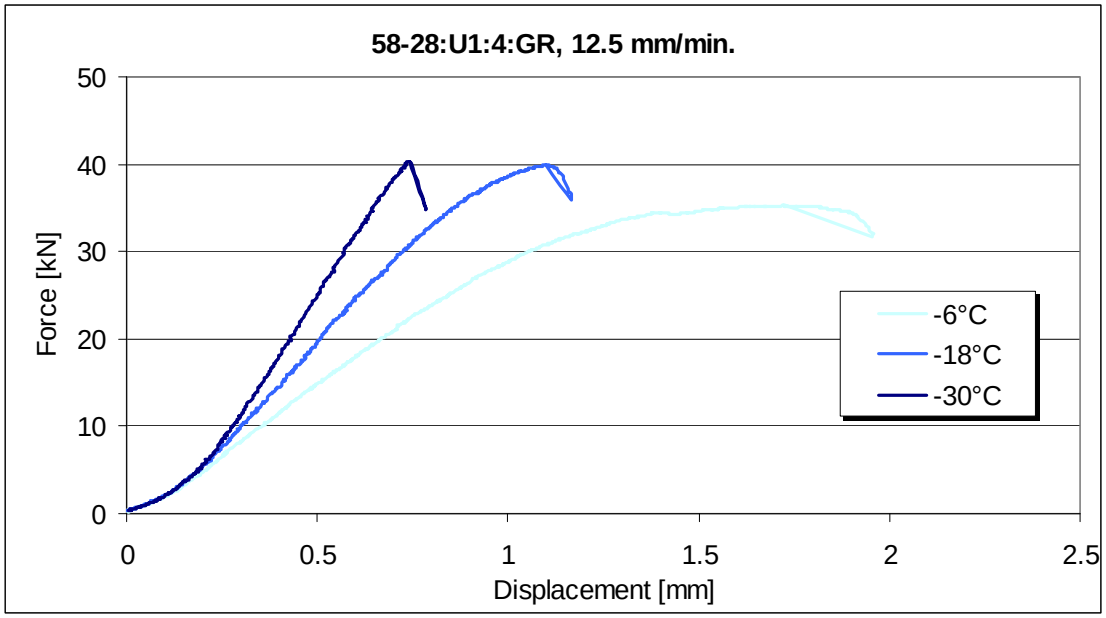

Figure 6.12. Example of the force-displacement curve during strength test at three different temperatures (58-28:U1:4:GR, 12.5 mm/min.).

AASHTO T 322-03 specifies a displacement rate of 12.5mm/min. To further investigate the influence of the loading rate on the strength, two other levels, 1 and 3 mm/min., were also used. The summary of the results is presented in Table 6.6.

Table 6.6. Tensile strength values for all the mixtures

Mixture	Temp. [°C]	Strength [MPa]		
		1 mm/min	3 mm/min	12.5 mm/min
58-40:M1:4:GR	-18	2.48	3.03	3.72
	-30	4.12	5.49	7.08
	-42	7.10	7.46	8.70
58-40:M1:4:GR:+0.5AC	-18	1.85	2.30	3.36
	-30	4.95	4.89	7.16
	-42	7.23	7.67	8.52
58-40:M1:4:LM	-18	2.42	2.30	3.93
	-30	4.78	5.31	6.05
	-42	5.38	6.60	6.56
58-34:M1:4:GR	-12	n/a	n/a	4.07
	-24	6.33	7.08	7.40
	-36	n/a	n/a	4.94
58-34:M1:4:GR:+0.5AC	-12	3.24	4.71	5.40
	-24	7.15	6.54	6.99
	-36	7.24	7.11	6.61
58-34:M1:4:LM	-12	2.84	4.39	4.86
	-24	5.45	4.94	5.06
	-36	5.42	4.64	3.94

58-34:M2:4:GR	-12	3.15	3.76	5.99
	-24	5.23	6.24	5.98
	-36	6.83	7.60	8.61
58-34:M2:4:LM	-12	2.89	3.99	5.11
	-24	5.83	6.30	5.55
	-36	6.24	6.04	5.43
58-28:U1:4:GR	-6	n/a	n/a	3.60
	-18	n/a	n/a	4.27
	-30	n/a	n/a	4.39
58-28:U1:4:GR:+0.5AC	-6	2.47	2.72	4.86
	-18	4.20	5.48	6.41
	-30	6.17	5.54	4.99
58-28:U1:4:LM	-6	2.31	2.78	3.76
	-18	3.43	4.68	4.76
	-30	4.37	4.63	4.62
58-28:U1:4:LM:+0.5AC	-6	2.24	3.18	4.07
	-18	3.97	4.11	4.99
	-30	4.29	4.52	4.45
58-28:U1:7:GR	-6	n/a	n/a	2.21
	-18	n/a	n/a	3.72
	-30	n/a	n/a	3.85
58-28:U1:7:GR:+0.5AC	-6	2.04	2.96	3.95
	-18	3.22	3.95	5.46
	-30	5.08	5.07	5.23
58-28:U1:7:LM	-6	1.66	2.67	3.17
	-18	3.66	3.66	3.77
	-30	4.02		3.42
58-28:U1:7:LM:+0.5AC	-6	1.90	2.44	2.82
	-18	3.66	3.76	3.71
	-30	3.62	3.53	3.17
58-28:U2:4:GR	-6	n/a	n/a	3.29
	-18	n/a	n/a	4.70
	-30	n/a	n/a	4.64
58-28:U2:4:LM	-6	2.87	3.72	4.26
	-18	4.27	4.93	4.79
	-30	4.74	4.18	3.93
64-34:M1:4:GR	-12	n/a	n/a	4.46
	-24	n/a	n/a	5.56
	-36	n/a	n/a	6.20
64-34:M1:4:LM	-12	2.83	4.57	5.63
	-24	5.35	6.99	7.22
	-36	5.76	6.08	6.00
64-34:M2:4:GR	-12	2.88	4.35	5.94
	-24	6.98	7.42	8.58
	-36	9.22	8.07	8.59
64-34:M2:4:LM	-12	3.02	3.71	4.55
	-24	6.42	6.94	7.30
	-36	7.20	8.26	7.95

64-28:U1:4:GR	-6	n/a	n/a	3.84
	-18	n/a	n/a	4.66
	-30	n/a	n/a	4.36
64-28:U1:4:LM	-6	2.27	3.47	4.76
	-18	5.17	4.39	5.09
	-30	4.21	4.79	4.35
64-28:M1:4:GR	-6	n/a	n/a	3.79
	-18	n/a	n/a	5.20
	-30	n/a	n/a	5.22
64-28:M1:4:LM	-6	2.32	3.37	4.00
	-18	5.14	4.83	6.01
	-30	5.76	5.71	5.10
64-22:U1:4:GR	0	2.58	2.77	4.16
	-12	4.50	5.34	5.98
	-24	6.27	6.30	6.28
64-22:U1:4:LM	0	2.09	2.73	3.56
	-12	3.92	4.44	5.08
	-24	4.71	4.42	4.59

Fracture and IDT Testing of the Asphalt Mixture Field Samples

This sub-chapter presents the results of fracture and IDT testing of field asphalt mixtures. As described in details in Chapter 3, four states delivered field samples cut from the pavements as beams and cores. All field samples received at the University of Minnesota and University of Illinois at Urbana-Champaign are presented in Table 6.7. Cores were cut into SCB, IDT, and DCT specimens whereas beams were used for SEB and TSRST specimens.

Table 6.7. Field samples received at UMN and UIUC

Site	Code name	University of Minnesota		University of Illinois at Urbana-Champaign	
		Cores	Beams	Cores	Beams
MnROAD Cell 03	MnROAD 03	27	1	9	4
MnROAD Cell 19	MnROAD 19	27	2	9	4
MnROAD Cell 33	MnROAD 33	18	2	9	4
MnROAD Cell 34	MnROAD 34	18	2	9	4
MnROAD Cell 35	MnROAD 35	18	2	9	5
MN CSAH-75, section 2 EB	MN75 2	14	1	13	2
MN CSAH-75, section 4 WB	MN75 4	14	2	13	4
WI US-45	WI US 45	27	5	9	4
WI STH-73	WI STH 73	27	5*	9	4

IL US-20, section 6	IL US20 6	18	4	9	6
IL US-20, section 7	IL US20 7	18	4	9	7
IL I-74	IL I74	36	0	18	9
ND SH-18	ND 18	12	0	0	0

* All beams received were broken.

Testing Overview

Similar to laboratory prepared mixtures, the test temperatures were determined based on the original PG grade of the binder. In some cases, this information was approximated using data provided by the appropriate state agency. Test temperatures and equivalent binder grades for all sites are given in Table 6.8.

Table 6.8. Equivalent binder PG grade and test temperatures

Site	Code name	Original binder grade	Equivalent binder grade	Test temperatures (SCB, IDT)			Test temperatures (DCT, SEB)		
		Temperature[1] ->		H	I	L	H	I	L
MnROAD Cell 03	MnROAD 03	120/150	PG 58-28	-6	-18	-30	-6	-18	-30
MnROAD Cell 19	MnROAD 19	AC-20	PG 64-22[2]	-12	-24	-36	0	-12	-24
MnROAD Cell 33	MnROAD 33	PG 58-28	PG 58-28	-6	-18	-30	-6	-18	-30
MnROAD Cell 34	MnROAD 34	PG 58-34	PG 58-34	-12	-24	-36	-12	-24	-36
MnROAD Cell 35	MnROAD 35	PG 58-40	PG 58-40	-18	-30	-42	-18	-30	-42
MN CSAH-75, section 2 EB	MN75 2	PG 58-28	PG 58-28	-6	-18	-30	-6	-18	-30
MN CSAH-75, section 4 WB	MN75 4	PG 58-34	PG 58-34	-12	-24	-36	-12	-24	-36
WI US-45	WI US 45	PG 58-34	PG 58-34[3]	-12	-24	-36	-6	-18	-30
WI STH-73	WI STH 73	PG 58-28	PG 58-28	-6	-18	-30	-6	-18	-30
IL US-20, section 6	IL US20 6	AC-10	PG 58-28	-6	-18	-30	-6	-18	-30
IL US-20, section 7	IL US20 7	AC-20	PG 64-22[2]	-12	-24	-36	0	-12	-24
IL I-74	IL I74	AC-20	PG 64-22[2]	-12	-24	-36	0	-12	-24
ND SH-18	ND 18	120/150	PG 58-28	-6	-18	-30	n/a	n/a	n/a

[1] H – high, I – intermediate, L – low
[2] test temperatures (for SCB and IDT) based on PG 64-34
[3] test temperatures (for DCT and SEB) based on PG 58-28

Table 6.9 gives an overview of all tests performed in this part. For all test but SEB, three replicates at each temperature were used which totals to nine specimens per site. If the top layer (wearing course) of the pavement was too thin (Illinois sites), the specimens were not cut (IDT testing) or the specimens were cut from the binder course (SEB tests). Also note that UIUC laboratory did not receive any field samples from North Dakota Highway 18.

Table 6.9. Fracture and IDT testing of field specimens

Site	Code name	Number of tests														
		SCB			IDT creep			IDT strength			DC(T)			SEB		
Temperature* ->		H	I	L	H	I	L	H	I	L	H	I	L	H	I	L
MnROAD Cell 03	MnROAD 03	3	3	3	3	3	3	3	3	3	2	3	3	2	2	2
MnROAD Cell 19	MnROAD 19	3	3	3	3	3	2	3	3	2	3	3	2	2	1	2
MnROAD Cell 33	MnROAD 33	3	3	3	3	3	3	3	3	3	3	3	3	2	2	2
MnROAD Cell 34	MnROAD 34	3	3	3	3	3	3	3	3	3	3	3	3	2	2	2
MnROAD Cell 35	MnROAD 35	3	3	3	3	3	3	3	3	3	3	3	3	2	2	2
MN CSAH-75, section 2 EB	MN75 2	2	3	3	2	2	3	2	1	3	3	3	3	1	1	2
MN CSAH-75, section 4 WB	MN75 4	3	3	3	2	2	3	2	2	3	3	3	3	2	2	2
WI US-45	WI US 45	3	2	3	3	3	3	3	3	3	3	3	2	2	2	2
WI STH-73	WI STH 73	3	3	3	3	3	3	2	3	3	3	3	3	2	2	2
IL US-20, section 6	IL US20 6	3	3	3	0	0	0	0	0	0	3	3	3	2	2	2
IL US-20, section 7	IL US20 7	3	3	3	0	0	0	0	0	0	3	3	3	2	2	2
IL I-74	IL I74	3	3	3	0	0	0	0	0	0	3	2	1	0	0	0
ND SH-18	ND 18	3	3	3	1	2	2	1	2	2	0	0	0	0	0	0

* Test temperature with reference to PG grade of the binder, H – high, I – intermediate, L – low.

Disc-Shaped Compact Tension [DC(T)]

For the DC(T), the fracture energy was found by taking the average of three test replicates. In some cases, due to fabrication or testing errors, only two DC(T) samples were tested. Table 6.10 shows DC(T) data for all of the field samples.

Table 6.10. DC(T) fracture energy for field mixtures

Field Section	Average Sample Thickness	Without Thickness Adjustment			With Thickness Adjustment		
		High (J/m^2)	Mid (J/m^2)	Low (J/m^2)	High (J/m^2)	Mid (J/m^2)	Low (J/m^2)
MnROAD 03	50 mm	703	317	203	-	-	-
MnROAD 19	50 mm	613	363	207	-	-	-
MnROAD 33	50 mm	605	378	270	-	-	-
MnROAD 34	50 mm	445	374	247	-	-	-
MnROAD 35	50 mm	414	427	339	-	-	-
MN75 2	25 mm	638	356	258	761	445	314
MN75 4	50 mm	1378	961	566	-	-	-
WI US 45	31 mm	801	437	387	890	496	448
WI STH 73	50 mm	604	471	299	-	-	-
IL US20 6	30 mm	349	343	177	417	389	199
IL US20 7	26 mm	377	312	164	454	378	205
IL I74	27 mm	213	202	196	249	235	245

When taking samples from the field, it is often difficult or impossible to obtain 50mm thick samples, especially when lift thicknesses are less than 50mm. Therefore, several of the field samples were less than 50mm thick. Because of size effects in fracture, thinner samples give lower fracture energy, even when normalized by the fracture face area. Therefore, the following equation was developed in order to correlate the fracture energy of thinner samples to a standard thickness (50mm).

$$\frac{F_{test}}{F_{50}} = A * \ln\left(\frac{T_{test}}{T_{50}}\right) + B$$

where: F_{test} = Fracture Energy at Testing Thickness, J/m^2

F_{50} = Normalized Fracture Energy at 50mm Thickness, J/m^2

T_{test} = Testing Thickness, mm

T_{50} = 50mm

A = 0.313; Regression Coefficient

B = 1.03; Regression Coefficient

This equation was developed for a limited set of data and at one temperature. Using this equation, the fracture energy was recalculated for the field samples that were less than 50mm. All of the MnROAD samples had a thickness of 50mm, as did MN75 4 and WI STH 73.

Single-Edge Notched Beam [SE(B)]

The Single-Edge Notched Beam, or SE(B), was also used to determine the low-temperature fracture properties of asphalt concrete test specimens. The SE(B)'s advantages include consistent

pure mode I (opening) loading, a simple loading configuration, and a flexibility to investigate other areas (including mixed-mode cracking and size effect). The SE(B) specimen dimensions are shown in Figure 6.13.

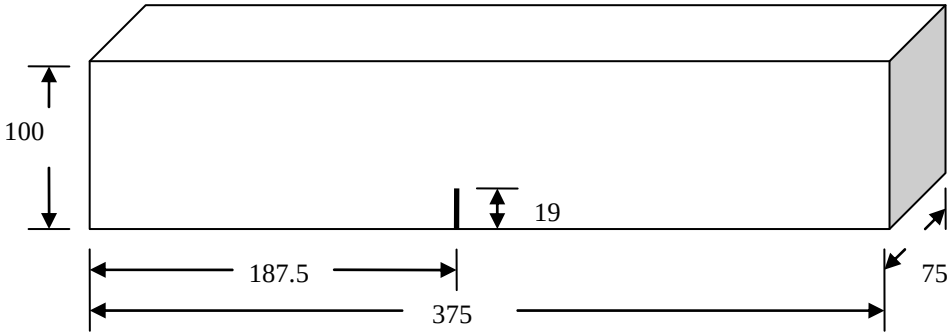

Figure 6.13. Specimen dimensions of the SE(B) sample (mm)

The SE(B) test is performed in a three point load configuration. A load is applied directly over the notch in order to achieve pure Mode I loading. The SE(B) test is controlled through a constant CMOD rate, 0.7 mm/min, to provide a stable post-peak fracture. The fracture energy is calculated by determining the area under the load-CMOD curve normalized by initial ligament length and thickness. Figure 6.14 shows the test configuration.

Figure 6.14. Test configuration of the SE(B)

Enough field beams were obtained from each site in order to run six SE(B) tests (two replicates at three temperatures). The only site not tested was Illinois I74 as the surface layer was two thin to obtain the proper specimen size. The first step in SE(B) specimen preparation is slicing the 375x100x75mm sample beams with the masonry saw. Next, a notch is cut with a tile saw 19mm deep into the beam, creating a ligament length of 81mm. Figure 6.15 shows a typical SE(B) sample after testing. Note the very straight fracture face which is indicative of a pure Mode I failure.

Figure 6.15. SE(B) specimen after testing

For the SE(B), the fracture energy was found by taking the average of two test replicates. In some cases, due to fabrication or testing errors, only one SE(B) sample was tested. Table 6.11 shows SE(B) data for all of the field samples.

Table 6.11. SE(B) fracture energy for field mixtures

Field Section	Low (J/m^2)	Med (J/m^2)	High (J/m^2)
MnROAD 03	279.4	257.6	450.2
MnROAD 19	165.9	269.4	307.0
MnROAD 33	233.8	338.3	507.4
MnROAD 34	339.2	357.4	763.7
MnROAD 35	273.3	363.5	793.6
MN75 2	430.2	480.8	451.7
MN75 4	628.6	716.5	884.2
WI US 45	467.8	442.2	744.5
WI STH 73	294.8	621.3	583.6
IL US20 6	256.1	377.9	539.4
IL US20 7	229.1	311.9	515.1

Semi-Circular Bending (SCB)

Semi circular bending (SCB) test was performed on all field mixtures according to the similar procedure outlined as for laboratory prepared specimens. Two SCB specimens were cut from one field sample (core) so total of 5 cores were needed to obtain sufficient number of SCB specimens per given mixture. Three replicates were tested at each temperature. Table 6.12 presents the results.

The acoustic emission (AE) study was not performed on field specimens.

Table 6.12. SCB fracture parameters for all field mixtures

Mixture	Temp(°C)	Fracture Toughness		Fracture Energy	
		Average ($MPa.m^{0.5}$)	CV (%)	Average (J/m^2)	CV (%)
MnROAD 03	-6	0.548	9.2	581.6	26.1
	-18	0.720	4.9	377.9	17.1
	-30	0.792	13.5	162.8	50.7
MnROAD 19	-12	0.661	8.2	253.9	53.4
	-24	0.690	17.3	257.9	20.2
	-36	0.768	16.7	108.0	62.0
MnROAD 33	-6	0.481	20.2	561.9	10.0
	-18	0.708	5.8	319.8	32.1
	-30	0.762	10.3	233.0	17.2
MnROAD 34	-12	0.625	8.4	584.8	22.4
	-24	0.882	5.7	424.3	41.3
	-36	0.956	10.6	373.6	22.2
MnROAD 35	-18	0.587	2.0	333.6	39.7
	-30	0.925	12.8	282.0	10.5
	-42	0.884	6.4	800.2	6.6
MN75 2	-6	0.545	12.4	419.4	27.8
	-18	0.774	8.6	353.9	16.5
	-30	0.795	23.0	356.5	16.2
MN75 4	-12	0.736	14.6	582.7	15.8
	-24	1.023	5.8	481.3	12.6
	-36	1.049	5.1	412.2	16.3
WI US 45	-12	0.751	7.5	668.4	3.2
	-24	0.702	26.6	320.6	46.9
	-36	0.795	7.6	266.5	7.8
WI STH 73	-6	0.690	0.6	303.3	17.4
	-18	0.820	11.1	375.9	6.0
	-30	0.930	7.4	231.1	95.4
IL US20 6	-6	0.392	4.5	321.6	18.5
	-18	0.707	2.0	367.4	43.0
	-30	0.732	7.2	180.7	62.6
IL US20 7	-12	0.594	4.4	315.3	22.8
	-24	0.677	16.0	309.1	117.0
	-36	0.574	40.4	166.2	54.1
IL I74	-12	0.644	8.6	307.6	51.0
	-24	0.586	25.1	213.0	n/a
	-36	0.579	51.1	294.0	52.2
ND 18	-6	0.585	3.7	444.2	28.3
	-18	0.618	10.0	205.8	22.9
	-30	0.606	6.3	163.3	83.6

Indirect Tensile Test (IDT) Creep Stiffness and Strength

Specimens cut from the field samples were also tested in IDT setup. Two parameters, creep stiffness and strength were determined using current AASHTO specification T 322-03. Creep stiffness was also calculated as a simple average over three replicates.

Table 6.13 presents creep stiffness values at 60sec and 500sec for all field mixtures. For cases when the number of replicates per temperature/mixture combination was smaller than 3, only simple average method was used.

Table 6.13. Creep stiffness values for all the mixtures at 60 and 500 seconds

Mixture	Temp (°C)	Creep stiffness @ 60sec [GPa]			Creep stiffness @ 500sec [GPa]		
		Simple average		AASHTO T 322-03	Simple average		AASHTO T 322-03
		Average	CV [%]		Average	CV [%]	
MnROAD 03	-6	7.03	21.9	9.00	3.37	28.6	4.11
	-18	15.86	4.0	16.02	10.09	8.2	10.61
	-30	30.69	12.9	32.33	25.24	3.4	27.35
MnROAD 19	-12	13.95	12.7	14.15	9.89	8.5	10.31
	-24	20.47	11.4	17.72	19.08	18.2	17.18
	-36	34.15	11.4	n/a	29.75	0.8	n/a
MnROAD 33	-6	8.80	25.0	9.65	4.27	35.9	4.43
	-18	14.45	15.7	16.17	9.93	19.2	11.06
	-30	21.67	14.7	22.40	15.78	18.3	16.43
MnROAD 34	-12	8.85	20.2	9.02	4.67	26.4	4.67
	-24	20.08	3.1	17.62	15.73	7.3	13.43
	-36	35.75	4.9	36.71	29.39	6.9	29.85
MnROAD 35	-18	9.75	12.5	10.96	6.72	36.0	7.56
	-30	15.60	2.2	14.04	11.59	2.3	10.41
	-42	30.41	16.5	34.74	24.92	15.7	28.58
MN75 2	-6	11.37	16.3	n/a	6.94	18.5	n/a
	-18	21.84	5.2	n/a	15.52	14.9	n/a
	-30	26.22	49.5	33.83	19.08	53.2	24.63
MN75 4	-12	14.04	22.2	n/a	7.60	29.1	n/a
	-24	24.72	26.2	n/a	18.39	29.9	n/a
	-36	30.47	5.0	26.45	26.35	3.5	23.41
WI US 45	-12	12.39	17.3	11.33	7.68	13.9	7.13
	-24	18.82	22.4	15.54	14.89	15.7	12.59
	-36	31.28	3.1	31.82	26.33	11.6	25.84
WI STH 73	-6	7.36	35.8	6.88	3.26	50.0	3.06
	-18	16.58	21.1	19.14	10.41	30.8	11.69
	-30	26.60	9.7	25.65	21.51	8.7	20.69
ND 18	-6	10.76	n/a	n/a	6.16	n/a	n/a
	-18	13.76	2.8	n/a	10.53	5.0	n/a
	-30	23.20	17.3	n/a	19.51	14.1	n/a

Tensile Strength

After creep test, each IDT specimen was used to measure tensile strength (AASHTO T 322-03). Only one (standard) loading rate was used (12.5mm/min). The summary of the results is presented in Table 6.14.

Table 6.14. Tensile strength values for all the mixtures

Mixture	Temp (°C)	Tensile strength [MPa]	
		Average	CV [%]
MnROAD 03	-6	4.941	5.2
	-18	5.077	17.9
	-30	4.199	3.4
MnROAD 19	-12	4.673	8.3
	-24	4.218	5.7
	-36	3.864	7.0
MnROAD 33	-6	4.496	4.8
	-18	5.251	1.8
	-30	3.928	18.6
MnROAD 34	-12	5.673	5.5
	-24	6.649	7.6
	-36	5.492	5.4
MnROAD 35	-18	4.282	13.9
	-30	5.483	4.5
	-42	5.519	2.3
MN75 2	-6	4.134	3.6
	-18	3.347	n/a
	-30	3.355	38.2
MN75 4	-12	5.589	6.5
	-24	5.625	6.4
	-36	4.618	6.2
WI US 45	-12	5.064	6.7
	-24	5.541	11.5
	-36	4.928	16.9
WI STH 73	-6	5.347	6.9
	-18	5.871	4.7
	-30	5.529	2.9
ND 18	-6	4.689	n/a
	-18	4.758	18.3
	-30	4.582	3.7

Thermal Stress Restrained Specimen Test (TSRST)

The TSRST system, developed under SHRP A-400 contract by Jung and Vinson (99), is an automated closed loop system which measures the tensile stress in an asphalt concrete specimen as it is cooled at constant rate. As the temperature drops, the specimen is restrained from

contracting thus inducing tensile stresses. The load and temperature are monitored and collected during the test using a load cell and four thermistors, respectively.

There are three major factors that influence the fracture resistance at low temperature: materials, environment and pavement geometry. Binder type, aggregate type and air void content are considered material factors. Temperature and cooling rate are included in environment factors. Pavement geometry factors include pavement width and thickness and the restraining effect of the aggregate base (100).

In this study only the two major factors were investigated using both field samples as well as mixtures produced in the laboratory. A total of twenty eight laboratory mixtures were tested as part of the comprehensive study on low temperature properties of asphalt materials. Additionally, twenty specimens obtained from US-45 located in Wisconsin and five MnROAD cells were used to evaluate field conditions. For the laboratory mixtures, two levels of air void content: 4% and 7% representing the design value and typical construction values, respectively, were chosen to study the effect of air voids on fracture resistance. Two levels of binder content, the design value and the design value plus 0.5%, were used to quantify the effect of asphalt content on the resistance to low temperature cracking. Two types of aggregate with different mechanical and physical properties, limestone and granite, were used to prepare the laboratory mixtures.

Materials

The experimental work included testing of field and laboratory specimens. A total of 76 specimens were tested in the TSRST system; 20 specimens recovered from the field and 56 specimens prepared in the laboratory. The test matrix for this study contains a combination of factors expected to have a significant effect on the low temperature fracture resistance of asphalt concrete.

Field Specimens

Several slabs were sawed from US-45 in Wisconsin and five cells at MnROAD. The slabs were brought to the lab where they were further sawed into prismatic specimens with the following dimensions: 50 ± 5 mm (2.0±0.15 in.) square and 250 ± 5 mm (10.0 ± 0.25 in.) in length. The asphalt binder and location of each slab is presented in Table 1.

Table 6.15. Field samples for TSRST

ID	PG binder	Location
WI US 45	58-34	Wisconsin
MnROAD 03	58-28	MnROAD
MnROAD 19	64-22	MnROAD
MnROAD 33	58-28	MnROAD
MnROAD 34	58-34	MnROAD
MnROAD 35	58-40	MnROAD

Laboratory Prepared Specimens

Laboratory specimens allow a better control of the factors that affect the thermal cracking properties of the asphalt concrete. Thus, statistical analysis can be performed to identify and quantitative evaluate the significance of the factors. These factors include binder type, aggregate type, binder content, and air void content.

The slabs were prepared and compacted at Iowa State University. Mixture 58-28:U1:7:LM was not available for testing during the TSRST program and slab 64-22:U1:4:LM was severely cracked before cutting.

Figure 6.16 shows some of the slabs used in TSRST testing. The laboratory prepared slabs were sawed in to prismatic specimens with the following dimensions: 50 ± 5 mm (2.0±0.15 in.) square and 250 ± 5 mm (10.0 ± 0.25 in.) in length.

Figure 6.16. Compacted slabs before cutting

Figure 6.17 shows typical laboratory specimens after sawing. A total of 56 tests were run, two replicates per mixture. Additional testing was done to investigate the effect of shape, size and cooling rate on the fracture properties of the mixtures.

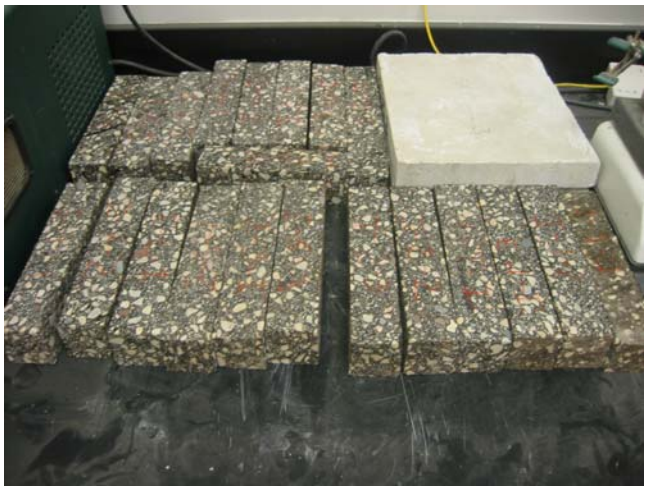

Figure 6.17. Laboratory specimens

Test Procedure

The TSRST system is design to measure the thermal induced tensile stress on an asphalt concrete specimen restrained from contracting when it is cooled at a constant rate. The cooling rate used in this study was 10°C/hr. Figure 6.18 shows a schematic picture of the system used for testing. The TSRST system consists of a chamber, load frame, computer, data acquisition system, temperature controller, two LVDT's, four thermistors, load cell and nitrogen cylinder.

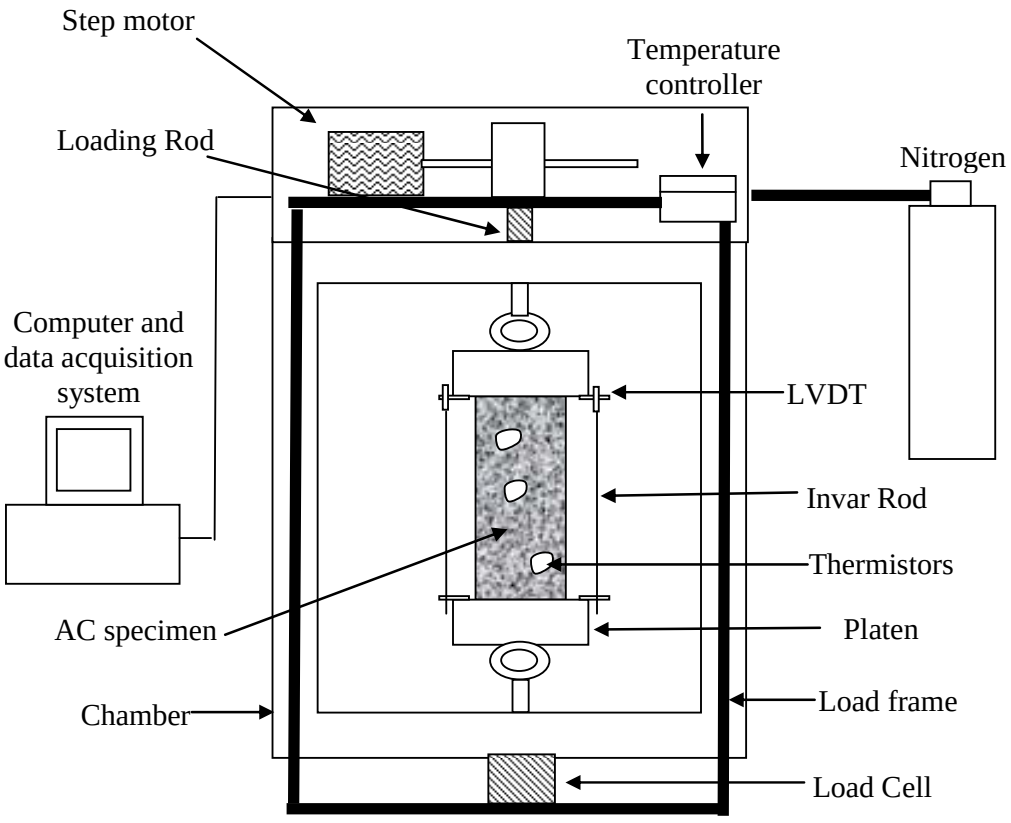

Figure 6.18. Schematic of TSRST (99)

The test procedure according to Jung and Vinson (99) is as follows:

1. Clean the platens with degreasing agent to remove previous material and use sand paper to make sure the surface is rough.
2. Prepare the epoxy: the mix proportion for plastic steel putty (hardener: resin) is 1: 9 by weight.
3. Attach the end platens to the specimen alignment stand and place the specimen between the platens with epoxy (see Figure 6.19). Make sure the specimen is aligned. Misalignment of the specimen will produce bending stresses during testing.
4. Leave the specimen in the stand until the epoxy is cured (e.g. at least 24 hours).
5. Remove the specimen with the end platens from the stand and store it at 5˚C for one hour for precooling (this time is used only if air is circulated otherwise 6 hours is used).
6. Connect the specimen-platen system to the TSRST machine. Attached the two LVDT's.
7. Attached the four thermistors using modeling clay in different locations and sides of the specimen. Close the chamber (see Figure 6.20).
8. Set the cooling rate (e.g. 10°C/hr) with the temperature controller and apply an initial tension load before starting the test.
9. Start program in the computer to correct position of the specimen and to record the surface temperature and load until the specimen fails.

Figure 6.19. Specimen alignment stand

Figure 6.20. TSRST test

In addition to the test protocol described before, ultrasound testing was performed on the laboratory specimens after the precooling cycle. The quality of the laboratory specimens was assessed by means of the UK1401 ultrasonic tester (see Figure 6.21). Khazanovich *et al.* (101) studied the applicability of the ultrasonic technology for evaluation of cracks and quality of flexible pavements. The wave velocity of the specimens was measured on its four different faces and an average was calculated. Larger wave velocities represent stiffer materials.

Figure 6.21. Ultrasonic tester UK1401

Results

Figure 6.22 shows a typical result from TSRST test. As the temperature inside the chamber drops at a constant rate, the thermally induced tensile stress increases until fracture occurs.

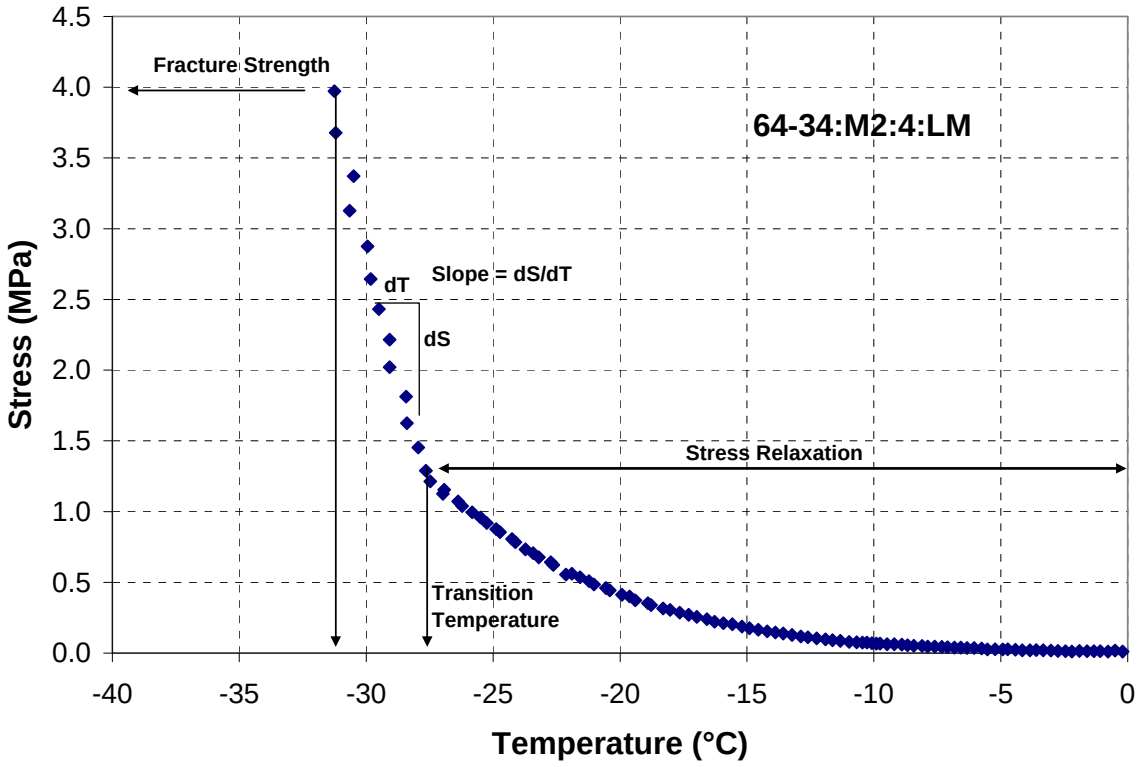

Figure 6.22. Typical stress-temperature curve from TSRST

The slope of the curve (dS/dT) shown in Figure 6.22 slowly increases until it reaches its maximum value at the transition temperature. After this temperature, dS/dT is constant and the stress temperature curve becomes linear until the specimen fails. The tensile stress and the temperature at the break point are the fracture strength and the fracture temperature, respectively.

Field Specimens

Fracture temperature, fracture strength, transition temperature, dS/dT, specific gravity and absorption of the field specimens are presented in Table 6.16.

Table 6.16. TSRST results for field specimens

ID	Replicate	PG binder	Fracture Temp (°C)	Fracture Strength (MPa)	dS/dT (MPa/°C)	Trans. Temp (°C)	Gs	Abs. (%)
WI US 45	1	58-34	-26.1	3.189	0.137	-10.8	2.368	0.072
WI US 45	2	58-34	-15.4	1.145	0.091	-10.0	2.362	0.086
MnROAD 03	1	58-28	-26.8	3.121	0.213	-16.2	2.387	0.058
MnROAD 03	2	58-28	-27.9	3.128	0.187	-15.6	2.372	0.045
MnROAD 19	1	64-22	-22.3	2.239	0.147	-12.6	2.284	0.048
MnROAD 19	2	64-22	-24.4	2.873	0.159	-10.0	2.292	0.061
MnROAD 19	3	64-22	-25.6	2.158	0.120	-11.0	2.297	0.073
MnROAD 19	4	64-22	-26.9	3.139	0.235	-20.2	2.326	0.060
MnROAD 33	1	58-28	-23.3	2.322	0.153	-14.6	2.350	0.079
MnROAD 33	2	58-28	-25.4	2.255	0.138	-14.8	2.357	0.089
MnROAD 33	3	58-28	-26.6	2.802	0.165	-14.6	2.377	0.087
MnROAD 33	4	58-28	-29.0	3.177	0.219	-22.3	2.363	0.069
MnROAD 34	1	58-34	-32.8	3.750	0.291	-25.9	2.355	0.049
MnROAD 34	2	58-34	-32.9	4.014	0.258	-25.2	2.374	0.078
MnROAD 34	3	58-34	-23.8	1.486	0.101	-13.6	2.378	0.039
MnROAD 34	4	58-34	-33.8	3.731	0.237	-23.9	2.364	0.049
MnROAD 35	1	58-40	-26.5	1.698	0.081	-14.8	2.374	0.083
MnROAD 35	2	58-40	-25.5	1.705	0.096	-19.6	2.373	0.052
MnROAD 35	3	58-40	-34.8	1.101	0.037	-14.8	2.356	0.046
MnROAD 35	4	58-40	-31.8	2.716	0.173	-24.2	2.370	0.071

Laboratory Prepared Specimens

Table 6.17 presents the results for the laboratory prepared mixtures. Fracture temperature, fracture strength, dS/dT, transition temperature, specific gravity, absorption and ultrasonic wave velocity for each specimen are shown in Table 6.17. The average fracture temperature for the laboratory specimens was -30.3°C. The lowest fracture temperature was -38.9°C and the highest was -25.0°C.

Table 6.17. TSRST results for laboratory specimens

ID	Rep.	Fracture Temp. (°C)	Fracture Strength (MPa)	dS/dT (MPa/°C)	Trans. Temp. (°C)	Gs	Abs. (%)	Velocity (m/s)
58-40:M1:4:GR	1	-31.0	4.049	0.573	-25.2	2.293	0.113	*
58-40:M1:4:GR	2	-36.8	4.078	0.543	-31.2	2.334	0.062	*
58-40:M1:4:GR:+0.5AC	1	-38.9	6.207	0.993	-34.5	2.361	0.044	3610
58-40:M1:4:GR:+0.5AC	2	-29.6	3.557	0.829	-26.2	2.361	0.031	2430
58-40:M1:4:LM	1	-34.8	2.959	0.322	-26.3	2.367	0.159	*
58-40:M1:4:LM	2	-31.7	4.012	0.673	-27.5	2.331	0.117	*
58-34:M1:4:GR	1	-30.9	3.005	0.393	-27.1	2.324	0.076	*
58-34:M1:4:GR	2	-27.9	3.200	0.397	-25.1	2.318	0.051	*
58-34:M1:4:GR	3	-32.8	4.323	0.303	-24.7	2.276	0.097	*
58-34:M1:4:GR:+0.5AC	1	-31.6	3.279	0.381	-25.1	2.318	0.085	3778
58-34:M1:4:GR:+0.5AC	2	-28.1	2.040	0.828	-27.0	2.338	0.077	3895
58-34:M1:4:LM	1	-31.1	3.834	0.533	-25.5	2.366	0.112	*
58-34:M1:4:LM	2	-34.1	3.289	0.322	-25.5	2.360	0.111	*
58-34:M1:4:LM	3	-32.6	2.862	0.259	-26.7	2.362	0.118	*
58-34:M1:4:LM	4	-26.6	2.531	1.415	-25.5	2.360	0.111	*
58-34:M2:4:GR	1	-27.0	3.156	1.704	-25.5	2.299	0.077	*
58-34:M2:4:GR	2	-34.6	2.764	0.496	-32.0	2.277	0.103	*
58-34:M2:4:LM	1	-32.3	3.167	0.537	-29.3	2.322	0.139	3578
58-34:M2:4:LM	2	-25.6	1.968	0.986	-24.7	2.300	0.115	3488
58-28:U1:4:GR	1	-28.0	2.636	0.509	-25.7	2.313	0.166	3820
58-28:U1:4:GR	2	-31.1	2.585	0.215	-25.2	2.313	0.095	3248
58-28:U1:4:GR:+0.5AC	1	-31.0	3.020	0.228	-23.0	2.321	0.110	3790
58-28:U1:4:GR:+0.5AC	2	-31.8	3.271	0.224	-22.4	2.328	0.059	3805
58-28:U1:4:LM	1	-25.5	1.136	0.410	-24.9	2.371	0.087	3673
58-28:U1:4:LM	2	-27.3	1.818	0.236	-25.2	2.366	0.088	*
58-28:U1:4:LM:+0.5AC	1	-27.6	2.555	0.503	-25.9	2.377	0.087	3878
58-28:U1:4:LM:+0.5AC	2	-28.5	2.789	0.502	-26.6	2.402	0.150	*
58-28:U1:7:GR	1	-34.2	2.293	0.342	-29.9	2.160	2.170	3203
58-28:U1:7:GR	2	-31.5	2.156	0.302	-27.0	2.160	2.126	3093
58-28:U1:7:GR:+0.5AC	1	-27.4	2.104	0.160	-20.7	2.259	0.262	3663
58-28:U1:7:GR:+0.5AC	2	-29.4	2.550	0.293	-25.7	2.261	0.254	3633
58-28:U1:7:LM:+0.5AC	1	-30.8	1.990	0.181	-26.0	2.239	0.570	3283
58-28:U1:7:LM:+0.5AC	2	-27.7	1.351	0.114	-20.1	2.268	0.345	3443
58-28:U2:4:GR	1	-32.7	3.012	0.215	-21.6	2.305	0.212	3758
58-28:U2:4:GR	2	-31.8	2.969	0.201	-21.4	2.310	0.135	3778
58-28:U2:4:LM	1	-26.7	1.670	0.182	-22.1	2.332	0.082	3568
58-28:U2:4:LM	2	-26.8	1.859	0.258	-23.6	2.322	0.084	3493
64-34:M1:4:GR	1	-30.8	3.090	0.197	-20.3	2.319	0.120	3813
64-34:M1:4:GR	2	-26.7	3.268	1.263	-25.5	2.309	0.103	3763
64-34:M1:4:LM	1	-32.7	2.934	0.221	-25.5	2.366	0.088	3873
64-34:M1:4:LM	2	-33.8	3.656	0.321	-28.7	2.358	0.108	3855
64-34:M2:4:GR	1	-26.8	3.184	1.126	-25.1	2.322	0.117	3795
64-34:M2:4:GR	2	-34.3	2.669	0.214	-25.3	2.313	0.155	3780

64-34:M2:4:LM	1	-31.3	3.972	0.702	-27.5	2.324	0.121	3580
64-34:M2:4:LM	2	-33.6	2.992	0.343	-29.5	2.329	0.115	3508
64-28:U1:4:GR	1	-31.0	2.958	0.221	-22.1	2.297	0.169	3880
64-28:U1:4:GR	2	-30.7	3.205	0.229	-21.9	2.315	0.078	3925
64-28:U1:4:LM	1	-28.1	2.468	0.185	-22.7	2.330	0.115	3705
64-28:U1:4:LM	2	-27.7	2.331	0.172	-19.6	2.337	0.096	3753
64-28:M1:4:GR	1	-31.0	3.164	0.475	-26.8	2.308	0.351	3748
64-28:M1:4:GR	2	-29.3	3.032	0.689	-26.6	2.294	0.921	3560
64-28:M1:4:LM	1	-28.3	2.629	0.397	-26.4	2.324	0.135	3598
64-22:U1:4:GR	1	-26.8	2.821	0.209	-19.6	2.296	0.247	3900
64-22:U1:4:GR	2	-25.0	3.023	0.206	-18.5	2.320	0.140	3935

* Ultrasonic tester not available

Dilatometric testing of the asphalt mixture slab compactor specimens and field beams samples

This section describes the results and the test method used to determine dilatometric properties of asphalt mixture slab compactor specimens (laboratory mixture) as well as field beams specimens. The laboratory samples were prepared by the research group at Iowa State University using a linear kneading slab compactor as described in Chapter 4. The field samples were delivered from the field in various beam sizes. The field-cut beams and the laboratory prepared slabs were used to cut prismatic beam samples of standard length and cross section suing a wet diamond-blade saw. The following sections describe the preparation and testing of samples.

Dilatometric Testing For Asphalt Mixture Slab Compactor Specimens

Materials

Samples for this test were obtained from Iowa State University for each mixture in the testing matrix for the project. A total of 54 slabs representing 27 mixtures of various combinations of binders, aggregates, voids content, and asphalt content were delivered (each with one replicate sample). From each slab two specimens were prepared for testing. Each slab sample supplied was approximately 200mm by 380mm by 65mm height and it has to be sawn with a masonry saw into specimen size of 65mm by 50mm by 380mm length. All mixtures were tested in duplicate for repeatability. Also all specimens where tested in a cooling as well as a heating cycle.

Specimen Preparation

Prior to testing the end caps and rods used to monitor length changes are mounted at both ends of the mixture specimens using epoxy adhesive as shown in Figure 6.23. The rods are made of a special polymer called " G7 polymer" which was chosen for this application because of its very low thermal coefficient of expansion and conductivity.

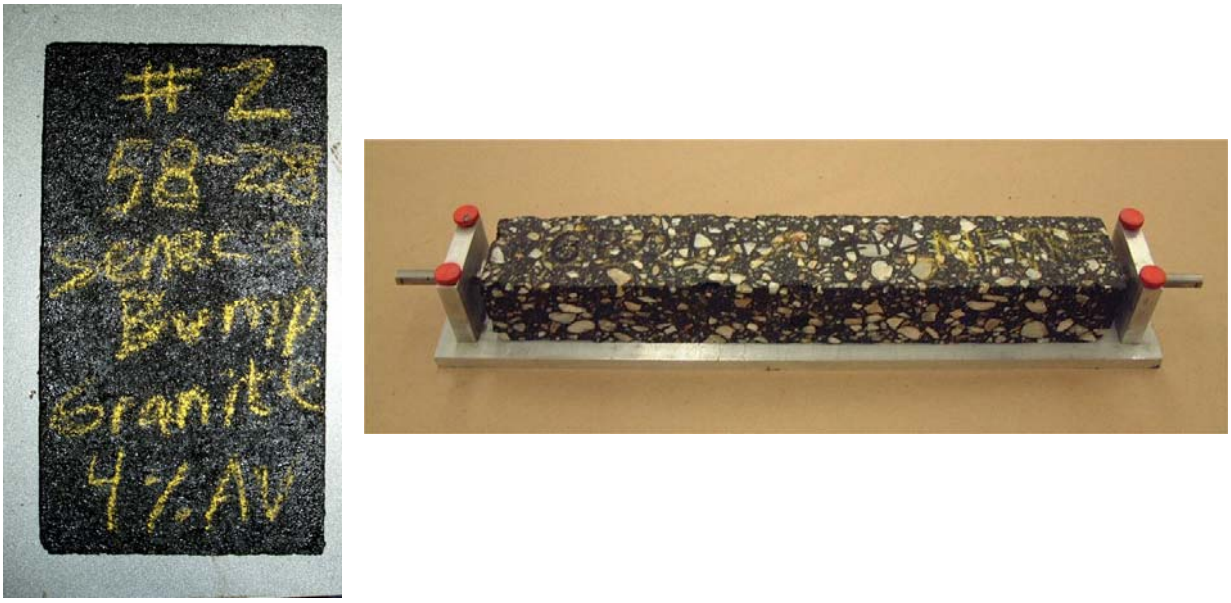

Figure 6.23. Received sample (left) and beam specimen prepared for testing (right)

Test Procedure

Testing starts by placing specimen on a frictionless Teflon base in an environmental chamber as shown in Figure 6.24. Heater is installed inside of the chamber to increase the temperature and chamber is cooled by means of liquid Nitrogen. The temperature measurements were made using a T-type thermocouple calibrated with a digital thermometer. A dummy specimen identical to the specimen used in the tests was placed on the bottom of the temperature control chamber for measuring the temperatures during tests. Two thermocouples were used one is on the surface of the specimen and the other in the center of the dummy specimen, and the third in approximately the same position as the mixture specimen. Specimens are held at 40°C for 10 min. before cooling the temperature to -80°C at the rate of 1°C/min. After reaching -80°C, the Specimens are held at this constant temperature for 10 minutes before the heating cycle starts and ends at 40°C using the same temperature change rate. The rate of temperature change, which was fixed for all the tests at 1ºC/min., was chosen for practical reasons and represented what had been used in previous studies (96). As the temperature changes, the two LVDTs placed at the end of G7 rods allow measuring changes in length of the specimen continuously while temperature is changing. The LVDTs readings were recorded at every minute. A system-controlling program (LabView software) was designed to control temperature heater and the inflow of liquid nitrogen and capture the temperature as well as the LVDTs' readings.

Computations

The following hyperbolic equation, which has been used to fit binder thermo-volumetric properties (97), was applied to the mixture data, and found to be effective to fit the nearly dual-linear curve.

$$v = c_v + a_g(T - T_g) + R(a_l - a_g)\ln\{1 + \exp[(T - T_g)/R]\}$$

where:

v = specific volume change in ml/g,

c_v = a constant, having no physical significance,

T_g = the glass transition temperature,

α_g = slope of lower asymptote of the v versus T curve,

a_l = slope of higher asymptote of the v versus T curve, and

R = a parameter representing the curvature between the asymptotes.

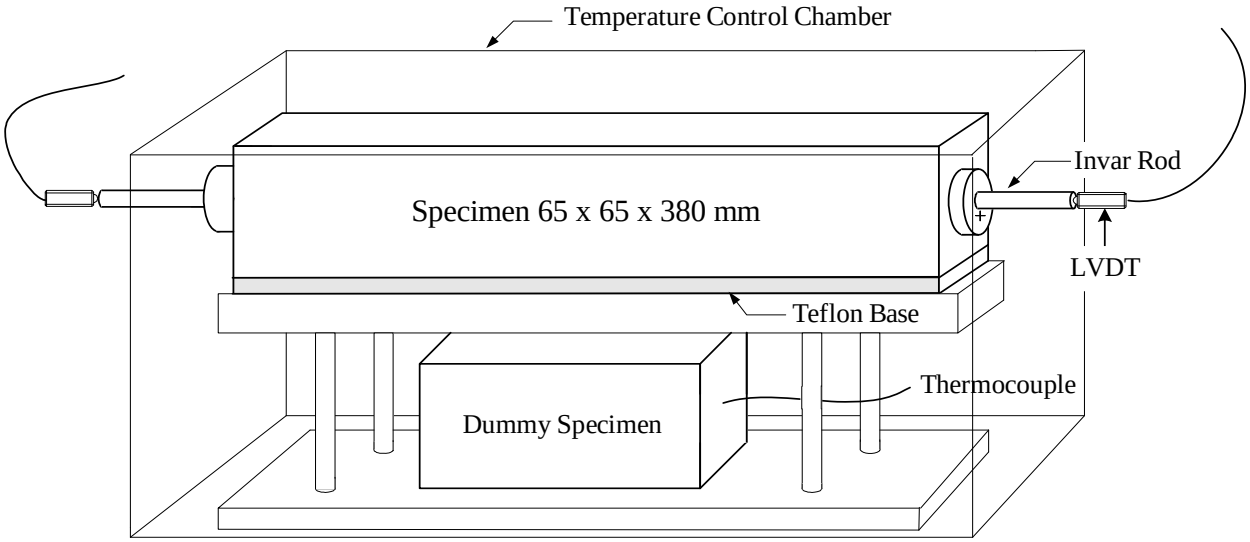

Figure 6.24. Specimen and LVDT position

Figure 6.25 depicts an example of the results of the temperatures measured on the surface and in the center of the dummy specimen. Because of the lag in sample temperature, it was decided to keep the dummy specimen and use the internal temperature in all analyses. The dummy specimen has the same dimensions as the regular sample and similar void content. It is thus assumed that the thermal conductivity is the same for all different mixtures tested. In the past researchers have use a calibration curve to adjust the chamber temperature and estimate sample internal temperature but in this study the dummy sample internal temperature was recorded continuously.

Figure 6.26 shows typical results of the testing in terms of thermal deformation versus the temperature of the specimen. The figure includes the cooling and the heating cycle. In the analysis, a separate fit of the model was used for the cooling than the heating cycle. This was done because it is clear that the trend of change in length during the cooling was different than the trend during the heating. This difference results in Tg values for cooling that are different than Tg values during heating.

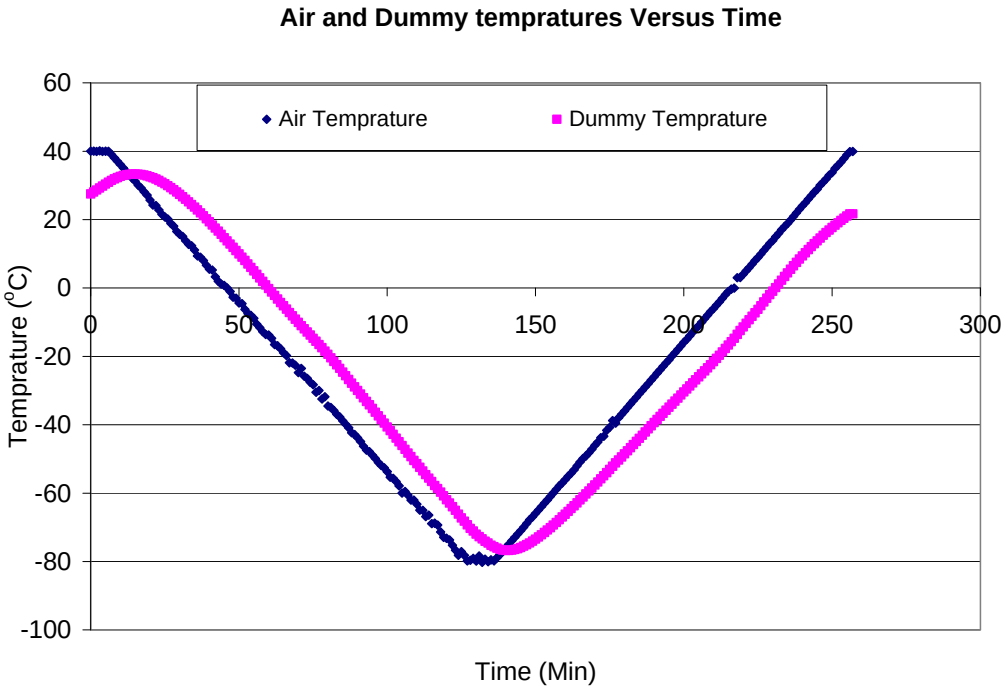

Figure 6.25. Temperature profile in the chamber during the test (cooling and heating)

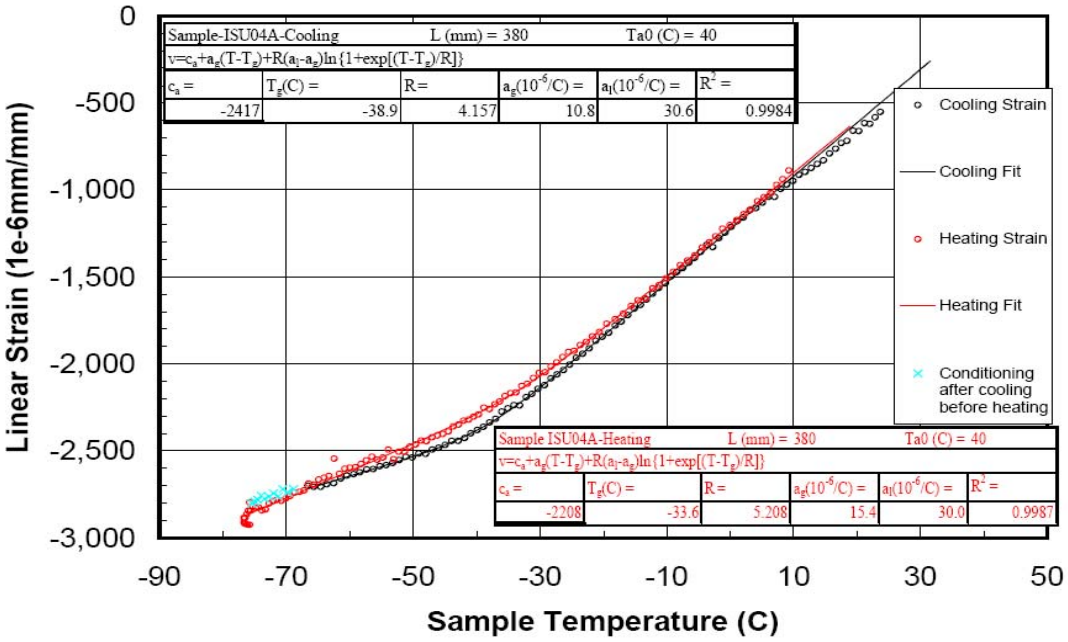

Figure 6.26. Typical results of the test

The results of the dilatometric measurements for all the laboratory produced mixtures are shown in Table 6.18. The results include glass transition temperature (Tg), the coefficients of contraction / expansion below and above glass transition temperature (α_g, α_l) and coefficient of regression for the cooling and the heating cycles for each sample. The results of the duplicate sample for each mixture were also listed in Table 6.18 to show the repeatability of the measurements. These duplicate samples were cut from the same slab but where tested in a random sequence to offset any time dependency bias. Table 6.19 is prepared to include only the average values of the glass transition parameters which can be used in modeling of the thermal cracking of these samples.

Table 6.18. Dilatometeric data for laboratory produced mixtures including replicates

Sample ID	Result Cooling				Result Heating			
	T_g(C)	a_g (10^{-6}/ C)	a_l (10^{-6}/C)	R^2	T_g(C)	a_g (10^{-6}/C)	a_l (10^{-6}/C)	R^2
58-40:M1:4:GR	-46.3	13.1	29.2	0.9993	-24.2	16.5	37.8	0.99855
58-40:M1:4:GR	-48.2	15.5	31.8	0.9928	-24.2	16.5	37.8	0.99855
58-40:M1:4:GR:+0.5AC	-46.3	12.6	35.2	0.9988	-30.4	12.2	46.9	0.99836
58-40:M1:4:GR:+0.5AC	-49.7	11.4	30.4	0.9947	-34.7	12.9	38.2	0.99847
58-40:M1:4:LM	-36.7	12.5	32.7	0.9960	-12.7	15.1	49.9	0.99834
58-40:M1:4:LM	-45.8	10.4	31.1	0.9996	-29.2	15.6	32.1	0.99801
58-34:M1:4:GR	-38.9	10.8	30.6	0.9984	-33.3	15.1	30.5	0.99879
58-34:M1:4:GR	-36.3	9.6	31.9	0.9974	-24.9	15.0	34.0	0.99881
58-34:M1:4:GR:+0.5AC	-37.5	6.6	37.4	0.9900	-29.4	14.8	33.9	0.99829
58-34:M1:4:GR:+0.5AC	-35.5	11.0	32.1	0.9978	-20.6	11.1	39.1	0.99431
58-34:M1:4:LM	-32.4	9.4	36.2	0.9967	-26.8	16.0	35.4	0.99887
58-34:M1:4:LM	-32.8	10.1	32.5	0.9892	-25.2	12.4	36.2	0.99695
58-34:M2:4:GR	-30.8	10.8	34.8	0.9984	-26.7	15.6	33.3	0.99718
58-34:M2:4:GR	-32.9	11.6	32.2	0.9996	-26.7	15.6	33.3	0.99718
58-34:M2:4:LM	-32.6	9.4	32.9	0.9994	-21.1	13.6	34.3	0.99727
58-34:M2:4:LM	-36.8	9.4	28.9	0.9965	-35.4	11.3	29.8	0.99734
58-28:U1:4:GR	-38.8	16.4	37.6	0.9892	-10.9	25.4	58.6	0.99927
58-28:U1:4:GR	-44.7	12.1	30.6	0.9983	-40.4	14.6	36.4	0.99945
58-28:U1:4:GR:+0.5AC	-43.3	13.3	35.8	0.9942	-32.7	17.7	39.3	0.99904
58-28:U1:4:GR:+0.5AC	-41.8	12.2	37.8	0.9968	-26.1	18.7	43.1	0.99931
58-28:U1:4:LM	-26.4	10.1	40.5	0.9871	-15.9	13.9	45.8	0.99632
58-28:U1:4:LM	-32.0	7.0	38.1	0.9998	-21.7	13.1	41.6	0.99885
58-28:U1:4:LM:+0.5AC	-29.9	10.9	39.6	0.9997	-19.3	13.7	42.2	0.99750
58-28:U1:4:LM:+0.5AC	-29.7	9.6	40.4	0.9998	-19.0	13.8	42.0	0.99810
58-28:U1:7:GR	-35.0	10.2	32.9	0.9936	-12.1	13.4	47.7	0.99948
58-28:U1:7:GR	-34.2	8.2	33.1	0.9886	-12.1	13.4	47.7	0.99948
58-28:U1:7:GR:+0.5AC	-31.0	6.6	38.4	0.9995	-18.0	16.3	38.8	0.99677
58-28:U1:7:GR:+0.5AC	-30.7	12.5	35.5	0.9992	-19.2	17.5	39.3	0.99840
58-28:U1:7:LM	-33.3	11.3	35.7	0.9994	-28.6	15.4	31.6	0.99271

58-28:U1:7:LM	-31.0	13.5	36.8	0.9996	-29.0	15.9	33.2	0.99745
58-28:U1:7:LM:+0.5AC	-30.8	9.9	41.7	0.9999	-22.4	14.4	42.9	0.99788
58-28:U1:7:LM:+0.5AC	-28.9	9.5	39.8	0.9827	-17.2	15.3	45.8	0.99809
58-28:U2:4:GR	-29.7	11.6	32.0	0.9970	-29.6	16.7	30.6	0.99848
58-28:U2:4:GR	-27.9	9.4	36.7	0.9994	-23.7	14.6	35.6	0.99935
58-28:U2:4:LM	-34.3	10.2	35.3	0.9973	-18.7	16.1	42.1	0.99961
58-28:U2:4:LM	-32.0	10.6	35.8	0.9980	-18.0	15.5	45.2	0.99820
64-34:M1:4:GR	-34.7	8.7	33.3	0.9941	-29.6	15.1	32.0	0.99968
64-34:M1:4:GR	-38.2	12.9	33.5	0.9963	-26.6	11.9	42.6	0.99699
64-34:M1:4:LM	-38.0	5.0	32.7	0.9974	-31.5	11.8	33.4	0.99780
64-34:M1:4:LM	-36.4	9.4	31.3	0.9998	-29.3	12.6	34.1	0.99899
64-34:M2:4:GR	-39.9	9.7	32.8	0.9980	-23.7	15.5	36.8	0.99810
64-34:M2:4:GR	-40.8	10.6	31.4	0.9986	-26.1	12.8	41.1	0.99832
64-34:M2:4:LM	-37.6	11.1	35.5	0.9997	-25.0	12.2	42.3	0.99927
64-34:M2:4:LM	-39.2	12.1	37.0	0.9993	-25.4	19.5	36.0	0.99807
64-28:U1:4:GR	-34.4	10.4	33.3	0.9957	-18.2	15.3	40.7	0.99906
64-28:U1:4:GR	-31.5	9.4	33.7	0.9986	-30.6	14.9	32.0	0.99780
64-28:U1:4:LM	-31.0	8.3	35.9	0.9998	-20.4	14.7	37.0	0.99767
64-28:U1:4:LM	-30.7	9.1	37.0	0.9991	-35.2	11.3	34.3	0.99892
64-28:M1:4:GR	-29.0	13.8	33.1	0.9996	-23.6	17.0	33.2	0.99728
64-28:M1:4:GR	-37.9	9.5	33.5	0.9943	-16.9	16.8	32.9	0.99912
64-28:M1:4:LM	-34.4	7.3	39.7	0.9994	-29.2	15.4	37.0	0.99687
64-28:M1:4:LM	-27.7	10.8	38.6	0.9995	-26.2	13.0	38.7	0.99847
64-22:U1:4:GR	-28.6	9.1	33.5	0.9995	-29.8	11.7	32.2	0.99914
64-22:U1:4:GR	-27.3	12.9	32.9	0.9997	-27.2	15.0	33.0	0.99859

Table 6.19. Dilatometeric average data for laboratory produced mixtures

Sample ID	Result Cooling				Result Heating			
	T_g(C)	a_g (10^{-6}/ C)	T_g(C)	a_g (10^{-6}/ C)	T_g(C)	a_g (10^{-6}/ C)	T_g(C)	a_g (10^{-6}/ C)
58-40:M1:4:GR	-47.24	14.31	30.48	0.9960	-24.25	16.47	37.84	0.9986
58-40:M1:4:GR:+0.5AC	-47.99	12.01	32.84	0.9967	-32.56	12.58	42.53	0.9984
58-40:M1:4:LM	-41.23	11.48	31.89	0.9978	-20.98	15.36	41.00	0.9982
58-34:M1:4:GR	-37.60	10.20	31.25	0.9979	-29.08	15.06	32.25	0.9988
58-34:M1:4:GR:+0.5AC	-36.54	8.82	34.79	0.9939	-25.01	12.93	36.51	0.9963
58-34:M1:4:LM	-32.62	9.76	34.38	0.9930	-26.00	14.20	35.78	0.9979
58-34:M2:4:GR	-31.83	11.19	33.51	0.9990	-26.71	15.59	33.30	0.9972
58-34:M2:4:LM	-34.70	9.38	30.89	0.9980	-28.21	12.43	32.09	0.9973
58-28:U1:4:GR	-41.79	14.27	34.11	0.9937	-25.66	20.02	47.54	0.9994
58-28:U1:4:GR:+0.5AC	-42.53	12.77	36.78	0.9955	-29.40	18.18	41.19	0.9992
58-28:U1:4:LM	-29.18	8.56	39.32	0.9935	-18.80	13.47	43.69	0.9976
58-28:U1:4:LM:+0.5AC	-29.81	10.28	40.03	0.9998	-19.15	13.72	42.10	0.9978
58-28:U1:7:GR	-34.64	9.19	33.01	0.9911	-12.12	13.38	47.66	0.9995
58-28:U1:7:GR:+0.5AC	-30.89	9.52	36.96	0.9993	-18.58	16.87	39.05	0.9976
58-28:U1:7:LM	-32.17	12.40	36.21	0.9995	-28.80	15.63	32.43	0.9951
58-28:U1:7:LM:+0.5AC	-29.82	9.72	40.74	0.9913	-19.78	14.83	44.31	0.9980
58-28:U2:4:GR	-28.78	10.53	34.35	0.9982	-26.67	15.66	33.07	0.9989
58-28:U2:4:LM	-33.12	10.39	35.58	0.9976	-18.38	15.81	43.64	0.9989
64-34:M1:4:GR	-36.46	10.81	33.44	0.9952	-28.12	13.50	37.27	0.9983
64-34:M1:4:LM	-37.21	7.19	31.99	0.9986	-30.40	12.21	33.75	0.9984
64-34:M2:4:GR	-40.37	10.15	32.12	0.9983	-24.91	14.15	38.95	0.9982
64-34:M2:4:LM	-38.39	11.57	36.27	0.9995	-25.19	15.86	39.15	0.9987
64-28:U1:4:GR	-32.91	9.88	33.50	0.9971	-24.37	15.09	36.33	0.9984
64-28:U1:4:LM	-30.86	8.67	36.43	0.9994	-27.75	13.01	35.64	0.9983
64-28:M1:4:GR	-33.41	11.69	33.28	0.9969	-20.22	16.89	33.04	0.9982
64-28:M1:4:LM	-31.06	9.05	39.16	0.9995	-27.71	14.17	37.86	0.9977
64-22:U1:4:GR	-27.94	10.95	33.20	0.9996	-28.49	13.35	32.64	0.9989

Testing of Asphalt Field Mixture Samples

The sample preparation and test method used for the field mixture are similar to laboratory prepared mixtures. Obviously no compaction was needed and the samples were sawed directly out of the field beam specimens.

Table 6.20 shows the field asphalt beam samples received together with their sizes. Each sample was sawn with a masonry saw into specimen size of 65mm by 50mm by 380mm length.

Table 6.20. List of Field samples received at University of Wisconsin

Site	Code name	Beams Size
MnROAD Cell 03	MnROAD 03	560x175x100
MnROAD Cell 19	MnROAD 19	475x200x150
MnROAD Cell 33	MnROAD 33	475x175x100
MnROAD Cell 34	MnROAD 34	475x175x100
MnROAD Cell 35	MnROAD 35	475x175x100
MN CSAH-75, section 2 EB	MN75 2	475x200x175
MN CSAH-75, section 4 WB	MN75 4	475x200x175
WI US-45	WI US 45	380x65x48
WI STH-73	WI STH 73	Samples not available
IL US-20, section 6	IL US20 6	380x65x50
IL US-20, section 7	IL US20 7	380x65x50
IL I-74	IL I74	Samples not available
ND SH-18	ND 18	Samples not available

The mixtures were tested in duplicate for repeatability. Also all specimens where tested in a cooling cycle as well as a heating cycle. Some of the samples could not be tested because they were not the top layer of the pavement and in some cases, the top layer thickness was less than the specimen size required. Table 6.21 shows test results of all samples. Table 6.22 shows the average values for the field mixtures that were tested

The results are limited in size and they are mainly needed for modeling of the thermal cracking. Thus no statistical analysis was conducted for this set of data. It can however be observed that the Tg values for the heating cycles are higher than the cooling cycles and the α_g values are higher during the heating cycles than the values during the cooling cycles. The relative trend for α_l is reversed as the values during the heating cycle is lower than the values during cooling. This asymmetrical behavior deserves further study.

Table 6.21. Dilatometric results for field mixtures

Field Location	Label	Result Cooling (Contraction)				Result Heating (Expansion)			
		T_g(C)	α_g (10^{-6}/C)	α_l (10^{-6}/C)	R^2	T_g(C)	α_g (10^{-6}/C)	α_l (10^{-6}/C)	R^2
Wisconsin US Highway 45	WI US 45A	-25.58	8.54	27.86	0.9996	-38.56	12.63	22.42	0.9973
Wisconsin US Highway 45	WI US 45B	-33.51	8.10	28.07	0.9996	-43.31	13.43	22.49	0.9992
MnROAD Test Cell 34	MnROAD 34A	-31.25	12.04	30.28	0.9984	-36.91	11.92	27.60	0.9981
MnROAD Test Cell 34	MnROAD 34B	-21.17	5.68	37.86	0.9994	-23.82	12.10	39.59	0.9994
MnROAD Test Cell 35	MnROAD 35A	-38.70	1.40	32.38	0.9986	-31.52	14.30	33.67	0.9995
MnROAD Test Cell 35	MnROAD 35B	-15.00	16.33	40.01	0.9989	-38.32	13.70	35.09	0.9988
MnROAD Test Cell 03	MnROAD 03A	-20.32	6.99	31.59	0.9992	-15.35	11.39	31.79	0.9994
MnROAD Test Cell 03	MnROAD 03B	-25.27	9.93	38.98	0.9984	-24.80	14.91	35.73	0.9993
MnROAD Test Cell 19	MnROAD 19A	-15.26	13.26	38.60	0.9983	-21.23	16.54	36.09	0.9968
MnROAD Test Cell 19	MnROAD 19B	Duplicate sample for top layer damaged							
MnROAD Test Cell 33	MnROAD 33	Broken sample							
Minnesota CSAH-75 Section 2 EB	MN75 2	Not tested (top layer too thin)							
Minnesota CSAH-75 Section 4 WB	MN75 4	Not tested (top layer too thin)							
Wisconsin State Highway 73	WI STH 73	Sample not available							
Illinois Interstate 74	IL I74	Sample not available							
Illinois US Highway 20 (AC10 Binder)	IL US20 6	Not tested (top layer too thin)							
Illinois US Highway 20 (AC20 Binder)	IL US20 7	Not tested (top layer too thin)							

Table 6.22. Dilatometric results for field mixtures - averages

Label	Result Cooling (Contraction)				Result Heating (Expansion)			
	T_g(C)	α_g(10^{-6}/C)	α_l(10^{-6}/C)	R^2	T_g(C)	α_g(10^{-6}/C)	α_l(10^{-6}/C)	R^2
WI US 45	-29.54	8.32	27.96	0.9996	-40.94	13.03	22.45	0.9983
MnROAD 35	-26.85	8.87	36.20	0.9988	-34.92	14.00	34.38	0.9991
MnROAD 34	-26.21	8.86	34.07	0.9989	-30.36	12.01	33.59	0.9987
MnROAD 19	-15.26	13.26	38.60	0.9983	-21.23	16.54	36.09	0.9968
MnROAD 03	-22.80	8.46	35.28	0.9988	-20.07	13.15	33.76	0.9994

CHAPTER 7

ANALYSIS OF EXPERIMENTAL DATA

Asphalt Binder Data

Dilatometric Results

PAV Binders

As explained in Chapter 5 a specially designed dilatometer was used for measuring the dilatometeric properties of the binders. Table 7.1 gives a summary of the dilatometeric properties of the binders based on averaging the measurements of the duplicate samples. The measurements include the glass transition temperature (T_g), thermal coefficient of contraction above T_g (liquid state α_l) and thermal coefficient of contraction below T_g, (glassy state α_g). The regression coefficient of curve fitting used for the model is also included in Table 7.1. Figure 7.1 includes a bar chart comparing the results as a function of binder source and grade.

Table 7.1. Summary of the dilatometeric properties of PAV aged binders

Binder Used			Thermal Properties			
S. No	**PG**	**NAME**	**T_g(^{o}C)**	**a_g(10^{-6}/^{o}C)**	**a_l(10^{-6}/^{o}C)**	**R^2**
LTCPB10	**PG 58-40**	**SEVAGE FHR7**	-24.98	333.4	538.3	.09989
LTCPB08	**PG 58-34**	**ELVALOY MURPHY**	-37.15	143.1	463.4	0.9998
LTCPB09	**PG 58-34**	**SEVAGE**	-29.64	195.9	583.3	0.9997
LTCPB01	**PG 58-28**	**NEAT SENECA**	-20.14	202.7	477.3	0.9994
LTCPB02	**PG 58-28**	**NEAT PAYNE & DOLAR**	-26.42	350.6	578.4	0.9998
LTCPB06	**PG 64-34**	**ELVALOY MURPHY**	-34.41	214.6	458.9	0.9998
LTCPB11	**PG 64-34**	**HUSKY**	-47.98	240.4	569.2	0.9994
LTCPB03	**PG 64-28**	**NEAT SENECA**	-31.03	224.5	545.4	0.9997
LTCPB04	**PG 64-28**	**SBS SENECA**	-24.26	262.7	456.2	0.9997
LTCPB05	**PG 64-22**	**NEAT SENECA**	-31.87	308.9	513.7	0.9995

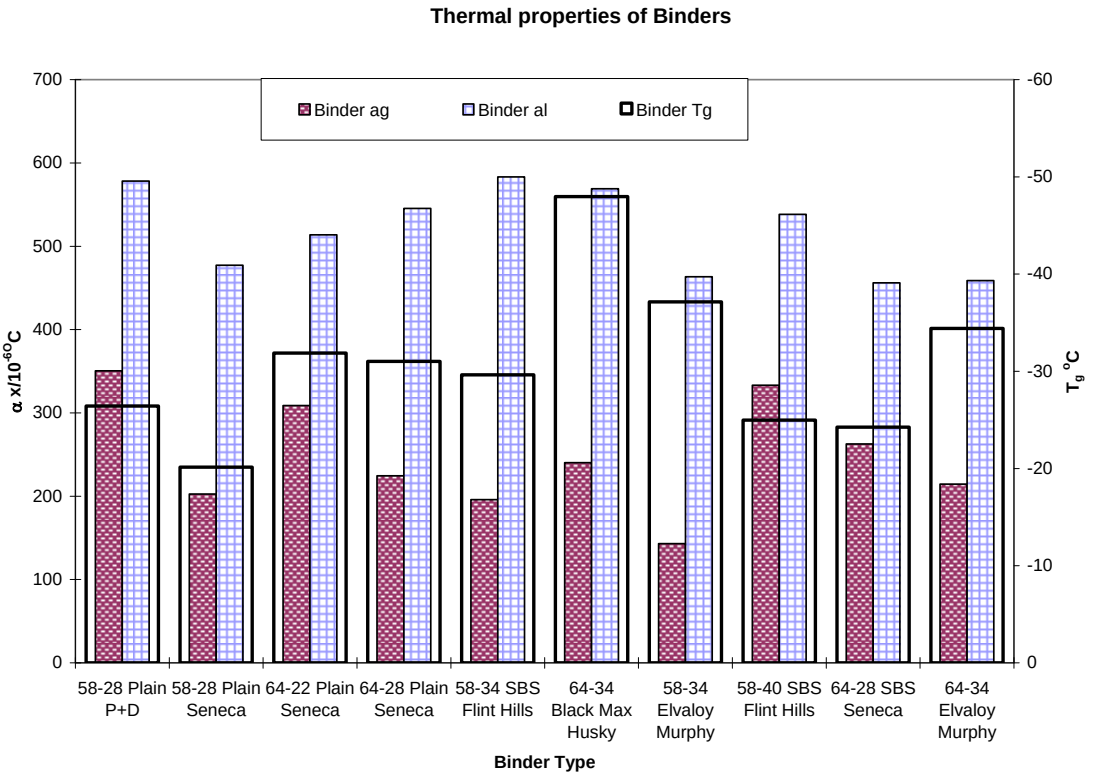

Figure 7.1. Dilatometeric properties of PAV aged binders

As shown in the Table 7.1 and Figure 7.1 the results include a wide range of Tg values with a minimum value of -48.00 °C and a maximum value of –21.1°C, a 27.0 °C range . The results also show a wide range (143.1 to 350.6 x 10^{-6}/ ^{o}C) for the thermal coefficients of contraction below Tg (glassy state α_g). The coefficients of contraction above Tg (liquid state, α_l) was in the range of 456.24 to 583.26 x 10^{-6}/°C, which is a narrower range than the values below Tg. As expected the values of α_g are always smaller than α_l and are in the range of 30% to 60% of α_l.

To show a simple statistical summary of the Tg test results of the PAV-aged binders, Table 7.2 is prepared. With two exceptions, the general trend in dilatometeric properties revealed that binders with a low-grade temperature (PG -yy) have lower T_g and higher thermal coefficients of contraction (α_g and α_l).

Table 7.2. Statistical summary of PAV aged binders test results

	Binder Cooling		
	T_g(°C)	α_g(10^{-6}/°C)	α_l(10^{-6}/°C)
Mean	-30.8	247.7	518.4
Standard Error	2.5	20.9	16.2
Median	-30.3	232. 5	525.9
Standard Deviation	7. 9	66.0	51.3
Sample Variance	62.3	4359.2	2628.2
Kurtosis	1.6887	-0.74911	-1.89109
Skewness	-1.02282	0.255199	-0.0411
Range	27.835	207.5	127.025
Minimum	-48.00	143.1	456.2
Maximum	-20.1	350.6	583.3
Count	10	10	10

RTFOT Binders

Summary of the results for the RTFO aged binders is shown in Figure 7.2. Similar to the PAV-aged samples, the testing was done in duplicate samples and the results for the two dilatometric cells were averaged.

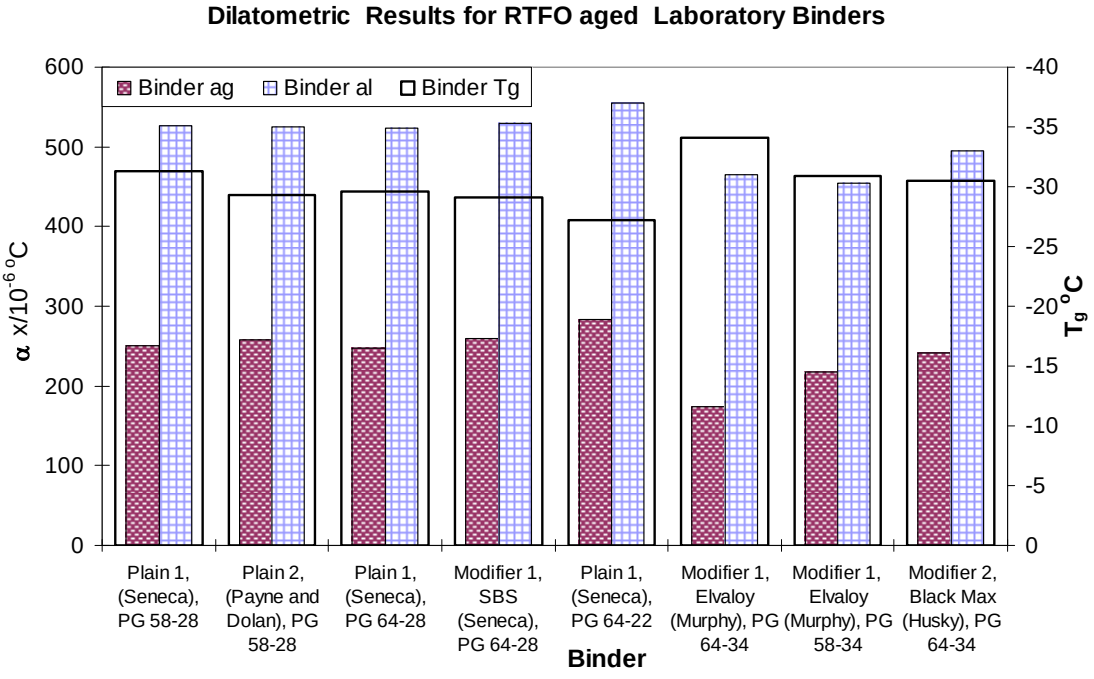

Figure 7.2. Dilatometeric properties of RTFO aged binders

Table 7.3 gives the statistical summary of the tested results for the RTFO-aged binders. When comparing the summary to the summary of the PAV-aged binders in Table 7.2 it can be observed that the average value of the Tg did not change significantly. Also the values of the coefficients of contractions for the PAV-aged samples are on average slightly higher than the averages for the RTOF-aged samples. No specific trends were found however for all binders. Some binders show an increase in coefficients of contraction after PAV aging compared to RTFO while others show a decrease. The lack of trends in changes due to PAV aging is consistent with earlier work conducted at University of Wisconsin. It appears that more testing of a larger population of binders is needed before a trend could be defined.

Table 7.3. Statistical summary of RTFO aged binders test results

	Binder Cooling		
	T_g(°C)	**$\alpha_g(10^{-6}/°C)$**	**$\alpha_l(10^{-6}/°C)$**
Mean	-30.26	241.29	509.22
Standard Error	0.71	11.65	12.25
Median	-30.09	248.85	523.72
Standard Deviation	2.00	32.96	34.66
Sample Variance	3.99	1086.30	1201.05
Kurtosis	1.54	2.13	-0.65
Skewness	-0.60	-1.26	-0.62
Range	6.85	109.04	101.41
Minimum	-34.06	173.90	454.20
Maximum	-27.21	282.94	555.61
Count	8	8	8

Extracted Binders

Summary of the results for the extracted binders are shown in Figure 7.3. Table 7.4 presents basic statistical summary of dilatometric results.

The results listed in Tables 7.3 and 7.4 indicate that the range in dilatometeric properties of the extracted binders are as follows:

- Binder Tg ranges between -20.11°C and –40.69°C
- Thermal coefficients of contraction below Tg (α_g) range between 220.76 and 335.16 x 10-6/°C
- While the thermal coefficients of contraction above Tg (α_l) was between 481.54 and 660.64 x 10-6/°C.

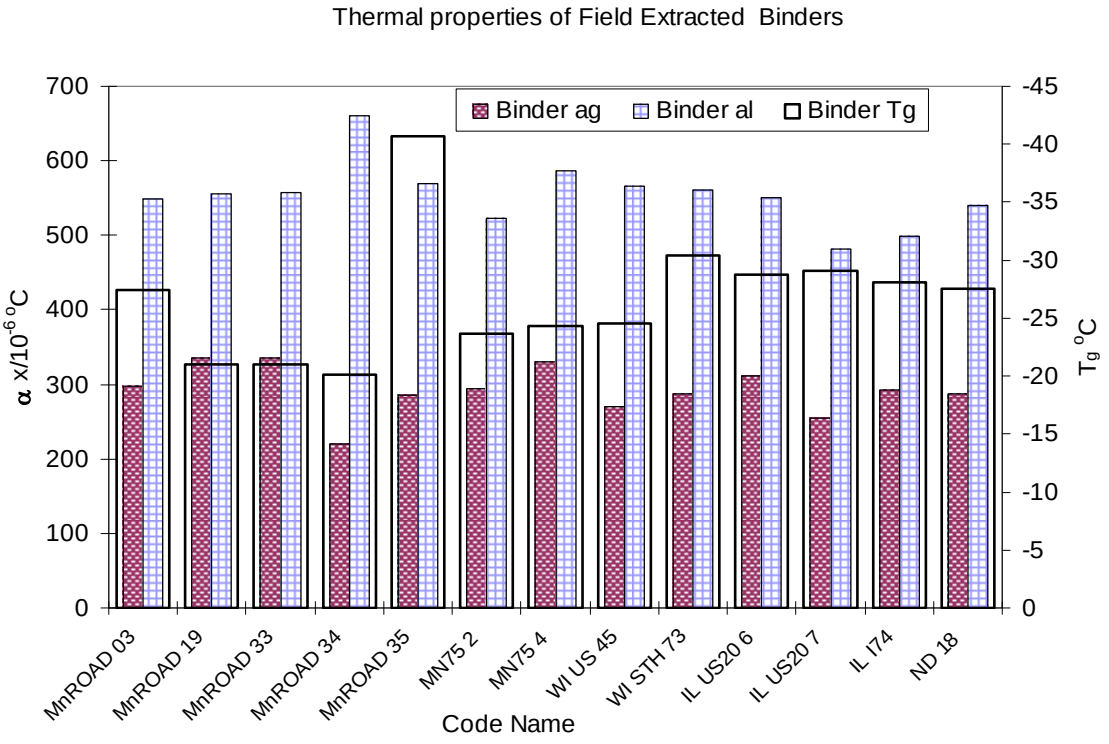

Figure 7.3. Dilatometeric properties of field extracted binders

Table 7.4. Statistical summary of extracted binders test results

	Binder Cooling		
	T_g(°C)	α_g(10^{-6}/°C)	α_l(10^{-6}/°C)
Mean	-26.66	292.44	553.65
Standard Error	1.50	9.00	11.96
Median	-27.40	292.80	556.31
Standard Deviation	5.40	32.46	43.11
Sample Variance	29.18	1053.91	1858.66
Kurtosis	3.05	0.73	2.82
Skewness	-1.34	-0.61	0.85
Range	20.58	114.39	179.11
Minimum	-40.69	220.76	481.54
Maximum	-20.11	335.16	660.64
Count	13	13	13

Rheological Results

Bending Beam Rheometer (BBR) Results

Data after 1h of conditioning was used to generate bar plots presented in Figures 7.4-7.7 that sort the binders in terms of *S* and *m* separately for three test temperatures. Figures 7.8-7.11 present the effect of hardening in terms of the change in creep stiffness. This effect, simulated by 20 hours specimen conditioning prior to testing in BBR, is the largest for RTFOT binders. It can be also noticed that this effect weakens with the amount of aging and becomes less temperature dependent for PAV binders. The influence of hardening on critical temperatures is presented in Figure 7.11. The criterion assumed for critical temperatures was BBR creep stiffness equal to 300MPa. As expected, critical temperatures increase when binders become stiffer.

Double Edge Notch Tension (DENT) and Direct Tension (DT) Results

Comparison between DENT and DT tests for RTFOT binder at two temperatures is presented in Figure 7.12. To make relative comparison, all rankings included in this figure have been sorted by failure stress in DT (top-left plot). It can be noticed that DT and DENT do not rank binders, at least not at these temperatures, in the same way either in terms of failure stresses or failure strains. Figure 7.13 compares four different methods for calculating critical temperatures Tcr based only on binder data. MP1a is a current AASHTO method (4)(5) for calculating Tcr, DENT method uses DENT results instead of DT to obtain binder strength mastercurves, and S and m-value methods use BBR data to find temperature (=Tcr) at which S=300MPa and m-value=0.300. It can be observed that all four methods follow similar trend and confirm PG grading system of the binders.

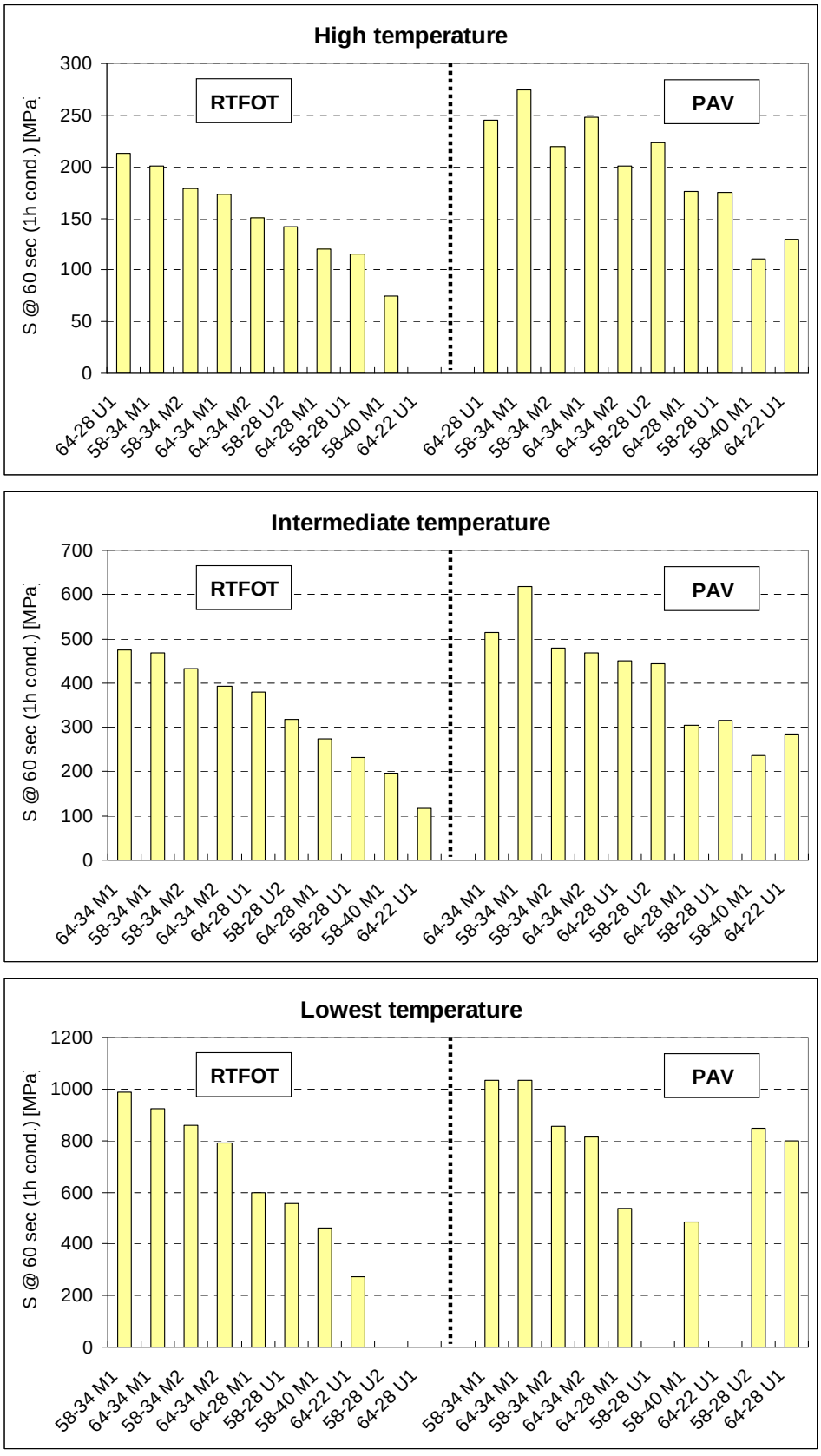

Figure 7.4. Creep stiffness ranking for RTFOT and PAV binders

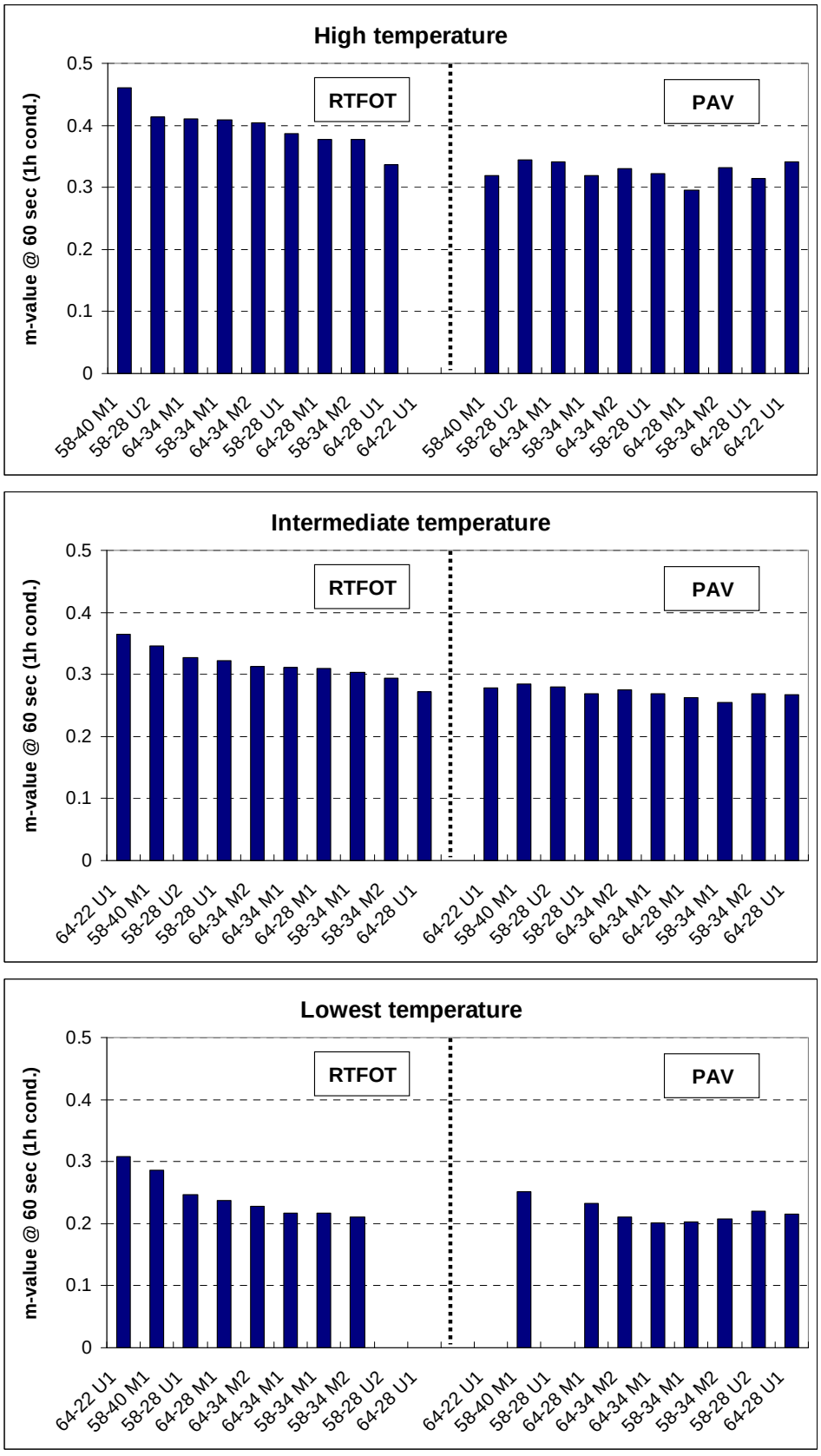

Figure 7.5. m-value ranking for RTFOT and PAV binders

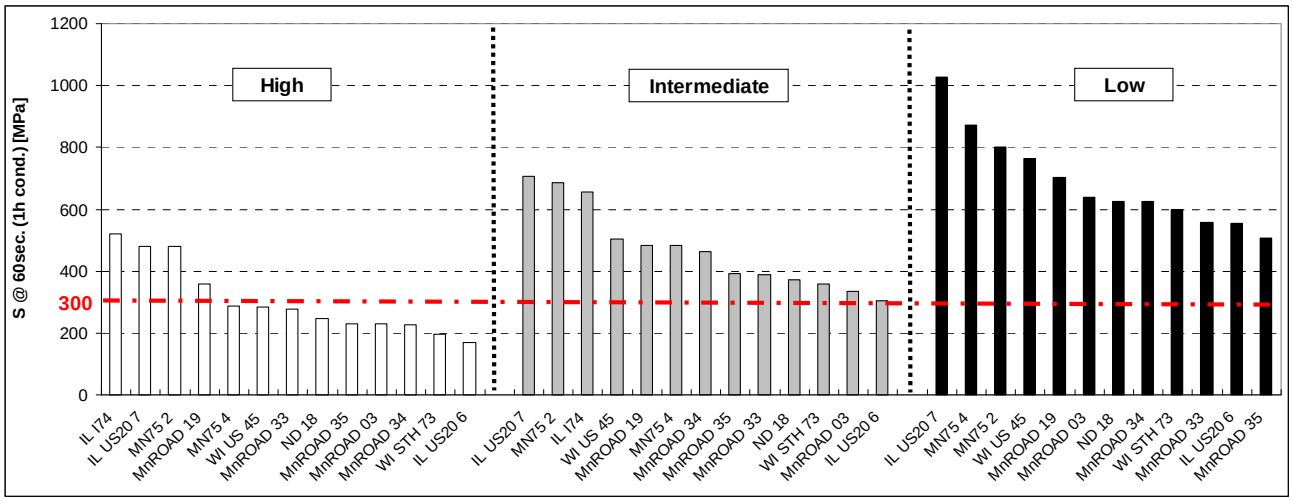

Figure 7.6. Creep stiffness ranking for extracted binders

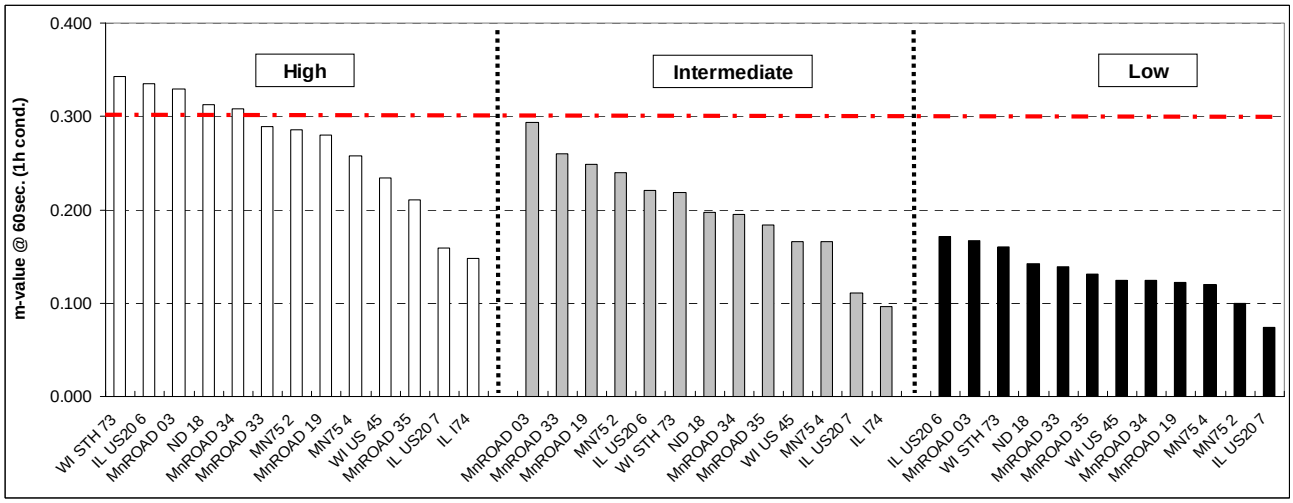

Figure 7.7. m-value ranking for extracted binders

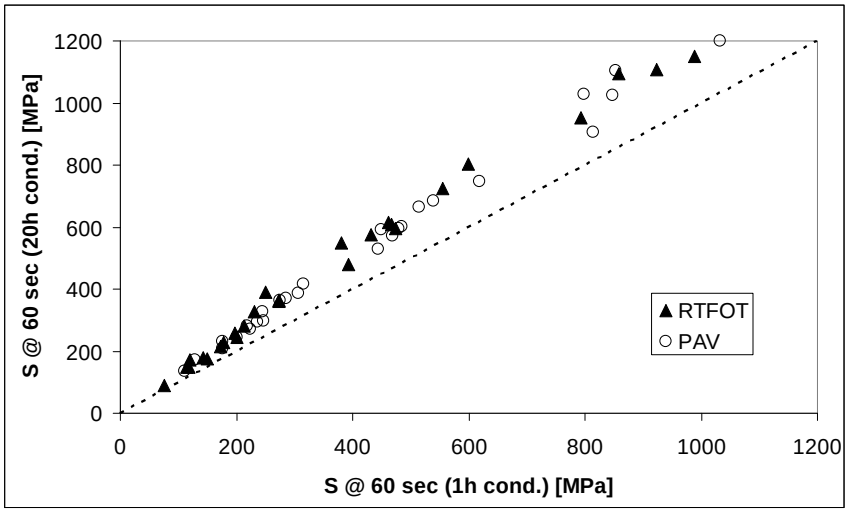

Figure 7.8. Influence of conditioning time on creep stiffness (laboratory binders)

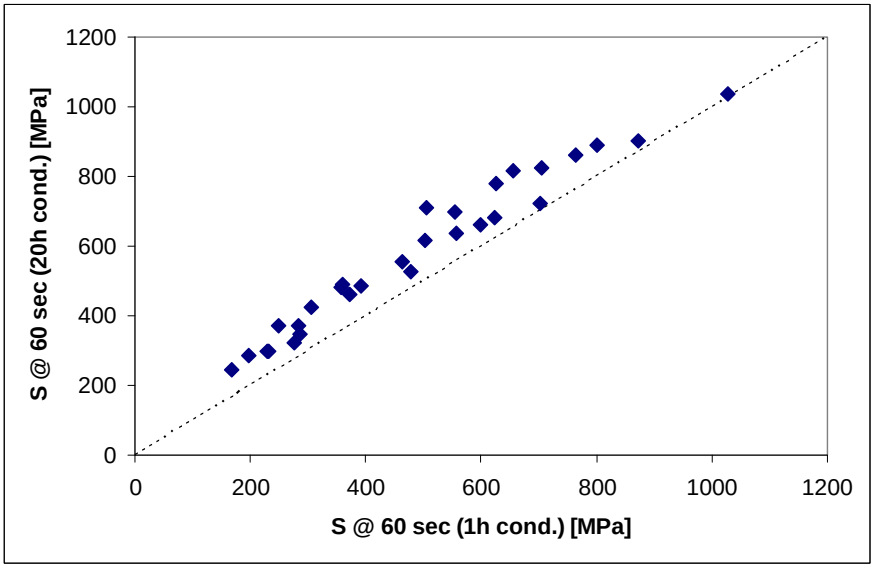

Figure 7.9. Influence of conditioning time on creep stiffness (extracted binders)

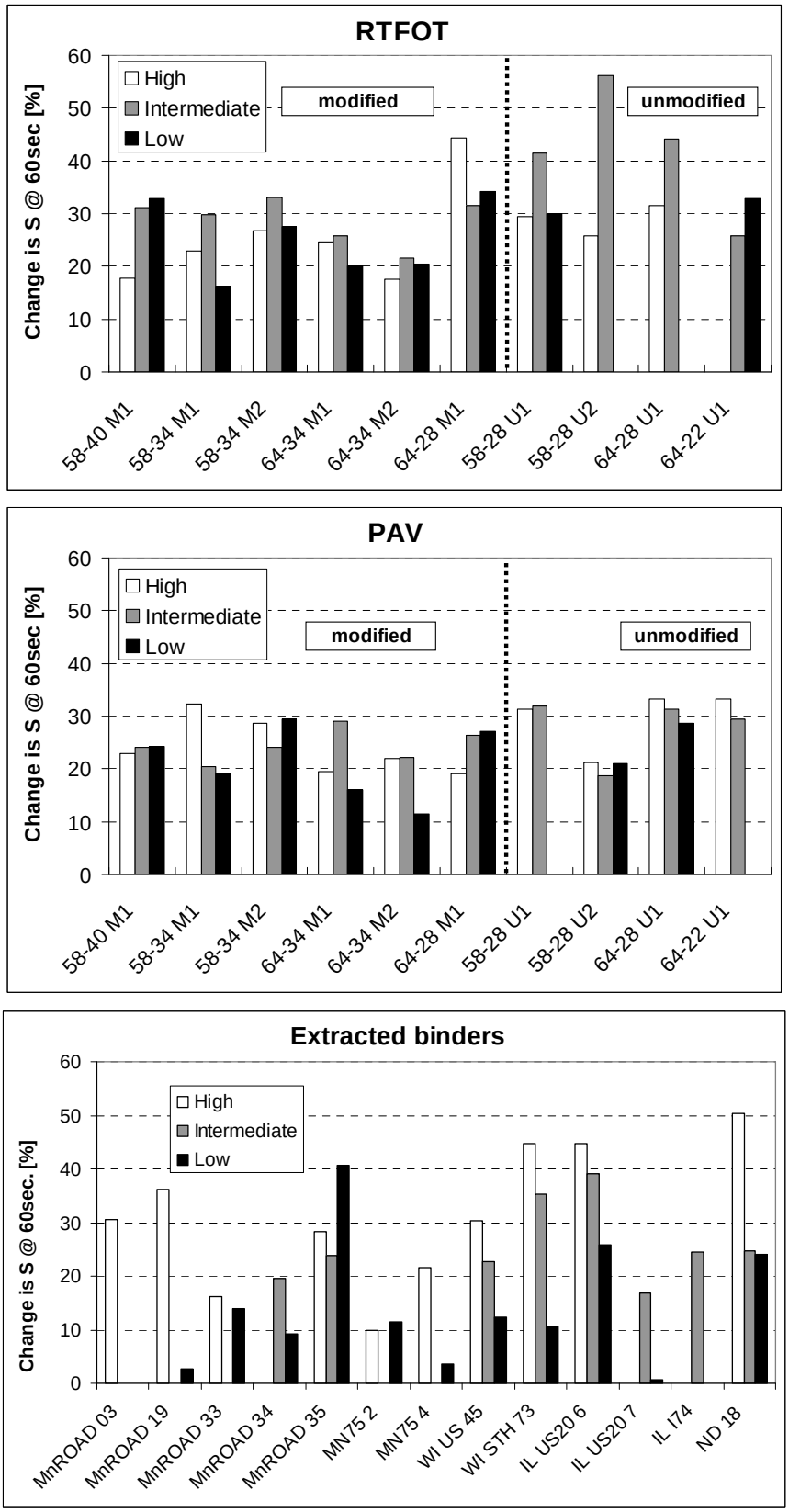

Figure 7.10. Increase in S after 20h

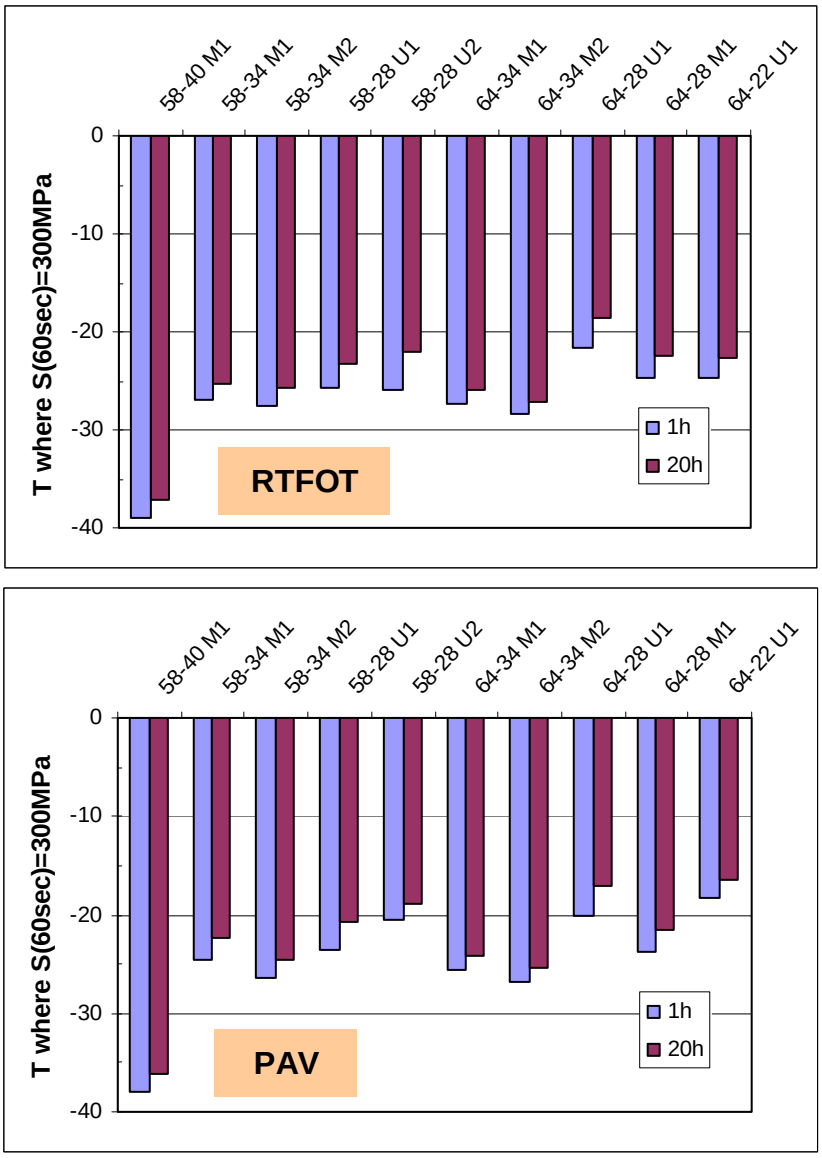

Figure 7.11. Influence of hardening on S critical temperatures

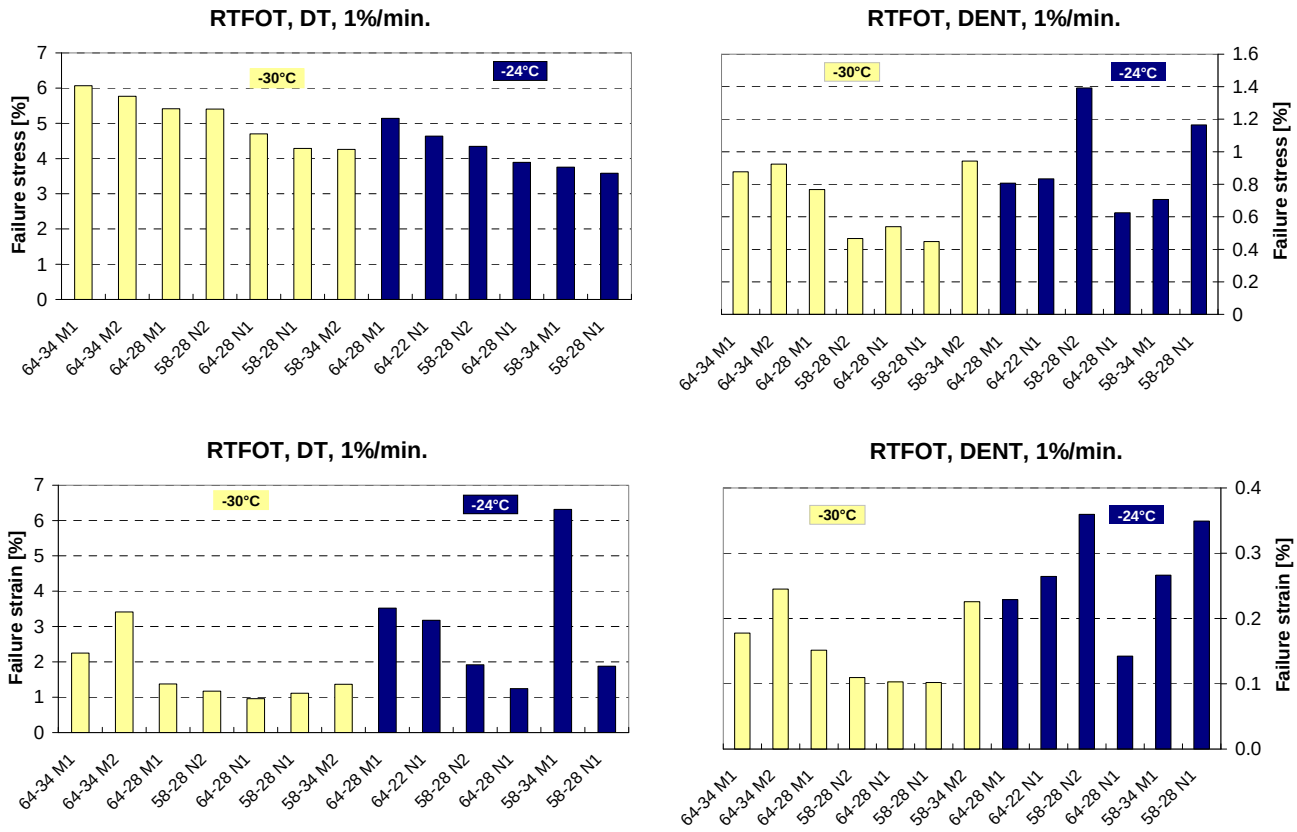

Figure 7.12. Comparison of DENT and DT for RTFOT binders

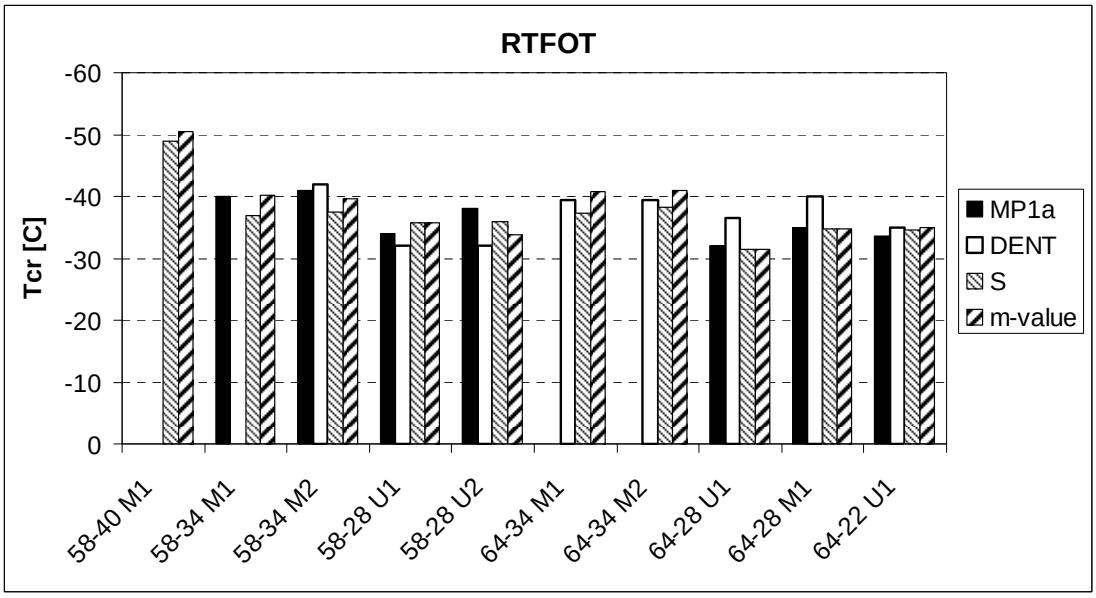

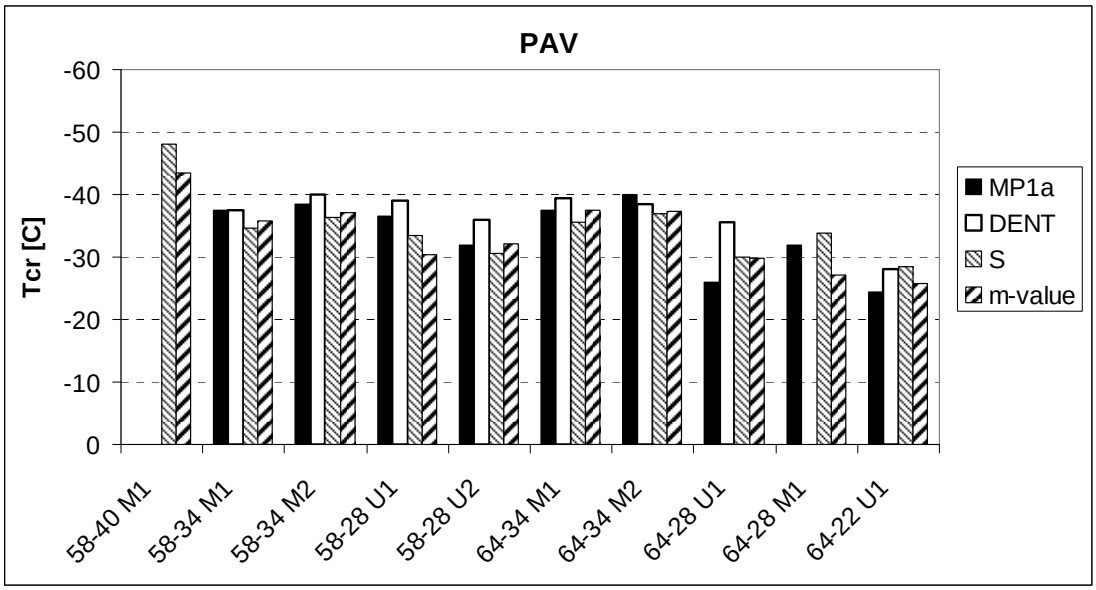

Figure 7.13. Comparison of critical temperatures for PAV and RTFOT binders

Asphalt Mixture Data

Fracture and IDT Testing of Laboratory Prepared Specimens

DC(T) Results

Figures 7.14 to 7.16 summarize DC(T) results on laboratory mixes at all three testing temperatures.

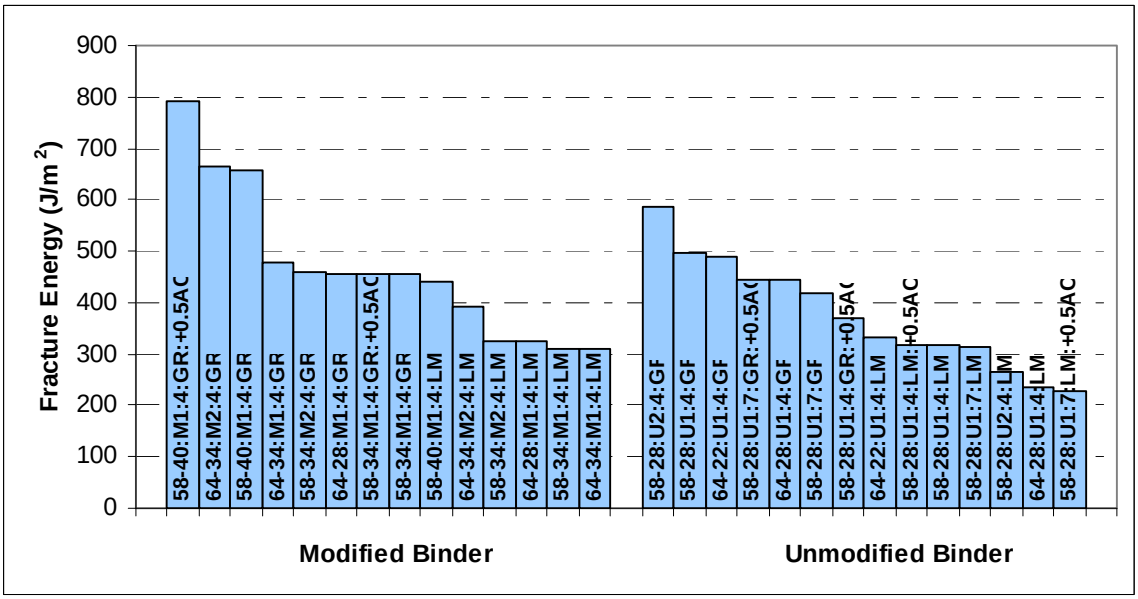

Figure 7.14. DC(T) test results at low testing temperature

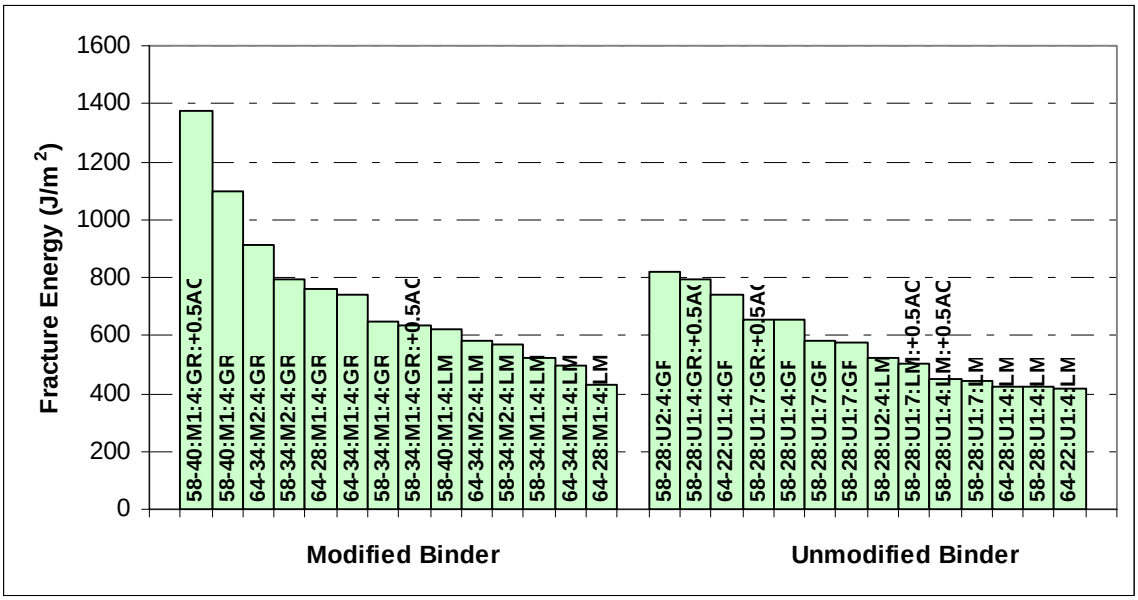

Figure 7.15. DC(T) test results at intermediate testing temperature

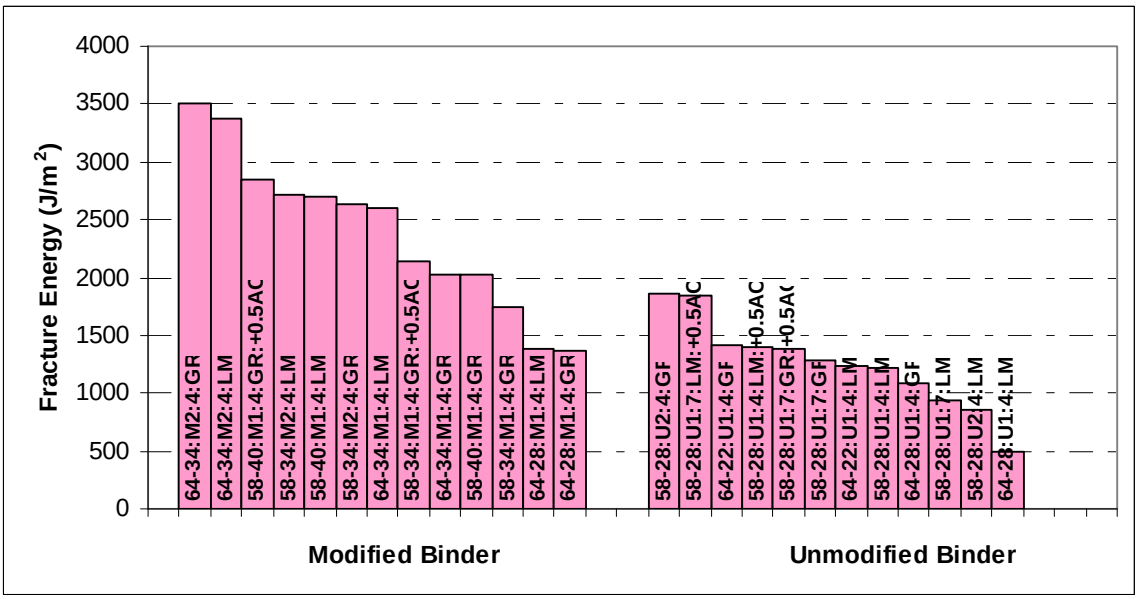

Figure 7.16. DC(T) test results at high testing temperature

Figure 7.17 shows a typical set of Load/CMOD curves that is recorded from three replicates during the DC(T) test.

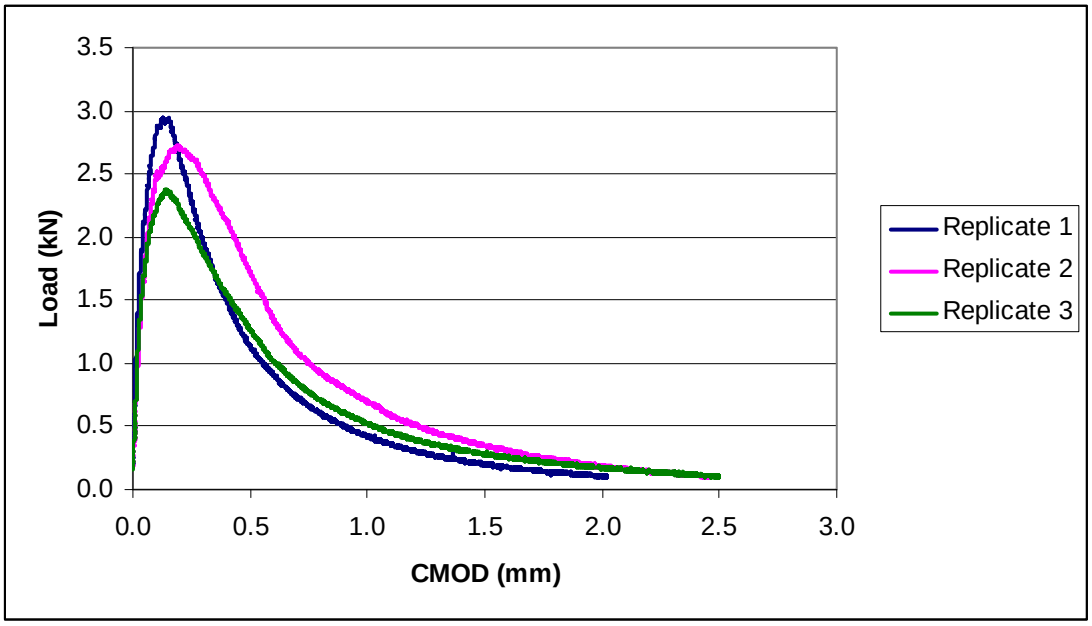

Figure 7.17. DC(T) load versus CMOD curves for 58-28:U1:4:LM at -18°C

Figure 7.18 shows the same mixture, but at the three different testing temperatures.

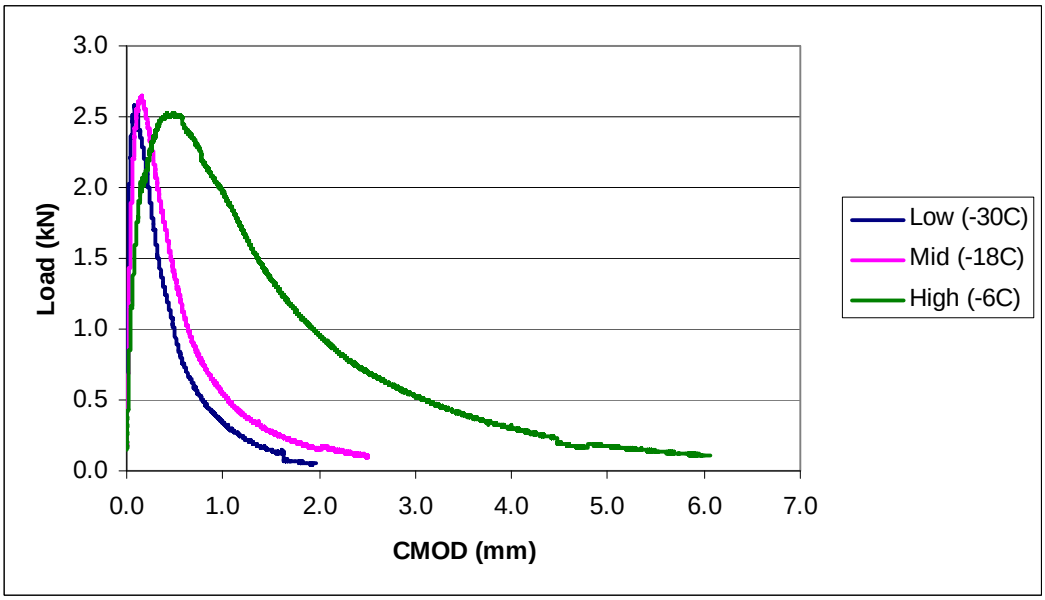

Figure 7.18. DC(T) load versus CMOD curves for 58-28:U1:4:LM at three testing temperatures

Figure 7.18 shows as the testing temperature increases, the peak load occurs at a higher CMOD. In addition the area under the Load/CMOD curve, or the fracture energy, increases. When running the DC(T) test, the test is complete when the load reaches 0.1kN. However, the CMOD gage has a maximum value of 6.5mm. Therefore, if the gage has opened to 6.5mm, but the load

has not reached 0.1kN, the test did not finish. In order to determine fracture energy for these mixes, we had to extrapolate the data. For this report, we simply took 60% of the peak load (25), and fitted the rest of the data to an exponential function, as shown in Figure 7.19.

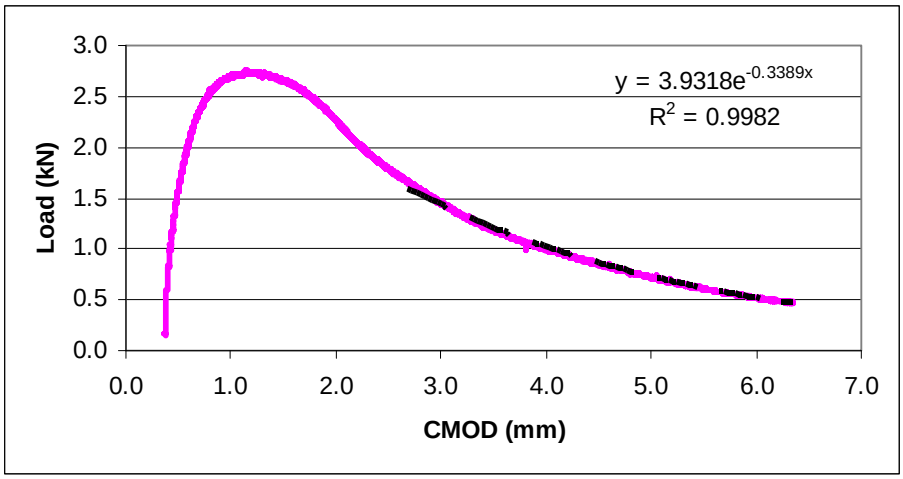

Figure 7.19. DC(T) extrapolation curve for 58-28:U1:7:LM:+0.5AC

SCB results

A typical plot for the fracture energy and toughness as a function of temperature is presented in Figure 7.20. The plots indicate that the fracture energy decreases when temperature decreases, while the fracture toughness increases when temperature decreases. The plots also indicate that the mixture made with granite has higher fracture energy and fracture toughness than the mixture made with limestone when the other variables are the same.

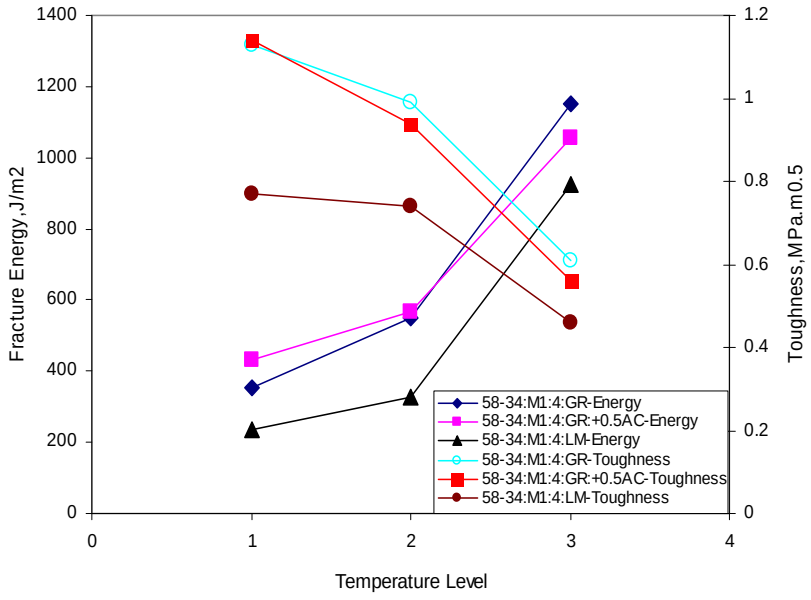

Figure 7.20. SCB fracture parameters for three mixtures with PG 58-34 and modifier 1

Another representative plot for mixtures with different PG high limit but the same low limit is shown in Figure 7.21. It can be observed that mixture with higher PG high limit had higher fracture energy and toughness values than the mixtures with lower PG high limit.

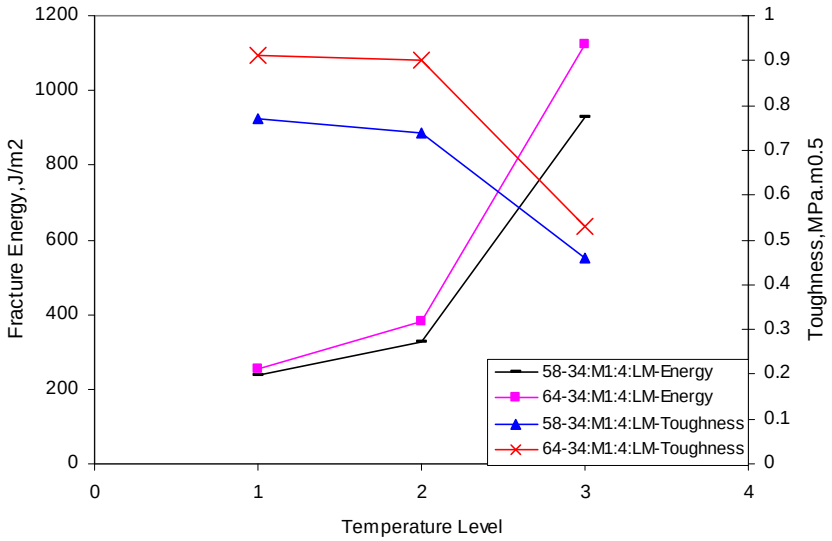

Figure 7.21. SCB fracture parameters for two mixtures with different PG high limit

The ranking from high to low based on fracture toughness for the three temperature levels is plotted in Figures 7.22-7.24. Similar plots with rankings based on fracture energy are shown in Figures 7.25-7.27.

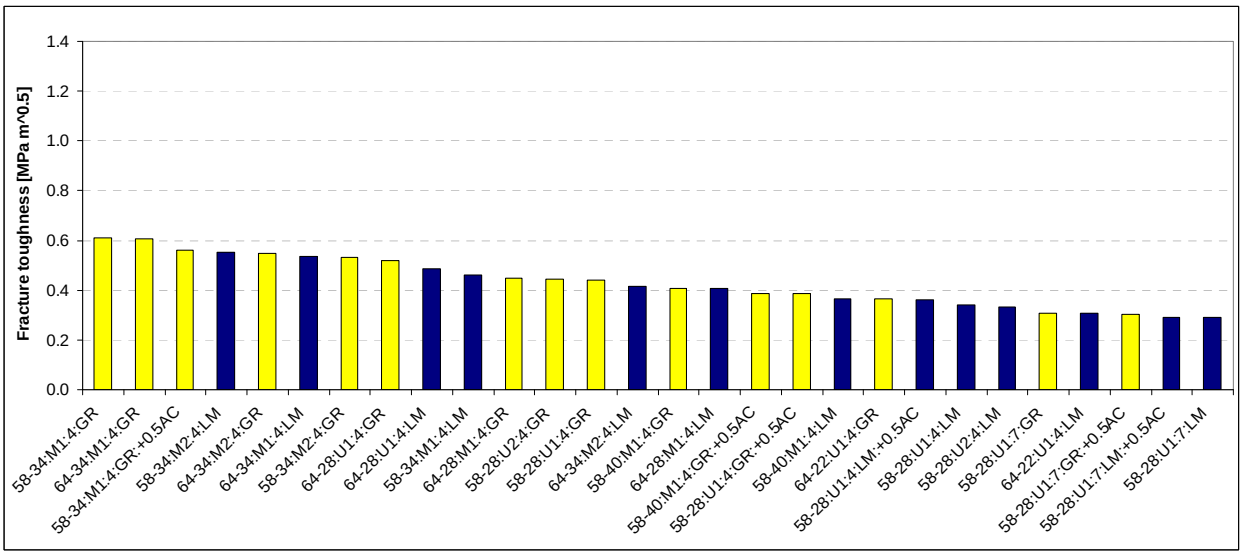

Figure 7.22. Mixture ranking for SCB fracture toughness at high test temperature

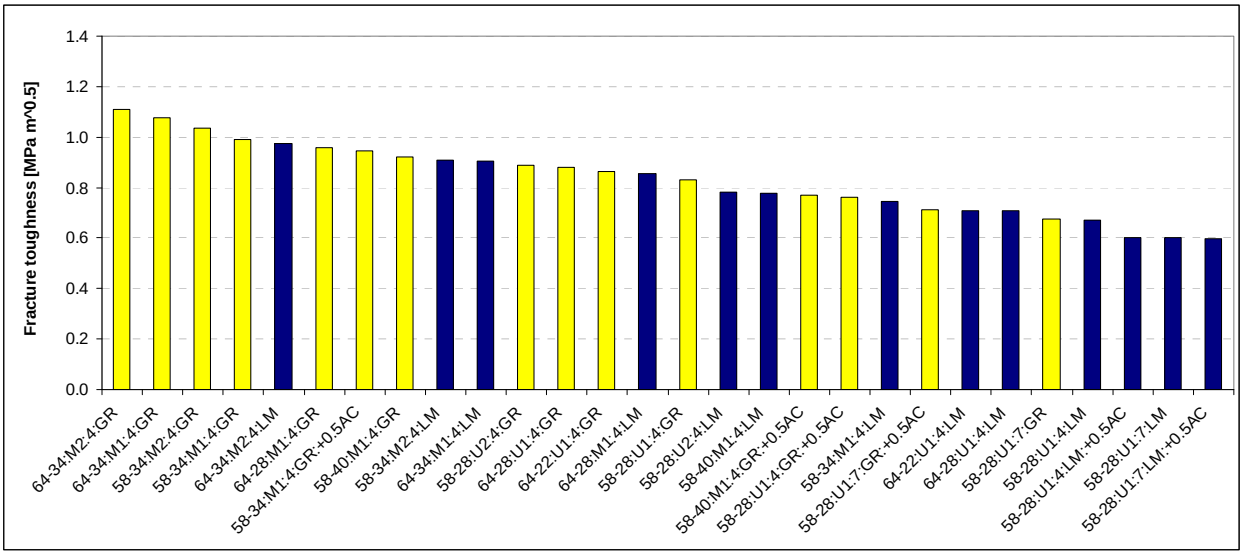

Figure 7.23. Mixture ranking for SCB fracture toughness at intermediate test temperature

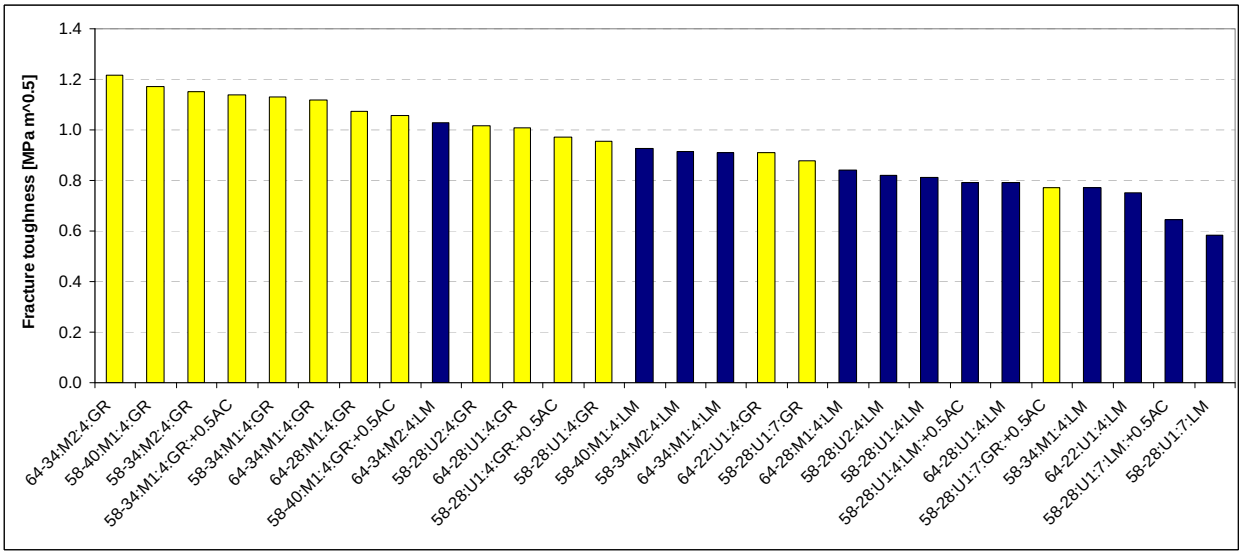

Figure 7.24. Mixture ranking for SCB fracture toughness at low test temperature

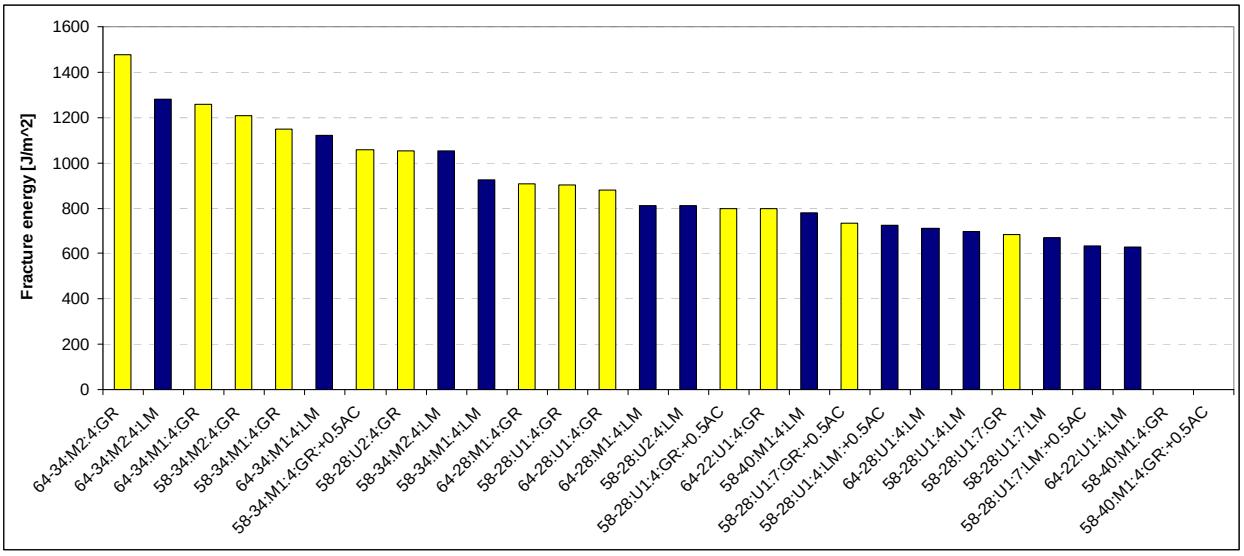

Figure 7.25. Mixture ranking for SCB fracture energy at high test temperature

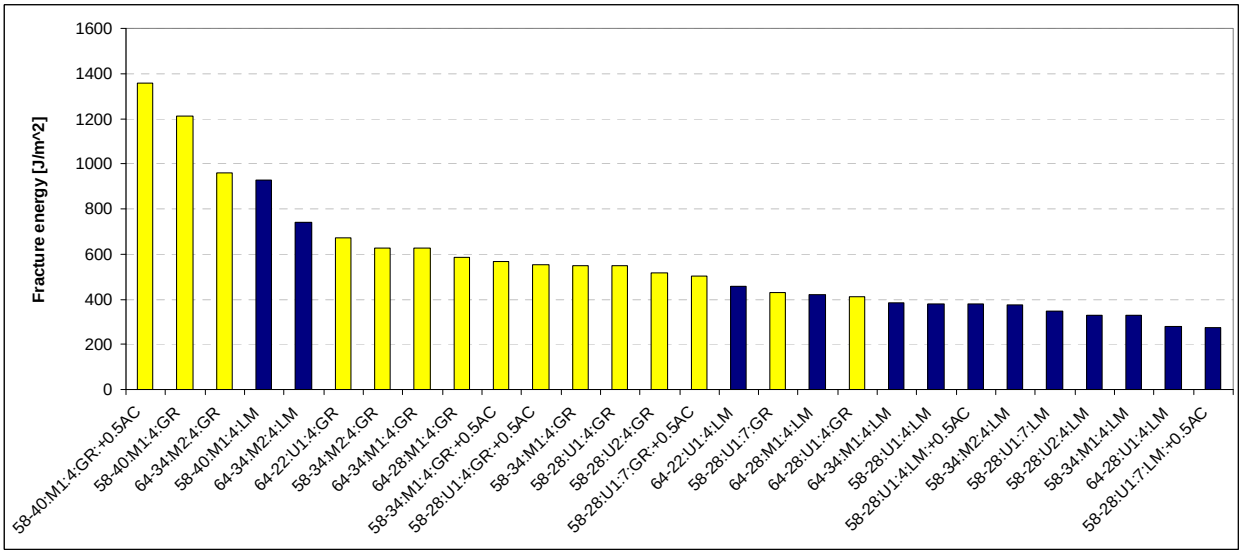

Figure 7.26. Mixture ranking for SCB fracture energy at intermediate test temperature

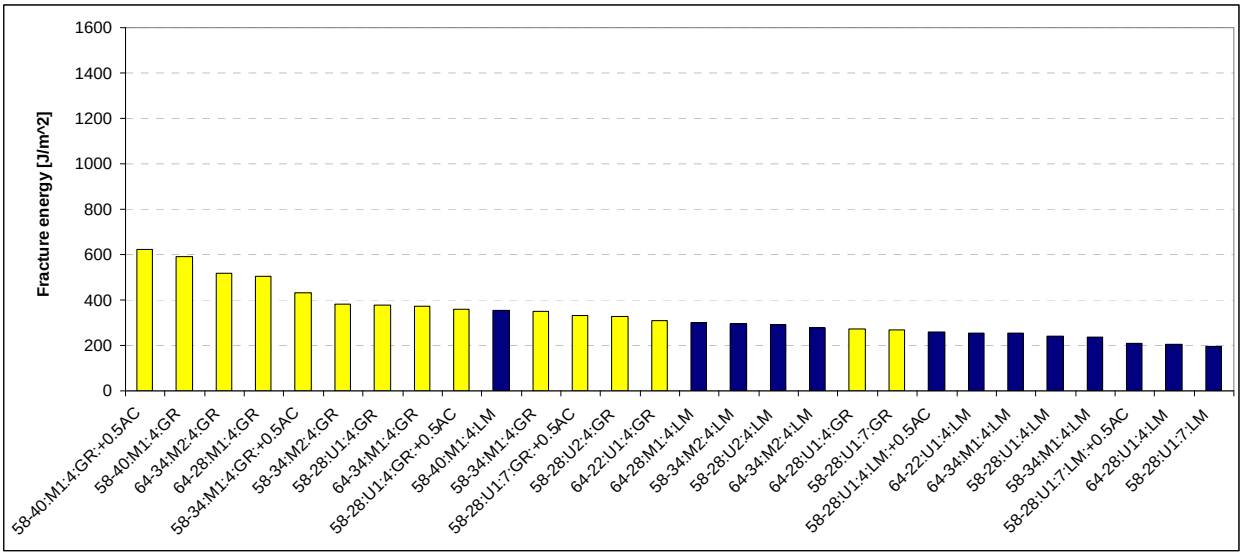

Figure 7.27. Mixture ranking for SCB fracture energy at low test temperature

From the ranking plots for fracture toughness shown above, we can see that the two mixtures with PG 58-28 plain 1 binder, 7% air voids and limestone aggregate type have the lowest toughness values for all three temperature levels. At the two higher temperature levels, mixture with PG 64-34 modified by modifier 2 binder, granite aggregate, 4% air voids and optimum asphalt content has the highest toughness value. However, mixture with PG 58-34 and modified by modifier 1 binder, granite aggregate, 4% air voids and optimum asphalt content has the highest toughness value at the highest temperature level. As for the fracture energy, the three mixtures 58-40:M1:4:GR:+0.5AC, 58-40:M1:4:GR and 64-34:M2:4:GR have the first, second and third highest values, respectively, at the two lower temperatures. For the highest temperature, mixture 64-34:M2:4:GR has the highest fracture energy. From the previous description, we know that the fracture energy values for the two mixtures 58-40:M1:4:GR:+0.5AC and 58-40:M1:4:GR were not obtained. Similar to the fracture toughness, we can also find that mixtures with PG 58-28 plain 1 binder, 7% air voids and limestone aggregate type have very low toughness values for all three temperature levels.

SCB Fracture Acoustic Emission Results

In addition, acoustic emission techniques were used to obtain relevant information about the fracture process in asphalt mixtures. AE represents a useful tool to obtain information about the microscopic damage during fracture and allows for a better understanding of the relation between the microstructural events and the macroscopic performance. In this study AE was used to obtain the number of AE events, the AE energy, and the AE event location during the fracture process. A total of 84 SCB fracture testing were monitored using acoustic emission. For the samples tested the recorded events number varied between 79 and 7647. The recorded event number changed with test sample and test condition. Typical plots of the loading and AE event count as a function of the load line displacement are shown in Figure 7.28. The numbers of AE events for all samples are presented in Table 7.5.

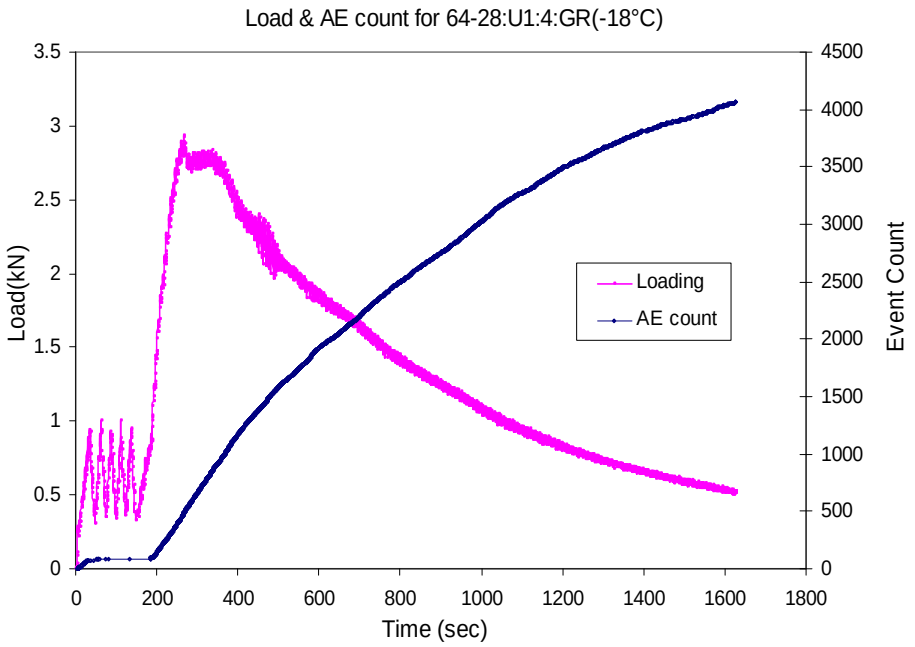

Figure 7.28. Typical loading and AE event count with load line displacement

Table 7.5. AE event count

Mixture	Sample ID	Temp (°C)	Event Count
58-40:M1:4:GR	1-21	-18	795
	2-31	-30	3065
	2-22	-42	7647
	3-32	-42	4501
58-40:M1:4:GR:+0.5AC	1-21	-18	412
	2-22	-30	2467
	3-31	-42	6107
58-40:M1:4:LM	2-31	-18	193
	1-32	-30	669
	2-22	-30	750
	3-21	-42	3227
58-34:M1:4:GR	2-21	-12	945
	1-22	-24	3848
	1-31	-36	6051
58-34:M1:4:GR:+0.5AC	2-22	-12	2355
	1-21	-24	4200
	3-31	-36	5723
58-34:M1:4:LM	7-32	-12	186
	4-22	-24	1105
	2-31	-36	5354
58-28:U1:4:GR	1-21	-6	446
	2-22	-18	1554
	3-31	-30	6572
58-28:U1:4:GR:+0.5AC	1-21	-6	509
	3-31	-18	3025
	4-32	-30	6384
58-28:U1:4:LM	1-22	-6	272
	2-31	-18	1171
	3-32	-30	4760
58-28:U1:4:LM:+0.5AC	2-21	-6	407
	3-31	-18	1106
	4-32	-30	4719
58-28:U1:7:GR	2-21	-6	1008
	2-22	-18	1915
	3-31	-30	6100
58-28:U1:7:GR:+0.5AC	3-21	-6	307
	4-22	-18	2814
	5-31	-30	4275
58-28:U1:7:LM	1-21	-6	79
	2-22	-18	1004
	9-31	-30	5504
58-28:U1:7:LM:+0.5AC	1-21	-6	117
	2-22	-18	1252
	5-31	-30	1585
58-34:M2:4:GR	1-21	-12	668
	4-22	-24	4861
	12-31	-36	5254
58-34:M2:4:LM	3-22	-12	173
	2-21	-24	1943
	4-31	-36	6260
58-28:U2:4:GR	2-32	-18	3668
	3-22	-30	5546
58-28:U2:4:LM	1-32	-6	102
	5-22	-18	1235
	6-31	-30	7284
64-34:M1:4:GR	1-21	-12	906
	2-22	-24	2662
	3-31	-36	6380
64-34:M1:4:LM	1-32	-12	292
	4-22	-24	1786
	4-21	-36	4325
64-34:M2:4:GR	2-21	-12	510
	3-22	-24	3820
	6-31	-36	7500
64-34:M2:4:LM	3-21	-12	671
	6-22	-24	1351
	8-31	-36	4065
64-28:U1:4:GR	1-32	-6	861
	2-22	-18	4836
	3-31	-30	5326
64-28:U1:4:LM	1-22	-6	161
	2-21	-18	2431
	7-31	-30	5016
64-28:M1:4:GR	1-21	-6	882
	2-22	-18	3170
	3-31	-30	4687
64-28:M1:4:LM	8-11	-6	240
	8-22	-18	1249
	8-51	-30	5398
64-22:U1:4:GR	3-21	0	500
	5-31	-12	1467
	7-32	-24	6393
64-22:U1:4:LM	2-21	0	102
	5-22	-12	835
	7-31	-24	3431

After the AE events were recorded, the locations of the AE event source were determined. An example of source location is given in Figure 7.29 that plots the location for all recorded events during the entire loading process.

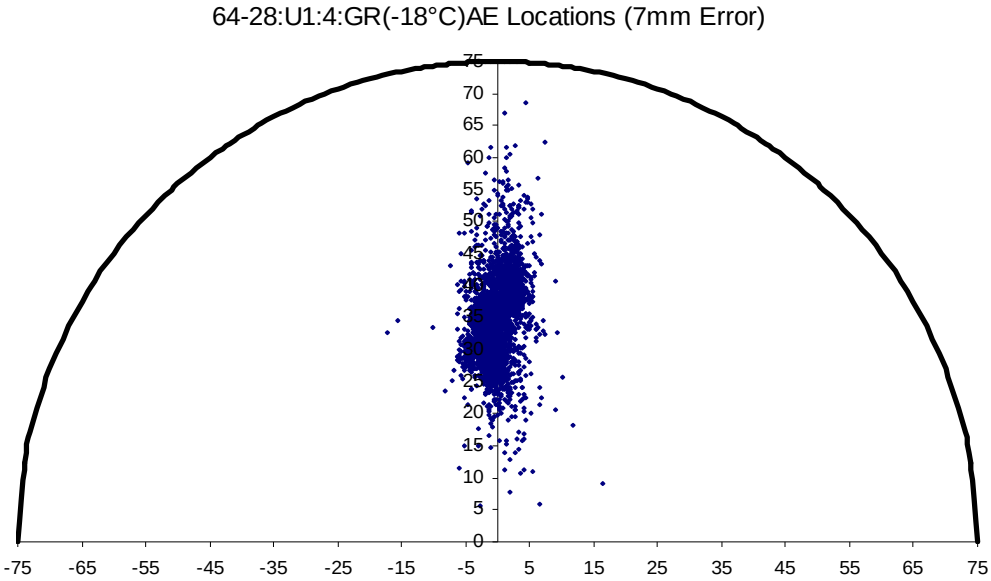

Figure 7.29. Example of AE source locations

IDT Results

The IDT data was used to generate plots which rank the mixtures according to the creep stiffness values at 60sec and 500sec derived using AASHTO T322-03 method. The rankings were done separately for the lowest, intermediate, and the highest test temperatures and they are presented in Figures 7.30 and 7.31. To better distinguish between aggregate types, the darker bars are used for the mixtures with limestone aggregate. This leads to the interesting observation that mixtures containing granite are not always superior, in terms of the creep stiffness, comparing to limestone mixtures. However, granite mixtures produce higher tensile strength, especially at lower temperatures (Figure 7.32).

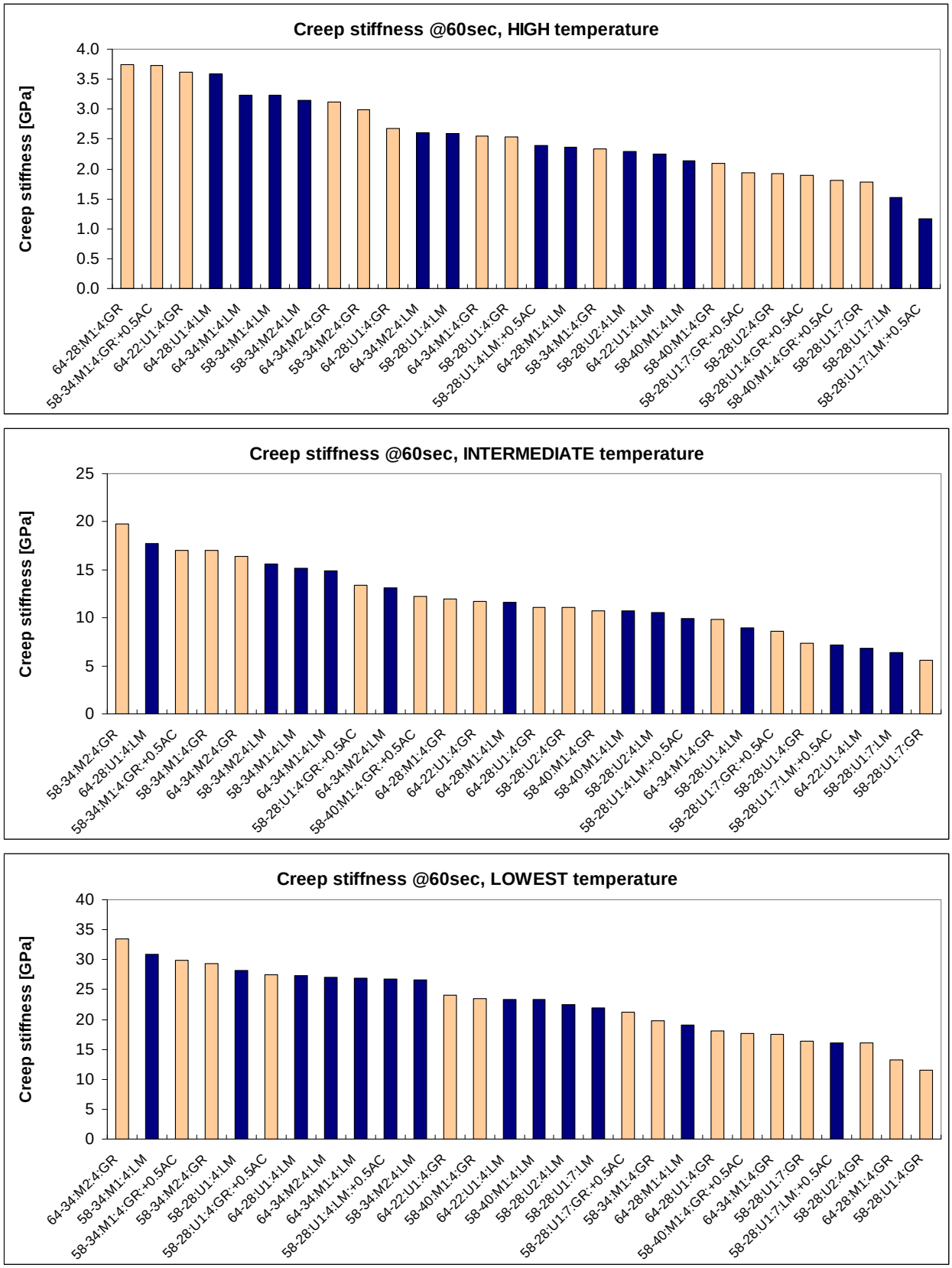

Figure 7.30. Creep stiffness at 60 sec. determined by the AASHTO method

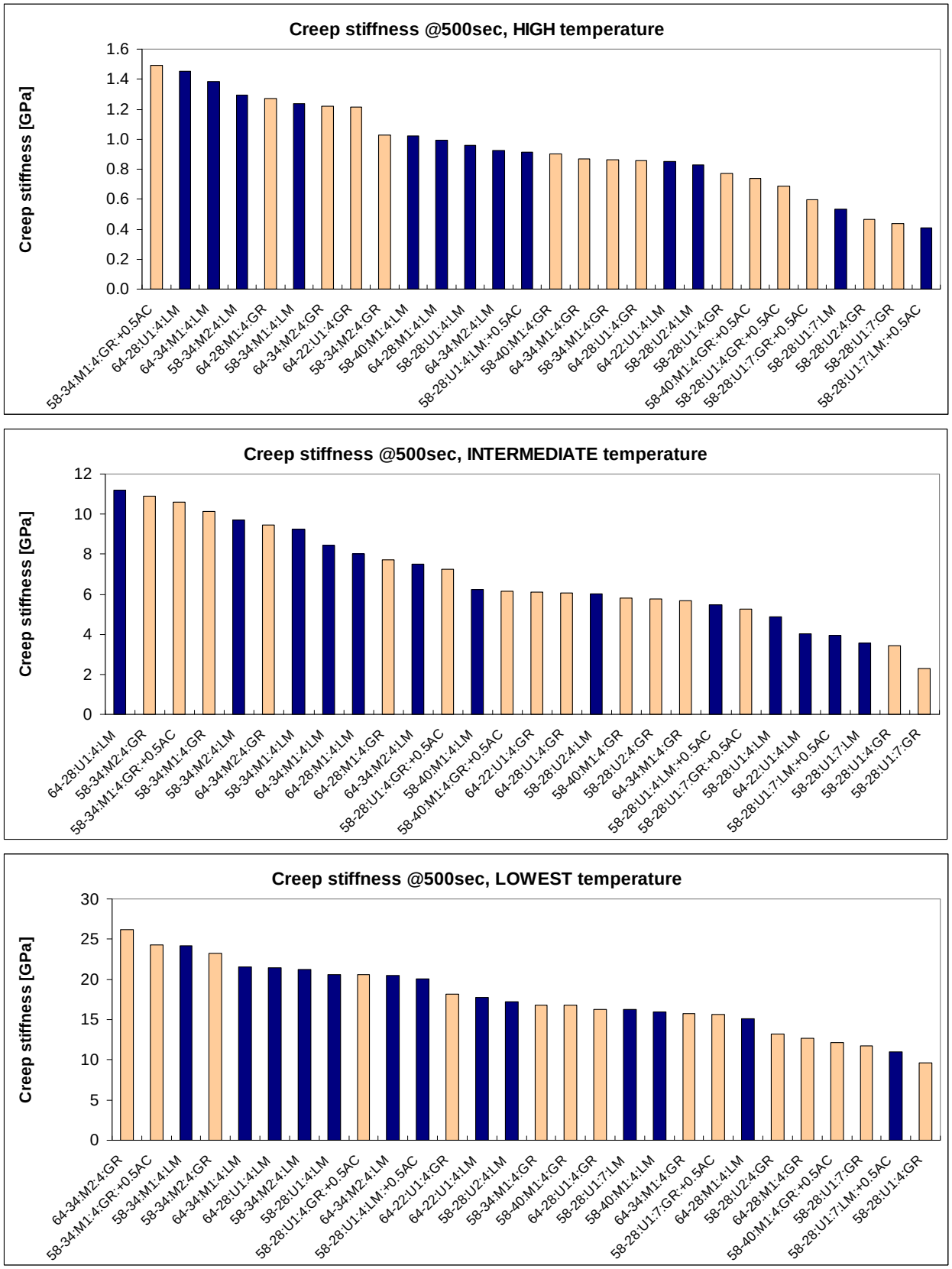

Figure 7.31. Creep stiffness at 500 sec. determined by the AASHTO method

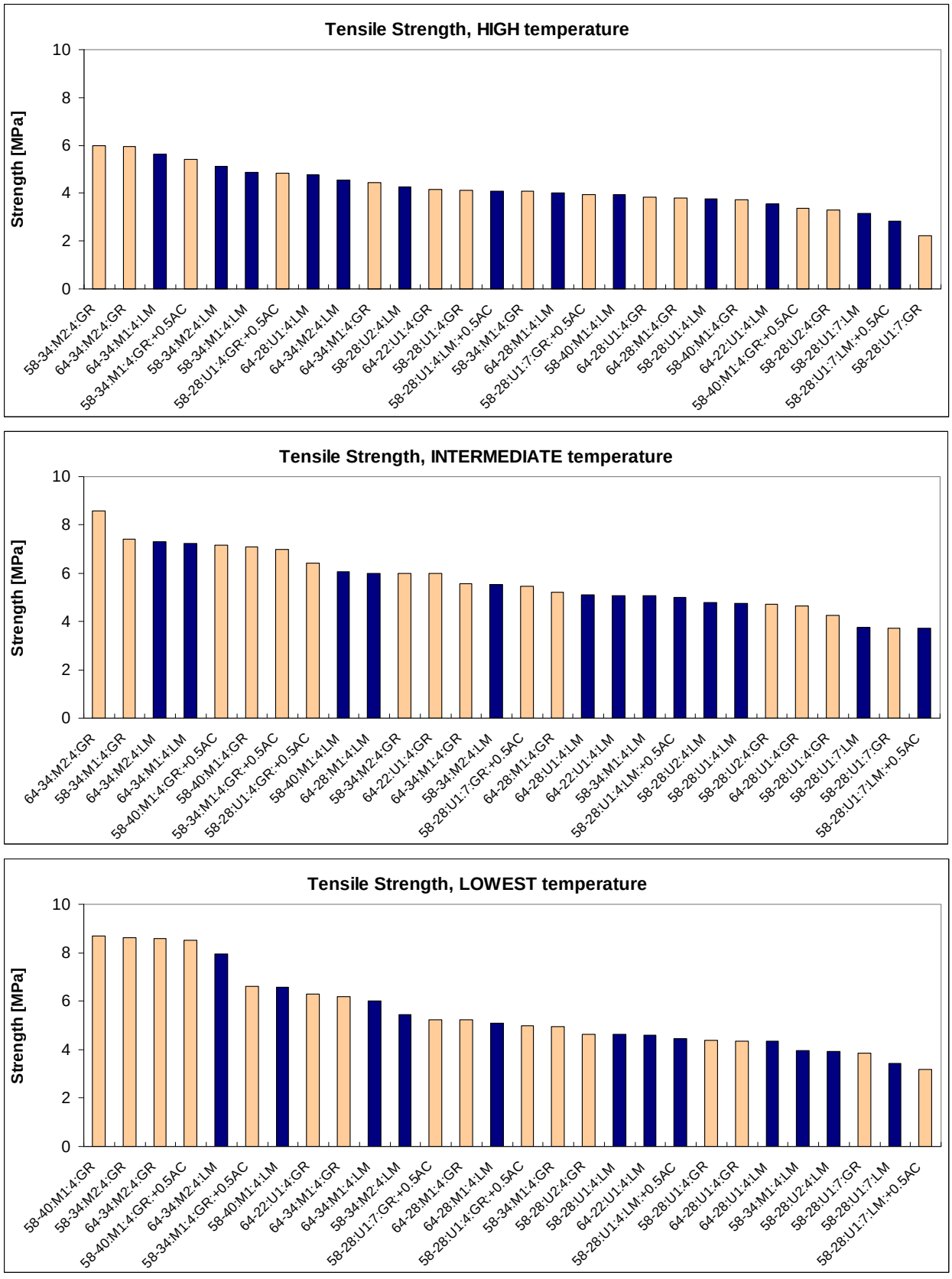

Figure 7.32. Tensile strength determined by the AASHTO method

Fracture and IDT Testing of Field Specimens

DC(T) Results

The following figures show the DC(T) fracture energy for field specimens with the adjusted thickness.

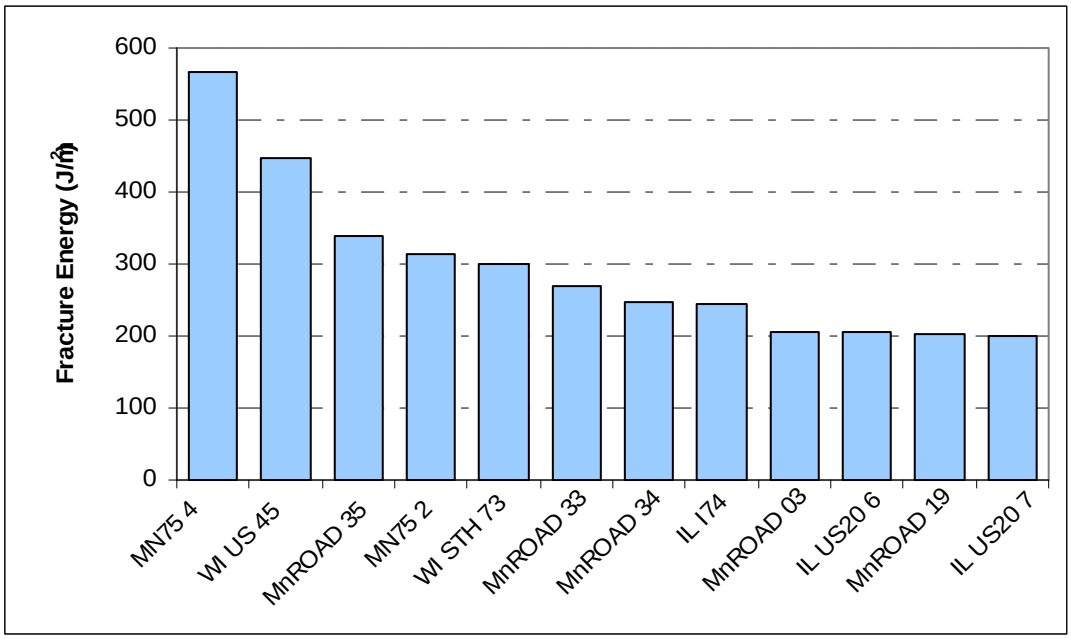

Figure 7.33. DC(T) test results at low testing temperature

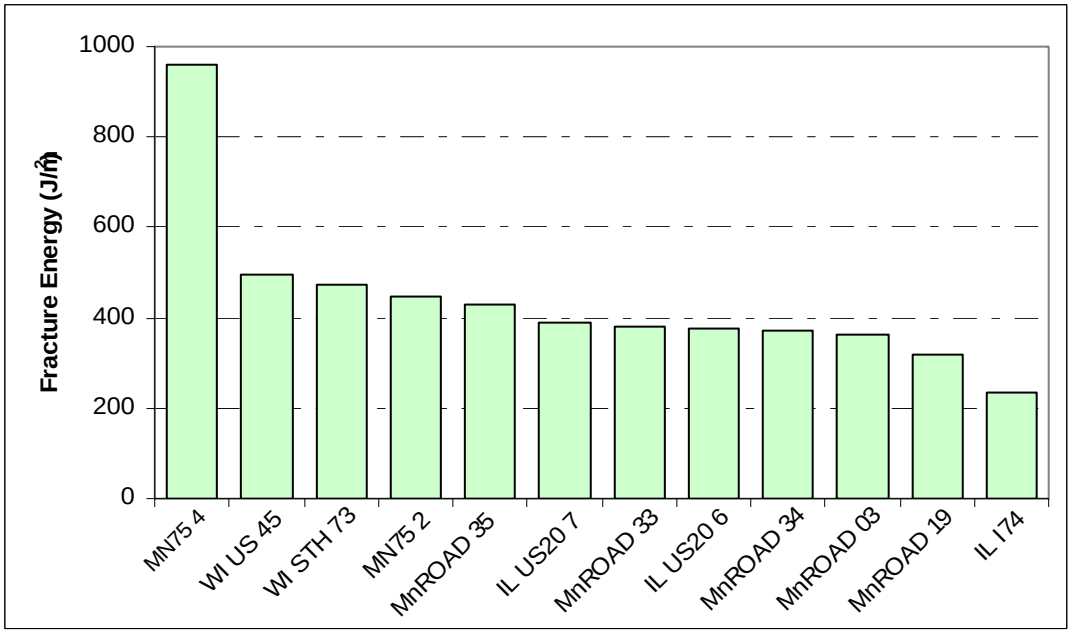

Figure 7.34. DC(T) test results at mid testing temperature

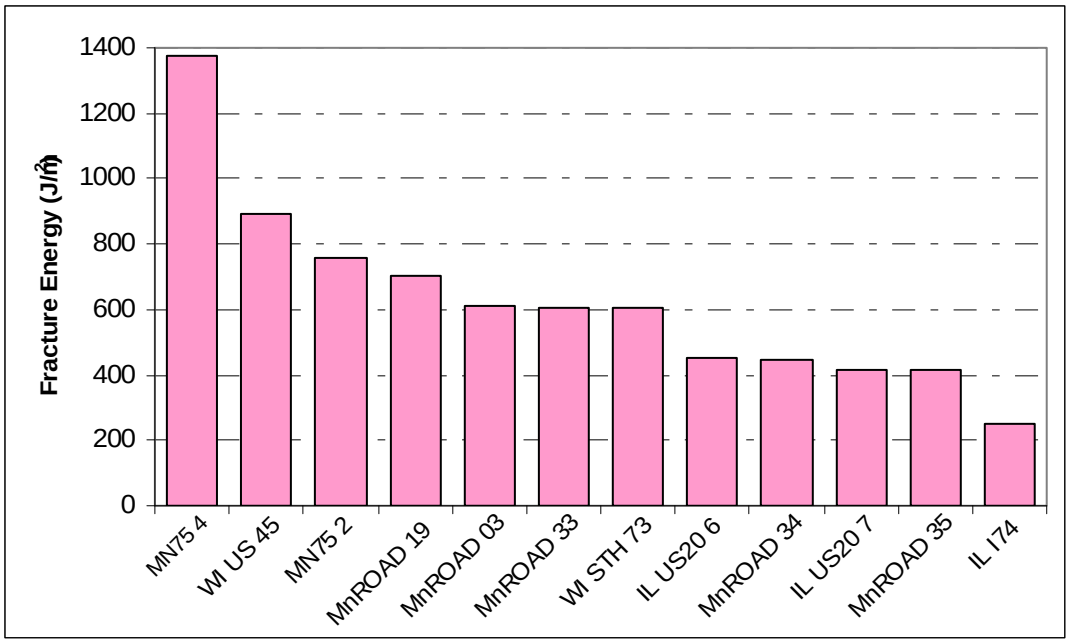

Figure 7.35. DC(T) test results at high testing temperature

SE(B) Results

The IL US20 SE(B) field samples were taken from the binder course, not the upper most layer (it would have been too thin). Therefore, the IL US20 data results are not shown in Figures 7.36-7.38.

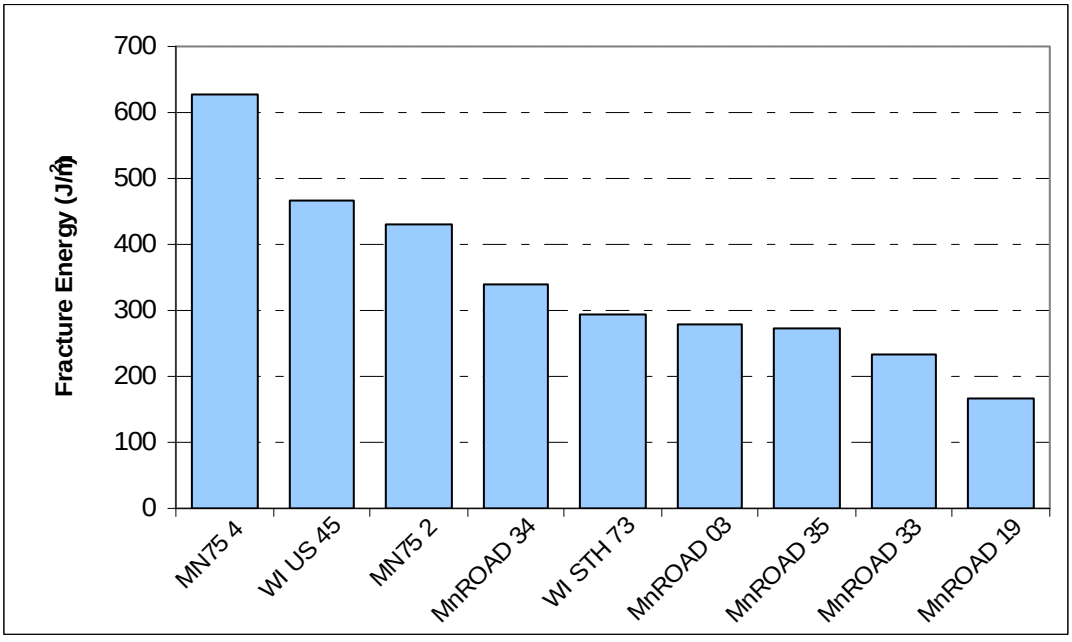

Figure 7.36. SE(B) test results at low testing temperature

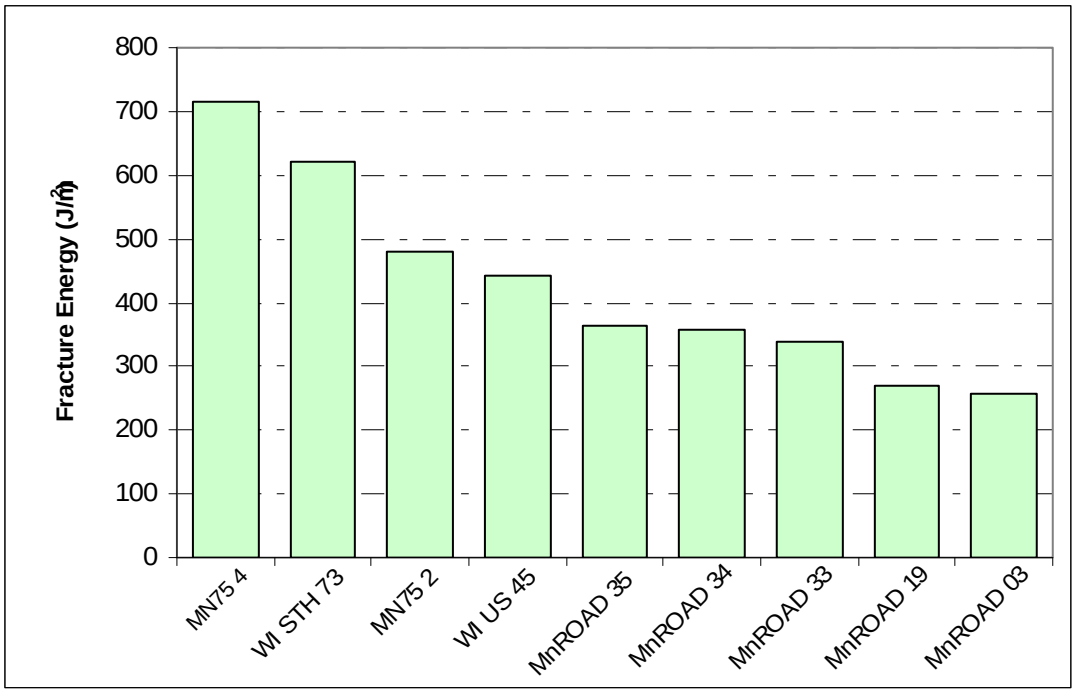

Figure 7.37. SE(B) test results at mid testing temperature.

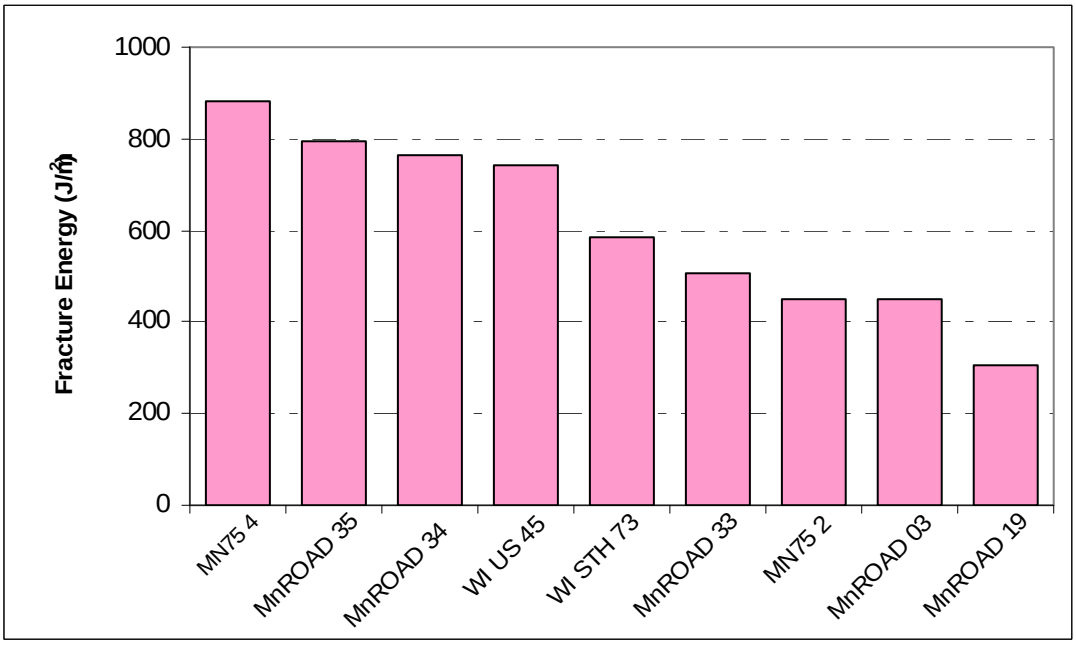

Figure 7.38. SE(B) test results at high testing temperature

SCB Results

Fractuire toughness, K_{Ic}, and fracture energy results for field specimens are presented in Figure 7.39 and 7.40. Observed trends, in terms of fracture energy, are similar to DC(T) and SE(B).

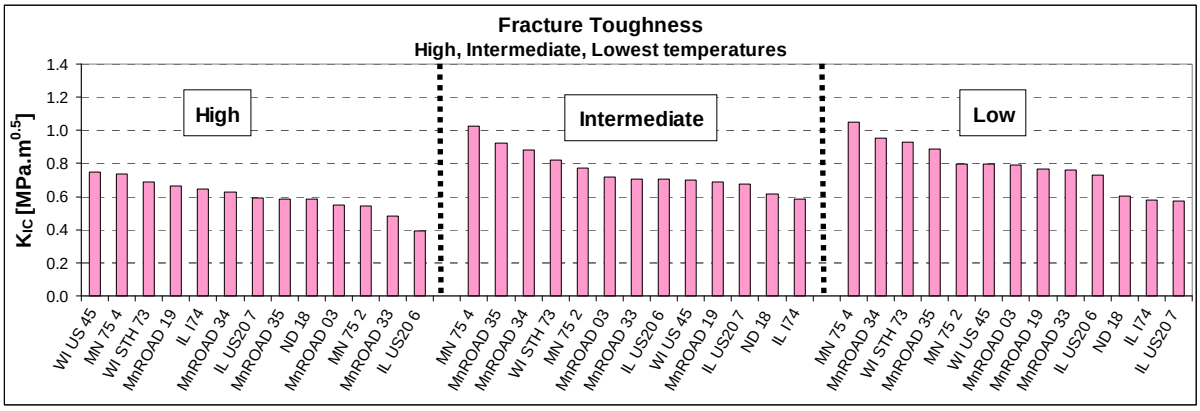

Figure 7.39. Field mixture ranking in terms of fracture toughness (SCB)

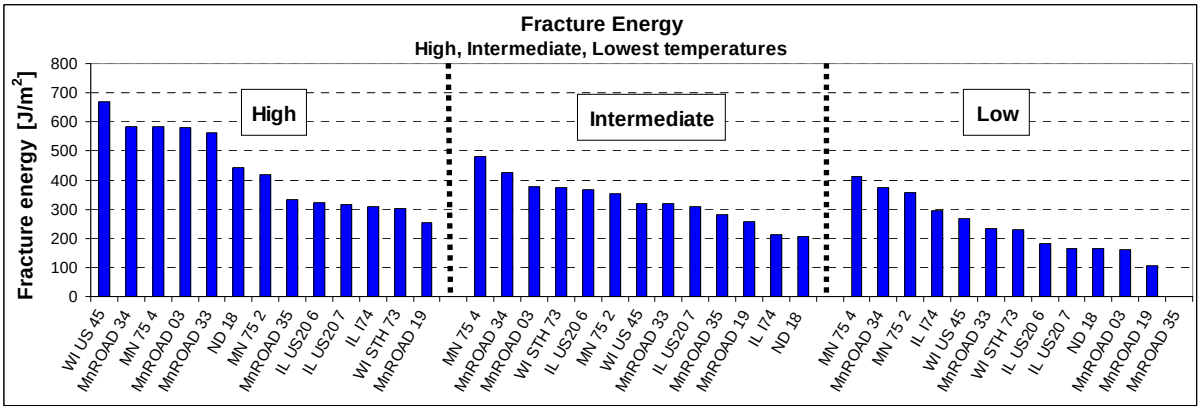

Figure 7.40. Field mixture ranking in terms of fracture energy (SCB)

IDT Results

The creep data was used to generate plots which rank the mixtures according to the creep stiffness values at 60sec and 500sec derived using simple average method. The ranking was done separately for the lowest, intermediate, and the highest test temperatures and it is presented in Figure 7.41-7.43.

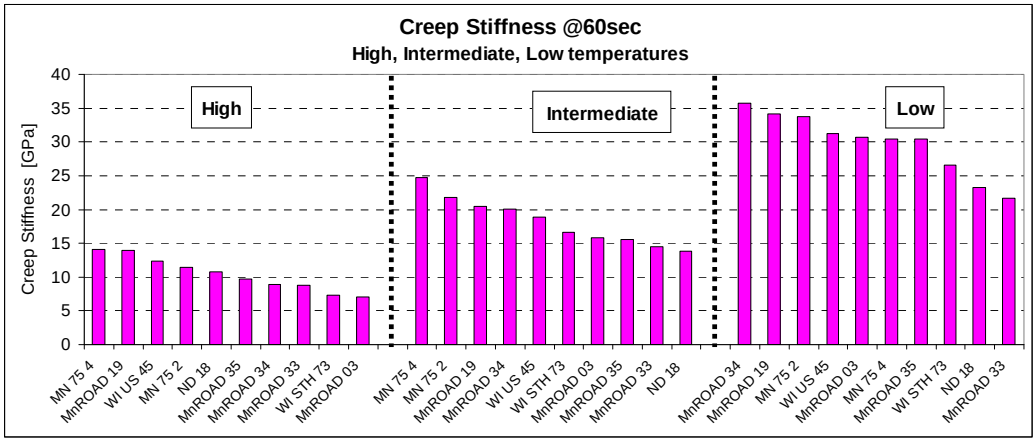

Figure 7.41. Creep stiffness at 60 sec. determined by the simple average method

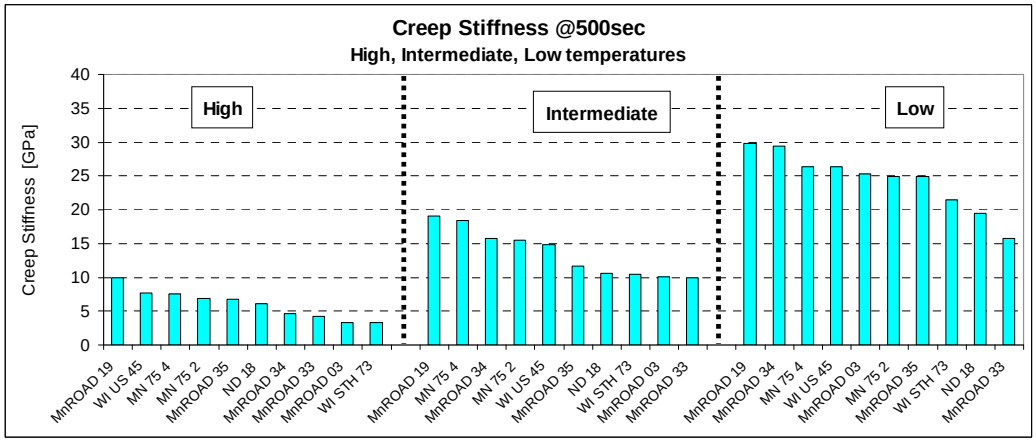

Figure 7.42. Creep stiffness at 500 sec. determined by the simple average method

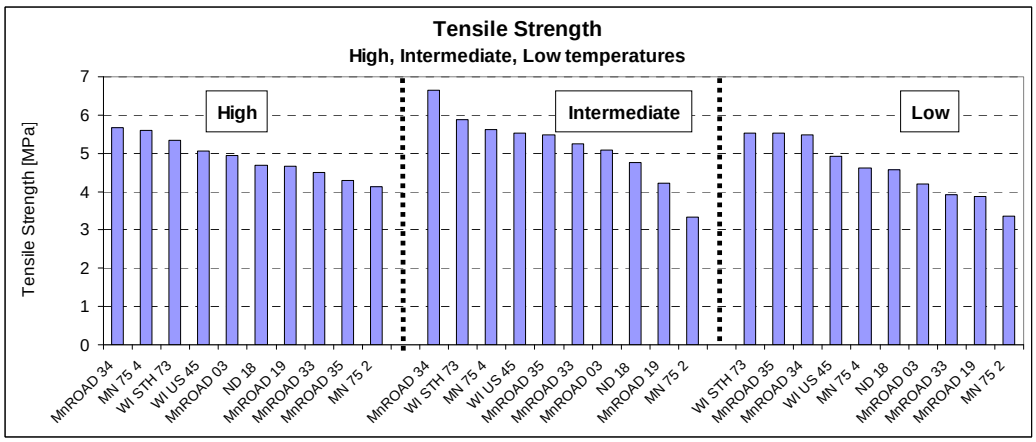

Figure 7.43. Tensile strength determined by the AASHTO method

TSRST Analysis

TSRST for Field Specimens

Figure 7.44 and 7.45 show the fracture temperature and fracture strength of the field specimens.

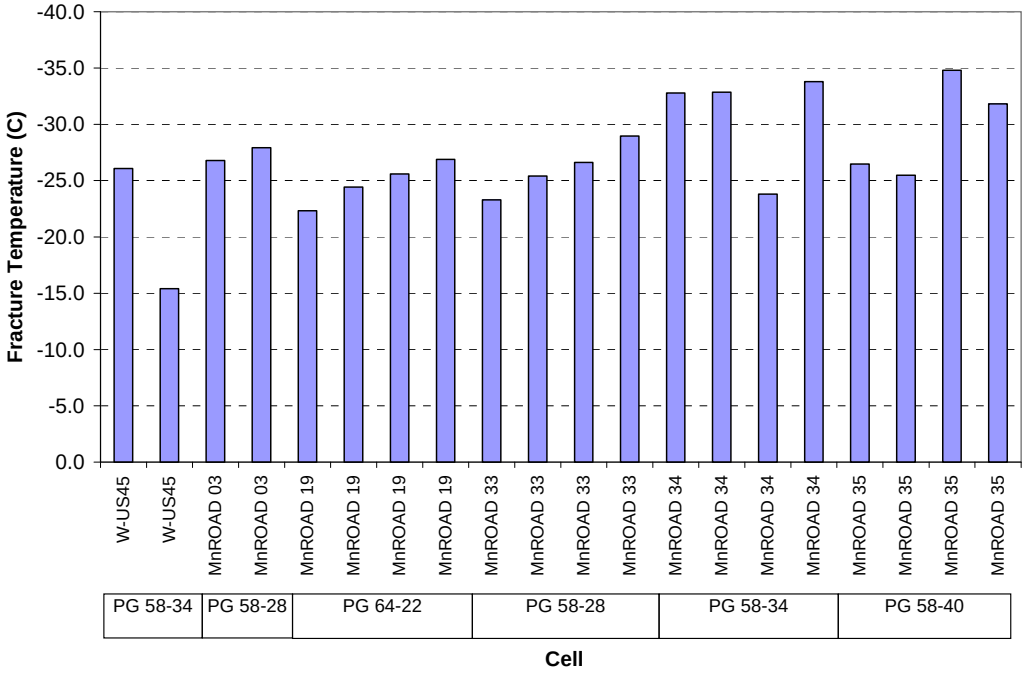

Figure 7.44. TSRST fracture temperature for field specimens

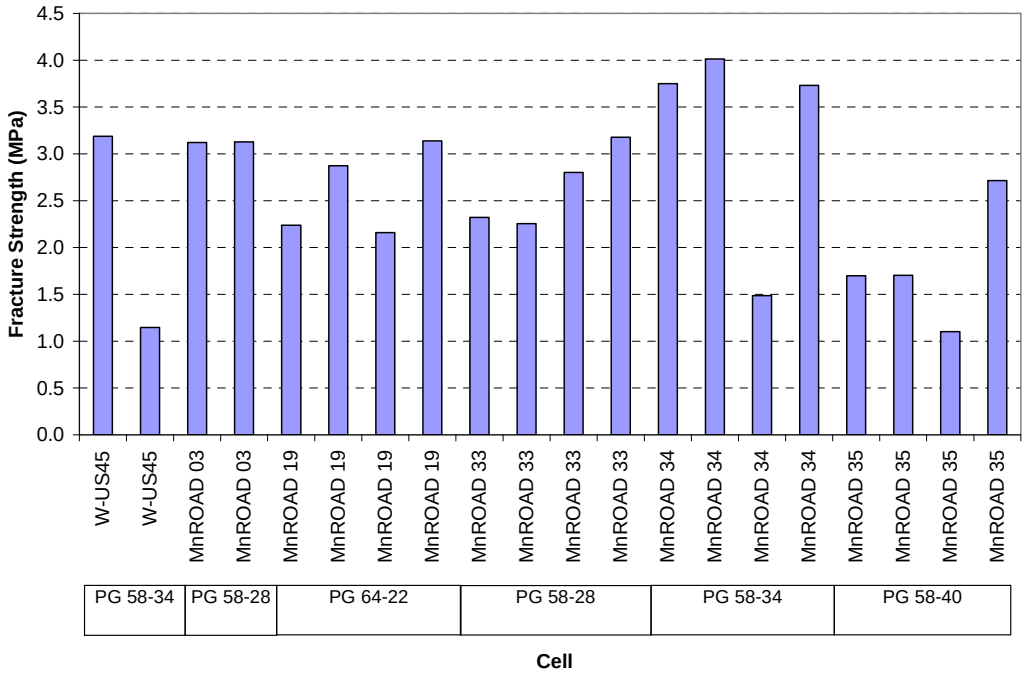

Figure 7.45. TSRST fracture strength for field specimens

The minimum fracture temperature from the field specimens was -34.8°C (MnROAD 35). The maximum fracture temperature was -15.4°C (WI US 45). This high temperature is due to the fact that for that specific specimen the epoxy was not properly cured and thus it failed during the test. The average fracture temperature for the field specimens is -27.7°C if the Wisconsin specimen with the epoxy problem is not included. The average fracture strength for these specimens is 2.6 MPa.

Differences between specimens in the same cell can be seen in Figure 7.45. For example, for MnROAD 35 there are two different fracture temperatures. The first two specimens have an average fracture temperature of -26°C while the other two (e.g. #3 and #4) have an average fracture temperature of -33.3°C. It is not clear why the results are different since the specimens are coming from the same location on the road.

The coefficient of variation for the fracture strength measurements (e.g. 33%) is significantly higher compare to the coefficient of variation for the fracture temperature (e.g. 16%). Figure 7.45 shows clearly more variability than Figure 7.44. This is one of the reasons fracture temperature instead of fracture strength is used to rank the low temperature resistance of the samples. On average the best performance for low temperature cracking was MnROAD 34 with the PG 58-34 binder (see Figure 7.46). The least resistant to thermal cracking was MnROAD 19 with a PG 64-22 binder as it was expected because it has the highest lower limit grade.

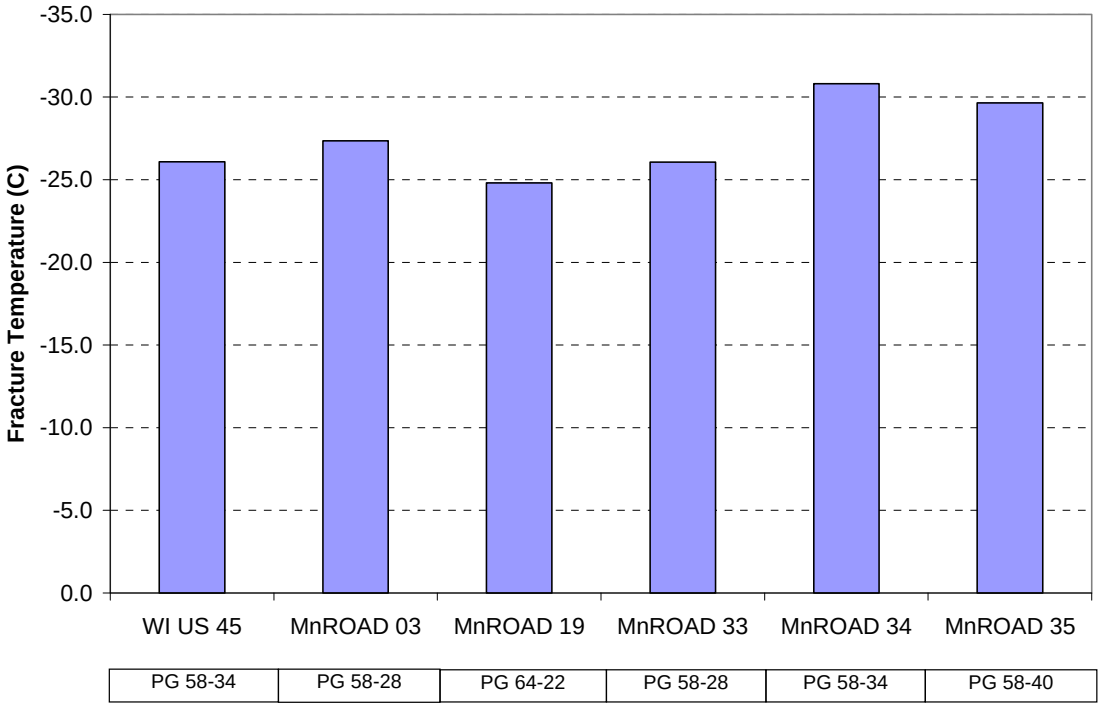

Figure 7.46. Average fracture temperature for field specimens

TSRST for Laboratory Specimens

Again the fracture strength shows more variability than the fracture temperature. The maximum and minimum fracture strength was 6.21 MPa and 1.14 MPa, respectively. Figure 7.47 and 7.48 show the fracture temperature and strength for all the laboratory prepared mixtures.

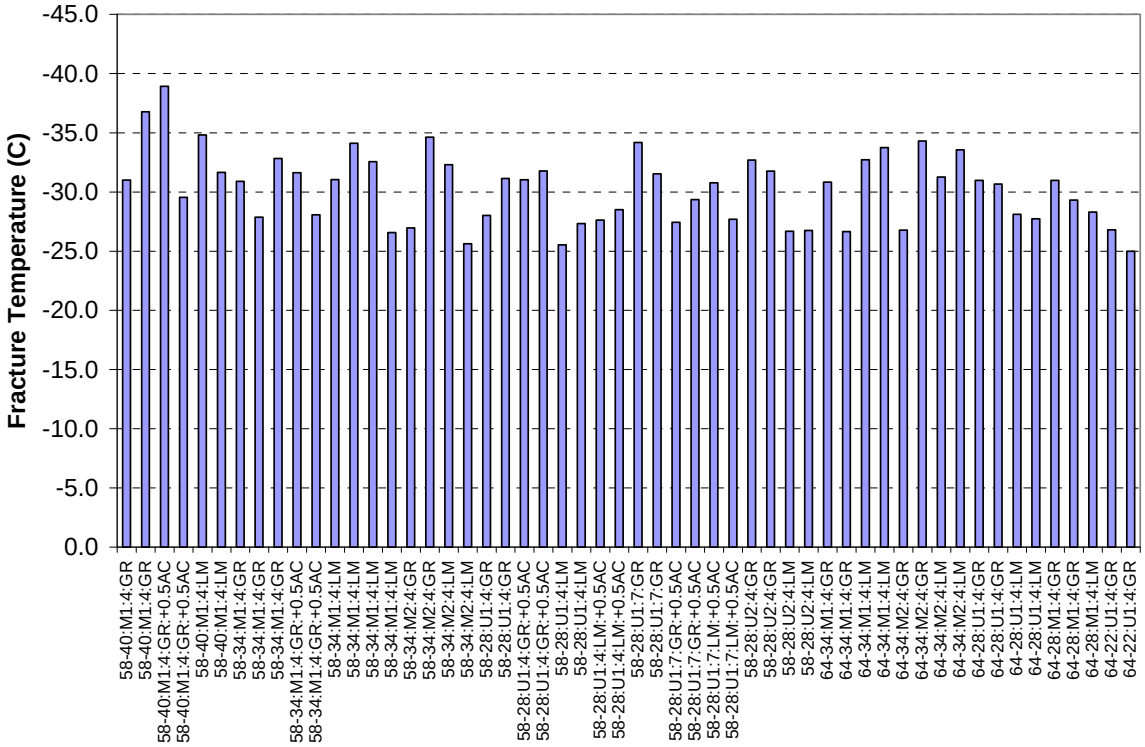

Figure 7.47. TSRST fracture temperature for laboratory specimens

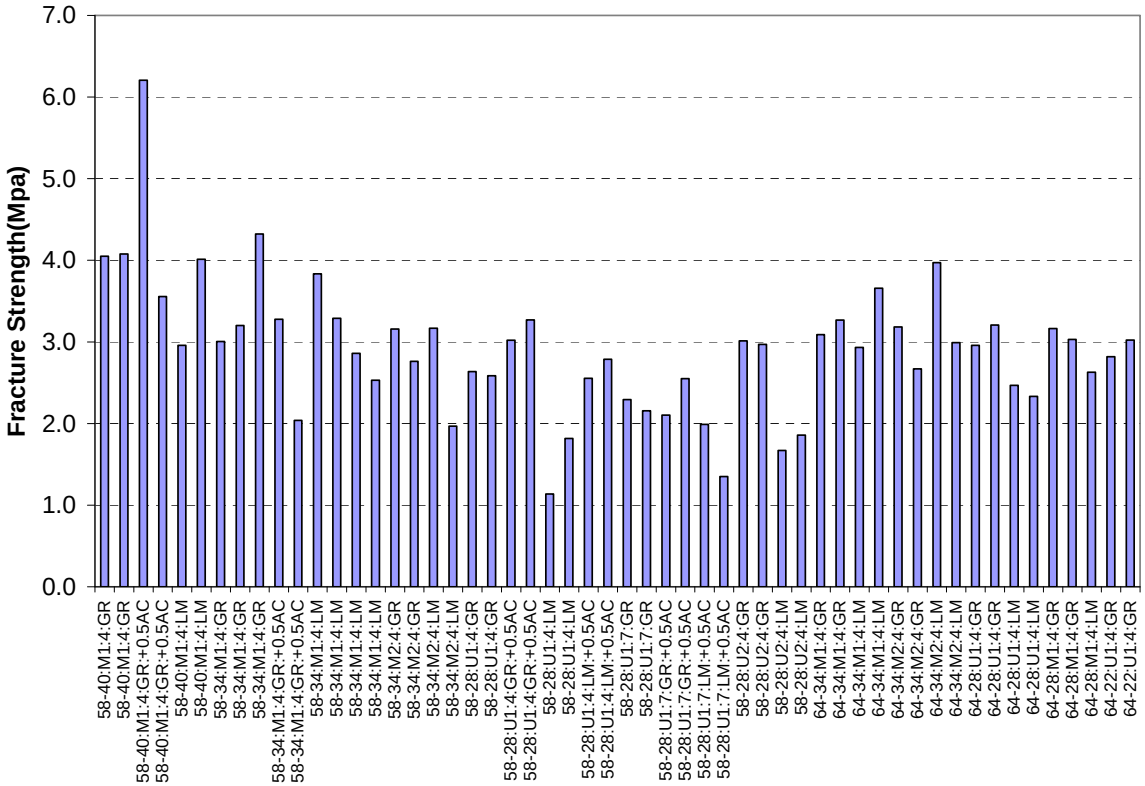

Figure 7.48. TSRST fracture strength for laboratory specimens

Based on the fracture temperature, on average the laboratory mixture that performed the best was 58-40:M1:4:GR:+0.5AC. The least satisfactory mixture in low temperature resistance was 64-22:U1:4:GR. As expected, the mixture containing binder with the highest lower limit grade (e.g. -22) was ranked as the lowest in thermal cracking resistance. Figure 7.49 shows the average fracture temperature for each laboratory prepared mixture. There is a high correlation between the lower PG grade of the asphalt binder and the resistance to low temperature of the mixture as it was expected. The best binder was PG 58-40 with the SBS modifier, followed by the PG 64-34 Elvaloy binder. Moreover for those mixtures, 4% of air voids seems to work better than 7%. The highest fracture temperatures were obtained when PG 64-22 and PG 58-28 unmodified binders were used. Additionally, on average the mixtures containing granite as aggregate performed slightly better than the mixture with limestone.

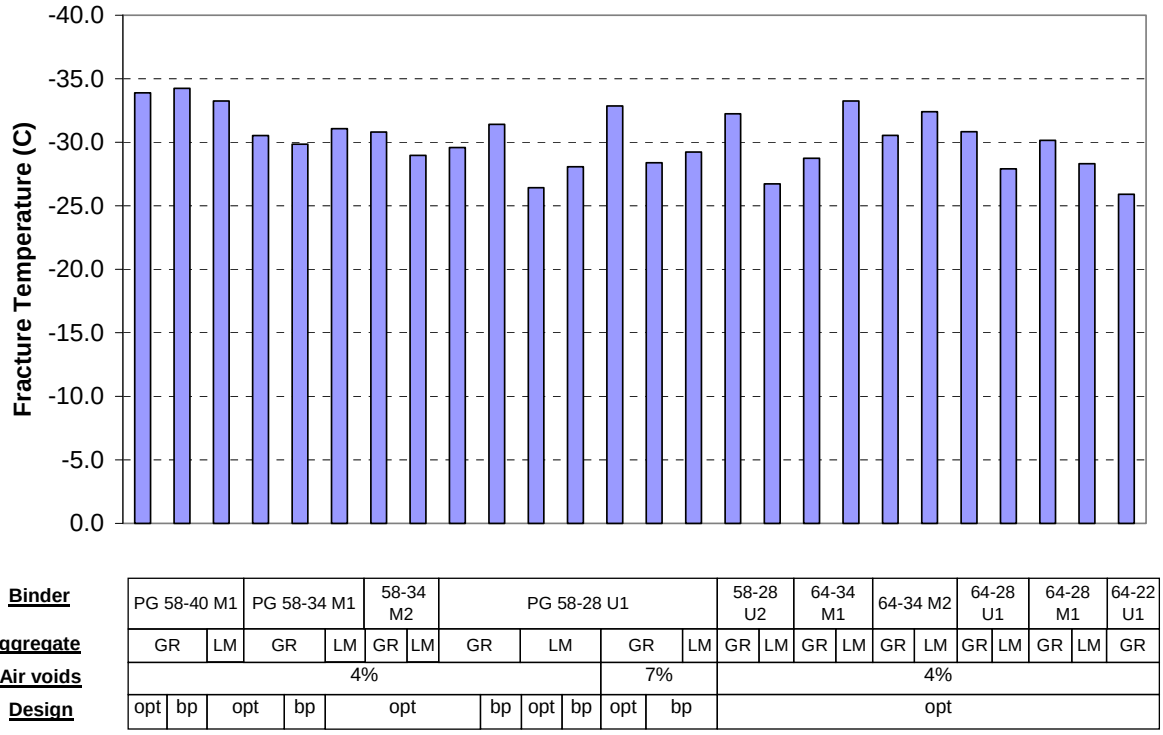

Figure 7.49. Average fracture temperature for laboratory specimens

Cooling Rate Effect

Preliminary testing was done to study the effect of the cooling rate on the TSRST test. The field cooling rates reported in the literature varying from 0.5°C/hr to 2.7°C/hr (99). Although the TSRST is the low temperature performance test that closest simulates field conditions, running each test with these cooling rates will result in an extremely long experiment program (e.g. one test will take up to more than 24 hours). Thus, the tests conducted in this study were done using a cooling rate of 10.0°C/hr. However, two TSRST tests were performed using a cooling rate of 2.0°C/hr to investigate the effect on the fracture strength and temperature if the cooling process is slowed down. Figure 7.50 shows a comparison of TSRST test using two different cooling rates for the 58-40:M1:4:LM mixture. As it is reported in the literature, when the cooling rate is decreased, the fracture temperature decreases as well. However, the reported behavior for the

fracture strength with the cooling rate was not observed in the two experiments performed. It is expected that when the cooling rate increases, the fracture strength increases. To capture the real influence of the cooling rate on the fracture strength more testing needs to be done.

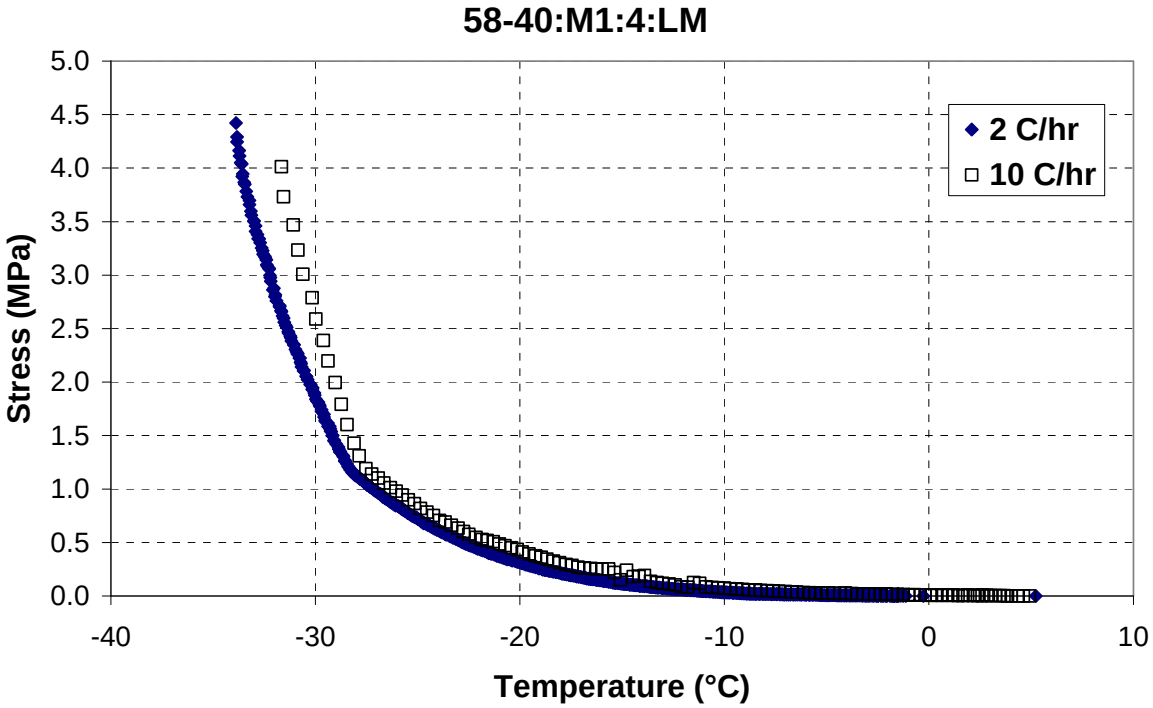

Figure 7.50. TSRST test using different cooling rates

Specimen Shape Effect

Limited evaluation of using cylindrical shape instead of prismatic shape for the test specimen was done in this study. Figure 7.51 shows specimens with prismatic and cylindrical geometry before and after the test. Cylindrical specimens showed slightly lower fracture temperature and slightly higher fracture strength as can be observed in Figure 7.52. However, it is recommended to conduct a larger testing program regarding the shape factor.

Figure 7.51. TSRST specimens with different shapes

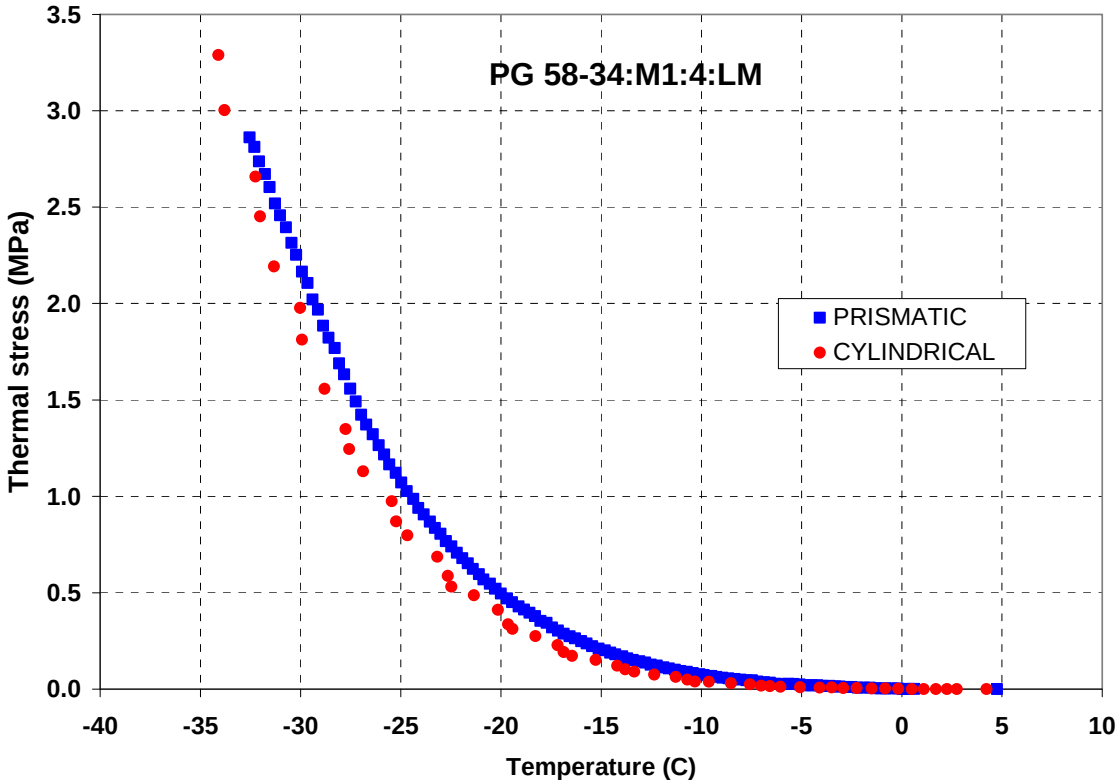

Figure 7.52. Influence of specimen shape in TSRST results.

TSRST – Statistical Analysis

The correlation factors between the parameters obtained during TSRST testing for the laboratory prepared specimens were calculated. Correlation factors more than $2/\sqrt{n}$ (rule of thumb) where n is the number of samples indicates high correlation between the parameters .Table 7.6 shows the correlation factors for the TSRST test parameters. Factors larger than 0.27 (n = 54) are significant and are presented in bold.

Table 7.6. Correlation matrix for TSRST test parameters

Frac_Str	**-0.600**						
PG-LL	**0.499**	**-0.580**					
Air_Void	0.015	**-0.367**	0.276				
Gs	0.050	**0.214**	-0.283	**-0.736**			
Abs	-0.130	-0.220	0.254	**0.644**	-0.763		
dS/dT	0.179	**0.290**	**-0.463**	-0.237	0.146	-0.109	
Trans_T	**0.585**	**-0.418**	**0.580**	0.039	-0.038	-0.163	**-0.383**
	Frac_T	**Frac_Str**	**PG-LL**	**Air_Void**	**Gs**	**Abs**	**dS/dT**

Fracture strength has a negative correlation with fracture temperature meaning that if the fracture temperature increases then the fracture strength decreases. The lower PG grade for the binder has a positive correlation with fracture temperature. As it was expected the correlation is significant and represents that if a binder with a higher PG–low limit is used then a higher fracture temperature for the mixture is expected. Additionally, it can be conclude from the correlation matrix that higher fracture temperature means higher transition temperatures.

According to the correlation factors the fracture strength is proportional to dS/dT and the specific gravity. Thus, specimens with a higher density will break at a higher thermally induced tensile load. Moreover, the fracture strength is inversely proportional to the transition temperature, air void content and the PG–lower limit. Thus, it is recommended to use lower air void content and a lower performance grade limit to obtain a better low temperature cracking performance of the mixture. Another important observation from Table 7.6 is that the slope of the linear part of the stress temperature curve (e.g. dS/dT) becomes steeper as the transition temperature decreases.

Quality control of the laboratory specimens was assessed with the ultrasonic tester. Preliminary evaluation of this technique was done by means of the correlation factors. Table 7.7 shows the result from this analysis.

Table 7.7. Correlation factors between ultrasonic velocity and the TSRST test parameters.

	Ultrasonic velocity
Fracture temperature	0.0968
Fracture strength	0.0941
PG lower limit	**0.2718**
dS/dT	-0.1341
Transition Temperature	**0.3108**
Specific Gravity	**0.3391**
Air_Void	**-0.3789**
Absorption	**-0.4063**

Correlation factors higher than 0.32 are significant for the ultrasonic tests (n = 39). It is clear that no relation was found between the ultrasonic wave velocity and the fracture temperature and strength. However, significant correlation was found between some physical parameters of the mixture (e.g. air void content, specific gravity and absorption) and the ultrasonic wave velocity. Table 7.7 shows that higher specific gravity means higher ultrasonic velocities and the opposite apply for the air void content and the absorption.

Based on the results from the laboratory specimens, a formal statistic comparison using test of hypothesis was performed. The objective of this analysis was to study the differences between the fracture temperature population means of the specimens made with:

- Limestone and granite.
- 4% and 7% air void content.
- Optimum and bump (optimum+0.5%) binder content.

The Student's t-distribution was used to compare the population means of the three cases described above. When the t-distribution is used, both sampled populations have to be approximately normal distributed with equal standard deviation (see Figure 7.53), also the samples must be selected independently (102). The assumptions of normality and equal variances imply that the relative frequency distributions for the two populations would look as shown in Figure 7.53a.

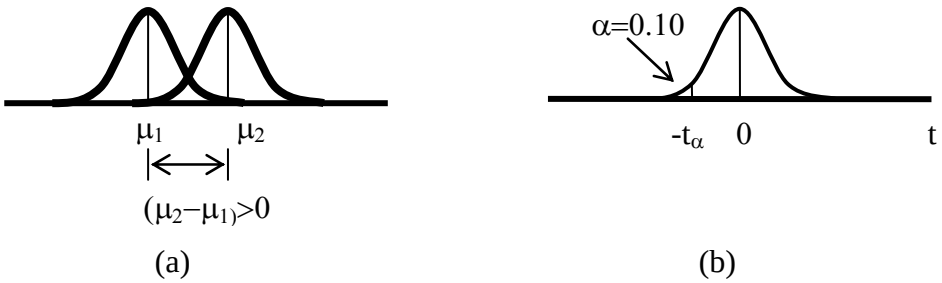

Figure 7.53. Assumptions for Two-Sample test (a), and rejection region for Test of Hypothesis (b)

Both assumptions can be made from the populations, Figure 7.54 shows that the normality assumption for one the population means hold (e.g. the probability plot is linear).

The variance can be assumed to be approximately equal because the same procedure, preparation and testing machine and operator were used to obtain the TSRST results. Therefore the human error and material's intrinsic variability was the same for the populations.

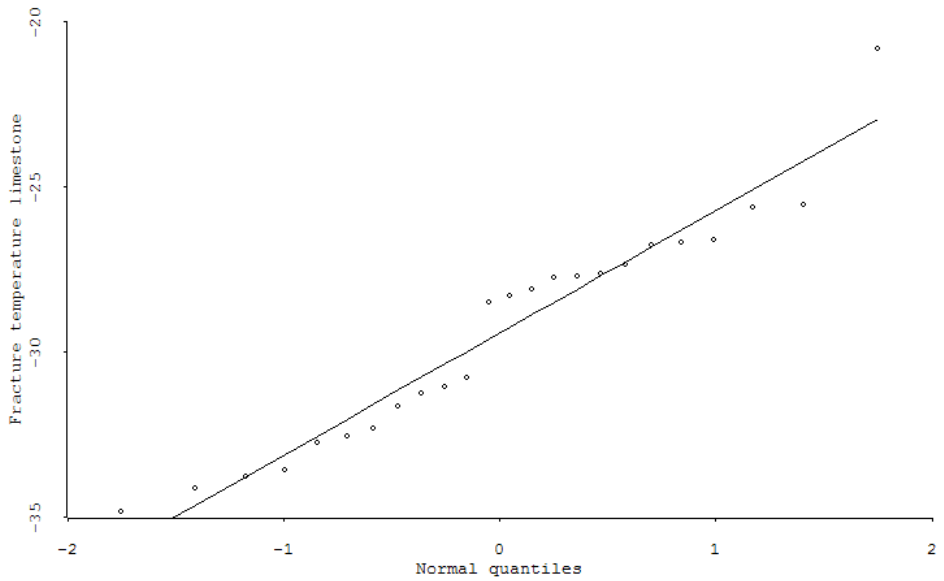

Figure 7.54. Probability plot for the fracture temperature mean population of specimens made with limestone

If the two populations are assumed to have equal variances ($\sigma^2_1=\sigma^2_2$), then it is reasonable to use the information of both samples to calculate a pooled sample estimator of σ^2 to be used in the calculation of tests of hypothesis (102). The following formula was used to estimate the variance of the each population:

$$S_p^2 = \frac{(n_1 - 1)s_1^2 + (n_2 - 1)s_2^2}{n_1 + n_2 - 2} \qquad [1]$$

where:

S^2_p= variance pooled estimator.

s^2_1= calculated variance for population 1 (e.g. specimens made of granite).

s^2_2= calculated variance for population 2 (e.g. specimens made of limestone).

n_1= number of samples in population 1 (e.g. specimens made of granite).

n_2= number of samples in population 2 (e.g. specimens made of limestone).

For the test of hypotheses a one-tailed test was used (see Figure 7.53b). The following null and alternative hypotheses were used with α = 0.10 (type I error, reject H_o when H_o is true):

$$H_0 : \mu_1 - \mu_2 = 0$$
$$H_a : \mu_1 - \mu_2 < 0 \qquad [2]$$

with the test statistic:

$$t = \frac{\bar{X}_1 - \bar{X}_2}{\sqrt{S_p^2\left(\frac{1}{n_1} + \frac{1}{n_2}\right)}} \qquad [3]$$

where,

X_1= mean estimator for population 1.

X_2= mean estimator for population 2.

n_1= number of samples in population 1.

n_2= number of samples in population 2.

S^2_p= variance pooled estimator.

and rejection region (values of the test statistic for which the null hypotheses is rejected): $t < -t_\alpha$

Table 7.8 shows the result for the test of hypothesis on the fracture temperature population means. It can be conclude that there is no significant difference between the population means of the fracture temperature of the specimens mixed with granite and limestone. It was also noted that the population means of the fracture temperature of specimens with 4% and 7% voids were almost the same. Moreover, no significant difference was observed between the fracture temperature population means of specimens with the optimum and the bump binder content.

Table 7.8. Test of hypothesis for the fracture temperature populations.

granite			limestone			S_p^2	$-t_\alpha$	$t_{statistic}$	Reject Region
n_1	$\bar{x}_1$	Std. Dev.	n_2	$\bar{x}_2$	Std. Dev.				$t<-t_\alpha$
31	-30.7	3.10	23	-29.8	2.98	9.317	-1.290	-1.042	Fail to reject Ho
4% air void			7% air void						
48	-30.3	3.14	6	-30.2	2.55	9.510	-1.290	-0.104	Fail to reject Ho
optimum			bump						
43	-30.3	3.06	12	-30.2	3.17	9.507	-1.290	-0.110	Fail to reject Ho

The same analysis described above was done with the results from the ultrasonic testing. Table 7.9 shows the test of hypothesis for the ultrasonic wave velocity populations. In this test, there is a significant difference between the mean of the ultrasonic velocity of specimens with 4% and 7% air void content. Thus, indicating that this equipment might be used for quality control (e.g. crack detection) purposes.

Table 7.9. Test of hypothesis for the ultrasonic velocity populations.

limestone			granite			S_p^2	$-t_\alpha$	$t_{statistic}$	Reject Region
n_1	$\bar{x}_1$	Std. Dev.	n_2	$\bar{x}_2$	Std. Dev.				$t<-t_\alpha$
16	3618	166	24	3650	343	82061	-1.305	-0.344	Fail to reject Ho
7% air void			4% air void						
6	3386	233	34	3682	270	70580	-1.305	-2.514	Reject Ho
bump			optimum						
11	3564	419	29	3665	214	80182	-1.305	-1.006	Fail to reject Ho

No statistically differences were found between the ultrasonic wave velocities of specimens mixed with limestone and granite and with specimens that contained the optimum and the bump binder content.

TSRST - Recommendations and General Comments

Based on the fracture temperature of the TSRST test and the limited number of experiments performed, the resistance to low temperature cracking of the mixtures is ranked in Table 7.10.

Table 7.10. Low temperature ranking of mixtures based on TSRST.

Ranking position	ID	Description	Aggregate	Binder Content	Air voids [%]
1	58-40:M1:4:GR:+0.5AC	SBS	granite	bump	4
2	58-40:M1:4:GR	SBS	granite	opt	4
3	58-40:M1:4:LM	SBS	limestone	opt	4
4	64-34:M1:4:LM	Elvaloy	limestone	opt	4
5	58-28:U1:7:GR	Unmodified 1	granite	opt	7
6	64-34:M2:4:LM	Black Max ™	limestone	opt	4
7	58-28:U2:4:GR	Unmodified 2	granite	opt	4
8	58-28:U1:4:GR:+0.5AC	Unmodified 1	granite	bump	4
9	58-34:M1:4:LM	Elvaloy	limestone	opt	4
10	64-28:U1:4:GR	Unmodified 1	granite	opt	4
11	58-34:M2:4:GR	SBS	granite	opt	4
12	64-34:M2:4:GR	Black Max ™	granite	opt	4
13	58-34:M1:4:GR	Elvaloy	granite	opt	4
14	64-28:M1:4:GR	SBS	granite	opt	4
15	58-34:M1:4:GR:+0.5AC	Elvaloy	granite	bump	4
16	58-28:U1:4:GR	Unmodified 1	granite	opt	4
17	58-28:U1:7:LM:+0.5AC	Unmodified 1	limestone	bump	7
18	58-34:M2:4:LM	SBS	limestone	opt	4
19	64-34:M1:4:GR	Elvaloy	granite	opt	4
20	58-28:U1:7:GR:+0.5AC	Unmodified 1	granite	bump	7
21	64-28:M1:4:LM	SBS	limestone	opt	4
22	58-28:U1:4:LM:+0.5AC	Unmodified 1	limestone	bump	4
23	64-28:U1:4:LM	Unmodified 1	limestone	opt	4
24	58-28:U2:4:LM	Unmodified 2	limestone	opt	4
25	58-28:U1:4:LM	Unmodified 1	limestone	opt	4
26	64-22:U1:4:GR	Unmodified 1	granite	opt	4

Mixtures with PG 58-40 binder and SBS modifier performed the best in TSRST testing. The mixtures prepared with that binder represent the top 3 of the rank shown in Table 7.10. Additionally, mixtures with 4% of air void content are less prone to low temperature cracking than mixtures with 7% air void. Additionally, on average the mixtures containing granite as aggregate performed slightly better than the mixtures with limestone. From Table 7.10 asphalt mixtures with PG 58-28 and PG 64-22 are the most susceptible to thermal cracking. As it was expected, there is a high correlation between the lower PG grade of the asphalt binder and the resistance to low temperature of the mixture.

Based on the limited experimental program performed in this study the following conclusions can be drawn:

- TSRST test results provide a good quantitative indication of low temperature resistance for asphalt mixtures.
- For the field samples, the best performance was obtained for MnROAD 34 with the PG 58-34 binder. Specimens recovered from MnROAD 19 with a PG 64-22 binder were the most susceptible to thermal cracking as it was expected because it has the highest lower limit grade.
- TSRST test results ranking for thermal cracking were consistent with the rankings based on the physical properties of the asphalt binder.
- TSRST test results are sensitive to the asphalt binder type, air void content, asphalt binder content and the type of aggregate.
- Preliminary results showed that ultrasonic tests can be used to asses the quality of the laboratory specimens before testing. Formal statistical analysis showed that variation on density and voids of the specimens can be detected with this technique.
- Cylindrical specimens showed slightly lower fracture temperature and slightly higher fracture strength compare to prismatic specimens.
- TSRST test results are sensitive to the cooling rate. If it is decreased, the fracture temperature decreases as well. The reported behavior for the fracture strength with the cooling rate was not observed. Fracture strength is expected to increase when the cooling rate increases.

Dilatometric Results for Laboratory Prepared Specimens

Table 7.11 includes a summary of the statistical analysis of the results collected for the laboratory prepared samples. The analysis gives a basic view about ranges in measurements and averages. The highlights are as follows:

For the thermal properties in the cooling condition:

- Mixture Tg ranges between -27.94°C and –47.98°C
- Thermal coefficients of contraction below Tg (α_g) range between 7.18 and 14.30 x $10^{-6}/^{o}C$
- The thermal coefficients of contraction above Tg (α_l) was between 10.26 and 30.48 x $10^{-6}/^{o}C$

For the thermal properties in the heating condition:

- Tg range is between -12.12°C.and -32.56°C,
- The range for the thermal coefficients of expansion below Tg (α_g) is between 12.21 to 20.02 x $10^{-6}/^{o}C$ and
- The range for the coefficients of expansion above Tg (α_l) is between 32.08 and 47.66 x $10^{-6}/^{o}C$.

Table 7.11. Statistical summary of dilatometric properties of laboratory mixture samples

Statistical Parameters	Mixture During Cooling Condition			Mixture During Heating Condition		
	Tg(C)	α_g(10-6/C)	α_l(10-6/C)	Tg(C)	α_g(10-6/C)	α_l(10-6/C)
Mean	-35.2259	10.5467	34.6851	-24.7148	14.8301	38.1699
Standard Error	1.0509	0.3219	0.5414	0.9087	0.3553	0.9092
Median	-33.4115	10.2803	34.1105	-25.6633	14.8320	37.8436
Mode	#N/A	#N/A	#N/A	#N/A	#N/A	#N/A
Standard Deviation	5.4607	1.6724	2.8133	4.7219	1.8461	4.7244
Sample Variance	29.8189	2.7970	7.9145	22.2965	3.4079	22.3199
Kurtosis	0.0625	0.4239	-0.3305	0.3436	0.9780	-0.7679
Skewness	-0.8553	0.5488	0.6491	0.7869	0.8785	0.4469
Range	20.0481	7.1213	10.2641	20.4389	7.8059	15.5729
Minimum	-47.9897	7.1883	30.4784	-32.5609	12.2137	32.0872
Maximum	-27.9417	14.3096	40.7424	-12.1220	20.0195	47.6601
Count	27	27	27	27	27	27

Therefore, it can be concluded that the thermal coefficients of expansion during heating (expansion) are higher than coefficients of contraction during cooling. This could be due to the asymmetrical volume change during heating and the possible effect of the sudden increase in pressure exerted by the asphalt films in the mix causing the aggregates to separate. The results also indicate that cyclic thermal loading may affect the thermal properties of mixtures. This may be related to the 'thermal fatigue behavior' of the asphalt pavements. These topics were not part of the objectives of this phase of the study and it is recommended that thermal cycling and asymmetrical thermal behavior be considered for future phases of the project.

Cross comparison between mixture and binder

Figure 7.55 presents mixtures critical temperatures calculated from IDT data as a function of PG low grade of the binder. It can be noticed that in general PG grade system performs well for all the mixtures – the lower PG grade the lower critical temperature. Two mixtures marked with "??" do not follow general trend and are probably due to the calculation error. It should be also mentioned that within the same PG grade, mixtures with granite tends to have lower critical temperatures comparing to limestone mixtures. This confirms earlier observation that granite mixtures produce higher tensile strength in IDT test. Figures 7.56 and 7.57 show comparisons between BBR creep stiffness data at 60sec and mixture fracture energy from SCB test. For laboratory prepared specimens, the lower creep stiffness *S* the higher fracture energy for both types of aggregate. This trend varies with temperature and it is stronger at -24°C. For the field data this relationship seems to be weaker regardless the temperature.

Figure 7.58 shows relationship between SCB and DC(T) tests in terms of fracture energy. Both tests produce very close results at low and intermediate temperatures but they deviate significantly at high temperatures. This discrepancy is caused by the different algorithms used to predict the tail of the load vs. load line displacement curve.

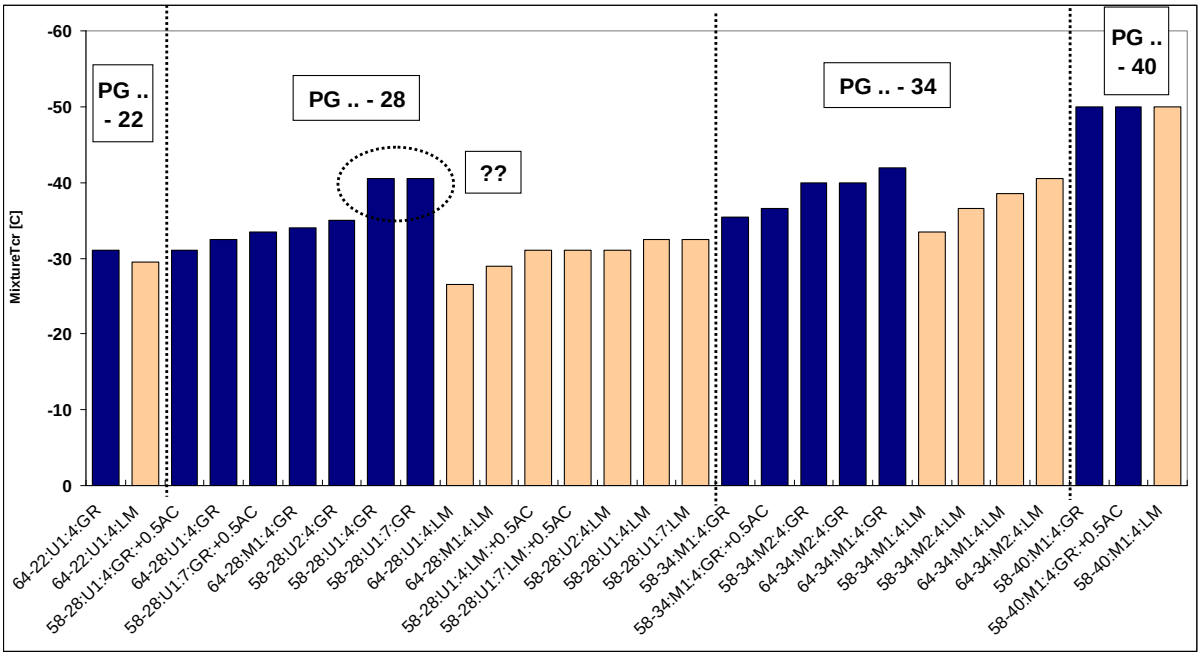

Figure 7.55. Critical temperatures calculated based on IDT vs. binder PG grade and aggregate type

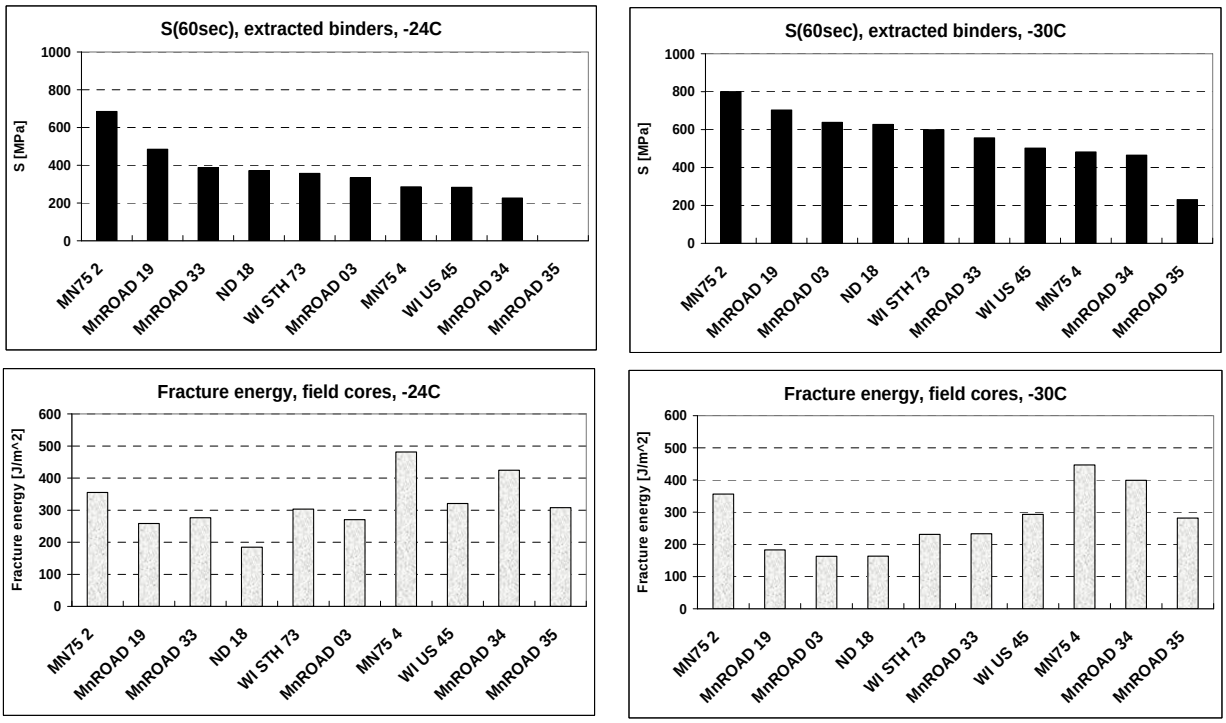

Figure 7.56. Comparison between binder BBR creep stiffness and SCB fracture energy for field materials at two temperatures

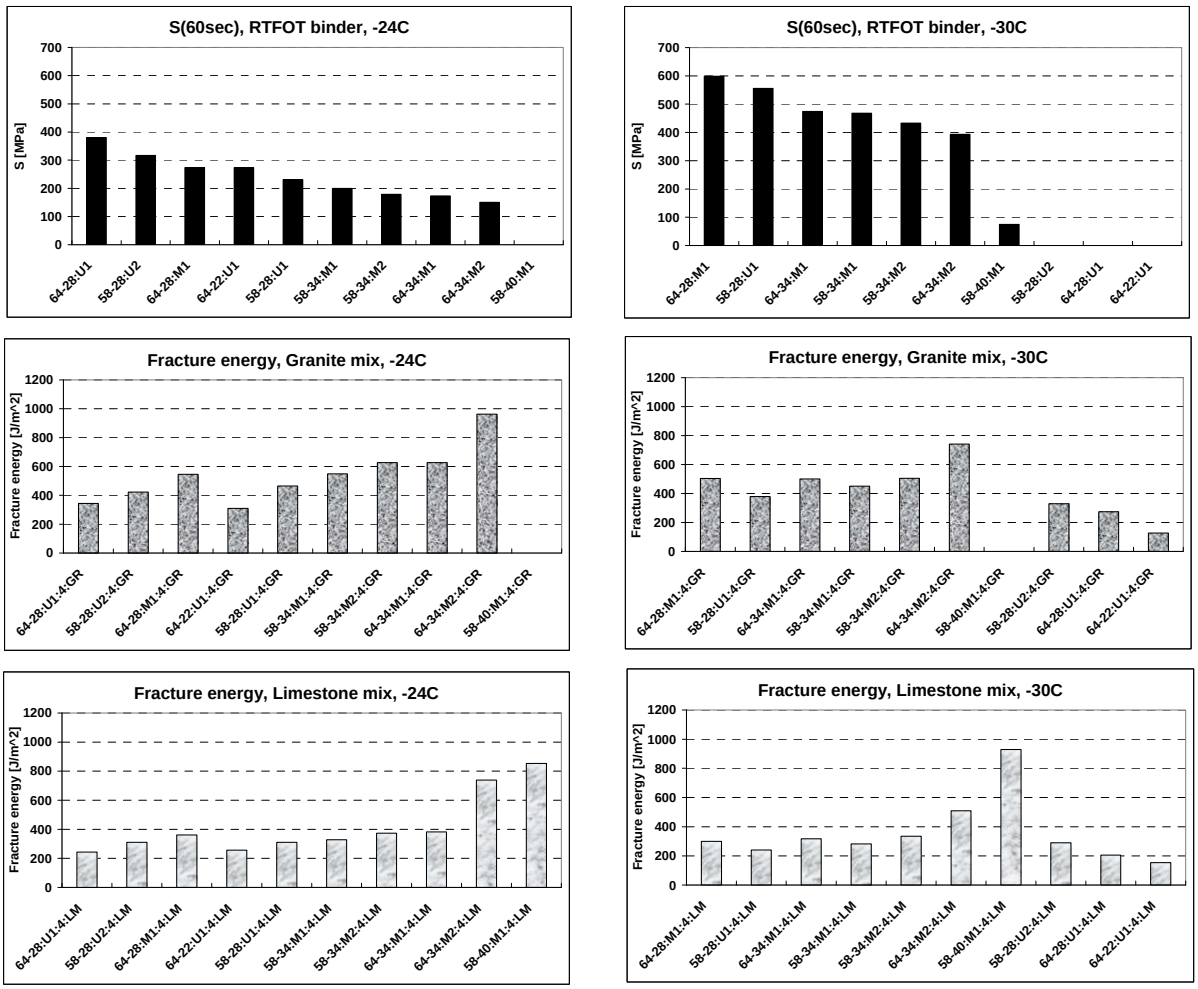

Figure 7.57. Comparison between binder BBR creep stiffness and SCB fracture energy for laboratory materials at two temperatures

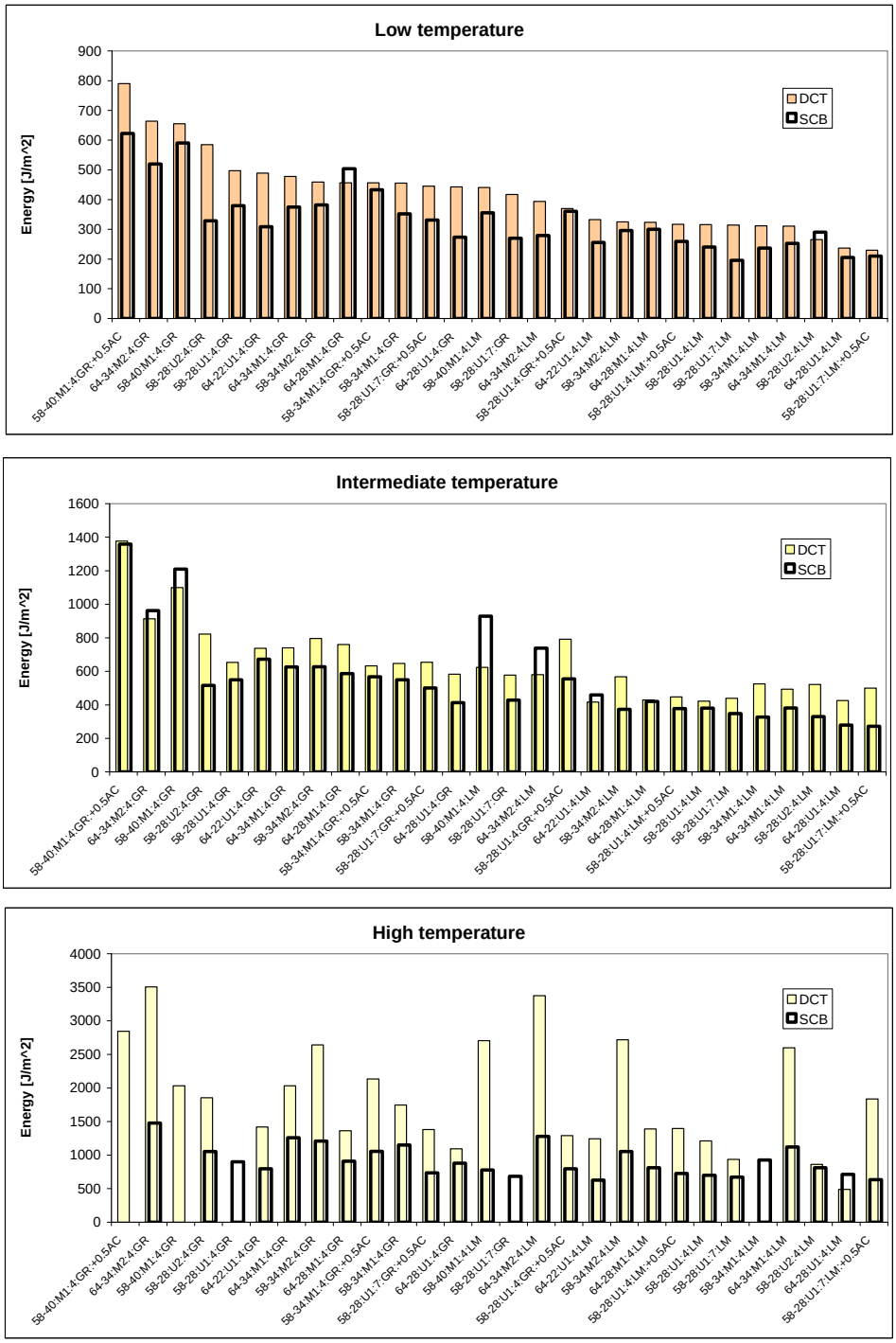

Figure 7.58. Comparison between DC(T) and SCB tests in terms of fracture energy

Cross comparison between laboratory data and field performance

Field samples and performance data received within the scope of this project were used to investigate the relationship between laboratory testing results and low-temperature cracking

susceptibility of the mixtures in the field. Table 7.12a and 7.12b present mixture and binder parameters that were chosen as potential predictors of mixture performance in the field. All parameters were correlated with one of the pavement distresses - *total length of transverse cracking* which was assumed as good estimator of low-temperature cracking. The comparisons were made at temperatures representative for each site to take into account local climate conditions. Table 7.13 presents *low pavement temperature at 50% reliability level* values that were obtained for each site from LTPP database and LTPPBIND software. Since laboratory parameters were not obtained at those temperatures linear interpolation was used to get appropriate values. Table 7.14a and 7.14b present all laboratory parameters at critical pavement temperatures (LTPP) and transverse cracking values used in this comparison.

Table 7.12a. Mixture laboratory parameters

	SCB Fracture Energy	IDT Creep Stiffness @60sec	IDT Creep Stiffness @500sec	SCB, Fracture Toughness	IDT, Tensile Strength	DCT Fracture Energy	SEB Fracture Energy
IL I74	x			x		x	
MN75 2	x	x	x	x	x	x	x
MN75 4	x	x	x	x	x	x	x
MnROAD 03	x	x	x	x	x	x	x
MnROAD 19	x	x	x	x	x	x	x
MnROAD 33	x	x	x	x	x	x	x
MnROAD 34	x	x	x	x	x	x	x
MnROAD 35	x	x	x	x	x	x	x
US20 6	x			x		x	
US20 7	x			x		x	
WI STH 73	x	x	x	x	x	x	x

Table 7.12b. Binder laboratory parameters

	BBR Creep Stiffness @60sec	BBR m-value @60sec	DT Strain at Failure	DENT Strain at Failure	DENT Stress at Failure
IL I74	x	x	x	x	x
MN75 2	x	x	x	x	x
MN75 4	x	x	x	x	x
MnROAD 03	x	x	x	x	x
MnROAD 19	x	x	x	x	x
MnROAD 33	x	x	x	x	x
MnROAD 34	x	x	x	x	x
MnROAD 35					
US20 6	x	x	x	x	x
US20 7	x	x	x	x	x
WI STH 73	x	x	x	x	x

Table 7.13. LTPP low pavement temperature at 50% reliability level

	Station	Temp. [°C]
IL I74	Urbana, IL	-16.4
MN75 2	Collegeville, MN	-24.4
MN75 4	Collegeville, MN	-24.4
MnROAD 03	Buffalo, MN	-23.8
MnROAD 19	Buffalo, MN	-23.8
MnROAD 33	Buffalo, MN	-23.8
MnROAD 34	Buffalo, MN	-23.8
MnROAD 35	Buffalo, MN	-23.8
US20 6	Freeport, IL	-19.7
US20 7	Freeport, IL	-19.7
WI STH 73	Stanley, WI	-24.7

Table 7.14a. Mixture laboratory parameter values and total length of transverse cracking

	SCB Fracture Energy [J/m^2]	IDT Creep Stiffness @60sec [GPa]	IDT Creep Stiffness @500sec [GPa]	SCB, Fracture Toughness [MPa m$^{0.5}$]	IDT, Tensile Strength [MPa]	DCT Fracture Energy [J/m^2]	SEB Fracture Energy [J/m^2]	Length of transverse cracking [ft/500ft]
IL I74	161.7			0.591		199.7		**1200**
MN75 2	355.3	24.2	17.4	0.785	3.35	303.5	453.8	**76**
MN75 4	479.0	24.9	18.7	1.024	5.59	947.9	713.5	**30**
MnROAD 03	273.9	23.0	17.4	0.755	4.65	228.2	268.1	**182**
MnROAD 19	260.4	20.2	18.9	0.689	4.22	203.6	271.1	**547**
MnROAD 33	277.8	17.9	12.8	0.734	4.61	312.2	287.8	**91**
MnROAD 34	425.1	19.8	15.5	0.881	6.67	380.1	357.7	**5.5**
MnROAD 35	308.6	12.6	4.7	0.750	4.86	473.1	410.1	**747**
US20 6	341.0			0.711		319.3		**84**
US20 7	360.4			0.714		217.0		**60**
WI STH 73	295.0	22.2	16.6	0.881	5.68	375.3	439.0	**0**

Table 7.14b. Binder laboratory parameter values and total length of transverse cracking

	BBR Creep Stiffness @60sec [MPa]	BBR m-value @60sec	DT Strain at Failure	DENT Strain at Failure	DENT Stress at Failure [MPa]	Length of transverse cracking [ft/500ft]
IL I74	350.0	0.214	0.196			**1200**
MN75 2	692.5	0.231	0.590	0.598	0.138	**76**
MN75 4	299.5	0.252	1.652	0.612	0.137	**30**
MnROAD 03	324.5	0.298	1.190	0.569	0.129	**182**
MnROAD 19	477.7	0.253	0.789	0.537	0.118	**547**
MnROAD 33	382.1	0.264	1.343	0.531	0.105	**91**
MnROAD 34	218.9	0.312	2.220	0.461	0.161	**5.5**
MnROAD 35						**747**
US20 6	125.8	0.257	1.470	0.519	0.111	**84**
US20 7	318.0	0.194	0.820	0.716	0.116	**60**
WI STH 73	385.1	0.211	1.423	0.504	0.115	**0**

Based on the data shown in above tables two correlation coefficients were calculated:

- Pearson correlation coefficient, ***r***:

$$r = \frac{\sum (x_i - \bar{x})(y_i - \bar{y})}{(n-1)s_x s_y}, \text{ where}$$

  x and y are sample means of x_i and y_i

  s_x and s_y are sample standard deviations

- Spearman's rank correlation coefficient, $\boldsymbol{\rho}$:

$$\rho = 1 - \frac{6\sum d_i^2}{n(n^2-1)}, \text{ where}$$

  d^2_i – difference between each rank of corresponding values in datasets,

  n – number of datasets pairs.

Pearson correlation coefficient reflects the linear relationship between two data sets whereas Spearman's rank correlation coefficient does not require linear relationship and thus is more flexible for investigating unknown trends.

Table 7.15. Correlation coefficients between laboratory parameters and field data

Laboratory parameters		Correlation coefficients	
		Pearson	**Spearman***
Mixture parameters	SCB, fracture energy	-0.708	**-0.718**
	IDT, S(60sec)	-0.713	-0.405
	IDT S(500sec)	-0.590	-0.071
	SCB, Fracture Toughness	-0.639	**-0.736**
	IDT, strength	-0.325	**-0.571**
	DCT, fracture energy	-0.265	**-0.500**
	SEB energy	-0.291	**-0.500**
Binder parameters	BBR S @ 60sec	0.105	0.248
	m-value S @ 60sec	-0.252	0.152
	DT strain at 3%	-0.694	**-0.673**
	DENT Stress at failure	-0.045	0.217
	DENT Strain at failure	-0.239	-0.250

* Values significant at 10% level are highlighted

Table 7.15 presents Pearson and Spearman correlation coefficients between laboratory parameters and transverse cracking. Using 10% significance level and Spearman's correlation coefficient, two important observations can be made:

1. Only fracture parameters are significant.
2. 5 out of 6 significant parameters are related to fracture properties of the mixtures.

Figure 7.59 shows significant relationships between laboratory data and transverse cracking. For all parameters the susceptibility to low-temperature cracking increases when parameter value decreases.

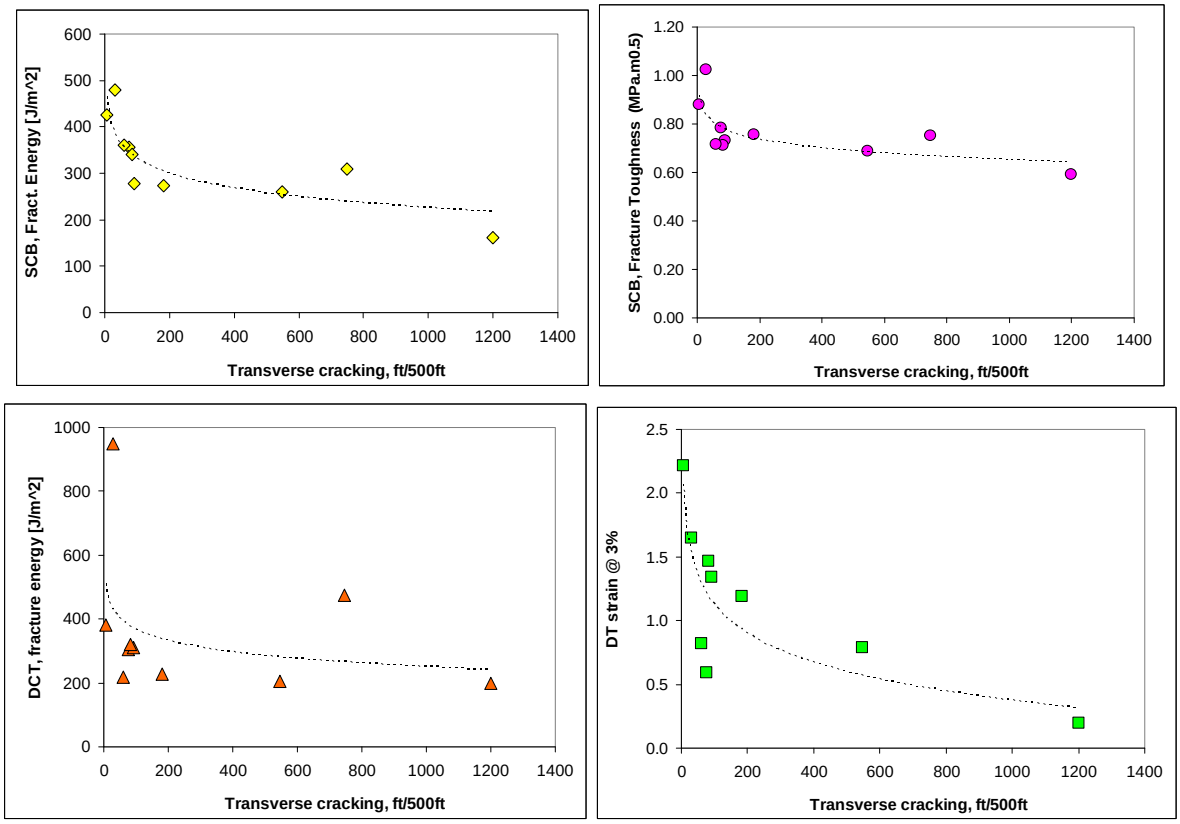

Figure 7.59. Relationship between laboratory parameters and transverse cracking

Additional Statistical Analysis

Statistical analysis was done on the various tests conducted on asphalt binders and hot mix asphalt samples. The analysis was done to evaluate the various test parameters for the tests conducted on laboratory binders and mix as well as recovered field binders and field mixes. A second statistical analysis utilizing regression analysis was done to develop predictive models for mixture tests utilizing binder and mixture volumetric data.

Statistical Analysis for Binders

Statistical analysis was performed on the binder test results of the asphalt binders provided by suppliers as well as recovered binders from field samples. These tests included bending beam rheometer, direct tension, and double edge notched tension tests. The ensuing sections describe the outcomes of the statistical analysis for each of the test apparatus and associated binder populations (asphalt suppliers and field recovered).

Bending Beam Rheometer RTFO

An analysis of variance (ANOVA) was conducted on both creep stiffness and m-value datasets. It was found that PG low temperature grade, storage time, testing time, testing temperature, and modifier significantly affect both creep stiffness and m-values. However, PG high temperature was not deemed a significant effect for either creep stiffness or m-values. The

summary of the ANOVA is summarized in showing the p-values of the variables in Table 7.16 and 7.18 for creep stiffness and m-value.

Table 7.16. Bending Beam Rheometer creep stiffness

Source	Parameter Estimate	Pr > F
PG High Temperature	5413.44	0.4056
PG Low Temperature	1093357.81	< .0001
Type of Modifier	88295.33	0.0115
Aging Time, hrs	425594.71	< .0001
Test Time	1995447.16	< .0001
Test Temperature	8729303.77	< .0001

Table 7.17. Bending Beam Rheometer m-value

Source	Parameter Estimate	Pr > F
PG High Temperature	0.00181015	0.0541
PG Low Temperature	0.02715603	< .0001
Type of Modifier	0.02067448	< .0001
Aging Time, hrs	0.1325295	< .0001
Test Time	0.33539619	< .0001
Test Temperature	0.83352818	< .0001

Mean comparisons were conducted at a 95% level of confidence by grouping data by PG low temperature, modifier, aging time, and testing time. All of the mean comparisons by test temperature were deemed statistically different when evaluating creep stiffness. The low test temperature yielded the highest creep stiffness values. When the m-value was evaluated for the same groupings, there were several groups not deemed statistically different. Table 7.18 summarizes the results of the mean comparisons. An "A" indicates the group with the highest mean while a "C" represents the group with the lowest mean. Groups with the same letter designation are not deemed statistically different, whereas groups with different letters are statistically different. Binders with a PG low temperature of -28ºC and modifier 3 yield m-values for both the intermediate and high temperatures that cannot be deemed statistically different. Grouping by PG high temperature in lieu of PG low temperature is not presented since PG high temperature was not deemed a factor to significantly affect either creep stiffness or m-values.

The next set of mean comparisons evaluated creep stiffness and m-values by modifier within aging time, testing time, and testing temperature. Table 7.19 summarizes the results of the m-value mean comparisons. Modifier 3 does emerge several times as being statistically different than the other modifiers. There were no differences identified when creep stiffness was evaluated.

Table 7.18. Mean comparisons of m-value by test temperature

PG Low Temperature	Modifier	Aging Time (hr)	Test Temperature		
			Low	*Intermediate*	*High*
-40	*SBS*	*1*	A	B	B
		20	A	B	C
-34	*SBS*	*1*	A	B	C
		20	A	B	C
	Elvaloy	*1*	A	B	C
		20	A	B	C
-28	*SBS*	*1*	A	B	C
		20	A	B	C
	Plain 1	*1*	A	B	B
		20	A	B	B
	Plain 2	*1*	A	B	N/A
		20	A	B	N/A
-22	*Plain 1*	*1*	A	B	N/A
		20	A	B	N/A

Table 7.19. Mean comparisons by modifier

Aging Time (hr)	Test Temperature	Modifier			
		SBS	*Elvaloy*	*Plain 1*	*Plain 2*
1	*1*	B	AB	A	AB
	2	A	A	A	A
	3	A	A	A	A
20	*1*	B	B	A	B
	2	B	B	A	B
	3	A	A	A	A

Direct Tension RTFO

An ANOVA was conducted on both the stress and strain at failure. The variables deemed significant for both stress and strain were PG low temperature, modifier, direct tension (DT) stress at percent strain, and test temperature. In both cases, PG high temperature was not deemed significant.

Mean comparisons of stress and strain at failure were conducted grouping the data by PG low temperature, modifier, and test temperature. Table 7.20 summarizes the results of mean comparisons of stress values at failure between DT 1% and 3%. For most comparisons, there is no difference between the two percentage levels. Table 7.21 summarizes the results of the strain mean comparisons between DT 1% and 3%. Unlike the stress mean comparisons, numerous comparisons resulted in deeming the strain values at the two percentage levels as statistically different.

Table 7.20. Stress mean comparison between Direct Tension percent strain

PG Low Temperature	Modifier	Test Temperature	DT %	
			1	*3*
-34	*SBS*	*1*	B	A
		2	A	A
		3	N/A	N/A
	Elvaloy	*1*	B	A
		2	B	A
		3	N/A	N/A
-28	*SBS*	*1*	B	A
		2	A	A
		3	A	A
	Plain 1	*1*	A	A
		2	A	A
		3	A	A
	Plain 2	*1*	N/A	N/A
		2	A	A
		3	A	A
-22	*Plain 1*	*1*	N/A	N/A
		2	A	B
		3	A	A

Table 7.21. Strain mean comparisons between Direct Tension percent strain

PG Low Temperature	Modifier	Test Temperature	DT %	
			1	*3*
-34	*SBS*	*1*	A	B
		2	A	A
		3	N/A	N/A
	Elvaloy	*1*	A	A
		2	A	A
		3	N/A	N/A
-28	*SBS*	*1*	A	A
		2	A	B
		3	A	A
	Plain 1	*1*	A	B
		2	A	A
		3	A	A
	Plain 2	*1*	N/A	N/A
		2	A	B
		3	A	B
-22	*Plain 1*	*1*	N/A	N/A
		2	A	B
		3	A	A

Double Edge Notched Tension (DENT) RTFO Lab

An ANOVA was conducted on stress at failure, strain at failure, and fracture toughness data. Both stress at failure and fracture toughness are significantly affected by modifier and test temperature. Strain at failure is significantly affected by PG low temperature and test temperature. These analyses are summarized in Tables 7.22 through 7.24.

Mean comparisons of all three datasets were conducted to compare values between those obtained at the three different test temperatures. Table 7.25 summarizes the results of the mean comparisons by modifier type. It can be seen that the low and intermediate test temperatures yielded similar results for all four modifiers. Table 7.26 summarizes the results for strain mean comparisons. Table 7.27 summarizes the results of fracture toughness mean comparisons. The fracture toughness mean comparison results were equivalent to the ones for stress mean comparisons.

Table 7.22. DENT stress at failure

Source	Parameter Estimate	Pr > F
PG High Temperature	0.01936467	0.6489
PG Low Temperature	0.5167714	0.0669
Type of Modifier	0.93416633	0.0221
Test Temperature	2.64734231	< .0001

Table 7.23. DENT strain at failure

Source	Parameter Estimate	Pr > F
PG High Temperature	0.0568368	0.2063
PG Low Temperature	0.29371427	0.0181
Type of Modifier	0.13778255	0.2763
Test Temperature	1.7599468	< .0001

Table 7.24. DENT fracture toughness

Source	Parameter Estimate	Pr > F
PG High Temperature	126.84717	0.6593
PG Low Temperature	2788.73633	0.1221
Type of Modifier	5365.45302	0.0466
Test Temperature	18495.1343	< .0001

Table 7.25. Stress mean comparisons between test temperatures

Modifier	Test Temperature		
	1	***2***	***3***
SBS	A	A	A
Elvaloy	A	A	N/A
Plain 1	B	B	A
Plain 2	B	B	A

Table 7.26. Strain mean comparisons between test temperatures

Modifier	Test Temperature		
	1	***2***	***3***
SBS	A	B	B
Elvaloy	A	B	N/A
Plain 1	A	B	B
Plain 2	B	B	A

Table 7.27. Fracture toughness mean comparisons between mean comparisons

Modifier	Test Temperature		
	1	***2***	***3***
SBS	A	A	A
Elvaloy	A	A	N/A
Plain 1	B	B	A
Plain 2	B	B	A

Direct Tension Analysis of Field Extracted Binders

Mean comparisons grouping stress and strain, obtained via direct tension (DT) testing, were conducted by test temperature. In both cases the comparison between samples tested at -18˚C versus those tested at -24˚C were deemed statistically significant. However, the mean stresses at -30˚C were deemed significantly different than those at -18˚C, but the strain means were not deemed significant. Both mean stresses and mean strains were not significantly different when comparing -30˚C and -24˚C. ANOVAs conducted for stress and strain deemed test temperature significant for both. The summary of the statistical analyses are summarized in Tables 7.28 through 7.31.

Table 7.28. Direct Tension of field extracted binders strain sum of squares Type I

Source	Degrees of Freedom	SS I	Mean Square	F value	Pr > F
Temperature	2	8.291959	4.145979	4.3	0.0161
Binder	12	35.86226	2.988521	3.1	0.0009

Table 7.29. Direct Tension on extracted binders strain sum of squares Type III

Source	Degrees of Freedom	SS III	Mean Square	F value	Pr > F
Temperature	2	8.725066	4.362533	4.52	0.0131
Binder	12	35.86226	2.988521	3.1	0.0009

Table 7.30. Direct Tension stress sum of squares Type I

Source	Degrees of Freedom	SS I	Mean Square	F value	Pr > F
Temperature	2	132.0638	66.03188	14.6	<.0001
Binder	12	278.4882	23.20735	5.13	<.0001

Table 7.31. Direct Tension stress sum of squares Type III

Source	Degrees of Freedom	SS III	Mean Square	F value	Pr > F
Temperature	2	137.5076	68.75381	15.2	<.0001
Binder	12	278.4882	23.20735	5.13	<.0001

Double Edge Notched Tension (DENT) Field Binders Analysis

Binders were extracted from field mixes to conduct DENT tests. Mean comparisons of stress, strain, and fracture energy were conducted with datasets grouped by test temperature. Mean comparisons of stress, strain, and fracture energy between -18˚C and -30˚C and between -18˚C and -24˚C were deemed statistically different. No other comparisons by test temperature were deemed statistically different. The summary of the analyses are summarized in Tables 7.32 through 7.37.

Table 7.32. DENT stress SSI

Source	Degrees of Freedom	SS I	Mean Square	F value	Pr > F
Binder	1	2.075529	2.075529	5.45	0.0213
Temperature	2	5.869416	2.934708	7.7	0.0007

Table 7.33. DENT stress SS III

Source	Degrees of Freedom	SS III	Mean Square	F value	Pr > F
Binder	1	2.185348	2.185348	5.74	0.0182
Temperature	2	5.869416	2.934708	7.7	0.0007

Table 7.34. Strain SS I

Source	Degrees of Freedom	SS I	Mean Square	F value	Pr > F
Binder	1	0.70218	0.70218	3.71	0.0564
Temperature	2	2.618029	1.309015	6.92	0.0014

Table 7.35. Strain SS III

Source	Degrees of Freedom	SS III	Mean Square	F value	Pr > F
Binder	1	0.743727	0.743727	3.93	0.0497
Temperature	2	2.618029	1.309015	6.92	0.0014

Table 7.36. Fracture Toughness SS I

Source	Degrees of Freedom	SS I	Mean Square	F value	Pr > F
Binder	1	3839.735	3839.735	8.3	0.0047
Temperature	2	7189.727	3594.864	7.77	0.0007

Table 7.37. Fracture Toughness SS III

Source	Degrees of Freedom	SS III	Mean Square	F value	Pr > F
Binder	1	4002.2	4002.2	8.65	0.004
Temperature	2	7189.727	3594.864	7.77	0.0007

Statistical Analysis for Laboratory Prepared Specimens

ANOVAs were conducted to evaluate which variables significantly affect the results from the various mix tests performed. Table 7.38 summarizes results from the ANOVAs. A solid dot indicates that a factor significantly affect the test results. PG low temperature and test temperature were significant variables for all seven of the eight types of mix test results. Use of optimal binder content or a binder bump of 0.5 percent does not seem to have a significant effect on any of the mix results evaluated. Analysis of the two fracture energy test results indicate that the two methods yield statistically different results. Indirect tensile test (IDT) creep stiffness at 60 seconds was also deemed statistically different than IDT creep stiffness at 500 seconds.

Table 7.38. Variables significantly affecting laboratory mix test results

Variable	DC Fracture Energy	SCB Fracture Toughness	SCB Fracture Energy	IDT Creep Stiffness @ 60 sec	IDT Creep Stiffness @ 500 sec	TSRST Fracture Temp	TSRST Fracture Strength	TSRST Slope
PG High Temperature		●	●					
PG Low Temperature	●	●	●	●	●	●	●	
Type of Modifier	●	●	●			●	●	●
Target Air Voids		●		●	●		●	
Aggregate Type	●	●	●				●	
Asphalt Content Bump								
Test Temperature	●	●	●	●	●	No comparison		

Predictive Models for Laboratory Prepared Mixes

Stepwise regression was used to evaluate different model possibilities. A level of confidence of 95 percent was used to evaluate the individual parameters of all of the developed models. The ensuing sections summarize the developed statistical models for the disc-shaped compact tension test (DC Energy), the semi-circular beam fracture toughness and energy, and the indirect tensile test at 60 seconds and 500 seconds.

Mallow's Cp was used to evaluate the benefits of the independent variables' contributions to a regression model. Mallow's Cp is a statistical tool used to select an appropriate model. A propitious model will have a Cp value close to the number of variables in the model plus 1. Mallow's Cp is calculated as follows:

$$Cp = \frac{SSE}{MSE} - N + 2 \bullet p$$

where:

SSE= Residual sum of squares,

MSE= Mean sum of squares,

N= Number of observations, and

p=Number of factors +1.

Disc-shaped Compact Tension (DC) Energy

The model selected for DC energy data consists of 4 variables with an R^2 of 0.788. Mallow's Cp is rather poor at 70.536 indicating that there is a significant amount of error. It should be noted however that the model selected offered the lowest Cp value.

$$DC\ Energy = 1948.8 - 53.3High - 46.3Low - 210.5aggregate + 328.5DT_{strain@1\%}$$

where:

High=PG high temperature,

Low=PG low temperature,

Aggregate Type=Type of Aggregate (e.g. granite=0, limestone=1), and

$DT_{strain1\%}$=Temperature when the Strain at Failure for DT at 1%.

Table 7.39 summarizes the statistics for the independent variables for the developed DC energy equation.

Table 7.39. DC Energy parameter estimates

Variable	Parameter Estimate	Pr > F
Intercept	3252.6776	<.0001
PG High Temperature	-65.64533	<.0001
PG Low Temperature	-34.10013	0.0003
Aggregate Type	-205.47585	0.0001
DT Strain at 1%	320.59607	<.0001

Semi-Circular Bending (SCB) Fracture Toughness

The model selected for SCB fracture toughness consists of 10 variables with an R^2 of 0.9334. Mallow's Cp for the model is 24.5658, which is fair. Table 7.40 summarizes the parameter estimates for the fracture toughness regression analysis.

Table 7.40. SCB fracture toughness parameter estimates

Variable	Parameter Estimate	Pr > F
Intercept	-0.48432	0.0115
PG High Temperature	0.01411	< .0001
Type of Modifier	-0.04126	< .0001
Test Temperature	0.34181	< .0001
Target Air Voids	-0.03434	< .0001
Aggregate Type	-0.11475	< .0001
DT Stress at 3%, MPa	-0.03768	< .0001
DT Strain at 3%	-0.01237	0.0178
Dent Stress, MPa	1003.2388	< .0001
Dent Strain	-0.18031	< .0001
Dent Toughness, kPa-$m^{0.5}$	-11.99714	< .0001

Semi-Circular Bending (SCB) Fracture Energy

The model selected for SCB fracture energy consists of 12 variables with an R^2 of 0.9281. Mallow's Cp for the model is 8.6. Table 7.41 lists the parameter estimates for the SCB fracture energy regression analysis.

Table 7.41. SCB fracture energy parameter estimates

Variable	Parameter Estimate	Standard Error	Type II SS	F Value	Pr > F
Intercept	-613.55223	231.3232	61242	7.04	0.0089
PG Low	-9.85286	5.06565	32934	3.78	0.0537
Type of Modifier	67.34232	13.6709	211235	24.27	<.0001
Temperature	-70.94488	44.09458	22535	2.59	0.1099
Target Air Voids	-25.03129	6.93642	113365	13.02	0.0004
Aggregate Type	-158.57569	15.11339	958370	110.09	<.0001
BBR Creep Stiffness @ 60 sec, MPa	0.44844	0.18533	50971	5.86	0.0168
BBR m-value @ 60 sec	1280.1028	605.6555	38889	4.47	0.0363
DT Stress 1%, MPa	50.9235	15.60927	92652	10.64	0.0014
DT Strain 1%	148.66762	15.66797	783774	90.03	<.0001
DT Strain 3%	18.47838	7.67721	50432	5.79	0.0174

Indirect Tensile (IDT) Creep at 60 Seconds

The model selected for IDT creep stiffness at 60 seconds consists of 4 variables with an R^2 of 0.8647. Mallow's Cp for the model is 26.3648. Table 7.42 lists the parameter estimates.

Table 7.42. IDT creep stiffness at 60 second parameter estimates

Variable	Parameter Estimate	Pr > F
Intercept	-1.67001	0.0822
Test Temperature	5.04796	<.0001
Target Air Voids	-0.90192	<.0001
Asphalt Content Bump	3.02186	0.0056
BBR Creep Stiffness	0.01656	<.0001

Indirect Tensile (IDT) Creep at 500 Seconds

The model selected for IDT creep stiffness at 500 seconds consists of 6 variables with an R^2 of 0.8900. Mallow's Cp for the model is 16.5696. Table 7.43 lists the parameter estimates.

Table 7.43. IDT creep stiffness at 500 second parameter estimates

Variable	Parameter Estimate	Pr > F
Intercept	-2.19468	0.2294
Test Temperature	4.59159	<.0001
Target Air Voids	-0.6564	<.0001
Asphalt Content Bump	1.96723	0.0138
BBR Creep Stiffness	0.01681	<.0001
DT Stress @ 1%	-1.0386	<.0001
DT Strain @ 1%	0.45843	0.0212

CHAPTER 8

MODELING OF LOW TEMPERATURE CRACKING IN ASPHALT PAVEMENTS

Development of Baseline Thermal Cracking Models

The first part of this chapter details the development of analytical/baseline low temperature cracking models for asphalt pavements considering construction materials and fracture mechanisms. It is helpful to compare and contrast modeling efforts associated with this project, as follows:

- **Analytical (or Closed-Form) Baseline Models.** This modeling approach involves the development of exact (with some exceptions) mathematical expressions that describe the behavior of a pavement system with relatively simple geometry and loading conditions. The advantages of this approach are that: 1) the expressions can be used to obtain instantaneous results (in a spreadsheet, for instance) and thus rapid sensitivity analyses can be performed over ranges of model inputs or parameters; 2) the solutions are exact, or have known accuracy over their entire stated validity range, and therefore can provide reliable benchmarks for more complex numerical models. The main disadvantage of this modeling approach is that the development of solutions becomes exceedingly complicated or impossible with increasing complexity of model geometry, material complexity, and other complex model inputs (load conditions, interfaces between layers, temperature gradients, etc.). This will become apparent later in this report, as it can be observed that even relatively simple models can quickly lead to rather complicated derivations and mathematical solutions. For complex problems, approximate numerical models or simulations are required.
- **Numerical Simulation Models.** Used for more complex problems, as described above, this method typically involves the use of the finite element modeling technique (other techniques, such as discrete element modeling are also possible) to provide a numerical estimation of pavement response and/or distress. The main advantage of this approach is the ability to handle complex model geometry, complex material properties, and complex boundary conditions (frictional sliding, complex tire loads, temperature gradients which change with time, and existing and/or developing cracks and discontinuities). While this approach clearly provides a means for developing realistic models which may lead to new insights about thermal cracking mechanisms and key factors, the disadvantages of this approach are: 1) the computational time may be excessive for complex problems, thereby limiting the number of cases that can be routinely considered; 2) development and proper interpretation of the model requires a highly trained analyst and/or considerable work is needed to develop a non-proprietary user-friendly model for general use; 3) model convergence is not guaranteed, and; 4) model inputs may be more difficult and/or expensive to obtain.

Clearly, there are tradeoffs for each of the two modeling approaches described above, and in fact, it was necessary to utilize both in the current study. The analytical models, which will be described in this section, are being used on this project primarily to provide baseline results (i.e., thermal stresses under temperature change, crack spacing, etc.) which will be used to verify the numerical FE models before invoking the complex aspects of these models. Verification against

benchmark solutions is a crucial step in ensuring that realistic and accurate results are being obtained from the approximate numerical models. Researchers at the University of Illinois at Urbana-Champaign (UIUC) have completed the extension of baseline analytical thermal cracking models, originally developed by researchers in the University of Minnesota in the previous low temperature cracking project (108), from one dimensional solution to two dimensional solutions. These new models allow engineers and practitioners to rapidly evaluate how various materials, structural (layers/thicknesses), and climatic factors may effect low temperature cracking development in asphalt pavements.

It should be noted that while this part can be regarded as a standalone document that provides closed-form solutions for the evaluation of thermal cracking under specific modeling assumptions, the importance of this work will become even more apparent in the second part of this chapter when the development and findings of numerical simulation models of field sections are complete. Nevertheless, the current report provides several new insights into thermal cracking mechanisms, such as the propensity for close crack spacing in instances when thermal cracks do not penetrate the entire depth of the HMA layers during their initial development. Close crack spacing has been observed in many field sections, including conventional hot-mix asphalt (HMA), full-depth, and composite pavements.

Readers interested in the details of model development, including modeling assumptions, derivations, and verification with other solutions, should read Sections 2 through 5 in detail. Readers more interested in the application of model results can skim over Sections 2 through 5 and then read Section 6 in detail. In this project, the analysis efforts focus on the thermal cracking within the asphalt overlay, so fractures in the base-layer or along the interface are not considered. Section 2 provides general modeling assumptions and solutions. Then, three types of solutions are obtained for corresponding interface conditions, as follows:

- **Section 3** - First, an asphalt overlay resting on a granular base is considered. Because the constraint from the base-layer is enacted via friction, a frictional boundary condition is employed to derive the explicit solution for elastic fields (stress, strain, deflection) within the asphalt overlay with full-depth cracks. By considering the strength of the pavement materials, a procedure for estimating the thermal crack spacing is then presented. Using the shear stress solution, a method for evaluating the propensity for debonding along the interface between the pavement and base layer in the vicinity of discontinuities is presented.
- **Section 4** - Secondly, an asphalt overlay fully bonded to a thick base-layer is studied. A two dimensional elastic solution is derived for one section between two discontinuities within the overlay. From this solution, the energy release rate of the three-dimensional channeling cracks is calculated. Using Beuth's exact solution of energy release rate for one crack occurring in an infinitely long section yields the closed-form solution.
- **Section 5** - Finally, an asphalt overlay fully bonded by a rigid base-layer is investigated. In the first two cases, once a crack initiates, it is assumed to propagate across the thickness of the overlay and stop at the interface. However, in this case, because the rigid base-layer provides a very rigid constraint on the deformation in the overlay, cracks initiated along the surface may not reach the interface between the overlay and the base-layer. With the increase of thermal loading, the existing cracks may propagate in two directions: top-down plane strain cracking and three-dimensional channeling. A two-dimensional series form solution is obtained, and energy release rates are calculated from the model for the two types or cracks.

By comparing the energy release rates with the fracture toughness of the overlay, the propensity for crack propagation can be evaluated.

Background

Hot Mix Asphalt (HMA) pavements are typically overlay/substrate systems with one or more asphalt concrete layers constructed upon either: granular aggregate layers; compacted soil layers (sometimes cement- or pozzolanically-stabilized), or, in case of pavement rehabilitation; existing Portland Cement concrete slabs. When an asphalt pavement is subjected to a thermal loading due to the ambient temperature change, thermal cracking can form across the width of the pavement (109). Thermal cracking is one of the most devastating distresses that can occur in asphalt pavements in cold climates. Various empirical and "mechanistic-empirical" models [(109) - (111)] have been proposed, in which various field observations and laboratory experiments were conducted to predict crack spacing in asphalt pavements.

Although the aforementioned empirical models produced some good predictions of crack spacing in asphalt pavement, the thermal stress distribution in pavements, a dominant factor controlling thermal crack development, has not been directly investigated in those models. To analyze the elastic fields of pavements, finite element method has been widely used to calculate the local stress and strain [(112) - (114)]. Since the quality of numerical simulations depends on the quality of meshing (e.g. discretization aspects), it is not straightforward to extend the results to general cases. Thus, analytical solutions are a valuable tool for researchers for model verification, and ultimately, to gain a better insight into mechanical responses and damage mechanisms in pavements.

One-dimensional (1D) models [(108), (115), (116)] have been developed to predict tensile stress distribution in a pavement with frictional constraint. The frictional force from the substrate is balanced by a uniform tensile stress along the thickness of the overlay. Because the friction forces are driven from the bottom of the pavement, considerable shear stress will be induced along the bottom of the overlay but vanishes along the free surface. Since a 1D model can neither solve the shear stress distribution in the overlay nor consider the temperature field along the thickness, a two-dimensional (2D) model is necessary to accurately describe the thermal stress distribution.

Beuth (117) presented solutions for fully and partially cracked film problems for elastic films bonded to elastic substrates with one crack and showed that when an overlay is fully bonded to a rigid substrate, the crack tips will stop within the overlay. Hong et al. (118) developed a model to predict the crack spacing and crack depth in highway pavements assuming that the effect of a crack in the overlay could be described by an increase in effective compliance. Xia and Hutchinson (119) and Shenoy et al. (120), respectively, investigated the crack patterns in the overlay and proposed an elastic solution in the integral form using dislocations as the kernel functions.

Due to the diversity of pavement design and construction procedure, thermal cracking may develop within asphalt pavement in various forms, which depend on the corresponding loading conditions and boundary conditions.

Figure 8.1. Observation of an asphalt overlay bonded to a base-layer with uniformly distributed cracks due to low temperature loading

General Solution

Consider a long asphalt pavement (width w , thickness h , Young's modulus E, Poisson's ratio v, thermal expansion coefficient α) resting upon a base-layer (see Figure 8.1). With a drop in ambient temperature, the asphalt overlay is subjected to a larger contractive deformation than that in the base-layer. When the thermal stress reaches a certain value, uniformly spaced thermal cracks may initiate to release the high thermal stress. Because the width of pavements is much larger than the depth, the stress distribution changing in the width direction is small. Based on the periodic boundary condition, we can use two-dimensional stress/strain distributions in one section between two neighboring cracks to represent the mechanical fields in the overall pavement.

Because the pavement is assumed to be fully bonded with the base-layer, the cohesive force renders the bottom of the pavement to remain in plane (i.e., in a horizontal plane). Because the thickness of the pavement is much smaller than its length and the top surface is free, generally the top surface of the pavement remains approximately in plane during the temperature change if a negligible amount of uplift due to curling occurs. Thus, we assume that all points of a plane normal to the y direction is still in the same plane after deformation, i.e.,

$$u_y(x,y) = u_y(y). \tag{1}$$

For this two-dimensional elastic problem, the constitutive law reads

$$\sigma_x = E\left(\varepsilon_x - \bar{\alpha}T\right), \quad \tau_{xy} = \mu\gamma_{xy}, \tag{2}$$

where $\bar{\alpha}$ denotes the difference between the coefficients of thermal expansion for the asphalt overlay and the base-layer. Considering the equilibrium condition in x direction, we can write

$$Eu_{x,xx} + \mu u_{x,yy} = 0. \tag{3}$$

Using the method of separation of variables, we can find the general solution as

$$u_x(x,y) = \left(A_1 e^{cx/h} + A_2 e^{-cx/h}\right)\left[B_1 \sin(dy/h) + B_2 \cos(dy/h)\right], \quad (4)$$

where A_1, A_2, B_1 and B_2 are constants to be determined via boundary conditions, and where $d = \sqrt{E/\mu c}$.

From the symmetry of the geometry and the free upper surface, we can write

$$u_x(0,y) = 0; \quad u_{x,y}(x,h) = 0. \quad (5)$$

Using the above boundary conditions, we simplify Eq. (4) as follow:

$$u_x(x,y) = B \sinh(cx/h) \cos d(1 - y/h). \quad (6)$$

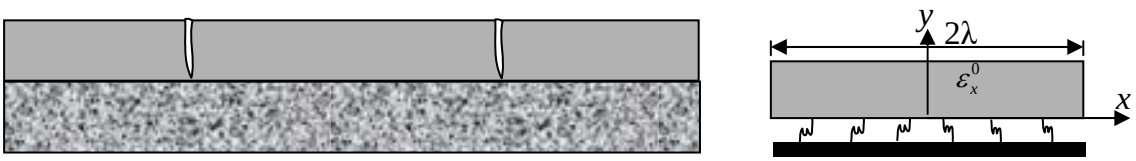

(a) (b)

Figure 8.2. An asphalt overlay resting on a granular base-layer

(a) the lateral view of the cracks, and; (b) one section between two cracks with a frictional interface

Full-Depth Cracks with Frictional Interface

Closed-Form Solution

For an asphalt layer resting upon a granular base as illustrated in Figure 8.2 (a), the constraint from the base-layer may be assumed through a frictional interface as Figure 8.2 (b). Along the bottom of the pavement, the interfacial frictional force may provide resistance to the displacement in the *x* direction such that

$$\tau_{xy}(x,0) = k u_x(x,0), \quad (7)$$

where *k* is the friction coefficient. Substituting Eq. (6) into Eq. (7), we obtain

$$d = \frac{kh}{\mu \tan(d)}; \quad c = \sqrt{\mu / E}\, d. \quad (8)$$

It is noted that d is solved numerically by recursive methods.

With a change in ambient temperature denoted as *T*, along the surface of the discontinuity, the stress σ_x should be zero. Due to the assumptions implied by Eq. (1), this boundary condition cannot be rigorously satisfied at every point. Here we set the total normal force as zero, namely

$$\int_{y=0}^{h} \sigma_x(\lambda, y)\, dy = 0. \quad (9)$$

Substituting Eq. (2) into Eq. (9) yields

$$B = \bar{\alpha} dh \frac{T}{c \sin d \cosh(c\lambda/h)}. \quad (10)$$

Thus, we obtain the explicit solution in Eq. (6) with constants d and c in Eq. (8), and B in Eq. (10).

Comparison with FEM Simulation

To verify the integrity of the proposed analytical model, comparisons are made with an FEM simulation using the software DIANA (DIsplacement ANAlyzer). Here we use typical values for HMA at low temperatures, with $E = 14.0GPa$; $v = 0.2$; $\alpha = 1.8*10^{-5}1/K$; $T_1 = -30K$; $T_2 = -25K$; $h = 0.2m$; $\lambda = 4m$. We draw the displacement distributions in the x direction at the top and the bottom of the pavement as seen in Figure 8.3. The model developed by Timm *et al.* [8] is also shown in this figure but note that it provides an identical prediction for the top and bottom of the pavement since it is a 1D model. Figure 8.3 shows that the proposed theoretical prediction is very close to FEM simulation whereas in the neighborhood of the discontinuity the FEM simulation provides a slightly lower estimate at the bottom and a higher estimate at the top. The 1D prediction provides a smaller prediction when x is small. In the neighborhood of the discontinuity, the prediction is between those at the top and bottom for either the FEM simulation or 2D theoretical prediction.

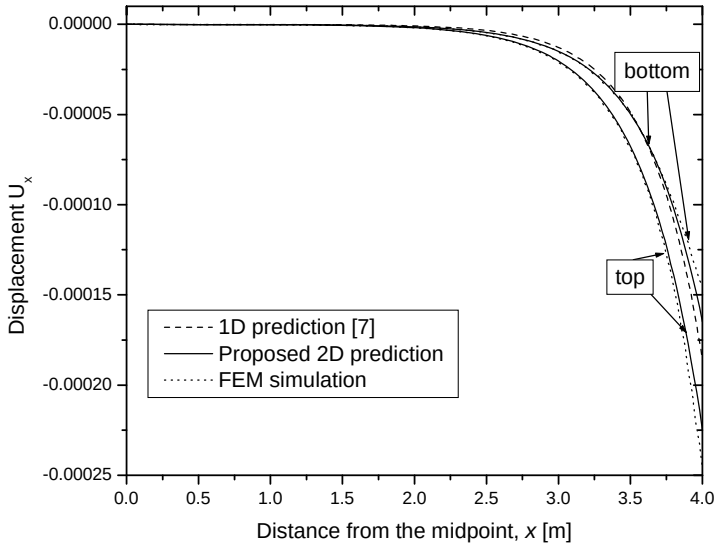

Figure 8.3. Displacement distributions along the top and bottom surface of pavement

Figure 8.4 shows the comparisons of stress distributions in the x direction at the top and the bottom of the pavement. Because three methods provide very close predictions in the range of $0 \le x \le 2.0m$ as seen in Figure 8.3, we only show the range of $2.0m \le x \le 4.0m$. In Figure 8.4(a) we can see that on the top surface the proposed 2D model produces results in good agreement with the FEM simulation for tensile stress, except at the neighborhood of the discontinuity (as expected), whereas the 1D prediction is in slightly less agreement with the FEM results. Figure 8.4(b) illustrates tensile stress and shear stress distributions along the bottom of the pavement. In the neighborhood of the discontinuity the FEM simulation presents a large change with respect to the proposed model solution due to the singularity effect. In the other range, the proposed 2D model fits well the FEM simulation for both tensile stress and shear stress. However, the 1D

prediction only provides tensile stress, which is lower than the 2D prediction and the FEM simulation.

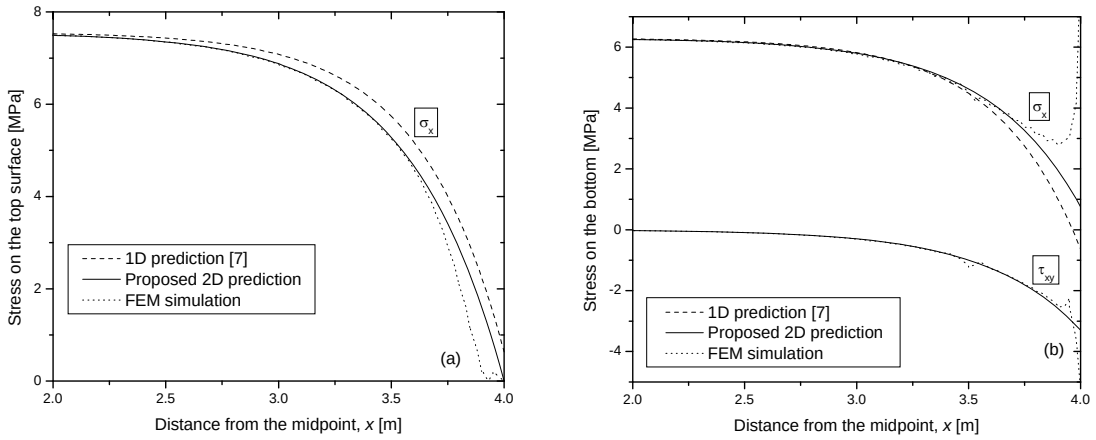

Figure 8.4. Stress distributions along (a) the top and (b) bottom surface of pavement

Application to Prediction of Crack Spacing

In Figure 8.4, the maximum tensile stress is at the midpoint of the top surface and the maximum shear stress is at the bottom at the discontinuities (existing cracks), and the maximum tensile stress is found to be higher than the maximum shear stress. Substituting Eq. (6) into Eq. (2) provides

$$\sigma_x^{\max} = E\left(\bar{\alpha} d \frac{T}{\sin(d)\cosh(c\lambda/h)} - \bar{\alpha} T \right); \quad \tau_{xy}^{\max} = \frac{\mu \bar{\alpha} d^2 T}{c} \tanh(c\lambda/h), \qquad (11)$$

where the former is positive and the latter is negative at low temperatures. With a decrease in ambient temperature, the maximum tensile stress increases. When this stress reaches the tensile strength of the pavement material, S, a new discontinuity would be initiated from the midpoint on the top surface. Then the maximum tensile stress will move to the midpoint of the new interval, and it will be much lower than the tensile strength. Thus given the geometry, material properties, and temperature distribution of a pavement, we can solve the critical discontinuity spacing λ^c, in which the maximum tensile stress is equal to the tensile strength, i.e. $\sigma_x^{\max}(\lambda^c) = S$. Thus, we can calculate the critical discontinuity spacing λ^c [(108), (121)]. Although the maximum shear stress is not as considerable as the tensile stress, when the interface between the pavement and the granular base is not strong, the shear stress may induce the debonding of the interface starting at the bottom of the discontinuities, which will cause curling of the pavement.

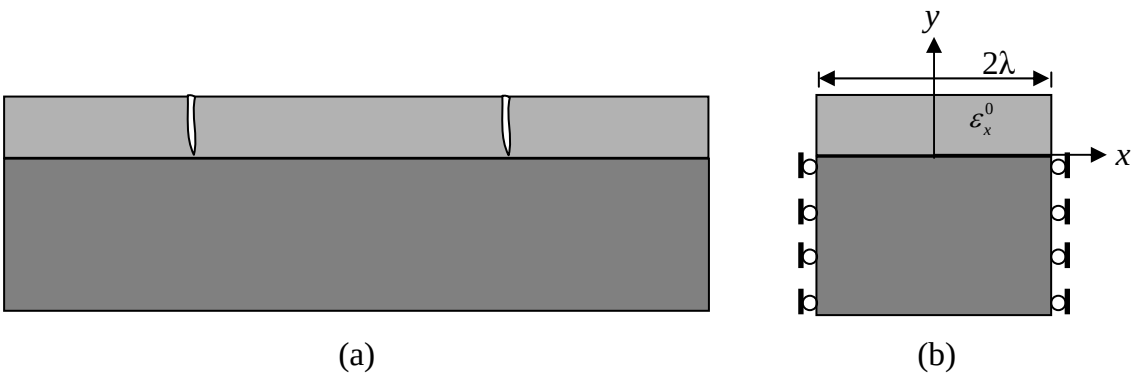

Figure 8.5. An asphalt overlay fully bonded to a thick base-layer

(a) the lateral view of the cracks, and; (b) one section between two cracks with a fully-bonded interface

Full-Depth Cracks with a Fully Bonded Interface

Consider an asphalt overlay fully bonded to a thick base-layer, as illustrated in Figure 8.5(a). Due to the temperature change, there exists a contractive mismatch thermal strain in the overlay, written as ε_x^0. Because the overlay is fully bonded to the thick base-layer, thermal stress will be induced and cracks may form when the stress is beyond the strength of the asphalt materials. To solve the stress distribution in the asphalt overlay, a 2D Cartesian coordinate system is setup with the origin at the central bottom of the section. The plane strain problem is considered.

Closed-Form Solution

The displacement field in the asphalt overlay in Figure 8.5(b) can be obtained by superposition of the following two problems: First, the asphalt overlay is subjected to both the thermal strain and an imaginary tensile stress (see Figure 8.6(b)), and the final displacement is zero. Second, the asphalt overlay is subjected to the corresponding compressive stress, but no thermal strain exists in the overlay. The displacement field can be obtained by the general displacement solution in Eq (6), in which two parameters are to be determined as B and c.

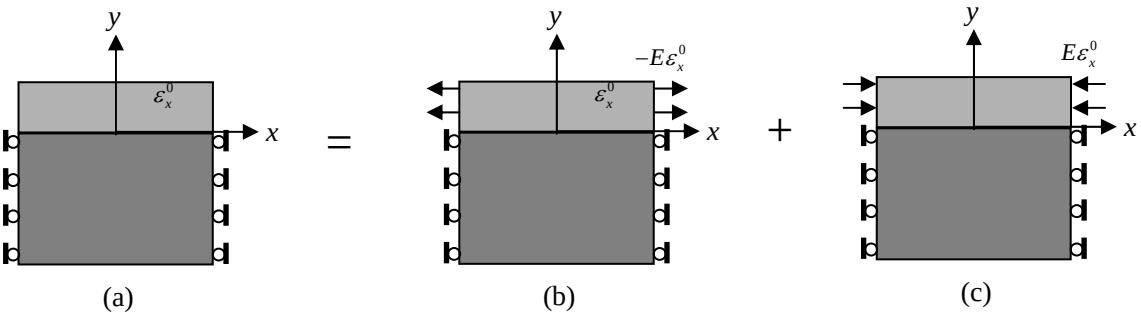

Figure 8.6. Schematic illustration for the solution of the displacement field in one section

At both ends, stress $\sigma_x = -\bar{E}_1 \varepsilon_x^0$. Due to assumptions of Eq. (1), this boundary condition cannot be rigorously satisfied at every point. However, the total normal force should be zero, namely

$$\frac{1}{h}\int_{y=0}^{h} \sigma_x(\lambda, y)\, dy = -\bar{E}_1 \varepsilon_x^0 . \tag{12}$$

The substitution of Eq (6) into Eq (2), and Eq (2) into Eq (12) yields

$$B = -\sqrt{\frac{\bar{E}_1}{\mu_1}}\, \frac{h\varepsilon_x^0}{\cosh(c\lambda/h)\sin d} . \tag{13}$$

To obtain the parameter c, Xia and Hutchinson's method (119) is used, in which comparison of the energy release rate with the exact solution provides

$$c = \frac{2}{\pi g(\alpha,\beta)}; \quad d = \sqrt{\frac{\bar{E}_1}{\mu_1}}\, c . \tag{14}$$

The detailed derivation of the above equation is given later. Here the function $g(\alpha,\beta)$ is illustrated in Figure 8.7. It depends on Dundur's parameters, α and β, namely,

$$\alpha = \frac{\bar{E}_1 - \bar{E}_0}{\bar{E}_1 + \bar{E}_0}, \quad \beta = \frac{\mu_1(1-2\nu_0) - \mu_0(1-2\nu_1)}{2\mu_1(1-\nu_0) + 2\mu_0(1-\nu_1)}, \tag{15}$$

with $\bar{E}_0 = E_0/(1-\nu_0^2)$ and $\mu_0 = E_0/[2(1-\nu_0)]$. Figure 8.7 shows the function $g(\alpha,\beta)$ for $\beta = 0$ and $\beta = \alpha/4$ [10], respectively. For convenience of the later simulation, $g(\alpha,\beta)$ is fitted by a function (see Figure 8.7) as:

$$g(\alpha,\beta) \approx \frac{1.258 - 0.40\alpha - 0.26\alpha^3 - 0.30\alpha^4}{1-\alpha} . \tag{16}$$

Figure 8.7 shows that the dependence of $g(\alpha,\beta)$ on β is weak except when α close to –1 (119). Thus, the fitted function in Eq (16) will be used to approximate $g(\alpha,\beta)$ in the following simulations.

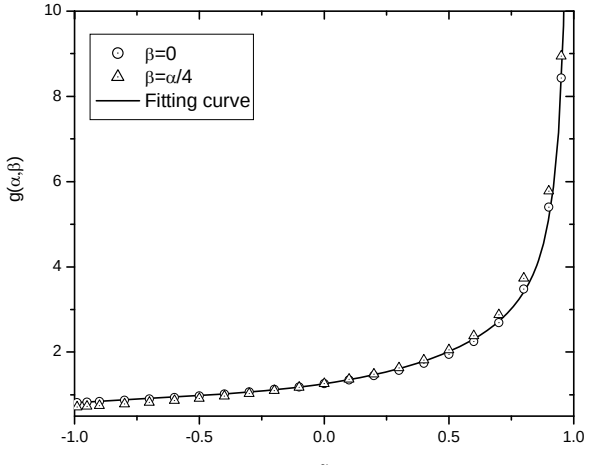

Figure 8.7. The function of $g(\alpha,\beta)$ vs. α for $\beta = 0$, $\beta = \alpha/4$ and the fitting curve

The combination of Eqs. (6), (13), and (14) provides a closed-form elastic solution for the reduced problem. Then, the total displacement and stress fields in Figure 8.1(b) read

$$u_x(x,y) = B\sinh(cx/h)\cos d(1-y/h), \qquad (17)$$

$$\sigma_x = \bar{E}_1\left(\varepsilon_x^0 + Bc/h\cosh(cx/h)\cos\left[d(1-y/h)\right]\right), \quad (18)$$

and

$$\tau_{xy} = \mu_1 Bd/h\sinh(cx/h)\sin d(1-y/h) \qquad (19)$$

with B in Eq (13), d and c in Eq (14).

Eq. (14) is derived by comparisons of the energy release rate of the crack in this solution with the exact solution provided by Beuth (117). Consider the section in Figure 8.1(b) with two discontinuities at the both ends and with a large width compared to the thickness. When the external mechanical loading in the substrate increases, a straight, steady-state channeling crack will initiate at the middle edge of the section and propagate in the $-z$ direction as seen in Figure 8.8. Far ahead of the crack front, the elastic fields are not influenced by the crack and are written in Eqs. (17)-(19). Thus the tensile stress at the symmetric plane is

$$\sigma_x(0,y) = \left(1 - \frac{d\cos\left[d(1-y/h)\right]}{\cosh(c\lambda/h)\sin d}\right)\sigma_x^0, \qquad (20)$$

with $\sigma_x^0 = \bar{E}_1\varepsilon_x^0$, and the shear stress is zero.

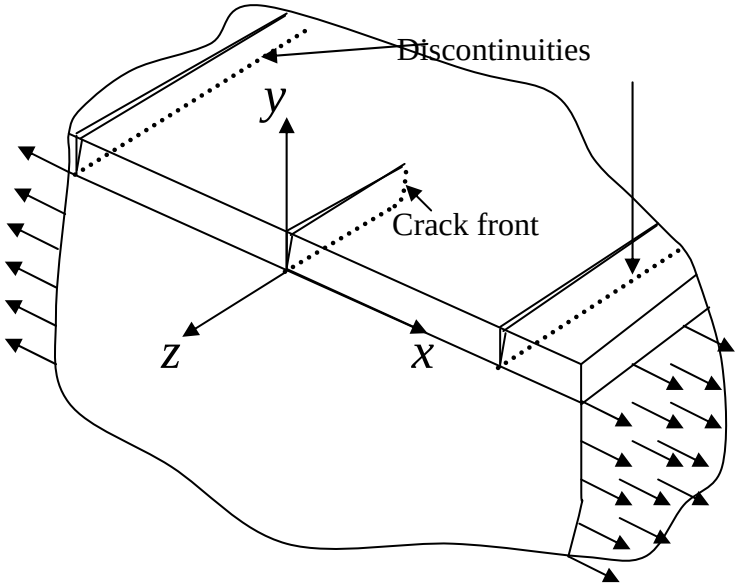

Figure 8.8. Schematic illustration of three-dimensional channeling

Far behind the crack front, the pavement is cracked into two sections, and the elastic fields in each section can also be obtained by Eq. (17) by replacing λ by $\lambda/2$ in the new local coordinate system. Then we can solve the crack opening displacement as:

$$\delta(0,y)=2\sqrt{\frac{\bar{E}_1}{\mu_1}}h\varepsilon_x^0\frac{\tanh\left(\frac{c\lambda}{2h}\right)}{\sin d}\cos\left[d\left(1-y/h\right)\right], \tag{21}$$

To recover this crack opening displacement, the stress in Eq. (20) has to be applied along the cracking surface. Thus, the energy release rate of the crack front can be obtained as the work done to close the crack opening displacement [10], namely,

$$G=\frac{1}{2h}\int_0^h\sigma_x(0,y)\delta(0,y)dy\,. \tag{22}$$

Because the free boundary condition in Eq. (12) cannot rigorously be satisfied at every point along the crack surface, we used the averaged stress along the thickness to represent the local stress. Here we also use the averaged stress in Eq. (22), such that the energy release rate can be explicitly written as

$$G=\frac{\left(\sigma_x^0\right)^2}{\bar{E}_1}\frac{h}{c}\left[2\tanh\left(\frac{c\lambda}{2h}\right)-\tanh\left(c\lambda/h\right)\right], \tag{23}$$

which provides the same form as Xia and Hutchinson's results [12] (Eq (30) of the Ref.) by setting $l=h/c$.

When the section is infinite long, i.e. $\lambda\to\infty$, Eq (22) is reduced to

$$G=\frac{\left(\sigma_x^0\right)^2 h}{\bar{E}_1 c}\,. \tag{24}$$

Beuth [10] also proposed the energy release rate averaged over the front of a semi-infinite isolated crack as

$$G=\frac{\left(\sigma_x^0\right)^2 h}{\bar{E}_1}\frac{\pi}{2}g(\alpha,\beta), \tag{25}$$

where $g(\alpha,\beta)$ can be further approximated by Eq (16) as a function of α. These two cases should be equivalent [12], so that the following is obtained

$$c=\frac{2}{\pi g(\alpha,\beta)}\,. \tag{26}$$

This equation has been used to calibrate the constants c and d as Eq (14).

Comparison with FEM Simulation

If this periodic section is extended to the total surface layer, the geometry and the loading at a crack surface is the same as the fully cracked problem of Beuth (1992) except that the former considers the periodically distributed discontinuities but the latter considers only a single crack. From Eqs. (6) and (13), we can solve the work done by the external loading as

$$W=\frac{\left(\sigma_x^0\right)^2}{\bar{E}_1 c}h^2\tanh\left(c\lambda/h\right). \tag{27}$$

To verify the integrity of the proposed analytical model, comparisons are made with the FEM simulation by ABAQUS. Two kinds of interfaces are considered. First, for a frictional interface, if the spring coefficient k is given, it is not necessary to consider the substrate. Due to the symmetry of the problem, only half of the section is modeled by 240×40 four-node quadrilateral elements with equal size under plane strain. Secondly, for a layer fully bonded to a substrate, we have to model both the layer and the substrate. Because a singular point exists at the edge of the interface, the FEM mesh shown in Figure 8.9 includes refined elements in the vicinity of that point. The *x*-directional displacement along the symmetric plane and the end of the substrate is constrained, which is consistent with Figure 8.1(d). Here the thickness of the substrate is 20 times as that of the surface layer, and 11260 four-node quadrilateral elements are used. To simulate the different length of the section, affine transformation of the mesh in the *x*-direction is used.

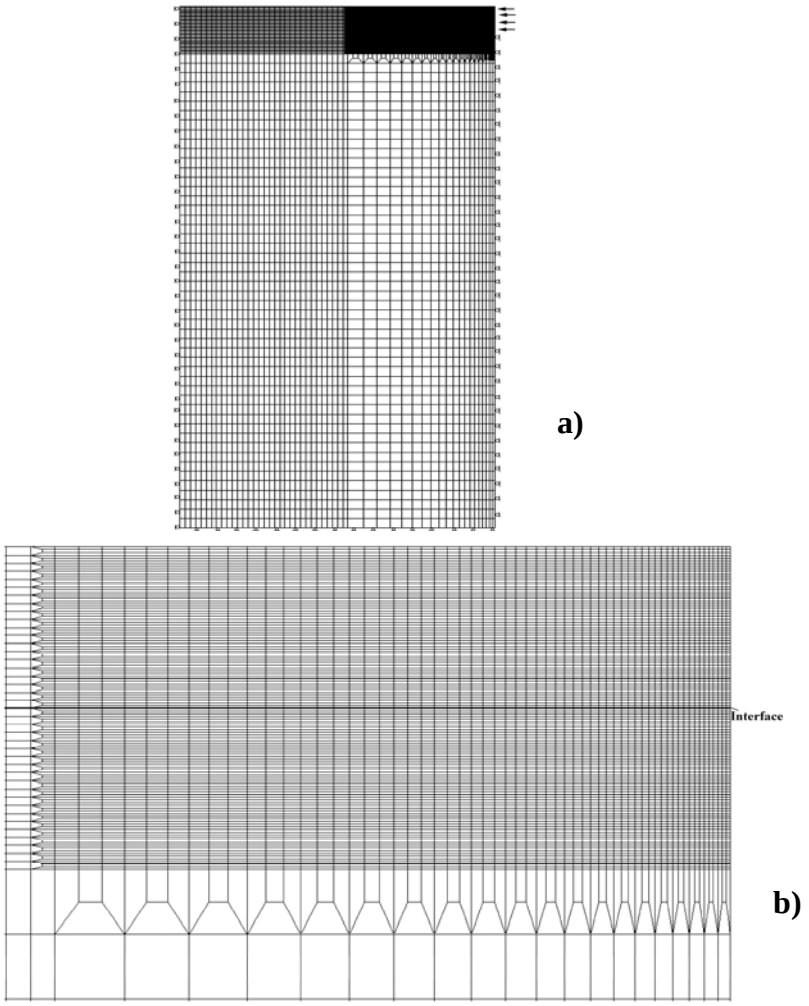

Figure 8.9. Finite element mesh used to model half of the geometry of the reduced problem

(a) Total mesh and (b) refined mesh at the vicinity of the singular point

Figure 8.10 shows the external work calculated by Eq (27) with comparisons to FEM simulations for two kinds of interfaces: a frictional interface and a fully bonded interface. With the increase of spring coefficient k or the Young's modulus of the substrate E_0, the external work reduces and is finally convergent to a constant. When the interface or substrate is stiff,

namely, $k > 0.25$ or $E_0 / E_1 > 1$, the cases of $\lambda = 12$ and $\lambda = 6$ provide the same result. Thus, the edge effect can be disregarded. However, when the interface or substrate is compliant, the case of $\lambda = 6$ gives a considerably lower result than that of $\lambda = 12$.

Comparing the theoretical predictions with the FEM results, we find that the proposed model is in excellent agreement with the numerical simulations for the frictional interface in Figure 8.10(a); whereas it provides a higher prediction for the fully bonded interface in the range of $E_0 / E_1 < 1$ in Figure 8.10(b). The reason for this difference is that the FEM simulation in Fig 10(b) constrains the *x*-directional displacement at the ends of the interface whereas the proposed model permits this deformation. In Figure 8.12(b), we can clearly observe this difference: the displacement along the bottom of the surface layer is zero at $x / \lambda = 1$ for the FEM results but it reaches the highest for the proposed model. In the extreme case, when $E_0 / E_1 \to 0$, the boundary condition for FEM simulation is reduced to a beam under uniform compression with the bottom constrained at both ends; whereas the proposed model is reduced to uniaxial compression of the beam. If the length of the section is permitted to be infinitely large, the half model of the current problem is the same as Beuth's problem. The external work for unit depth of the thickness in Eq. (27) is the same as Beuth's exact solution, which guarantees the accuracy of the proposed model for a surface layer with large crack spacing.

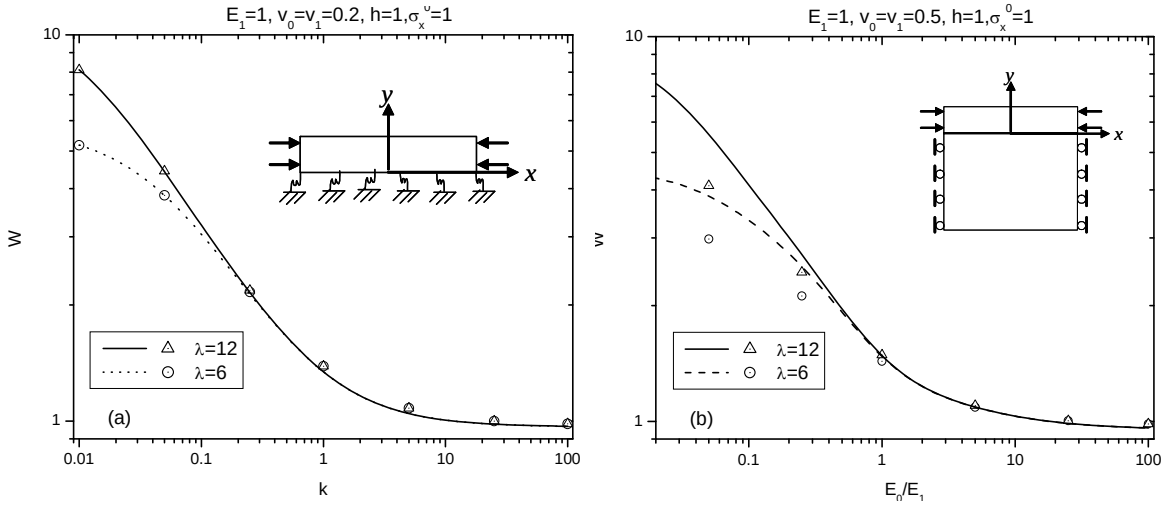

Figure 8.10. The work done by the force along the ends of the surface layer with two kinds of interfaces

(a) a frictional interface with the varying spring coefficient and (b) a fully bonded interface with the varying Young's modulus of the substrate. Curves denote the theoretical predications; symbols the FEM results.

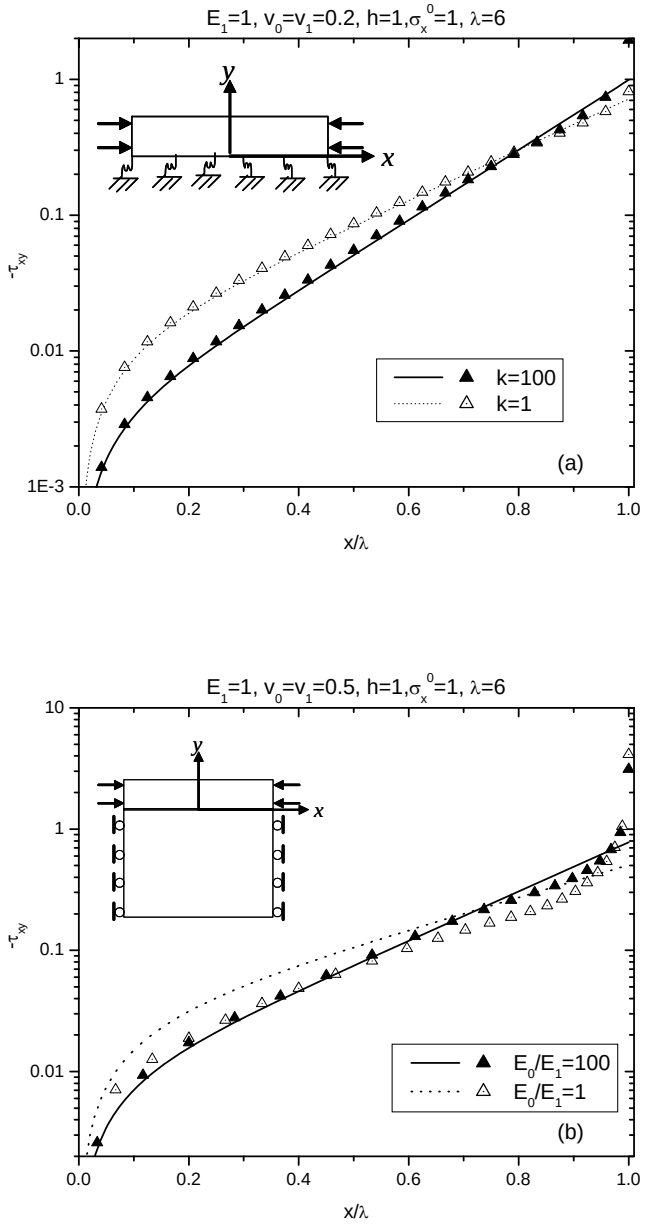

Figure 8.11. Interfacial shear stress distribution for two kinds of interfaces

(a) a frictional interface with the spring coefficient $k = 1$ and 100 and (b) a fully bonded interface with the Young's modulus of the substrate $E_0 = E_1$ and $100E_1$. Curves denote the theoretical predications; symbols the FEM results.

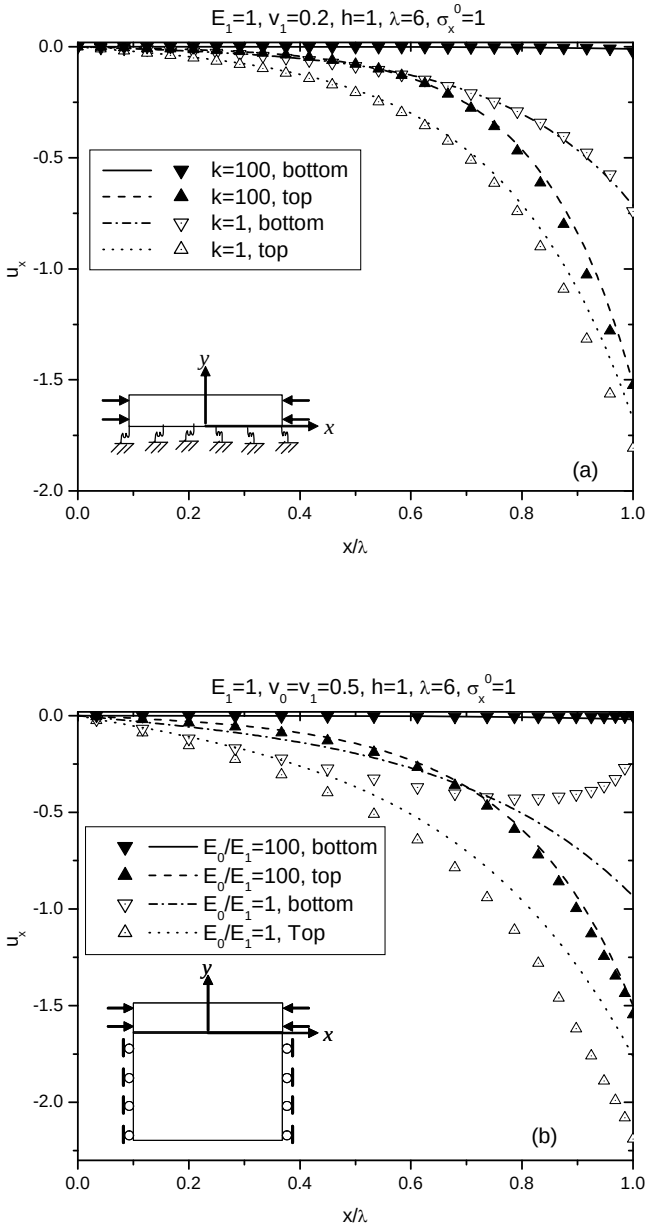

Figure 8.12. Displacement field along the top and bottom of the surface layer for two kinds of interfaces

(a) a frictional interface with the spring coefficient $k = 1$ and 100 and (b) a fully bonded interface with the Young's modulus of the substrate $E_0 = E_1$ and $100E_1$. Curves denote the theoretical predications; symbols the FEM results.

Figure 8.11 illustrates the interfacial shear stress distribution for two kinds of interfaces. In Figure 8.11(a) we can find that the theoretical solution agrees well with the FEM results even near the end of the surface layer for a frictional interface. However, for the fully bonded interface

in Figure 8.11(b), due to the singularity effect at the end of the surface layer, the FEM provides a higher result in the neighborhood of the singular point. In the other range, the two methods give comparable predictions, especially for $E_0/E_1=100$. In the vicinity of the singular point, our assumption in Eq. (1) can not be rigorously satisfied, which also leads to the approximate boundary condition in Eq (12). Thus, the accuracy of this analytical solution cannot be guaranteed in this region.

The displacement distributions of u_x along the top and bottom of the surface layer are shown in Figure 8.12. It is seen that, the stiffer the interface or substrate, the smaller the displacement field. The displacement field along the bottom of the surface layer is always smaller than that along the top due to the constraint of the interface. In Figure 8.12(a), the displacement monotonically changes with x along both the bottom and the top of the film; whereas for the FEM simulations in Figure 8.12(b) the displacement along the bottom of the film reaches the maximum in between and then decreases to zero at the end due to the rigid boundary condition. The proposed model is in good agreement with the FEM results in Figure 8.12(a) except for the case of $E_0/E_1=1$ in Figure 8.12(b) because the boundary conditions for the FEM simulations and analytical derivation are different.

Essentially, the proposed model is based on the assumption of the frictional interface. To accurately simulate the fully bonded interface, we followed Xia and Hutchinson's [12] method to make the energy release rate for both kinds of interfaces equivalent in Eqs. (24) and (25). Thus, this model provides a good prediction in terms of total strain energy or external work for the fully bonded interface, but it does not accurately predict the local elastic field especially in the vicinity of the singular point. However, in an average sense, the proposed model produces a good estimate of the local solution for the fully bonded interface, besides that it gives a very accurate solution for the general frictional interface.

Application to Fracture Analysis

The interfacial shear stress distribution is very important for evaluation of the interfacial shear strength [14, 15]. Combining Eqs. (13) and (19), we obtain an explicit solution of the interfacial shear stress as

$$\tau_{xy}=-c\sigma_x^0\frac{\sinh\left(cx/h\right)}{\cosh\left(c\lambda/h\right)}, \qquad (28)$$

from which we can solve the interfacial shear stress for both the frictional interface and the fully bonded interface with c defined by Eqs (8) and (14), respectively. Obviously, it is different from Agrwal and Raj's assumption (121) where they used a sine wave function to approximate the interfacial shear stress. In Figure 8.13, we see that at the singular point $\left(x/\lambda=1\right)$, the shear stress is almost same for each the ratio of h/λ because the thickness h is typically much smaller than the crack spacing and then $\tanh\left(c\lambda/h\right)$ is convergent to 1. The shear stress exponentially decrease from the singular point and is finally reduced to zero at the symmetric point. The smaller the ratio of h/λ, the higher the decreasing speed. Thus, for a very thin surface layer, the interfacial shear stress is only concentrated in the neighborhood of the singular point. When the shear strength along the interface is given, comparing the maximum shear stress and the shear strength, we can evaluate the propensity of the interfacial debonding.

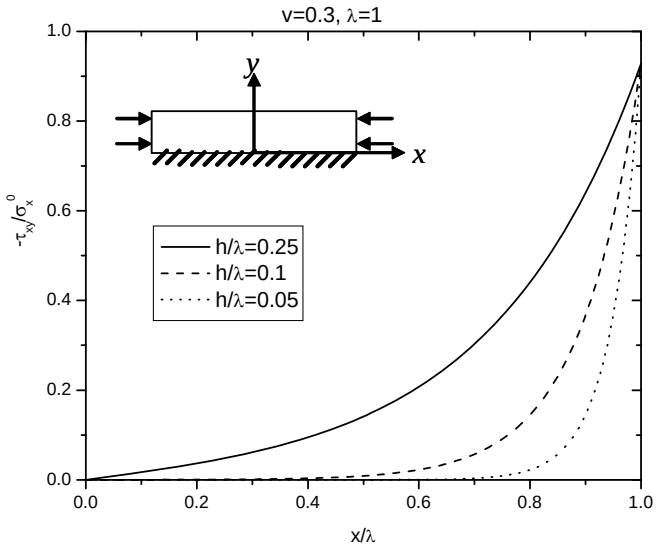

Figure 8.13. Interfacial shear stress distribution for the thin film fully bonded to a rigid substrate with the thickness $h/\lambda = 0.25,\ 0.1$, and 0.05**.**

In Eq (14), we find that c or d only depends on the material constants for a fully bonded film/substrate system. The interface can be simulated by a frictional interface with the equivalent spring coefficient denoted by Eq (8), i.e.,

$$k = \mu_1 d \tan d / h . \qquad (29)$$

Obviously, the frictional spring coefficient of the interface will increase along with the decrease of the thickness of the surface layer because μ_1 and d are material constants. Thus, the thinner the surface layer, the stronger the interface restraint for the fully bonded surface layer/substrate system. Xia and Hutchinson [12] employed 1D solution to simulate the fully bonded interface and also obtained the equivalent spring coefficient (Eq. (12) of reference [12]) as

$$k = \mu_1 d^2 / h . \quad (30)$$

Figure 8.14 illustrates the results of Eqs. (29) and (30) . When $E_0 / E_1 < 1$, two methods provide very close predictions. However, when $E_0 / E_1 > 1$, the proposed method gives a much higher prediction than Xia and Hutchinson's method. We know that for a surface layer bonded to a rigid substrate, i.e. $E_0 / E_1 \to \infty$, the spring coefficient will be infinitely large. Obviously, Xia and Hutchinson's method cannot predict this tendency, whereas the proposed method provides a very good explanation.

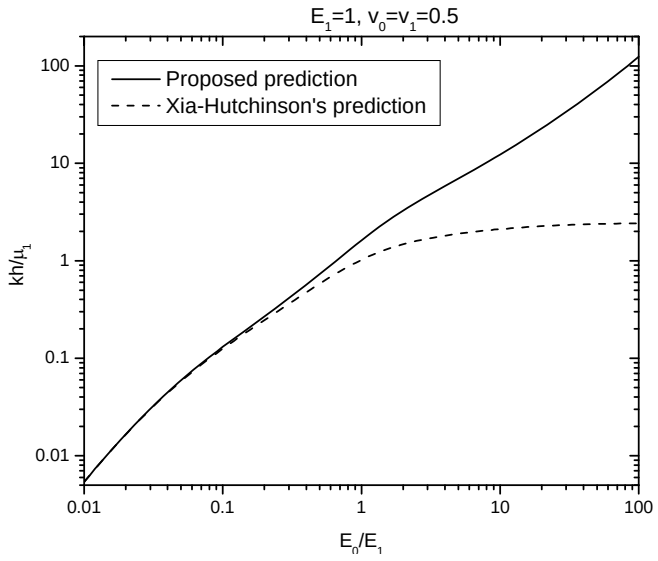

Figure 8.14. Equivalent spring coefficients for a fully bonded interface with the different Young's moduli of the substrate.

Partial-Depth Cracks with a Rigid Base Layer

Consider an asphalt overlay bonded to a rigid base-layer, which is subjected to an ambient temperature change *T*, as illustrated in Figure 8.15 (a). Because the overlay and the base-layer have different thermal expansion coefficients, a residual stress is induced in the overlay as:

$$\sigma_0 = -\frac{E}{1-\nu}\bar{\alpha}T\,. \tag{31}$$

Here the plane strain condition is considered for the overlay subjected to isotropic thermal strain. In this paper, we only consider the tensile stress, i.e. $\sigma_0 > 0$. The thermal strain of the substrate can be simply disregarded by treating it as a perfectly rigid body. With the increase of σ_0, uniformly spaced discontinuities with spacing of 2λ will form in the overlay and the stress will be redistributed. For a compliant overlay on a rigid substrate, the crack tips stop within the overlay (117). Here the length of the discontinuities is denoted as a. Using the periodic boundary condition, we assume that each section between two discontinuities has the same elastic fields. Considering the marked section, we set up the coordinates with the origin at the center of the bottom of the overlay as seen in Figure 8.1(a).

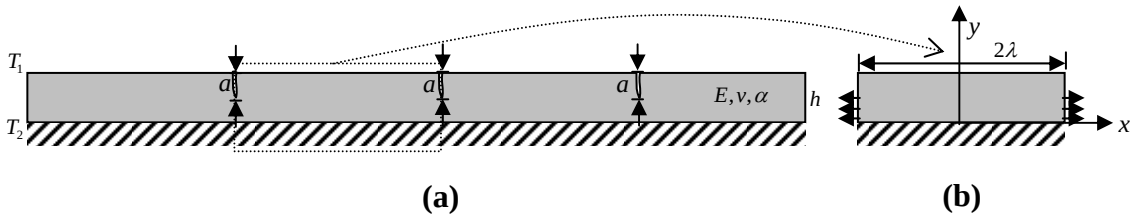

Figure 8.15. An asphalt overlay bonded to a rigid base-layer: (a) the lateral view of the cracks; and (b) the marked section between two cracks.

Series-Form Solution

Because the bottom of the asphalt overlay is fully bonded to the base-layer which is rigid, along the bottom of the overlay, the displacement should be fixed, i.e.,

$$u_x(x,0)=0, \tag{32}$$

Substituting the general solution Eq (6) into Eq (32) yields

$$d_i = i\pi - \frac{\pi}{2}; \quad c_i = \sqrt{\mu/\bar{E}}\, d_i, \tag{33}$$

with $i=1,2,\cdots$. Then, we write the displacement field as

$$u_x(x,y)=\sum_{i=1}^{N} B_i \sinh(c_i x/h)\cos\left[d_i(1-y/h)\right], \tag{34}$$

Here N can be a large number, whose value depends on the convergence of the solution, which will be discussed later; and $B_i\ (i=1,2,\cdots,N)$ is the displacement component corresponding to the basis function. Considering the boundary condition of the end, we know that the tensile stress above the discontinuity tip is zero due to the free surface and the displacement field under the discontinuity tip is zero due to the symmetric boundary condition. Thus, we write

$$\sum_{i=1}^{N} B_i c_i \cosh(c_i\lambda/h)\cos\left[d_i(1-y/h)\right]+\frac{h\sigma_0}{\bar{E}}=0, \text{ for } h-a\le y\le h \tag{35}$$

and

$$\sum_{i=1}^{N} B_i \sinh(c_i\lambda/h)\cos\left[d_i(1-y/h)\right]=0, \text{ for } 0\le y<h-a. \tag{36}$$

This boundary condition cannot be rigorously satisfied at every point by a selection of a finite number of functions in Eq. (34). Here we define a piecewise function to describe the error as

$$e(y)=\begin{cases}\displaystyle\sum_{i=1}^{N} B_i c_i \cosh(c_i\lambda/h)\cos\left[d_i(1-y/h)\right]+\frac{h\sigma_0}{\bar{E}} & h-a\le y\le h\\ \displaystyle\sum_{i=1}^{N} B_i \sinh(c_i\lambda/h)\cos\left[d_i(1-y/h)\right] & 0\le y<h-a\end{cases}. \tag{37}$$

Since there are N unknowns as B_i, we use N weight functions to establish weighted residual equations posed as follows:

$$\int_0^h e(y)\cos\left[d_i(1-y/h)\right]dy=0, \quad i=1,2,\cdots,N. \tag{38}$$

From the above N equations, we can solve for B_i. Substitution of Eq (37) into Eq (38) provides

$$A_{ij}B_j = f_i, \tag{39}$$

where

$$f_i=-\int_{h-a}^{h}\frac{h\sigma_0}{\bar{E}}\cos\left[d_i(1-y/h)\right]dy=-\frac{h^2\sigma_0}{\bar{E}d_i}\sin\frac{d_i a}{h}, \tag{40}$$

and

$$A_{ij}=\int_{h-a}^{h} c_j\cosh\left(c_j\lambda/h\right)\cos\left[d_j\left(1-y/h\right)\right]\cos\left[d_i\left(1-y/h\right)\right]dy \\ +\int_{0}^{h-a}\sinh\left(c_j\lambda/h\right)\cos\left[d_j\left(1-y/h\right)\right]\cos\left[d_i\left(1-y/h\right)\right]dy \quad . \tag{41}$$

For $i\neq j$, we have

$$A_{ij}=\frac{1}{2}\left[\frac{h}{d_i-d_j}\sin\frac{\left(d_i-d_j\right)a}{h}+\frac{h}{d_i+d_j}\sin\frac{\left(d_i+d_j\right)a}{h}\right]\left[c_j\cosh\left(\frac{c_j\lambda}{h}\right)-\sinh\left(\frac{c_j\lambda}{h}\right)\right],$$

and for $i=j$, we have

$$A_{ij}=\frac{ac_j}{2}\cosh\left(\frac{c_j\lambda}{h}\right)+\frac{h-a}{2}\sinh\left(\frac{c_j\lambda}{h}\right)+\frac{h}{4d_i}\sin\frac{2d_ia}{h}\left[c_j\cosh\left(\frac{c_j\lambda}{h}\right)-\sinh\left(\frac{c_j\lambda}{h}\right)\right].$$

From Eq (39), B_i can be solved, and then the displacement field in Eq (34) can be obtained, from which the stress fields can easily be derived as

$$\sigma_x=\sum_{i=1}^{N}\frac{\bar{E}B_ic_i}{h}\cosh\left(c_ix/h\right)\cos\left[d_i\left(1-y/h\right)\right]+\sigma_0\,, \tag{42}$$

and

$$\tau_{xy}=\sum_{i=1}^{N}\mu\frac{B_id_i}{h}\sinh\left(c_ix/h\right)\sin\left[d_i\left(1-y/h\right)\right]. \tag{43}$$

Because the error function in Eq (37) is piecewise, and the assumption of Eqs. (1) is used, the series form solution with a limited number of basis functions in Eq (34) may not approach the exact solution, the convergence and accuracy of the solution are explored in the following section.

Calibration of the Crack Opening Displacement

To show the convergence of the proposed solution, we investigate the displacement field changing with the discontinuity spacing and discontinuity depth when using a finite number of functions in Eq. (34). In the numerical simulations, $v=0.2$ and $h=1$ are used. Figure 8.16 shows the displacement field distribution along the cracked end for $\lambda/h=4.0$. In Figure 8.16(a), the overlay is fully cracked. Notice that, when $N=3$, the results are very close to those for $N=10$, which indicates that the solution converges very fast. However, for a partial-depth crack with $a/h=0.4$, Figure 8.16 (b) shows that the solution converges more slowly. When N is large, the displacement under the crack tip will be convergent to zero, but the rate of convergence is slow. As a minimal requirement, we suggest $N>h/\left(2a\right)+1$ so that the piecewise boundary condition along the cracked end will be minimally embodied. For instance, in the case of the example shown in Figure 8.16(b)

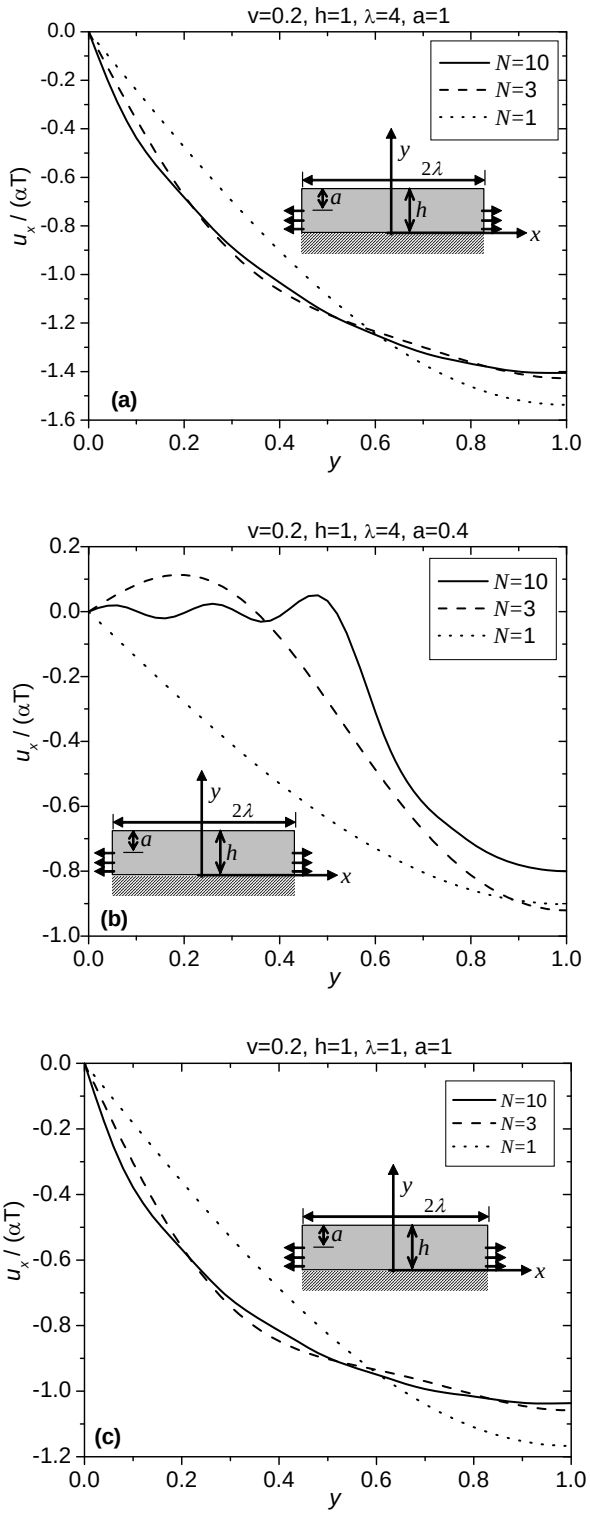

Figure 8.16. Convergence of the solution due to the crack depth and the crack spacing:

(a) $a = h; \lambda = 4h$; (b) $a = 0.4h; \lambda = 4h$; and (c) $a = h; \lambda = h$.

The curve for $N=1$ $(N<3)$, which is a monotonic decreasing function, can not illustrate the piecewise boundary condition with a connection point at $y=0.6$. Figure 8.16(c) shows the displacement field distribution along the fully cracked end for a smaller crack spacing $(\lambda/h=1.0)$. It can be observed that the convergence rate is somewhat slower than that for $\lambda/h=4.0$ in Figure 8.16(a) but the difference is relatively small. Thus, the crack spacing only has a minor effect on the rate of convergence.

Figure 8.17 illustrates the convergence of the solution along the boundary condition. The results for normalized discontinuity depths $a/h=1,\ 0.6,$ and 0.2 are presented. A large number of functions are used as $N=80$. In Figure 8.17(a), the displacement field under the discontinuity tip is apparently zero but that above the discontinuity tip is negative; whereas, in Figure 8.17(b), the stress along the cracked surface is zero but that under the discontinuity tip is tensile as predicted. In addition, in Figure 8.17(b), it can be observed that the stress is very high in the neighborhood of the discontinuity tip due to the singularity at the discontinuity tip. However, a nonphysical fluctuation of the stress under the discontinuity tip is also seen in Figure 8.17(b). The reason is that assumption in Eq. (1) cannot be exactly satisfied, and thus the stress distribution cannot be exactly approached by the set of the basis functions in Eq. (34). To calibrate this model, we construct a multiplier k on all the displacement components B_i by normalizing the crack opening displacement (COD) on the overlay surface. Then the actual displacement components are written as

$$\bar{B}_i = kB_i\,. \tag{44}$$

From Eq. (34), we can write COD as

$$\delta(a) = \sum_{i=1}^{N} 2kB_i \sinh\left(c_i\lambda/h\right). \tag{45}$$

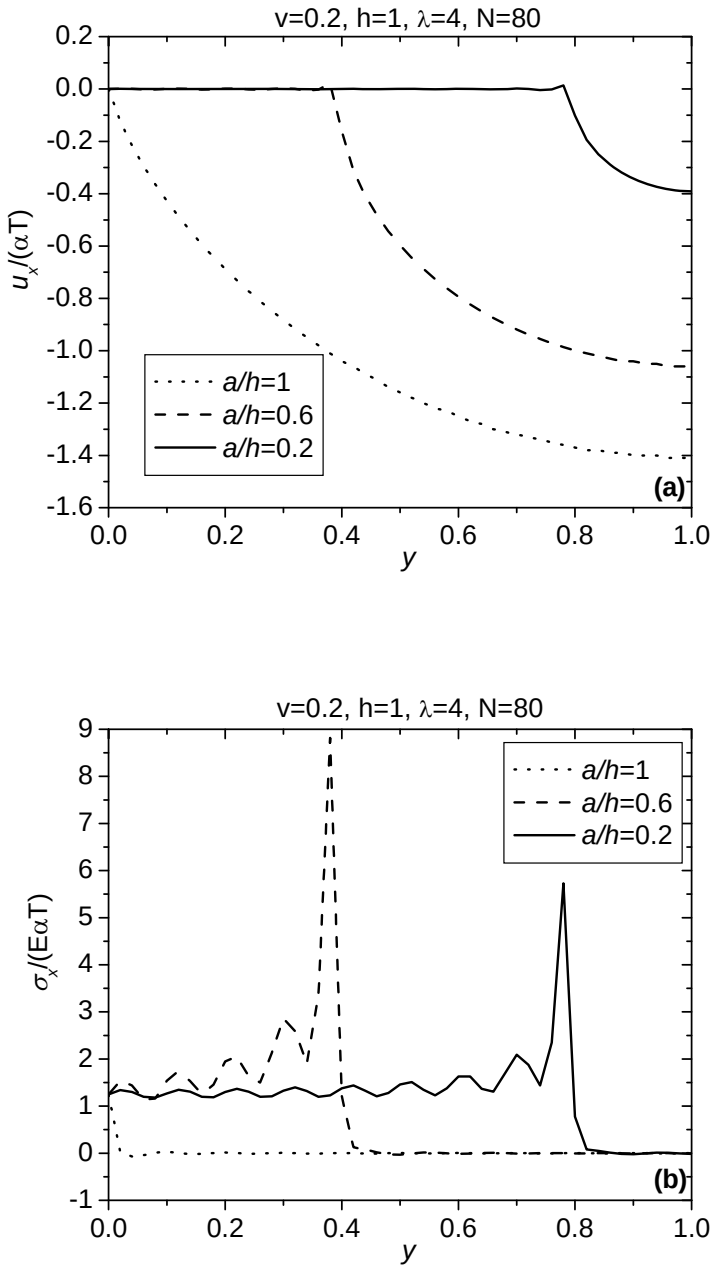

Figure 8.17. Elastic fields along the cracked end

(a) Displacement field; and (b) stress field.

Shenoy et al. [13] showed that when the crack spacing is larger than 5 times of the thickness of the overlay, i.e. $\lambda / h > 2.5$, the effect of the crack spacing on COD can be disregarded. Fitting the curve for $\alpha = -0.99$ and $\lambda / h > 2.5$ given by Shenoy et al. [13], we obtain the COD as,

$$\delta(a) = 0.2456\left(\frac{a}{h}\right)\left(\frac{a}{h} - 2.574\right)\left(\frac{a}{h} - 9.777\right)\frac{h\sigma_0}{\bar{E}}. \tag{46}$$

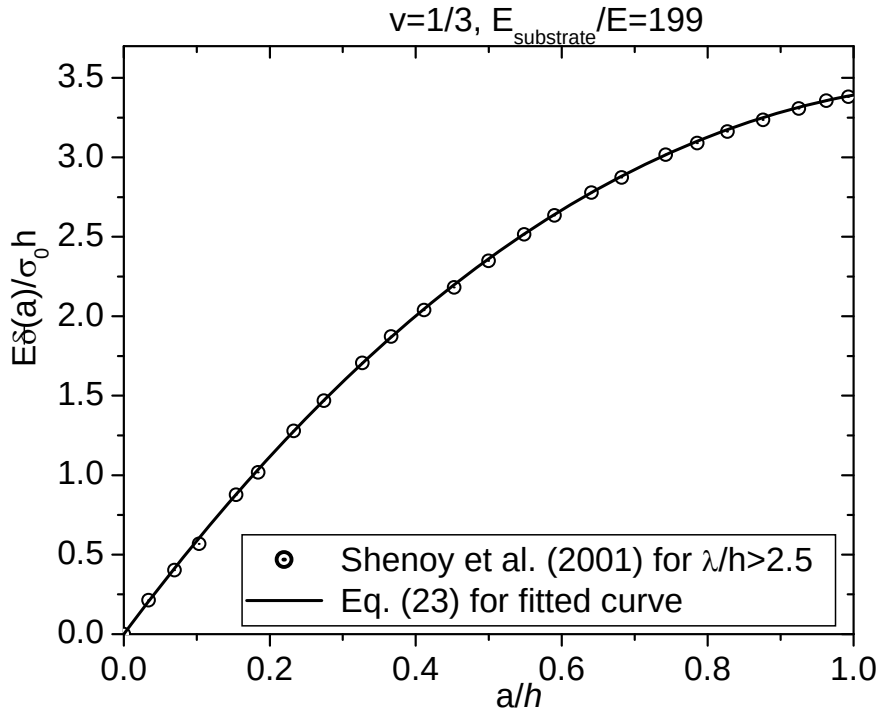

Figure 8.18. Normalized crack opening displacement on the overlay surface as a function of crack depth a/h.

Figure 8.18 illustrates the comparisons of the fitted function with the data presented by Shenoy et al. (120). It is noted that the above equation is approximately obtained for $\nu = 1/3$ and $E_{substrate}/E = 199$. Obviously, the substrate is so stiff as compared with the overlay that it can be assumed as a rigid substrate. Beuth (117) and Xia and Hutchinson (119) showed that the Poisson's ratio only has a minor effect and can be disregarded. Comparing Eq. (45) with Eq. (46), we obtain

$$k = -0.1228\left(\frac{a}{h}\right)\left(\frac{a}{h}-2.574\right)\left(\frac{a}{h}-9.777\right)\frac{h\sigma_0}{\bar{E}\sum_{i=1}^{N} B_i \sinh\left(c_i \lambda / h\right)}. \tag{47}$$

Substituting Eqs. (44) into (34), we can find that the calibrated solution not only satisfies the displacement boundary condition under the discontinuity tip as zero but also provides an accurate displacement for COD. Thus, this calibrated solution will give a good prediction of the displacement field. However, a constant stress along the cracked free surface is produced due to this calibration.

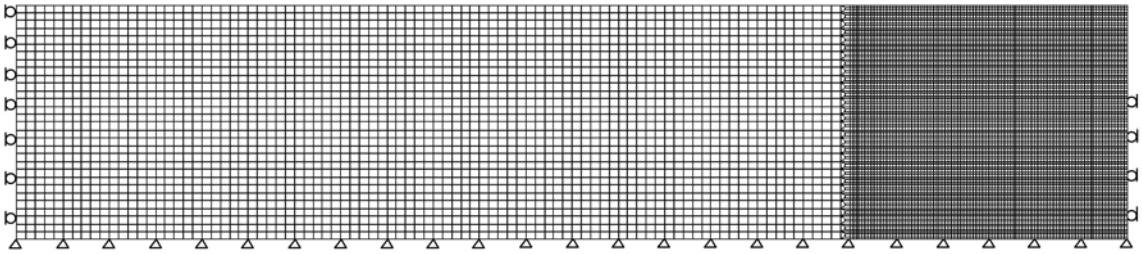

Figure 8.19. Finite element mesh used to model half of the section between two cracks.

The bottom is fixed, x-directional displacements along two ends are constrained except for the cracked free surface.

Comparison with FEM Simulation

To verify the proposed model, comparisons are made with the finite element method (FEM) simulations by ABAQUS. Due to the symmetry of the problem, only half of the section is modeled by 10890 four-node quadrilateral elements under plane strain condition. The mesh and the boundary condition are shown in Figure 8.19. In the numerical simulation, the following parameters are used: $v = 0.2$; $h = 1$; and $\lambda = 4$.

Because most thermal cracks initiate at the surface, Figure 8.20 shows the comparisons of the proposed prediction with the FEM simulations for elastic fields along the surface of the overlay for different crack depths. The following features can be observed:

In Figure 8.20(a), the displacement field is zero at the symmetric point, decreases along with x, and reaches the minimum at the cracked end. The proposed model is in good agreement with the FEM results.

For the full crack with $a/h = 1$ in Figure 8.20(b), the stress on the surface of the overlay monotonically decreases along with x and reaches the minimum with negative values at the cracked end. The proposed model provides good agreement with the FEM results.

For the partial-depth crack with $a/h = 0.6$ or 0.2 in Figure 8.20(b), the proposed predictions of the tensile stress along the surface still monotonically decrease with *x*; whereas the FEM results reach a minimum at a peak point and then increase to zero at the end. The proposed model cannot capture the non-monotonic tendency in the neighborhood of the end, but the results still fit well with the FEM results in areas of interest away from the existing discontinuities.

In the neighborhood of the crack tip, because no basis function in Eq. (34) can reflect the inflection point of the stress distribution, it is impossible to find a solution from the set of basis functions, which both satisfies the stress boundary condition and provides a good prediction for the displacement field. Using the calibration in Eq. (44),

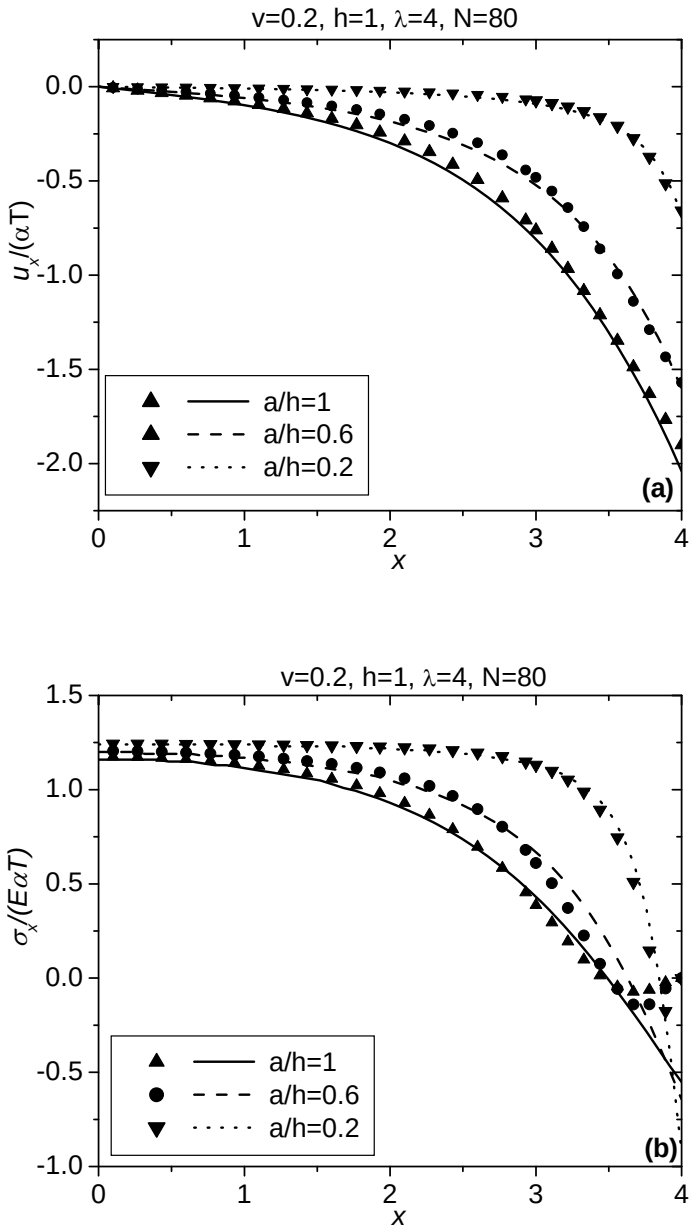

Figure 8.20. Comparisons of elastic fields along the top of the overlay.

(a) Displacement field; (b) stress field. Symbols denote the FEM results; curves the theoretical predictions

we obtain a good agreement with FEM results for the displacement field but the stress-free boundary condition is not exactly satisfied at the cracked end. Instead, for case where response away from the free end is needed, i.e., for determining crack spacing, this method works very well. However, for case where stress distribution close to the discontinuity is desired, this solution is not recommended.

Application to Fracture Analysis

With the increase of the thermal loading, a crack will initiate at a flaw on the surface of the overlay and propagate in two modes: the top-down plane strain cracking toward the interface and the 3-D channeling across the overlay as seen in Figure 8.21(a) and Figure 8.21(b), respectively. For plane strain cracking, using Eqs. (34), (42), and (43) with the calibrated displacement components in Eq. (44), we can solve the elastic fields in the section of the overlay. Considering the periodic distribution of the elastic fields in Figure 8.15(a), we can expand the solution of the section to all other sections, and then calculate the path-independent J-integral along a counter-clockwise contour line. For instance, we compute it along a line with four segments as seen in Figure 8.21(a): $S_1 : y = 0$ and x is from 0 to 2λ; $S_2 : x = 2\lambda$ and y is from 0 to h; $S_3 : y = h$ and x is from 2λ to 0; and $S_4 : x = 0$ and y is from h to 0. Thus, we can calculate the energy release rate for top-down plane strain cracking. For 3-D channeling, the energy release rate can be calculated as the work done to close the crack opening displacement for unit length of the channeling advance. Given a crack depth, if σ_x^0 is applied along the crack surface, it will be closed. Therefore, we can calculate the energy release rate [10] as

$$G = \frac{\sigma_x^0}{2a}\int_{h-a}^{h} \delta(y)\,dy = -\frac{\sigma_x^0}{a}\sum_{i=1}^{N}\frac{B_i h}{d_i}\sinh\left(c_i\lambda/h\right)\sin\left(d_i a/h\right) \quad (48)$$

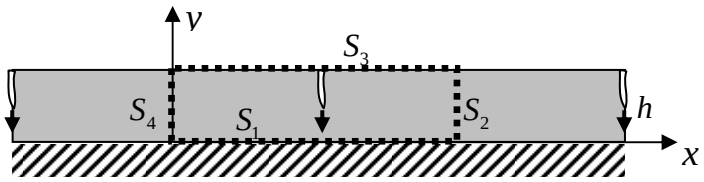

(a)

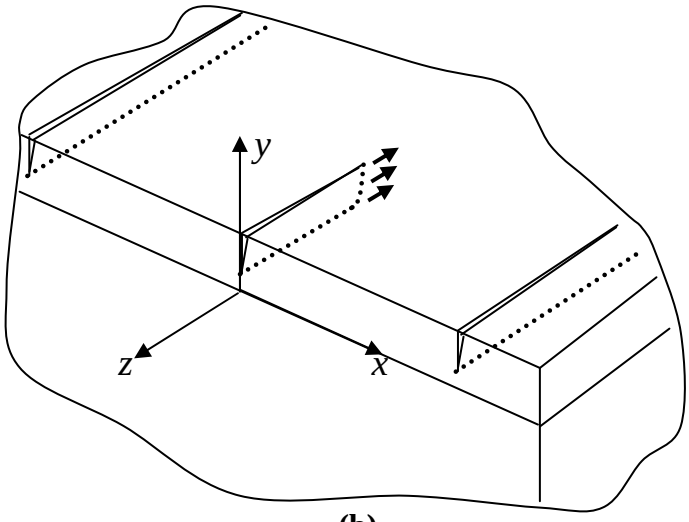

(b)

Figure 8.21 Schematic illustration of thermal cracking in asphalt overlays

(a) top-down plane strain cracking and (b) three-dimensional channeling

Fig. 22 illustrates the energy release rates for plane strain cracking and 3-D channeling. It can be seen that the local maximum energy release rates g_1 and g_2 exist at a_1 and a_2 for 2-D cracking and 3-D channeling, respectively. This is similar to the results of Beuth (117) for a single crack and Shenoy et al. (120) for periodic cracks. From this figure, we can see that when the crack depth is small, given a thermal loading the crack driving forces for both modes are small, and the crack will not initiate. If the thermal loading is so large that the driving force is larger than the fracture toughness, plane cracking will occur. Because the driving force increases with the crack depth for $a < a_1$, the cracking quickly propagates until the crack depth becomes larger than a_1. Thus, when the crack depth is smaller than a_1, the cracking is unstable. When $a_1 < a < a_3$, further loading is needed to make the crack to propagate toward the interface. Before $a > a_3$, because the crack driving force for plane strain cracking is larger than that for 3D channeling, the crack may stop within the overlay in the width direction. However, when $a_3 \le a$, channeling cracks will propagate first under thermal loading. Thus, the crack will fully cross the overlay. With the increment of the loading, it is more difficult for cracks to propagate toward the interface, but as the stress in the overlay keeps increasing, a new crack will initiate and thus the stress will be relaxed again. It should be noted that Fig. 22 shows that the energy release rate for plane strain cracking is reduced to zero at

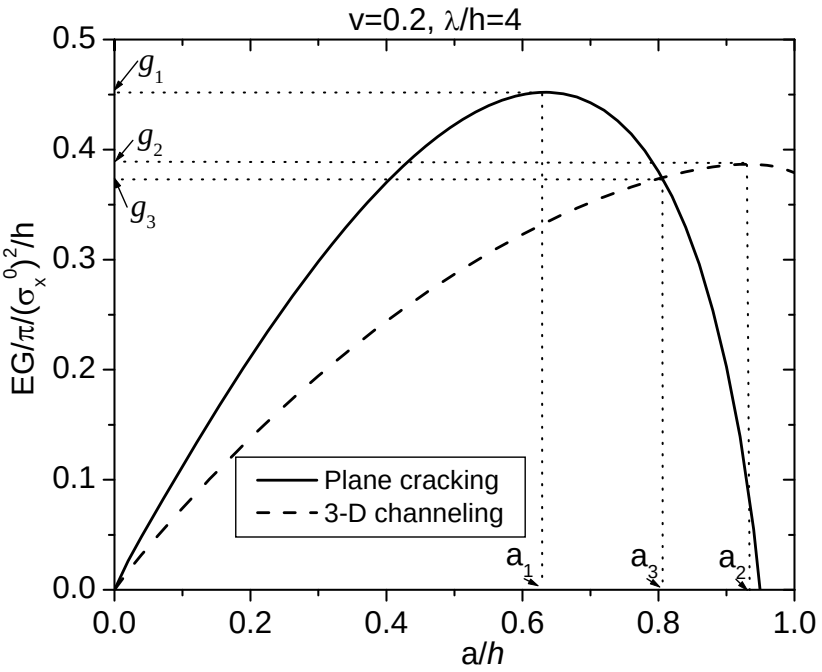

Figure 8.22. Energy release rates for plane strain cracking and three-dimensional channeling

Discussion and Results

The key accomplishments and findings described in sections 2 though 5 will now be summarized. Table 1 provides a quick overview of the models developed, their underlying

assumptions, and general uses. The current report provides several new insights into thermal cracking mechanisms, such as prediction of crack spacing for pavements prone to thermal cracking, and the propensity for very close crack spacing (as little as two or three times the crack depth) in instances when thermal cracks do not penetrate the entire depth of the HMA layers during their initial development. Close crack spacing has been observed in many field sections, including conventional hot-mix asphalt (HMA), full-depth, and composite pavements. This phenomenon will be evaluated in later stages of the current study for Interstate 74 in Champaign, Illinois.

Although several assumptions are made in the current model to derive the explicit solution, it is shown that the accuracy of the solutions is very good under the associated modeling assumptions, as verified with finite element simulations. Compared to existing closed-form solutions, the proposed models are more general and therefore more widely applicable. The solutions are valuable to the pavement analyst who seeks to understand the general mechanisms of thermally-induced pavement deterioration and for the researcher wishing to perform early stage verification of more complex pavement models. The models are particularly accurate under extreme weather conditions where the temperature drops very fast and the contribution of HMA on stress relaxation is minor. These elastic models can provide a reasonable explanation for the development of severe thermal cracking, which has been observed in the northern regions of USA.

Clearly, there is a need to develop more comprehensive models beyond those presented herein to consider the following factors: HMA viscoelasticity, other pavement configurations (for instance, HMA on a more flexible support layer, such as asphalt treated base, or multi-layered HMA pavements), non-linear/non-uniform temperature cooling, combined thermal and truck loadings, and the use of fracture models which more directly related to HMA fracture tests. In these endeavors, the closed-form models developed herein will serve as useful benchmarks for the development of approximate numerical solutions (finite element).

A series of analytical models are presented to investigate thermal cracking in asphalt pavements. Using the boundary and loading conditions, we obtain the solutions for three cases: an asphalt overlay resting on a granular base-layer; an asphalt overlay fully bonded to a thick base-layer, and; an asphalt overlay bonded to a rigid base-layer. Comparisons of the solution with the FEM simulations show that the proposed models provides good predictions of the elastic fields. Using this solution, the energy release rates can be calculated for plane strain cracking and 3D channeling. Fracture analysis of asphalt pavements is conducted based on strength and energy criteria.

In the current work, the material of the overlay is limited to linear elasticity. However, the asphalt pavement materials typically exhibit a viscoelastic behavior even at low temperatures. Thus, a viscoelastic constitutive model is ultimately needed. In addition, the temperature distribution in the thickness direction of the pavement varies along with the ambient temperature change, and then the effect of the nonlinear temperature gradients needs to be studied further. Future modeling efforts are planned to compare this model with field data and laboratory data and use this model to predict low temperature cracking in asphalt pavements. It should be noted that though this study is motivated by the thermal cracking in asphalt pavements and overlays, this method is applicable for other overlay/substrate structures such as protective coatings.

CHAPTER 9

THERMAL CRACKING PREDICTIONS

Introduction

For decades asphalt technologists have attempted to link binder and mixture physical properties to field distresses. Under the penetration grading system, higher penetration grade binders were used in cold climates. In the AC grading system, temperature susceptibility was controlled by specifying binder physical properties at three broadly spaced test temperatures, namely 135, 60, and 25 C. In the Superpave system, a bending beam rheometer is used to control low temperature binder properties. Although seldom specified, engineers have also attempted to link low temperature mixture properties directly to thermal cracking resistance. For instance, measurements from the very important St. Anne Test Road study in Canada suggested that thermal cracking was strongly related to instances where mixture stiffness at the design low air temperature were found to exceed 1 GPa at 7200 seconds loading time. However, there are clearly important factors which are not accounted for when attempting to form such links, i.e., mixture physical properties, pavement thickness, pavement layer and layer interface properties, cooling rates, etc.

During the Strategic Highway Research Program (SHRP), a first attempt was made to develop true performance-based models which directly predicted distress levels versus time using mechanistic-empirical structural response and distress models. For thermal cracking, the program TCMODEL was developed and completed in 1993, and after minor improvements and several recalibration iterations, is being used in the Mechanistic-Empirical Design Guide (M-E PDG) Software developed under the National Cooperative Highway Research Program (NCHRP) project 1-37A, which is under review by the American Association of State Transportation and Highway Officials (AASHTO). The first official public release of the program (version 1.0) is expected in the Spring of 2007. At the time of this writing, however, version 0.964 was available and thus used for all predictions reported herein.

One of the key features of TCMODEL is the ability to predict thermal stress versus time and depth in the pavements, based upon pavement temperatures computed using air temperatures. Arguably, the weakest link in TCMODEL is the use of a simple, phenomenological model (Paris Law, developed in 1961) to estimate crack growth rate, using tensile strength and m-value obtained from testing with the Superpave indirect tension test (IDT). That notwithstanding, TCMODEL is a verified, calibrated, and validated model, and thus can be viewed as a state-of-the-art tool for performance-based thermal cracking prediction, which is a key element of an integrated mixture and pavement design system (such as the M-E PDG). The computer code in the version of TCMODEL used in the M-E PDG was independently verified by researchers on the NCHRP 9-22 project as part of the development of software for performance-related construction specifications.

Over the past decade, significant advances have been made in the development of asphalt concrete fracture tests, such as the semi-circular bend test and the disk-shaped compact tension test, or DC(T), now specified in ASTM D7313-06. These tests have been found to be vastly superior in their ability to distinguish between mixtures with different aggregate types and binders, particularly polymer-modified binders, as shown in previous chapters. New fracture

models, such as the cohesive zone model (CZM), are now available for asphalt concrete, and can be used in powerful finite element simulation to capture the combined effects of traffic and climate on crack initiation and propagation in asphalt pavements. These models directly utilize laboratory fracture test data. These tools represent the cutting edge, and if deemed useful, could be feasibly implemented as a replacement to the fracture 'engine' in TCMODEL in a relatively short time frame (2-3 years), pending development of efficient code, tailored for the study of flexible pavements.

This chapter presents thermal cracking predictions using both the state-of-the-art TCMODEL program, followed by demonstrative simulations using cutting edge finite element techniques. The goals of the analyses presented were two-fold: 1) to evaluate the predictive accuracy of TCMODEL under the current release of the M-E PDG, and; 2) to describe and demonstrate new fracture-based thermal cracking prediction tools. Finally, a comparison and contrast of the two modeling approaches is made, focused on describing the advantages and disadvantages of each approach, along with recommendations for further research and field validation.

Thermal Cracking Predictions Using TCMODEL

This section describes the analysis methods used to obtain thermal cracking predictions using the M-E PDG software, presents thermal cracking predictions of the LTC study field sections, and makes recommendations for future improvement of TCMODEL. The M-E PDG provides three levels of analysis rigor, e.g., level 1, level 2, and level 3. Level 1 requires extensive measured laboratory data, while level 3 simply requires general knowledge of mixture design variables, pavement layering, and asphalt grade. Level 2 is intermediate to levels and 1 and 3, but in the case of thermal cracking, is performed when measured mixture data is only available at a single temperature (-10C). Thus, for the analysis presented herein, level 1 and level 3 predictions were performed. The main difference between level 1 and level 3 predictions for the analyses performed herein were the type of properties used to describe the HMA surface layer. Identical model inputs were used for all other pavement layers. From the standpoint of thermal cracking predictions using TCMODEL, the lower pavement layers were expected to have minimal impact on overall predictions, as the model is entirely non-load associated. The lower pavement layers will affect climatic model results; however, the impact of these properties on the near-surface pavement temperatures which drive thermal cracking in TCMODEL was expected to be negligible. The following sections present specific analysis methods used in level 1 and level 3 predictions, along with typical input and output file examples.

Level 3 Analysis Methods

For convenience (and as explained in the following section), level 3 analyses were first conducted. The M-E PDG input dialog boxes related to asphalt thermal cracking are provided in Figures 9.1 through 9.3. Because TCMODEL does not consider traffic effects, it is not necessary to change the traffic related parameters from their default values. Thus, although traffic-related dialog boxes are normally encountered first when running the M-E PDG, the presentation herein begins at the Environment/Climatic dialog box.

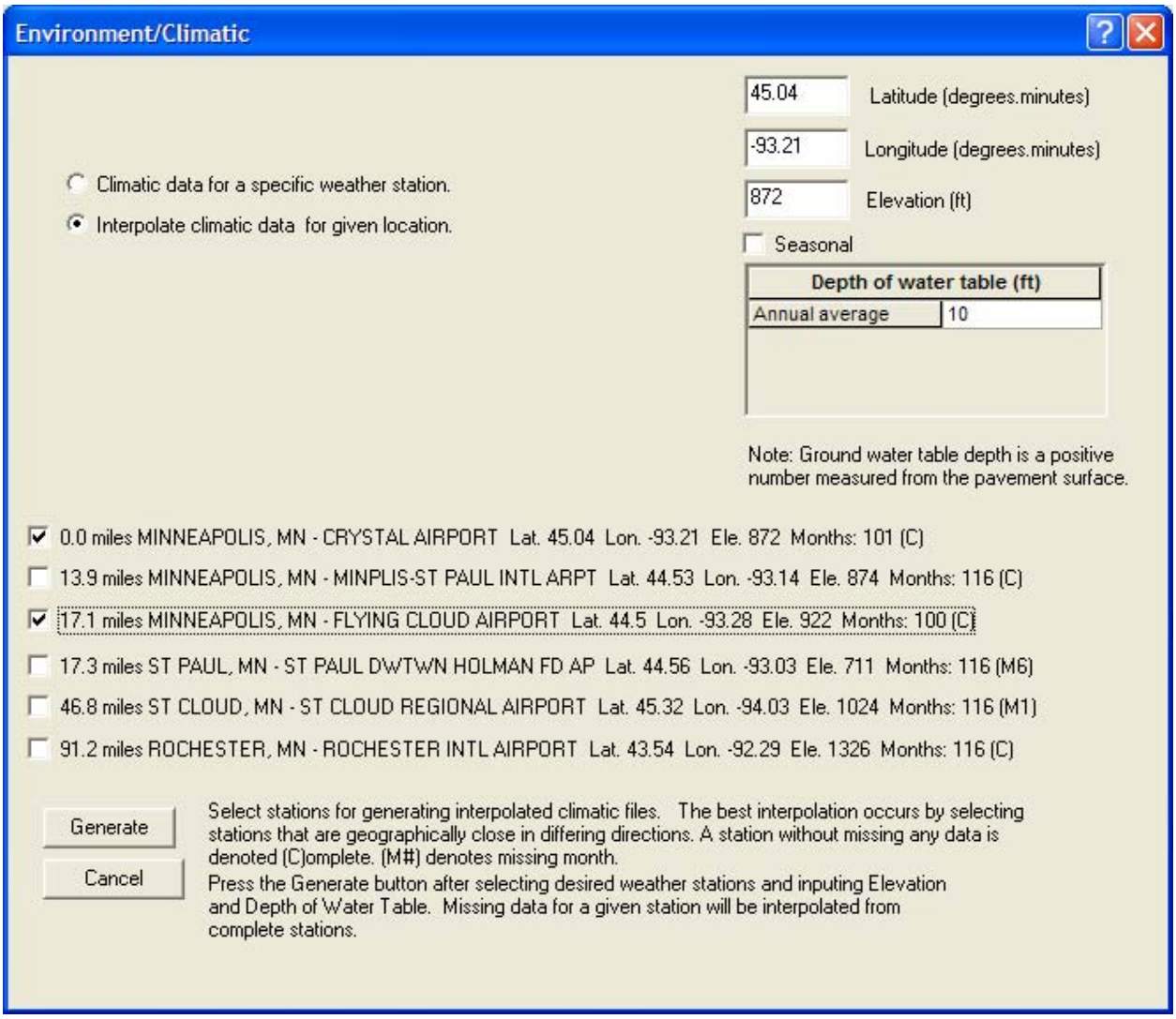

Figure 9.1. Typical climatic file generation dialog box, including interpolation between weather stations

Figure 9.1 demonstrates the weather station interpolation feature in the M-E PDG. The interpolation feature is generally used for one of two reasons: 1) an available weather station is not in direct proximity to the area of interest, or; 2) the weather station of interest has incomplete records. It is not known if the interpolation feature tends to reduce the severity of critical cooling events due to averaging effects. However, assuming that the selected stations are not separated by excessive distance and assuming that there are no major changes in elevation or other geographical differences between the stations, this effect is expected to be fairly minimal. Figure 9.2 shows the typical HMA input dialog box, while Figure 9.3 shows the thermal cracking dialog box. Note that for a level 3 analysis, the creep compliance and tensile strength values are automatically generated. These values a generated by the M-E PDG using empirical formulas developed at Arizona State University during the NCHRP 1-37A project.

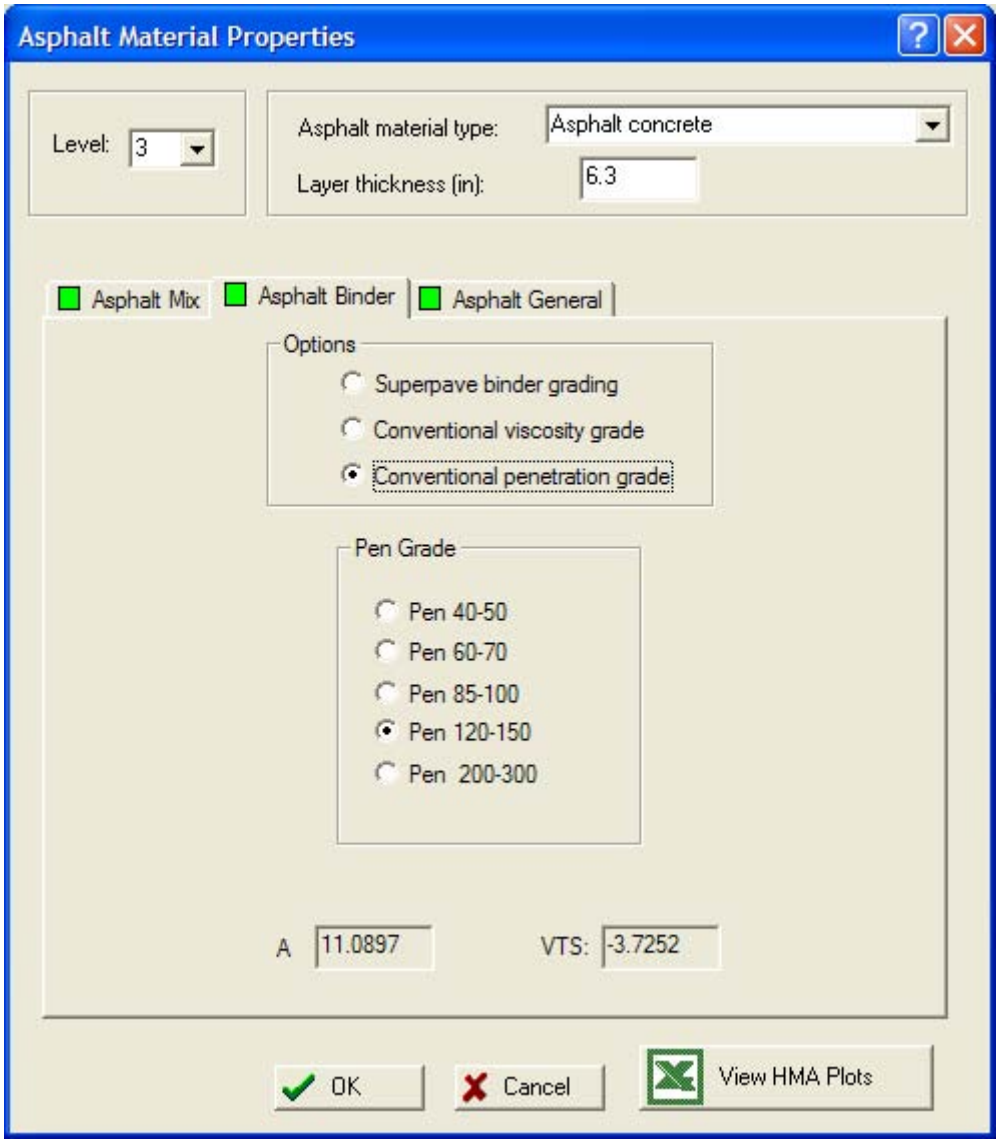

Figure 9.2. Typical HMA input dialog box

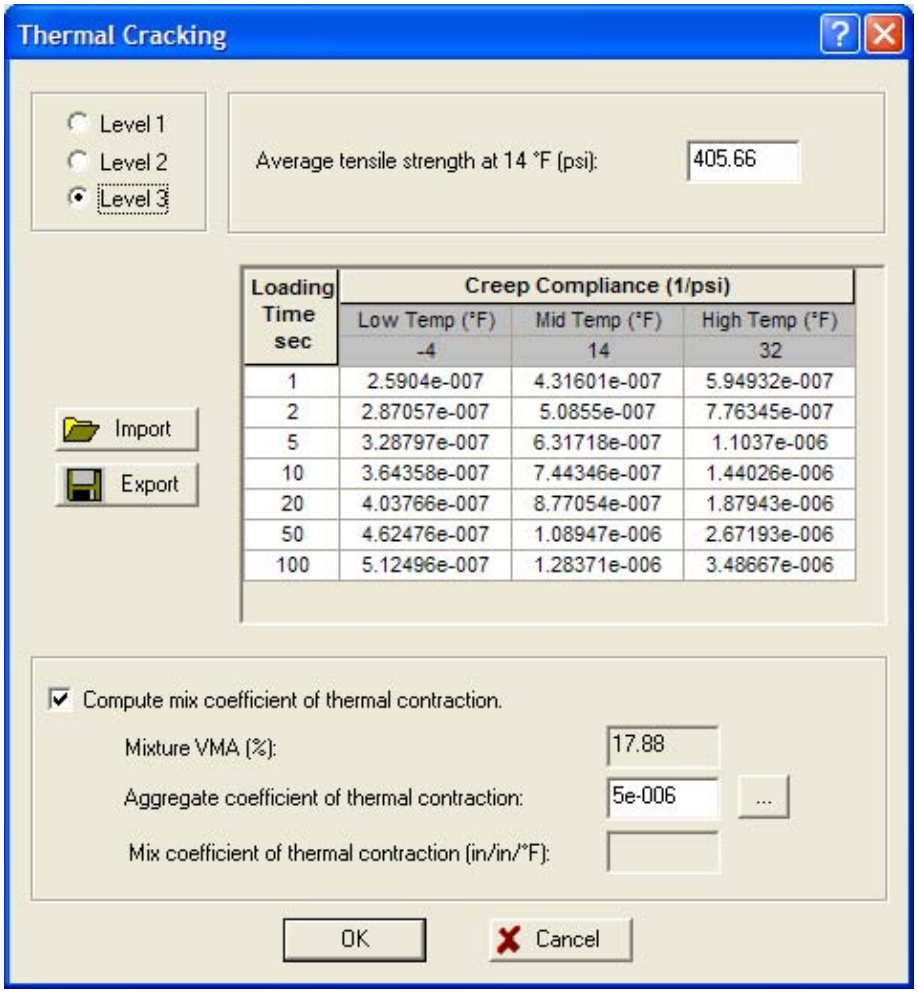

Figure 9.3. The thermal cracking dialogue box within the M-E PDG

Once all of the data is input into the M-E PDG, the 'Run Analysis' button is pressed. Most of the analysis time is related to the generation of the climatic files. This can take anywhere from a few seconds to a few minutes, depending upon the speed of the PC and the selected design life. Once the thermal cracking predictions are complete, the user can terminate the execution of the program (assuming that fatigue and rutting analyses are not desired). However, in this case, thermal cracking results must be manually extracted from the M-E PDG subdirectories on the local computer's hard drive, whereas a completed M-E PDG analysis is presented in a convenient spreadsheet. Figures 9.4, 9.5, and 9.6 demonstrate some of the key output files generated by the M-E PDG. Figure 9.4 is an example of the 'Data.in' file, which contains program inputs such as pavement thickness, tensile strength, thermal coefficient, and calibration factor (beta2, which equals 6.0 for level 3), etc. Figure 9.5 is an example of the 'Comply.in' file, which is a summary of the viscoelastic material models which were fit to the creep compliance data by a program called 'Master.exe', which is executed just prior to TCMODEL. The main purpose of Master.exe is to obtain shift factors by applying the time-temperature superposition principle, and then to fit two specific functional forms (viscoelastic models) to the data; namely, the generalized Voight-Kelvin Model, and Power Law Model, as described in Chapter 2. Figure 9.6 shows an example of the '.tcr' file created by TCMODEL, which summarizes the average cracking length and total amount of cracking (ft/500ft) as a function of time in months.

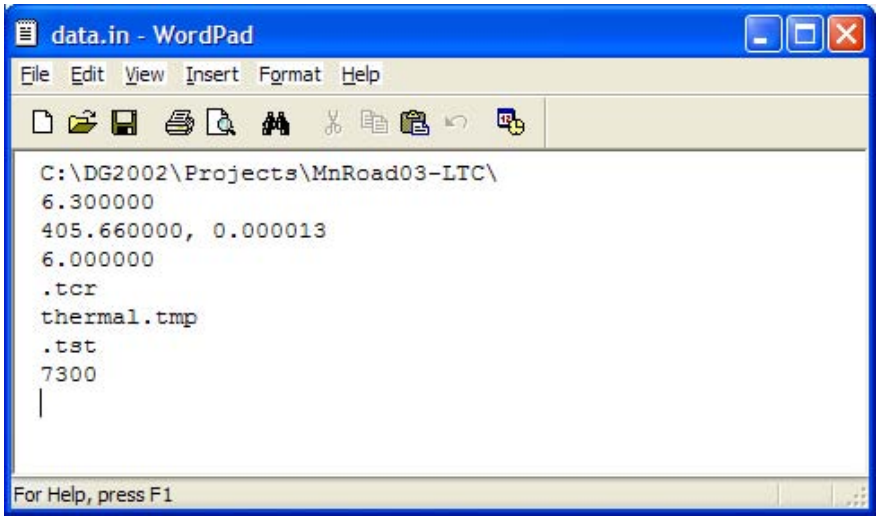

Figure 9.4. Typical Data.in input file

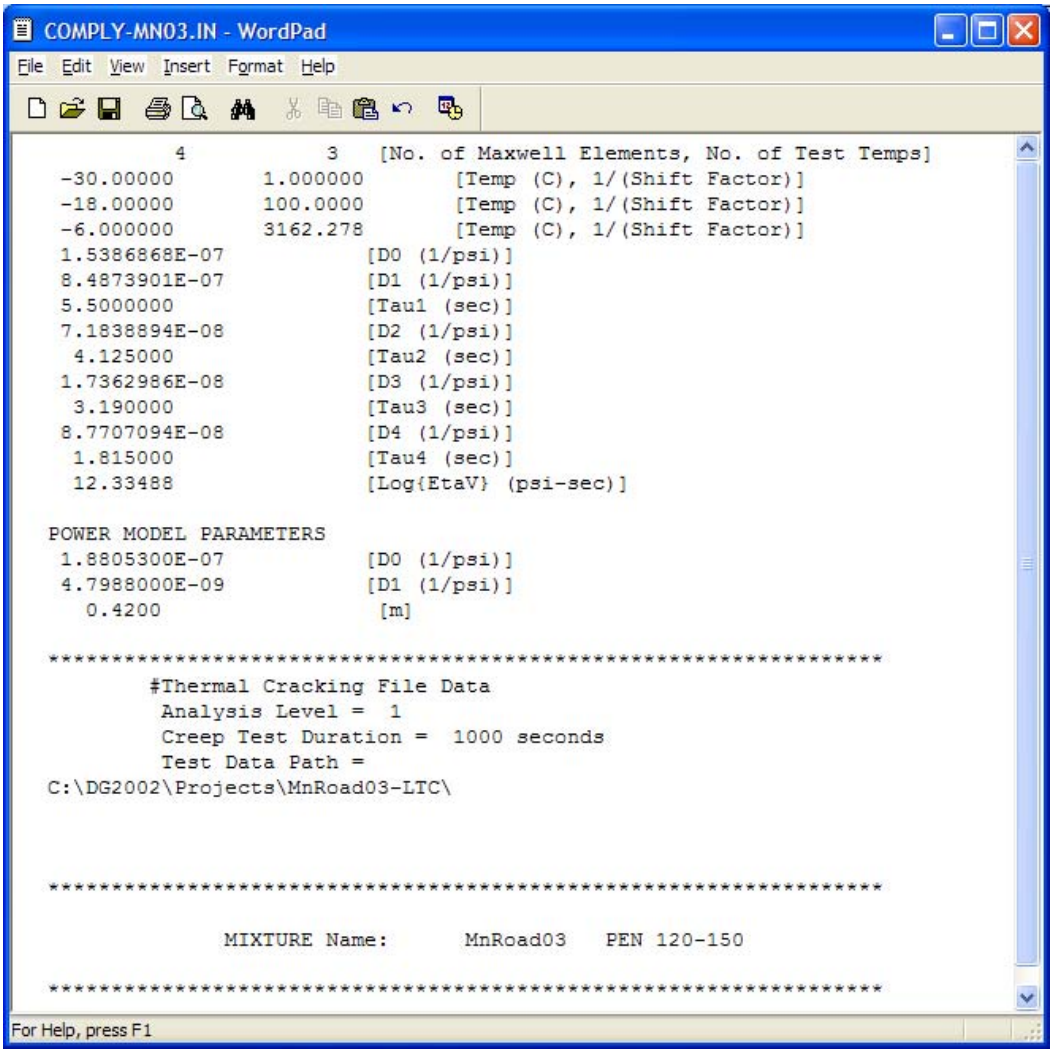

Figure 9.5. Typical Comply.in input file

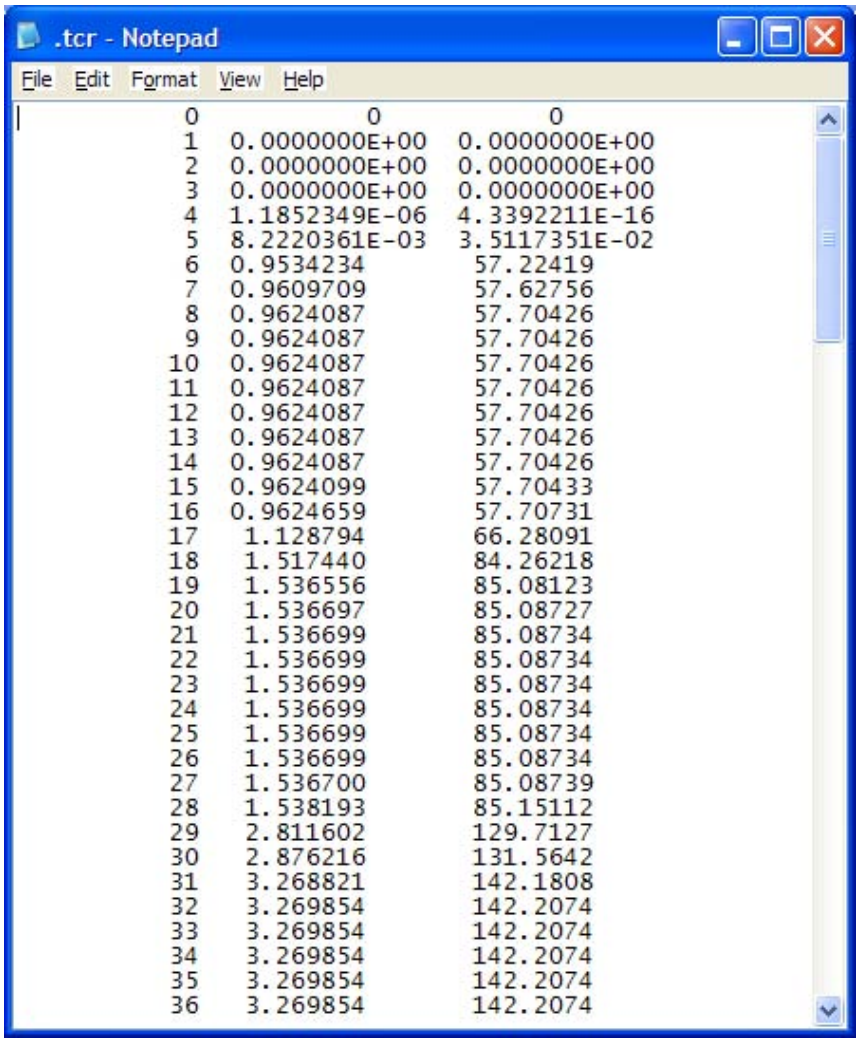

Figure 9.6. Typical thermal cracking output file

Level 1 Analysis Methods

The primary HMA properties required for TCMODEL are the creep compliance master curve and associated shift factors, mixture tensile strength at -10C, and the coefficient of thermal contraction. Although the M-E PDG provides an interface where creep compliances can be directly entered, an 'expert mode' approach was used in this study. The main reason this approach was taken, was to allow extra care to be used in assembling creep compliance data. The Superpave Indirect Tension Test data collected in this study was noted to have questionable values at short loading times. Thus, a spreadsheet was developed which allowed the master curves to be visually constructed by hand. An example is provided in Figure 9.7. It should be noted that the M-E PDG only provides input of up to 100 seconds of creep data, regardless of the analysis level. However, when using the expert mode approach, additional creep data can be used in the formation of the master curve. For instance, 1000 second creep curves were used herein. The spreadsheet results were used to create Comply.in files, as shown in Figure 9.8. Next, the Data.in files generated during the level 3 analysis were manipulated to include measured IDT tensile strength, measured coefficient of thermal expansion, and the level 1 calibration factor (beta2 = 1.0) was applied, as shown in Figure 9.9. It should be noted that true

tensile strength values were not available, since clip on gages were not used in the IDT tests performed in this study, and subsequently had to be estimated as 80 percent of the bulk indirect tensile strength (based upon experience of the UIUC research team). A detailed summary of model inputs is included in Appendix G.

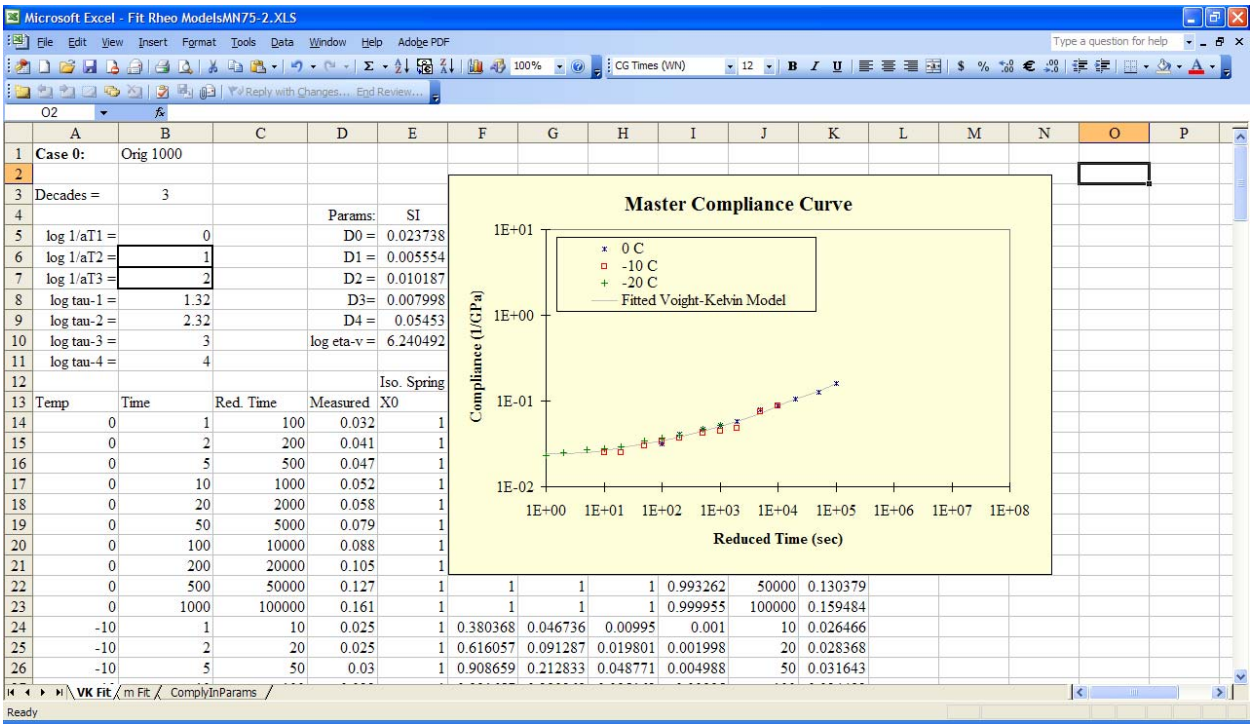

	A	B	C	D	E	F	G	H	I	J	K
1	**Case 0:**	Orig 1000									
2											
3	Decades =	3									
4				Params:	SI						
5	log 1/aT1 =	0		D0 =	0.023738						
6	log 1/aT2 =	1		D1 =	0.005554						
7	log 1/aT3 =	2		D2 =	0.010187						
8	log tau-1 =	1.32		D3=	0.007998						
9	log tau-2 =	2.32		D4 =	0.05453						
10	log tau-3 =	3		log eta-v =	6.240492						
11	log tau-4 =	4									
12					Iso. Spring						
13	Temp	Time	Red. Time	Measured	X0						
14	0	1	100	0.032	1						
15	0	2	200	0.041	1						
16	0	5	500	0.047	1						
17	0	10	1000	0.052	1						
18	0	20	2000	0.058	1						
19	0	50	5000	0.079	1						
20	0	100	10000	0.088	1						
21	0	200	20000	0.105	1						
22	0	500	50000	0.127	1	1	1	1	0.993262	50000	0.130379
23	0	1000	100000	0.161	1	1	1	1	0.999955	100000	0.159484
24	-10	1	10	0.025	1	0.380368	0.046736	0.00995	0.001	10	0.026466
25	-10	2	20	0.025	1	0.616057	0.091287	0.019801	0.001998	20	0.028368
26	-10	5	50	0.03	1	0.908659	0.212833	0.048771	0.004988	50	0.031643

Figure 9.7. Typical Spreadsheet manipulation of IDT creep data to obtain master curve parameters

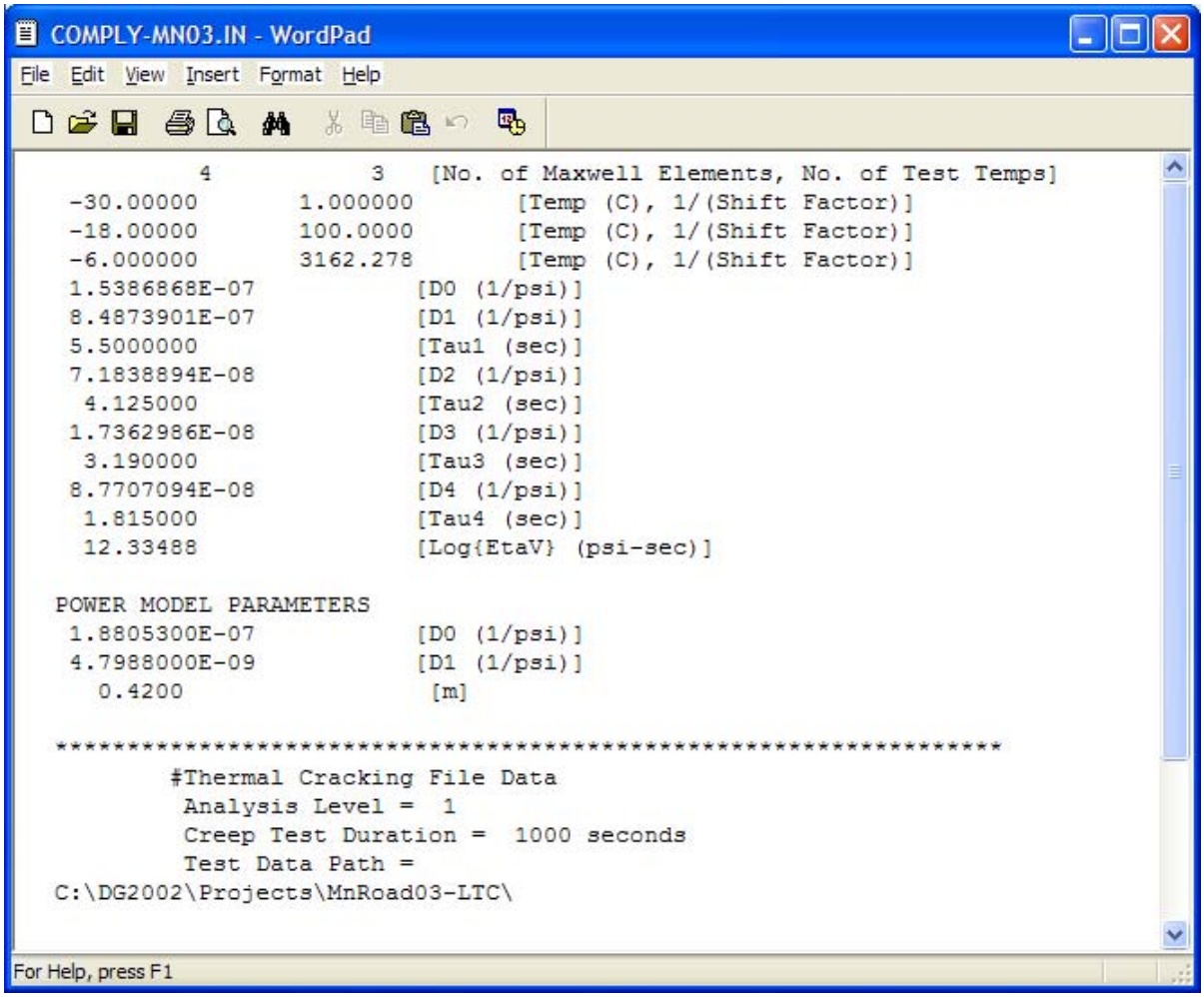

Figure 9.8. Example of Comply.in file used in Level 1 analysis

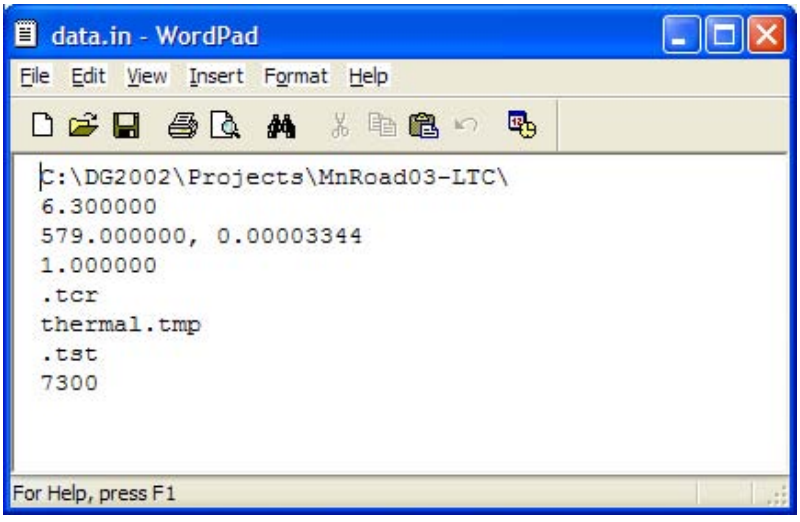

Figure 9.9. Example of Data.in file for Level 1 analysis

TCMODEL Model Predictions and Discussion

Selected typical thermal cracking versus time results are presented in Figure 9.10. Note that the MnROAD sections 03 and 19 were predicted by TCMODEL to develop rapid thermal cracking, while the MnROAD sections 33, 34, and 35 were not predicted to develop significant thermal cracking.

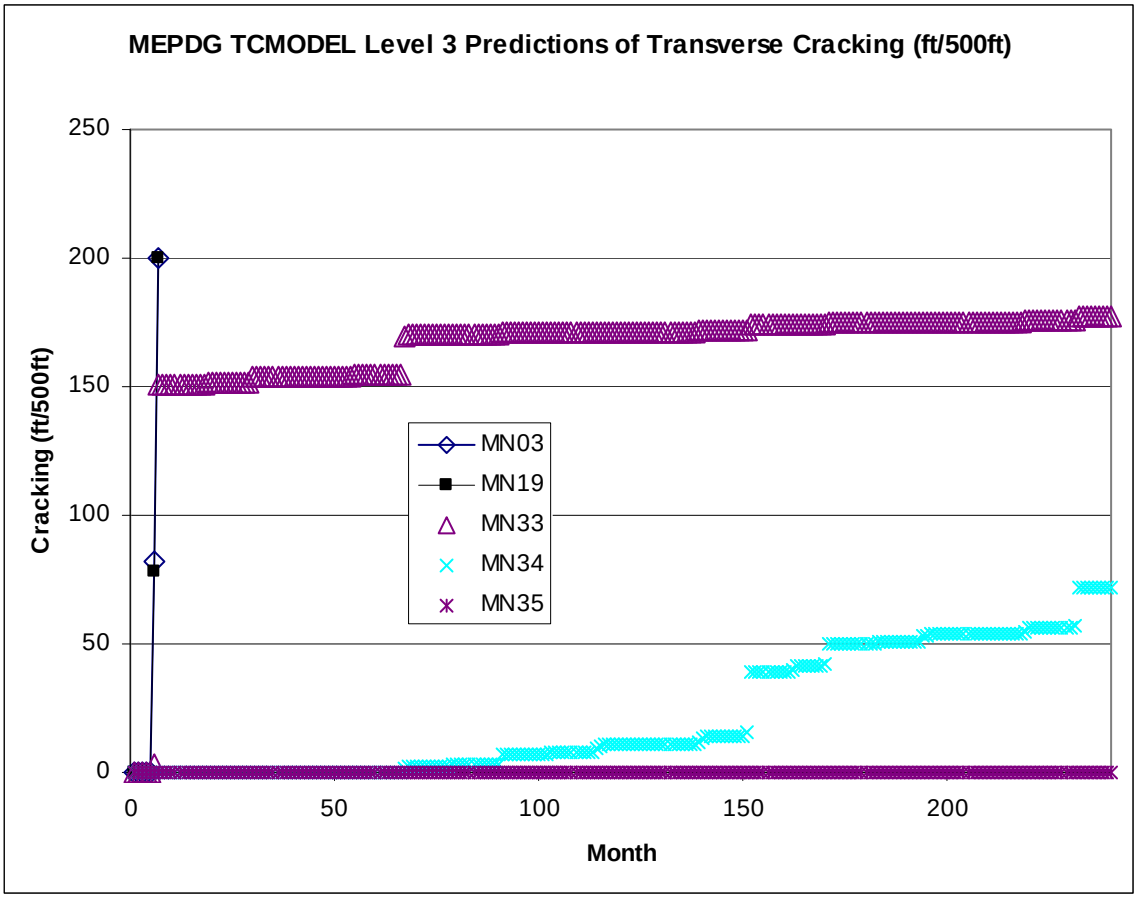

Figure 9.10. Selected thermal cracking vs. time data

Table 9.1 provides a summary of all level 1 and level 3 predictions, along with observed cracking levels. Observed cracking levels were obtained from the Pooled Fund Study state participants, and were typically reported in either number of full width cracks per unit length of pavement, or total feet of transverse cracking per length of pavement. Because TCMODEL only predicts amount of cracking per time (and not severity), all transverse crack severity levels were added together to arrive at total feet of transverse cracking. All cracking data was normalized to a uniform basis of 500 feet of pavement length, to be consistent with TCMODEL output. In the case of the Minnesota sections, all crack counts were reported for 500 foot test sections and therefore did not require normalization. Because IDT creep data was unavailable for all three Illinois sections (surfaces were too thin to fabricate test specimens after saw cutting), model predictions are not provided for these sections.

The most accurate predictions obtained were for the carefully controlled MnROAD sections, with the exception of MnROAD cell 35, which had high levels of reported transverse cracking. However, upon future examination of crack maps collected in the field, the exact mechanism of

the cracking cannot be confidently categorized as traditional low temperature cracking (Figure 9.11), since many partial width, distributed cracks were observed. Adding to the suspicion is the fact that the binder grade used, PG 58-40, was much softer than the grades used in the adjacent sections 33 and 34 (PG 58-28 and PG 58-34, respectively), but demonstrated higher levels of cracking. The second portion of this chapter, which deals with finite element modeling of HMA pavements, provides insight towards a possible mechanism behind the cracking exhibited in MnROAD cell 35.

More erratic prediction trends were noted for the other field sections, including WI 45 and 73, and MN 75-2 and 75-4. In the latter three cases, the level of thermal cracking in the field was over-predicted using TCMDODEL. Reasons for model discrepancies will be presented in the following section. It should be noted that an exact estimate of the cracking levels on WI 73 was not available at the time of this study.

Table 9.1. Thermal cracking predictions from M-E PDG and TCMODEL

	MN 03	MN 19	MN 33	MN 34	MN 35	WI 45	WI 73	MN 75-2	MN 75-4
Yr. Open	1994	1994	1999	1999	1999	1995	2000	1996	1996
Last Survey Yr.	2006	2006	2006	2006	2006	2004	2003	2005	2005
# Months	152	152	92	92	92	108	36	108	108
Observed Cracking (ft/500ft)	182	547	91	6	747	60[a]	0	76	54
L1 Predicted Cracking (ft/500ft)	192.3	>>200	24	0	0	0	>>200	>>200	>>200
L3 Predicted Cracking (ft/500ft)	>>200	>>200	171	7	0	25	>>200	>>200	---[b]

[a]Estimated. Range of 1 to 5 cracks per 100-ft of pavement reported in pavement management database. However, good overall performance was indicated in the project nomination form.

[b]Master curve program 'Master.exe' did not function properly for this level 3 prediction run using M-E PDG version 0.964. This issue will be resolved in version 1.0.

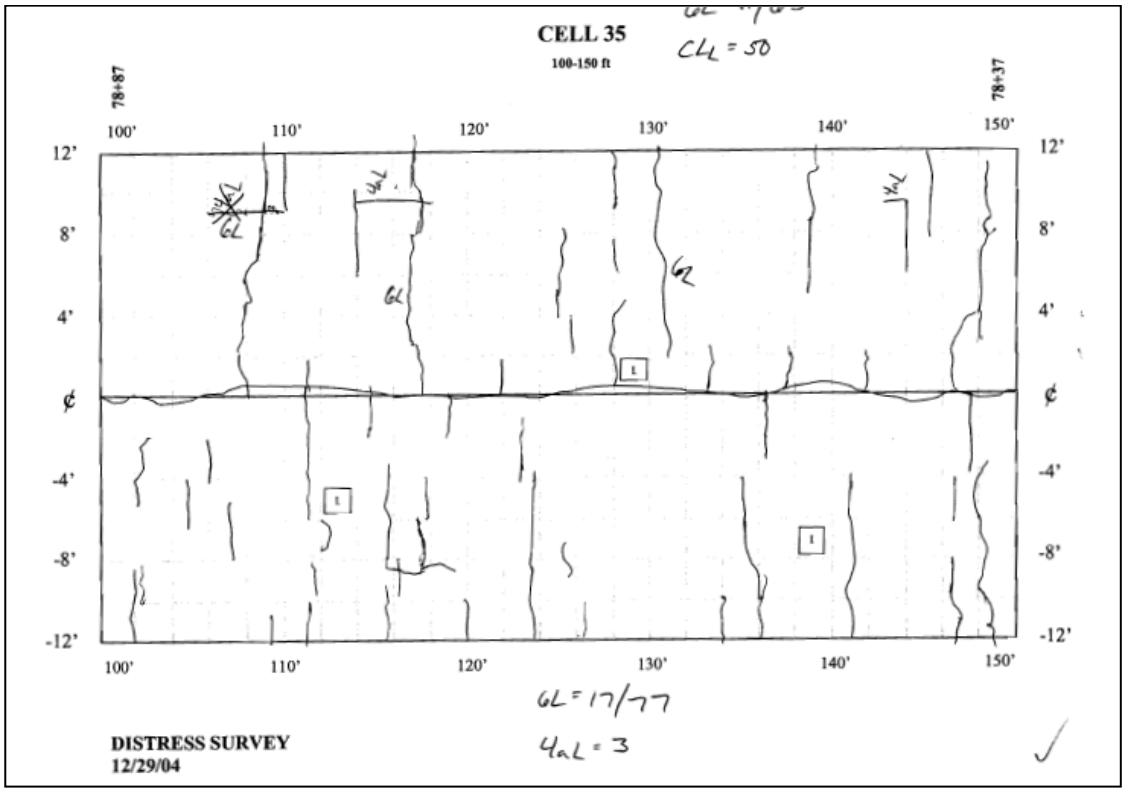

Figure 9.11. Crack map of MnROAD section 35

(source: MnROAD webpage: http://mnroad.dot.state.mn.us/research/cell_info/cell35.asp)

Sources of Modeling Error and Recommendations for Improvement of TCMODEL

It is important to bear in mind that performance prediction models have associated assumptions and limitations and, even after calibration, discrepancies with actual field performance should be expected. This section outlines sources of model prediction errors with TCMODEL, both in general and with specific reference to unique features of this study. Recommendations for improved modeling results, where applicable, are provided.

1. **National versus Local Calibration** – The M-E PDG has been calibrated to a national data base of material properties and field cracking observations. Because of the extreme breath of climates, traffic levels, pavement structures, and materials represented in the M-E PDG, regional and/or local calibration of the M-E PDG is highly recommended.
2. **Beta Version of M-E PDG** – A beta testing version (0.964) of the M-E PDG was utilized. At the time of the writing of this report, a critical software bug was reported in the Master.exe program, which affected the Level 3 thermal cracking predictions reported herein. Once the bug is fixed and the model is recalibrated, it is recommended to revisit the predictions made herein. This could be accomplished in Phase II of the study.
3. **Need for Accurate IDT data** – Most of the IDT tests were performed at temperatures well below the test temperatures recommended in the AASHTO standard. The IDT device used for collection of creep compliance data in this study produced suspect data, particularly at short loading times. As a result, for the purpose of Level 1 predictions, data fitting, data smoothing and other manipulations were necessary to render the data

usable in the M-E PDG models. In addition, the true tensile strength value was not available, since clip on gages were not used in the tests performed, and subsequently had to be estimated from bulk indirect tensile strength. In the future, having a well calibrated device, participating in round-robin testing programs, and the use of clip on gages during the strength test will serve to improve level 1 thermal cracking predictions.

4. **Better Understanding of the Role of Aging**. The role of aging of asphalt paving mixtures in thermal cracking development and thermal cracking predictions is not well understood. Currently, the M-E PDG does not have a provision for the HMA properties in the thermal cracking analysis to age harden with depth and time. Furthermore, the vast majority of the calibration set used to calibrate TCMODEL were from existing field sections where it was only possible to test materials at one point in time (generally, towards the end of the pavement's service life). Having a better match between the age of the samples used in a research investigation to those used in the calibration of the model would be expected to produce better prediction accuracy. Moreover, in the future, methods to more accurately account for material aging with depth and time in model predictions will lead to a more robust prediction system.
5. **Improvement of Climatic Files in the M-E PDG**. There are two issues which could be improved with respect to climatic files and thermal cracking modeling. 1) Currently, the M-E PDG has databases of up to 9 years of climatic data. Some data sets only contain around 6 years of data. For analyses where the design life exceeds the number of years of climatic data, the M-E PDG software repeats the climatic data. The problem with this approach is that thermal cracking is sensitive to critical winter cooling events, which may occur infrequently. Thus, the effect of repeating climatic data may be to underpredict or overpredict the severity of the climate, depending upon the criticality of the repeated range of years. 2) For specific thermal cracking predictions of existing pavements, such as MnROAD, it is not possible to match the year of the database climatic files with the years that the actual pavement was in service. This can lead to discrepancies between the rate of crack propagation, particularly in the case of MnROAD, where a very severe winter occurred within the first two years of pavement life.
6. **Improved Fracture Properties**. The ability for the predictive accuracy of TCMODEL to be improved in the future will likely be limited by the weakest physical link in the model. It is presumed that the weakest link in the model at present is the Paris-law based crack prediction model, which was discussed in the literature review section of this report. As was also shown earlier in this report, material fracture energy was found to be highly correlated to field cracking. Thus, by employing fracture energy into future thermal cracking models, it would be expected that even better results could be obtained.
7. **Improved Crack Modeling Technique**. The following section demonstrates how the finite element method can be used to model crack initiation and propagation, and account for both thermal and traffic induced loading. The ability of the model to capture the key physics associated with a moving crack (changing boundary value problem) and relation of fracture process zone with layer thickness and proximity to other material layers is expected to produce more realistic results. In the near future, it will be possible to construct a finite element based model which can be used to predict daily temperature cycles and to track thermal crack growth with time.

Now that the state-of-the-art in thermal cracking prediction using the M-E PDG has been presented, in-depth look forward at a cutting edge, fracture-based thermal cracking prediction modeling approach is now presented.

Cohesive Zone Fracture Modeling of Thermal Cracking

Perhaps the most compelling reason to continue to strive towards further developments in thermal cracking modeling capabilities is the logical need to address a fracture-dominated phenomenon such as thermal cracking with appropriate fracture tests and models. Fortunately, as described in Chapter 8, significant strides have been made in developing true HMA fracture tests, which are suitably repeatable and relatively easy to perform. In this section, a powerful finite element based modeling approach is demonstrated, which utilizes this fracture information in the prediction of thermal crack initiation and propagation. While this section presents a specific modeling approach and others certainly exist, the intent is to provide the reader with a general idea of how fracture energy based fracture model simulations work, what information is obtained from them, their advantages relative to TCMODEL, and the remaining challenges in moving these models towards implementation as part of a practical HMA design system.

Background

This section provides background information on the development of fracture-based, finite element simulation models. The numerical simulations were performed using the finite-element (FE) analysis technique in the commercially available software program ABAQUS. The program was customized by developing and implementing several user-subroutine codes to enable fracture tools to be employed in the simulation of low temperature pavement cracking. This section is subdivided into the following sub-sections:

- Overview of Finite Element Pavement Modeling:
  - Bulk Material Constitutive Model (Viscoelastic Model)
  - Fracture Constitutive Model (Cohesive Zone Interface Elements)
  - Typical Pavement Mesh
  - Loading Conditions
  - Boundary Conditions
  - Input Properties
  - Standard Scheme for Presentation of Results
- Model Predictions
- Summary of Simulation Results
- Conclusions and Recommendations

Overview of Finite Element Pavement Modeling

Bulk Material Constitutive Models

An appropriate bulk material constitutive model is crucial to the accurate simulation of material behavior in the FE modeling technique. Asphalt concrete material is known to have time and temperature dependent behavior across most of the in-service temperature range. Creep tests on asphalt concrete materials have suggested that linear viscoelastic behavior at low and moderate temperatures can be reasonably assumed for the purposes of thermal cracking simulations. For

the numerical simulations, asphalt concrete was modeled using the generalized Maxwell model as illustrated in Figure 9.12, where the following Prony series function is used to describe the experimental data:

$$E(t) = \sum_{i=1}^{N} E_i \left[\exp(-t / \tau_i)\right]$$

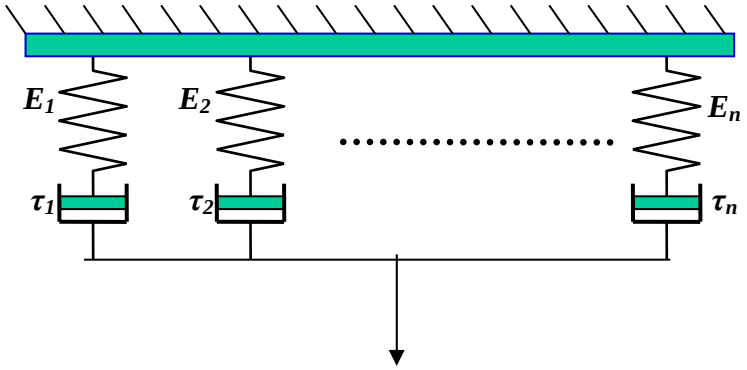

Figure 9.12. Schematic representation of the Generalized Maxwell Model

The generalized Maxwell model is available in ABAQUS; however to capture the dependence of asphalt concrete properties on temperature by use of the time-temperature superposition principle, a customized user-subroutine was used. Asphalt concrete coefficient of thermal expansion and contraction were studied extensively during the course of this project. The thermal coefficient of asphalt concrete material was modeled in form of a temperature dependent parameter on basis of the experimental findings described in Chapter 7. The temperature-dependent thermal coefficient was implemented within ABAQUS FE simulations by means of a user subroutine, taking the relationship as bi-linear using the two coefficients and glass transition temperature provided in Chapter 10 for each field mixture. A similar bi-linear, user defined subroutine was implemented in ABAQUS to model the temperature shift factors, as provided in Chapter 6. Granular bases and subgrade materials were modeled using a linear elastic material model. Typical values for elastic modulus and Poisson's ratio of granular base and subgrade were used on basis of the information obtained from previously available reports (For example, *"MnRoad Aggregate Base Profile Summary"* report). In the case of field section simulations, the use of an elastic model for the granular base and subgrade was deemed adequate due to the relatively low stress levels in the base and subgrade layers. The finite element technique provides excellent flexibility in implementing more complex material models for various pavement layers, but added sophistication comes with added computational expense and typically requires a more costly laboratory testing program. Thus, engineering judgment must be applied in evaluating the tradeoffs between model sophistication and model practicality within the context of the specific distress being simulated.

Fracture Constitutive Model

A robust fracture mechanics based concept to account for cracking should be used to model thermal cracking in asphalt concrete pavements. A typical "strength of material" type analysis

may not be suitable because of non-linear behavior in the vicinity of crack tip and introduction of material separation, which defies the use of standard continuum-type approaches. For simulation of crack initiation and propagation, a cohesive zone model was used due to its capability to account for material damage ahead of a macro-crack. This zone of damage is typically known as the fracture process zone. Song et al. (103) demonstrated the capability of the cohesive zone model in the simulation of cracking in asphalt concrete materials.

Cohesive Zone Concept

The cohesive zone model is an efficient technique to predict the damage occurring in a process zone located ahead of a crack tip in a material. This approach, which involves nonlinear constitutive laws described by displacement jump and the corresponding traction along the interfaces, provides a simple, yet powerful phenomenological model to simulate complex fracture behavior such as crack nucleation, crack initiation, pure mode-I and mixed-mode crack propagation. In other words the cohesive zone model describes the relationship at any material point between its capacity to transfer load (traction) and potential opening (displacement jump) due to damage or cracking.

Figure 9.13 (a) illustrates the process zone, defined herein as the distance between a cohesive crack tip where the traction is maximum and a material crack tip where a traction-free region develops. Therefore the process zone describes the region between the point of no damage (full load carrying capacity) and the point of complete failure (no load-bearing capacity). Along this zone, crack nucleation, initiation, and propagation behavior such as microcracking, crack bridging, crack branching, and other complex non-linear damage effects occur. Figure 9.13 (b) shows a schematic illustration of the relation between displacement jump and the traction along the process zone. The cohesive surfaces are joined together by a cohesive traction, which varies depending upon the displacement jump across the crack faces. As the displacement jump increases due to an increase of external force or compliance in the structure, the traction first increases, reaches a maximum, and finally decays to zero. This softening relationship can be developed fundamental fracture properties of asphalt mixtures such as the material strength (σ_c), a critical displacement (δ_c) and cohesive fracture energy (G_f).

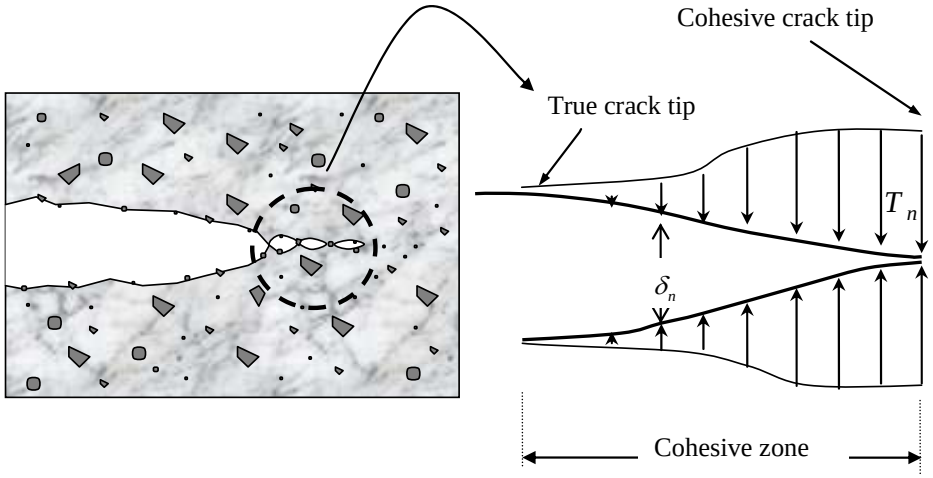

Figure 9.13. (a) Illustration of fracture behavior near crack tip and (b) Displacement jump (δ) and correspondent traction (T_n)

Bilinear Cohesive Zone Model

A bilinear cohesive zone model (103) was used in this study, where the non-dimensional effective displacement (λ) and effective traction (t) are defined as follows:

$$\lambda = \sqrt{\left(\frac{\delta_n}{\delta_n^c}\right)^2 + \beta^2\left(\frac{\delta_s}{\delta_s^c}\right)^2} \qquad \text{and} \qquad t(\lambda) = \frac{(1-\lambda)}{(1-\lambda_{cr})}\sigma_c,$$

where β is the ratio between maximum normal and shear traction; σ_c is a critical traction, which is one of cohesive parameters; δ_n and δ_s denote normal opening and shear sliding displacements, respectively; and δ_n^c are δ_s^c critical values where complete separation, i.e. zero traction, occurs. Notice that λ_{cr}, which is a non-dimensional parameter, is incorporated to reduce the compliance by adjusting the slope of the elasticity of the cohesive law.

The normal and shear tractions are given as

$$t_n = \frac{1-\lambda'}{\lambda'}\left(\frac{\delta_n}{\delta_n^c}\right)\frac{\sigma_c}{1-\lambda_{cr}} \text{ and } t_s = \beta^2\left(\frac{\delta_n^c}{\delta_s^c}\right)\frac{1-\lambda'}{\lambda'}\left(\frac{\delta_s}{\delta_s^c}\right)\frac{\sigma_c}{1-\lambda_{cr}},$$

where λ' is monotonically increasing and given by

$$\lambda' = \max(\lambda_{\max}, \lambda),$$

in which $\lambda_{max}=\lambda_{cr}$ initially and $\lambda_{max}=\lambda_{cr}$ if $\lambda > \lambda_{max}$. Figure 9.14 illustrates a normal displacement jump versus normal traction curve. For illustration purposes, $\lambda_{cr}=0.25$ is used.

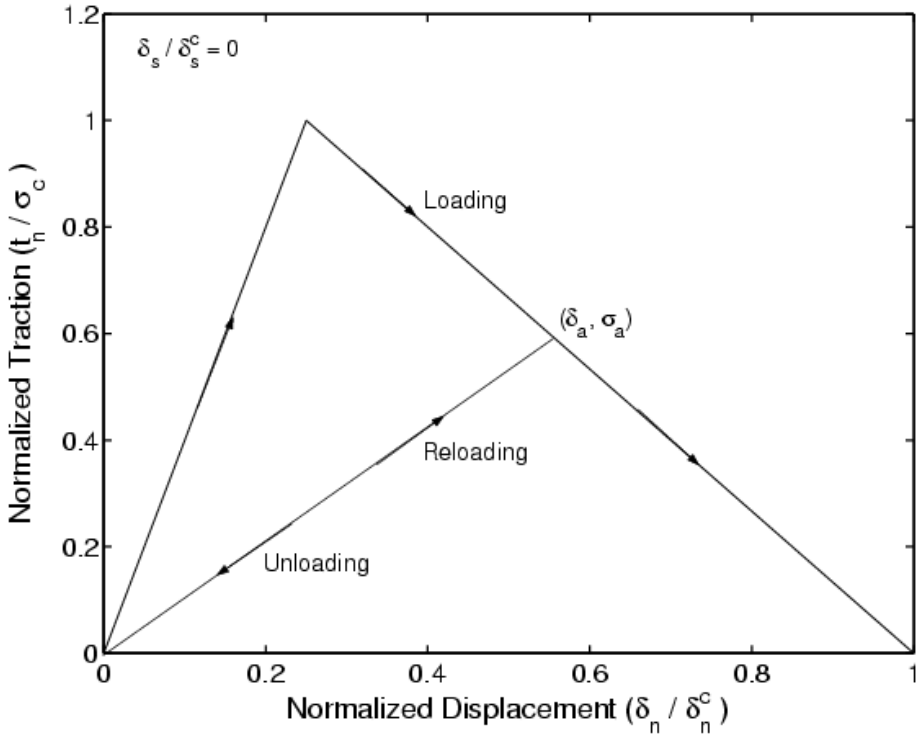

Figure 9.14. Schematic representation of loading and unloading in terms of displacement jump and the traction in the Bilinear Cohesive Model

The bilinear cohesive zone model was implemented in the form of a user element (UEL) subroutine in ABAQUS. The material parameters used in the cohesive fracture model are derived from experimental fracture energy and tensile strength. Based upon previous studies, the local fracture energy required in the CZM can be estimated as approximately 70 percent of the experimental fracture energy obtained in the Disk-Shaped Compact Tension Test, or DC(T) using load-CMOD data. The DC(T) test is now specified by ASTM D7313-06. The tensile strength from the IDT test can be used without calibration as an estimate of the local material strength in lieu of a more accurate measurement without significant detriment to model predictions. It is anticipated that a standardized procedure will be available in the near future to obtain local fracture energy and tensile strength from the DC(T) test.

In the current cohesive fracture approach, cracking in the pavement is simulated in the FE model by means of a specialized cohesive zone (CZ) element. These elements are inserted in the mesh along the interfaces between elements, thus allowing fracture surfaces to develop, as governed by a local softening law controlling the load-displacement separation behavior of the interface elements.

Typical Pavement Mesh

The FE models for low-temperature cracking simulations were constructed using graded meshes, which are used to significantly reduce the computational time. Graded meshes typically have a finer element size close to the regions of high stress variations and potential separation, whereas in the regions of low stress gradients, larger elements are used. Figure 9.15 shows the region of pavement that is modeling using the FE analysis. Note that the simulations in this study were performed by simplifying the pavement section to a two-dimensional FE model created along the longitudinal direction (taking section along the direction of traffic movement). The FE model dimensions (a.k.a. 'domain extent') were selected on basis of the previous studies carried out during the NSF-GOALI (NSF-GOALI Project # 0219566) research project at the University of Illinois at Urbana-Champaign. The FE model was generated using a domain length of 12192-mm (40-ft). The subgrade depth was selected as 6096-mm (20-ft), and the extent of subgrade was modeled as a semi-infinite boundary by use of special infinite elements in both length and depth directions. Figure 9.16 shows a typical mesh used in this study, where the mesh in close vicinity to a potential thermal cracking region is constructed with smaller elements (~2 mm).

Figure 9.16(b) shows an area in the vicinity of a potential crack path. Also notice that the frictional interfaces between various pavement layers are indicated in this figure. Figure 9.16(c) shows the details in the region where cohesive zone elements are embedded in the mesh to allow for cracking. Note that the current set of simulations is limited to the study of a single crack site for simplicity in the presentation of results. In this approach, it is not difficult to add additional cracks and to study crack interaction behavior. Due to the two-dimensional simulation approach used herein, each crack represents a transverse crack through the width of pavement. The frictional contact interfaces between asphalt concrete and granular base, and granular base and soil subgrade are indicated in the figure. More discussions on contact interfaces are described later in this chapter.

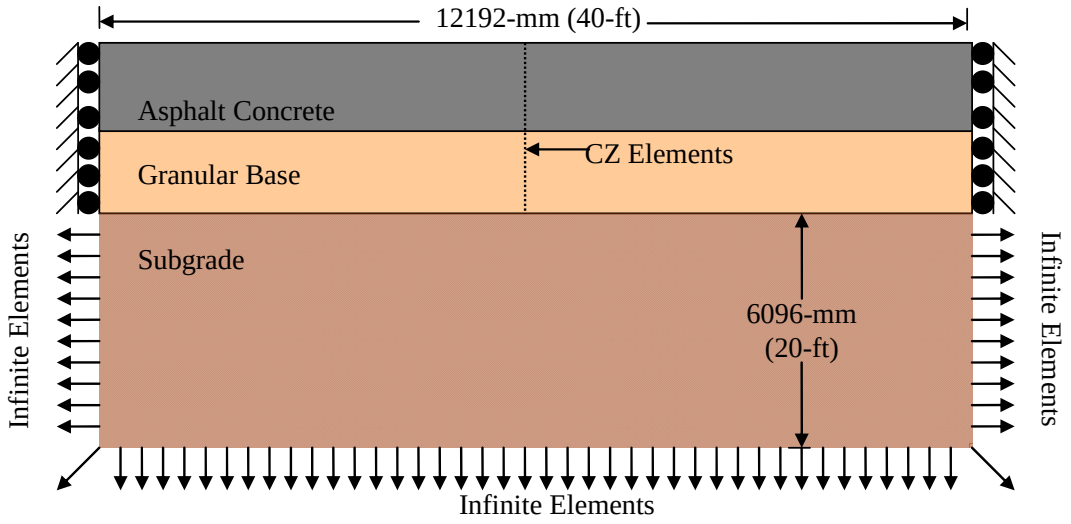

Figure 9.15. Schematic showing FE Model of pavement

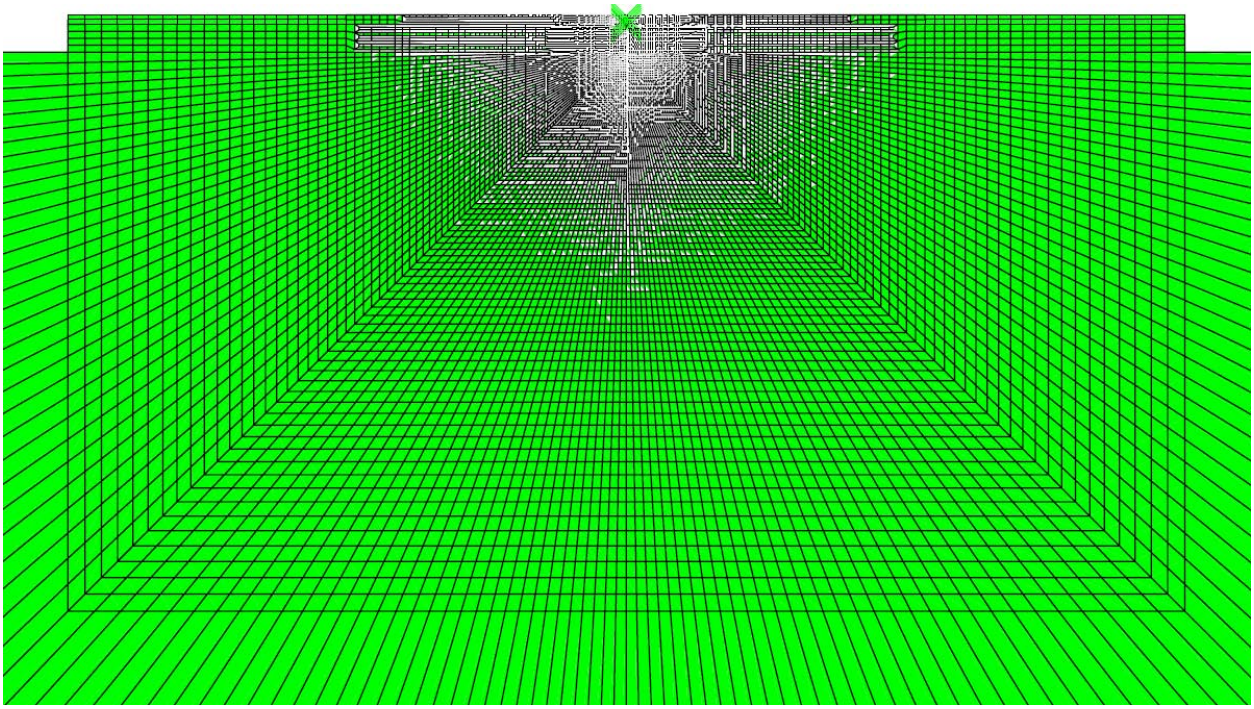

(a) FE Model (Entire Domain)

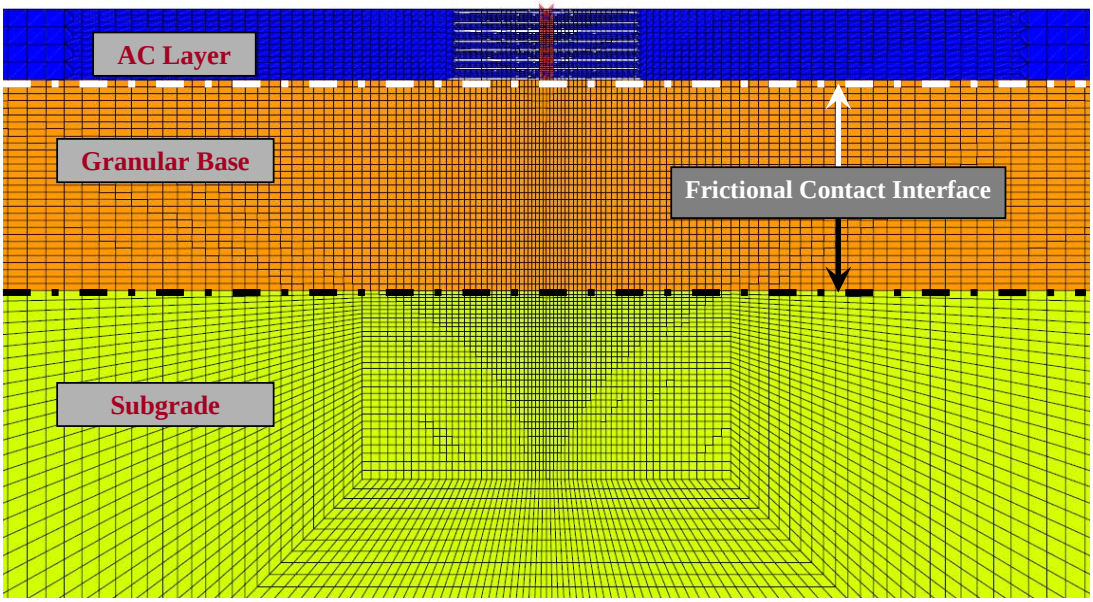

(b) FE Model Mesh Details, Slightly Magnified in Crack Path Region

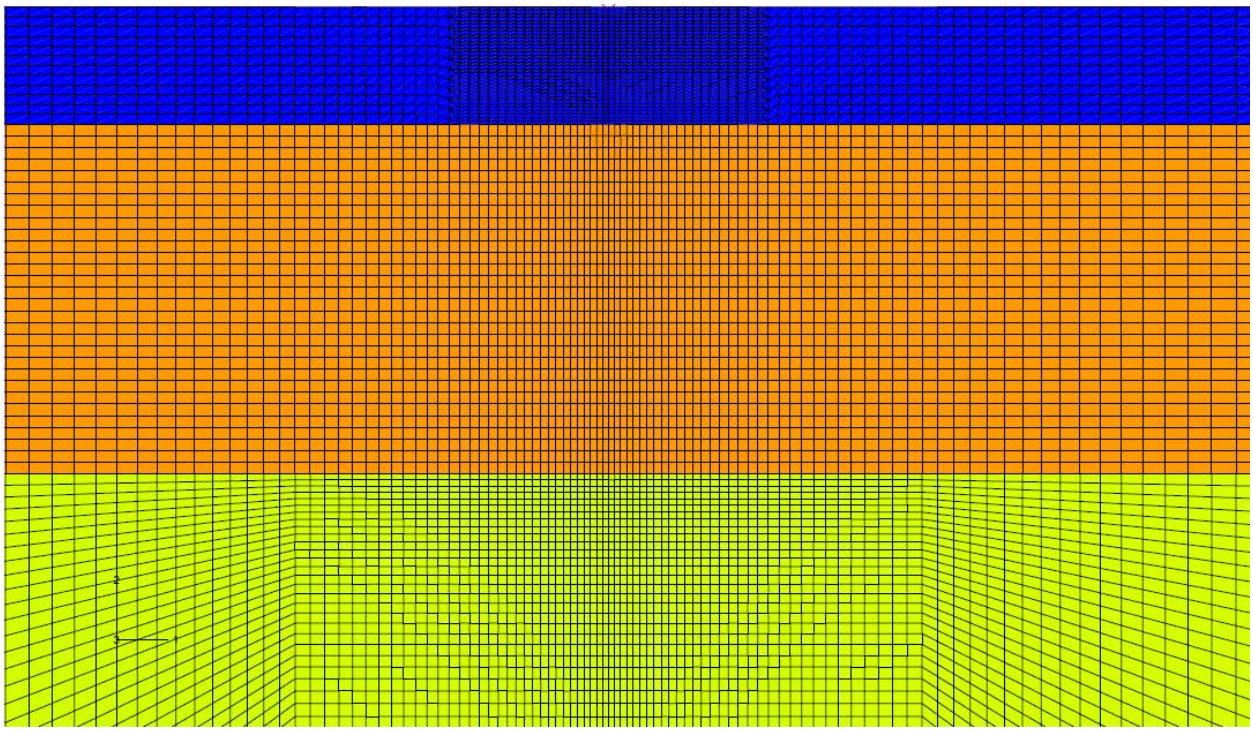

(c) FE Model Mesh Details, with Additional Magnification in Crack Path Region

Figure 9.16. Typical Finite Element mesh

Loading Conditions

Pavements undergo relatively complicated loading conditions during the course of their service life. The three main loads which were imposed on the pavement model include:

- Gravity loads;

- Thermal loads, and;
- Tire loads

The gravity loads are imposed in the FE model using an initial loading step, with time independent loading conditions. For all of the simulations performed in this project, gravity loading conditions were imposed. The FE code ABAQUS calculates gravity loads automatically based upon the density of materials and the geometry of the model structure. The thermal (or temperature) loads and tire loads are discussed in detail in the next two subsections.

Thermal Loads and Critical Conditions Analysis

Thermal loads on the pavement structure are transient and depend on factors including air temperature, percent sunshine, wind speed, latitude, etc. The thermal loads for various pavement sections in this project were evaluated using Enhanced Integrated Climatic Model (EICM) developed by Dempsey et al. (105). The EICM is built into the AASHTO M-E PDG software; this was used to generate the pavement temperature profiles as functions of depth and time. The temperature loads were applied to the model in terms of transient temperature values for each node in asphalt concrete. A user-subroutine was developed to automatically evaluate the nodal temperatures values based on the node location and time in the simulation.

The coolest pavement temperatures reached during the course of pavement life were generally selected for simulations in an effort to focus on a **critical conditions** analysis. In certain cases, additional critical conditions were identified where the highest rates of pavement cooling occurred (in combination with very low temperatures, but perhaps not the coldest absolute temperature reached). The rational for taking the aforementioned critical conditions approach focusing on very low temperatures stemmed from three considerations:

(1) experimental fracture energies were noted to drop significantly at very low temperature;

(2) the ability of the bulk material to relax stress is greatly reduced at low temperatures, and;

(3) most cracking in the field studies were reported to have occurred over the winter months.

Another motivation for limiting the analyses to colder temperatures is associated to the overall emphasis of this project (low temperature cracking) and the difficulty in obtaining and modeling bulk and fracture properties at higher temperatures. For bulk materials tested at higher temperatures, material nonlinearity (necessitating multiple stress states), and the need for triaxial testing arrangements, require additional testing and modeling resources. Material fracture will not occur at higher temperatures in general (as noted in laboratory testing, for temperatures about 0C and greater depending upon asphalt characteristics). Instead, a form of viscous separation is observed. This type of material response has received little attention and would be very difficult to obtain experimentally. In the future, as computational speeds are increased, it would be more feasible to model continuously throughout the year, as is done in TCMODEL. Still, improvements in material characterization and models will need to occur first. Only at this point can the veracity of the critical conditions approach be validated.

Tire Loads

A limited number of simulations were performed with tire loads applied to the pavement in simulation models. Tire loads can be applied to pavement models through various approaches. In the current study, and on the basis of previous work performed by Kim and Buttlar (106) and Buttlar et al. (107), tire loads were discritized as a number of point loads applied over the nodes. In this approach, the magnitude of the point load depends upon the magnitude of local load intensity and the distribution of load across elements having the particular common nodes. This

discretization procedure is based on the principle of equivalent work. This type of approach is especially important for loads applied in regions of varying element sizes.

Boundary Conditions

Selection of boundary conditions is arguably just as important as setting realistic loading conditions. The first step in determining boundary conditions includes determination of domain extent (how much of the pavement is modeled). As described earlier the domain extent for this study was determined on basis of the previous experience obtained during other pavement simulations performed in other projects.

Due to the infinite nature of the soil subgrade the boundary conditions were represented using a specialized type of elements known as "infinite" elements. These types of elements are used to represent an infinite extension of the subgrade. Another important aspect of boundary conditions involves the type of boundary conditions imposed at the lateral boundaries of the pavement model (e.g., pinned versus roller support at nodes). In general, asphalt pavement continuity in the x-direction is established by placing vertical rollers at the model edge so that horizontal thermal stresses can develop upon cooling. Thermal contraction strains lead to tensile stress development due to the restrained boundary condition. Vertical contraction is not restrained, but is relatively small and inconsequential in the scope of thermal crack simulation.

Other boundary considerations include the interface conditions between various pavement layers. The interface between asphalt concrete and granular base and granular base and soil subgrade is especially important because of the potential for relative movement between these layers. In the current project these interfaces were modeled using a small-sliding frictional interface model available in ABAQUS. This model allows for a frictional sliding of the asphalt concrete due to thermal expansion/contraction. In the current model simulations, the interface behavior is important for the proper simulation of pavement response under traffic loading and combined thermal and traffic loadings. Although beyond the scope of the current simulations, interface behavior is also very important for multiple crack simulations, where frictional sliding of pavement sections and development of associated thermal stresses is critical in determining crack spacing versus time.

Input Parameters for FE Model

Various inputs that are utilized in the simulation of low temperature cracking of asphalt concrete are described in this section. Various material properties/inputs utilized for the current FE modeling approach are as follows:

- Asphalt Concrete Mixtures:
  - Relaxation modulus master curve
  - Temperature shift factors
  - Fracture energy at low temperature
  - Tensile strength
  - Coefficient of thermal expansion (coefficients above and below glass transition temperature and glass transition temperature)
- Granular Base and Soil Subgrade
  - Material Classification

Pavement layer thicknesses are required for construction of the pavement model. This includes layer thicknesses of asphalt concrete layer(s), base and sub-base. For imposing the thermal

loading the climatic and geographic conditions are required. Climatic information associated with field sections to be simulated is available in form of hourly climatic databases which can be generated through the AASHTO M-E PDG software. The hourly climatic databases in the M-E PDG generally date back a maximum of 9 years – thus in absence of the hourly climatic databases for older pavements, the climatic inputs can be determined from the National Oceanic and Atmospheric Administration (NOAA) climatic databases available from their website (www.noaa.gov).

Standard Schemes for Presentation of Simulation Results

The results from FE analyses of pavements can be presented in a number of different ways using available post-processing techniques. For instance, stress contour plots are often generated and presented. Because of the complexity of low-temperature cracking simulation outputs and the need to track crack propagation and other crack front response, a special scheme has been developed in an attempt to allow the reader to better visualize the analysis results and to rapidly compare results between various sections. This section details standard formats used for x-y style plots. Simulation results are typically presented in this report in two ways:

1. Graphical plots showing opening displacements and thresholds of softening and complete separation: These results are very useful for the detailed examination of pavement response (CZ element opening, separation, and fracture).
2. Tabulated results: Useful for more detailed examinations of numerical results, as well as for quick, relative comparisons.

These procedures will be discussed using an example that involves a simple simulation of a beam loaded in 3-point bending. As discussed earlier a bilinear cohesive zone model was used for simulation of low temperature cracking in various pavement sections. This model provides the behavior of material within the cohesive zone (between interface elements). The model represents the opening (displacement jump), δ, and the load carrying capacity between the two faces, or traction T_n. Figure 9.17 illustrates the bilinear cohesive zone model. The model indicates the threshold for the opening between two faces of material at which the linear material behavior is transformed to softening region. The label '**S**' marks the displacement threshold separating these two regions. Similarly the displacement threshold for fully separated (cracked) region is indicated by the label '**C**'.

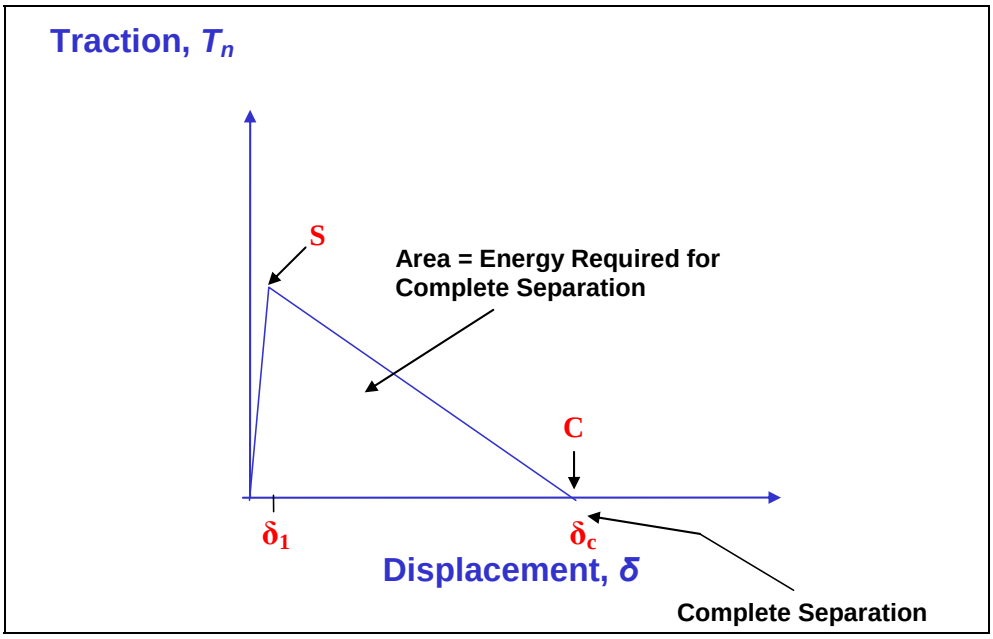

Figure 9.17. Parameters associated to the Bilinear Cohesive Zone Model

Figure 9.18 shows the schematic of a beam in 3-point bending with cracking at the center span. The label 'S' indicates the boundary between softened region and linear material behavior and label 'C' indicates the location of crack tip. The simulation result for this problem is presented in Figure 9.19. The plot provides the opening displacement for the cohesive zone elements along the height of beam. The thresholds for beginning of softening and cracking (complete separation) are also indicated on the plot using vertical lines at displacements of δ_1 and δ_c respectively. Table 9.2 indicates the positions within the beam which have completely separated (cracked) and the positions which are in the softening regime.

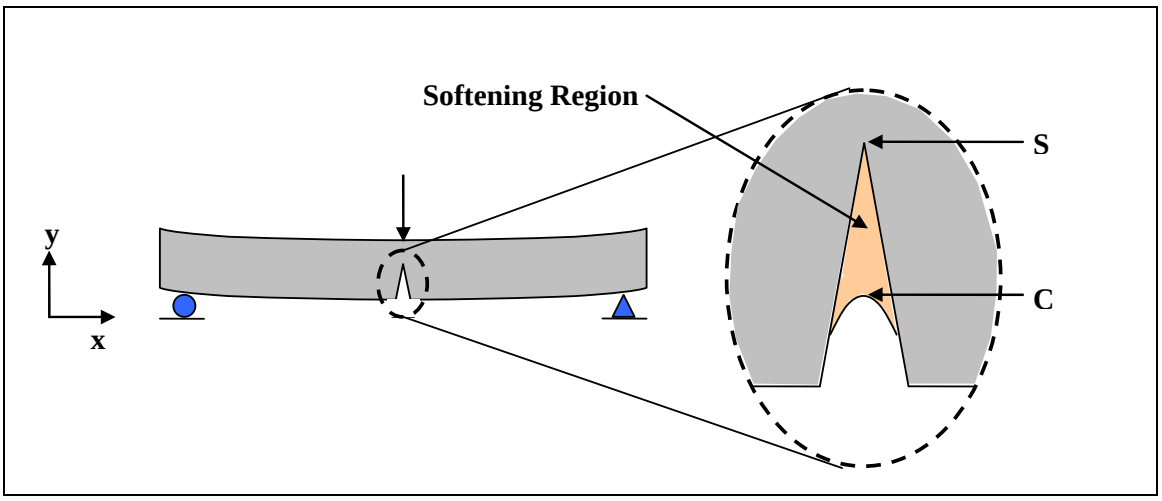

Figure 9.18. Schematic showing softening and separation regions

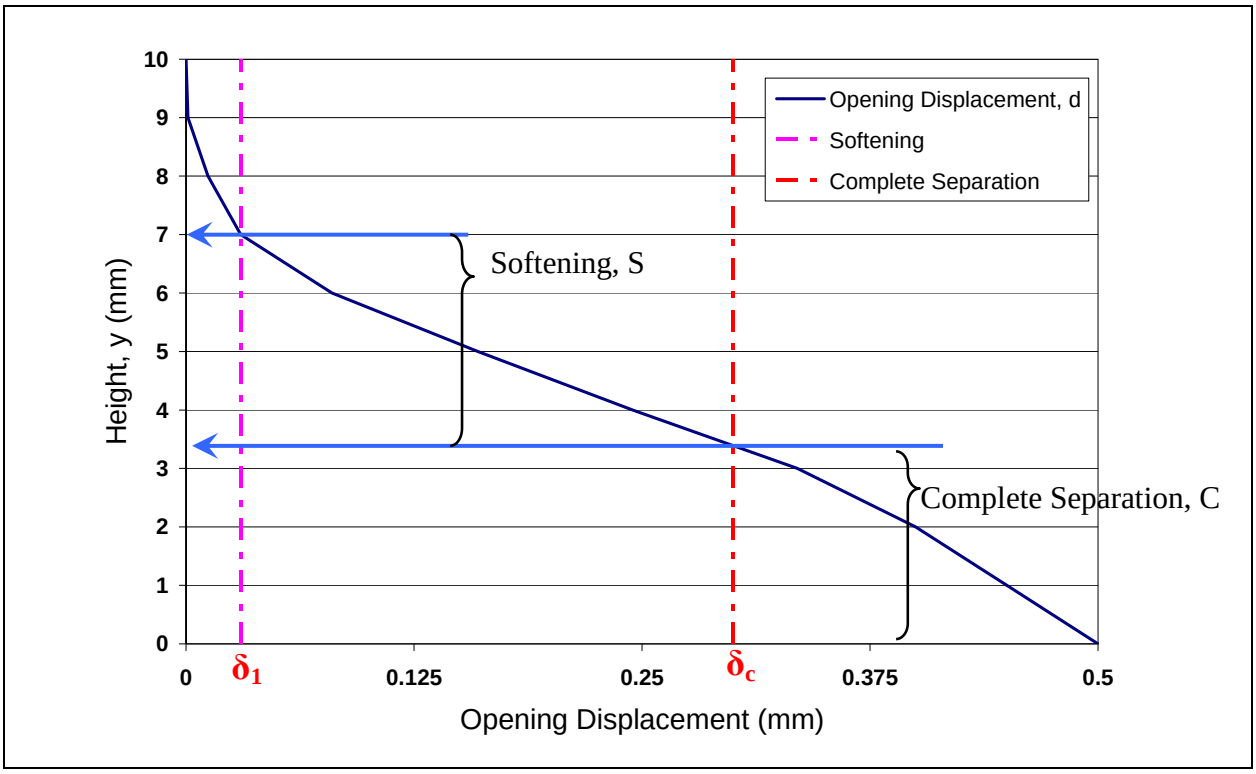

Figure 9.19. Graphical plots for beam example

Table 9.2. Tabulated result for beam example

Layer (thickness)	Length of Crack from the bottom of layer (mm)	Length of softened region (mm)
Beam (10mm)	3.4	3.6

Model Predictions

The results for various FE simulations of pavement sections are discussed in this section. The following pavement sections have been studied using the FE modeling approach described in the previous section:

1. MnROAD Cell 03
2. MnROAD Cell 19
3. MnROAD Cell 33
4. MnROAD Cell 34
5. MnROAD Cell 35

Cells 03 and 19 were constructed in the same year and are part of the high volume (Interstate 94) traffic sections at MnROAD. Cells 33, 34 and 35 were constructed in the same year, and are in the low-volume loop at MnROAD and have very similar paving structures, but utilize different PG binder grades in the HMA surface.

MnROAD Cells 03 and 19

Figure 9.20 illustrates the structure and material details for the FE model of cells 03 and 19. Figure 9.21 shows the temperature profiles for the asphalt concrete layers during the coolest temperature event. The coolest event for cells 03 and 19 occurred February 1st – 2nd, 1996. During this coolest event the air temperature dropped to -39.7 C. The pavement surface temperature was predicted to reach a minimum of -33.8 C.

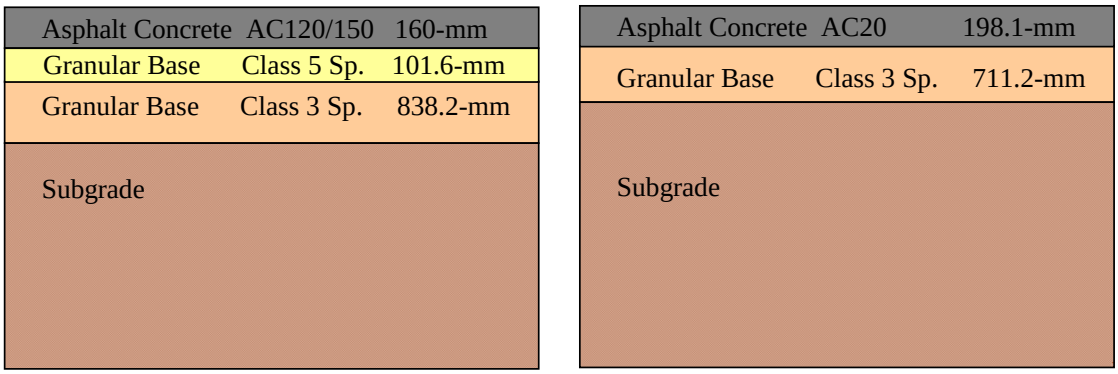

MnRoad Cell 03 MnRoad Cell 19

Figure 9.20. Material and structure details of Cells 03 and 19

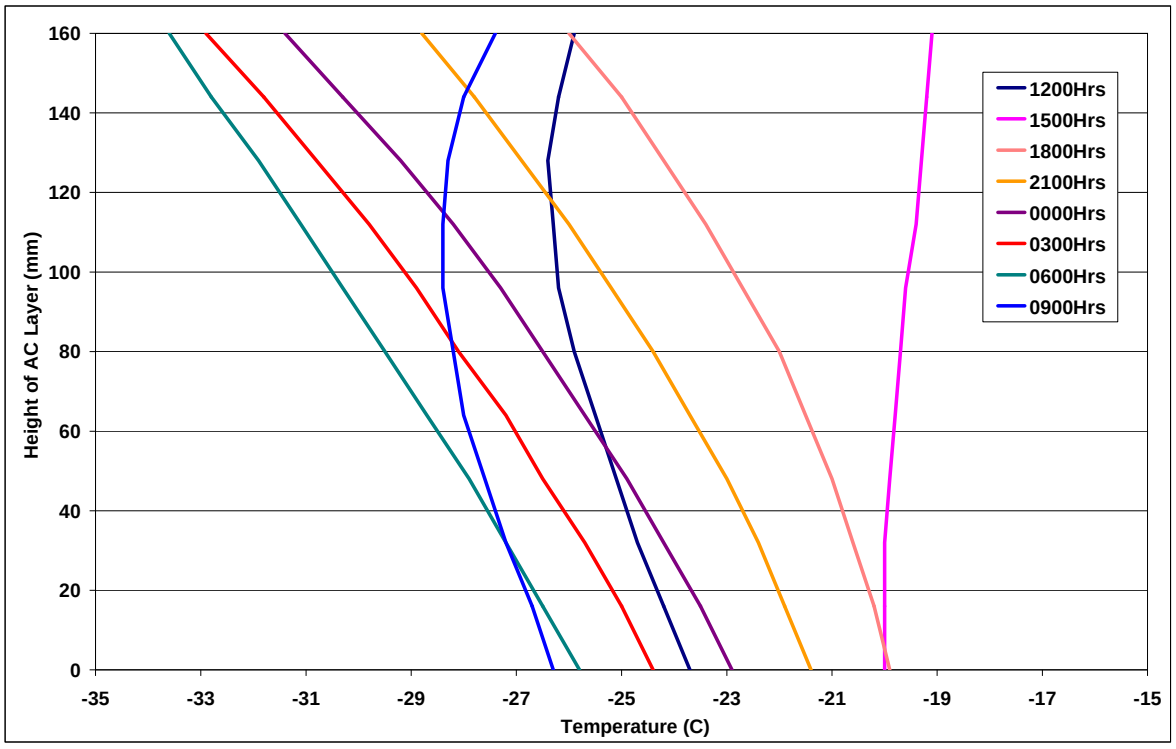

(a) MnROAD Cell 03

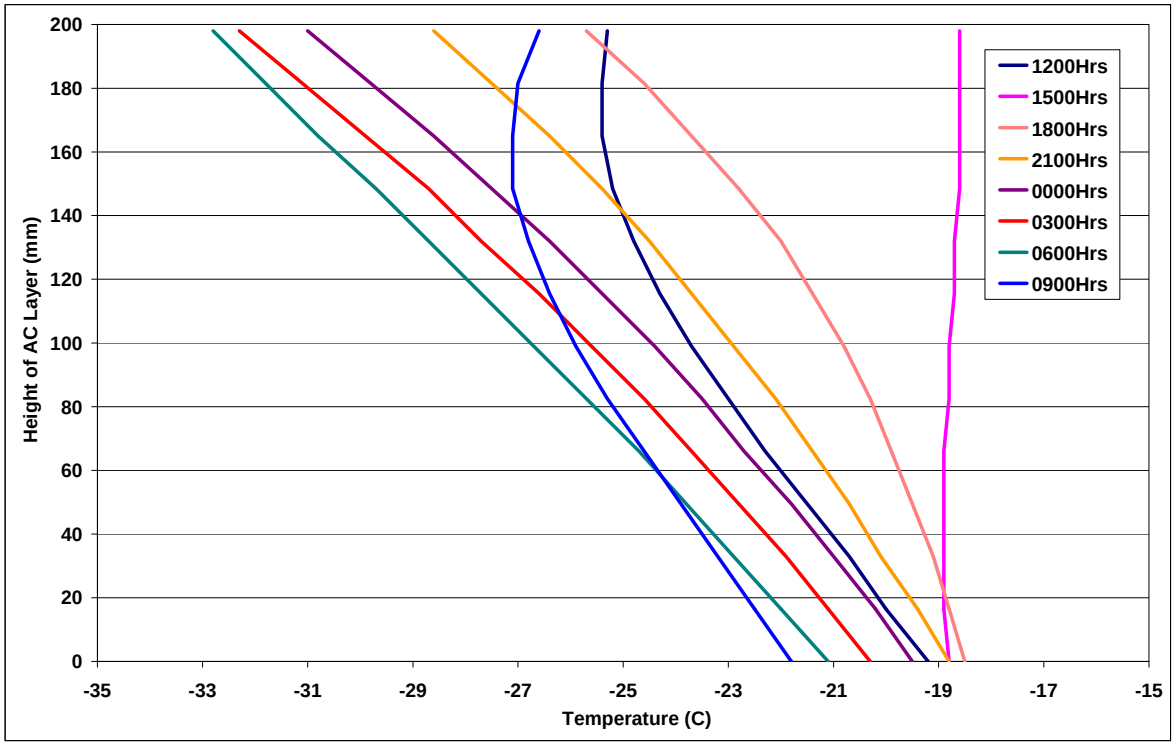

(b) MnROAD Cell 19

Figure 9.21. Critical cooling event (02/01 – 02/02/1996); pavement temperature profiles for Cells 03 and 19

The temperature profiles shown above were applied to the FE models in the form of thermal loads. The simulations were performed with hourly temperature load increments assuming that temperature variations are linearly varying for each hour. The simulations for both MnROAD cells 03 and 19 predicted thermal cracking throughout the thickness of asphalt concrete during the single event cooling cycle. The cohesive zone opening displacement plots for these sections are shown in Figure 22. The simulations indicated a crack starting at the surface of asphalt concrete extending to the bottom. Cell 03 underwent the thermal cracking at lower temperatures compared to cell 19, indicating that cell 19 has higher possibility of thermal cracking. It is also apparent from the extent of crack opening (crack width), which is more than two-folds higher in case of cell 19. Although multiple cracks were not simulated herein, it is anticipated that fairly close crack spacing would have been predicted had multiple cracks been simulated, based upon the relatively large contractions predicted at the crack sites.

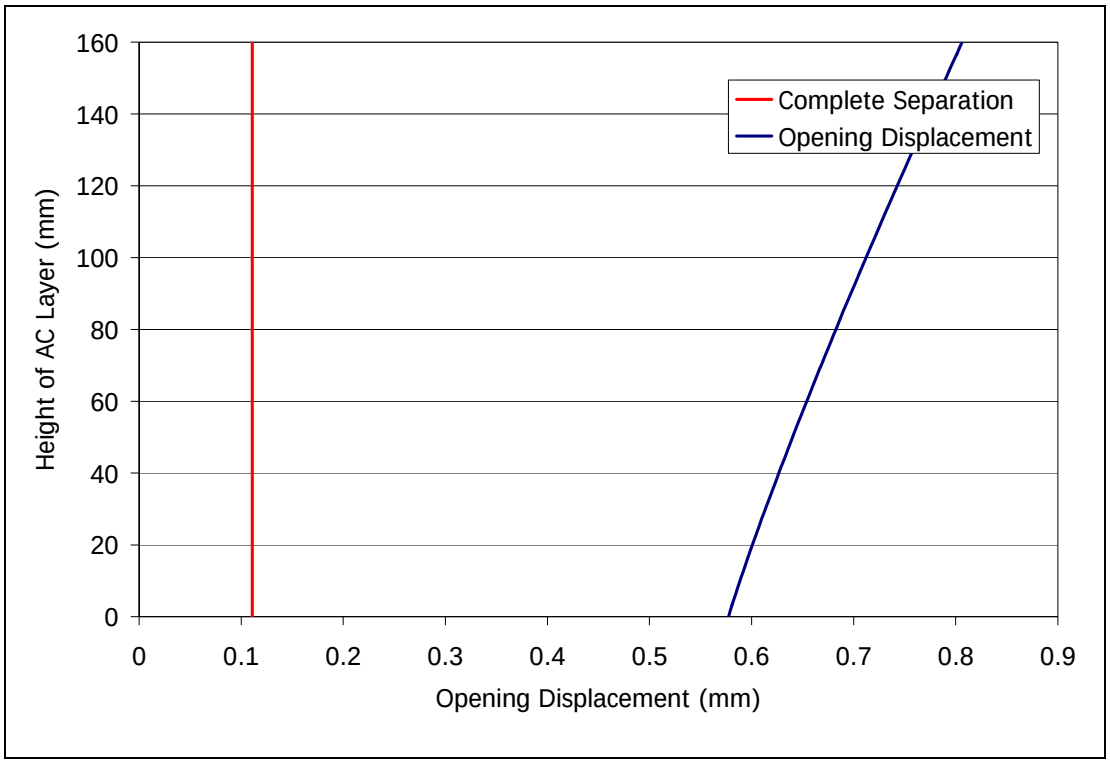

(a) Cell 03

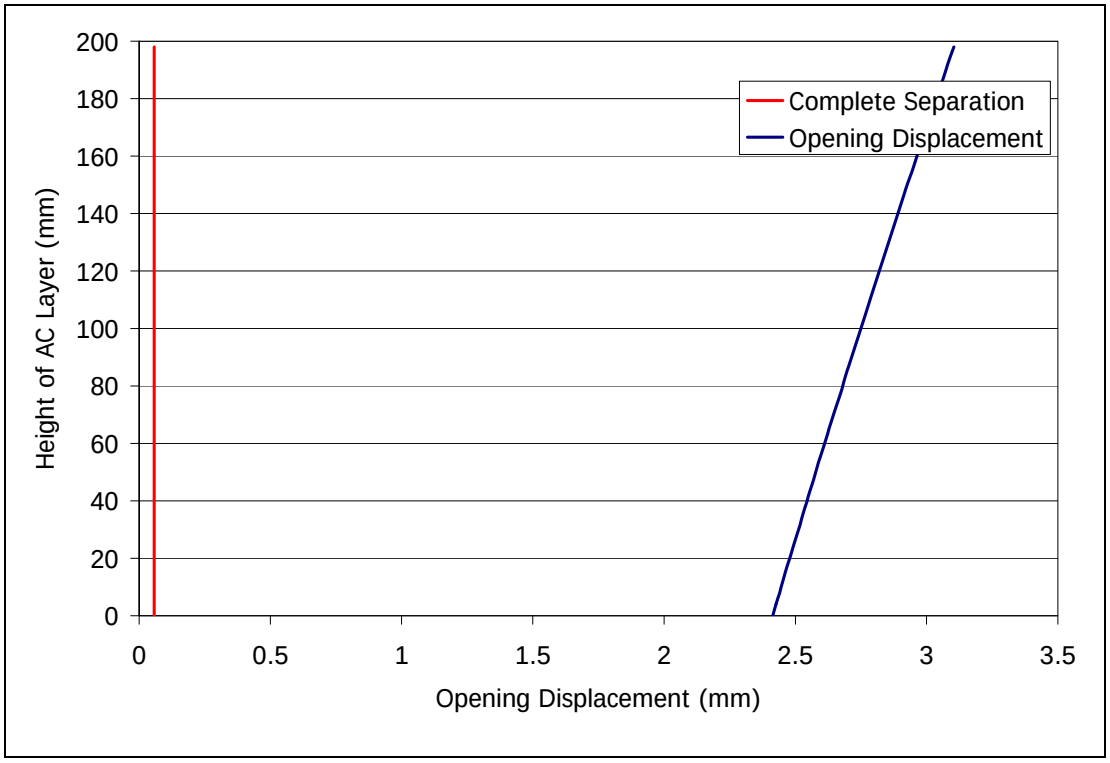

(b) Cell 19

Figure 9.22. Opening displacement plots showing thermal cracking in Cell 03 and 19 due to single event cooling

Table 9.3. Extent of Cracking and Softening in Cells 03 and 19 due to Single Event Cooling

Layers (Thickness)	Length of Crack from the top of layer (mm)	Length of softened region (mm)
Cell 03		
AC Course (160-mm)	160-mm	--
Cell 19		
AC Course (198-mm)	198-mm	--

MnROAD Cells 33, 34 and 35

The structure for sections 33, 34, and 35 are very similar, differing only in the PG binder grade used in the asphalt concrete mixtures. Figure 9.23 illustrates the structure and material details for the FE model. Figure 9.24 shows the temperature profile for the asphalt concrete layers during the coolest temperature event. During the service period of these pavement sections, the coolest event occurred during the 30th – 31st of January, 2004. During the coolest event, the lowest air temperature reached -31.1 C. **The pavement surface temperature was predicted to reach a minimum of -26.2 C. Thus, all three PG binder grades used, e.g., PG 58-28, PG 58-34, and PG 58-40, would be expected to prevent thermal cracking under this critical cooling event.**

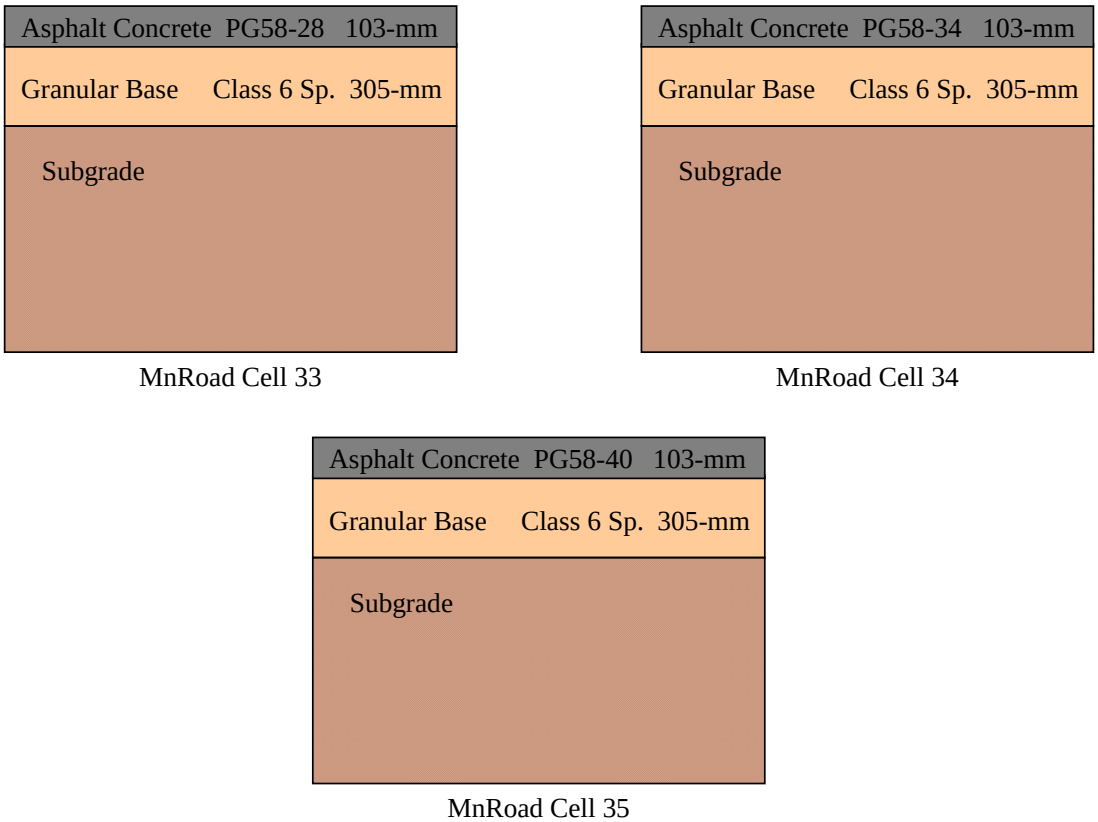

Figure 9.23. Material and Structure Details of Cells 33, 34 and 35

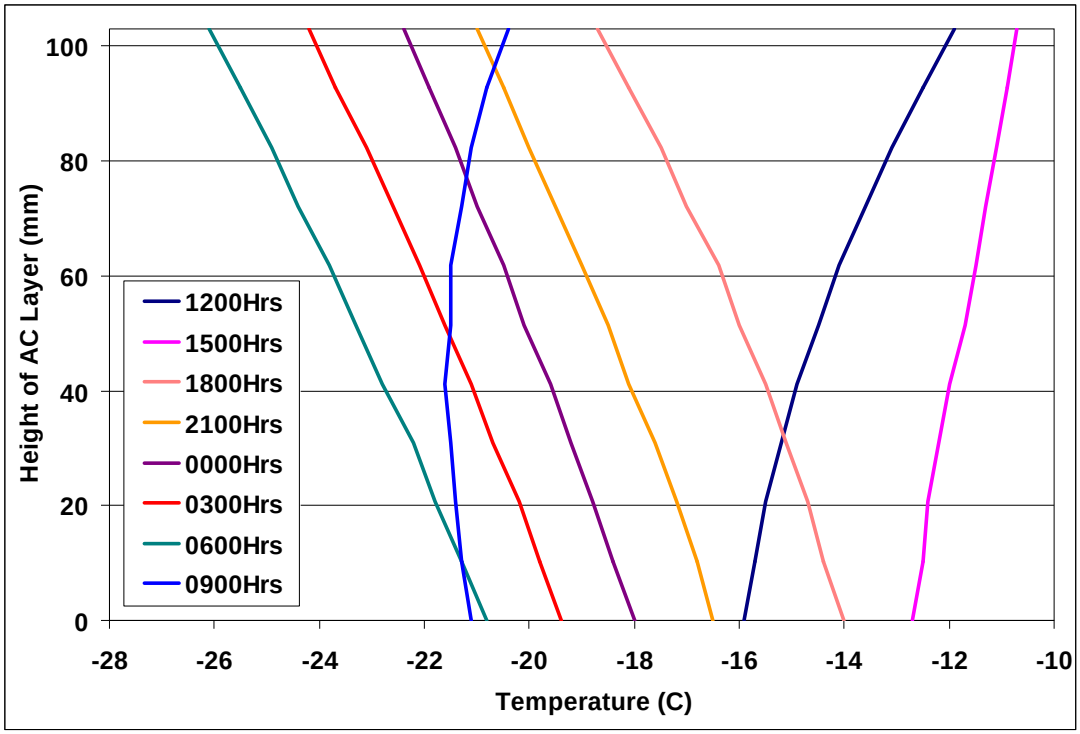

Figure 9.24. Coolest event on record (01/30 – 01/31/2004); pavement temperature profile for Cells 33, 34 and 35

FE simulations were performed for cells 33, 34 and 35 using the thermal loads for the coolest event shown above. The results of the thermal loading suggest the following conclusions:

- Not surprisingly, the simulations predicted that thermal cracking would not occur in any of the cells due to this single event thermal loading. The cohesive zone opening displacement plots for these sections are shown in Figure 9.25. The plots show that there was no cracking or softening in any of these sections under the critical cooling event.
- However, it can be clearly seen that the response of the pavement with the PG 58-28 binder was approaching a critical level of tension on the surface, which is reasonable for a critical cooling event so close to -28 C (e.g., the surface reached a minimum temperature of -26.2 C).
- Interestingly, the PG 58-40 binder showed slightly worse thermal behavior that the PG 58-34 binder, which was not intuitively expected. This can be observed by comparing Figures 9.25b and 9.25c, where the blue line for the PG 58-40 binder actually indicates 'worse' response than the PG 58-34 binder. Although neither response is remotely critical under this cooling cycle, the reverse ranking might suggest an anomaly in the mechanical properties of the PG 58-40 binder.

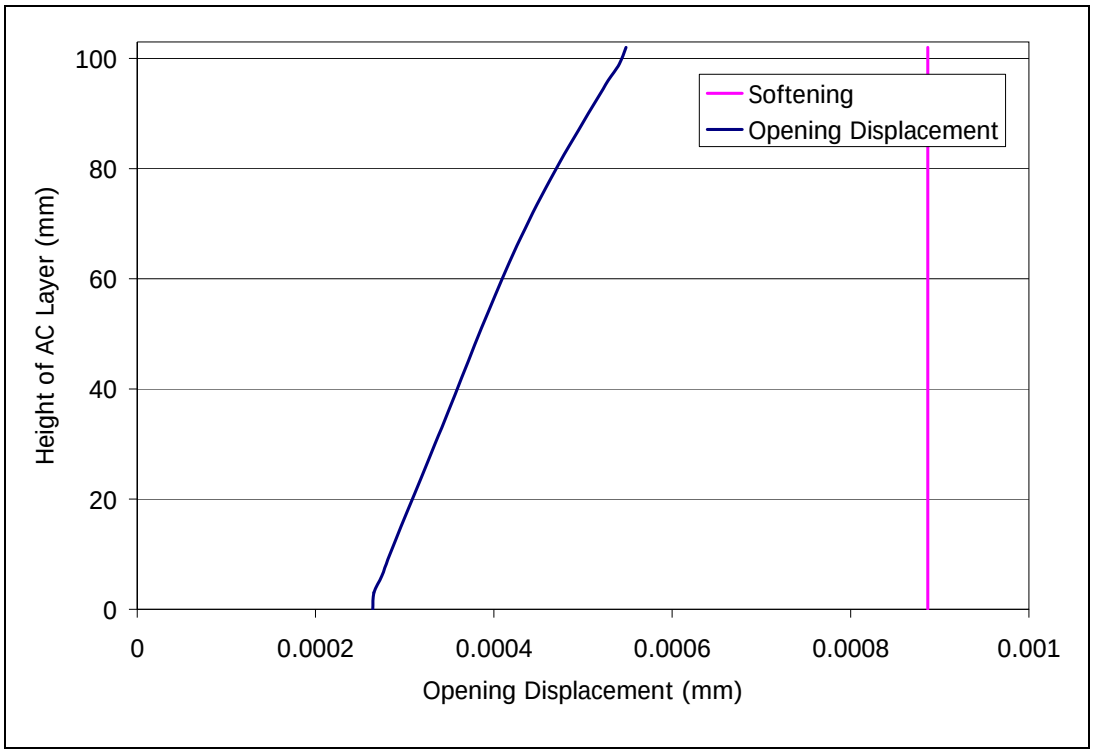

(a) Cell 33

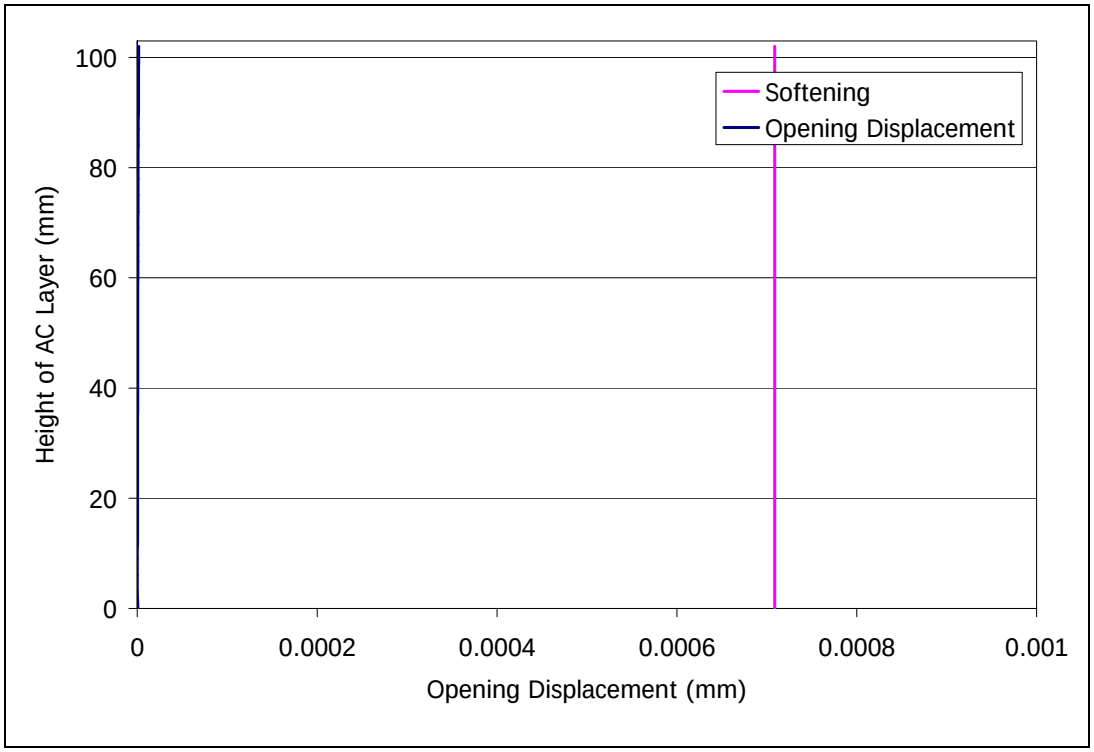

(b) Cell 34

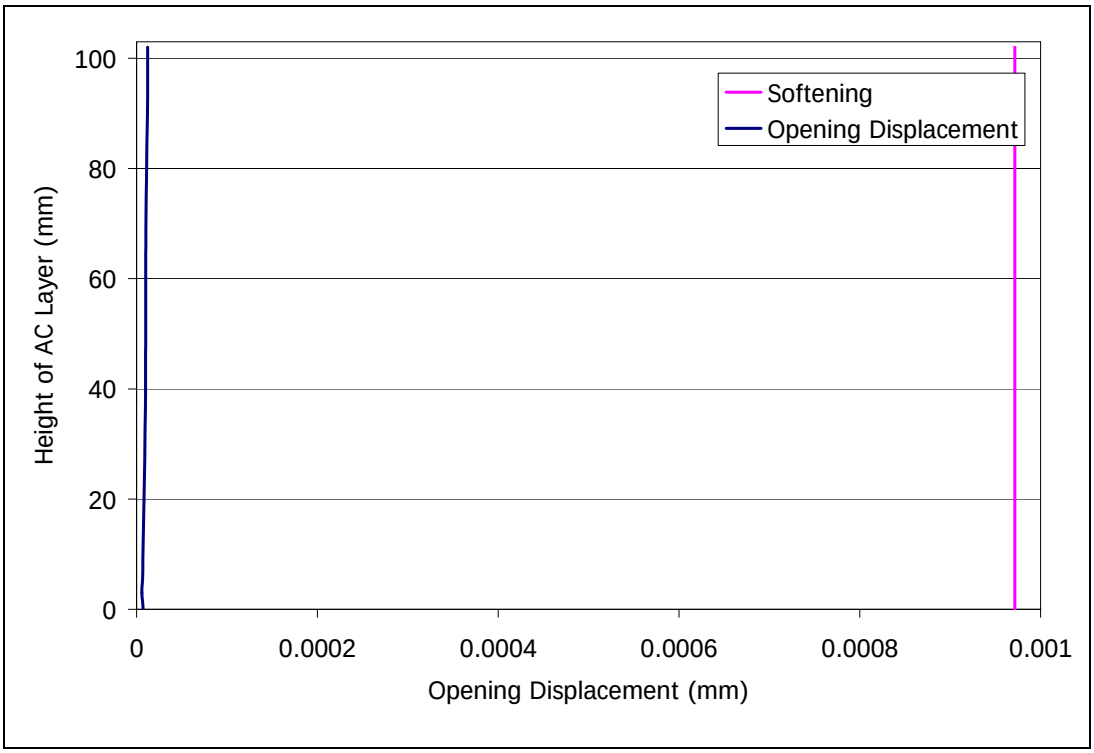

(c) Cell 35

Figure 9.25. Opening displacement plots showing due to single event cooling cycle for Cells 33, 34 and 35

Table 9.4. Extent of cracking and softening in Cells 33, 34 and 35 due to Single Event Cooling

Layers (Thickness)	Length of Crack from the top of layer (mm)	Length of softened region (mm)
Cell 33		
AC Course (103-mm)	--	--
Cell 34		
AC Course (103-mm)	--	--
Cell 35		
AC Course (103-mm)	--	--

In order to evaluate the possibility of cracking due to the effects of traffic loads combined with thermal loading, a limited set of analyses were conducted. For cells 33, 34 and 35 a single tire load was applied at the coolest temperature. In the case of two-dimensional model, the tire load is approximated in the form of an infinitely long strip along the depth of model (width of pavement). The load was applied in the form of a 9-kip (40-KN) single tire load. Figure 9.26 provides a schematic for the application of a tire load in the FE model. The cohesive element

displacement plots for cells 33, 34, and 35 with tire loading are shown in Figure 9.27. The results are provided in Table 9.5.

The results of the thermo-mechanical (combined) loading suggest the following conclusions:

- The model did not predict that cracking would occur due to a single tire load occurring at the coolest event in each of the three cells.
- However, cells 33 and 35 were predicted to have experienced a significant amount of softening from the 'bottom up,' while cell 34 was predicted to have only a very limited extent of this type of softening.

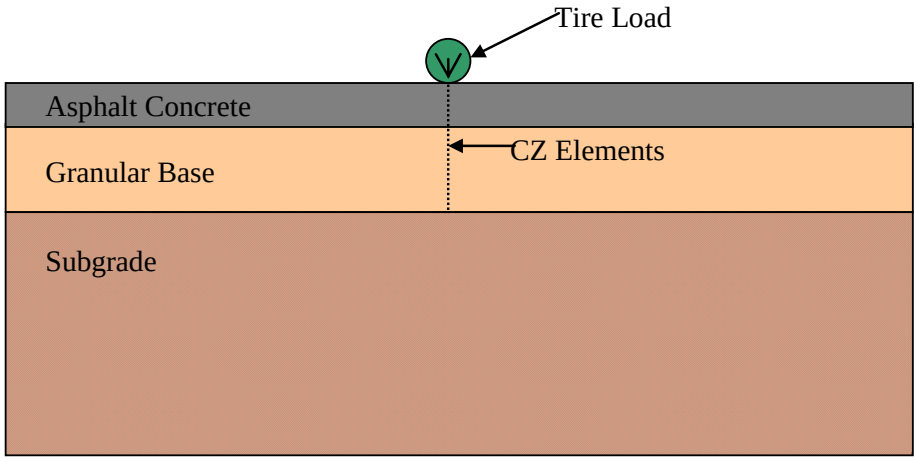

Figure 9.26. Schematics for tire load simulations

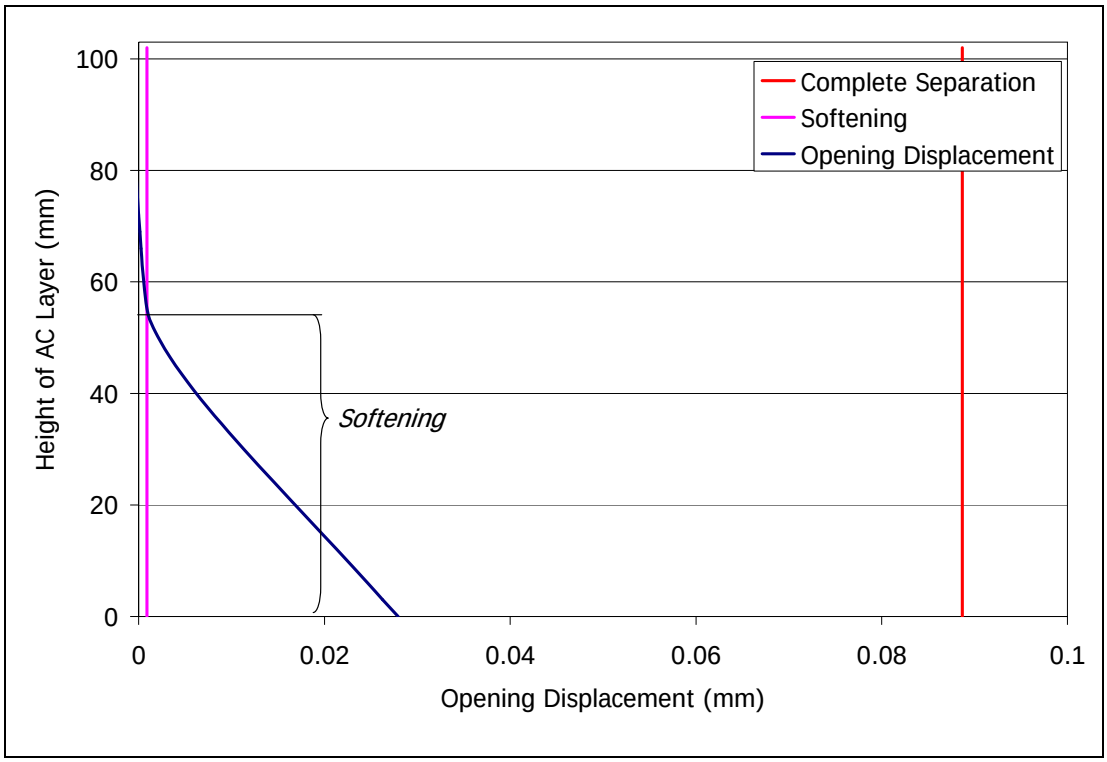

(a) Cell 33

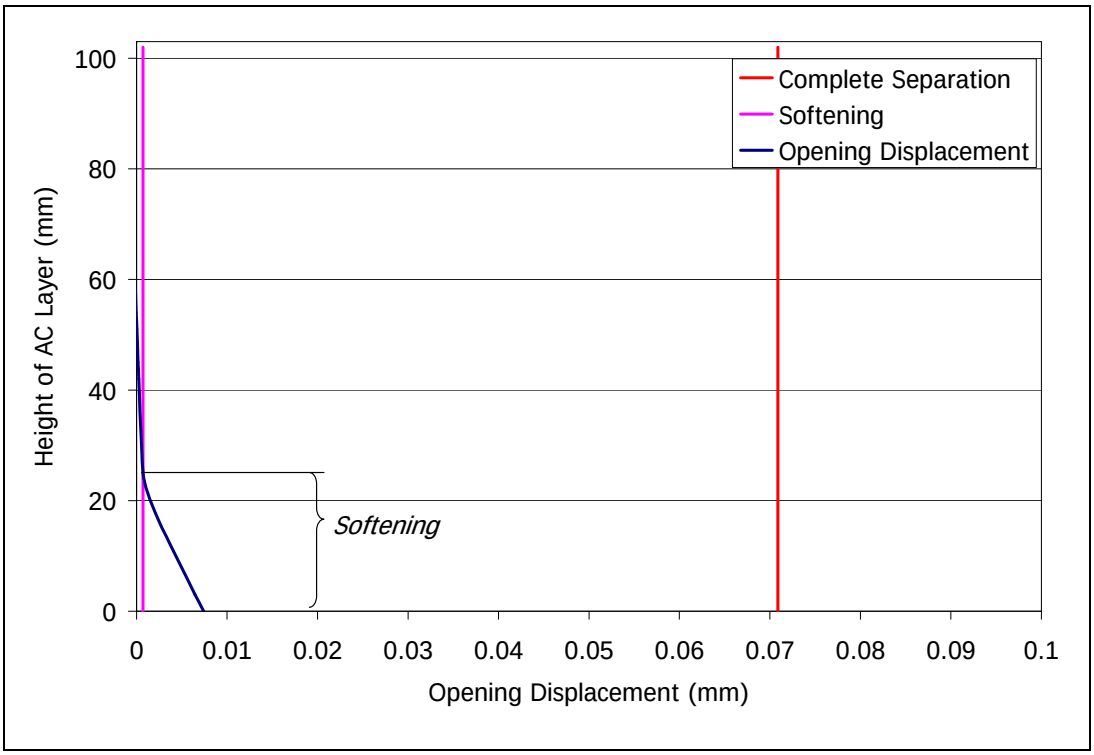

(b) Cell 34

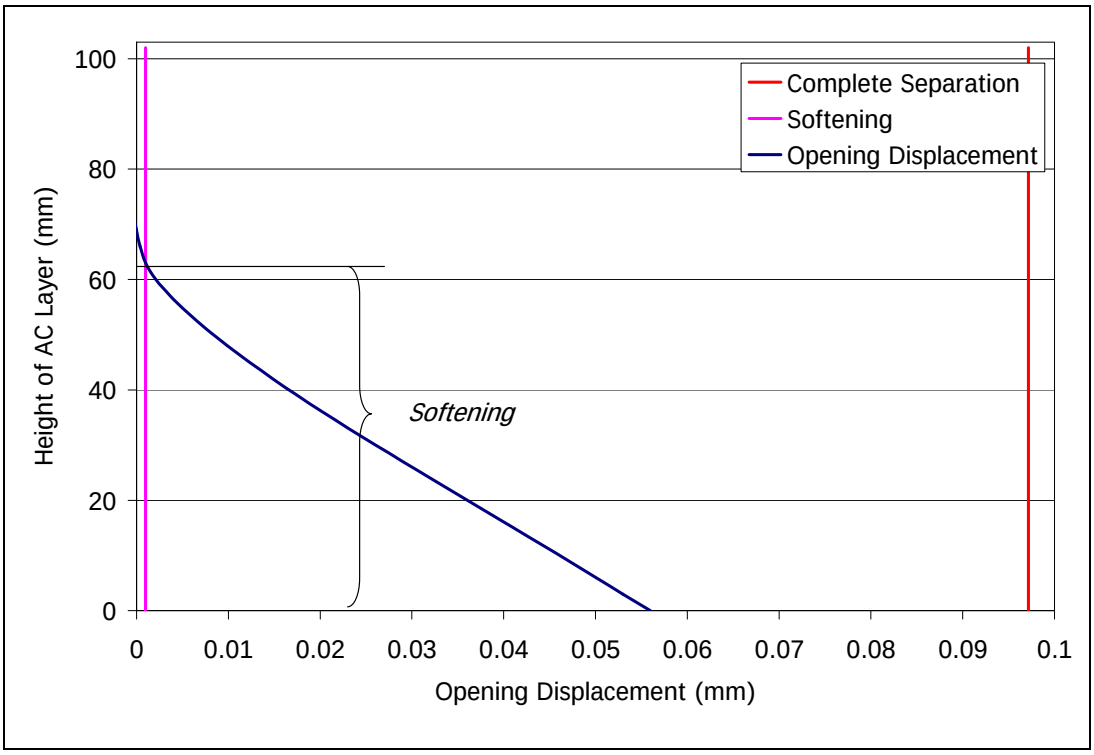

(c) Cell 35

Figure 9.27. Opening displacement plots for Cells 33, 34 and 35 due to a single tire load applied during a coolest event

Table 9.5. Extent of cracking and softening in Cells 33, 34 and 35 due to single tire load applied during the coolest event

Layers (Thickness)	Length of Crack (mm)	Length of softened region (mm)
Cell 33		
AC Course (103-mm)	--	54-mm from bottom
Cell 34		
AC Course (103-mm)	--	24-mm from bottom
Cell 35		
AC Course (103-mm)	--	63-mm from bottom

Summary of Finite Element Simulation Results

The results for the FE-based thermal cracking modeling of the MnROAD cells can be summarized as follows:

- Cells 03 and 19 were found to be highly susceptible to low temperature thermal cracking during the coolest single event (24-hour) thermal cycle during the winter for 1995-96.
- Cell 19 showed higher thermal cracking potential compared to cell 03. The higher thermal cracking potential of cell 19 is attributed to an inferior asphalt binder grade for the mixture (AC-20 vs. PEN 120-150), which concurs with field performance. Cell 19 asphalt concrete fracture properties are inferior to those of cell 03 and the viscoelastic properties indicate that the mixture is less compliant, thus leading to increased thermal stress and even more rapid crack development.
- Although the analyses were limited to non-interacting cracks at the present time, the results strongly suggest that additional cracks would have developed in a multiple crack simulation.
- Cells 33, 34 and 35 showed very limited potential for thermal cracking under the most critical single event thermal cycle experienced to date (winter of 2003-04). Interestingly, the ranking of the material response along the analyzed cracking plane did not directly follow the ranking of the PG binder grades, indicating that the PG 58-40 binder may actually be inferior to the PG 58-34 grade on the basis of response to thermal loading.
- Simulations of cells 33, 34 and 35 subjected to a single tire loading during the critical cooling event indicated that cell 35 has the highest amount of potential for damage (softening) followed by cell 33. Again, the ranking of the material response along the analyzed cracking plane did not directly follow the ranking of the PG binder grades, indicating that the PG 58-40 binder may actually be inferior to both the PG 58-28 and PG 58-34 grades on the basis of response to combined thermal and traffic loading.
- The prediction of the higher extent of softening damage in cell 35 is due to the highly compliant asphalt mixture (PG58-40), which causes excessive deformation under the tire load. At the same time the fracture properties for this mixture is very similar to those of the cell 33 (PG58-28) mixture.

Summary, Conclusions and Recommendations

This chapter presented thermal cracking model predictions using the state-of-the-art TCMODEL program, along with demonstrative simulations using cutting edge finite element techniques. The goals of the analyses presented were two-fold: 1) to evaluate the predictive accuracy of TCMODEL under the current release of the M-E PDG, and; 2) to describe and demonstrate new fracture-based thermal cracking prediction tools.

Some difficulties were encountered in the evaluation of field sections using the TCMODEL program, including missing field performance data, the presence of very thin surface lifts on some field sections, and poor quality of IDT creep compliance data in a number of sections. In addition, the version of the M-E PDG used, version 0.964, is already outdated, as a bug was encountered and fixed, and the model was under recalibration at the time of this report. All those difficulties notwithstanding, it was still possible to evaluate TCMODEL in the context of version 0.964 by running the model in a semi-manual fashion using the available lab and field data. In general, the TCMODEL predictions using levels 1 and 3 were similar, with the level 3 predictions being slightly more conservative. Difficulties were encountered in interpreting the differences between reported transverse cracking in MnROAD cell 35 and TCMODEL predictions; however, finite element modeling provided some insight towards the discrepancies noted. The results of the analysis suggest that the TCMODEL program appears to do a reasonable job of predicting thermal cracking in the 'out of the box' form; e.g., using national calibration factors. By employing regional calibration, it seems reasonable to conclude that the model would be a useful tool for the design of pavements to resist thermal cracking, as it could be to identify mixtures with creep compliance, thermal coefficient, and/or tensile strength values which are inappropriate for a given selected climate. This would provide extra reliability against thermal cracking when used in combination with the PG binder selection system. The two weakest links in the TCMODEL system were: 1) the lack of true mixture fracture inputs, and; 2) the inability to directly consider traffic loading.

A series of thermal cracking simulations were carried out using cutting-edge finite element techniques with cohesive zone fracture modeling. Bulk material behavior was modeled with IDT creep compliance master curve information, while mixture fracture properties were obtained from disk-shaped compact tension tests. The finite element simulations were able to capture the damaging effects of the critical cooling event of February 1^{st} – 2^{nd}, 1996. Furthermore, the simulations were able to provide insight towards the unexpected ranking of field performance in MnROAD cells 33, 34, and 35, where the section with the softest binder experienced the most transverse cracking. The FE modeling helped quantify the manifestation of deficiencies (or at least anomalies) in the compliance and fracture properties of the PG 58-40 binder. A potential bottom-up cracking mechanisms was identified, which may explain the diffuse, non-continuous cracking pattern observed (Figure 9.11).

Based upon the findings of this investigation, the following recommendations are suggested:

- Consideration should be given to local or regional calibration of TCMODEL, followed by model validation
- Finite element analysis should be expanded to include: multiple cracks, thermal fatigue under multiple cycles, and extended to 3D.
- Although the ABAQUS program was very useful in proof of concept simulations, a standalone finite element thermal cracking code w/ a user-friendly interface is needed. Because of the relative simplicity of the CZM approach, the development of such a

standalone code is a relative straightforward task. This code could utilize portions of the existing TCMODEL code, and would serve as a next-generation TCMODEL program, capable of considering mixture fracture properties.

CHAPTER 10

SUMMARY, CONCLUSIONS AND RECOMMENDATIONS

This comprehensive research study brought together different experimental protocols and analyses and compared them based on a common set of asphalt materials and on well documented field performance data to determine the best combination of experimental work and analyses to improve the low temperature fracture resistance of asphalt pavements. The study was comprised of three major components:

1) Field investigation of 13 pavement sections, consisting of a range of laboratory tests and analyses performed on cores and beams cut from the pavements as well as field performance.
2) Comprehensive laboratory study in which the effect of two different aggregate types, ten different asphalt binders consisting of multiple crude sources and PG grades, two levels of air voids, and two levels of asphalt binder contents, on the fracture properties of asphalt mixtures were examined.
3) Advanced modeling of the low temperature cracking mechanism in asphalt pavements based upon the field and laboratory components.

Although this study investigated low temperature cracking, the research approach used can be extended to a wide variety of issues that many states have in common including fatigue, reflective, and top down cracking.

Summary

The literature review performed at the beginning of this study has shown that, although most researchers agree that fracture properties of both asphalt binders and asphalt mixtures is a critical requirement for both the material selection process and the stress analyses of the pavement, there is no consensus with respect to what experimental method to use. In addition, there is little understanding of the relations between the conventional material properties, used in the current specifications, and the fracture mechanics properties. The review also showed that the stress analyses methods available at this time to investigate asphalt pavements exposed to severe low temperatures and low temperature cycles have important limitations that make their applicability questionable. It appears that an analysis based on the fracture mechanics models, such as the cohesive zone model, may offer a more realistic approach to modeling the crack propagation in asphalt pavements.

The comprehensive experimental effort on both laboratory prepared specimens as well as field samples has resulted in a number of important findings.

The asphalt binder dilatometric results obtained for the PAV condition indicate a wide range of T_g values with a minimum value of -48.00 ºC and a maximum value of –21.1°C, a 27.0 ºC range. The results also show a wide range (143.1 to 350.6 x 10^{-6}/ ºC) for the thermal coefficients of contraction below T_g (glassy state α_g). The coefficients of contraction above T_g (liquid state, α_l) was in the range of 456.24 to 583.26 x 10^{-6}/°C, which is a narrower range than the values below T_g. As expected the values of α_g are always smaller than α_l and are in the range of 30% to 60%

of α_l. With two exceptions, the general trend in dilatometeric properties revealed that binders with a low-grade temperature (PG -yy) have lower T_g and higher thermal coefficients of contraction (α_g and α_l). When comparing the results for the PAV-aged versus the RTFOT-aged binders it was observed that the average value of the T_g did not change significantly. Also the values of the coefficients of contractions for the PAV-aged samples are on average slightly higher than the averages for the RTOF-aged samples. However, no specific trends were found as some binders showed an increase in coefficients of contraction after PAV aging compared to RTFOT, while others showed a decrease. For the binders extracted from the field mixture samples the T_g values ranged between -20.11°C and –40.69°C, the thermal coefficients of contraction below Tg (α_g) were between 220.76 and 335.16 x 10^{-6}/°C, while the thermal coefficients of contraction above Tg (α_l) were between 481.54 and 660.64 x 10^{-6}/°C.

The asphalt binders BBR results on the laboratory aged specimens followed the expected trends. Physical hardening, simulated by 20 hours specimen conditioning prior to testing was found to be significant and the largest effect was noticed in the RTFOT-aged binders. It was also noticed that this effect weakened with the amount of aging and became less temperature dependent for the PAV-aged binders. The results for the extracted binders indicated that for most of the samples the stiffness and the m-values were much higher, and respectively lower, even at the highest of the three temperatures which is above the approximate PG of the original binder.

The asphalt binders DT and DENT results did not rank binders similarly in terms of failure stresses or failure strains. However, a comparison of the critical temperatures T_{cr} calculated using four different methods showed that all four methods follow similar trends that partially support the PG system.

The asphalt mixture fracture tests showed that in terms of fracture toughness two mixtures with PG 58-28 plain 1 binder, 7% air voids and limestone aggregate type had the lowest toughness values for all three temperature levels. At the two higher temperature levels, mixture with PG 64-34 modified by modifier 2 binder, granite aggregate, 4% air voids and optimum asphalt content had the highest toughness value. However, mixture with PG 58-34 and modified by modifier 1 binder, granite aggregate, 4% air voids and optimum asphalt content had the highest toughness value at the highest temperature level. For the fracture energy, the three mixtures 58-40:M1:4:GR:+0.5AC, 58-40:M1:4:GR and 64-34:M2:4:GR had the first, second and third highest values, respectively, at the two lower temperatures. For the highest temperature, mixture 64-34:M2:4:GR had the highest fracture energy. Similar to the fracture toughness, the mixtures with PG 58-28 plain 1 binder, 7% air voids and limestone aggregate type had very low toughness values for all three temperature levels.

The trends observed from the fracture testing did not match the trends observed in the IDT results. The mixtures containing granite are not always superior, in terms of the creep stiffness, compared to the limestone mixtures. However, the granite mixtures produced most of the time higher tensile strength, especially at the lower temperatures.

The TSRST results indicated that the laboratory mixture that performed best was 58-40:M1:4:GR:+0.5AC. The least satisfactory mixture was 64-22:U1:4:GR. As expected, the mixture containing binder with the highest lower limit grade (e.g. -22) was ranked as the lowest in thermal cracking resistance. There is a high correlation between the lower PG grade of the asphalt binder and the resistance to low temperature of the mixture as it was expected. The best binder was PG 58-40 with the SBS modifier, followed by the PG 64-34 Elvaloy binder. For these mixtures, 4% of air voids seems to work better than 7%. The highest fracture temperatures

were obtained when PG 64-22 and PG 58-28 unmodified binders were used. Additionally, on average the mixtures containing granite as aggregate performed slightly better than the mixture with limestone. For the field samples, the lowest fracture temperature was measured for MnROAD cell 35 at -34.8°C. On the average, the fracture temperature for the field specimens was -27.7°C and the average fracture strength was 2.6 MPa, much smaller than the strength values determined in the IDT.

A comparison of the rankings generated using similar parameters for binders and mixtures, respectively, indicated noticeable differences and the magnitude of these differences varied with temperatures. Also, within the same PG grade, mixtures with granite aggregates had lower critical temperatures compared to limestone mixtures.

Simple descriptive statistical parameters, such as Pearson and Spearman correlation coefficients, between the material parameters for the field samples calculated at the low pavement temperature at 50% reliability obtained for each site from LTPP database and LTPPBIND software and transverse cracking showed that only the fracture parameters were significant, in particular the mixture SCB fracture toughness and energy and the binder DT failure strain.

Based on the parameters and field information presented in the previous chapters a series of thermal cracking simulations were carried out using finite element techniques with cohesive zone fracture modeling. Bulk material behavior was modeled with IDT creep compliance master curve information, while mixture fracture properties were obtained from disk-shaped compact tension tests. The finite element simulations were able to capture the damaging effects of the critical cooling event of February 1st – 2nd, 1996. Furthermore, the simulations were able to provide insight towards the unexpected ranking of field performance in Mn/ROAD cells 33, 34, and 35, where the section with the softest binder experienced the most transverse cracking. The FE modeling helped quantify the manifestation of deficiencies (or at least anomalies) in the compliance and fracture properties of the PG 58-40 binder. A potential bottom-up cracking mechanisms was identified, which may explain the diffuse, non-continuous cracking pattern observed in MnROAD cell 35.

A database containing all the experimental results obtained in this study was developed and delivered to MnDOT for further use in conjunction with MnROAD dataset and the pavement management system database.

Conclusions

Based on the research performed in this study, the following important conclusions can be drawn:

- The current specifications for low temperature cracking for both asphalt binders and mixtures are based on static creep tests and do not include a fracture test. It is strongly recommended that the selection of fracture resistant binders and mixtures be based on simple-to-perform true fracture tests.
  - In this study two simple mixture tests were investigated and were successfully used to provide relevant fracture properties. The statistical analysis indicated that the fracture toughness and energy obtained from these new tests correlate best with the field distresses measured in the selected pavement sections.
  - These tests can be used to select materials with better fracture resistance and provide input parameters needed in an improved thermal cracking analysis that would replace the empirical analysis part of the current Mechanistic Empirical Pavement Design Guide

  - The current binder direct tension test protocol also provided a fracture parameter, the failure strain, which is highly correlated to thermal cracking occurrence in the selected pavement section. This test can be further improved, as shown in this research, to obtain binder characteristics needed for more accurate ranking at low temperature.
  - The current indirect tensile test provides useful information for the complete evaluation of low temperature behavior of asphalt mixtures, but is not the best choice for a simple screening test.
  - The current thermal stress restrained specimen test can become a useful research tool to analyze the stress development and fracture mechanism in asphalt mixtures at low temperatures if further refined.
- Asphalt binder properties represent a key factor in designing asphalt mixtures resistant to low temperature cracking. However, the current asphalt binder testing does not provide sufficient reliability to predict low temperature cracking of asphalt pavements
  - The aggregate type has a significant effect on the fracture properties of similar types of mixtures made with the same asphalt binder.
  - The volumetric properties also influence the low temperature cracking of asphalt mixtures.
  - The PG system provides a good starting point in the selection of asphalt binders. However, this study showed the need for further refinement of the current AASHTO M320 specification which seems to be "blind" to improved fracture properties at low temperature due to polymer modification.
  - Physical hardening has a significant effect on measured binder properties and appears to be an important variable for bending beam rheometer and fracture testing.
- Even at low temperatures asphalt mixtures are complex viscoelastic composite materials that are significantly temperature and loading rate dependent
  - This study clearly demonstrated that the effect of temperature is significant as the behavior changes from brittle-ductile to brittle; therefore, when conducting low temperature tests on asphalt mixtures, testing temperatures should be established relative to the expected low pavement temperature and/or relative to the low temperature Superpave PG grade for the location of interest.
  - The mixture and binder test temperatures should be matched as much as possible to better understand the contribution of the binder to the fracture properties of mixtures. This contribution needs to be further investigated and modeled.
  - The effect of loading rate also needs to be further investigated to better match true field cooling rates.
- The mixture coefficient of thermal contraction is a critical parameter for estimation of field performance for low temperature cracking.
  - This study showed that the coefficients are affected by binder grades and by mixture variables.
  - The tests level of difficulty warrants the creation of the database of values for different types of binders and mixtures that can be used for future analyses.

Recommendations for future research

The findings of this study represent a very good start in developing an improved asphalt binder and asphalt mixture specifications, as well as improving the low temperature cracking model that is included in the current Mechanistic-Empirical Pavement Design Guide. However, this research effort needs to be continued to address the following key issues:

- Develop a specification for selecting asphalt mixtures with increased fracture resistance similar to the PG system for binders.
  - Low temperature cracking performance cannot rely entirely on the PG of the binder. There is a critical need for an asphalt mixture specification.
  - This study identified test protocols that can be used to obtain fracture parameters that control the fracture resistance of the mixtures.
  - These test methods need to be applied to a wider range of mix designs (SMA, warm mixtures, porous mixtures) and aggregate size, since in this study only one type of mix was used.
  - These methods need to be used to test cored samples from top performing pavements to develop limiting criteria for fracture energy and fracture toughness in order to obtain limiting temperatures at which these materials will perform well.
- Improve the current PG system for asphalt binders.
  - This reseach identified a number of issues not included in the current PG specification that can influence the performance of asphalt binders significantly
  - The analysis indicated that the failure strain at the minimum pavement temperature obtained with the direct tension test correlated best with field occurrence of thermal cracking. It becomes important to have a fracture parameter as part of criterion to obtain the critical low temperature and therefore, there is a critical need to develop a robust fracture test for asphalt binders.
  - Physical hardening needs to be further investigated to understand its role in predicting pavement performance.
- Improve the modeling approach developed in this study.
  - This study clearly indicated that the empirical model that is used to predict low temperature cracking in the mechanistic empirical pavement design can be successfully replaced with a robust mechanics based model that can significantly increase the accuracy of the prediction model.
  - This work needs to be continued in order to improve the models developed in this work by providing additional experimental data and additional pavement performance data.
- Apply test methods and analyses to asphalt pavements built with RAP.
  - Most of the pavements built today contain various degrees of RAP. It becomes therefore important to investigate the fracture resistance of RAP mixtures using the set of tools developed for “clean” mixtures
  - The fracture properties will most likely represent the controlling factors that will dictate the amount of RAP and the type of binder to be used since the addition of RAP influences the most the fracture properties of the resulting mixture.

One key recommendation is that the construction of instrumented field test sections under well controlled conditions and the evaluation of additional existing field sections are needed to validate the findings of this study. Based on such a study, the development of revised binder and mixture design specifications could be achieved.

REFERENCES

(1). Anderson, D. A., Christensen, D. W., Bahia, H. U., Dongre, R., Sharma, M. G., Antle, C. E., and Button, J. (1994), *Binder Characterization and Evaluation, SHRP A-369, Vol. 3, Physical Characterization Strategic Highway Research Program* National Research Council, Washington, D.C.

(2). American Association of State Highway and Transportation Officials (AASHTO) Standard T 313-05 (2005), "Standard Method of Test for Determining the Flexural Creep Stiffness of Asphalt Binder Using the Bending Beam Rheometer (BBR) ", *Standard Specifications for Transportation Materials and Methods of Sampling and Testing, 25th Edition*, Washington, D.C.

(3). American Association of State Highway and Transportation Officials (AASHTO) Designation T314-02 (2002), "Standard Method of Test for Determining the Fracture Properties of Asphalt Binder in Direct Tension (DT) ", *Standard Specifications for Transportation Materials and Methods of Sampling and Testing, Part 2B: Tests*,"22nd Edition, Washington, D.C.

(4). American Association of State Highway and Transportation Officials (AASHTO) Designation T313-02 (2002), "Standard Method of Test for Determining the Flexural Creep Stiffness of Asphalt Binder Using the Bending Beam Rheometer (BBR) ", *Standard Specifications for Transportation Materials and Methods of Sampling and Testing, Part 2B: Tests*, 22nd Edition, Washington, D.C.

(5). American Association of State Highway and Transportation Officials (AASHTO) Designation MP1a-02 (2002), "Standard Specification for Performance Graded Asphalt Binder", *AASHTO Provisional Standards*, May 2002 Edition, Washington, D.C.

(6). American Association of State Highway and Transportation Officials (AASHTO) Designation T322-03 (2003), "Standard Method of Test for Determining the Creep Compliance and Strength of Hot-Mix Asphalt (HMA) Using the Indirect Tensile Test Device", *Standard Specifications for Transportation Materials and Methods of Sampling and Testing, Part 2B: Tests*, 22nd Edition, Washington, D.C.

(7). Bienawski, Z.T., and Hawkes, I. (1978), "Suggested methods for determining tensile strength of rock materials." *International Journal of Rock Mechanics and Mining Sciences*, 15, 99-103.

(8). ASTM Method C496/C496M-04 (2004). "Standard Test Method for Splitting Tensile Strength of Cylindrical Concrete Specimens". *Annual book of ASTM Standards, Vol. 04.02*. American Society for Testing and Materials, Philadelphia, PA.

(9). John P. Hallin (2004), *Development of the 2002 Guide for the Design of New and Rehabilitated Pavement Structures: Phase II*, National Cooperative Highway Research Program, NCHRP 1-37A, Washington, D.C.

(10). Monismith, C.L., Secor, G.A., and Secor, K.E. (1965), "Temperature Induced Stresses and Deformations in Asphalt Concrete." *Journal of the Association of Asphalt Paving Technologist*, Vol.34, 248-285.

(11). Carpenter, S.H. (1983), *Thermal Cracking in Asphalt Pavements: An Examination of Models and Input Parameters*»,USA CREEL.

(12). Janoo, V. (1989), Performances *of 'Soft' Asphalt Pavements in Cold Regions* USA CRREL Special Report.

(13). Stock, A.F., Arand, W. (1993), "Low Tempertature Cracking in Plymer Modified Binders." *Journal of the Association of Asphalt Paving Technologist*, Vol.62, 23-53.

(14). Jung, D., Vinson, T.S. (1993), "Low Temperature Cracking Resistance of Asphalt Concrete Mixtures." *Journal of the Association of Asphalt Paving Technologist*, Vol.62, 54-92.

(15). Pucci T.; Dumont A.-G., Di Benedetto H. (2004), "Thermomechanical and mechanical behavior of asphalt mixtures at cold temperature: Road and laboratory investigations, " *Road materials and pavement design*, vol. 5, no. 1: 45-72.

(16). Fortier R.; Vinson T. S. (1998) "Low-temperature cracking and aging performance of modified asphalt concrete specimens", *Transportation Research Record 1630*, 77-86.

(17). Moavenzadeh, F. (1967) "Asphalt fracture". *Journal of the Association of Asphalt Paving Technologist*, Vol. 36, 51-79.

(18). ASTM Method E399-90, "Plane-Strain Fracture Toughness for Metallic Materials", *Annual book of ASTM Standards, Vol. 03.01*. (2002) American Society for Testing and Materials, Philadelphia, PA

(19). Lee, N. K. and Hesp, S. A. M. (1994) "Low Temperature Fracture Toughness of Polyethylene-Modified Asphalt binders." *Transportation Research Record 1436*, 54-59.

(20). Lee, N.K., Morrison,G. R. and Hesp, S.A.M. (1995) "Low Temperature Fracture of Poluethylene-Modified Asphalt binders and Asphalt Concrete Mixes." *Journal of the Association of Asphalt Paving Technologists*, Vol. 64, 534-574.

(21). Dongre, R., Sharma, M.G., Anderson, D.A. (1989). "Development of Fracture Criterion for Asphalt Mixtures at Low Temperatures", *Transportation Research Record 1228*, 94-105.

(22). Hoare, T.R. and Hesp, S.A.M., (2000). "Low-temperature Fracture Testing of Asphalt Binders". *Transportation Research Record 1728*, 36-42.

(23). Anderson, D.A., Champion-Lapalu, L., Marasteanu, M.O., LeHir, Y.M., Planche, J.P. and Martin, D., (2001). "Low-Temperature Thermal Cracking of Asphalt Binders as Ranked by Strength and Fracture Properties", *Transportation Research Record 1766*, 1-6.

(24). Olard, F. and Di Benedetto, H. (2004). "Fracture Toughness and Fracture Energy of Bituminous Binders at Low Temperatures". *Proceedings of 5th RILEM International Conference on Cracking in Pavements*, May 5-7, Limoges, France.

(25). Li, X., Marasteanu, M.O. (2004). "Evaluation of the Low Temperature Fracture Resistance of Asphalt Mixtures Using the Semi Circular Bend Test.", *Journal of the Association of Asphalt Paving Technologist*, Vol. 73, 401-426.

(26). Andriescu, A., Hesp, S.A.M., and Youtcheff, J.S. (2004). "On the Essential and Plastic Works of Ductile Fracture in Asphalt Binders." *Presentation at the 2004 Transportation Research Board annual meeting*, paper 04-2459, Washington D.C.

(27). Cotterell, B. and Reddel, J.K. (1977). "The Essential Work of Plane Stress Ductile Fracture", *International Journal of Fracture*, 13(3), 267-277.

(28). Roy, S.D. and Hesp, S.A.M. (2001) "Low-Temperature Binder Specification Development: Thermal Stress Restrained Specimen Testing of Asphalt Binders and Mixtures".

Presentation at the 2001 Transportation Research Board annual meeting, paper 01-2027, Washington D.C.

(29). Zofka A., Marasteanu M. (2007), "Development of Double Edge Notched Tension (DENT) Test for Asphalt Binders", *Journal of Testing and Evaluation*, ASCE, Vol. 35, No. 3.

(30). Gauthier G. G., Anderson D. (2006), "Fracture mechanics and asphalt binders", *International Journal of Road Materials and Pavement Design*, Vol. 7, pp. 9-35

(31). Majidzadeh, K., Kauffmann, E., Ramsamooj, D. (1971), "Application of Fracture Mechanics in the Analysis of Pavement Fatigue", *Proceedings of the Association of Asphalt Paving Technologists*, Vol. 40, pp. 227-246.

(32). Labuz, J.F. and Dai, S. (1994) *Cracking of Asphalt Concrete at Low Temperatures*, Final report, submitted to Center for Transportation Studies, University of Minnesota, Minneapolis, MN.

(33). Ramsamooj, D. (1991), "Prediction of Fatigue Life of Asphalt Concrete Beams for Fracture Tests" *Journal of Testing and Evaluation*, Vol. 19, No. 3, pp. 231-239.

(34). Kim, K. W., El Hussein, M. (1997) "Variation of Racture Toughness of Asphalt Concrete under Low Temperature", *Construction and Building Materials*, Vol. 11, No. 7-8, 403-411.

(35). Karihaloo, B.L. and Nallathambi, P. (1989). "An Improved Effective Crack Model for the Determination of Fracture Toughness of Concrete", *Cement and Concrete Research*, Vol. 19, 603-610.

(36). Mobasher, B., Mamlouk, M.S. and Lin, H-M. (1997) "Evaluation of Crack Propagation Properties of Asphalt Mixtures", *Journal of Transportation Engineering*. Vol. 123, No. 5, pp. 405-413.

(37). Hossain, M., Swartz, S., Hoque, E. (1999), "Fracture and Tensile Characteristics of Asphalt-Rubber Concrete", *ASCE Journal of Materials in Civil Engineering*, Vol. 11, No. 4, pp. 287-294.

(38). Wagoner, M. P., Buttlar, W. G., Paulino, G.H. (2005), "Development of a Single-Edge Notched Beam Test for Asphalt Concrete Mixtures", *Journal of Testing and Evaluation*, Vol. 33, No. 6, pp. 452-460.

(39). Wagoner, M. P., Buttlar, W. G., Paulino, G.H. (2005), "Development of a Single-Edge Notched Beam Test for the Study of Asphalt Concrete Fracture", *Geotechnical Special Publication No. 130: Advances in Pavement Engineering, Proceedings of Sessions of the GeoFrontiers 2005 Congress*, Austin, TX.

(40). American Association of State Highway and Transportation Officials (AASHTO) Provisional Standards TP4-00 (2000), "Method for Preparing and Determining the Density of Hot-Mix Asphalt (HMA) Specimens by Means of the Superpave Gyratory Compactor", American Association of State Highway Transportation Officials, Washington, D.C., April 2000 edition.

(41). Roque, R., Zhang, Z. and Sankar, B. (1999) "Determination of Crack Growth Rate Parameters of Asphalt Mixtures Using the Superpave IDT." *Journal of the Association of Asphalt Paving Technologists*, Vol. 68, 404-433.

(42). Paris, P.C. and Erdogan, F., (1963) "A Critical Analysis of Crack Propagation Laws", *Transactions of the ASME, Journal of Basic Engineering*, Series D, 85, No. 3.

(43). Zhang, Z., Roque, R. and Birgisson, B. (2001) "Evaluation of laboratory Measured Crack Growth rate for asphalt Mixtures", *Transportation Research Record*, 1767, 67-75.

(44). Roque, R., Birgisson, B., Sangpetngam, B., and Zhang, Z. (2001). "Hot Mix Asphalt Fracture Mechanics : A Fundamental Crack Growth Law for Asphalt Mixtures ", *Journal of the Association of Asphalt Paving Technologist*, Vol.70, 816-827.

(45). Chong, K.P. and Kuruppu, M.D. (1984) "New Specimen for Fracture Toughness Determination for Rock and Other Materials", *International Journal of Fracture*, Vol. 26, R59-R62.

(46). Chong, K.P. and Kuruppu, M.D. (1988) "New Specimens for Mixed Mode Fracture Investigations of Geomaterials", *Engineering Fracture Mechanics*, Vol. 30, No. 5, 701-712.

(47). Lim, I. L., Johnston, I.W., Choi, S.K. and Boland, J.N. (1994). "Fracture Testing of a Soft Rock with Semi-Circular Specimens Under Three point Bending. Part1-Mode I." *International Journal of Rock Mechanics, Mining Science* 31, 199-212.

(48). Ingraffea, A.R., Gaunsallus, K.L., Beech, J.F., and Nelson, P.P. (1984), "A Short Rod Based System for Fracture Toughness Testing of Rock", ASTM STP 885, *Chevron-Notched Specimens: Testing and Stress Analysis*, Louisville, KY, 152-266.

(49). Lim, I. L., Johnston, I. W. and Choi, S.K. (1993) "Stress Intensity factors for Semi-Circular Specimens Under Three-Point Bending." *Engineering Fracture Mechanics*, Vol.44, No.3, 363-382.

(50). Molenaar, J. M. M. and Molenaar, A.A.A. (2000) "Fracture Toughness of Asphalt in the Semi-Circular Bend Test", *Proceedings, 2nd Eurasphalt and Eurobitume Congress*, Barcelona, Spain.

(51). Li, X., Marasteanu, M.O., Dai, S., and Lukanen, E. (2005) "Prediction of Low Temperature Crack Spacing in Asphalt Pavements", *Proceedings, the 7th International Conference on the Bearing Capacity of Roads, Railways and Airfields*, Trondheim, Norway.

(52). Li, X. (2005) *Investigation of the Fracture Resistance of Asphalt Mixtures at Low Temperature with a Semi Circular Bend (SCB) Test*. Ph.D. Thesis, University of Minnesota, Minneapolis, MN.

(53). Underwood, J.H., Newman, J.C., Jr., and Seeley, R.R. (1980) "A proposed standard round compact specimen for plane strain fracture toughness testing", *Journal of Testing and Evaluation*, Vol. 8, No. 6, Nov., 308-313.

(54). Wagoner, M.P., Buttlar, W.G., and Blankenship, P. (2005). "Investigation of the Fracture Resistance of Hot-Mix Asphalt Concrete Using a Disk-shaped Compact Tension Test", *Presentation at the 2005Transportation Research Board annual meeting*, paper 05-2394, Washington D.C.

(55). Lee, K. W., Soupharath, N., Shukla, A., Fraanco, C. A., Manning, F. J. (1999), "Rheological and Mechanical Properties of Blended Asphalts Containing Recycled Asphalt Pavement Binders", *Proceedings of the Association of Asphalt Paving Technologists*, Vol. 68, pp. 89-128.

(56). Wagoner, M.P., Buttlar, W.G., Paulino, G.H. (2005) "Disk-Shaped Compact Tension Test for Asphalt Concrete Fracture" *Society for Experimental Mechanics*, Vol. 45, No. 3, pp. 270-277.

(57). Wagoner, M. P., Buttlar, W.G., Paulino, G.H., Blankenship, P. (2007), "Laboratory Testing Quite for Characterization of Asphalt Concrete Mixtures Obtained from Field Cores", submitted to *Proceedings of the Association of Asphalt Paving Technologists*.

(58). Littlefield, G. (1967), "Thermal Expansion and Contraction Characteristics of Utah Asphaltic Concretes", *Proceedings of the Association of Asphalt Paving Technologists*, Vol. 36, pp. 673-702.

(59). Jones, G.M., Darter, M.I. and Littlefield, G. (1968) "Thermal Expansion-Contraction of Asphaltic Concrete", *Journal of the Association of Asphalt Paving Technologists*, Vol. 37, 56-97.

(60). Stoffels, S., Kwanda, F.D. (1996), "Determination of the Coefficient of Thermal Contraction of Asphalt Concrete Using the Resistant Strain Gage Technique", *Proceedings of the Association of Asphalt Paving Technologists*, Vol. 65, pp. 73-90.

(61). Mehta, Y.A., Stoffels, S.A., Christensen, D.W. (1999), "Determination of Coefficient of Thermal Contraction of Asphalt Concrete Using Indirect Tensile Test Hardware", *Proceedings of the Association of Asphalt Paving Technologists*, Vol. 68, pp. 349-368.

(62). Zeng, M., Shields, D.H. (1999), "Nonlinear Thermal Expansion and Contraction of Asphalt Concrete", *Canadian Journal of Civil Engineering*, Vol. 26, pp. 26-34.

(63). Bahia, H.U., Zeng, M., Nam, K. (2000), "Consideration of Strain at Failure and Strength in Prediction of Pavement Thermal Cracking", *Proceedings of the Association of Asphalt Paving Technologists*, Vol. 69, pp. 497-539.

(64). Nam, K. and Bahia, H.U. (2004), "Effect of Binder and Mixture Variables on Glass Transition Behavior of Asphalt Mixtures", *Proceedings of the Association of Asphalt Paving Technologists*, Vol. 73.

(65). Mamlouk, M.S., Witczak, M.W., Kaloush, K.E., Hasan, N. (2005), "Determination of Thermal Properties of Asphalt Mixtures", *Journal of Testing and Evaluation*, Vol. 33, No. 2, pp. 1-9.

(66). Fromm, H.J. and Phang, W.A. (1972) "A Study of Transverse Cracking of Bituminous Pavements", *Proceedings, the Association of Asphalt Paving Technologists*, Vol. 41, 383-423.

(67). Van Draat, W.E.F. and Sommer, P. (1966), "Ein Great zur Bestimmung der Dynamishcen Elastizitattsmoduln von Asphalt", *Strasse und Autobahn*, Vol. 35.

(68). Bazin, P. and Saunier, J.B. (1967), "Deformability, Fatigue and Healing Properties of Asphalt Mixes", *Proceedings, Second International Conference on the Structural Design of Asphalt Pavements*, Ann Arbor, Michigan, 553-569.

(69). Haas, R., Meyer, F., Assaf, G. and Lee, H. (1987) "A Comprehensive Study of Cold Climate Airport Pavement Cracking", *Proceedings of the Association of Asphalt Paving Technologists*, Vol. 56, 198-245.

(70). Hills, J.F. and Brien, D. (1966) "The Fracture of Bitumens and Asphalt Mixes by Temperature Induced Stresses", Prepared Discussion, *Proceedings, the Association of Asphalt Paving Technologists*, Vol. 35, 292 – 309.

(71). Haas, R.C.G. (1973) *A Method of Design Asphalt Pavements to Minimize Low-Temperature Shrinkage Cracking*, The Asphalt Institute, Research Report RR-73-1, College Park, Maryland.

(72). Christison, J.T., Murray, D.W. and Anderson, K.O. (1972) "Stress Prediction and Low Temperature Fracture Susceptibility of Asphaltic Concrete Pavements", *Proceedings of the Association of Asphalt Paving Technologists*, Vol. 41, 494-523.

(73). Shields, B.P., Anderson, K.O. and Dacyszyn, J.M. (1969) "An Investigation of Low Temperature Transverse Cracking of Flexible Pavements", *Proceedings of the Canadian Good Roads Association*.

(74). Young, F.D., Deme, I., Burgess, R.A., and Kopvillem, O. (1969) "Ste. Anne Test Road – Construction Summary and Performance After Two Years of Service", *Proceedings of the Canadian Technical Asphalt Association*.

(75). Finn, F., Saraf, C.L., Kulkarni, R., Nair, K., Smith, W., and Abdullah, A. (1977), *User's Manual for the Computer Program Cold*, NCHRP Report 1-10B, Transportation Research Board, Washington, D.C.

(76). Finn, F., Saraf, C.L., Kulkarni, R., Nair, K., Smith, W., and Abdullah, A. (1986) *Development of Pavement Subsystems*, NCHRP Report 291, Transportation Research Board, Washington, D.C.

(77). Hiltunen, D.R. and Roque, R. (1994) "A Mechanics-Based Prediction Model for Thermal Cracking of Asphaltic Concrete Pavements", *Journal of the Association of Asphalt Paving Technologists*, Vol. 63, 81-117.

(78). American Association of State Highway and Transportation Officials (AASHTO) Provisional Standards TP9-96 (2000), "Method for Determining the Creep Compliance and Strength of Hot Mix Asphalt (HMA) Using the Indirect Tensile Test Device", Washington, D.C., April 2000 edition.

(79). Soules, T.F., Busbey, R.F., Rekhson, S.M., Markovsky, A. and Burke, M.A. (1987) "Finite Element Calculation of Stress in Glass Parts Undergoing Viscous Relaxation", *Journal of the American Ceramic Society*, Vol. 70, No. 2, 90-95

(80). Chang, H.S., Lytton, L.R. and Carpenter, H.S. (1976) *Prediction of Thermal Reflection Cracks in West Texas*, Report TTI-2-8-73-18-3, Texas Transportation Institute, Texas.

(81). Schapery, R.A. (1986) "Time-Dependent Fracture: Continuation Aspects of Crack Growth", *Encyclopedia of Materials Science and Engineering*, M.B. Bever (Ed.), Permagon Press, Elmsford, NY.

(82). Molenaar, A.A.A. (1983) *Structural Performance and Design of Flexible Road Constructions and Asphalt Concrete Overlays*, Ph.D. Dissertation, Delft University of Technology, Delft, Netherlands..

(83). Lytton, R.L., Shanmugham, U. and Garrett, B.D. (1983) *Design of Asphalt Pavements for Thermal Fatigue Cracking*, Research Report 284-4, Texas Transportation Institute, Texas.

(84). Hillerborg, A., Modeer, M., Peterson, P.E. (1976) "Analysis of Crack Formation and Crack Growth in Concrete by Meams of Fracture Mechanics and Finite Elements", *Cement and Concrete Research*, Vol. 6, 773-782.

(85). Hillerborg, A. (1983) "Analysis of One Single Crack", *Fracture Mechanics of Concrete*, Elsevier Science Publishers, Amsterdam, Netherlands, 223-249.

(86). Petersson, P. E. (1981) *Crack Growth and Development of Fracture Zones in Plain Concrete and Similar Materials*, Ph. D. Thesis, Lund Institute of Technology, Lund, Sweden.

(87). Jenq, Y-S and Perng, J-D (1991) "Analysis of Crack Propagation in Asphalt Concrete Using Cohesive Crack Model", *Transportation Research Record 1317*, 90-99.

(88). Shen, W., Kirkner, D.J. (1999) "Distributed thermal cracking of AC pavement with frictional constraint", ASCE *Journal of Engineering Mechanics 125*, 554–560.

(89). Shen, W., Kirkner, D.J. (2001) "Thermal Cracking of Viscoelastic Asphalt-Concrete Pavement", ASCE *Journal of Engineering Mechanics 127*, 554–560.

(90). Dugdale, D.S. (1960) "Yielding of Steel Sheets Containing Slits", *Journal of the Mechanics and Physics of Solids*, Vol. 8, 100-108.

(91). Barenblatt, G.I. (1962) "The Mathematical Theory of Equilibrium Vracks in Brittle Fracture", *Advances in Applied Mechanics*, Vol. VII, Academic Press, 55-129.

(92). Soares, J.B., Colares de Freitas, F. A. and Allen, D. H., (2003) "Considering Heterogeneity of the Material in Crack Modeling of Asphaltic Mixtures", *Transportation Research Record 1832*, 113-120.

(93). Paulino, G.H., Song, S. H., Buttlar, W.G. (2004) "Cohesive Zone Modeling of Fracture in Asphalt Concrete", *5th International Conference RILEM "Cracking in Pavements"*, Limoges, France.

(94). Hannele K. Zubeck, Ted S. Vinson (1996). "Prediction of Low Temperature Cracking of Asphalt Concrete Mixtures with Thermal Stress Restrained Specimen Test Results", *Transportation Research Record 1545*, National Research Council, Washington, D.C.

(95). Timm, D. and Voller, V. (2003) "Field Validation and Parametric Study of a Thermal Crack Spacing Model", *Journal of the Association of Asphalt Paving Technologist*, Vol. 72, 356-387.

(96). Schmidt, R.J and. Santucci, L.E (1966), "A Practical Method for Determining the Glass Transition Temperature of Asphalts and Calculation of Their Low Temperature Viscosities", *Proceedings of the Association of Asphalt Paving Technologists*, Vol. 35, p. 61.

(97). Bahia H.U. Anderson and D.A (1993), "Glass Transition Behavior and Physical Hardening of Asphalt Binders", *Proceedings of the Association of Asphalt Paving Technologists*, Vol. 62, pp. 93-129

(98). Anderson T.L. (1995), *Fracture Mechanics, Fundamentals and Application*, CRC Press, Second Edition.

(99). Jung, D.H., Vinson, T.S., (1994), *Strategic Highway Research Program. SHRP A-400*. "Low-Temperature Cracking: Test selection", Washington, D.C.

(100). Strategic Highway Research Program (1994), *SHRP-A-417*, "Accelerated Performance Related Tests for Asphalt-Aggregate Mixes and Their Use in Mix Design and Analysis Systems", Washington, D.C.

(101). Khazanovich, L., Velasquez, R., and Nesvijski, E., (2005) "Evaluation of top-down cracks in asphalt pavements using a self-calibrating ultrasonic technique". *Transportation Research Record*, Washington D.C.

(102). McClave, J. and Sincich,T., (2003), *Statistics*, Ninth Edition. Prentice Hall.

(103). Song, S. H., G. H. Paulino and W.G. Buttlar (2006) "A Bilinear Cohesive Zone Model Tailored for Fracture of Asphalt Concrete considering Rate Effects in Bulk Materials", *Engineering Fracture Mechanics*, Vol-73, No. 18, p 2829-48.

(104). Xu, X.-P. and A. Needleman (1994), "Numerical simulations of fast crack growth in brittle solids", *Journal of the Mechanics and Physics of Solids*, Vol. 42(9), pp. 1397-1434.

(105). Dempsey, B. J., R. L. Litton, D. E. Pufahl, C. H. Michalak, and H. S. Lang (1993), *An Integrated Model for the Climatic Effects on Pavement*, FHWA, Report No. FHWA-RD-90-033, Washington, D.C.

(106). Kim, J, and W.G. Buttlar (2001), "Analysis of Reflective Crack Control System Involving Reinforcing Grid Over Base-Isolating Interlayer Mixture", *ASCE Journal of Transportation Engineering*, Vol. 128 No. 4, pp. 375-384.

(107). Buttlar, W G, D. Bozkurt, M.R. Thompson, and S.M. Smith (2001), "The Rantoul Demonstration Project: Techniques for Reflective Crack Mitigation at GA Airports", *Proceedings of the 2001 Airfield Pavement Specialty Conference*, pp. 322-335.

(108). Timm, D.H., Guzina, B.B., and Voller, V.R. (2003). "Prediction of thermal crack spacing". *Int. J. Solids Struct*., 40,125-142.

(109). Roque R., Hiltunnen D.R., Buttlar W.G. (1995). "Thermal cracking performance and design of mixtures using superpaveTM", J. *Assoc. Asphalt Paving Technol*. 64, 718-733.

(110). Fromm, H.F., and Phang, W.A. (1972). "A study of transverse cracking of bituminous pavements", *Proc. Assoc. Asphalt Paving Techno*., 41, 383-423.

(111). Haas, R., Meyer, F., Assaf, G., and Lee, H. (1987). "A comprehensive study of cold climate airport pavement cracking", Proc. *Assoc. Asphalt Paving Techno*., 56, 198-245.

(112). Yang, Y.B., and Lin, B.H. (1995). "Vehicle-bridge interaction analysis by dynamic condensation method", *J. Struct. Eng*., 121, 1636-1643.

(113). Shalaby, A., Abd, E.l., Halim, A.O., and Easa, S.M. (1996). "Low-temperature stresses and fracture analysis of asphalt overlays" *Transp. Res. Rec*. *1539*, 132-139.

(114). Waldhoff A.S., Buttlar W.G., Kim J. (2000). "Investigation of thermal cracking at Mn/ROAD using the Superpave IDT", Proc. *Assoc. Asphalt Paving Techno 45*, 228-259.

(115). Shen W., Kirkner D.J. (1999). "Distributed thermal cracking of AC pavement with frictional constraint", J. *Eng*. *Mech*. 125(5), 554–560.

(116). Chen, G., and Baker, G. (2004). "Analytical model for predication of crack spacing due to shrinkage in concrete pavements", *J. Struct. Eng.*, 130, 1529-1533.

(117). Beuth, J.L. (1992). "Cracking of thin bonded films in residual tension", *Int. J. Solids Struct*. *29*, 1657-1675.

(118). Hong, A.P., Li, Y.N., and Bažant, Z.P. (1997). "Theory of crack spacing in concrete pavements", *J. Eng. Mech*. *123*, 267-275.

(119). Xia, Z.C., and Hutchinson, J.W. (2000). "Crack patterns in thin films" *J. Mech. Phys. Solids.*, 48, 1107-1131.

(120). Shenoy, V.B., Schwartzman, A.F., and Freund, L.B. (2001). "Crack patterns in brittle thin films", *Int. J. Fract.*, 109, 29-45.

(121). Agrawal, D.C., and Raj, R. (1989). "Measurement of the ultimate shear-strength of a metal ceramic interface", *Acta Metall*. 37, 1265-1270.

(122). Chen, B.F., Hwang, J., Chen, I.F., Yu, G.P., Huang, J.-H. (2000). "A tensile-film-cracking model for evaluating interfacial shear strength of elastic film on ductile substrate", *Surf. Coat. Tech*. 126, 91-95.

(123). Marasteanu, M.O., Li, X., Clyne, T.R., Voller, V.R., Timm, D.H., Newcomb, D.E. (2004). *Low temperature cracking of asphalt concrete pavements*, Final Report, Center for Transportation Studies, University of Minnesota, Minneapolis, MN.

APPENDIX A

Nomination of State Field Test Sites

Nomination of State Field Test Sites

The selection of field samples was of critical importance to the project and therefore the site identification and sample acquisition should was a lot of consideration and was performed with a lot of care. Asphalt overlays and asphalt pavements that include RAP were not considered in this study to eliminate to eliminate additional factors that influence performance.

The selection of field sites was based upon the recommendations made by the participating states. The site nomination form was used by the states to provide the preliminary information required by the research team for the selection of the field sites is attached at the end of this document.

State Field Sampling

Based on the different types of tests and sample geometry requirements the following number of samples and original material quantities are required as a reasonable minimum:

Table A-1. Overall samples required per site

Field Sample Types	Number of Samples
(18” x 6” x core depth) Beams, see figure 1	**9**
6” Cores (outside diameter)	**36**
Loose HMA Mix , kg	**300kg**
AC Binder (1-gallon bucket)	**1**

For the field samples both 6” outside diameter cores and 6”x18” beams were obtained, as indicated in Table A-1. The depth of the samples were as large as practically possible and should include the asphalt layers and the interface with the aggregate base.

The samples were marked on the top surface to show the direction of traffic and should be labeled in the manner shown in Table A-2.

Table A-2. Sample identification

Investigation of Low Temperature Cracking in Asphalt Pavements	
State	
Roadway	
Direction	**EB – WB – NB – SB**
Date Sampled	**/ /**
Sample Type	**Beam / Core** **Loose HMA / AC Binder**
Sample Number	**_____Of _____**
Other Observations	

Sampling was performed between the wheel paths at 50-foot intervals as shown in Figure A-1. A suggested detail of the sampling area is shown in Figure A-2. .

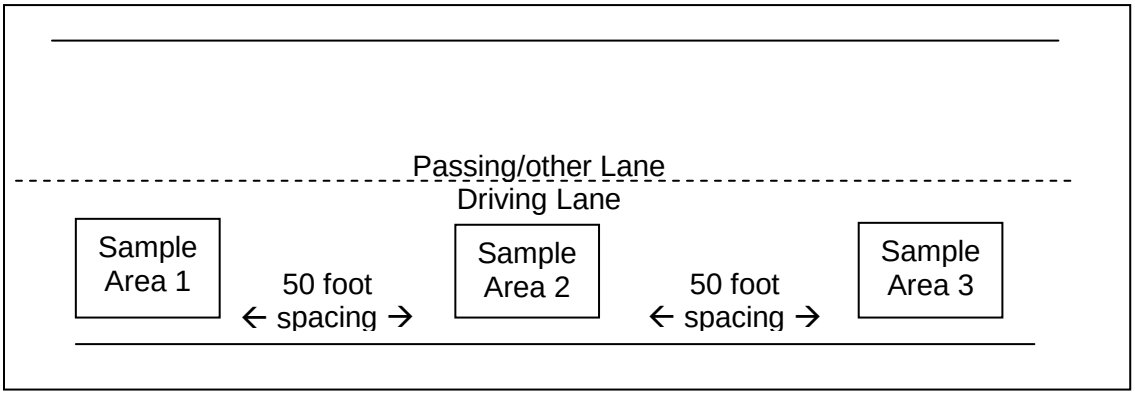

Figure A-1. Sampling areas in the 500' test section centered between the wheel paths

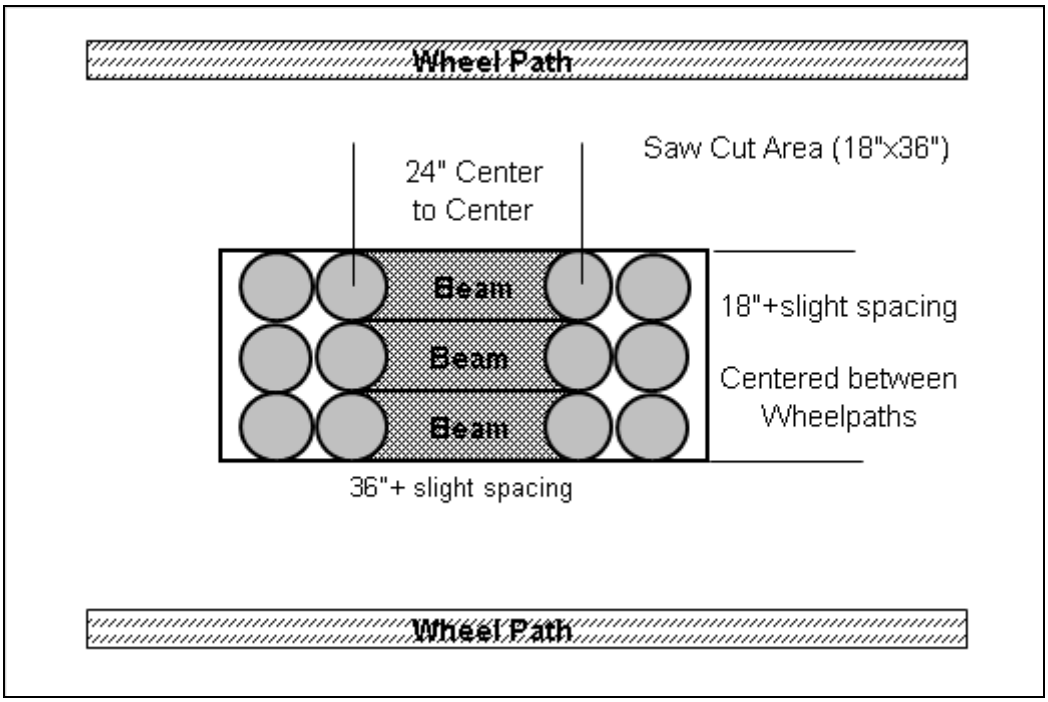

Figure A-2. Example of sampling area detail (12 cores and 3 beams)

Table A-3. Low temperature project nomination form

State			
Type–Number (I-35, US-12, ST-11)	-		
Nearest City (# miles west of ___)			
Latitude/Longitude (estimated)	Lat= Long=		
Traffic (ADT / %trucks / ESALS)	/ /		
Pavement Layer Description (HMA – PG Grade per lift) (Base) (Subbase) (Subgrade – Existing Soil)	**Layer Description**	**Thickness**	**Year**
HMA Aggregate Description			
Performance Ranking (circle)	(1=Best) **1 – 2 – 3 – 4 – 5** (5=Worst)		
Record/Sample Availability	**Answer**	**Comment**	
Construction Records	**Yes/No**		
Original Construction Lab Testing	**Yes/No**		
Historical Research Data (Part of another research study?)	**Yes/No**		
Pavement Management Data (# Years of ride, distress, video)	**Yes/No**		
Pavement Instrumentation	**Yes/No**		
Original HMA Loose Mix*	**Yes/No**		
Original Asphalt Binder*	**Yes/No**		
Original HMA Aggregates*	**Yes/No**		
*** If not available are other "typical" materials obtainable?**	**Yes/No**		
Other items worth reporting:			

APPENDIX B

Nominated Sites

Table B-1. Sites nominated by Illinois DOT

Site	#	Structure	Thickness	Comments
I-155	1	mill & replace	2" (2001)	
		19 mm mix	13.5" (1991)	
		lime-stabilized subgrade	12" (1991)	
US-50	2	surface	1.5"	demonstration project built in 1986 with several different pavement sections
		19 mm mix	9.5, 11.0, 12.5"	
		with & without lime-stabilized subgrade	with & without underdrains	
US-20	3	AC-10, AC-20	1.5"	
		AC-10, AC-20 19 mm mixes	11.5"	
		w/ rock - no drains, w/ soil has drains	variable	
I-74	4	AC-20 surface	1.5"	original surface will soon be milled and replaced 2-foot transverse crack spacing confined to surface layer, probably not thermal cracking
		AC-20, 19 mm mix	15.5"	
		lime-stabilized subgrade	12"	

Table B-2. Sites nominated by Minnesota DOT

Site	#	Structure	Thickness	Comments
Cell 33	1	HMA PG 58-28 crushed granite base - class 5	4" (1999) 12"	silty clay subgrade constructed in 1994
Cell 34	2	HMA PG 58-34 crushed granite base - class 5	4" (1999) 12"	silty clay subgrade constructed in 1994
Cell 35	3	HMA PG 58-40 crushed granite base - Class 5	4" (1999) 12"	silty clay subgrade constructed in 1994
Cell 3	4	HMA 120/150 crushed base - class 5 crushed subbase - class 3	6.3" 4" 33"	silty clay subgrade constructed in 1992
Cell 19	5	HMA AC-20 crushed subbase - class 3	7.8" 28"	silty clay subgrade constructed in 1992
CSAH-75 section 4WB	6	HMA PG 58-34 HMA PG 58-34 recycled mix (32B) crushed base - class 5	2" 2" 2.5" ~12"	sand-gravel subgrade constructed in 1955
CSAH-75 section 2EB	7	HMA PG 58-28 recycled mix (42B) recycled mix (32B) crushed base - class 5	2" 2" 2.5" ~12"	sand-gravel subgrade constructed in 1955

Table B-3. Sites nominated by North Dakota DOT

Site	#	Structure	Thickness	Comments
SH-18	1	HBP 120/150	4" (1997)	a thin lift overlay has been placed over part of this project
		blended base	12" (1997)	
		bituminous treated base	3" (1954)	
US-12	2	HBP PG 58-34	2" (1999)	grade constructed in 1948
		HBP PG 58-28	2.5" (1999)	
		blended base	15.5" (1999)	
US-83	3	HBP PG 58-34	2" (2000)	grade constructed in 1979
		HBP PG 58-28	3.5" (2000)	
		blended base	16" (2000)	
		aggregate base	2" (1980)	

Table B-4. Sites nominated by Wisconsin DOT

Site	#	Structure	Thickness	Comments
US-45	1	58-34, 58-40 (SB) 85/100 (NB)	4"	only difference in NB and SB lanes is the binder
		58-34, 58-40 (SB) 120/150 (NB)	4"	
		51-34 (SB) 120/150 (NB)	2"	sand to silt loam subgrade
		milled HMA subbase	9-10"	
STH-73	2	58-28 mix	3"	subbase stabilized with asphaltic base course entire route was pulverized and relayed
		milled HMA base	2"	
STH-64	3	12.5 mm mix	125"	No low temperature cracks reported in the 3.91 mile project
		19 mm mix	1.5"	
		19 mm mix	1.75"	
		pulverized and re-lay existing HMA	6"	

Table B-5. Accepted sites

State	Road	Asphalt Binder	Performance (1=Good) (5=Bad)	Age (Years)	Pavement Comment	Recommendation
IL	I-155	AC-20	5	14	Surface milled & replaced in 2000	Not recommended: surface milled and replaced
IL	US-50	AC-10, AC-20	2	20	demonstration project built in 1986	Projects 2 or 3 State pick one of the two sites to be accepted - similar cases
IL	US-20	AC-10, AC-20	2	20		Projects 2 or 3 State pick one of the two sites to be accepted - similar cases
IL	I-74	AC-20	2	15	original surface will soon be milled and replaced	Accepted
MN	Cell 33	PG 58-28	3	6	silty clay subgrade constructed in 1994	Accepted
MN	Cell 34	PG 58-34	1	6	silty clay subgrade constructed in 1994	Accepted
MN	Cell 35	PG 58-40	4	6	silty clay subgrade constructed in 1994	Accepted
MN	Cell 3	PG 58-28 120/150	3	14	silty clay subgrade constructed in 1992	Accepted
MN	Cell 19	PG 64-22 AC-20	4	14	silty clay subgrade constructed in 1992	Accepted
MN	CSAH-75 section 4WB	PG 58-34	3	10	sand-gravel subgrade constructed in 1955	Accepted
MN	CSAH-75 section 2EB	PG 58-28	4	10	sand-gravel subgrade constructed in 1955	Accepted
ND	SH-18	120/150	4	8	A thin lift overlay has been placed over part of this project	Not recommended: overlay placed on original pavement
ND	US-12	PG 58-34, 58-28	1	6	grade constructed in 1948	Projects 9 or 10 State pick one of the two sites to be accepted - similar cases
ND	US-83	PG 58-34, 58-28	1	5	grade constructed in 1979	Projects 9 or 10 State pick one of the two sites to be accepted - similar cases
WI	US-45	PG 58-34, 58-40 85/100, 120/150	2	10	only difference in NB and SB lanes was binder	Accepted
WI	STH-73	PG 58-28	1	5	subbase stabilized with asphaltic base course	Accepted
WI	STH-64	PG 58-34	1	2	No low temperature cracks reported in the 3.91 mile project	Not recommended: too recent

Note that the following recommendations were made to Illinois DOT and to North Dakota DOT, respectively, in terms of selecting the second site:

- US 50 demonstration project may offer more information than US 20. If this is not the case it is suggested to select the mix with higher air voids; if the same, the one with the higher traffic. State makes the final call.
- It is suggested to select the mix with higher air voids; if the same, the one with the higher traffic. State makes the final call.

APPENDIX C

MnROAD Coring Experience

(provided by Tim Clyne, Mn/DOT)

Field samples were taken from five sections at MnROAD May 23-24, 2005. The following samples were taken (note: the University of Minnesota had previously obtained 9 cores from each of the three latter sections):

Table C-1. Field samples from MnROAD

Cell	Lane	# 6" x 18" Beams	# 6" Cores
3	Driving	9	36
19	Driving	9	36
33	80 kip	9	27
34	80 kip	9	27
35	80 kip	9	27

Two groups of samples were taken for each cell, one on each end. Previous to coring, lines were marked on the pavement as shown in Figure C-1. The samples were centered between the wheelpaths. Three beams were marked side by side with a width of 7 inches each to allow for imperfect saw cuts in the field. The length was marked at 18 inches, which would allow the beams to be trimmed back to 15 inches for laboratory testing. A string line was snapped to draw a straight line, and the lines were spray painted onto the pavement. On one end of each cell a second set of beams was marked directly behind the first set. A straight line was then painted back from the center of the beams to denote core locations. Arrows marked the direction of traffic.

The first step in the sampling operation was to core along the pre-painted lines (Figure C-2). A core rig with a 6 inch inside diameter core barrel was used to take the cores. Water was used to cool the barrel and minimize the dust. Next a 20 inch saw was used to cut the beams and also to cut a large rectangular area around the core holes. Figure C-3 shows the cutting operation. Figure C-4 shows the sample area after the cores were removed and the saw cuts have been made. Figure C-5 is another picture of the sample area along with the tools used to remove the beams. A crowbar was used to loosen the beams, and a special tool was used to clamp the beams for easy removal. The cores were then measured, labeled, and recorded onto data sheets for later reference. Once all of the samples and extra material were removed from the holes, loose mix from a local HMA plant was used to patch the holes. The mix was compacted with a vibratory plate compactor before the roadway was allowed back open for traffic.

Figure C-1. Core and beam layout prior to cutting

Figure C-2. Coring with core truck

Figure C-3. Saw cutting beam samples

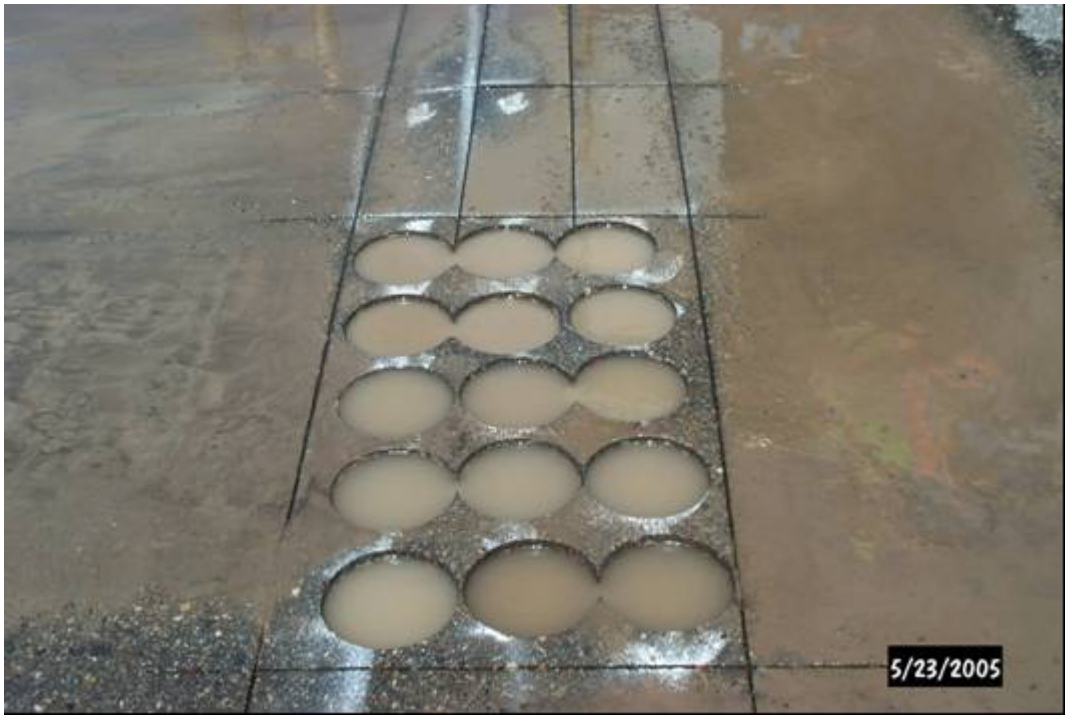

Figure C-4. Sample area after coring and cutting

Figure C-5. Sample area and tools for removing beams

APPENDIX D

Illinois Coring Experience

(provided by Andrew Braham, UIUC)

Field samples were taken from two sections of US Highway 20 in northern Illinois, just outside of Freeport, on November 1, 2005. From the two sections, three sample sets were obtained. Table 1 shows the sampling distribution.

Table D-1. Field samples from Illinois

Station	Asphalt Binder	Number of 6" x 18" Beams	Number of 5.75" Cores
695+00	AC-10	3	12
695+50	AC-10	3	12
696+00	AC-10	3	12
735+00	AC-20	3	12
735+50	AC-20	3	12
736+00	AC-20	3	12

Illinois Department of Transportation had laid out the sample orientation as shown in Figure D-1. The samples were clustered between the wheelpaths with the length of the beams aligned with the traffic flow.

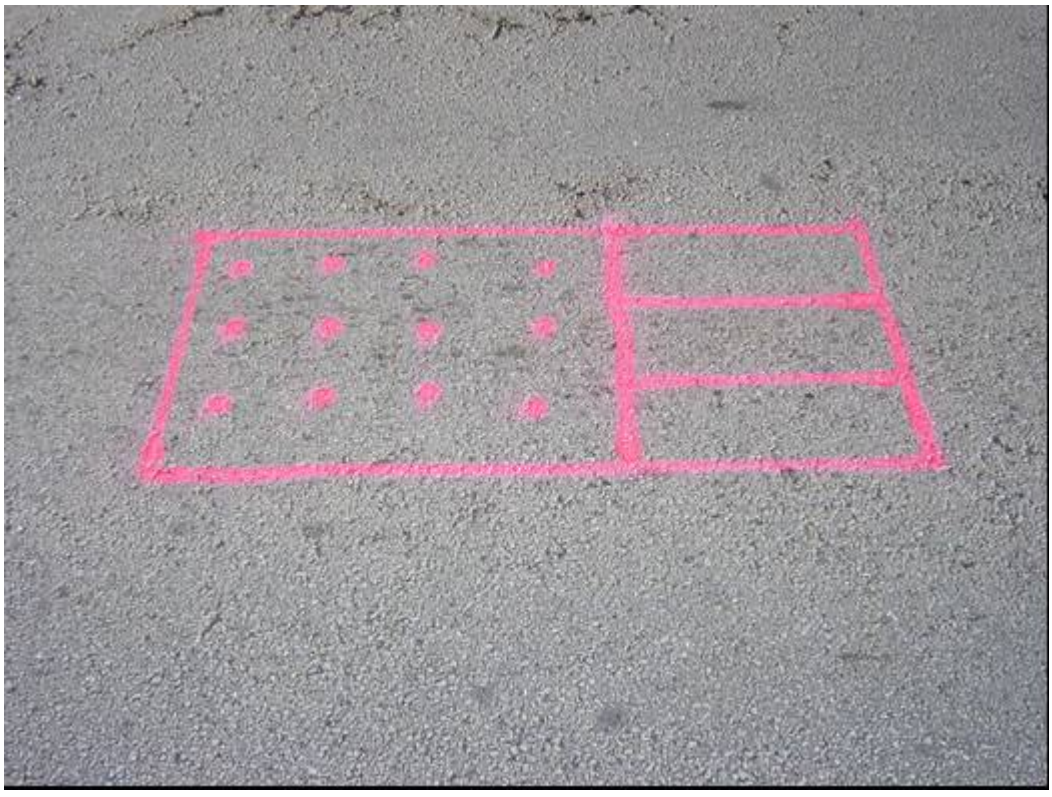

Figure D-1. Sample orientation

The cores were cut first and extracted as shown in Figure D-2. Two portable coring rigs were onsite, with 5.75" inside diameter core bits.

Figure D-2. Coring operation

Twelve cores were taken from each station. The pavement was approximately 13" deep, with 11.5" of binder course and a 1.5" surface mix. Figure 3 shows the extracted cores.

Figure D-3. Extracted cores

To extract the beams, a 36" diameter saw was brought in. Figure D-4 shows the saw in action.

Figure D-4. Saw cutting

The saw cut the full depth of the pavement (Figure D-5) and the beams were extracted.

Figure D-5. Cut beams in road

All of the samples were extracted in Rantoul, IL. Sample distribution were as follows. Minnesota, Iowa State, Wisconsin, and Illinois each received eighteen cores, three from each station. In addition, Minnesota, Wisconsin, and Illinois had six beams, one from each station. The beam sizes are shown in Table D-2 to D-4.

Table D-2. Minnesota beams

Station	Number	Length (in)	Width (in)	Height (in)
695+00	2	21.50	7.50	10.75
695+50	1	19.50	9.50	12.00
696+00	2	20.00	9.00	10.50
735+00	3	20.00	8.75	11.75
735+50	1	18.50	9.50	9.00
736+00	2	20.75	9.75	10.50

Table D-3. Wisconsin beams

Station	Number	Length (in)	Width (in)	Height (in)
695+00	1	21.25	7.50	12.00
695+50	3	19.50	7.50	10.75
696+00	1	21.50	9.00	12.00
735+00	2	20.00	9.50	9.00
735+50	2	18.50	7.50	9.00
736+00	3	20.75	10.25	9.00

Table D-4. Illinois beams

Station	Number	Length (in)	Width (in)	Height (in)
695+00	1	21.50	10.00	12.00
695+50	2	19.25	9.50	12.00
696+00	3	20.00	9.25	12.00
735+00	1	20.00	10.75	12.00
735+50	3	18.25	8.50	12.00
736+00	1	20.75	9.50	12.00

APPENDIX E

Pavement Condition Survey - US Highway 20
November 2, 2005

(provided by Andrew Braham, UIUC)

Huiming Yin and Andrew Braham of the University of Illinois and Jim Trepanier of Illinois DOT conducted a pavement condition survey of US Highway 20 just outside of Freeport, IL. This road was constructed approximately twenty years ago with a full depth HMA structure. Two sections were surveyed. The first section, section A, used an AC-10 binder and the second section, section B, used an AC-20 binder.

Over the entire two sections, there was very little mainline thermal cracking. Except for random transverse cracking, there were only two short sections that were obviously thermal cracking. One of the sections was in section A and the other was in section B. Both sections were in the eastbound lanes. The section A thermal cracking had 8-10 full width cracks approximately 20-30 feet apart just after a bridge. The section B thermal cracking had 8-10 full width cracks approximately 20-30 apart as well, but these cracks were on an approach to a bridge. Figure E-1 shows a mainline crack example.

Figure E-1. Full-width thermal cracking

There was quite a bit of thermal cracking on the shoulders. Jim mentioned that they probably used a different mix on the shoulders and that mix would have included RAP. This would decrease the shoulder's ability to withstand the thermal stresses. When there was shoulder thermal cracking, there were often small cracks that went into the mainline, but these seemed to be caused by the crack in the shoulder. Figure E-2 shows an example of this phenomenon.

Figure E-2. Shoulder cracking

The most common distress observed on both sections was end load segregation. This occurred on a very regular basis throughout the project. Figure E-3 shows an example of this distress. Although it looks severe, the ride quality while traveling over these distresses was decent. You could feel the roughness but it did not feel obtrusive.

Figure E-3. End load segregation

The two pavement sections were instrumented. Since these were a part of a large test section, strain gages and other gages were imbedded in the pavement. In addition, three surface treatments were placed on Section B, a ¾" HMA overlay, a slurry seal, and a chip seal. The chip seal provided the best surface protection and covered all surface distresses from the underlying pavement. This indicates that the pavement overall is very structurally sound and most of the distresses observed were simply surface distresses.

Overall, the pavement did look twenty years old, with random cracks here and there (besides the previously mentioned). In addition, there may have been some fatigue cracking in Section B. This was very mild and may have just been on the surface.

Since this is a test section, there have been reports written about it. UIUC will attempt to obtain these reports.

In conclusion, it was difficult to observe any visual differences between the AC-10 section and the AC-20 section. This will provide an interesting opportunity for analysis in the lab to see if the two mixes perform differently.

APPENDIX F

TEST METHODS – OVERVIEW

Asphalt Mixtures

Indirect Tensile (IDT) Test

AASHTO specification recommends performing creep and strength tests at 0C, -10C, and -20C. For creep, a constant load is applied to the specimen for 1000sec and vertical and horizontal displacements are measured using extensometers mounted on both faces of the specimen. Based on the recorded load and displacement values, the creep compliance is calculated. The creep compliance can be further converted to relaxation modulus which is used in thermal cracking calculations and modeling.

For the strength test the specimen is loaded at a constant loading rate (12.5mm/min) until it breaks, and the tensile strength of the specimen is calculated.

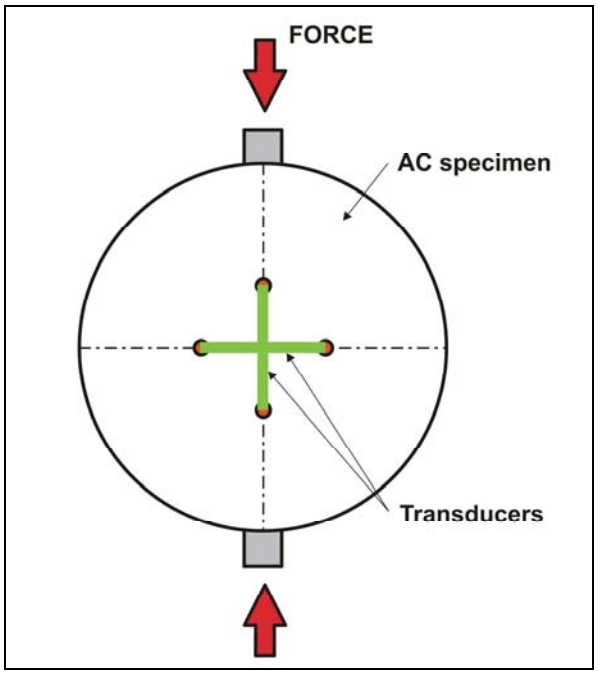

Figure F-1. IDT

SCB

Semi Circular Bending (SCB) test is performed to determine the fracture toughness and fracture energy of an asphalt mixture specimen. A load, controlled by the constant crack mouth opening displacement measured at the notch at the bottom of the specimen, is applied vertically at the top of the semi-circular specimen using value and the load line displacement (LLD) is measured using a vertically mounted extensometer. The fracture toughness is calculated from the peak load and fracture energy is determined from the area under load-LLD curve.

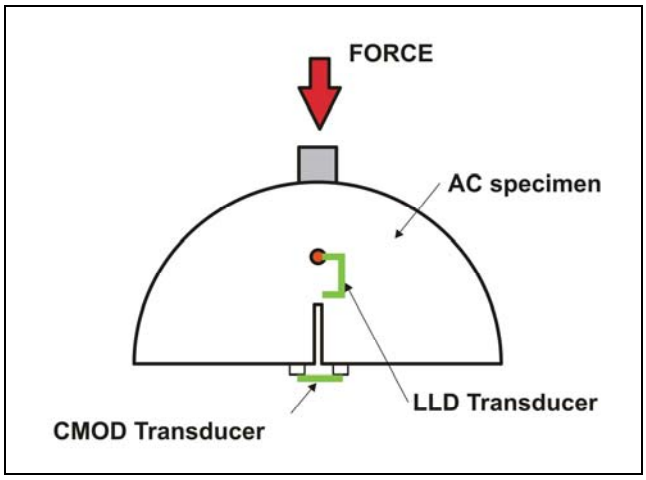

Figure F-2. SCB

DC(T)

Similar to SCB, Disc-Shaped Compact Tension test DC(T) is performed to determine fracture energy of the asphalt mixture specimen. A tensile force is applied at the loading holes and the crack mouth opening displacement (CMOD) is measured with a clip-on gage at the face of the crack mouth. The fracture energy is calculated by determining the area under the load-CMOD curve.

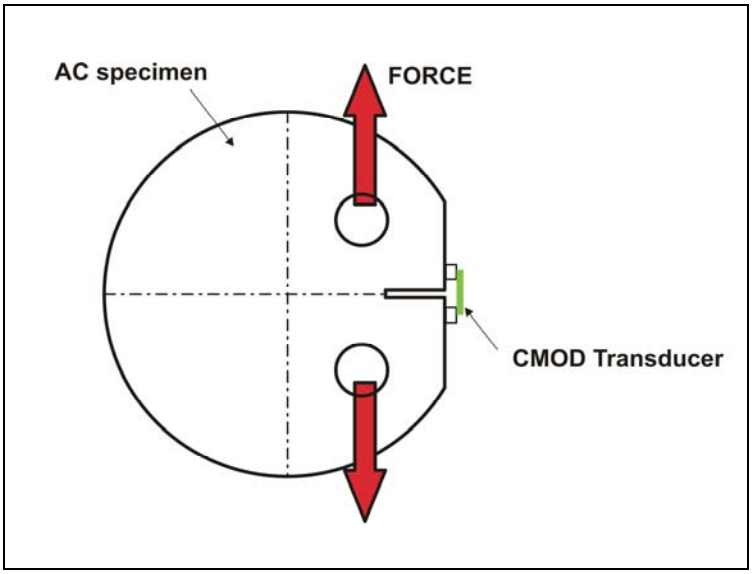

Figure F-3. DC(T)

SE(B)

Single-Edge Notched Beam, SE(B), is a classical fracture test to determine fracture toughness and fracture energy of the asphalt mixture. A mixture beam is tested using the 3-point bending setup shown below. Similar to SCB test, loading is controlled to obtain a constant CMOD rate and the fracture energy is calculated from the area under the load-CMOD curve.

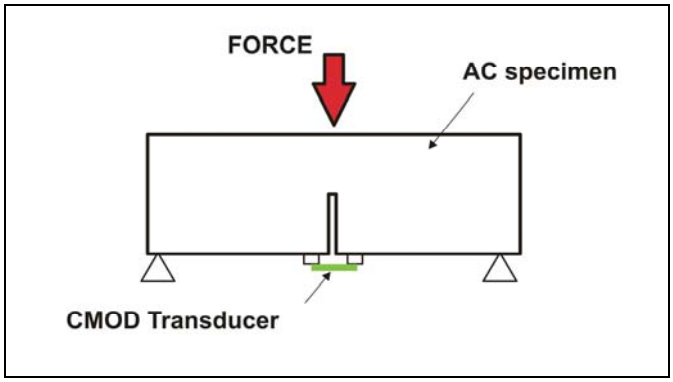

Figure F-4. SE(B)

Asphalt Binders

DENT

Double Edge Notch Tension (DENT) test is performed in Direct Tension setup to determine asphalt binder fracture toughness. The specimen is pulled apart with a constant rate until it breaks. Fracture toughness is calculated from the peak load using appropriate formula.

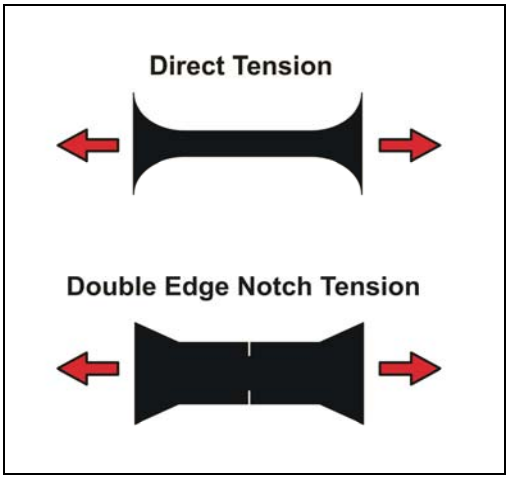

Figure F-5. DT and DENT comaparison

APPENDIX G

TCMODEL inputs

(provided by Eshan Dave, UIUC)

Organization of Appendix

This section presents the details regarding the viscoelastic material inputs for various asphalt concrete mixtures from the LTC study. For each of the mixtures the AASHTO MEPDG Level-I and Level-III inputs are presented. The details include the model parameters for creep compliance master curve (Generalized Kelvin Model and Power Law Model)) and relaxation modulus master curve (Generalized Maxwell Model).

MnRoad Cell Level-I inputs are used to describe various quantities presented for each set of mixtures and input levels. All the other set of properties follow similar presentation scheme.

MnRoad Cell 03 ← Name of section

Level – 1 ← Level of MEPDG Input

Creep-Compliance Model Parameters

```
   4           3   [No. of Maxwell Elements, No. of Test Temps]
 -30.00000       1.000000       [Temp (C), 1/(Shift Factor)]
 -18.00000       100.0000       [Temp (C), 1/(Shift Factor)]
 -6.000000       3162.278       [Temp (C), 1/(Shift Factor)]
 1.5386868E-07            [D0 (1/psi)]
 8.4873901E-07            [D1 (1/psi)]
 5.5000000                [Tau1 (sec)]
 7.1838894E-08            [D2 (1/psi)]
  4.125000                [Tau2 (sec)]
 1.7362986E-08            [D3 (1/psi)]
  3.190000                [Tau3 (sec)]
 8.7707094E-08            [D4 (1/psi)]
  1.815000                [Tau4 (sec)]
  12.33488                [Log{EtaV} (psi-sec)]

POWER MODEL PARAMETERS
 1.8805300E-07            [D0 (1/psi)]
 4.7988000E-09            [D1 (1/psi)]
   0.4200                  [m]
```

Time-Temperature Shift Factors

Gen. Kelvin Model Parameters, $D0$, D_i,, Tau_i, and etaV

Power Law Model Parameters, D0, D1, and m

```
**********************************************************************
        #Thermal Cracking File Data
         Analysis Level =  1
         Creep Test Duration =  1000 seconds
         Test Data Path =
C:\DG2002\Projects\MnRoad03-LTC\


**********************************************************************

              MIXTURE Name:      Asphalt

**********************************************************************
```

Generalized Maxwell Model Parameters

```
          5
  2375828.
  41.51828
  297267.7
  1441.181
  997349.6
  10158.86
  2120135.
  83800.66
  708470.3
  2785992.
```

Number of Maxwell Units in the Model (n)

E_1, Tau_1, E_2, Tau_2, . . . E_n Tau_n

Gen. Maxwell Model Parameters, Spring (E_i (psi)) and Dashpot (Tau_i (sec)) Constants

MnRoad Cell 03

Level – 3

Creep-Compliance Model Parameters

```
          4           3   [No. of Maxwell Elements, No. of Test Temps]
 -20.00000       1.000000       [Temp (C), 1/(Shift Factor)]
 -10.00000       50.11873       [Temp (C), 1/(Shift Factor)]
 0.0000000E+00   398.1073       [Temp (C), 1/(Shift Factor)]
 2.5969592E-07           [D0 (1/psi)]
 9.9811921E-08           [D1 (1/psi)]
 0.9200001               [Tau1 (sec)]
 1.5383424E-07           [D2 (1/psi)]
  1.840000               [Tau2 (sec)]
 7.9900005E-08           [D3 (1/psi)]
  2.760000               [Tau3 (sec)]
 1.0775500E-06           [D4 (1/psi)]
  3.680000               [Tau4 (sec)]
  10.32779               [Log{EtaV} (psi-sec)]

POWER MODEL PARAMETERS
 2.1097617E-07           [D0 (1/psi)]
 6.4747361E-08           [D1 (1/psi)]
   0.3313                 [m]

*****************************************************************
        #Thermal Cracking File Data
         Analysis Level =  1
         Creep Test Duration =  100 seconds
         Test Data Path =
C:\DG2002\Projects\MnRoad03-LTC\



*****************************************************************

              MIXTURE Name:      Asphalt

*****************************************************************
```

Generalized Maxwell Model Parameters

```
          5
  1173274.
  5.895430
  802369.6
  48.45251
  388361.8
  479.3508
  986261.3
  1648.052
  500391.8
  38797.10
```

MnRoad Cell 19

Level – 1

Creep-Compliance Model Parameters

```
          4           3   [No. of Maxwell Elements, No. of Test Temps]
 -36.00000       1.000000       [Temp (C), 1/(Shift Factor)]
 -24.00000       501.1872       [Temp (C), 1/(Shift Factor)]
 -12.00000       1258.925       [Temp (C), 1/(Shift Factor)]
 1.6044640E-07           [D0 (1/psi)]
 2.4892869E-07           [D1 (1/psi)]
 5.1000000               [Tau1 (sec)]
 7.1838894E-08           [D2 (1/psi)]
  3.825000               [Tau2 (sec)]
 5.1386913E-08           [D3 (1/psi)]
  2.960000               [Tau3 (sec)]
 4.0108114E-08           [D4 (1/psi)]
  1.683000               [Tau4 (sec)]
  12.73620               [Log{EtaV} (psi-sec)]

POWER MODEL PARAMETERS
 1.4478600E-07           [D0 (1/psi)]
 1.5918400E-08           [D1 (1/psi)]
   0.2650                 [m]

*****************************************************************
        #Thermal Cracking File Data
         Analysis Level =  1
         Creep Test Duration =  1000 seconds
         Test Data Path =
C:\DG2002\Projects\MnRoad19-LTC\



*****************************************************************

              MIXTURE Name:      Asphalt

*****************************************************************
```

Generalized Maxwell Model Parameters

```
          5
  1281213.
  38.42208
  1070844.
  720.3898
  863313.9
  5198.856
  1333769.
  70712.32
  1683470.
  3176720.
```

MnRoad Cell 19

Level – 3

Creep-Compliance Model Parameters

```
          4           3   [No. of Maxwell Elements, No. of Test Temps]
 -20.00000       1.000000       [Temp (C), 1/(Shift Factor)]
 -10.00000       63.09575       [Temp (C), 1/(Shift Factor)]
 0.0000000E+00   501.1873       [Temp (C), 1/(Shift Factor)]
 2.9180146E-07           [D0 (1/psi)]
 1.0675233E-07           [D1 (1/psi)]
 0.9399999               [Tau1 (sec)]
 1.3238784E-07           [D2 (1/psi)]
  1.880000               [Tau2 (sec)]
 1.1725867E-07           [D3 (1/psi)]
  2.820000               [Tau3 (sec)]
 9.6871304E-07           [D4 (1/psi)]
  3.760000               [Tau4 (sec)]
  10.50589               [Log{EtaV} (psi-sec)]

POWER MODEL PARAMETERS
 2.4321758E-07           [D0 (1/psi)]
 6.5418426E-08           [D1 (1/psi)]
   0.3169                 [m]

*****************************************************************
        #Thermal Cracking File Data
         Analysis Level =  1
         Creep Test Duration =  100 seconds
         Test Data Path =
C:\DG2002\Projects\MnRoad19-LTC\



*****************************************************************

              MIXTURE Name:      Asphalt

*****************************************************************
```

Generalized Maxwell Model Parameters

```
          5
  986206.6
  6.289618
  616221.6
  56.83013
  442245.0
  522.2338
  843913.4
  2268.888
  538399.4
  55474.88
```

MnRoad Cell 33

Level – 1

Creep-Compliance Model Parameters

```
          4           3   [No. of Maxwell Elements, No. of Test Temps]
 -30.00000       1.000000       [Temp (C), 1/(Shift Factor)]
 -18.00000       5.011872       [Temp (C), 1/(Shift Factor)]
 -6.000000       316.2277       [Temp (C), 1/(Shift Factor)]
 2.0406834E-07           [D0 (1/psi)]
 1.1029457E-06           [D1 (1/psi)]
 4.5000000               [Tau1 (sec)]
 1.2453272E-07           [D2 (1/psi)]
  3.375000               [Tau2 (sec)]
 1.1784107E-08           [D3 (1/psi)]
  2.610000               [Tau3 (sec)]
 9.8678596E-08           [D4 (1/psi)]
  1.485000               [Tau4 (sec)]
  11.06899               [Log{EtaV} (psi-sec)]

POWER MODEL PARAMETERS
 2.4492700E-07           [D0 (1/psi)]
 6.7368000E-08           [D1 (1/psi)]
   0.5050                 [m]

*****************************************************************
        #Thermal Cracking File Data
         Analysis Level =  1
         Creep Test Duration =  1000 seconds
         Test Data Path =
C:\DG2002\Projects\MnRoad33-LTC\



*****************************************************************

              MIXTURE Name:      Asphalt

*****************************************************************
```

Generalized Maxwell Model Parameters

```
          5
  1624867.
  20.50556
  154138.3
  390.3123
  1206062.
  1580.863
  1411540.
  8624.940
  503714.3
  204564.8
```

MnRoad Cell 33

Level – 3

Creep-Compliance Model Parameters

```
          4           3   [No. of Maxwell Elements, No. of Test Temps]
 -20.00000       1.000000       [Temp (C), 1/(Shift Factor)]
 -10.00000       44.66836       [Temp (C), 1/(Shift Factor)]
 0.0000000E+00   354.8134       [Temp (C), 1/(Shift Factor)]
 2.5541232E-07           [D0 (1/psi)]
 1.0376309E-07           [D1 (1/psi)]
 0.9100000               [Tau1 (sec)]
 2.0427845E-07           [D2 (1/psi)]
  1.820000               [Tau2 (sec)]
 3.6664552E-08           [D3 (1/psi)]
  2.730000               [Tau3 (sec)]
 1.3819121E-06           [D4 (1/psi)]
  3.640000               [Tau4 (sec)]
  10.12560               [Log{EtaV} (psi-sec)]

POWER MODEL PARAMETERS
 2.0119543E-07           [D0 (1/psi)]
 7.1360539E-08           [D1 (1/psi)]
   0.3453                 [m]

*****************************************************************
        #Thermal Cracking File Data
         Analysis Level =  1
         Creep Test Duration =  100 seconds
         Test Data Path =
C:\DG2002\Projects\MnRoad33-LTC\



*****************************************************************

              MIXTURE Name:      Asphalt

*****************************************************************
```

Generalized Maxwell Model Parameters

```
          5
  1275597.
  5.629682
  940370.7
  42.31982
  212369.9
  490.3797
  1087274.
  1238.838
  399627.5
  29666.55
```

MnRoad Cell 34

Level – 1

Creep-Compliance Model Parameters

```
          4           3   [No. of Maxwell Elements, No. of Test Temps]
 -36.00000       1.000000       [Temp (C), 1/(Shift Factor)]
 -24.00000       199.5200       [Temp (C), 1/(Shift Factor)]
 -12.00000       10000.00       [Temp (C), 1/(Shift Factor)]
 1.6752464E-07           [D0 (1/psi)]
 5.7900048E-07           [D1 (1/psi)]
 6.0000000               [Tau1 (sec)]
 1.2922754E-07           [D2 (1/psi)]
  4.500000               [Tau2 (sec)]
 6.3191336E-08           [D3 (1/psi)]
  3.480000               [Tau3 (sec)]
 6.1582119E-08           [D4 (1/psi)]
  1.980000               [Tau4 (sec)]
  13.02235               [Log{EtaV} (psi-sec)]

POWER MODEL PARAMETERS
 1.9214500E-07           [D0 (1/psi)]
 3.2074900E-09           [D1 (1/psi)]
   0.3900                 [m]

*****************************************************************
        #Thermal Cracking File Data
         Analysis Level =  1
         Creep Test Duration =  1000 seconds
         Test Data Path =
C:\DG2002\Projects\MnRoad34-LTC\



*****************************************************************

              MIXTURE Name:      Asphalt

*****************************************************************
```

Generalized Maxwell Model Parameters

```
          5
  1630206.
  69.62388
  1000302.
  2345.564
  1046359.
  21821.91
  1400458.
  405216.7
  891946.2
 1.1138931E+07
```

MnRoad Cell 34

Level – 3

Creep-Compliance Model Parameters

```
          3           3   [No. of Maxwell Elements, No. of Test Temps]
 -20.00000       1.000000       [Temp (C), 1/(Shift Factor)]
 -10.00000       14.12537       [Temp (C), 1/(Shift Factor)]
 0.0000000E+00   89.12511       [Temp (C), 1/(Shift Factor)]
 3.6802354E-07           [D0 (1/psi)]
 2.8987586E-07           [D1 (1/psi)]
 0.9875000               [Tau1 (sec)]
 4.9844033E-08           [D2 (1/psi)]
  1.975000               [Tau2 (sec)]
 1.6282386E-06           [D3 (1/psi)]
  2.962500               [Tau3 (sec)]
  9.259657               [Log{EtaV} (psi-sec)]

POWER MODEL PARAMETERS
 2.7247276E-07           [D0 (1/psi)]
 1.2331586E-07           [D1 (1/psi)]
   0.3748                 [m]

*********************************************************************
        #Thermal Cracking File Data
         Analysis Level =  1
         Creep Test Duration =  100 seconds
         Test Data Path =
C:\DG2002\Projects\MnRoad34-LTC\



*********************************************************************

              MIXTURE Name:      Asphalt

*********************************************************************
```

Generalized Maxwell Model Parameters

```
          4
  1254514.
  5.332341
  185617.4
  85.53444
  961545.1
  250.5259
  315540.4
  4927.438
```

MnRoad Cell 35

Level – 1

Creep-Compliance Model Parameters

```
          4           3   [No. of Maxwell Elements, No. of Test Temps]
 -42.00000       1.000000       [Temp (C), 1/(Shift Factor)]
 -30.00000       199.5200       [Temp (C), 1/(Shift Factor)]
 -18.00000       1000.000       [Temp (C), 1/(Shift Factor)]
 1.5301106E-07           [D0 (1/psi)]
 2.9820978E-07           [D1 (1/psi)]
 5.0000000               [Tau1 (sec)]
 1.5560941E-07           [D2 (1/psi)]
  3.750000               [Tau2 (sec)]
 5.7182416E-08           [D3 (1/psi)]
  2.900000               [Tau3 (sec)]
 7.3396190E-08           [D4 (1/psi)]
  1.650000               [Tau4 (sec)]
  12.51837               [Log{EtaV} (psi-sec)]

POWER MODEL PARAMETERS
 1.0460800E-07           [D0 (1/psi)]
 4.1574500E-08           [D1 (1/psi)]
   0.2250                 [m]

*****************************************************************
        #Thermal Cracking File Data
         Analysis Level =  1
         Creep Test Duration =  1000 seconds
         Test Data Path =
C:\DG2002\Projects\MnRoad35-LTC\



*****************************************************************

              MIXTURE Name:      Asphalt

*****************************************************************
```

Generalized Maxwell Model Parameters

```
          5
  2178714.
  29.98187
  984396.2
  624.6755
  1169488.
  3650.803
  893627.1
  59506.54
  1309251.
  2475292.
```

MnRoad Cell 35

Level – 3

Creep-Compliance Model Parameters

```
          2           3   [No. of Maxwell Elements, No. of Test Temps]
 -20.00000       1.000000       [Temp (C), 1/(Shift Factor)]
 -10.00000       7.943283       [Temp (C), 1/(Shift Factor)]
 0.0000000E+00   50.11873       [Temp (C), 1/(Shift Factor)]
 6.8917166E-07           [D0 (1/psi)]
 1.9157369E-07           [D1 (1/psi)]
  1.233333               [Tau1 (sec)]
 2.0957777E-06           [D2 (1/psi)]
  2.466667               [Tau2 (sec)]
  8.629397               [Log{EtaV} (psi-sec)]

POWER MODEL PARAMETERS
 4.0752161E-07           [D0 (1/psi)]
 1.9174908E-07           [D1 (1/psi)]
   0.4211                 [m]

*****************************************************************
        #Thermal Cracking File Data
         Analysis Level =  1
         Creep Test Duration =  100 seconds
         Test Data Path =
C:\DG2002\Projects\MnRoad35-LTC\



*****************************************************************

              MIXTURE Name:      Asphalt

*****************************************************************
```

Generalized Maxwell Model Parameters

```
          3
  425215.4
  12.77208
  783921.1
  77.43507
  241880.7
  1487.734
```

MN State Highway 75-2

Level – 1

Creep-Compliance Model Parameters

```
          4           3   [No. of Maxwell Elements, No. of Test Temps]
 -20.00000       1.000000       [Temp (C), 1/(Shift Factor)]
 -10.00000       10.00000       [Temp (C), 1/(Shift Factor)]
 0.0000000E+00   100.0000       [Temp (C), 1/(Shift Factor)]
 1.6370721E-07           [D0 (1/psi)]
 3.8306105E-08           [D1 (1/psi)]
 1.3200000               [Tau1 (sec)]
 7.0253410E-08           [D2 (1/psi)]
  2.320000               [Tau2 (sec)]
 5.5161747E-08           [D3 (1/psi)]
  3.000000               [Tau3 (sec)]
 3.7606945E-07           [D4 (1/psi)]
  4.000000               [Tau4 (sec)]
  11.40200               [Log{EtaV} (psi-sec)]

POWER MODEL PARAMETERS
 1.3479201E-07           [D0 (1/psi)]
 2.2966390E-08           [D1 (1/psi)]
   0.3250                 [m]

*****************************************************************
        #Thermal Cracking File Data
         Analysis Level =  1
         Creep Test Duration =  1000 seconds
         Test Data Path =
C:\DG2002\Projects\MN 75-2\



*****************************************************************

              MIXTURE Name:      Asphalt

*****************************************************************
```

Generalized Maxwell Model Parameters

```
          5
  1251502.
  16.77270
  1351454.
  152.8914
  641607.3
  824.9756
  1528753.
  4655.188
  1335151.
  183106.5
```

MN State Highway 75-2

Level – 3

Creep-Compliance Model Parameters

```
          4           3   [No. of Maxwell Elements, No. of Test Temps]
 -20.00000       1.000000       [Temp (C), 1/(Shift Factor)]
 -10.00000       70.79458       [Temp (C), 1/(Shift Factor)]
 0.0000000E+00   630.9573       [Temp (C), 1/(Shift Factor)]
 2.4417150E-07           [D0 (1/psi)]
 1.0266121E-07           [D1 (1/psi)]
 0.9600000               [Tau1 (sec)]
 1.7576103E-07           [D2 (1/psi)]
  1.920000               [Tau2 (sec)]
 7.8141440E-08           [D3 (1/psi)]
  2.880000               [Tau3 (sec)]
 1.1823320E-06           [D4 (1/psi)]
  3.840000               [Tau4 (sec)]
  10.47039               [Log{EtaV} (psi-sec)]

POWER MODEL PARAMETERS
 1.9903881E-07           [D0 (1/psi)]
 6.2716417E-08           [D1 (1/psi)]
   0.3295                 [m]

*****************************************************************
        #Thermal Cracking File Data
         Analysis Level =  1
         Creep Test Duration =  100 seconds
         Test Data Path =
C:\DG2002\Projects\MN 75-2\



*****************************************************************

              MIXTURE Name:      Asphalt

*****************************************************************
```

Generalized Maxwell Model Parameters

```
          5
  1331404.
  6.287349
  919969.5
  55.34569
  365535.0
  636.9067
  1009388.
  2253.688
  469184.3
  57486.32
```

MN State Highway 75-4

Level – 1

Creep-Compliance Model Parameters

```
          4           3   [No. of Maxwell Elements, No. of Test Temps]
 -20.00000       1.000000       [Temp (C), 1/(Shift Factor)]
 -10.00000       3.162300       [Temp (C), 1/(Shift Factor)]
 0.0000000E+00   316.2280       [Temp (C), 1/(Shift Factor)]
 1.5604174E-07           [D0 (1/psi)]
 7.0674791E-08           [D1 (1/psi)]
 1.4850000               [Tau1 (sec)]
 1.6840443E-08           [D2 (1/psi)]
  2.610000               [Tau2 (sec)]
 1.2442274E-07           [D3 (1/psi)]
  3.375000               [Tau3 (sec)]
 3.7861602E-07           [D4 (1/psi)]
  4.500000               [Tau4 (sec)]
  11.60065               [Log{EtaV} (psi-sec)]

POWER MODEL PARAMETERS
 1.6654729E-07           [D0 (1/psi)]
 7.9340388E-09           [D1 (1/psi)]
   0.4050                 [m]

*****************************************************************
        #Thermal Cracking File Data
         Analysis Level =  1
         Creep Test Duration =  1000 seconds
         Test Data Path =
C:\DG2002\Projects\MN 75-4\



*****************************************************************

              MIXTURE Name:      Asphalt

*****************************************************************
```

Generalized Maxwell Model Parameters

```
          5
  2038979.
  20.92745
  368301.4
  376.3135
  1471940.
  1533.999
  1335711.
  15262.10
  1193610.
  314908.9
```

MN State Highway 75-4

Level – 3

Creep-Compliance Model Parameters

```
           3           3    [No. of Maxwell Elements, No. of Test
Temps]
       -20.0       1.000   [Temp (C), 1/(Shift Factor)]
       -10.0      19.953   [Temp (C), 1/(Shift Factor)]
         0.0     141.254   [Temp (C), 1/(Shift Factor)]
  3.3894884E-07             [D0 (1/psi)]
  3.2539606E-07             [D1 (1/psi)]
   1.037500                 [Tau1 (sec)]
  4.3603048E-08             [D2 (1/psi)]
   2.075000                 [Tau2 (sec)]
  1.8122009E-06             [D3 (1/psi)]
   3.112500                 [Tau3 (sec)]
   9.396045                 [Log{EtaV} (psi-sec)]

 POWER MODEL PARAMETERS
  4.2738463E-07             [D0 (1/psi)]
  2.9063020E-08             [D1 (1/psi)]
    0.5832                  [m]

 ****************************************************************
         #Thermal Cracking File Data
          Analysis Level =  1
          Creep Test Duration =  100 seconds
          Test Data Path =
 C:\DG2002\Projects\MN 75-4\



 ****************************************************************

               MIXTURE Name:      Asphalt

 ****************************************************************
```

Generalized Maxwell Model Parameters

```
           4
   1497791.
   5.464139
   159725.7
   109.1371
   998320.6
   327.3104
   294459.8
   7256.464
```

WI State Highway 45

Level – 1

Creep-Compliance Model Parameters

```
          4           3   [No. of Maxwell Elements, No. of Test Temps]
 -36.00000       1.000000       [Temp (C), 1/(Shift Factor)]
 -24.00000       199.5260       [Temp (C), 1/(Shift Factor)]
 -12.000000      1000.000       [Temp (C), 1/(Shift Factor)]
 1.6438647E-07           [D0 (1/psi)]
 1.4414000E-07           [D1 (1/psi)]
 5.0000000               [Tau1 (sec)]
 1.3170000E-07           [D2 (1/psi)]
  3.750000               [Tau2 (sec)]
 4.6204000E-08           [D3 (1/psi)]
  2.900000               [Tau3 (sec)]
 5.4167000E-08           [D4 (1/psi)]
  1.650000               [Tau4 (sec)]
  12.29100               [Log{EtaV} (psi-sec)]

POWER MODEL PARAMETERS
 1.7108000E-07           [D0 (1/psi)]
 1.1194800E-08           [D1 (1/psi)]
   0.3100                 [m]

*****************************************************************
        #Thermal Cracking File Data
         Analysis Level =  1
         Creep Test Duration =  1000 seconds
         Test Data Path =
C:\DG2002\Projects\WI45-LTC\



*****************************************************************

              MIXTURE Name:      Asphalt

*****************************************************************
```

Generalized Maxwell Model Parameters

```
          5
  1547972.
  33.44953
  884065.5
  647.7313
  1179140.
  3780.198
  726080.4
  72035.46
  1745969.
  1086478.
```

WI State Highway 45

Level – 3

Creep-Compliance Model Parameters

```
          3           3   [No. of Maxwell Elements, No. of Test Temps]
 -20.00000       1.000000       [Temp (C), 1/(Shift Factor)]
 -10.00000       14.12537       [Temp (C), 1/(Shift Factor)]
 0.0000000E+00   89.12511       [Temp (C), 1/(Shift Factor)]
 3.6802354E-07           [D0 (1/psi)]
 2.8987586E-07           [D1 (1/psi)]
 0.9875000               [Tau1 (sec)]
 4.9844033E-08           [D2 (1/psi)]
  1.975000               [Tau2 (sec)]
 1.6282386E-06           [D3 (1/psi)]
  2.962500               [Tau3 (sec)]
  9.259657               [Log{EtaV} (psi-sec)]

POWER MODEL PARAMETERS
 2.7247276E-07           [D0 (1/psi)]
 1.2331586E-07           [D1 (1/psi)]
   0.3748                 [m]

*********************************************************************
        #Thermal Cracking File Data
         Analysis Level =  1
         Creep Test Duration =  100 seconds
         Test Data Path =
C:\DG2002\Projects\WI45-LTC\



*********************************************************************

              MIXTURE Name:      Asphalt

*********************************************************************
```

Generalized Maxwell Model Parameters

```
          4
  1254514.
  5.332341
  185617.4
  85.53444
  961545.1
  250.5259
  315540.4
  4927.438
```

WI State Highway 73

Level – 1

Creep-Compliance Model Parameters

```
          4           3   [No. of Maxwell Elements, No. of Test Temps]
 -30.00000       1.000000       [Temp (C), 1/(Shift Factor)]
 -18.00000       10.00000       [Temp (C), 1/(Shift Factor)]
 -6.000000       501.1870       [Temp (C), 1/(Shift Factor)]
 1.7661721E-07           [D0 (1/psi)]
 6.7235500E-07           [D1 (1/psi)]
 4.7000000               [Tau1 (sec)]
 2.1543122E-07           [D2 (1/psi)]
  3.525000               [Tau2 (sec)]
 7.7699063E-08           [D3 (1/psi)]
  2.726000               [Tau3 (sec)]
 6.6995714E-08           [D4 (1/psi)]
  1.551000               [Tau4 (sec)]
  11.39703               [Log{EtaV} (psi-sec)]

POWER MODEL PARAMETERS
 2.0652594E-07           [D0 (1/psi)]
 5.7419118E-09           [D1 (1/psi)]
   0.4750                [m]

*****************************************************************
        #Thermal Cracking File Data
         Analysis Level =  1
         Creep Test Duration =  1000 seconds
         Test Data Path =
C:\DG2002\Projects\WI73-LTC\



*****************************************************************

              MIXTURE Name:      Asphalt

*****************************************************************
```

Generalized Maxwell Model Parameters

```
          5
  1635987.
  25.53529
  1167586.
  390.8605
  1172355.
  1989.549
  1007645.
  21230.15
  678389.6
  332041.7
```

WI State Highway 73

Level – 3

Creep-Compliance Model Parameters

```
          4           3   [No. of Maxwell Elements, No. of Test Temps]
 -20.00000       1.000000       [Temp (C), 1/(Shift Factor)]
 -10.00000       31.62278       [Temp (C), 1/(Shift Factor)]
 0.0000000E+00   223.8721       [Temp (C), 1/(Shift Factor)]
 2.6777286E-07           [D0 (1/psi)]
 1.0090142E-07           [D1 (1/psi)]
 0.8700000               [Tau1 (sec)]
 1.7749379E-07           [D2 (1/psi)]
  1.740000               [Tau2 (sec)]
 4.5885631E-08           [D3 (1/psi)]
  2.610000               [Tau3 (sec)]
 1.2566449E-06           [D4 (1/psi)]
  3.480000               [Tau4 (sec)]
  9.981516               [Log{EtaV} (psi-sec)]

POWER MODEL PARAMETERS
 2.0846578E-07           [D0 (1/psi)]
 7.4485762E-08           [D1 (1/psi)]
   0.3465                 [m]

*****************************************************************
        #Thermal Cracking File Data
         Analysis Level =  1
         Creep Test Duration =  100 seconds
         Test Data Path =
C:\DG2002\Projects\WI73-LTC\



*****************************************************************

              MIXTURE Name:      Asphalt

*****************************************************************
```

Generalized Maxwell Model Parameters

```
          5
  1152203.
  5.254822
  836043.1
  37.12948
  274853.1
  362.5125
  1044418.
  914.3461
  426991.2
  19887.12
```